polymers

Special Issue Reprint

Advances in Sustainable Polymeric Materials, 3rd Edition

Edited by
Cristina Cazan and Mihai Alin Pop

mdpi.com/journal/polymers

MDPI

Advances in Sustainable Polymeric Materials, 3rd Edition

Advances in Sustainable Polymeric Materials, 3rd Edition

Guest Editors

Cristina Cazan
Mihai Alin Pop

MDPI

Basel • Beijing • Wuhan • Barcelona • Belgrade • Novi Sad • Cluj • Manchester

Guest Editors

Cristina Cazan
Department of Product Design, Mechatronics and Environment
Transilvania University of Brasov
Brasov
Romania

Mihai Alin Pop
Department of Materials Science
Transilvania University of Brasov
Brasov
Romania

Editorial Office
MDPI AG
Grosspeteranlage 5
4052 Basel, Switzerland

This is a reprint of the Special Issue, published open access by the journal *Polymers* (ISSN 2073-4360), freely accessible at: https://www.mdpi.com/journal/polymers/special_issues/1WGC728322.

For citation purposes, cite each article independently as indicated on the article page online and as indicated below:

Lastname, A.A.; Lastname, B.B. Article Title. *Journal Name* **Year**, *Volume Number*, Page Range.

ISBN 978-3-7258-7559-7 (Hbk)
ISBN 978-3-7258-7560-3 (PDF)
https://doi.org/10.3390/books978-3-7258-7560-3

© 2026 by the authors. Articles in this reprint are Open Access and distributed under the Creative Commons Attribution (CC BY) license. The reprint as a whole is distributed by MDPI under the terms and conditions of the Creative Commons Attribution-NonCommercial-NoDerivs (CC BY-NC-ND) license (https://creativecommons.org/licenses/by-nc-nd/4.0/).

Contents

Cristina Cazan and Mihai Alin Pop
Advances in Sustainable Polymeric Materials, 3rd Edition
Reprinted from: *Polymers* **2026**, *18*, 729, https://doi.org/10.3390/polym18060729 . . . . . **1**

Johan Stanley, Eleftheria Xanthopoulou, Margaritis Kostoglou, Lidija Fras Zemljič, Dimitra A. Lambropoulou and Dimitrios N. Bikiaris
Study on Impact of Monomers Towards High Molecular Weight Bio-Based Poly(ethylene Furanoate) via Solid State Polymerization Technique
Reprinted from: *Polymers* **2024**, *16*, 3305, https://doi.org/10.3390/polym16233305 . . . . . **6**

Isaac Karimi, Mahnaz Ghowsi, Layth Jasim Mohammed, Zohreh Haidari, Kosar Nazari and Helgi B. Schiöth
Inulin as a Biopolymer; Chemical Structure, Anticancer Effects, Nutraceutical Potential and Industrial Applications: A Comprehensive Review
Reprinted from: *Polymers* **2025**, *17*, 412, https://doi.org/10.3390/polym17030412 . . . . . **24**

Ane García-García, Unai Silván, Leyre Pérez-Álvarez and Senentxu Lanceros
Comparing the Printability, Biological and Physicochemical Properties of Bio-Based Photo-Crosslinkable Hydrogels
Reprinted from: *Polymers* **2025**, *17*, 2867, https://doi.org/10.3390/polym17212867 . . . . . **42**

Cem Gök, Arzum Işıtan, Massimo Bersani, Paolo Bettotti, Laura Pasquardini, Michele Fedrizzi, et al.
Physicochemical and Antimicrobial Evaluation of Bacterial Cellulose Derived from Spent Tea Waste
Reprinted from: *Polymers* **2025**, *17*, 2521, https://doi.org/10.3390/ polym17182521 . . . . . **59**

Siyang Wu, Lixing Ren, Xiaochun Qiu, Qiance Qi, Bo Li, Peijie Xu, et al.
Interface Enhancement and Tribological Properties of Cattle Manure-Derived Corn Stalk Fibers for Friction Materials: The Role of Silane Treatment Concentration
Reprinted from: *Polymers* **2025**, *17*, 22, https://doi.org/10.3390/polym17010022 . . . . . **80**

Zaineb Mchich, Daniela Simina Stefan, Rachid Mamouni, Nabil Saffaj and Magdalena Bosomoiu
Eco-Friendly Hydrogel Beads from Seashell Waste for Efficient Removal of Heavy Metals from Water
Reprinted from: *Polymers* **2024**, *16*, 3257, https://doi.org/10.3390/polym16233257 . . . . . **105**

Adina-Elena Segneanu, Ionela Amalia Bradu, Mihaela Simona Calinescu (Bocanici), Gabriela Vlase, Titus Vlase, Daniel-Dumitru Herea, et al.
Novel Nanocomposites and Biopolymer-Based Nanocomposites for Hexavalent Chromium Removal from Aqueous Media
Reprinted from: *Polymers* **2024**, *16*, 3469, https://doi.org/10.3390/polym16243469 . . . . . **118**

Hugo Duarte, João Brás, El Mokhtar Saoudi Hassani, María José Aliaño-Gonzalez, Solange Magalhães, Luís Alves, et al.
Lignin-Furanic Rigid Foams: Enhanced Methylene Blue Removal Capacity, Recyclability, and Flame Retardancy
Reprinted from: *Polymers* **2024**, *16*, 3315, https://doi.org/10.3390/polym16233315 . . . . . **154**

Tutik Sriani, Muslim Mahardika, Shofa Aulia Aldhama, Chandrawati Putri Wulandari and Gunawan Setia Prihandana
Upcycling of Expanded Polystyrene Waste-Impregnated PVP Using Wet-Phase Inversion for Effective Microalgae Harvesting
Reprinted from: *Polymers* **2024**, *16*, 2703, https://doi.org/10.3390/polym16192703 . . . . . **174**

Yeong-Min Kim, Kyungnam Kim and Tri Ho Minh Le
Advancing Sustainability and Performance with Crushed Bottom Ash as Filler in Polymer-Modified Asphalt Concrete Mixtures
Reprinted from: *Polymers* **2024**, *16*, 1683, https://doi.org/10.3390/polym16121683 . . . . . **185**

Byungsik Ohm, Sang Yum Lee and Tri Ho Minh Le
Utilizing Crushed Recycled Marble Stone Powder as a Sustainable Filler in SBS-Modified Asphalt Containing Recycled Tire Rubber
Reprinted from: *Polymers* **2025**, *17*, 70, https://doi.org/10.3390/polym17010070 . . . . . **204**

polymers

MDPI

Editorial

Advances in Sustainable Polymeric Materials, 3rd Edition

Cristina Cazan [1,*] and Mihai Alin Pop [2,*]

[1] Department of Product Design, Mechatronics and Environment, Transilvania University of Brasov, 500036 Brasov, Romania
[2] Department of Materials Science, Transilvania University of Brasov, 500036 Brasov, Romania
* Correspondence: c.vladuta@unitbv.ro (C.C.); mihai.pop@unitbv.ro (M.A.P.)

The increasing global demand for polymeric materials, combined with growing environmental concerns about fossil-based plastics, has significantly accelerated research into sustainable polymer systems. Conventional petroleum-derived polymers have contributed substantially to modern technological development, supporting applications in packaging, construction, transportation, electronics, and biomedical engineering. However, their extensive production and accumulation have resulted in serious environmental challenges, including greenhouse gas emissions, depletion of non-renewable resources, and persistent plastic pollution. These concerns have driven the development of sustainable polymeric materials designed to reduce environmental impacts while maintaining high performance and durability [1–3].

One key strategy in sustainable polymer science is the development of bio-based polymers derived from renewable resources, such as lignin, cellulose, starch, and other biomass feedstocks. These materials offer significant environmental advantages, including reduced carbon footprint, biodegradability, and lower dependence on fossil resources. In addition, advances in recycling technologies—including mechanical, chemical, and emerging biological recycling approaches—have enabled more efficient recovery and reuse of polymeric materials, supporting circular material flows and reducing waste accumulation [1,4,5]. Sustainable polymer composites incorporating industrial and agricultural waste have also emerged as promising alternatives to conventional materials, offering improved resource efficiency and reduced environmental impact while maintaining desirable mechanical and functional properties [6,7].

The circular economy concept has become a fundamental framework guiding the development of sustainable polymer systems. By promoting material reuse, recycling, and waste valorization, circular economy strategies can minimize environmental impact while maximizing resource efficiency. Waste-derived materials, including recycled plastics, industrial by-products, and biomass residues, can be successfully integrated into polymer matrices to produce high-performance composite materials suitable for engineering applications [5,7–10]. These approaches transform waste streams into valuable material resources, contributing to sustainable material management and reducing environmental pollution.

Sustainable polymeric materials have demonstrated significant potential across a wide range of advanced applications. Bio-based and recycled polymer systems are increasingly being utilized in construction, environmental remediation, biomedical engineering, and infrastructure development. Polymer composites reinforced with natural fibers or waste-derived fillers exhibit improved structural performance, durability, and environmental compatibility [11,12]. These developments highlight the important role of sustainable

polymer science in addressing global environmental challenges and enabling the transition toward more resource-efficient material systems.

The rapid evolution of sustainable polymer science reflects its inherently multidisciplinary nature, integrating materials science, chemistry, environmental engineering, and industrial innovation. Advances in polymer synthesis, recycling technologies, and composite engineering have expanded the range of sustainable materials available for industrial and technological applications. As a result, sustainable polymer systems are widely recognized as essential components in achieving long-term environmental sustainability and supporting circular economic models [13].

One of the main research directions addressed in this Special Issue, "Advances in Sustainable Polymeric Materials, 3rd Edition", is the development of bio-based polymers as viable alternatives to petroleum-derived materials. Stanley et al. [14] investigated the synthesis of high-molecular-weight poly(ethylene furanoate) (PEF), a fully bio-based polyester with strong potential to replace poly(ethylene terephthalate) in packaging applications. By optimizing solid-state polymerization parameters, the authors achieved significant improvements in molecular weight, crystallinity, and thermal stability, confirming the feasibility of producing high-performance renewable polymers suitable for industrial use. Complementing this work, Karimi et al. [15] presented a comprehensive review of inulin, a naturally occurring polysaccharide with a wide range of applications in pharmaceutical, biomedical, and industrial systems. The unique chemical structure, biodegradability, and functional versatility of inulin make it a promising sustainable biopolymer for advanced material applications.

Recent advances in bio-based functional polymer systems also include important developments in biomedical engineering and advanced manufacturing technologies. García-García et al. [16] investigated photo-crosslinkable hydrogels derived from natural polymers, including gelatin, alginate, and chitosan, demonstrating their excellent printability, mechanical stability, and biocompatibility for extrusion-based 3D printing applications. These hydrogels show strong potential for use in tissue engineering, regenerative medicine, and personalized biomedical devices. Similarly, Gök et al. [17] reported the sustainable production of bacterial cellulose using spent tea waste as a renewable carbon source. The resulting materials exhibited excellent mechanical properties, antimicrobial activity, and structural uniformity, confirming the feasibility of converting food waste into high-value, functional biomaterials suitable for biomedical, electronic, and environmental applications.

The valorization of agricultural and organic waste represents another important focus of this Special Issue. Agricultural residues and biomass waste offer abundant renewable resources for developing sustainable polymer composites. Wu et al. [18] demonstrated the successful utilization of corn stalk fibers recovered from cattle manure as reinforcement materials in friction composites. The biological pre-treatment and optimized silane modification improved fiber–matrix compatibility, reduced water absorption, and enhanced tribological performance. These results highlight the potential of agricultural waste fibers as sustainable reinforcement materials that can improve composite performance while simultaneously reducing environmental impacts.

In addition to structural applications, sustainable polymer materials have demonstrated significant potential in environmental remediation technologies. Mchich et al. [19] developed eco-friendly hydrogel beads derived from seashell waste and alginate for the removal of heavy metals from aqueous solutions. These materials exhibited excellent adsorption capacity, favourable kinetics, and good reusability, demonstrating their suitability for water purification applications. Similarly, Segneanu et al. [20] developed innovative nanocomposites based on waste-derived components, including eggshells, fly ash, mag-

https://doi.org/10.3390/polym18060729

netite nanoparticles, and biopolymers such as carrageenan and chitosan. The engineered materials achieved very high chromium removal efficiency, highlighting the synergistic effects of combining inorganic waste-derived materials with polymer matrices to develop advanced environmental remediation systems.

Further contributions focused on the removal of organic pollutants and the development of sustainable functional polymer systems. Duarte et al. [21] developed lignin-based rigid foams with excellent adsorption capacity for methylene blue, as well as flame-retardant and recyclable properties. The use of lignin, a widely available renewable aromatic biopolymer, represents an important step toward replacing fossil-based phenolic materials. In addition, Sriani et al. [22] demonstrated the successful upcycling of expanded polystyrene waste into functional membrane systems for microalgae harvesting. The developed membranes showed excellent permeability, structural stability, and biomass recovery efficiency, demonstrating the potential to convert plastic waste into valuable functional materials for environmental and industrial applications.

Sustainable polymer composites have also demonstrated their effectiveness in important applications in infrastructure and construction materials. Kim et al. [23] investigated the use of crushed bottom ash as a filler in polymer-modified asphalt mixtures. Their results demonstrated improved mechanical performance, moisture resistance, and durability, confirming the feasibility of incorporating industrial waste into high-performance infrastructure materials. Similarly, Ohm et al. [24] evaluated the use of crushed recycled marble stone powder as a sustainable filler in asphalt mixtures containing recycled tyre rubber. The incorporation of waste-derived fillers improved structural stability, deformation resistance, and mechanical performance, highlighting the effectiveness of circular economy approaches in infrastructure development.

Collectively, the studies in this Special Issue demonstrate significant progress in sustainable polymer science. Bio-based polymers derived from renewable resources have demonstrated strong potential to replace conventional petroleum-based materials while maintaining comparable or improved performance. The use of waste-derived materials in polymer composites represents an effective strategy for reducing environmental impact, improving resource efficiency, and supporting circular economic principles.

Furthermore, sustainable polymer systems have shown great potential for environmental remediation, biomedical engineering, advanced manufacturing, and infrastructure applications. These developments highlight the versatility and adaptability of polymer materials in addressing current environmental and technological challenges.

Despite these advances, several challenges remain in scaling laboratory-scale developments for industrial production. Future research should focus on improving material performance, optimizing processing methods, and evaluating long-term durability and lifecycle sustainability. Interdisciplinary collaboration among materials scientists, chemists, engineers, and environmental researchers will be essential to accelerating the development and implementation of sustainable polymer technologies.

In conclusion, the contributions presented in this Special Issue demonstrate the transformative potential of sustainable polymeric materials derived from renewable resources and waste streams. These advances support the transition toward more sustainable material systems, reduce environmental impact, and contribute to the development of circular economic solutions. Sustainable polymer science will continue to play a critical role in addressing global environmental challenges and enabling future technological innovation.

https://doi.org/10.3390/polym18060729

Author Contributions: Conceptualization, C.C. and M.A.P.; methodology, C.C. and M.A.P.; writing—original draft preparation, C.C.; writing—review and editing, C.C. and M.A.P.; visualization, M.A.P. All authors have read and agreed to the published version of the manuscript.

Funding: This research received no external funding.

Conflicts of Interest: The authors declare no conflict of interest.

References

1. Niaounakis, M. Recycling of biopolymers—The patent perspective. *Eur. Polym. J.* **2019**, *114*, 464–475. [CrossRef]
2. Hottle, T.; Bilec, M.M.; Landis, A.E. Sustainability Assessments of Bio-Based Polymers. *Polym. Degrad. Stab.* **2013**, *98*, 1898–1907. [CrossRef]
3. Rosenboom, J.-G.; Langer, R.; Traverso, G. Bioplastics for a Circular Economy. *Nat. Rev. Mater.* **2022**, *7*, 117–137. [CrossRef] [PubMed]
4. European Commission. *Circular Economy Action Plan Progress Report*; European Commission: Brussels, Belgium, 2023.
5. Collias, D.I.; James, M.I.; Layman, J.M. Introduction—Circular Economy of Polymers and Recycling Technologies. In *Circular Economy of Polymers: Topics in Recycling Technologies*; ACS Symposium Series; American Chemical Society: Washington, DC, USA, 2021.
6. Singh, M.K.; Siengchin, S.; Sanjay, M.R. Recent Advances of Sustainable Composites in Manufacturing Sector. *J. Appl. Sci. Eng. Technol. Manag.* **2023**, *1*, 1–2. [CrossRef]
7. Cosnita, M.; Cazan, C.; Duta, A. Interfaces and Mechanical Properties of Recycled Rubber–Polyethylene Terephthalate–Wood Composites. *J. Compos. Mater.* **2014**, *48*, 683–694. [CrossRef]
8. Cazan, C.; Enesca, A.; Cosnita, M. Accelerated Aging of Polymeric Composites Based on Waste with TiO_2 Fillers. *ACS Appl. Polym. Mater.* **2023**, *5*, 3958–3970. [CrossRef]
9. Cazan, C.; Cosnita, M. Sustainable Composites with Synergistic Combinations of Construction and Demolition Waste: Behavior of Rubber, HDPE, PS, and Brick after Short-Term Water Immersion. *J. Clean. Prod.* **2024**, *471*, 143342. [CrossRef]
10. Vladuta, C.; Andronic, L.; Duta, A. Effect of TiO_2 Nanoparticles on the Interface in the PET–Rubber Composites. *J. Nanosci. Nanotechnol.* **2010**, *10*, 2518–2526. [CrossRef]
11. Okolie, O.; Kumar, A.; Edwards, C.; Njuguna, J. Bio-Based Sustainable Polymers and Materials: From Processing to Biodegradation. *J. Compos. Sci.* **2023**, *7*, 213. [CrossRef]
12. Kaya, Y.; Kobya, V.; Ünverdi, M.; Mardani, A. Polymers in Sustainable Construction Composites: Rheology, Mechanical Performance, and Durability. *Polymers* **2025**, *17*, 2186. [CrossRef]
13. Mohanty, A.; Wu, F.; Mincheva, R.; Misra, M. Sustainable Polymers. *Nat. Rev. Methods Primers* **2022**, *2*, 46. [CrossRef]
14. Stanley, J.; Xanthopoulou, E.; Kostoglou, M.; Fras Zemljič, L.; Lambropoulou, D.A.; Bikiaris, D.N. Study on Impact of Monomers Towards High Molecular Weight Bio-Based Poly(ethylene Furanoate) via Solid State Polymerization Technique. *Polymers* **2024**, *16*, 3305. [CrossRef] [PubMed]
15. Karimi, I.; Ghowsi, M.; Mohammed, L.J.; Haidari, Z.; Nazari, K.; Schiöth, H.B. Inulin as a Biopolymer; Chemical Structure, Anticancer Effects, Nutraceutical Potential and Industrial Applications: A Comprehensive Review. *Polymers* **2025**, *17*, 412. [CrossRef] [PubMed]
16. García-García, A.; Silván, U.; Pérez-Álvarez, L.; Lanceros, S. Comparing the Printability, Biological and Physicochemical Properties of Bio-Based Photo-Crosslinkable Hydrogels. *Polymers* **2025**, *17*, 2867. [CrossRef] [PubMed]
17. Gök, C.; Işıtan, A.; Bersani, M.; Bettotti, P.; Pasquardini, L.; Fedrizzi, M.; D'Angelo, D.; Boyacıoğlu, H.; Koluman, A. Physicochemical and Antimicrobial Evaluation of Bacterial Cellulose Derived from Spent Tea Waste. *Polymers* **2025**, *17*, 2521. [CrossRef]
18. Wu, S.; Ren, L.; Qiu, X.; Qi, Q.; Li, B.; Xu, P.; Guo, M.; Zhao, J. Interface Enhancement and Tribological Properties of Cattle Manure-Derived Corn Stalk Fibers for Friction Materials: The Role of Silane Treatment Concentration. *Polymers* **2025**, *17*, 22. [CrossRef]
19. Mchich, Z.; Ștefan, D.S.; Mamouni, R.; Saffaj, N.; Bosomoiu, M. Eco-Friendly Hydrogel Beads from Seashell Waste for Efficient Removal of Heavy Metals from Water. *Polymers* **2024**, *16*, 3257. [CrossRef]
20. Segneanu, A.-E.; Bradu, I.A.; Călinescu, M.S.; Vlase, G.; Vlase, T.; Herea, D.-D.; Buema, G.; Mihailescu, M.; Grozescu, I. Novel Nanocomposites and Biopolymer-Based Nanocomposites for Hexavalent Chromium Removal from Aqueous Media. *Polymers* **2024**, *16*, 3469. [CrossRef]
21. Duarte, H.; Brás, J.; Saoudi Hassani, E.M.; Aliaño-Gonzalez, M.J.; Magalhães, S.; Alves, L.; Valente, A.J.M.; Eivazi, A.; Norgren, M.; Romano, A.; et al. Lignin-Furanic Rigid Foams: Enhanced Methylene Blue Removal Capacity, Recyclability, and Flame Retardancy. *Polymers* **2024**, *16*, 3315. [CrossRef]

22. Sriani, T.; Mahardika, M.; Aldhama, S.A.; Wulandari, C.P.; Prihandana, G.S. Upcycling of Expanded Polystyrene Waste-Impregnated PVP Using Wet-Phase Inversion for Effective Microalgae Harvesting. *Polymers* **2024**, *16*, 2703. [CrossRef]
23. Kim, Y.-M.; Kim, K.; Le, T.H.M. Advancing Sustainability and Performance with Crushed Bottom Ash as Filler in Polymer-Modified Asphalt Concrete Mixtures. *Polymers* **2024**, *16*, 1683. [CrossRef]
24. Ohm, B.; Lee, S.Y.; Le, T.H.M. Utilizing Crushed Recycled Marble Stone Powder as a Sustainable Filler in SBS-Modified Asphalt Containing Recycled Tire Rubber. *Polymers* **2025**, *17*, 70. [CrossRef]

Disclaimer/Publisher's Note: The statements, opinions and data contained in all publications are solely those of the individual author(s) and contributor(s) and not of MDPI and/or the editor(s). MDPI and/or the editor(s) disclaim responsibility for any injury to people or property resulting from any ideas, methods, instructions or products referred to in the content.

https://doi.org/10.3390/polym18060729

polymers

MDPI

Article

Study on Impact of Monomers Towards High Molecular Weight Bio-Based Poly(ethylene Furanoate) via Solid State Polymerization Technique

Johan Stanley [1], Eleftheria Xanthopoulou [1], Margaritis Kostoglou [2], Lidija Fras Zemljič [3], Dimitra A. Lambropoulou [4,5] and Dimitrios N. Bikiaris [1,*]

[1] Laboratory of Chemistry and Technology of Polymers and Colors, Department of Chemistry, Aristotle University of Thessaloniki, GR-541 24 Thessaloniki, Greece; johansta@chem.auth.gr (J.S.); exanthoa@chem.auth.gr (E.X.)
[2] Laboratory of Chemical and Environmental Technology, Department of Chemistry, Aristotle University of Thessaloniki, GR-541 24 Thessaloniki, Greece; kostoglu@chem.auth.gr
[3] Faculty of Mechanical Engineering, University of Maribor, SI-2000 Maribor, Slovenia; lidija.fras@um.si
[4] Laboratory of Environmental Pollution Control, Department of Chemistry, Aristotle University of Thessaloniki, GR-541 24 Thessaloniki, Greece; dlambro@chem.auth.gr
[5] Center for Interdisciplinary Research and Innovation (CIRI-AUTH), Balkan Center, GR-570 01 Thessaloniki, Greece
* Correspondence: dbic@chem.auth.gr

Abstract: In recent years, bio-based poly(ethylene furanoate) has gained the attention of packaging industries owing to its remarkable properties as a promising alternative to fossil-based polymers. It is necessary to synthesize high-molecular-weight polymers using effective and straightforward techniques for their commercialization. In this present work, poly(ethylene 2,5-furan dicarboxylate) (PEF) was produced with a high molecular weight of 0.43 dL/g using 2,5-furan dicarboxylic acid (FDCA) or its derivative Dimethyl-2,5-Furan dicarboxylate (DMFD), followed by solid-state polymerization (SSP) conducted at different temperatures and reaction times. The intrinsic viscosity ([η]), carboxyl end-group concentration (–COOH), and thermal properties of the produced polyesters were evaluated using differential scanning calorimetry (DSC). The results indicated that the SSP process improved the melting temperature and crystallinity of both the PEF samples as the reaction times and temperatures increased, as corroborated by DSC and X-ray diffraction (XRD) analyses. Additionally, both intrinsic viscosity and number-average molecular weight saw an increase with longer SSP durations and higher temperatures, while the concentration of carboxyl end groups decreased, aligning with expectations. The overall results indicate that PEF (DMFD) samples exhibited a significant increase in crystallization and molecular weight, attributed to their lower degree of crystallinity and their monomer's high purity.

Keywords: bio-based polymers; 2,5-furan dicarboxylic acid; Dimethyl 2,5-furan dicarboxylate; poly(ethylene 2,5-furan dicarboxylate); poly(ethylene furanoate); solid state polymerization; thermal properties

1. Introduction

The bio-based market is currently dominated by drop-in bio-based polymers (from renewable raw materials with comparable material properties to their fossil counterparts; e.g., bio-based poly(ethylene terephthalate) (PET)) and non-biodegradable polymers [1,2]. Other than the resistance to biodegradability, greenhouse gas (GHG) emissions constitute the major issue forcing the chemical industry to shift from petroleum-derived plastics towards bio-based, benign polymers. Poly(ethylene 2,5-furandicarboxylate) (PEF) is a bio-based polymer with a striking ability to reduce GHG emissions and promising properties to replace fossil-based PET in packaging industries. A recent study conducted by Eerhart et al.

on life cycle assessment (LCA) of corn-starch-based PEF shows a reduction in GHG emission by about 45–55% (with fossil-based ethylene glycol (EG)) or by 68–82% (with bio-based EG) relative to fossil-based PET [3]. Due to its low GHG emissions, PEF gains increasing attention from the chemical industries and governmental agencies as an alternative to conventional polymers [4]. Avantium (Amsterdam, Netherlands) has already started to produce PEF on a pilot scale aiming to operate the world's first 2,5-furan dicarboxylic acid (FDCA) flagship plant in 2024 to produce 5000 tons of FDCA per annum (5 kta), which is the key building block for the PEF polyester [5].

PEF is a 100% recyclable bio-based polyester with better barrier, mechanical, and thermal characteristics than PET, making it ideal for demanding applications like food packaging, bottles, and fibers [6–8]. For example, the automotive, electrical, and electronics sectors can take advantage of enhanced PEF-based thermoplastics due to their outstanding mechanical characteristics, ability to be remolded or reshaped, thermal stability, and dimensional consistency. Additionally, it is possible to develop sustainable, recyclable, and durable adhesives modified with PEF [9,10]. Due to the rigidity and polarity of its furan ring, it exhibits lower O_2, CO_2, and H_2O permeability compared to PET. PEF exhibits similar mechanical properties to PET, with a slightly higher elastic modulus and smaller elongation at break [11]. The thermal stability of PEF is slightly lower than PET, but it is stable until 350 °C [12]. A recent study by Pluta et al. aimed to investigate the thermal behavior of PEF in relation to varying cold-crystallization temperatures. The study concluded that the cold-crystallization temperature significantly influences the morphology and thermal properties of PEF [13]. Van der Mass et al. demonstrated a novel method for producing high-molecular-weight PEF polyesters using diguaiacyl oxalate (DGO) as a traceless chain extender, which allows for the coupling of lower molecular weight polymer chains and eliminating the need for metal catalysts [14].

Solid-state polymerization (SSP) is a highly efficient technique for synthesizing high-molecular-weight polymers suitable for various industrial applications, such as bottles, films, and fibers. It offers an optimized approach for achieving high production efficiency and consistent product quality, as evidenced in the polyester industry. This process stands out for its low energy requirements and solvent-free nature, reducing environmental impact and eliminating the need for solvent recovery systems, making it a greener alternative to solution polymerization [15]. Additionally, SSP is cost-effective due to its straightforward process design and the absence of costly catalysts often used in other polymerization methods. Operating at lower temperatures than melt polymerization, SSP minimizes energy consumption and reduces the risk of side reactions that could compromise polymer quality. Its versatility allows for its application across a wide range of polymers, including biodegradable polymers, thermoplastics, and liquid crystalline polymers, making it suitable for various industrial uses [16].

Knoop et al. studied the preparation of high-molecular-weight furan-based polyesters using a combination of melt polycondensation and solid-state polycondensation techniques. Dimethyl furan-2,5-dicarboxylate (DMFD) was chosen as a starting monomer due to its purity after two recrystallization cycles and less color formation. A tenfold increase in the *Mw* (83,000 g/mol) of PEF was observed after 72 h of SSP, which was sufficiently high for bottle and fiber application [17]. Hong et al. have managed to synthesize PEF with 0.60 dL/g intrinsic viscosity [η] using DMFD as the starting monomer via a melt polycondensation technique. In order to expand the usage of PEF for bottles and packaging applications, the SSP technique was applied. After 48 h of SSP, a moderate increase in intrinsic viscosity of 0.72 dL/g was observed [18]. Gabirondo et al. conducted an interesting study on the depolymerization of commercial PEF and further repolymerization. The repolymerization was conducted using melt polycondensation and further SSP was carried out up to 48 h. The successful formation of biopolymers with similar chemical and thermal properties like virgin PEF offers a sustainable end-of-life option for PEF [19].

Our research group also conducted various studies on SSP to improve the molecular weight of PEF. Kasmi et al. aimed to synthesize high-molecular-weight PEF polyesters

using DMFD as the starting monomer, catalyzed by tetrabutyl titanate (TBT) and followed by SSP carried out at different reaction times and temperatures. Following SSP, the intrinsic viscosity increased significantly, exceeding 1 dL/g after just 5 h of reaction at 205 °C, demonstrating its suitability for industrial manufacturing processes [20]. Papadopoulos et al. have made a comparative study between poly(propylene furanoate) (PPF) and poly(butylene furanoate) (PBF), which were synthesized via two-step melt polycondensation using DMFD as starting monomers, followed by SSP performed at different temperatures and reaction times [21].

Our previous work was focused on a comparative study of synthesizing high-molecular-weight poly(ethylene furanoate) using FDCA or its derivative DMFD as the starting monomer for food packaging applications. Our research group observed that FDCA promoted the production of high-molecular-weight PEF [22]. Although much research has been carried out to improve the molecular weight of furan-based polyesters using different monomers, catalysts, and nanocomposites, to the best of our knowledge, no comparative study has been performed regarding the effect of monomer type on improving the molecular weight of PEF by using melt polycondensation followed by the SSP technique. Thus, in this work, PEF was synthesized using both FDCA and DMFD as starting monomers using the melt polycondensation technique and subjected to the SSP technique for further improving the molecular weight of the PEF. Our aim was to see which monomer gives the higher molecular weight increase during SSP. The effect of temperature and time on the increase of molecular weight of both PEF (FDCA) and PEF (DMFD) samples was monitored, while complementary data were provided by means of XRD and DSC.

2. Materials and Methods

2.1. Materials

2,5-Furan dicarboxylic acid (BioFDCA X000230-2003) was purchased from Corbion (Gorinchem, The Netherlands). Diethylene glycol (DEG) (anhydrous, 99.8%), titanium butoxide, and antimony trioxide were purchased from Aldrich Co. (London, UK). DMFD was synthesized using FDCA and methanol. All other reagents and solvents utilized in the process were of analytical grade.

2.2. Synthesis of PEF Using Dimethyl 2,5-Furandicarboxylate (DMFD)

The PEF polyesters were synthesized in a glass batch reactor through a two-stage melt polycondensation process consisting of transesterification and polycondensation steps. A 1:1.5 molar ratio of DMFD and diethylene glycol (DEG) was used, with titanium butoxide (TBT) (400 ppm) serving as the catalyst. To eliminate air, the reactor containing the reagents was evacuated and purged with nitrogen multiple times before commencing the reaction.

In the transesterification step, the reaction mixture was heated at 160–190 °C for 4 h under a nitrogen atmosphere while being continuously stirred at 200 rpm. Nearly all the theoretical methanol produced during the reaction was removed via distillation, marking the completion of this step.

For the polycondensation step, a vacuum of 5.0 Pa was gradually applied over 15 min to prevent excessive foaming, reduce oligomer sublimation, and remove excess diols. The reaction was then carried out at 220–240 °C for 4 h to complete the polycondensation process. The reaction mixture was continuously stirred at 100–150 rpm under vacuum conditions. Upon completion of the polycondensation reaction, the resulting polyesters were extracted, milled, and subsequently washed with methanol [22].

2.3. Synthesis of PEF Using 2,5-Furandicarboxylic Acid (FDCA)

In the initial esterification step, FDCA and DEG were combined in a 1:2.1 molar ratio. The flask was evacuated and purged with nitrogen three times to ensure the complete removal of air. The reaction mixture was preheated to 170 °C for 30 min, followed by heating at 190–210 °C for 2 h while stirring at 200 rpm under a nitrogen atmosphere.

Generally, within the first 1–1.5 h of the first step, EG distillation occurs. After 2.5 h, the oligomers were removed with a heating pistol.

Antimony trioxide (Sb_2O_3) (300 ppm) was charged into the polymerization reactor as a catalyst before the polycondensation step. A vacuum (5.0 Pa) was applied slowly for 15 min to begin the polycondensation process. The vacuum was applied slowly to avoid evacuating reaction solutions from the flask. The increase in the temperature took place at the same time as the vacuum. Then, the temperature increased to 250 °C for 4 h, and 260 °C for 2 h. At the same time, the stirring speed decreased (100-70-50 rpm) to avoid high shear stress. Finally, the samples were retrieved from the reaction mixture, washed with methanol, milled, and characterized [22].

2.4. Solid State Polymerization

The SSP process was carried out using an apparatus that included four test tubes linked to a vacuum line and placed in a thermostatically controlled salt bath. About 1.5 g of milled PEF polyester was added to each glass tube while maintaining a vacuum of 3–4 Pa. The reaction was conducted at steady temperatures of 185 °C, 190 °C, and 195 °C for PEF polyesters made from both FDCA and its derivative DMFD monomers. The test tubes were taken out of the bath at intervals of 1, 2, 4, and 6 h, and the resulting polymers were analyzed for intrinsic viscosity ([η]), carboxyl end-group content, and thermal characteristics.

2.5. Characterization

2.5.1. Intrinsic Viscosity

The intrinsic viscosity of the materials was determined using an Ubbelohde viscometer (Schott Gerate GmbH, Hofheim, Germany) at 25 °C. The samples were dissolved in a 60/40 (w/w) solution of phenol and tetrachloroethane by heating the mixture at 80 °C for 10 min. After cooling, the samples were filtered to remove any solid particles. The intrinsic viscosity ([η]) was then calculated using the Solomon–Ciuta Equation (1):

$$[\eta] = \frac{\left[2\left\{\frac{t}{t_0} - \ln\left(\frac{t}{t_0}\right) - 1\right\}\right]^{\frac{1}{2}}}{c} \quad (1)$$

where c is the concentration of the solution, t_0 is the flow time of pure solvent, and t is the flow time of solution.

The number-average molecular weight ($\overline{M_n}$) of the samples was determined using Equation (2) following the Berkowitz equation [22]:

$$\overline{M_n} = 3.29 \times 10^4 \, [\eta]^{1.54} \quad (2)$$

2.5.2. End-Group Analysis

The content of carboxyl end groups in the synthesized polyesters was determined by employing a titration method in a mixture of benzyl alcohol and chloroform, in accordance with Pohl's approach [23]. The titration was conducted using a standard NaOH solution dissolved in benzyl alcohol, with phenol red serving as the indicator. This titration procedure was repeated three times, and the mean value of [COOH] was computed.

2.5.3. Differential Scanning Calorimetry (DSC)

A PerkinElmer Pyris DSC-6 differential scanning calorimeter calibrated using pure indium and zinc standards was employed for the thermal analysis. Samples weighing 6–8 mg were sealed in aluminum pans, and all measurements were conducted under a nitrogen atmosphere with a flow rate of 20 mL/min. The PEF (FDCA) and PEF (DMFD) samples were first heated from 30 °C to 210 °C with a heating rate of 20 °C/min. The glass transition temperature (T_g), melting temperature (T_m), cold crystallization temperature

(T_{cc}), and enthalpies (ΔH_m and ΔH_{cc}) of the PEF (FDCA) and PEF (DMFD) samples were determined from these scans. Crystallinity degree ($X_c{}^a$) was calculated with Equation (3):

$$X_{c^a}(\%) = \left(\frac{\Delta H_m - \Delta H_{cc}}{\Delta H_m^0}\right) \times 100 \quad (3)$$

where $\Delta H^0{}_m$ = 137 J/g, the heat of melting of the 100% crystalline PEF.

2.5.4. Wide Angle X-Ray Diffraction Patterns (WAXRD)

X-ray powder diffraction (XRD) patterns were obtained using a MiniFlex II XRD system (Rigaku Co., Tokyo, Japan) with Cu Ka radiation (0.154 nm). All materials were analyzed at 2θ range of 5° to 50° with a scan speed of 1°/min. The % crystallinity was calculated from the XRD graphs through origin software (OriginPro 2024b-Learning edition) using Equation (4):

$$X_{c^b}(\%) = \left(1 + \frac{A_{am}}{A_c}\right)^{-1} \quad (4)$$

A_{am} is the area of the amorphous halo, and A_c is the area of the crystalline peaks.

3. Modeling of the Solid-State Polymerization of PEF Polyesters Kinetics

3.1. Reaction Mechanism

The main reaction mechanisms occurring during the solid-state polymerization (SSP) of PEF polyesters include polycondensation/transesterification, esterification, thermal degradation, and the polycondensation of vinyl end groups [24]. The reaction mechanism is detailed in Equations (5)–(8), where k_1 and K_1 denote the forward and equilibrium rate constants for the transesterification process (Equation (5)), while k_2 and K_2 correspond to the rate constants associated with the esterification process (Equation (6)). The kinetic rate constants for the degradation and polycondensation of reactions involving vinyl end groups, regarded as one-way processes, are represented as k_d and k_v in Equations (7) and (8), respectively.

Polycondensation/transesterification

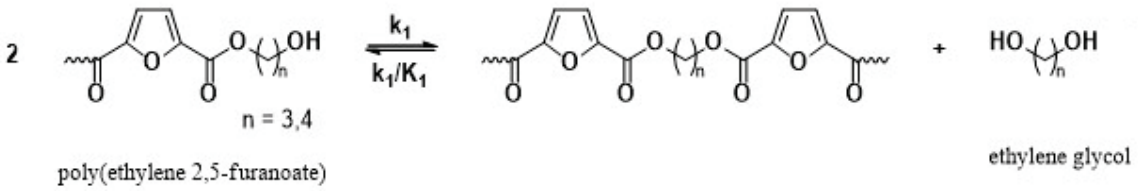

(5)

Esterification

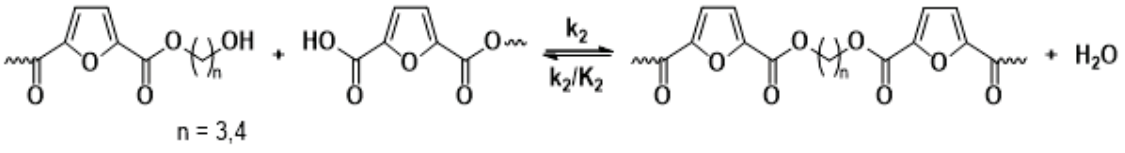

(6)

Thermal degradation

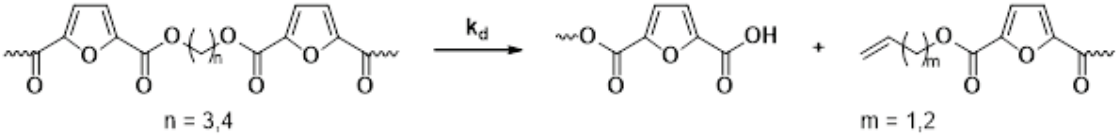

(7)

Polycondensation of vinyl end groups

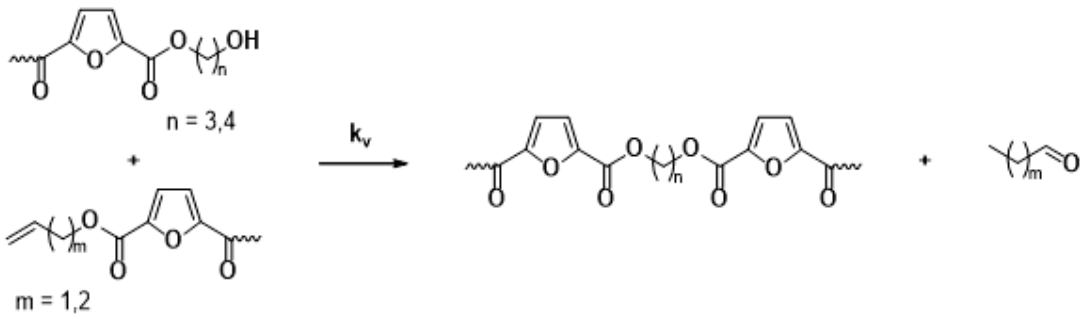

(8)

The molecular weight of the PEF polyesters was enhanced by means of three distinct reactions. In the first reaction, ethylene glycol was produced through the reaction of two hydroxyl end groups, as shown in Equation (5). In the second reaction, a carboxyl end group reacts with a hydroxyl group, producing water as a byproduct, as depicted in Equation (6). Additionally, a side reaction between a vinyl ester end group and a hydroxyl end group can release acetaldehyde, which also contributes to an increase in the molecular weight, as illustrated in Equation (8). On the other hand, when thermal degradation occurs, an ester bond in the macromolecular chain cleaves, producing a vinyl ester end group and a carboxyl end group, which can reduce the molecular weight of the polyester, as illustrated in Equation (7). The overall reaction rate can be influenced by intrinsic reaction kinetics, changes in the polymer's degree of crystallization, diffusional limitations of the reactive end groups, and the desorption of volatile byproducts such as water and glycol [20,25].

3.2. Simplified Mathematical Model

The modeling of SSP kinetics presents significant challenges because it requires consideration of chemical kinetics and diffusion phenomena to accurately depict the change in concentration of reactive species throughout the reaction process [24]. This results in additional variation based on the distance from the interface. Consequently, to represent the reaction, a model that includes two independent variables and a series of partial differential equations encompassing multiple diffusional, kinetic, and crystallization parameters is essential [26]. Using such complex models to simulate just a few experimental data points lacks physical relevance. In this study, only five data points were recorded at each experimental condition, leading to the adoption of a simpler kinetic model as proposed by Ma and co-workers [27,28]. While this model was initially developed for the SSP of PET, our research group has effectively applied it to model the SSP of pristine PEF and also for nanocomposites of PEF and PET [20,21,29].

The mathematical model was developed based on the following assumptions.

- The kinetic rate constants are found to be unaffected by the polymer chain lengths, focusing solely on the reactivity of the end groups.
- The glycols and water are efficiently removed from the reaction mixture through the application of a high vacuum (below 3–4 Pa), leading to the omission of the reverse reactions presented in Equations (5) and (6).
- Owing to the polycondensation process operating at comparatively low temperatures (185–195 °C), neither thermal degradation nor acetaldehyde formation are considered side reactions (Equations (7) and (8) are eliminated).
- Any diffusional limitations resulting from the desorption of volatile species are disregarded.

Once these simplifications are taken into account, the change in rates of hydroxyl [OH] and carboxyl [COOH] end groups can be represented by Equations (9) and (10) [27,28].

$$\frac{d[OH]_t}{dt} = -2k_1\left[OH\right]_t^2 - k_2[COOH]_t[OH]_t \quad (9)$$

$$\frac{d[COOH]_t}{dt} = -k_2[COOH]_t[OH]_t \quad (10)$$

where $[COOH]_t$ and $[OH]_t$ denote the actual "true" carboxyl and hydroxyl end-group concentration, respectively.

Ma and co-workers [27,28] coined the term "actual hydroxyl and carboxyl end-groups" to explain the slowdown in SSP kinetics at high [η] values. As a result, it was determined that a portion of the hydroxyl and carboxyl end groups ($[OH]_i$ and $[COOH]_i$, respectively) had been rendered temporarily inactive, and the actual concentration of OH and COOH in Equations (9) and (10) can be written as:

$$[OH]_t = [OH] - [OH]_i \quad (11)$$

$$[COOH]_t = [COOH] - [COOH]_i \quad (12)$$

where [COOH], [OH], $[COOH]_i$, and $[OH]_i$ stand for the total and temporarily inactivated concentrations of the COOH and OH groups, respectively.

Moreover, the end-group concentration can be used to determine the number-average molecular weight:

$$\overline{M_n} = \frac{2}{[COOH] + [OH]} \quad (13)$$

In conjunction with Equations (2) and (11)–(13), along with (9) and (10), these equations form a collection of ordinary differential equations that are solved numerically utilizing the varying step-size Runge–Kutta method. The outcomes of this approach reveal changes in the concentrations of –COOH and –OH end groups, as well as the intrinsic viscosity over time during SSP. By concurrently fitting the concentrations of [OH], [COOH], and [η] to the experimental data points based on time, four adjustable parameters—k_1, k_2, $[OH]_I$, and $[COOH]_i$—are estimated for each experimental condition.

4. Results and Discussion

4.1. Synthesis and Kinetic Study of PEF Polyesters After SSP

The SSP of both PEF (FDCA) and PEF (DMFD) polyesters was carried out at 185, 190, and 195 °C for 1, 2, 4, and 6 h under vacuum. The values of intrinsic viscosity [η] and number-average molecular weight ($\overline{M_n}$) for the PEF (FDCA) and PEF (DMFD) polyesters, which were produced after solid-state polymerization (SSP) at various temperatures and durations, are presented in Table 1. The number-average molecular weights ($\overline{M_n}$) were calculated experimentally, measuring the intrinsic viscosity [η] using Equation (2).

Table 1. Intrinsic viscosity ([η], dL/g) and number-average molecular weights ($\overline{M_n}$, g/mol) of PEF (FDCA) and PEF (DMFD) polyesters obtained after SSP at different temperatures and times. The degree of polymerization (DP) appears in parentheses.

Temperature (°C)	SSP Time (h)	PEF (FDCA)		PEF (DMFD)	
		[η]	$\overline{M_n}$	[η]	$\overline{M_n}$
as received	0	0.43	8969 (49)	0.41	6822 (37)
185	1	0.43	8969 (49)	0.46	9950 (54)
	2	0.44	9292 (50)	0.49	10,967 (59)
	4	0.44	9292 (50)	0.51	11,664 (63)
	6	0.45	9619 (52)	0.54	12,737 (69)
190	1	0.45	9619 (52)	0.49	10,967 (59)
	2	0.45	9619 (52)	0.50	11,313 (63)
	4	0.46	9950 (54)	0.53	12,376 (67)
	6	0.46	9950 (54)	0.56	13,471 (73)
195	1	0.46	9950 (54)	0.49	10,967 (59)
	2	0.46	9950 (54)	0.52	12,018 (65)
	4	0.47	10,285 (56)	0.58	14,219 (77)
	6	0.48	10,624 (57)	0.61	15,367 (83)

After SSP, the PEF polyesters showed an increase in average molecular weight with respect to the increase in SSP time and temperature. The hydroxyl end groups of macromolecular chains reacted more readily with carboxyl end groups at temperatures that are close to PEF's melting point, joining the chains and increasing PEF's molecular weight. Moreover, the diffusion of generated byproducts, like ethylene glycol and water, was substantially slower at low SSP temperatures. Another factor is the increase in crystallinity that slows the diffusion rate of by-products that are formed [20]. For these reasons, the SSP temperature was chosen close to PEF's melting point from 185 °C to 195 °C. As anticipated, due to the esterification and transesterification reactions taking place, the carboxyl end groups consistently diminished with longer SSP durations at every temperature tested, leading to an observed rise in the molecular weight of PEF [30]. Both SSP time and temperature played an important role in increasing the PEF's molecular weight.

Figure 1a,b displays the increase in intrinsic viscosity values of synthesized PEF (FDCA) and PEF (DMFD) polyesters with respect to SSP time and temperatures. Although many research publications have been reported on the increase in the molecular weight of PEF polyesters, to overcome the inferior properties of PEF polyesters, to the best of our knowledge, no comparative study has been performed regarding the effect of monomers on improving the molecular weight of PEF. The initial intrinsic viscosity values of PEF (FDCA) and PEF (DMFD) polyesters were 0.43 dL/g and 0.41 dL/g, respectively. The intrinsic viscosity of the PEF (FDCA) sample was increased at a slow rate from 0.43 dL/g up to 0.45 dL/g at 185 °C after 6 h of SSP, up to 0.46 dL/g at 190 °C after 6 h of SSP, and up to 0.48 dL/g at 195 °C after 6 h of SSP.

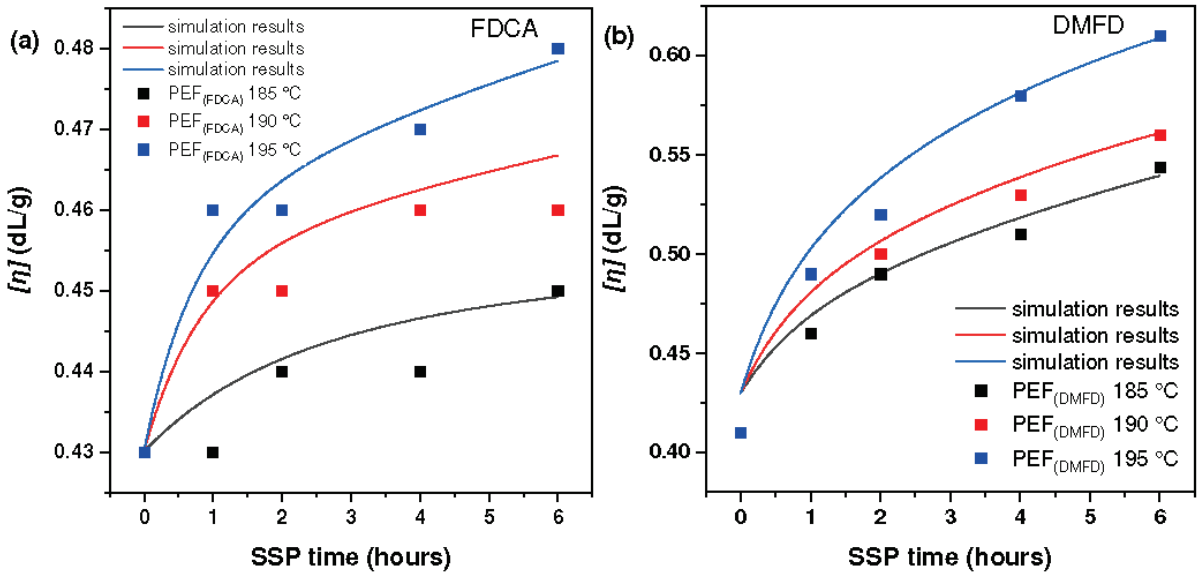

Figure 1. Variation of intrinsic viscosity [η] with respect to time (h) during SSP at different temperatures; (**a**) PEF (FDCA); (**b**) PEF (DMFD).

The intrinsic viscosity of the PEF (DMFD) sample showed a higher increase from 0.41 dL/g up to 0.54 dL/g at 185 °C after 6 h of SSP, up to 0.56 dL/g at 190 °C after 6 h of SSP, and up to 0.61 dL/g at 195 °C after 6 h of SSP. It may be inferred that the PEF (DMFD) sample's rapid growth in molecular weight was related to its lower degree of crystallinity since crystallinity has a significant impact on the mobility and diffusion rate of the polymer chain-end groups, which are found in the amorphous phase of semi-crystalline polyesters [21]. Also, the high purity of DMFD monomers obtained via esterification of FDCA with methanol under acidic conditions assisted in the rise of the molecular weight of the samples [31].

Also, as anticipated, raising the SSP reaction temperature from 185 to 195 °C, both transesterification and esterification were accelerated, which obviously favors the increase

in intrinsic viscosity. The diffusion of the corresponding glycol and water controlled the corresponding reactions. The diffusion of byproducts was slower at low SSP temperatures. Increasing the SSP temperature close to the melting point of PEF polyesters, the carboxyl end groups of the polymer reacted more readily with hydroxyl end groups to form macromolecular chains, which raised the intrinsic viscosity of the polyester. Therefore, regardless of the type of polyester, intrinsic viscosity increased slowly at 185 to 195 °C [21,30]. It can be said that the [η] range achieved in this research was adequate to meet particular end-use necessities for food packaging, including beverage containers and sheets [20].

Figure 2 shows the effect of reaction temperature and time during SSP on the carboxyl end-group concentration for PEF (FDCA) and PEF (DMFD) samples. The terminal carboxylic groups (–COOH) are the second variable that was utilized to track the effects of SSP time and temperature. The presence of carboxyl end groups is proof of the degradation reaction that happened during polycondensation step [32]. These formed carboxyl end groups that might react through esterification, which increases the molecular weight. From the results, it is understood that the concentration of the carboxyl end group decreased with an increase in SSP time and temperature in both PEF (FDCA) and PEF (DMFD) samples. The carboxyl end-group concentration was mostly dependent on time, whereas temperature had less of an effect on the variation.

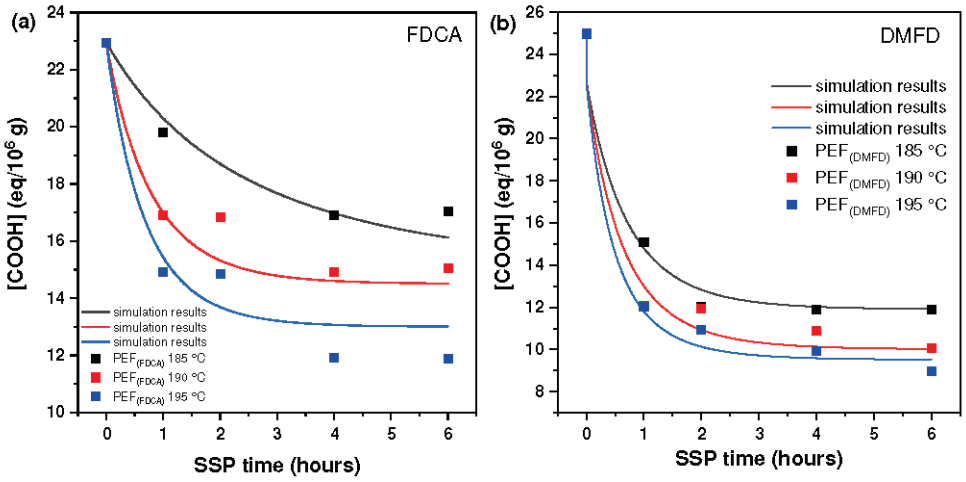

Figure 2. The concentration of carboxyl (−COOH) end group changes with time during the SSP of (**a**) PEF (FDCA) and (**b**) PEF (DMFD) at various temperatures. The continuous lines reflect the theoretical data collected from the kinetic model simulation.

The carboxyl group reduction rate was increased at 195 °C for both PEF (FDCA) and PEF (DMFD) samples, compared to 190 °C and 185 °C. The initial carboxyl end-group concentration of PEF (FDCA) 195 °C sample started at 22.95 eq/10^6 g and reached 11.88 eq/10^6 g after 6 h, whereas PEF (DMFD) 195 °C samples began at 25 eq/10^6 g and reached 8.96 eq/10^6 g after 6 h. Hence, it can be concluded that the carboxyl end-group concentration showed a consistent downward trend as the SSP time increased and a more significant reduction was observed in PEF (DMFD) samples compared to PEF (FDCA) samples.

Figure 3 displays the hydroxyl (–OH) end-group concentration of PEF (FDCA) and PEF (DMFD) samples. The (–OH) end-group concentration was the third variable that clarified how temperature and time affected SSP. As anticipated, and consistent with the previously described findings, the concentration of (–OH) end groups reduced over time. The PEF (FDCA) and PEF (DMFD) samples studied at 195 °C show the highest reduction compared to 185 °C and 190 °C. This rapid decrease in the (–OH) end-group concentration was in accordance with the [η] results. In comparison to FDCA, DMFD samples showed a faster and more consistent reduction trend as the SSP time increased. For example, the hydroxyl end-group concentration of PEF (FDCA) 195 °C samples started at 200 eq/10^6 g

and reduced to 176.37 eq/10^6 g after 6 h of SSP, whereas PEF (DMFD) samples began at 209.24 eq/10^6 g and decreased up to 121.18 eq/10^6 g under the same conditions. Finally, during SSP of PEF (FDCA) and PEF (DMFD) polyesters, the mobility of the end groups was increased with respect to time and temperature, resulting in the chain extension of the polymers.

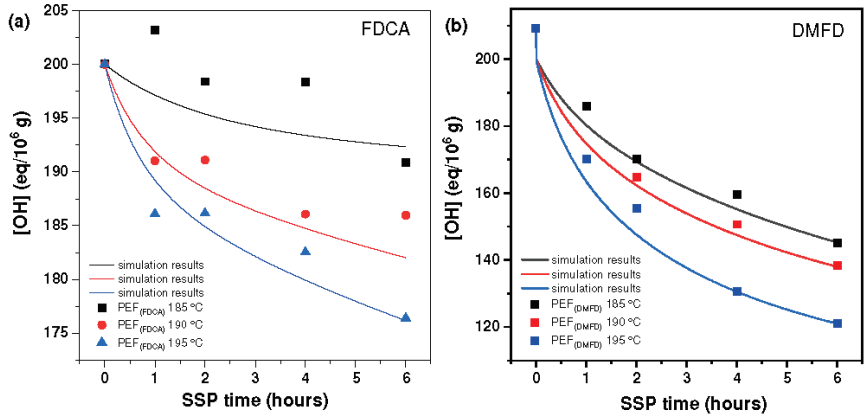

Figure 3. The concentration of hydroxyl (–OH) end group changes with time during the SSP of (**a**) PEF (FDCA) and (**b**) PEF (DMFD) at various temperatures. The continuous lines reflect the theoretical data collected from the kinetic model simulation.

The comparison between the fitted model curves and the experimental data appears in Figure 4. The values of the parameters found by fitting the experimental data are presented in Table 2. It was observed that the constant k_2 was much larger than the constant k_1. The larger values of k_2 are compensated by the fact that the concentration of active carboxyls is much smaller than the one of active hydroxyls, so the two reactions (between chain-end hydroxyls and between chain-end hydroxyls and carboxyl's) proceed in a comparable rate for a while until the elimination of chain-end carboxyl's. The concentration of inactive species was reduced as the temperature increased, with the only exception being one of the hydroxyls for FDCA, where the inactive material remained almost constant with temperature.

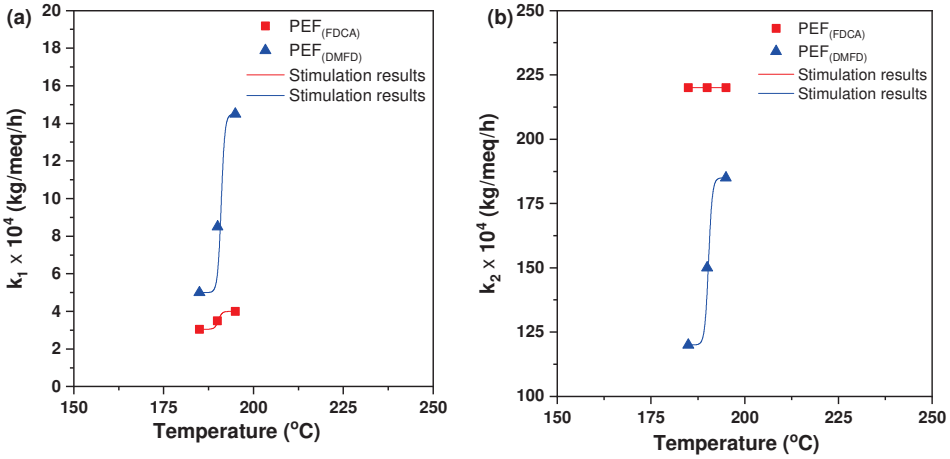

Figure 4. The calculated kinetic rate constants for the (**a**) polycondensation/transesterification (k_1) and (**b**) esterification (k_2) processes of PEF (FDCA) with PEF (DMFD) samples increased as a function of temperature.

Table 2. Parameter values resulted by fitting the simplified model to the experimental data of chain-end hydroxyl and carboxyl evolution.

Sample	k_1 (kg/meq/h)	k_2 (kg/meq/h)	$[OH]_i$ (meq/kg)	$[COOH]_i$ (meq/kg)
FDCA				
185 °C	0.000305	0.022	80	15
190 °C	0.00035	0.022	90	14.5
195 °C	0.0004	0.022	85	13
DFMD				
185 °C	0.0005	0.012	180	12
190 °C	0.00085	0.015	140	10
195 °C	0.00145	0.0185	130	9.5

The reaction constants increased with temperature, so the values of activation energy can be computed. By fitting an Arrhenius equation, it can be found that for DFMD, the reaction "1" between hydroxyls has activation energy E/R = 22,500 K (where R is the ideal gas constant) and the reaction "2" between hydroxyls and carboxyls has activation energy E/R = 9500 K. The corresponding values of the preexponential constant are $1.08 \cdot 10^{18}$ kg/meq/h and $1.22 \cdot 10^{7}$ kg/meq/h, respectively. Regarding FDCA, the activation energies for the reactions "1" and "2" were E/R = 5900 K and E/R = 0 K, respectively. The corresponding preexponential constants were 120 kg/meq/h and 0.022 kg/meq/h, respectively. The activation energy appeared to be much smaller for reaction "2" compared to reaction "1". In addition, it appears to be much smaller for FDCA compared to DFMD. The zero value of activation energy of reaction "2" for FDCA implicated that the actual activation energy was small and could not be estimated with accuracy by the present experimental data.

4.2. Thermal Analysis of Polyesters After SSP

4.2.1. DSC Analysis

The thermal characteristics of PEF polyesters synthesized using FDCA and DMFD monomers were investigated using DSC thermograms. Figure 5a–f clearly illustrates that SSP time and temperature have a significant impact on the thermal properties of prepared PEF polyesters. The melting temperature and degree of crystallinity rose as the time and temperature of SSP increased, which is related to the rise in intrinsic viscosity and molecular weight (Table 1).

The degree of crystallinity ($X_c{}^a$ (%)) of the PEF polyesters was calculated using Equation (3) from the values of enthalpy (ΔH_m), displayed in Table 3. The evolution of the crystallinity of both PEF (FDCA) and PEF (DMFD) samples with respect to SSP time and temperature are displayed in Figure 6a,b, respectively. The PEF (FDCA) samples reached a maximum degree of crystallinity of 36.4%; on the other hand, the PEF (DMFD) samples reached a maximum of 52%. From the results, it is clear from the data that SSP occurs in the polymer's amorphous regions. PEF (DMFD) samples' rapid rise in molecular weight is associated with a lower degree of crystallinity. Because the undesirable byproducts were eliminated more quickly, the molecular weight increased. This claim is also supported by the values of $\overline{M_n}$ /η found in the current investigation and the results of previous research on the SSP of PEF [15].

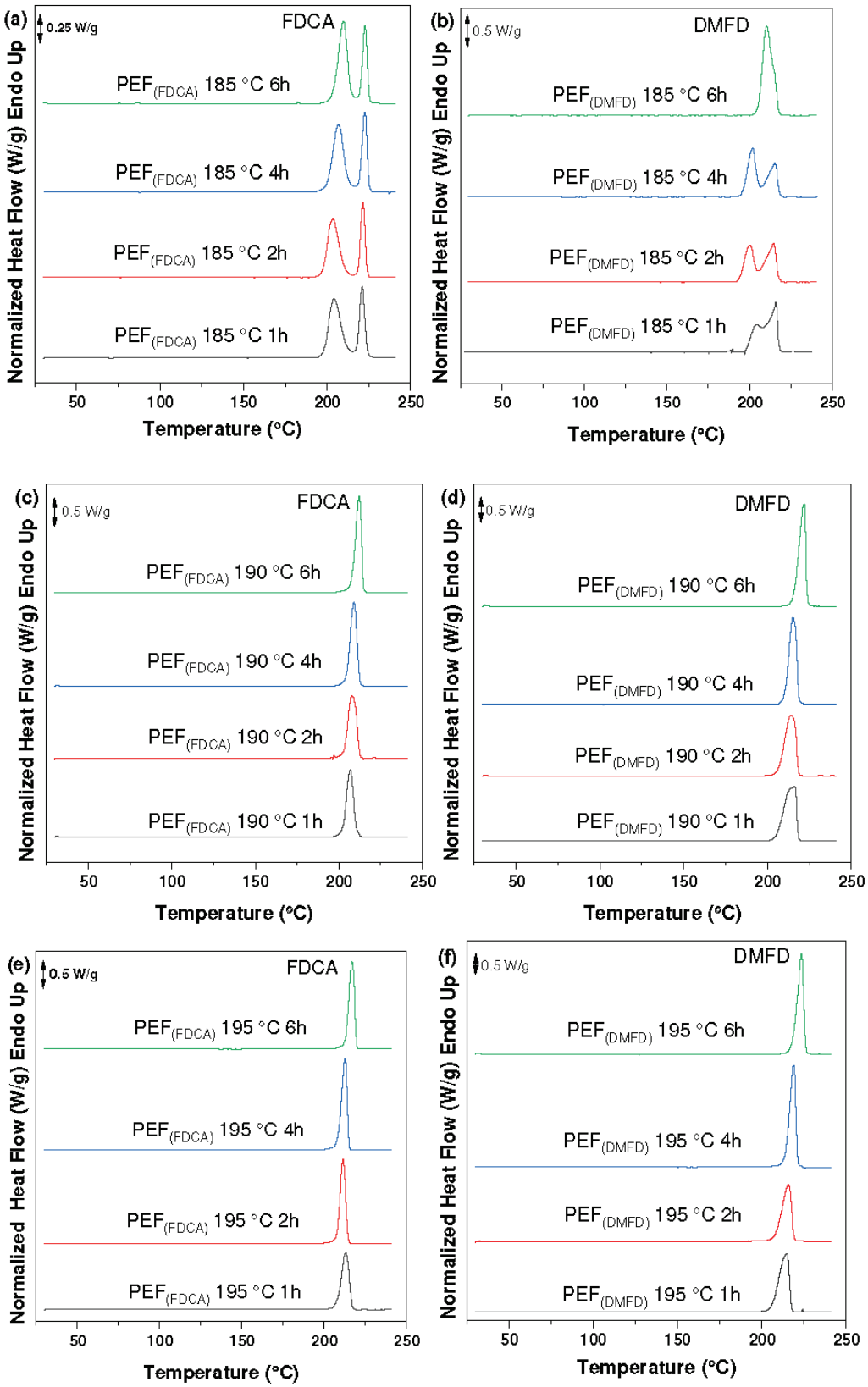

Figure 5. DSC thermograms of the PEF polyesters after SSP at 185 °C for (**a**) PEF (FDCA) and (**b**) PEF (DMFD), after SSP at 190 °C for (**c**) PEF (FDCA) and (**d**) PEF (DMFD), and after SSP at 195 °C for (**e**) PEF (FDCA) and (**f**) PEF (DMFD).

Table 3. Crystallinity degree ($X_c{}^a$ (%)) of PEF (FDCA) and PEF (DMFD) samples after SSP calculated from DSC using melting enthalpy (ΔH_m).

SSP Temperature (°C)	SSP Time (h)	PEF (FDCA) ($X_c{}^a$ (%))	PEF (DMFD) ($X_c{}^a$ (%))
As received	0	29.5	28
185	1	29.6	37.8
	2	29.7	41.2
	4	32.5	41.6
	6	33.9	48.6
190	1	29.6	42.3
	2	33.3	47.9
	4	34.7	48.7
	6	36	49.5
195	1	31.7	49.6
	2	34.7	51
	4	35.3	51.7
	6	36.4	52

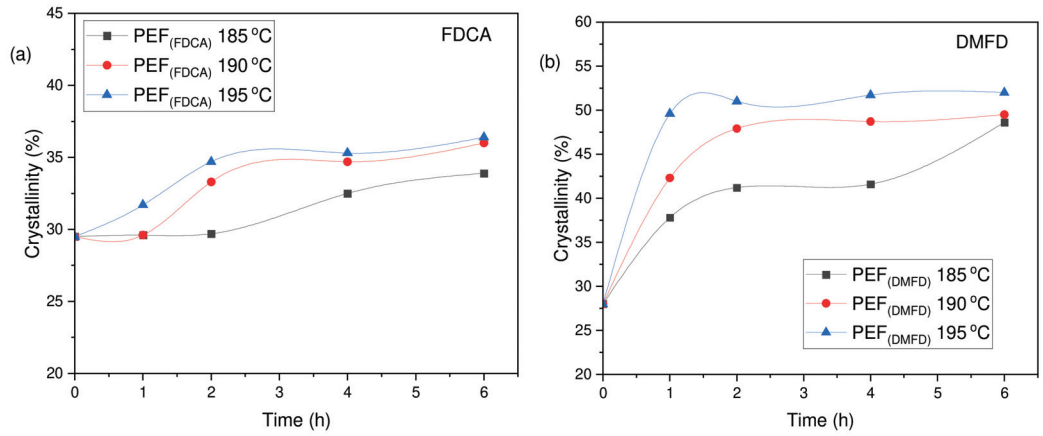

Figure 6. Evolution of the crystallinity degree ($X_c{}^a$ (%)) with respect to SSP time and temperature for (**a**) PEF (FDCA) and (**b**) PEF (DMFD) polyesters.

4.2.2. XRD Analysis

The crystalline structure of the prepared PEF polyesters after SSP was investigated using XRD analysis. The resulting patterns of PEF (FDCA) and PEF (DMFD) samples are presented in Figure 7a–f. As observed, with respect to the increase in time and temperature, the crystallinity was increased in both the FDCA and DMFD samples. All the PEF polyesters exhibited four main diffraction peaks at $2\theta \approx 16.5°$, $2\theta \approx 18°$, $2\theta \approx 23°$, and $2\theta \approx 26°$, which indicated the influence of crystallization in samples after SSP [33]. However, the intensity of the peak in PEF (FDCA) samples was lower compared to the PEF (DMFD) samples. As reported in our previous work, FDCA samples have limited chain mobility, which causes a decrease in the crystallization rate. The higher DEG concentration (6%) in FDCA samples affected the crystallinity of polyesters due to the mobility of the ether block. Furthermore, decreasing DEG concentration (1–2%) in DMFD samples contributed to the increased crystallization rate [22,34].

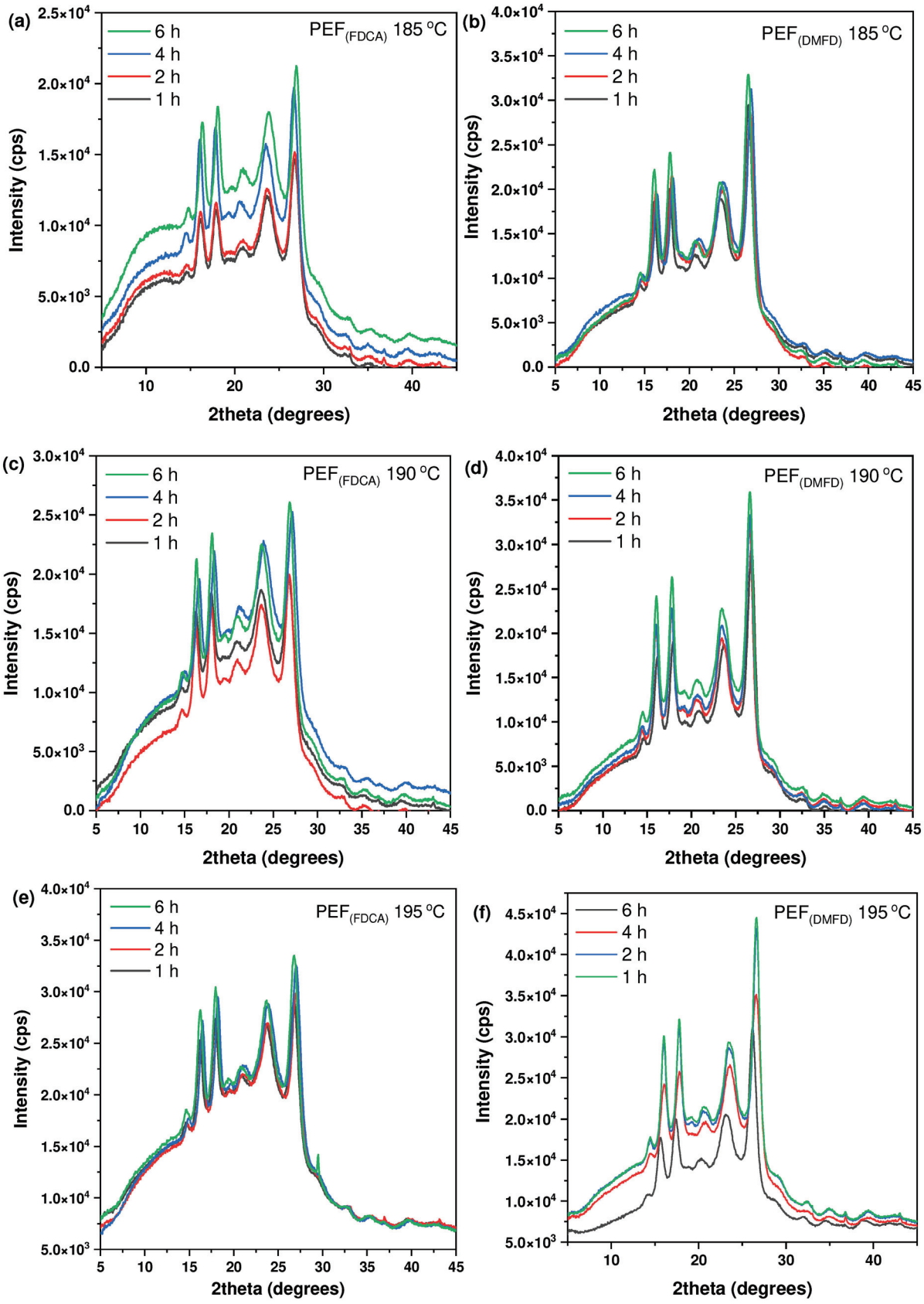

Figure 7. XRD patterns PEF polyesters after SSP at 185 °C for (**a**) PEF (FDCA) and (**b**) PEF (DMFD), after SSP at 190 °C for (**c**) PEF (FDCA) and (**d**) PEF (DMFD), and after SSP at 195 °C for (**e**) PEF (FDCA) and (**f**) PEF (DMFD).

The degree of crystallinity ($X_c{}^b$) has been calculated using Equation (4) displayed in Table 4. From the results, it is observed that PEF (DMFD) samples show an increase in crystallinity with respect to SSP time and temperature compared to the PEF (FDCA) samples, as displayed in Figure 8a,b, respectively. PEF (FDCA) samples reached the highest crystallinity of 18.9%, whereas PEF (DMFD) samples reached the highest crystallinity of 31.2%. This finding shows that the SSP was performed in the amorphous regions of polymers and in agreement with the ($X_c{}^a$) and $\overline{M_n}/\eta$ values obtained in this present study.

Table 4. Crystallinity degree ($X_c{}^b$ (%)) of PEF (FDCA) and PEF (DMFD) samples after SSP calculated from XRD thermograms.

SSP Temperature (°C)	SSP Time (h)	PEF (FDCA) ($X_c{}^b$ (%))	PEF (DMFD) ($X_c{}^b$ (%))
As received	0	15.3	14
185	1	15.3	15.4
	2	15.7	17.3
	4	16.2	20
	6	16.6	21.8
190	1	15.9	16.2
	2	16.3	17.4
	4	16.8	21.5
	6	17.2	23.8
195	1	16.1	17.6
	2	17.3	21.5
	4	18	26.8
	6	18.9	31.2

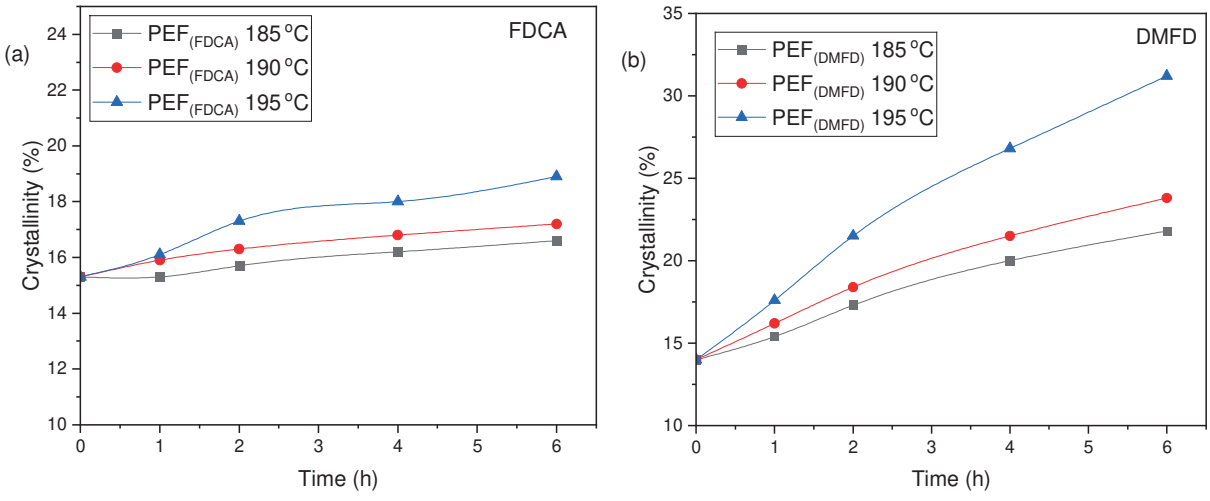

Figure 8. Evolution of the crystallinity degree ($X_c{}^b$ (%)) with respect to SSP time and temperature for (**a**) PEF (FDCA) and (**b**) PEF (DMFD) polyesters.

5. Conclusions

High-molecular-weight (0.43 dL/g) poly(ethylene 2,5-furan dicarboxylate) (PEF) polyesters were synthesized using 2,5-furan dicarboxylic acid (FDCA) and/or its derivative Dimethyl-2,5-Furan dicarboxylate (DMFD) monomers, followed by solid-state polymerization (SSP) conducted at different reaction times and temperatures. As expected, both

PEF (FDCA) and PEF (DMFD) samples showed an increase in intrinsic viscosity [η] and number-average molecular weight ($\overline{M_n}$) with respect to SSP time and temperature. The SSP kinetics of PEF (FDCA) and PEF (DMFD) samples were investigated at different temperatures, 185 °C, 190 °C, and 195 °C, both experimentally and by simple kinetic modeling. The results indicated that the kinetic rate constant k_2 was found to be significantly greater than the kinetic rate constant k_1 due to the lower concentration of active carboxyls than that of active hydroxyls. The thermal analysis of both PEF polyester samples after SSP was performed by differential scanning calorimetry (DSC) technique revealed that the prepared PEF samples' melting temperatures increased gradually in response to SSP temperature and reaction time. All SSP samples that were subjected to DSC and X-ray diffraction (XRD) analysis showed an increase in crystallinity. The PEF (DMFD) samples showed a rapid increase in crystallization and molecular weight due to their lower degree of crystallinity and high purity of monomer. The overall results showed that SSP occurs in the amorphous regions of the polymer, as anticipated for all SSP samples, and that the intrinsic viscosity and number-average molecular weight of prepared PEF polyester increased as the SSP temperature and time increased, while the concentration of carboxyl end groups decreased.

Author Contributions: Conceptualization, methodology, formal analysis, investigation, J.S., E.X., M.K., L.F.Z. and D.N.B.; writing—original draft preparation, J.S., E.X., M.K. and D.N.B.; writing—review and editing, J.S., E.X., M.K., L.F.Z. and D.N.B.; supervision, D.N.B., L.F.Z. and D.A.L.; project administration, D.N.B., L.F.Z. and D.A.L.; funding acquisition, D.N.B., L.F.Z. and D.A.L. All authors have read and agreed to the published version of the manuscript.

Funding: This research is funded by EU Horizon 2020 research and innovation program under the project 'Advanced Research and Training Network in Food quality, safety, and security'—FoodTraNet—H2020-MSCA-ITN-2020′ (grant agreement no. 956265).

Institutional Review Board Statement: Not applicable.

Data Availability Statement: Data are contained within the article.

Conflicts of Interest: The authors declare no conflicts of interest.

Abbreviations

The following abbreviations are used in the manuscript.

PEF	Poly(ethylene 2,5-furan dicarboxylate)
DMFD	Dimethyl-2,5 furandicarboxylate
FDCA	2,5-furan dicarboxylic acid
XRD	X-ray diffraction
PET	Poly(ethylene terephthalate)
GHG	Greenhouse gas
LCA	Life cycle assessment
EG	Ethylene glycol
SSP	Solid-state polymerization
PPF	Poly(propylene furanoate
PBF	Poly(butylene furanoate
DSC	Differential scanning calorimetry
WAXD	Wide Angle X-ray Diffraction Patterns
DGO	Diguaiacyl oxalate

References

1. Prieto, A. To Be, or Not to Be Biodegradable. . . That Is the Question for the Bio-Based Plastics. *Microb. Biotechnol.* **2016**, *9*, 652–657. [CrossRef] [PubMed]
2. Salgado, P.R.; Di Giorgio, L.; Musso, Y.S.; Mauri, A.N. Recent Developments in Smart Food Packaging Focused on Biobased and Biodegradable Polymers. *Front. Sustain. Food Syst.* **2021**, *5*, 630393. [CrossRef]
3. Eerhart, A.J.J.E.; Faaij, A.P.C.; Patel, M.K. Replacing Fossil Based PET with Biobased PEF; Process Analysis, Energy and GHG Balance. *Energy Environ. Sci.* **2012**, *5*, 6407. [CrossRef]

4. Kim, T.; Bamford, J.; Gracida-Alvarez, U.R.; Benavides, P.T. Life Cycle Greenhouse Gas Emissions and Water and Fossil-Fuel Consumptions for Polyethylene Furanoate and Its Coproducts from Wheat Straw. *ACS Sustain. Chem. Eng.* **2022**, *10*, 2830–2843. [CrossRef]
5. De Jong, E.; Dam, M.A.; Sipos, L.; Gruter, G.-J.M. *Furandicarboxylic Acid (FDCA), A Versatile Building Block for a Very Interesting Class of Polyesters*; ACS Publications: Washington, DC, USA, 2012; pp. 1–13.
6. De Jong, E.; Visser, H.A.; Dias, A.S.; Harvey, C.; Gruter, G.-J.M. The Road to Bring FDCA and PEF to the Market. *Polymers* **2022**, *14*, 943. [CrossRef]
7. Gomes, F.W.; Lima, R.C.; Piombini, C.R.; Sinfitele, J.F.; De Souza, F.G.; Coutinho, P.L.A.; Pinto, J.C. Comparative Analyses of Poly(Ethylene 2,5-Furandicarboxylate)−PEF−and Poly(Ethylene Terephthalate) − PET − Resins and Production Processes. *Macromol. Symp.* **2018**, *381*, 1800129. [CrossRef]
8. Louw, J.; Farzad, S.; Görgens, J.F. Polyethylene Furanoate: Technoeconomic Analysis of Biobased Production. *Biofuels Bioprod. Biorefining* **2023**, *17*, 135–152. [CrossRef]
9. Sanders, J.H.; Cunniffe, J.; Carrejo, E.; Burke, C.; Reynolds, A.M.; Dey, S.C.; Islam, M.N.; Wagner, O.; Argyropoulos, D. Biobased Polyethylene Furanoate: Production Processes, Sustainability, and Techno-Economics. *Adv. Sustain. Syst.* **2024**, *8*, 2400074. [CrossRef]
10. Eid, N.; Ameduri, B.; Boutevin, B. Synthesis and Properties of Furan Derivatives for Epoxy Resins. *ACS Sustain. Chem. Eng.* **2021**, *9*, 8018–8031. [CrossRef]
11. Van Berkel, J.G.; Guigo, N.; Visser, H.A.; Sbirrazzuoli, N. Chain Structure and Molecular Weight Dependent Mechanics of Poly(Ethylene 2,5-Furandicarboxylate) Compared to Poly(Ethylene Terephthalate). *Macromolecules* **2018**, *51*, 8539–8549. [CrossRef]
12. Jensen, M.H.; Riisager, A. Advances in the Synthesis and Application of 2,5-Furandicarboxylic Acid. In *Biomass, Biofuels, Biochemicals*; Elsevier: Amsterdam, The Netherlands, 2020; pp. 135–170.
13. Pluta, M.; Bojda, J.; Svyntkivska, M.; Makowski, T.; De Boer, E.L.; Piorkowska, E. Crystallization-Controlled Structure and Thermal Properties of Biobased Poly(Ethylene2,5-Furandicarboxylate). *Polymers* **2024**, *16*, 3052. [CrossRef] [PubMed]
14. Van der Maas, K.; Weinland, D.H.; Van Putten, R.J.; Wang, B.; Gruter, G.J.M. Catalyst Free PET and PEF Polyesters Using a New Traceless Oxalate Chain Extender. *Green. Chemistry* **2024**, *26*, 11182–11195. [CrossRef] [PubMed]
15. Yao, B.; Ni, C.; Chen, M.; Song, H. Self-Assembly and Solid-State Photo Polymerization of Acrylamide Crystal Film. *Colloid. Polym. Sci.* **2009**, *287*, 73–79. [CrossRef]
16. Bernabé Vírseda, I.; Beltrán, F.R.; De la Orden, M.U.; Martínez Urreaga, J. Effects of Solid-State Polymerization on the Structure and Properties of Degraded Poly(3-Hydroxybutyrate-Co-3-Hydroxyvalerate). *Polym. Degrad. Stab.* **2024**, *220*, 110630. [CrossRef]
17. Knoop, R.J.I.; Vogelzang, W.; Van Haveren, J.; Van Es, D.S. High Molecular Weight Poly(Ethylene-2,5-Furanoate); Critical Aspects in Synthesis and Mechanical Property Determination. *J. Polym. Sci. A Polym. Chem.* **2013**, *51*, 4191–4199. [CrossRef]
18. Hong, S.; Min, K.D.; Nam, B.U.; Park, O.O. High Molecular Weight Bio Furan-Based Co-Polyesters for Food Packaging Applications: Synthesis, Characterization and Solid-State Polymerization. *Green. Chemistry* **2016**, *18*, 5142–5150. [CrossRef]
19. Gabirondo, E.; Melendez-Rodriguez, B.; Arnal, C.; Lagaron, J.M.; Martínez De Ilarduya, A.; Sardon, H.; Torres-Giner, S. Organocatalyzed Closed-Loop Chemical Recycling of Thermo-Compressed Food Packaging Films of Poly(Ethylene Furanoate). *Polym. Chem.* **2021**. [CrossRef]
20. Kasmi, N.; Papageorgiou, G.; Achilias, D.; Bikiaris, D. Solid-State Polymerization of Poly(Ethylene Furanoate) Biobased Polyester, II: An Efficient and Facile Method to Synthesize High Molecular Weight Polyester Appropriate for Food Packaging Applications. *Polymers* **2018**, *10*, 471. [CrossRef]
21. Papadopoulos, L.; Xanthopoulou, E.; Nikolaidis, G.N.; Zamboulis, A.; Achilias, D.S.; Papageorgiou, G.Z.; Bikiaris, D.N. Towards High Molecular Weight Furan-Based Polyesters: Solid State Polymerization Study of Bio-Based Poly(Propylene Furanoate) and Poly(Butylene Furanoate). *Materials* **2020**, *13*, 4880. [CrossRef]
22. Stanley, J.; Terzopoulou, Z.; Klonos, P.A.; Zamboulis, A.; Xanthopoulou, E.; Koltsakidis, S.; Tzetzis, D.; Zemljič, L.F.; Lambropoulou, D.A.; Kyritsis, A.; et al. Effect of Monomer Type on the Synthesis and Properties of Poly(Ethylene Furanoate). *Polymers* **2023**, *15*, 2707. [CrossRef]
23. Pohl, H.A. Determination of Carboxyl End Groups in Polyester, Polyethylene Terephthalate. *Anal. Chem.* **1954**, *26*, 1614–1616. [CrossRef]
24. Vouyiouka, S.N.; Karakatsani, E.K.; Papaspyrides, C.D. Solid State Polymerization. *Prog. Polym. Sci.* **2005**, *30*, 10–37. [CrossRef]
25. Ravindranath, K.; Mashelkar, R.A. Modeling of Poly(Ethylene Terephthalate) Reactors. I. A Semibatch Ester Interchange Reactor. *J. Appl. Polym. Sci.* **1981**, *26*, 3179–3204. [CrossRef]
26. Mallon, F.K.; Ray, W.H. Modeling of Solid-State Polycondensation. II. Reactor Design Issues. *J. Appl. Polym. Sci.* **1998**, *69*, 1775–1788. [CrossRef]
27. Ma, Y.; Agarwal, U.S.; Sikkema, D.J.; Lemstra, P.J. Solid-State Polymerization of PET: Influence of Nitrogen Sweep and High Vacuum. *Polymer (Guildf)* **2003**, *44*, 4085–4096. [CrossRef]
28. Ma, Y.; Agarwal, U.S. Solvent Assisted Post-Polymerization of PET. *Polymer* **2005**, *46*, 5447–5455. [CrossRef]
29. Achilias, D.S.; Chondroyiannis, A.; Nerantzaki, M.; Adam, K.V.; Terzopoulou, Z.; Papageorgiou, G.Z.; Bikiaris, D.N. Solid State Polymerization of Poly(Ethylene Furanoate) and Its Nanocomposites with SiO_2 and TiO_2. *Macromol. Mater. Eng.* **2017**, *302*, 1700012. [CrossRef]

30. Kasmi, N.; Majdoub, M.; Papageorgiou, G.; Achilias, D.; Bikiaris, D. Solid-State Polymerization of Poly(Ethylene Furanoate) Biobased Polyester, I: Effect of Catalyst Type on Molecular Weight Increase. *Polymers* **2017**, *9*, 607. [CrossRef]
31. Qu, X.; Zhou, G.; Wang, R.; Zhang, H.; Wang, Z.; Jiang, M.; Tang, J. Insights into High Molecular Weight Poly(Ethylene 2,5-Furandicarboxylate) with Satisfactory Appearance: Roles of in-Situ Catalysis of Metal Zinc. *J. Ind. Eng. Chem.* **2021**, *99*, 422–430. [CrossRef]
32. Zhang, T.; Howell, B.A.; Smith, P.B. Thermal Degradation of Glycerol/Adipic Acid Hyperbranched Poly(Ester)s Containing Either Hydroxyl or Carboxyl End-Groups. *J. Therm. Anal. Calorim.* **2015**, *122*, 1221–1229. [CrossRef]
33. Stoclet, G.; Gobius du Sart, G.; Yeniad, B.; De Vos, S.; Lefebvre, J.M. Isothermal Crystallization and Structural Characterization of Poly(Ethylene-2,5-Furanoate). *Polymer* **2015**, *72*, 165–176. [CrossRef]
34. Fei, X.; Wang, J.; Zhu, J.; Wang, X.; Liu, X. Biobased Poly(Ethylene 2,5-Furanoate): No Longer an Alternative, but an Irreplaceable Polyester in the Polymer Industry. *ACS Sustain. Chem. Eng.* **2020**, *8*, 8471–8485. [CrossRef]

Disclaimer/Publisher's Note: The statements, opinions and data contained in all publications are solely those of the individual author(s) and contributor(s) and not of MDPI and/or the editor(s). MDPI and/or the editor(s) disclaim responsibility for any injury to people or property resulting from any ideas, methods, instructions or products referred to in the content.

polymers

MDPI

Review

Inulin as a Biopolymer; Chemical Structure, Anticancer Effects, Nutraceutical Potential and Industrial Applications: A Comprehensive Review

Isaac Karimi [1,2,*], Mahnaz Ghowsi [2], Layth Jasim Mohammed [3], Zohreh Haidari [1], Kosar Nazari [1] and Helgi B. Schiöth [4,*]

[1] Research Group of Bioengineering and Biotechnology, Laboratory for Computational Physiology, Department of Biology, Faculty of Science, Razi University, P.O. Box 67149-67346, Kermanshah, Iran; z.haidari@stu.razi.ac.ir (Z.H.); kosarnazari@stu.razi.ac.ir (K.N.)
[2] Department of Biology, Faculty of Science, Razi University, P.O. Box 67149-67346, Kermanshah, Iran; ghowsi.mahnaz@razi.ac.ir
[3] Department of Medical Microbiology, College of Medicine, Babylon University, Hilla City 51002, Babylon Governorate, Iraq; med996.layth.jasim@uobabylon.edu.iq
[4] Department of Surgical Sciences, Functional Pharmacology and Neuroscience, Uppsala University, 751 24 Uppsala, Sweden
* Correspondence: isaac_karimi2000@yahoo.com or karimiisaac@razi.ac.ir (I.K.); helgi.schioth@uu.se (H.B.S.); Tel./Fax: +98-83-34274545 (I.K.); +46-18-4714160 (H.B.S.)

Abstract: Inulin is a versatile biopolymer that is non-digestible in the upper alimentary tract and acts as a bifidogenic prebiotic which selectively promotes gut health and modulates gut–organ axes through short-chain fatty acids and possibly yet-to-be-known interactions. Inulin usage as a fiber ingredient in food has been approved by the FDA since June 2018 and it is predicted that the universal inulin market demand will skyrocket in the near future because of its novel applications in health and diseases. This comprehensive review outlines the known applications of inulin in various disciplines ranging from medicine to industry, covering its benefits in gut health and diseases, metabolism, drug delivery, therapeutic pharmacology, nutrition, and the prebiotics industry. Furthermore, this review acknowledges the attention of researchers to knowledge gaps regarding the usages of inulin as a key modulator in the gut–organ axes.

Keywords: fructans; inulin; prebiotics; *Bifidobacterium*; pharmaceutics; nutraceuticals

1. Introduction

Valentin Rose the Younger, a German pharmacologist, isolated inulin, a fructan, from the roots of *Inula helenium* in 1804, and Thomson coined the term inulin in 1917 (for a review see [1]. Inulin is the second most abundant carbohydrate storage in plants and is distributed across various parts such as bulbs, roots, root tubers, leaf bases, grains, and fruits. Dicotyledonous plants such as the Asteraceae and Campanulaceae families are rich sources of inulin. Nutritional inulin-containing plants include leek, onion, garlic, asparagus, Jerusalem artichoke, dahlia, chicory, yacon, etc. (Figure 1; [2]). Therefore, inulins with various origins are found in nature, and inulin and its inulin-laden products have been used in different applications, mainly in the food and drug industries, in all countries for more than two centuries.

Figure 1. Well-known plant resources of inulin. From left to right, the root of chicory (*Cichorium intybus*), sunchoke (*Jerusalem artichoke*), and dahlia tubers (*Dahlia pinnata*).

Inulin is not enzymatically assimilated in the upper alimentary tract; therefore, it does not alter blood glucose levels nor interfere with the insulin–glucagon counter-balance [3]. Basically, inulin is a prebiotic, which is a non-digestible ingredient resistant to gastric acidity and enzymatic digestion. At the same time, inulin can be fermented by the colonic microbiota and can stimulate the growth and activity of some colonic beneficial bacteria necessary for health and well-being. The inulin-type fructans (inulin and fructooligosaccharides (FOS)) have prebiotic effects. Because inulin has β (2→1) linkages, it reaches the colon intact, without enzymatic hydrolysis in the upper gastrointestinal tract. It is hydrolyzed by β-fructosidase-producing bacteria and increases the *Bifidobacteria* population (bifidogenic effect) in the colon [4]. Therefore, the demand for inulin-based products will skyrocket in the next decade mainly because of their usage as prebiotics in health and diseases (www.transparencymarketresearch.com; accessed on 20 December 2024; [5]).

2. Methodology of Literature Review

An electronic literature search of various databases was stochastically performed for publications in English. These databases included PubMed, Web of sciences, Embase, and Scopus. This stochastic review recaps the chemical characteristics and various applications of inulin.

3. Chemical Structure

In the inulin structure, linear chains of fructosyl groups are linked by (2→1) glycosidic bonds and α-D-(1→2) glucopyranoside rings are at their ends (Figure 2; Table 1). Plant-derived inulins have 2–100 fructose units and their aqueous solubility depends on chain length (Figure 2; [6]). Usually, inulin has a linear structure but some inulins have branches connected by β-(2→6) linkages. Based on their degree of polymerization (DP), inulin-type fructans can be divided into FOS (DP $\leq$ 10) and inulin (DP > 10; [7]). The DP of plant-derived inulin varies from 2–60 and its molecular weight is less than 10^4 Da; however, microbial inulin has a higher molecular weight of $>10^6$ Da. Nonetheless, it is not completely clear whether their physiological properties are different or not [8]; however, various FOS compounds (n = 13) and FOS substances (n = 113) were reported with their DP in PubChem (https://pubchem.ncbi.nlm.nih.gov/ accessed on 12 December 2024; Supplementary File S1). It seems that the physicochemical properties of various FOSs and inulins are different and dependent on DP. In essence, the molecular diversity of FOS and inulin enables investigation into their quantitative structure-activity relationship for the discovery of novel variants in both plant and microbial resources.

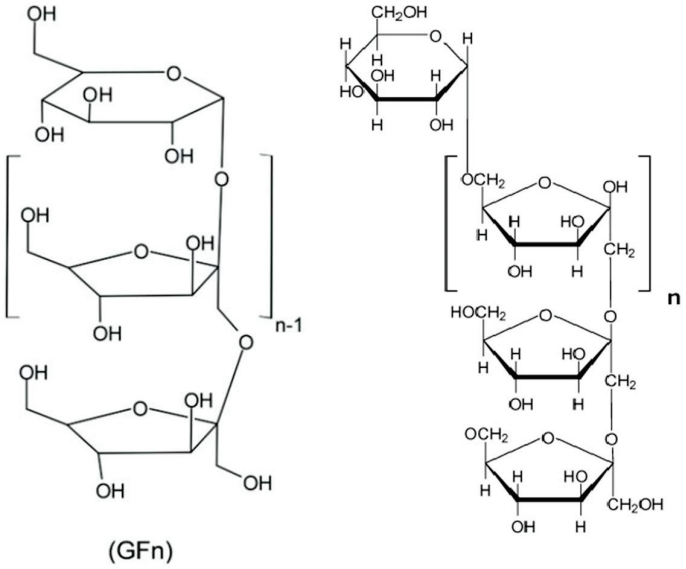

Figure 2. Inulin $(C_6H_{10}O_5)_n$ (**left**) and fructooligosaccharide $(C_6H_{10}O_5)_n$ (**right**) structure [9].

The molecular weight of short-chain inulin depends on its chain length and varies between 1500–1600 Da [2]. For fructan production in plants, sucrose–sucrose fructosyltransferase (EC 2.4.1.99) catalyzes the transfer of a fructose molecule from one sucrose moiety to another for the formation of a kestose known as glucosyl-1, 2 fructosyl-1, 2 fructose. Fructan–fructan–fructosyltransferase (EC 2.4.1.100) elongates the inulin chain [10]. In addition, inulin can be produced by some microorganisms via a fructosyltransferase called inulosucrase (EC 2.4.1.9, sucrose: 2, 1-β-D-fructan 1-β-D-fructosyltransferase). This enzyme transfers fructose residues from sucrose and during this process, a polysaccharide chain connected by β-(2, 1) fructosyl linkages is formed and inulin polymers are generated [11]. Interestingly, one study performed enzymatic production of inulin. The recombinant *Lactobacillus gasseri* inulosucrase produced inulin from sucrose as the sole substrate with an average molecular weight of 5.858×10^6 Da under the optimal conditions of pH 5.5, 25 °C, an enzyme dosage of 4.5 U/g sucrose, a sucrose concentration of 50% (*w*/*v*), and a reaction time of 1.5 h [12]. In addition, neo-inulin and neo-levan types of fructans with internal glucose residues can also be found [13]. Interestingly, another study [14] demonstrated that furanose-based polysaccharides, such as inulin, levan, and arabinan, exhibit a variety of conformational states. At the level of mono-, di-, or polysaccharides, the dynamic geometries of both the glycosidic linkages and the furanose rings remain largely unchanged and independent of one another. In summary, because of increased demands for inulin with different physicochemical and pharmaceutical features (for a review see [15], more tools in bioengineering and biotechnology must be employed to produce various inulin biopolymers or bio-oligomers with novel applications.

Despite the high market demand for inulin and inulin-based products, inulin faces several limitations in industrial applications, including its temperature sensitivity, which leads to degradation at high temperatures, restricting its use in processes like baking [16,17]. Its low solubility in water limits its functionality in certain beverages and syrups, while its variability in molecular weight can result in inconsistent properties, necessitating additional processing [18]. High doses of inulin may cause digestive discomfort, reducing its suitability for sensitive consumers, and its extraction and purification can be costly, making it less competitive compared to other fibers [19]. Furthermore, its functional benefits are concentration-dependent, and it is prone to hydrolysis in acidic conditions, limiting its stability in low-pH products. Limited consumer awareness and regulatory

challenges in some regions also hinder its broader adoption. Addressing these issues through improved technologies, formulations, and education can help expand inulin's industrial potential.

Table 1. The physicochemical properties of inulin compounds reported by https://pubchem.ncbi.nlm.nih.gov/ accessed on 12 December 2024.

	Name/ PubChem CID	Molecular Weight g/mol	XLogP3-AA	Hydrogen Bond Donor Count	Hydrogen Bond Acceptor Count	Rotatable Bond Count	Topological Polar Surface Area Å	Canonicalized
$C_{228}H_{382}O_{191}$ 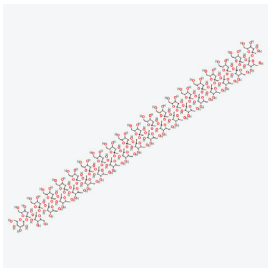	Inulin [USP: BAN]/ 18772499]	6179	−70.2	116	191	149	3040	Yes
$C_{24}H_{42}O_{21}$ 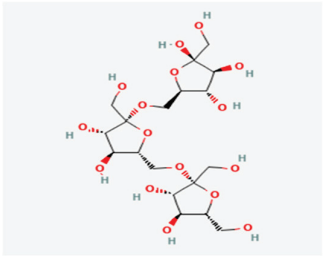	Inulin—chicory Inulin—*Jerusalem artichoke*/ 132932783	666.6	−7.4	14	21	13	384	Yes
$C_{18}H_{32}O_{16}$ 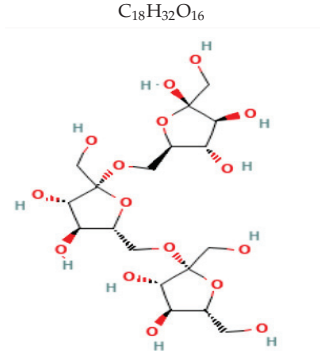	Levan—*Erwinia herbicola* 440946	504.4	−6	11	16	10	296	Yes

Note: Inulin; Linear chain of β(2→1)-linked fructosyl groups with α-D-(1→2) glucopyranoside at the end and Levan; linear or branched chain of β(2→6)-linked fructosyl groups, with possible β(2→1) branches.

4. Pharmaceutical and Pharmacological Applications of Inulin

The LADMET (liberation, absorption, distribution, metabolism, excretion, and toxicity) of beta-D-Fructofuranose, FOS, and inulin were discussed in a review [15], which highlighted the liberation of drugs from various inulin-based drug delivery systems (DDSs) and the findings are partly presented in Supplementary File S2. Inulin has many pharmaceutical applications (Figure 3). In this context, inulin can be used orally to deliver drugs to the colon. Physicochemically, inulin has a high molecular weight and melting temperature, low solubility, and it is slightly viscous when dissolved. Inulin has high molecular flexibility and low glass transition (Tg) in comparison with other oligo- or polysaccharides because of its (2→1) linked d-fructosyl backbone [20]. Because inulin has a low number of reducing groups, it is a suitable excipient for drugs, although the reducing groups can cause protein

degradation. Inulin has low hygroscopicity and its crystallization rate is low. The aforementioned features make inulin a good stabilizer for proteins [21]. In this context, some studies have also shown that similarly to small sugars such as trehalose, mannitol and so on, inulin may be a good stabilizer for some pharmaceutical systems against physical and chemical degradation. For instance, one study showed that lyophilization of alkaline phosphatase with inulin preserved its activity [22]. Moreover, inulin renders a protective property to bovine plasma protein against denaturation during the freeze-drying procedure [23,24]. Inulin can be used for the spray freeze-drying of acyl-homoserine-lactone (AHL) acylases without loss of their activities [21]. This may be due to high molecular flexibility and because of the low steric hindrance of inulin [21]. In this regard, it has been shown that inulin protects PEGylated lipoplexes against aggregation during lyophilization and storage for three months. Likewise, inulin can be an appropriate stabilizer for different PEGylated nanoparticles [21]. One study suggested that inulin preserves doxorubicin-loaded (PEG) 3-PLA nanopolymers during lyophilization [25]. Inulin sugar glasses conserved the activity and structural integrity of influenza virosomes during freeze-drying and storage [26]. In this vein, inulin can stabilize hemagglutinin during freezing and freeze-drying and it is a suitable cryo-and lyo-protectant for this subunit of influenza vaccine [27]. The inclusion of Δ^9-tetrahydrocanabidol (THC) as an unstable drug in inulin by spray-freeze drying and lyophilization strongly increased its stability [28,29]. To sum up, the genuine aforementioned features of inulin can be bio-mimicked for use in various industries ranging from fabricating sugar glasses to coating enzymes and therapeutic peptides.

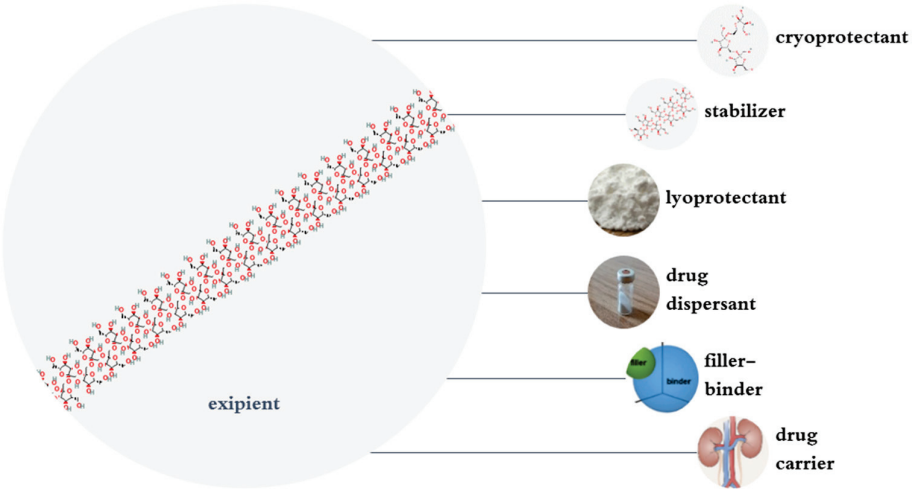

Figure 3. Various applications of inulin in the pharmaceutical industry.

One of the most promising methods for the improvement of the oral bioavailability of poorly water-soluble drugs is solid dispersion using compounds like inulin. In the gastrointestinal tract, these drugs dissolve slowly and their bioavailability is low. Inulin exhibits high solubility, particularly in water at elevated temperatures, which facilitates faster hydration and improved dissolution of poorly soluble drugs. This property makes it a valuable excipient in pharmaceutical formulations for enhancing drug bioavailability [21]. In this regard, one study compared the applicability of inulin, one surface-active derivative of inulin called inutec R Sp1, and polyvinylpyrolodone (PVP), as carriers in solid dispersions prepared by spray-freeze drying [30]. These carriers served to enhance the solubility of some lipophilic drugs such as diazepam, fenofibrate, ritonavir, efavirenz. The results showed that the dissolution rate of these drugs in the solution of various drugs was raised in the following order: inulin 2.3 kDa < PVP k30 << inutec R SP1. Another study showed

that the incorporation of super disintegrants in solid dispersion tablets that contain the drug enhanced the solubility level of fenofibrate [31]. Solid dispersion tablets composed of inulin 4 kDa showed a fast dissolution capability and excellent storage stability [31]. A fast-dissolving, inulin-based solid dispersion tablet containing poorly soluble human immunodeficiency virus protease inhibitor, TMC240, has been marketed [32]. Research findings showed that solid dispersion of TMC240 in an inulin matrix amplified the in vitro and in vivo release of TMC2400. Different amorphous inulin types can be used as filler binders for tablets prepared by direct compaction and inulins with longer chains that have slower dissolution can be used as filler binders for chewable tablets or lozenges [21]. One study investigated the dissolution behavior of tablets composed of poorly aqueous soluble diazepam and inulin DP11 and inulin DP23. In this case, diazepam was incorporated in these inulin types in the amorphous state by freeze-drying using solvents like water and tertiary butyl alcohol. The study showed that fast dissolution of diazepam was observed with slow-dissolving carriers, such as these types of inulins [28]. In another study, labile lipophilic THC molecules were incorporated in a glassy matrix of inulin and the authors showed that this inulin-based solid dispersion may be an approach to fabricating tablets of THC for sublingual administration because this formulation released the THC very fast—in around 3 min [33]. Therefore, inulin-based biopolymers can enhance the bioavailability of an array of drugs that have low human intestinal absorption and may improve the LADME criteria of drugs.

In addition to the aforementioned role of inulin as a stabilizer, it was employed as a drug carrier for various organs [15–34]. Routinely, inulin has been used as the "gold standard" for measuring glomerular filtration rate (GFR) because after intravenous administration, inulin does not bind to the blood proteins and after its filtration by the kidneys, it is not reabsorbed, metabolized or secreted by kidneys. These properties make inulin a unique material for measuring GFR [9] and an effective drug carrier for nephron-related pathologies. Accordingly, potential DDSs were manufactured, which can be employed for the direct delivery of anti-infective or anti-inflammatory drugs straight to the urinary tract [9]. Moreover, inulin can be used to form a self-assembled micelle system in water which incorporates vitamin E (hydrophobic drug) and releases it in a well-ordered manner. For instance, vitamin E-succinate was linked to inulin by an ester bond and formed amphiphilic inulin-based polymers with hydrolyzable groups. In this context, particulates of hydroxyapatite inulin incorporated in novel poly(e-caprolactone) (PCL) microporous matrices have been used to produce bone substitutes and for the precise delivery of bioactive macromolecules that may be used in formulating long-term, controlled release devices for bioactive molecules such as hormones and extended-residence supports for tissue development and cell growth [35]. One of the most important challenges in medical research is targeting drugs to the large intestine for treating colonic disorders. Free films were prepared using a combination of inulin as a bacterially degradable system and time- or pH-dependent polymers as a coating formulation for colonic DDSs [36]. The utilization of inulin as a preparatory polymer starting material for the production of DDSs is based on its unique properties. For example, it is degradable by colon bacteria and it and its metabolites are nontoxic [35]. Inulin was also mixed with divinyl sulfone and succinic anhydride to formulate a biodegradable hydrogel through crosslinking with trimethylolpropane tris (3-mercaptopropionate). The resulting hydrogels were saturated with the 2-anti-cancer model drug methoxyestradiol (2-ME), an endogenous angiogenic metabolite of estrogen, and evaluated for their therapeutic potential in colorectal carcinoma and in vitro release. These pH-sensitive hydrogels had extraordinary properties such as swelling, stability in virtual gastric fluid, and biodegradability in the presence of inulinase and esterase. These

worthy features make hydrogels suitable candidates for treating colorectal cancer through their efficient drug delivery [37,38]. To prepare amphiphilic inulin graft copolymer that can self-assemble in water into a micelle-type structure and to deliver the anticancer model drug doxorubicin, inulin was chemically modified and conjugated with polyethylene glycol 2000 and succinyl-ceramide [39]. These polymeric micelles released intact doxorubicin for a sustained period without a first burst release. An inulin-based glycovesicle was reported for pathogen-targeted drug delivery to control salmonellosis [40]. In summary, these are a few examples of the many applications of inulin in modern pharmaceutical technology and DDSs.

Inulin can also be applied in pharmaceutics as an auxiliary therapeutic agent for certain diseases (for a review see [21]. In this context, inulin-type fructans hasten the absorption of some minerals such as calcium, magnesium, copper, iron, and zinc in both humans and animals [41,42]. Broadly, various studies show that inulin can increase the calcium absorption and deposition of calcium in the bone of rats and humans (for a review see [43] and may be helpful in the prevention of calcium-deficient conditions like osteoporosis and rapid somatic growth. Similarly, the administration of inulin-type fructans increased the absorption of minerals and bone mineral accretion when combined with probiotic *Lactobacilli*. Inulin may increase absorption surface and expression of calcium-binding proteins in the large intestine and decrease intestinal lumen pH which in turn, increases the solubility of minerals in the gut. Furthermore, inulin suppresses bone resorption and increases the bioavailability of phytoestrogens by stimulating beneficial microorganisms in the gut. In addition, ITFs can improve mineral absorption by stabilizing the intestinal flora and reducing inflammation. Therefore, its consumption may be beneficial in the prevention and treatment of musculoskeletal diseases [41–44]. Consistently with the aforementioned studies, consumption of short- and long-chain inulin fructans (8 g/day for one year) in young adolescents increased calcium absorption and bone mineral density [45]. Butyrate is the main fermentative product of inulin and is a strong stimulator of CaBP-9kDa expression that stimulates the calcium absorption pathway through increasing 1, 25 (OH)2D3 receptor binding [46]. Similarly, two studies reported that 75 g/kg inulin in a semi-purified diet stimulated the absorption of magnesium, copper, and zinc in rats of different ages [47,48]. In this context, young male rats treated with inulin-type fructans increased the phosphorus content of bone in two weeks [49]. Various factors such as the dietary content of minerals or fructans and background diet, sex, age, and hormonal status may alter the effects of inulin-type fructans on the absorption of minerals [41]. In essence, the mechanisms of improved intestinal absorption of minerals in the presence of inulin-based formulation need to be investigated more deeply. Technically, various industrial efforts are welcomed to investigate the fermentative products of inulin using different bioreactors to develop formulations for the better absorption of minerals.

Inulin has many therapeutic potentials in metabolic and infectious diseases. For instance, high doses of inulin (40–100 g/d) are effective in diabetic patients [50]. The dietary supplementation of 8 g of FOS for two weeks reduced serum glucose levels in type II diabetic patients, while dietary supplementation with FOS did not alter serum glucose in healthy subjects [51]. As mentioned above, inulin has (2–1) linkages and human digestive enzymes such as α-glucosidase, maltase, isomaltase, and sucrase cannot hydrolyze these linkages; therefore, pristine inulin will be fermented and converted to lactate, gases, and short-chain fatty acids (SCFAs) such as acetate, propionate, and butyrate in ceco-colon [10–52]. Perhaps the hypoglycemic effects of inulin may be due to propionate production because it exerts a hypoglycemic effect via inhibition of hepatic gluconeogenesis [26–52]. Inulin decreases blood levels of fatty acids and triacylglycerols and their hepatic

biosynthesis. An intake of 8 g of short-chain FOS/d for two weeks decreased fasting blood glucose and serum total cholesterol levels in diabetic patients. Nonetheless, serum high-density-lipoprotein (HDL) cholesterol, triacylglycerols, and fatty acids were not significantly altered. The mechanisms by which short-chain FOS can modulate glucose and lipid metabolism are not completely known [53]. Moreover, some animal and human studies have demonstrated that inulin and oligofructoses obtained from inulin have lipid-lowering effects [54]. In rats, long-term consumption of high doses of oligofructoses reduced blood cholesterol levels [54–56]. It has been reported that inulin consumption in breakfast cereal (9 g/d) or as a powdered addition to beverages and meals (10 g/d) reduced fasting triacylglycerols up to 27 and 19%, respectively [54]. These effects may be mediated by reducing the secretion of very low-density lipoprotein (VLDL) particles from the liver and reducing the activity and gene expression of fatty acid synthetase [54]. One study hitherto showed that consumption of 14 g/day inulin for 4 weeks did not affect the fasting total, low-density lipoprotein (LDL) or HDL cholesterol, or serum triacylglycerols [57]. Likewise, the modest hyperlipidemic subjects taking inulin showed reduced LDL levels without concomitant alteration in HDL cholesterol and serum triacylglycerols levels [58]. Inulin may be useful in regulating nitrogen balance by reducing blood urea and uric acid concentration [10]. In an impressive review [59] the lipid-lowering properties of dietary polysaccharides like inulin have been discussed.

The exact therapeutic and prophylactic effects of inulin for metabolic syndrome have not been determined, but an array of reviews have focused on the improvement of some of the therapeutic effects of inulin in this case [60–64]. These systematic reviews pertained to the microbial community of the gut and its roles in stabilizing the gut barrier and producing useful postbiotics that modulate some receptors that are involved in glucose and fatty acid metabolism. To the best of our knowledge, the direct interaction of inulins and FOSs with the mucous membrane of the gut has not been discussed (Figure 4).

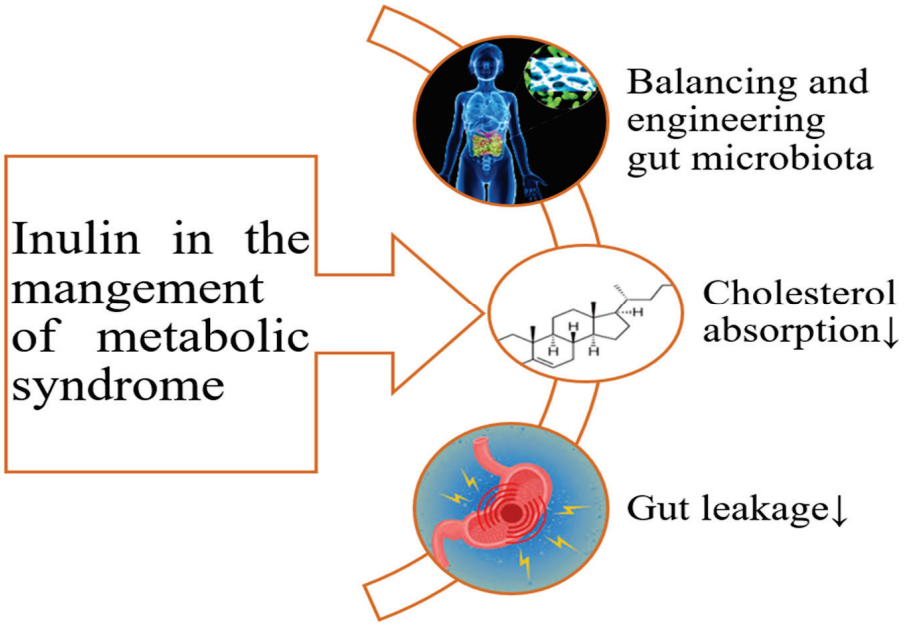

Figure 4. The impact of inulin on the management of metabolic syndrome; Note: ↓ shows decline.

Inulin may be useful in regulating nitrogen balance by reducing blood urea and uric acid concentrations [10]. Despite the many reviews (e.g., [65,66]) that report on the metabolic effects of inulin in health and diseases, there is no study that pertains to the

impact of inulin on amino acid and nucleotide intermediary metabolism. In conclusion, the mechanisms by which inulin and inulin-derived oligofructoses, and short-chain FOS can modulate glucose, amino acid, and fatty acid metabolism are mysterious and warrant future investigations.

5. Anticancer Effects of Inulin

Cancer is a leading cause of death, with a profound impact on healthcare systems worldwide. Challenges in prophylaxis and oncotherapy include chemotherapy resistance, off-target effects of chemotherapeutic agents that exhibit severe adverse effects, and the expensiveness of current chemotherapeutic agents. In recent years, inulin as a naturally occurring prebiotic fiber has gained ample attention for its potential in cancer treatment owing to its unique structure, stability, and nutritional properties which highlight it as an effective auxiliary therapeutic, adjuvant and carrier for drug delivery in cancer therapy (for a review see [34,67–70]; Figure 5). In this vein, efforts towards the development of therapeutic inulin-based nanomaterials and nanocomposites with a special emphasis on the multifunctional role of inulin in oncotherapy as a signaling, synergistic, immunomodulatory and anticarcinogenic molecule have been pursued [68–70]. A recent review [70], provides a succinct overview of current clinical trials and observational studies associated with inulin-based oncotherapy. Over the past decades, natural polysaccharides, as well as biopolymers, have been widely developed for targeting colon cancer using various DDSs [68]. Inulin was used in colorectal tumors not only as an entrapment material concerning its degradation by enzymes in the colonic microflora and its drug release behavior in a sustained and controlled manner, but also as a dietary fiber with added well-being benefits. In conclusion, to the best of our knowledge, mechanisms beyond the anti-cancer effects of inulin have not been addressed until now.

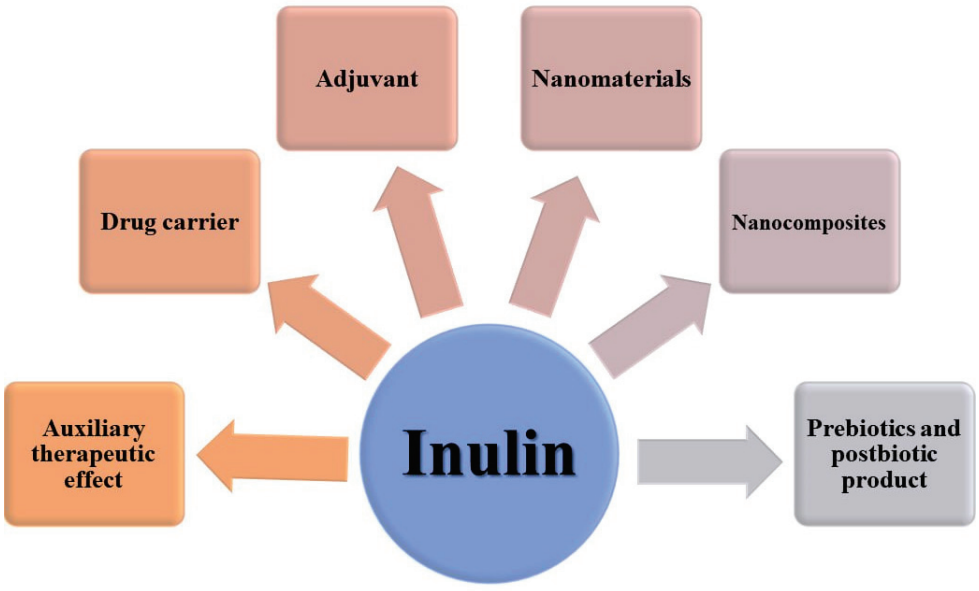

Figure 5. The various portals of inulin applications in oncotherapy.

6. Nutraceutical Potentials of Inulin

Several studies have evaluated the antioxidative activity of inulin (for a review see [71]). In this regard, one study showed that dietary supplementation with inulin improved the feed consumption and egg production rate of laying hens and increased the antioxidative activities of superoxide dismutase (SOD), catalase (CAT), glutathione peroxidase (GSH-Px),

and serum total antioxidant capacity and reduced levels of malondialdehyde, an index of lipid peroxidation [72]. It has been reported that dietary supplementation of inulin increased *Bifidobacteria* and *Lactobacilli* counts in the ceca of laying hens. *Bifidobacterium* spp. are lactic acid-producing bacteria that have SOD and lactic acid, both of which help scavenge free radicals. Another study indicated that pre-treatment with inulin prevents impairment of the colonic smooth muscle cell contractility induced by lipopolysaccharide exposure by a decrease in mucosal production of free radicals [73]. Another study focused on the antioxidative activity of inulin-based prebiotics, which promotes the development of functional fermented goat milk, indicated that the radical scavenging rate reached 75.52% and the scavenging rate of superoxide radicals was 21.09%. The researchers pointed out that inulin improved the nutritional value of functional foods [74]. In a similar vein, an impressive and seminal study reported on the consumption of a combination of the probiotic bacteria *Lactobacillus casei* (4×10^8 colony-forming unit (CFU)) and prebiotic inulin (400 mg) and suggested that dietary supplementation with this symbiotic may prevent oxidative stress in the plasma of healthy volunteers by increasing the ferric reducing ability of plasma (FRAP) and CAT activity [75]. In another study, the antioxidant activity of carboxymethyl inulin (CMI) was enhanced by chemical modification. The results revealed a significant enhancement in antioxidant activity upon the introduction of cationic Schiff bases into CMI as compared to the commercially available antioxidant Vc [76]. Therefore, the direct and indirect antioxidative effects of inulin that are mediated through the improvement of gut microbiota place inulin in a superior position to combat oxidative stress in both health and disease.

The regular intake of dietary fiber boosts the gut microbiome and health of the host in several ways. Dietary fibers (DFs) are indigestible products that have become a vital ingredient to be included in every healthy diet. DF is defined as carbohydrate polymers containing ≥ 10 monomeric units that resist digestion by endogenous enzymes in the small intestine. DF includes edible carbohydrate polymers, and synthesized carbohydrate polymers [65]. DF can be divided into "soluble DF" (SDF) and "insoluble DF" (IDF) according to solubility, and it can be further categorized into "partially fermentable fiber" and "completely fermentable fiber" based on its fermentability [65]. The health benefits of DF for hosts are revealed mainly by changes in gut microbiota composition and microbial metabolites. In this context, the role of inulin as a prebiotic DF is at the heart of the biopharmaceutical applications of this biopolymer, which may be due to its ability to modulate gut microbiota, enhance gut health and gut–organ axes (e.g., gut–kidney axis; Figure 6), and improve metabolic processes (for a review see [5–15]). Prebiotics can be described as "selectively fermented ingredients that alter the configuration and activity in the gastrointestinal microbiota that confer positive effect". In a seminal review [77], the beneficial impact of the dietary inclusion of inulin in human and animal models was discussed. The authors concluded that inulin as a fructan prebiotic can be a part of functional food products that promote health benefits to consumers. The review also vindicates the efficacy of inulin as a stabilizer, fat replacer, component in nanoformulations, and humectant in the cosmetic industry. Interestingly, hydrophobically modified inulin (HMI) has applications like the targeted release of drugs. In essence, it is important to explore the properties of SCFA inulin esters because they are less studied. Furthermore, HMI stabilizes various dispersion formulations as an excipient for producing hydrophobic drugs because inulin is generally recognized as safe (Figure 7; [78]). Therefore, inulin and inulin-based products may have health-promoting activities such as acting as DF, prebiotics, and drug carriers in the gut.

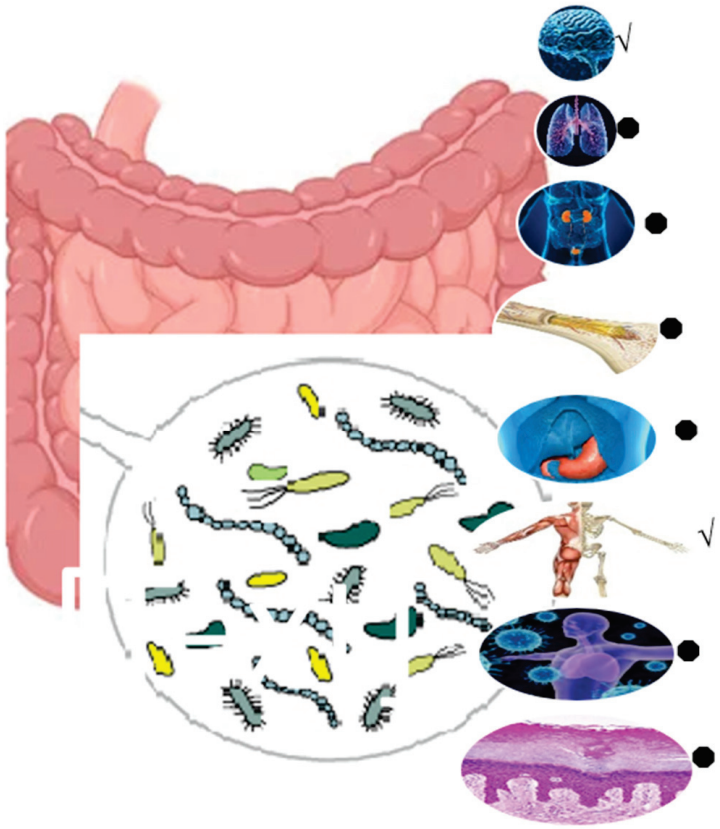

Figure 6. The effect of inulin on the gut–organ axes. √ and • express axes with greater and fewer publications, respectively.

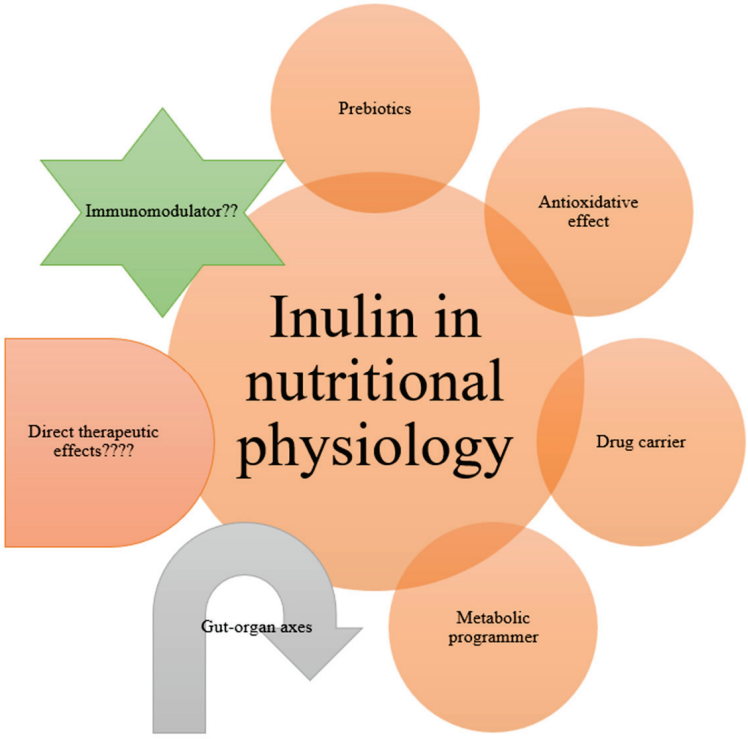

Figure 7. The role of inulin in nutritional physiology.

The prebiotic impact of inulin on the management of gastrointestinal disorder has been the subject of many studies (for a review see [79]). These researchers reviewed the positive

impact of prebiotics in experimental colitis and human inflammatory bowel disease (IBD), and concluded that inulin has trophic effects on gut microflora via the enhancement of colonic production of short-chain fatty acids (SCFAs) and the subsequent growth of indigenous lactobacilli and bifidobacteria, decreasing mucosal lesion and mucosal inflammation by promoting host defense against invasion and pathogen translocation, and inhibiting gastrointestinal diseases like IBD. The therapeutic effects of prebiotic inulin-type fructans in severe bowel diseases like active and inactive Crohn's disease need more deep investigations [80]. In another review [19], the history of inulin as a prebiotic and its ability to enhance the growth and functionality of Bifidobacterium bacteria, as well as its effect on host gene expression and metabolism, were discussed. Finally, the authors proposed symbiotic (inulin plus probiotics) applications in the management of a group of diseases including cardiometabolic diseases after a deep discussion about various controversies regarding the effects of inulin on the health and diseases of the gut. In this continuum, the symbiotic formulations of inulin and other probiotics were reviewed [19–81]. Moreover, a bibliographic review focused on human clinical studies highlighted the main effects of inulin on human metabolic health, with a special focus on the mechanisms of action of this prebiotic. The authors concluded that inulin supplementation contributes to anthropometric indices control and improves metabolic status mainly through the selective favoring of SCFA-producer species from the genera Bifidobacterium and Anaerostipes [66]. In a seminal review [82], the role of inulin in the establishment of the gut microbial community during the first 1000 days of a child's life was discussed, and the impact of inulin on the prevention of enteric diseases in adulthood was highlighted, in addition to the role of fructans in metabolic programming. In this context, another review [83] pertained to the microbial-derived products, including SCFAs, lipopolysaccharides and secondary bile acids, that may be involved in the regulation of hepatic lipid metabolism. Finally, they concluded that the relationships between bacterial species (e.g., competition and mutualism), play key roles in the degradation of inulin and the regulation of the microbial structure. Regarding the therapeutic effects of inulin-type fructans (ITFs) and prebiotics on IBDs and Crohn's disease, the findings of different studies are controversial, possibly due to the altering microbial community (for a review see [84,85]. In a systematic review [86], all aspects of inulin-type fructans including short-chain fructooligosaccharides (scFOS), oligofructose, and inulin were deeply discussed and the authors proposed the personalization of prebiotic applications in precise and personalized medicine. To personalize the ITFs, we must focus on the plasticity of the microbial community of the intestine, postbiotics produced during microbial modulation, and their effects on extra-intestinal tissues (for a review, see [87,88]. In addition to the DF formulation of inulin, innovative synthetic or semi-synthetic inulin-based delivery systems, such as hydrogels and nanoparticles, are designed for their sustained and controlled-release formulations. The mechanisms and bacterial enzymes involved in inulin degradation by gut microbiota have been reviewed [89]. An inulin-rich flour has been formulated from *Smallanthus sonchifolius*, popularly known as yacon, which is a member of the *Asteraceae* family (for a review see [64]. The authors showed that the intake of yacon flour can reduce glycemia, HbA1c, advanced glycation ends, plasma lipids, body fat mass, body weight, and waist circumference and improve intestinal microbiota and antioxidant status. In conclusion, inulin has many applications in the nutraceutical sector, especially for innovating new functional formulations in feed/food technologies; however, further studies are welcomed to assess its effects on gut–organ axes.

An array of investigations focused on the food and feed markets and the associated technologies of inulin and its byproducts (Figure 8) [7,20,21,34,71,81,90–98].

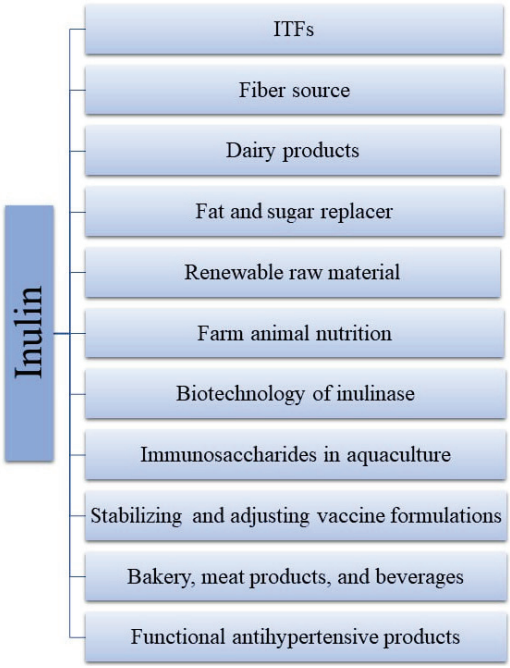

Figure 8. Schematic summary of possible applications for the global market of inulin. ITFs: inulin-type fructans.

7. Conclusions and Remark

Inulin can be considered a treasure trove for many applications in various industries, and many countries are involved in mass producing this economic polysaccharide (https://www.fortunebusinessinsights.com/industry-reports/inulin-market-101512, accessed on 23 January 2025). In this overview, we have tried to consolidate the current and possible applications of inulin by reviewing seminal studies, current reviews, and systematic reviews focused on inulin to offer an integrated package, and to highlight the knowledge gaps. Nowadays, inulin and ITFs are predominantly used as prebiotics to engineer gut microbiota and alleviate metabolic diseases like diabetes mellitus; however, inulin's role in modulating gut–organ axes remains to be investigated deeply. In addition, studies on the non-medical applications of inulin in synthesizing new bio-engineering products are scarce. Key areas for the usage of inulin products are the dairy, bakery, beverage, and meat industries as sugar and fat replacements, despite their shortcomings. The application of inulin as an immunosaccharide in the aquaculture sector would be a new opportunity that warrants more investigation. In conclusion, a quick search of inulin in Google images will clarify the many medicinal and industrial products made of inulin in the global market. This review has tried to demonstrate the economic importance of inulin in a comprehensive manner.

Supplementary Materials: The following supporting information can be downloaded at: https://www.mdpi.com/article/10.3390/polym17030412/s1, File S1: Physicochemical features and degree of polymerization of fructooligosaccharides; File S2: FOS, beta-D-fructofuranose, levan, and inulin.

Author Contributions: Conceptualization, I.K. and H.B.S.; methodology, I.K.; software, I.K. and L.J.M.; validation, I.K., L.J.M. and Z.H.; formal analysis, Z.H. and K.N.; investigation, I.K. and M.G.; resources, L.J.M.; data curation, I.K., K.N., Z.H. and L.J.M.; writing—original draft preparation, M.G. and I.K.; writing—review and editing, I.K. visualization, I.K. and H.B.S.; supervision, I.K. and H.B.S.; project administration, I.K. and H.B.S.; funding acquisition, L.J.M. and H.B.S. All authors have read and agreed to the published version of the manuscript.

Funding: The APC was funded by Uppsala University.

Acknowledgments: The authors are thankful to Razi University, Babylon University, and Uppsala University for supporting this study.

Conflicts of Interest: We declare no conflict of interest among authors in publishing this review paper.

References

1. Boeckner, L.S.; Schnepf, M.I.; Tungland, B.C. Inulin: A review of nutritional and health implications. **2001**. *Adv. Food Nutr. Res.* **2001**, *43*, 1–63. [PubMed]
2. Singh, R. Enzymatic preparation of high fructose syrup from inulin. In *Bioprocessing of Foods*; Asiatech Publishing Inc.: New Delhi, India, 2011; pp. 77–98.
3. Delzenne, N.M.; Kok, N.N. Nutritional and health benefits of inulin and oligofructose. *J. Nutr.* **1999**, *129*, 1402S–1406S.
4. Gibson, G.R.; Probert, H.M.; Van Loo, J.; Rastall, R.A.; Roberfroid, M.B. Dietary modulation of the human colonic microbiota: Updating the concept of prebiotics. *Nutr. Res. Rev.* **2004**, *17*, 259–275. [CrossRef] [PubMed]
5. Tiwari, R.; Sethi, P.; Rudrangi, S.R.S.; Padarthi, P.K.; Kumar, V.; Rudrangi, S.; Vaghela, K. Inulin: A multifaceted ingredient in pharmaceutical sciences. *J. Biomater. Sci. Polym. Ed.* **2024**, *35*, 2570–2595. [CrossRef]
6. Barclay, T.; Ginic-Markovic, M.; Johnston, M.R.; Cooper, P.D.; Petrovsky, N. Analysis of the hydrolysis of inulin using real time 1H NMR spectroscopy. *Carbohydr. Res.* **2012**, *352*, 117–125. [CrossRef]
7. Ni, D.; Xu, W.; Zhu, Y.; Zhang, W.; Zhang, T.; Guang, C.; Mu, W. Inulin and its enzymatic production by inulosucrase: Characteristics, structural features, molecular modifications and applications. *Biotechnol. Adv.* **2019**, *37*, 306–318. [CrossRef]
8. Slavin, J. Fiber and prebiotics: Mechanisms and health benefits. *Nutrients* **2013**, *5*, 1417–1435. [CrossRef]
9. Mandracchia, D.; Tripodo, G.; Latrofa, A.; Dorati, R. Amphiphilic inulin-d-α-tocopherol succinate (INVITE) bioconjugates for biomedical applications. *Carbohydr. Polym.* **2014**, *103*, 46–54. [CrossRef]
10. Kaur, N.; Gupta, A.K. Applications of inulin and oligofructose in health and nutrition. *J. Biosci.* **2002**, *27*, 703–714. [CrossRef]
11. Banguela, A.; Hernández, L. Fructans: From natural sources to transgenic plants. *Biotecnol. Apl.* **2006**, *23*, 202–210.
12. Ni, D.; Zhu, Y.; Xu, W.; Bai, Y.; Zhang, T.; Mu, W. Biosynthesis of inulin from sucrose using inulosucrase from Lactobacillus gasseri DSM 20604. *Int. J. Biol. Macromol.* **2018**, *109*, 1209–1218. [CrossRef] [PubMed]
13. Peshev, D.; Van den Ende, W. Fructans: Prebiotics and immunomodulators. *J. Funct. Foods* **2014**, *8*, 348–357. [CrossRef]
14. Nester, K.; Plazinski, W. Conformational properties of inulin, levan and arabinan studied by molecular dynamics simulations. *Carbohydr. Polym.* **2020**, *240*, 116266. [CrossRef] [PubMed]
15. Akram, W.; Pandey, V.; Sharma, R.; Joshi, R.; Mishra, N.; Garud, N.; Haider, T. Inulin: Unveiling its potential as a multifaceted biopolymer in prebiotics, drug delivery, and therapeutics. *Int. J. Biol. Macromol.* **2024**, *259*, 129131. [CrossRef]
16. Böhm, A.; Kaiser, I.; Trebstein, A.; Henle, T. Heat-induced degradation of inulin. *Eur. Food Res. Technol.* **2005**, *220*, 466–471. [CrossRef]
17. Glibowski, P.; Bukowska, A. The effect of pH, temperature and heating time on inulin chemical stability. *Acta Sci. Pol. Technol. Aliment.* **2011**, *10*, 189–196.
18. Du, M.; Cheng, X.; Qian, L.; Huo, A.; Chen, J.; Sun, Y. Extraction, physicochemical properties, functional activities and applications of inulin polysaccharide: A review. *Plant Foods Hum. Nutr.* **2023**, *78*, 243–252. [CrossRef]
19. Tawfick, M.M.; Xie, H.; Zhao, C.; Shao, P.; Farag, M.A. Inulin fructans in diet: Role in gut homeostasis, immunity, health outcomes and potential therapeutics. *Int. J. Biol. Macromol.* **2022**, *208*, 948–961. [CrossRef]
20. Mensink, M.A.; Frijlink, H.W.; van der Voort Maarschalk, K.; Hinrichs, W.L. Inulin, a flexible oligosaccharide I: Review of its physicochemical characteristics. *Carbohydr. Polym.* **2015**, *130*, 405–419. [CrossRef]
21. Mensink, M.A.; Frijlink, H.W.; van der Voort Maarschalk, K.; Hinrichs, W.L. Inulin, a flexible oligosaccharide. II: Review of its pharmaceutical applications. *Carbohydr. Polym.* **2015**, *134*, 418–428. [CrossRef]
22. Hinrichs, W.; Prinsen, M.; Frijlink, H. Inulin glasses for the stabilization of therapeutic proteins. *Int. J. Pharm.* **2001**, *215*, 163–174. [CrossRef] [PubMed]
23. Furlán, L.T.R.; Padilla, A.P.; Campderrós, M.E. Inulin like lyoprotectant of bovine plasma proteins concentrated by ultrafiltration. *Int. Food Res.* **2010**, *43*, 788–796. [CrossRef]
24. Furlán, L.T.R.; Lecot, J.; Padilla, A.P.; Campderrós, M.E.; Zaritzky, N. Effect of saccharides on glass transition temperatures of frozen and freeze dried bovine plasma protein. *J. Food Eng.* **2011**, *106*, 74–79. [CrossRef]

25. Ayen, W.Y.; Kumar, N. A systematic study on lyophilization process of polymersomes for long-term storage using doxorubicin-loaded (PEG) 3–PLA nanopolymersomes. *Eur. J. Pharm. Sci.* **2012**, *46*, 405–414. [CrossRef] [PubMed]
26. de Jonge, J.; Amorij, J.-P.; Hinrichs, W.L.; Wilschut, J.; Huckriede, A.; Frijlink, H.W. Inulin sugar glasses preserve the structural integrity and biological activity of influenza virosomes during freeze-drying and storage. *Eur. J. Pharm. Sci.* **2007**, *32*, 33–44. [CrossRef]
27. Amorij, J.; Meulenaar, J.; Hinrichs, W.; Stegmann, T.; Huckriede, A.; Coenen, F.; Frijlink, H. Rational design of an influenza subunit vaccine powder with sugar glass technology: Preventing conformational changes of haemagglutinin during freezing and freeze-drying. *Vaccine* **2007**, *25*, 6447–6457. [CrossRef]
28. Van Drooge, D.; Hinrichs, W.; Frijlink, H. Anomalous dissolution behaviour of tablets prepared from sugar glass-based solid dispersions. *J. Control. Release* **2004**, *97*, 441–452. [CrossRef]
29. van Drooge, D.-J.; Hinrichs, W.L.; Dickhoff, B.H.; Elli, M.N.; Visser, M.R.; Zijlstra, G.S.; Frijlink, H.W. Spray freeze drying to produce a stable Δ9-tetrahydrocannabinol containing inulin-based solid dispersion powder suitable for inhalation. *Eur. J. Pharm. Sci.* **2005**, *26*, 231–240. [CrossRef]
30. Srinarong, P.; Hämäläinen, S.; Visser, M.R.; Hinrichs, W.L.; Ketolainen, J.; Frijlink, H.W. Surface-active derivative of inulin (Inutec® SP1) is a superior carrier for solid dispersions with a high drug load. *J. Pharm. Sci.* **2011**, *100*, 2333–2342. [CrossRef]
31. Srinarong, P.; Faber, J.; Visser, M.; Hinrichs, W.; Frijlink, H. Strongly enhanced dissolution rate of fenofibrate solid dispersion tablets by incorporation of superdisintegrants. *Eur. J. Pharm. Biopharm.* **2009**, *73*, 154–161. [CrossRef]
32. Visser, M.R.; Baert, L.; van't Klooster, G.; Schueller, L.; Geldof, M.; Vanwelkenhuysen, I.; De Kock, H.; De Meyer, S.; Frijlink, H.W.; Rosier, J. Inulin solid dispersion technology to improve the absorption of the BCS Class IV drug TMC240. *Eur. J. Pharm. Biopharm.* **2010**, *74*, 233–238. [CrossRef] [PubMed]
33. Van Drooge, D.; Hinrichs, W.; Wegman, K.; Visser, M.; Eissens, A.; Frijlink, H. Solid dispersions based on inulin for the stabilisation and formulation of Δ9-tetrahydrocannabinol. *Eur. J. Pharm. Sci.* **2004**, *21*, 511–518. [CrossRef] [PubMed]
34. Wan, X.; Guo, H.; Liang, Y.; Zhou, C.; Liu, Z.; Li, K.; Niu, F.; Zhai, X.; Wang, L. The physiological functions and pharmaceutical applications of inulin: A review. *Carbohydr. Polym.* **2020**, *246*, 116589. [CrossRef] [PubMed]
35. Coombes, A.; Rizzi, S.; Williamson, M.; Barralet, J.; Downes, S.; Wallace, W. Precipitation casting of polycaprolactone for applications in tissue engineering and drug delivery. *Biomaterials* **2004**, *25*, 315–325. [CrossRef]
36. Akhgari, A.; Farahmand, F.; Garekani, H.A.; Sadeghi, F.; Vandamme, T.F. Permeability and swelling studies on free films containing inulin in combination with different polymethacrylates aimed for colonic drug delivery. *Eur. J. Pharm. Sci.* **2006**, *28*, 307–314. [CrossRef]
37. Pitarresi, G.; Tripodo, G.; Calabrese, R.; Craparo, E.F.; Licciardi, M.; Giammona, G. Hydrogels for Potential Colon Drug Release by Thiol-ene Conjugate Addition of a New Inulin Derivative. *Macromol. Biosci.* **2008**, *8*, 891–902. [CrossRef]
38. Liang, X.; Lin, D.; Zhang, W.; Chen, S.; Ding, H.; Zhong, H.-J. Progress in the Preparation and Application of Inulin-Based Hydrogels. *Polymers* **2024**, *16*, 1492. [CrossRef]
39. Licciardi, M.; Scialabba, C.; Sardo, C.; Cavallaro, G.; Giammona, G. Amphiphilic inulin graft co-polymers as self-assembling micelles for doxorubicin delivery. *J. Mater. Chem. B* **2014**, *2*, 4262–4271. [CrossRef]
40. Xu, Y.; Niu, C.; Liang, S.; Guo, J.; Li, K.; Zhang, J.; Li, J.; Jin, Y.; Bai, J.; Dai, J. An inulin-based glycovesicle for pathogen-targeted drug delivery to ameliorate salmonellosis. *Int. J. Biol. Macromol.* **2024**, *267*, 131656. [CrossRef]
41. Scholz-Ahrens, K.E.; Schrezenmeir, J. Inulin and oligofructose and mineral metabolism: The evidence from animal trials. *J. Nutr.* **2007**, *137*, 2513S–2523S. [CrossRef]
42. Dunshea, F.; Pluske, J.; Ponnampalam, E. Dietary iron or inulin supplementation alters iron status, growth performance, intramuscular fat and meat quality in finisher pigs. *Meat Sci.* **2024**, *213*, 109496. [CrossRef] [PubMed]
43. Bakirhan, H.; Karabudak, E. Effects of inulin on calcium metabolism and bone health. *Int. J. Vitam. Nutr. Res.* **2023**, *93*, 85–96. [CrossRef] [PubMed]
44. Gao, S.; Zhao, X.; Leng, Y.; Xia, Z. Dietary supplementation with inulin improves burn-induced skeletal muscle atrophy by regulating gut microbiota disorders. *Sci. Rep.* **2024**, *14*, 2328. [CrossRef]
45. Abrams, S.A.; Griffin, I.J.; Hawthorne, K.M.; Liang, L.; Gunn, S.K.; Darlington, G.; Ellis, K.J. A combination of prebiotic short-and long-chain inulin-type fructans enhances calcium absorption and bone mineralization in young adolescents. *T. Am. J. Clin. Nutr.* **2005**, *82*, 471–476. [CrossRef] [PubMed]
46. Maiyar, A.C.; Norman, A.W. Effects of sodium butyrate on 1, 25-dihydroxyvitamin D3 receptor activity in primary chick kidney cells. *Mol. Cell. Endocrinol.* **1992**, *84*, 99–107. [CrossRef]
47. Coudray, C.; Rambeau, M.; Feillet-Coudray, C.; Tressol, J.C.; Demigne, C.; Gueux, E.; Mazur, A.; Rayssiguier, Y. Dietary inulin intake and age can significantly affect intestinal absorption of calcium and magnesium in rats: A stable isotope approach. *Nutr. J.* **2005**, *4*, 1–8. [CrossRef]

48. Coudray, C.; Feillet-Coudray, C.; Gueux, E.; Mazur, A.; Rayssiguier, Y. Dietary inulin intake and age can affect intestinal absorption of zinc and copper in rats. *J. Nutr.* **2006**, *136*, 117–122. [CrossRef]
49. Takahara, S.; Morohashi, T.; Sano, T.; Ohta, A.; Yamada, S.; Sasa, R. Fructooligosaccharide consumption enhances femoral bone volume and mineral concentrations in rats. *J. Nutr.* **2000**, *130*, 1792–1795. [CrossRef]
50. ROOT, H.F.; BAKER, M.L. Inulin and artichokes in the treatment of diabetes. *Arch. Intern. Med.* **1925**, *36*, 126–145. [CrossRef]
51. Costa, G.T.; Guimarães, S.B.; Sampaio, H.A.d.C. Fructo-oligosaccharide effects on blood glucose: An overview. *Acta Cir. Bras.* **2012**, *27*, 279–282. [CrossRef]
52. Roberfroid, M. Dietary fiber, inulin, and oligofructose: A review comparing their physiological effects. *Crit. Rev. Food Sci. Nutr.* **1993**, *33*, 103–148. [CrossRef] [PubMed]
53. Liu, F.; Prabhakar, M.; Ju, J.; Long, H.; Zhou, H. Effect of inulin-type fructans on blood lipid profile and glucose level: A systematic review and meta-analysis of randomized controlled trials. *Eur. J. Clin. Nutr.* **2017**, *71*, 9–20. [CrossRef] [PubMed]
54. Williams, C.M. Effects of inulin on lipid parameters in humans. *J. Nutr.* **1999**, *129*, 1471S–1473S. [CrossRef] [PubMed]
55. Delzenne, N.M.; Kok, N.; Fiordaliso, M.-F.; Deboyser, D.M.; Goethals, F.M.; Roberfroid, M.B. Dietary fructooligosaccharides modify lipid metabolism in rats. *Am. J. Clin. Nutr.* **1993**, *57*, 820S. [CrossRef]
56. Fiordaliso, M.; Kok, N.; Desager, J.P.; Goethals, F.; Deboyser, D.; Roberfroid, M.; Delzenne, N. Dietary oligofructose lowers triglycerides, phospholipids and cholesterol in serum and very low density lipoproteins of rats. *Lipids* **1995**, *30*, 163–167. [CrossRef]
57. Pedersen, A.; Sandström, B.; Van Amelsvoort, J.M. The effect of ingestion of inulin on blood lipids and gastrointestinal symptoms in healthy females. *Br. J. Nutr.* **1997**, *78*, 215–222. [CrossRef]
58. Davidson, M.H.; Maki, K.C.; Synecki, C.; Torri, S.A.; Drennan, K.B. Effects of dietary inulin on serum lipids in men and women with hypercholesterolemia. *Nutr. Res.* **1998**, *18*, 503–517. [CrossRef]
59. Yin, D.; Zhong, Y.; Liu, H.; Hu, J. Lipid metabolism regulation by dietary polysaccharides with different structural properties. *Int. J. Biol. Macromol.* **2024**, *270*, 132253. [CrossRef]
60. O'Connor, S.; Chouinard-Castonguay, S.; Gagnon, C.; Rudkowska, I. Prebiotics in the management of components of the metabolic syndrome. *Maturitas* **2017**, *104*, 11–18. [CrossRef]
61. Li, L.; Li, P.; Xu, L. Assessing the effects of inulin-type fructan intake on body weight, blood glucose, and lipid profile: A systematic review and meta-analysis of randomized controlled trials. *Food Sci. Nutr.* **2021**, *9*, 4598–4616. [CrossRef]
62. Mohammadi, F.; Shiri, A.; Tahmouzi, S.; Mollakhalili-Meybodi, N.; Nematollahi, A. Application of inulin in bread: A review of technological properties and factors affecting its stability. *Food Sci. Nutr.* **2023**, *11*, 639–650. [CrossRef] [PubMed]
63. El-Nashar, H.A.; Taleb, M.; EL-Shazly, M.; Zhao, C.; Farag, M.A. Polysaccharides (pectin, mucilage, and fructan inulin) and their fermented products: A critical analysis of their biochemical, gut interactions, and biological functions as antidiabetic agents. *Br. J. Nutr.* **2024**, *38*, 662–693. [CrossRef] [PubMed]
64. Silva, I.F.d.; Bragante, W.R.; Junior, R.C.M.; Laurindo, L.F.; Guiguer, E.L.; Araújo, A.C.; Fiorini, A.M.; Nicolau, C.C.; Oshiiwa, M.; Lima, E.P.d. Effects of Smallanthus sonchifolius Flour on Metabolic Parameters: A Systematic Review. *Pharmaceuticals* **2024**, *17*, 658. [CrossRef] [PubMed]
65. Sheng, W.; Ji, G.; Zhang, L. Immunomodulatory effects of inulin and its intestinal metabolites. *Front. Immunol.* **2023**, *14*, 1224092. [CrossRef]
66. Alonso-Allende, J.; Milagro, F.I.; Aranaz, P. Health Effects and Mechanisms of Inulin Action in Human Metabolism. *Nutrients* **2024**, *16*, 2935. [CrossRef]
67. Di Bartolomeo, F.; Startek, J.; Van den Ende, W. Prebiotics to fight diseases: Reality or fiction? *Phytother. Res.* **2013**, *27*, 1457–1473. [CrossRef]
68. Chadha, S.; Kumar, A.; Srivastava, S.A.; Behl, T.; Ranjan, R. Inulin as a delivery vehicle for targeting colon-specific cancer. *Curr. Drug Deliv.* **2020**, *17*, 651–674. [CrossRef]
69. Illippangama, A.U.; Jayasena, D.D.; Jo, C.; Mudannayake, D.C. Inulin as a functional ingredient and their applications in meat products. *Carbohydr. Polym.* **2022**, *275*, 118706. [CrossRef]
70. Ghali, E.N.H.K.; Chauhan, S.C.; Yallapu, M.M. Inulin-based formulations as an emerging therapeutic strategy for cancer: A comprehensive review. *Int. J. Biol. Macromol.* **2024**, *259*, 129216. [CrossRef]
71. Gupta, N.; Jangid, A.K.; Pooja, D.; Kulhari, H. Inulin: A novel and stretchy polysaccharide tool for biomedical and nutritional applications. *Int. J. Biol. Macromol.* **2019**, *132*, 852–863. [CrossRef]
72. Shang, H.-M.; Zhou, H.-Z.; Yang, J.-Y.; Li, R.; Song, H.; Wu, H.-X. In vitro and in vivo antioxidant activities of inulin. *PLoS ONE* **2018**, *13*, e0192273. [CrossRef] [PubMed]

73. Pasqualetti, V.; Altomare, A.; Guarino, M.P.L.; Locato, V.; Cocca, S.; Cimini, S.; Palma, R.; Alloni, R.; De Gara, L.; Cicala, M. Antioxidant activity of inulin and its role in the prevention of human colonic muscle cell impairment induced by lipopolysaccharide mucosal exposure. *PLoS ONE* **2014**, *9*, e98031. [CrossRef] [PubMed]
74. Shu, G.; He, Y.; Wan, H.; Hui, Y.; Li, H. Effects of prebiotics on antioxidant activity of goat milk fermented by Lactobacillus plantarum L60. *Acta Univ. Cibiniensis-Ser. E Food Technol.* **2017**, *21*, 11–18. [CrossRef]
75. Kleniewska, P.; Hoffmann, A.; Pniewska, E.; Pawliczak, R. The influence of probiotic Lactobacillus casei in combination with prebiotic inulin on the antioxidant capacity of human plasma. *Oxidative Med. Cell Longev.* **2016**, *2016*, 1340903. [CrossRef]
76. Chen, Y.; Zhang, H.; Chen, Q.; Mi, Y.; Guo, Z. Synthesis and characterization of novel carboxymethyl inulin derivatives bearing cationic Schiff bases with antioxidant potential. *Int. J. Biol. Macromol.* **2024**, *275*, 133761. [CrossRef]
77. Bhanja, A.; Sutar, P.P.; Mishra, M. Inulin-A polysaccharide: Review on its functional and prebiotic efficacy. *J. Food Biochem.* **2022**, *46*, e14386. [CrossRef]
78. Usman, M.; Zhang, C.; Patil, P.J.; Mehmood, A.; Li, X.; Bilal, M.; Haider, J.; Ahmad, S. Potential applications of hydrophobically modified inulin as an active ingredient in functional foods and drugs-A review. *Carbohydr. Polym.* **2021**, *252*, 117176. [CrossRef]
79. Akram, W.; Garud, N.; Joshi, R. Role of inulin as prebiotics on inflammatory bowel disease. *Drug Discov. Ther.* **2019**, *13*, 1–8. [CrossRef]
80. Anderson, J.L.; Hedin, C.R.; Benjamin, J.L.; Koutsoumpas, A.; Ng, S.C.; Hart, A.L.; Forbes, A.; Stagg, A.J.; Lindsay, J.O.; Whelan, K. Dietary intake of inulin-type fructans in active and inactive Crohn's disease and healthy controls: A case–control study. *J. Crohns Colitis* **2015**, *9*, 1024–1031. [CrossRef]
81. Yoo, S.; Jung, S.-C.; Kwak, K.; Kim, J.-S. The Role of Prebiotics in Modulating Gut Microbiota: Implications for Human Health. *Int. J. Mol. Sci.* **2024**, *25*, 4834. [CrossRef]
82. Vaughan, E.E.; Le Danh Tuyen, P.D.; Chongviriyaphan, N.; Wang, W.; Dillon, D.H.; Meyer, D.; Bindels, J.; Hautvast, J.; Ong, S.; Khan, N.C. Fructans in the first 1000 days of life and beyond, and for pregnancy. *Asia Pac. J. Clin. Nutr.* **2016**, *25*, 652–675.
83. Hu, Y.; He, J.; Zheng, P.; Mao, X.; Huang, Z.; Yan, H.; Luo, Y.; Yu, J.; Luo, J.; Yu, B. Prebiotic inulin as a treatment of obesity related nonalcoholic fatty liver disease through gut microbiota: A critical review. *Crit. Rev. Food Sci. Nutr.* **2023**, *63*, 862–872. [CrossRef] [PubMed]
84. Wilson, B.; Whelan, K. Prebiotic inulin-type fructans and galacto-oligosaccharides: Definition, specificity, function, and application in gastrointestinal disorders. *Asia. Pac. J. Clin. Nutr.* **2017**, *32*, 64–68. [CrossRef] [PubMed]
85. Man, S.; Liu, T.; Yao, Y.; Lu, Y.; Ma, L.; Lu, F. Friend or foe? The roles of inulin-type fructans. *Carbohydr. Polym.* **2021**, *252*, 117155. [CrossRef] [PubMed]
86. Hughes, R.L.; Alvarado, D.A.; Swanson, K.S.; Holscher, H.D. The prebiotic potential of inulin-type fructans: A systematic review. *Adv. nutr.* **2022**, *13*, 492–529. [CrossRef]
87. Swanson, K.; De Vos, W.; Martens, E.; Gilbert, J.; Menon, R.; Soto-Vaca, A.; Hautvast, J.; Meyer, P.; Borewicz, K.; Vaughan, E. Effect of fructans, prebiotics and fibres on the human gut microbiome assessed by 16S rRNA-based approaches: A review. *Benef. Microbes.* **2020**, *11*, 101–129. [CrossRef]
88. Tian, R.; Yu, L.; Tian, F.; Zhao, J.; Chen, W.; Zhai, Q. Effect of inulin, galacto-oligosaccharides, and polyphenols on the gut microbiota, with a focus on Akkermansia muciniphila. *Food Funct.* **2024**, *15*, 4763–4772. [CrossRef]
89. Wang, W.; Fan, Z.; Yan, Q.; Pan, T.; Luo, J.; Wei, Y.; Li, B.; Fang, Z.; Lu, W. Gut microbiota determines the fate of dietary fiber-targeted interventions in host health. *Gut Microbes* **2024**, *16*, 2416915. [CrossRef]
90. Yeo, S.-K.; Ooi, L.-G.; Lim, T.-J.; Liong, M.-T. Antihypertensive properties of plant-based prebiotics. *Int. J. Mol. Sci.* **2009**, *10*, 3517–3530. [CrossRef]
91. Apolinário, A.C.; de Lima Damasceno, B.P.G.; de Macêdo Beltrão, N.E.; Pessoa, A.; Converti, A.; da Silva, J.A. Inulin-type fructans: A review on different aspects of biochemical and pharmaceutical technology. *Carbohydr. Polym.* **2014**, *101*, 368–378. [CrossRef]
92. Buriti, F.C.; Saad, S.M. Chilled milk-based desserts as emerging probiotic and prebiotic products. *Crit. Rev. Food Sci. Nutr.* **2014**, *54*, 139–150. [CrossRef] [PubMed]
93. Nisha Rakhesh, N.R.; Fellows, C.; Sissons, M. Evaluation of the technological and sensory properties of durum wheat spaghetti enriched with different dietary fibres. *J. Sci. Food Agric.* **2014**, *95*, 2–11. [CrossRef] [PubMed]
94. Kumar Singh, P.; Kumar, V.; Yadav, R.; Shukla, P. Bioengineering for microbial inulinases: Trends and applications. *Curr. Protein Pept. Sci.* **2017**, *18*, 966–972.
95. Nawaz, A.; Irshad, S.; Hoseinifar, S.H.; Xiong, H. The functionality of prebiotics as immunostimulant: Evidences from trials on terrestrial and aquatic animals. *Fish Shellfish. Immunol.* **2018**, *76*, 272–278.
96. Yan, M.R.; Welch, R.; Rush, E.C.; Xiang, X.; Wang, X. A sustainable wholesome foodstuff; health effects and potential dietotherapy applications of yacon. *Nutrients* **2019**, *11*, 2632. [CrossRef]

97. Farag, M.A.; Jomaa, S.A.; Abd El-Wahed, A.; El-Seedi, H.R. The many faces of kefir fermented dairy products: Quality characteristics, flavour chemistry, nutritional value, health benefits, and safety. *Nutrients* **2020**, *12*, 346. [CrossRef]
98. de Carvalho Correa, A.; Lopes, M.S.; Perna, R.F.; Silva, E.K. Fructan-type prebiotic dietary fibers: Clinical studies reporting health impacts and recent advances in their technological application in bakery, dairy, meat products and beverages. *Carbohydr. Polym.* **2024**, *323*, 121396. [CrossRef]

Disclaimer/Publisher's Note: The statements, opinions and data contained in all publications are solely those of the individual author(s) and contributor(s) and not of MDPI and/or the editor(s). MDPI and/or the editor(s) disclaim responsibility for any injury to people or property resulting from any ideas, methods, instructions or products referred to in the content.

polymers

MDPI

Article

Comparing the Printability, Biological and Physicochemical Properties of Bio-Based Photo-Crosslinkable Hydrogels

Ane García-García [1,2], Unai Silván [2,3], Leyre Pérez-Álvarez [1,2,*] and Senentxu Lanceros [2,3]

[1] Innovative Macromolecular Materials Group (Imacromat), Physical Chemistry Department, Faculty of Science and Technology, University of the Basque Country UPV/EHU, 48940 Leioa, Spain; ane.garcia@bcmaterials.net
[2] BCMaterials, Basque Center for Materials, Applications and Nanostructures, UPV/EHU Science Park, 48940 Leioa, Spain; unai.silvan@bcmaterials.net (U.S.); senentxu.lanceros@bcmaterials.net (S.L.)
[3] Ikerbasque, Basque Foundation for Science, 48009 Bilbao, Spain
* Correspondence: leyre.perez@ehu.eus; Tel.: +34-946012709

Abstract: Bio-based photo-crosslinkable hydrogels are used in tissue engineering as three-dimensional printable scaffolds due to their functional and biological similarities with the extracellular matrix (ECM). In this work, emerging bioink candidates such as chitosan, alginate and gelatin-based photo-crosslinkable hydrogel were developed using extrusion-based 3D printing to establish a better understanding of their applicability. The polymers were methacrylated by the same methacrylation reaction pathway, which enabled successful light-induced 3D printing. Morphology, swelling (6–40%), mechanical (Young's modulus, 0.1–0.5 KPa) and rheological properties (300–1000 Pa), degradation kinetics (10->60 days) and printability of the gels were also characterized in identical conditions for the first time. 3D-printability results indicated that methacrylated gelatin enhanced printability, shape fidelity and integrity of printed structures compared to methacrylated alginate, which presents structural instability and poorer printing control due to its low crosslink density. Moreover, cell attachment and Live/Dead assays using bone marrow-derived mesenchymal stem cells (BM-MSCs) showed that all formulations have good biocompatibility for use as scaffolds. Specifically, gelatin-based hydrogels showed a higher level of BM-MSCs attachment and spreading than the other types of hydrogels. Overall, our results suggest that the hydrogels based on these three biopolymers present good potential as a biomaterial for light-induced extrusion-based 3D printing.

Keywords: photo-crosslinkable hydrogels; extrusion-based 3D printing; methacrylated alginate; methacrylated chitosan; methacrylated gelatin

1. Introduction

The development of materials that provide a three-dimensional environment capable of structural and biochemical support for the tissue, promoting cell proliferation and enhancing cell properties, is crucial for tissue engineering applications [1]. In this regard, 3D printing is identified as a promising technology for the precise fabrication of three-dimensional (3D) scaffolds.

Amongst the range of printing technologies, extrusion-based 3D printing has garnered significant attention due to its simplicity, scalability [2], cost-effectiveness, accessibility and the lack of energy-intensive sources, such as lasers, which could affect the cells [3].

Hydrogels are one of the most promising classes of ink for creating 3D-printed scaffolds, as they possess a high structural and functional similarity to the extracellular ma-

trix [4]. Meanwhile, hydrogel networks present good biocompatibility, biodegradability and high-water absorption capability. Furthermore, hydrogels can be easily modified and dynamically adapted to the changing needs of the culture of different cell types [1,5]. Among the different types of hydrogels, photo-crosslinkable hydrogels enable the fabrication of highly complex and precise 3D structures, since light controls the gelation process spatially and temporally. In addition, photo-crosslinking is a rapid method that works under mild conditions, ensuring the preservation of sensitive biological components such as proteins and cells [6].

Polysaccharides and polymers of peptidic origin are commonly used in the development of printable hydrogels [7]. Polysaccharides are a group of complex polymers isolated from a wide range of renewable resources, including plants, animals, and microbes [8]. This is the case of alginate, which is derived from diverse resources, such as the cell walls of brown seaweed or bacteria and is one of the most widely studied natural polymers [8]. Alginate is composed of two homopolymeric blocks, 1,4-β-D-mannuronic acid (M) and 1,4-α-L-guluronic acid (G) [9] and is typically studied for biomedical applications due to its good biocompatibility, solubility, porosity, hydrophilicity and injectability [7]. Another polysaccharide of natural origin that is commonly used in the form of a hydrogel in tissue engineering is chitosan, which is composed of D-glucosamine and N-acetyl glucosamine units linked by β-glycosidic bonds (1-4). This polymer exhibits excellent antimicrobial and antioxidant activity, mucoadhesivity, biodegradability and high biological compatibility [10–13]. As a bio-ink for 3D-printing, chitosan has demonstrated stability under physiological conditions, appropriate viscosity, and ability to support effective cell proliferation and differentiation [14]. Regarding natural polymers of peptidic origin, they are widely found in living organisms and generally have specific bioactive activities (including antibacterial, anti-inflammatory, tissue and cell adhesion, promotion of cell proliferation and migration, etc.) [7]. Among them, gelatin is a natural polymer derived from the hydrolyzation of collagen, the major component of cartilage, bone, skin, connective tissue and the extracellular matrix in animals, which presents biocompatibility, biodegradability, low antigenicity, easy processing, abundant availability in nature and cost-effectiveness [15,16]. Due to these valuable characteristics, gelatin is considered an ideal material that can be easily adapted as a bio-ink for 3D printing [17–20].

In recent years, hydrogels derived from these three biopolymers have emerged as among the most versatile and widely used materials in 3D bio-printing. These natural polymers have been adapted for use in a variety of additive manufacturing techniques, including extrusion-based bio-printing and digital light processing (DLP); however, it remains a challenge to print high-resolution constructs with adequate functionality [21–24].

In the case of alginate, ionotropic gelation of unmodified alginate is the most widely explored strategy for extrusion-based bio-printing, due to its rapid ionic crosslinking [25], but it results in low-resolution constructs. However, more complex formulations of alginate in combination with other biopolymers have shown high printing fidelity and applicability in a wide range of tissues, including bone [17] or skin [26]. Regarding photo-crosslinkable alginate, the direct 3D extrusion-based photo-printing of concentrated solutions of methacrylated alginate proves to be inefficient in the absence of external crosslinking agents [27]. However, Gharacheh et al. enhanced the printing quality of methacrylated alginate, together with the osteogenic differentiation of hMSCs cells, reducing the concentration of the biopolymer and incorporating human allograft bone particles [27].

On the other hand, gelatin, which presents good biodegradability and cell adhesiveness, has also been shown to be a suitable candidate for cell encapsulation and printing [18]. Specifically, methacrylated gelatin is commonly employed as bioink in extrusion-based

photo-printing. Methacrylated gelatin was 3D-printed with high fidelity via extrusion with photo-crosslinking (12.5 mW/cm^2) and successfully tested in vivo in a rat condyle defect [28].

Chitosan-based hydrogels, due to their antimicrobial and anti-inflammatory properties [19], have been widely incorporated into bio-printed scaffolds for applications in skin [19] and nerve regeneration [29]. We previously demonstrated the successful extrusion-based printability, biocompatibility and antimicrobial properties of slightly photo-cured methacrylated chitosan scaffolds [14]. However, photo-curing conditions led to poor mechanical properties, which could affect their long-term stability and applicability.

Taking the above into consideration, this study compares 3D printable scaffolds based on photo-crosslinkable alginate, chitosan and gelatin. In recent years, studies on these systems have proliferated, but there is no common criterion for methacrylation conditions, ink formulations, or printing conditions—the main parameters that serve as the basis for comparison. In this respect, the hydrogels were synthesized via photo-crosslinking after methacrylation of the biopolymers, using the same reaction conditions. They were also characterized under identical conditions in terms of morphology, swelling, degradation, rheological and mechanical stability, properties that are highly influenced by hydrogel composition. Additionally, the adhesion properties and cytocompatibility of hydrogels were synchronously and identically characterized in vitro to determine their potential to support cell attachment, proliferation, and viability as biomaterials. This work hypothesizes that by comparatively analyzing the individual properties of these commonly used biocompatible and printable hydrogels, we can provide a practical framework for the selection of suitable bio-inks for specific applications. In addition, these results add fundamental knowledge for the development of functional 3D-printed scaffolds suitable for regenerative medicine applications.

2. Materials and Methods

2.1. Materials

The synthesis of the photo-crosslinked hydrogels was performed by modifying sodium alginate (Sigma-Aldrich, Darmstadt, Germany, W201502, $M_w = 1.1 \times 10^5$ g/mol), chitosan from crab shells (Sigma-Aldrich, Darmstadt, Germany, 48165, $M_w = 8.7 \times 10^5 \pm 4 \times 10^4$ g/mol) and gelatin from porcine skin type A (Sigma-Aldrich, Darmstadt, Germany, G1890, $M_w = 1.7 \times 10^5$ g/mol) with methacrylic anhydride (Sigma-Aldrich, Darmstadt, Germany, 276685). In addition, the photoinitiator lithium phenyl-2,4,6-trimethylbenzoylphosphinate (LAP, Sigma-Aldrich, Darmstadt, Germany, 900889), acetic acid (Sigma Aldrich, Darmstadt, Germany, 33209 for analysis, ≥99.8%), potassium phosphate monobasic (Acros Organics, Geel, Belgium, 447670010, 99%, for analysis), sodium phosphate dibasic (Acros Organics, Geel, Belgium, 448140010, 98%, extra pure), sodium hydroxide (Panreac, Castellar del Valles, Spain, 141687.1211, pure, pharma grade), ethanol (Panreac, Castellar del Valles, Spain,141086.0716, absolute), glutaraldehyde aqueous solution (Sigma-Aldrich, Darmstadt, Germany, 354400, 25%), (3-aminopropyl)triethoxysilane (APTES, Sigma-Aldrich, Darmstadt, Germany, 440140), 3-(trimethylsilyl)-1-propanesulfonic acid sodium salt (TSP, Sigma-Aldrich, Darmstadt, Germany, 178837, 97%), deuterium oxide (Sigma-Aldrich, Darmstadt, Germany, 151882, 99 atom D), acetic acid-d_4 (Sigma-Aldrich, Darmstadt, Germany, 151785, ≥99.5% atom D), and Human Bone Marrow-derived Mesenchymal Stem Cells (BM-MSCs) were purchased by Cell Lines Service (Heidelberg, Alemania, Catalog number CLS-300665). Dulbecco's Modified Eagle Medium (DMEM, Gibco, Waltham, MA, USA, 30030), fetal bovine serum (FBS, Sigma-Aldrich, SV30160.03), formaldehyde (Sigma-Aldrich, Darmstadt, Germany, 50-00-0), penicillin and streptomycin antibiotics

(Gibco, 15140-122), phosphate-buffered saline (PBS, Gibco, 10010-023), NucBlue™ Live Cell Stain ReadyProbes™ Reagent (Thermo Fisher, Waltham, MA, USA, R37605), and LIVE/DEAD™ Cell Imaging kit (Thermo Fisher, Waltham, MA, USA, R37601) were used.

2.2. Preparation of Photo-Crosslinkable Hydrogels

2.2.1. Methacrylation of the Biopolymers

The modification of chitosan was carried out following the method proposed by Kolawole et al. [30] with slight modifications. Methacrylic anhydride (3.1 mL) was added to a 1.5% (*w*/*v*) chitosan solution (0.5% (*v*/*v*) in acetic acid solution and kept stirring at 45 °C for 24 h. The resulting product was then purified through dialysis (12–14 kDa membranes) over 5 days and lyophilized at −50 °C and 0.1 mBar.

For the modification of alginate, the procedure of Chou et al. was followed [31]. Briefly, a 2% (*w*/*v*) solution of sodium alginate in distilled water was prepared. Then, a 20% molar excess of methacrylic anhydride was added to the solution while maintaining the pH at 7.5 using a solution of NaOH 5 M, with constant magnetic stirring for 2 h. Then, the final solution was maintained at 4–8 °C for 24 h, and the reaction was washed with 200 mL of ethanol (30 min × 5 times). The product obtained was dissolved in 60 mL of distilled water, purified via dialysis (3.5 kDa membranes) against sterile water for 5 days and lyophilized at −50 °C and 0.1 mBar.

The modification of gelatin took place according to the procedure of Bektas et al. [32]. Firstly, 10 mL of methacrylic anhydride was added to a 10% (*w*/*v*) solution of gelatin from porcine skin type A (PBS, 50 °C). The obtained product was purified via dialysis (12–14 kDa membranes) against sterile water at 40 °C for 5 days and lyophilized at −50 °C and 0.1 mBar.

2.2.2. Synthesis of Photo-Crosslinkable Hydrogels

For the synthesis of the photo-crosslinked hydrogels of chitosan, a solution of methacrylated chitosan (CHIMe) 1.5% (*w*/*v*) was prepared in a 0.5% (*v*/*v*) acetic acid solution. Separately, the photoinitiator LAP, in a 0.1% (*w*/*w*) concentration with respect to the chitosan, was dissolved using a negligible volume of the previous acetic acid solution (300 µL approximately). Finally, the hydrogels were photo-crosslinked in situ under UV light LEDs (405 nm, 19 mW/cm^2) for 30 s. The same procedure was carried out for the photo-crosslinked hydrogels of alginate, but using a solution of methacrylated alginate (AlgMe) 3% (*w*/*v*) in PBS (pH = 7.4), and for the photo-crosslinked hydrogels of gelatin (GelMe), but employing a solution of methacrylated gelatin (GelMe) 8% (*w*/*v*) prepared in PBS (pH = 7.4).

2.3. Nuclear Magnetic Resonance (^{1}H-NMR)

The degree of methacrylation of the photo-crosslinked hydrogels was determined by nuclear magnetic resonance spectroscopy, using a Bruker Avance (Billerica, MA, USA, 500 MHz spectrometer. In the case of CHIMe, the spectrum was taken using a concentration of 20 mg/mL of the modified polymer in a 99.5% D_2O and 0.5% acetic acid-d_4 at 25 °C. According to literature [30], the methacrylation degree (MD) was calculated based on the ratio of the relative areas of the integration of the protons of the N-acetyl-glucosamine units of chitosan at 2.8–3.9 ppm, and those of the resonance peaks of the methacrylate groups at 5.6–6.0 ppm (Equation (1)).

$$\text{MD CHIMe } (\%) = \frac{\textit{Integral of methacrylate protons at } 5.6 - 6.0 \text{ ppm}/2}{\textit{Integral of chitosan cycle protons at } 2.8 - 3.9 \text{ ppm}/6} \times 100 \quad (1)$$

For AlgMe, the spectrum was taken using a concentration of 20 mg/mL in D_2O at 85 °C, in order to move the water signal out of the spectral region of interest [33]. Based on literature and under the assumption that methacrylation only occurs on guluronic (G) units, both the G unit ratio in the alginate chain and the degree of methacrylation were determined using Equations (2) and (3), respectively. The integral values of the anomeric proton signals of the guluronic and mannuronic units at 5 and 4.3 ppm correspond to H_G and H_M. Likewise, H_a and H_b refer to the integrals of the two vinyl protons of the methacrylic group, located at 5.7 and 6.2 ppm [34].

$$\text{G}\ (\%) = \frac{H_G}{H_M + H_G} \times 100 \tag{2}$$

$$\text{MD AlgMe}\ (\%) = \frac{\frac{H_a + H_b}{2}}{H_G} \times \text{G} \tag{3}$$

Finally, for GelMe, the spectrum was taken using a concentration of 20 mg/mL in D_2O and at 45 °C. To calculate the degree of methacrylation, the method of internal standard using 3-(trimethylsilyl)-1-propanesulfonic acid sodium salt (TSP) was used. The TSP signal appears at 0 ppm and corresponds to 9 protons (H_{TSP}). To calculate the amount of methacrylic units present in the gelatin derivatives, only the integral obtained for the peak with the highest chemical shift (5.6 ppm) was used, which corresponds to one proton (H_M) [35]. Equation (4) was used to calculate the degree of methacrylation of GelMe.

$$\text{MD GelMe}\ (\%) = \frac{H_M}{H_{TSP}} \times \frac{9}{1} \times \frac{n(TSP)[\text{mmol}]}{m(gelatin)[\text{g}]} \tag{4}$$

The shown data corresponds to the average of three samples.

2.4. Morphological Characterization

The morphology and the pore size of the hydrogels were studied using a Hitachi (Tokyo, Japan) S-4800 scanning electron microscope (SEM) (150 s, 20 mA, 15 kV). Hydrogels were previously lyophilized (−50 °C and 0.1 mBar) and then coated with gold. Pore size was determined using ImageJ 1.49 software and was the average of 20 diameters in each sample.

2.5. Physico-Chemical Characterization

2.5.1. In Vitro Swelling

Lyophilized hydrogels were immersed in phosphate buffer solution (PBS) at pH = 7.4 and 37 °C, and the swelling factor was calculated over time according to Equation (5):

$$\text{Swelling factor}\ = \frac{W_s - W_d}{W_d} \tag{5}$$

where W_s and W_d are the weights of the swollen and dried hydrogels, respectively. The shown data correspond to the average of three samples.

2.5.2. In Vitro Degradation

Fresh hydrogels were immersed in phosphate buffer solution (PBS) at pH = 7.4 and 37 °C. The mass loss over time was monitored as a quantification of the hydrolytic degradation using Equation (6):

$$\text{Mass loss}\ (\%)\ = \frac{W_0 - W_t}{W_t} \times 100 \tag{6}$$

where W_0 is the weight of the hydrogel at the initial time and W_t is the weight at a specific time. Three samples were evaluated for each data point.

Additionally, the sol-fraction was also measured. For this, lyophilized samples were weighed (W_{dry1}) and incubated in the corresponding solvent at 37 °C for 24 h. Then, each sample was lyophilized and weighed (W_{dry2}). The sol fraction (%) was calculated as follows (Equation (7)) [36]:

$$\text{Sol-fraction } (\%) = \frac{W_{dry1} - W_{dry2}}{W_{dry1}} \times 100 \quad (7)$$

2.5.3. Compressive Stress–Strain Test

A compression stress–strain test of hydrogels was performed using a Metrotec (Lezo, Spain) FTM-50 texture analyzer equipped with a 20 N load cell. Measurements were made at a constant rate of 10 mm/min until mechanical failure. Young's modulus (E) was determined from a linear regression on the stress–strain curves between 10–20% strain. A total of three replicates were analyzed for each sample.

2.5.4. Rheology

Rheological measurements of the photo-crosslinked hydrogels were carried out with a Rheometric Scientific Advanced Rheometric Expansion System (ARES, TA Instruments, Waters Corporation, New Castle, PA, USA) equipped with a 25 mm diameter parallel plate geometry and a 1.5 mm gap. The viscoelastic limit was determined through a shear strain sweep. Subsequently, the storage (G') and loss (G") modulus were measured at 25 °C over a frequency range of 0.1 to 500 rad/s, at a fixed strain of 1%.

2.5.5. 3D Printing Quality

Using the CellInk HeartWare designer 2.4 software, a square grid scaffold of 40 × 40 mm was designed with a space between lines of 5 × 5 mm. The printing quality of each hydrogel was evaluated using the CellInk (Gothenburg, Sweeden) printer INKREDIBLE + at optimized conditions, such as a printing speed of 600 mm/min, a pressure of 21, 25 and 18 kPa for CHIMe, AlgMe, and GelMe hydrogels, respectively and a nozzle's diameter of 0.254 mm. For this purpose, the parameters of uniformity factor (U), expansion ratio (α), size accuracy, and squareness (Equations (8), (9), (10), and (11), respectively) were calculated using the images taken with the microscope Nikon AZ100 Multizoom (Tokyo, Japan).

Uniformity factor (U) is defined as the difference between the length of the printed structures (l) and the theoretical length (L):

$$U = \frac{l}{L} \quad (8)$$

The expansion ratio (α) indicates the ability of the ink to spread over the printed surface. It is defined as the relation between the diameter of the printed filament (d) and the theoretical diameter of the nozzle (D):

$$\alpha = \frac{d}{D} \quad (9)$$

Size accuracy quantifies the printing fidelity by comparing the theoretical area (A_t) (25 mm^2) of the pores of the designed structure, with the real area (A) of the printed squares [37]:

$$Size\ accuracy = 1 - \frac{A_t - A}{A_t} \quad (10)$$

Squareness of the printed scaffolds was also calculated with the perimeter of the pore (L) and the area of the printed square scaffolds (A) [38]:

$$Squareness = \frac{L^2}{16A} \quad (11)$$

2.6. Cell Culture and Immunofluorescence

In order to adhere the hydrogels for easy handling in the culture place, the surface of coverslips (13 mm in diameter) after washing with ethanol and water was functionalized in a UV-ozone oven with -OH groups. Then, they were immersed in a 10% APTES solution in absolute ethanol for 1 h at 50 °C and subsequently washed with absolute ethanol (×3), Milli-Q water (×2), and PBS (×1). They were then immersed in a solution of glutaraldehyde 2.5% in PBS for 1 h at room temperature, washed with PBS (×3) and Milli-Q water (×3), and finally dried and kept at 4 °C until use.

For cell culture on hydrogels, the corresponding materials were deposited on a slide, and then the glutaraldehyde-functionalized coverslips were placed on top, with UV light used for photo-polymerization and adhesion. Then, Human Bone Marrow Mesenchymal Stem Cells (BM-MSCs) were cultured in DMEM medium (Gibco) supplemented with 10% (*v*/*v*) fetal bovine serum (FBS, Gibco), 1% (*v*/*v*) penicillin/streptomycin (Pen/Strep, Gibco) and 1% (*v*/*v*) GlutaMAX (Gibco) at 37 °C in a humidified atmosphere of 5% CO_2.

To analyze the adhesion of BM-MSCs to the materials, 10.000 cells were seeded onto photo-crosslinked hydrogels placed in 24-well cell culture plates. 24 h after cell seeding, samples were washed with PBS and chemically fixed using 4% formaldehyde. Next, samples were stained using NucBlue (ThermoFisher, Waltham, MA, USA) and ActinRed (ThermoFisher, Waltham, MA, USA), and fluorescence images were acquired using a Nikon Wclipse Ti DS-Qi2 (Tokyo, Japan) at ×10 fluorescence microscope. Images were processed with ImageJ software.

2.7. Cytotoxicity Assay of the "Medium"

Hydrogels were incubated in complete culture medium for 48 h at 37 °C. Simultaneously, BM-MSCs cells were seeded on a 24-well plate at a density of 10.000 cells/well and allowed to adhere for 24 h. Next, half of the culture medium volume of each well was replaced with the hydrogel-conditioned medium, and cells were then cultured for 24 h. Cells were then stained with NucBlue (Thermo Fisher, Waltham, MA, USA) and Live/Dead assay (Invitrogen, Carlsbad, CA, USA) following the manufacturer's protocol. Finally, five images of each well were acquired using a Nikon TiU (Tokyo, Japan) inverted fluorescence microscope.

3. Results

3.1. Hydrogel Preparation and Morphological Characterization

The modification of the three biopolymers was carried out via methacrylic acid-mediated methacrylation to introduce active groups for subsequent photo-crosslinking. Nuclear magnetic resonance (^{1}H-NMR) confirmed the successful methacrylation of the three polymers.

Figure 1 compares the ^{1}H-NMR spectra of chitosan and methacrylated chitosan. As can be observed, the characteristic signals of the protons of the glucosamine ring appearing in the range of 2.8 and 3.9 ppm decreased in the modified polymer, while two distinct singlets at 5.6 and 6.2 ppm corresponding to the vinyl hydrogens (H_a and H_b) of the methacrylate groups appeared, confirming the successful methacrylation. According to Equation (1), the degree of methacrylation was determined to be 41 ± 4%.

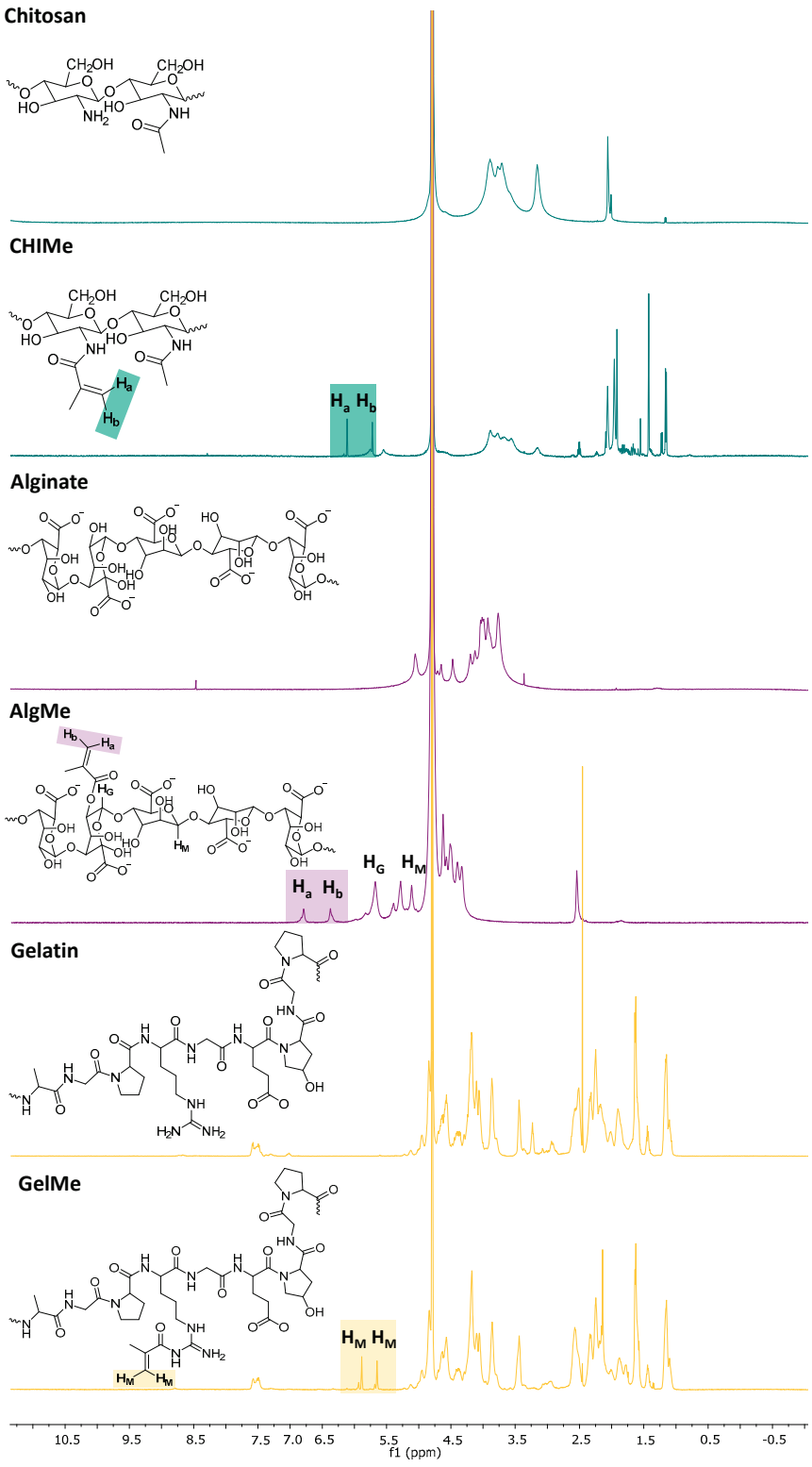

Figure 1. ^{1}H-NMR spectra of chitosan and methacrylated chitosan (green), alginate and methacrylated alginate (purple), and gelatin and methacrylated gelatin (orange).

In Figure 1, the ^{1}H-NMR spectra of alginate and methacrylated alginate display the expected signals between 3.5 and 4.5 ppm corresponding to the saccharide units of alginate. After modification, additional peaks emerge between 5.7 and 6.2 ppm, attributed to the vinyl protons (H_a and H_b) of the methacrylate groups. These peaks are absent in the

unmodified alginate spectrum, confirming the successful incorporation of methacrylate moieties in the alginate structure. The G proportion and the methacrylation degree were calculated according to Equations (2) and (3), resulting in a G proportion of 27± 4% and a methacrylation degree of 9 ± 4%.

The ^{1}H-NMR spectra of gelatin and methacrylated gelatin are also shown in Figure 1. The appearance of new peaks between 5.6 and 4.7 ppm (H_M) confirms the introduction of methacrylate groups in this biopolymer. The signal with the highest chemical shift gives the methacrylate amount present in the gelatin derivatives, while the signal with the smallest chemical shift was not used for quantifications because it was caused by a mixture of the methacrylamide groups and methacryl-modified hydroxyproline [22]. The degree of methacrylation for gelatin derivatives was quantified (32 ± 3%) based on the integration of the H_M peak according to Equation (4).

A significantly lower methacrylation degree was measured in the case of the functionalization of alginate due to the fact that only G units are modified in this polymer [21]. In addition, the nucleophilic attack of the carbonyl group of methacrylic anhydride in alginate takes place on -OH moieties, which display a lower nucleophilic nature than the -NH_2 moieties involved in the functionalization of gelatin and chitosan.

After successful methacrylation of the three biopolymers, photo-crosslinked hydrogels were prepared under the conditions described in the experimental section. The measured sol-fraction in all the samples was lower than 10% (CHIMe 7.5 ± 1.1, AlgMe 10.1 ± 0.3 and GelMe 8.3 ± 0.2). Taking into account the importance of porosity in terms of interaction with surrounding cells and tissues, affecting also oxygen and nutrient diffusion, cell migration and proliferation [39], the pore size of the hydrogels was analyzed by scanning electron microscope (SEM). SEM images confirmed that photo-crosslinking leads to interconnected porous three-dimensional structures (Figure 2), with average pore sizes of 0.37 ± 0.07 mm, 0.23 ± 0.08 mm, and 0.13 ± 0.02 mm, for AlgMe, CHIMe and GelMe, respectively. The largest pore size corresponds to AlgMe hydrogels, which is in line with the low methacrylation degree of this polymer, which seems to lead to a lower crosslinking density of the photo-cured network. In the cases of CHIMe and GelMe hydrogels, which display similar degrees of methacrylation (41% and 33%, respectively), the higher concentration of GelMe in the precursor hydrogel mixture (8% GelMe and 1.5% CHIMe) seems to be translated into a higher crosslinking density and, therefore, a smaller pore size.

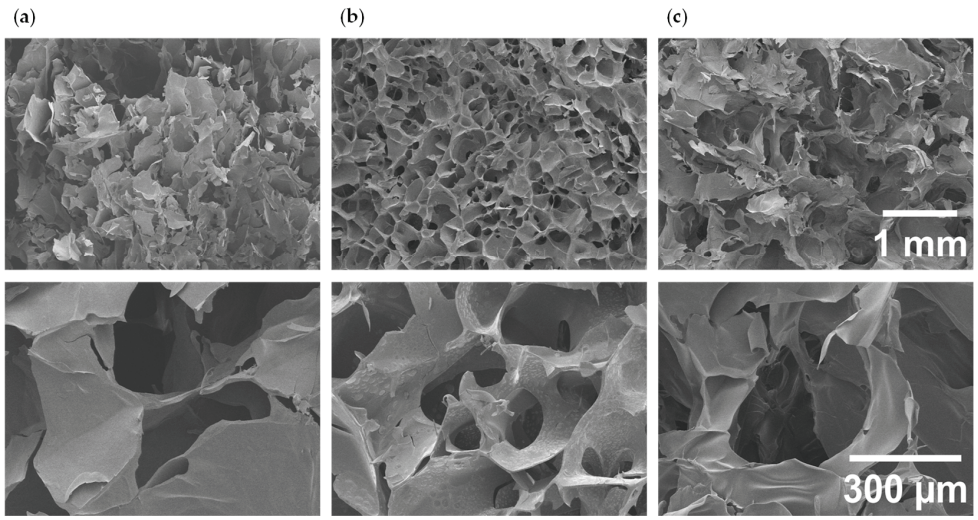

Figure 2. SEM images of (**a**) AlgMe; (**b**) GelMe, and (**c**) CHIMe hydrogels. At the top scale bar = 1 mm and at the bottom scale bar = 300 µm.

3.2. Physico-Chemical Characterization

The porous structure of the hydrogels allows them to absorb and retain water, influencing their mechanical properties and degradation rate. Figure 3a shows the swelling factors of the three hydrogels over time, calculated according to Equation (5). The water absorption capacity is a balance between the pore size of the polymer network, the concentration of the polymer, its methacrylation degree, and its own hydrophilicity. As shown in Figure 3a, in this study AlgMe exhibited the highest swelling factor (43%), which was attributed to its low concentration and methacrylation degree, resulting in a lower degree of crosslinking and consequently a higher water absorption capacity. This is in consonance with the high pore size measured by SEM (see Figure 2a). The considerable water absorption of AlgMe gels is also explained by the chemical nature of the biopolymer, which contains many carboxylate groups that at neutral pH are deprotonated, leading to repulsive electrostatic interactions and promoting higher water absorption by osmotic pressure, compared to gelatin and chitosan, which present more hydrophobic regions after methacrylation and higher crosslinking degrees. The data obtained are in agreement with those reported in the literature [10,40,41]. Regarding CHIMe and GelMe, their swelling factors are in accordance with their corresponding pore sizes measured by SEM. The higher concentration of GelMe that results in a higher crosslinking density leads to a more restricted swelling of GelMe hydrogels.

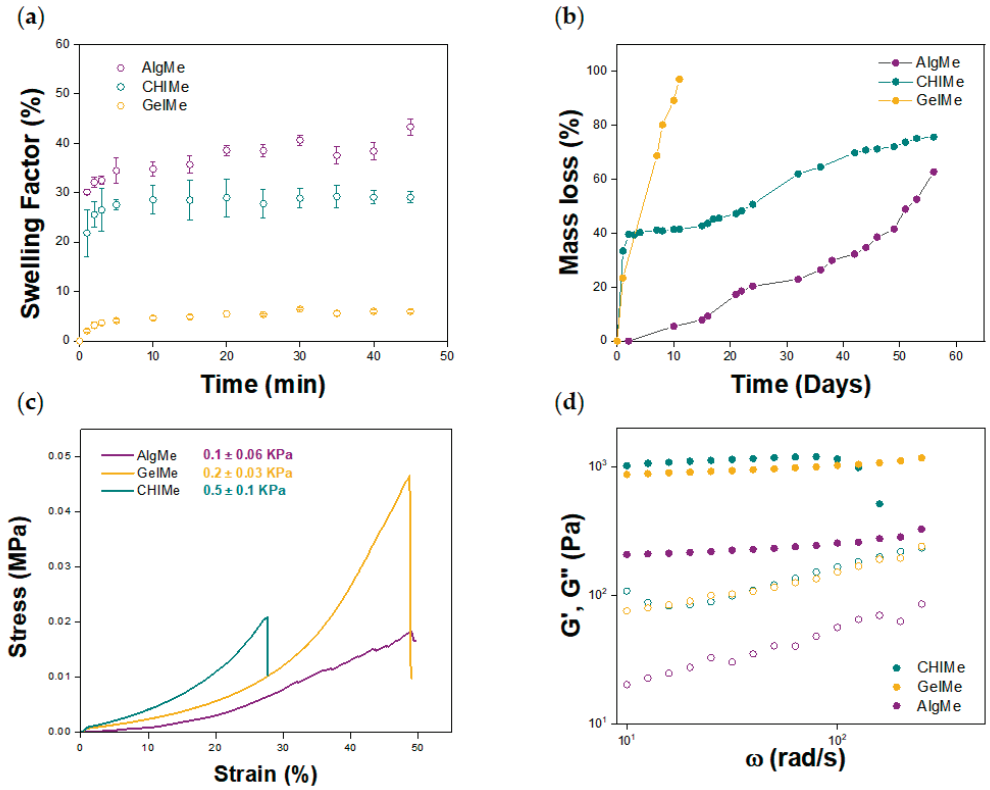

Figure 3. Physico-chemical characterization of the hydrogels. (**a**) Swelling factor; (**b**) Degradation of hydrogels over a period of 60 days; (**c**) Compression stress–strain test, and (**d**) Rheological properties o, CHIMe (green), AlgMe (purple), and GelMe (yellow) in a frequency scan being G′ the storage modulus (filled circles) and G″ the loss modulus (open circles).

The kinetics of degradation of the hydrogels is a critical parameter as it directly influences the material's stability and, subsequently, its potential applicability. Figure 3b shows the hydrolytic degradation under physiological conditions (pH = 7.4) of the three hydrogels after reaching their maximum swelling. Figure 3b shows that the polymer composition

governs the hydrogel degradation kinetics rather than the water content (swelling) of the networks. CHIMe achieved a degradation rate of 78% in a hydrolytic medium in 60 days of study. It is known that at pH values higher than its pK_a (6.5), chitosan establishes inter- and intramolecular hydrogen bonds due to the protonation of its amine groups, which increases hydrogel stability and consequently reduces its degradation rate [42].

As expected, the slowest degradation rate was obtained for AlgMe, reaching 72% mass loss in 60, which is consistent with reports in the literature [43,44]. The numerous carboxyl and hydroxyl groups on the molecular backbone of alginate can easily form intra- and intermolecular hydrogen bonds that reinforce the molecular network and limit chain mobility. This fact restricts the hydrolytic cleavage of the glycosidic bonds at physiological pH and makes this biopolymer degrade more slowly [45]. Finally, GelMe hydrogels showed the fastest degradation rate, reaching 100% mass loss in 18 days. Gelatin is thermally unstable at 37 °C, presents more disordered conformations, losing its structural integrity, which contributes to accelerating degradation via hydrolysis under physiological conditions [46,47].

Figure 3c shows the compression stress–strain curves measured for the prepared hydrogels. The results obtained indicate that the Young's modulus increases as the strain increases, showing the characteristic non-linear behavior of hydrogels across all samples [10]. Analyzing the Young's modulus, it can be observed that AlgMe is the softest hydrogel (lower Young's modulus), and therefore the most flexible and the one that withstands the highest stress and deformation until breakage. In the case of CHIMe and GelMe hydrogels, which showed more restricted swelling capacity, tougher hydrogels were obtained. Unlike swelling, which seems to be governed by the different concentrations of the polymer in the network, their mechanical behavior seems to be primarily influenced by differences in crosslinking density, as reflected in their degree of methacrylation. A higher degree of crosslinking leads to more rigid and fragile structures, especially in these hydrogels, in which the direct ester bonding between polymeric chains takes place in the absence of an intermediate and flexible crosslinking agent. Thus, CHIMe was the hardest and the most fragile material tested, suffering failure at 27% of compression. In comparison to previously reported data [14], the higher light intensity employed during the photo-printing of the ink (19 mW/cm^2 vs 0.2 mW/cm^2) in the present work, makes CHIMe gels capable of withstanding deformation forces 5 times greater.

Rheological tests were carried out to characterize the viscoelastic behavior of the photo-crosslinked hydrogels by measuring the energy stored (storage modulus, G') in the material during shear and the energy loss afterwards (loss modulus, G''). The shear stress was controlled by varying the oscillation amplitude. The results obtained are shown in Figure 3d. The rheological results suggest that all samples show the typical hydrogel behavior, as the storage moduli values are higher than the loss moduli in a frequency range (G' > G'') of 0.1 to 500 rad/s at a fixed strain of 1%, indicating that the materials exhibit predominantly elastic properties rather than viscous. In addition, G' presents a direct dependence on the composition of the hydrogel [48]. It is observed that hydrogels with higher swelling capacity (AlgMe), due to their lower crosslinking density, showed reduced G' values. This indicates that AlgMe-based hydrogels are the most elastic ones, which is in agreement with the data obtained in the analyses of the mechanical properties. On the other hand, hydrogels based on GelMe and CHIMe show higher values of both storage and loss modulus, derived from their higher crosslinking density and higher degree of methacrylation.

3.3. Printability

Hydrogels are excellent candidates as matrices for 3D printing. For the purpose of studying the quality of the printing of the prepared inks, square grids were printed

following the conditions described in the experimental part, and the uniformity factor expansion ratio, size accuracy and squareness were measured according to Equations (8), (9), (10), and (11), respectively.

According to Figure 4, it can be concluded that a high concentration of biopolymer and a high methacrylation degree in the hydrogels lead to a clear improvement of the printability of the ink, increasing the uniformity factor, size accuracy, and squareness, while decreasing the expansion ratio. It should be noted that the methacrylation degree and polymer concentration differ among the studied systems. These values were selected to yield printable, stable hydrogels for each polymer rather than to isolate specific physicochemical parameters. The selected conditions fall within experimentally and commercially relevant ranges. Thus, in the case of GelMe, high concentration and high methacrylation degree lead to a significant improvement in the printability of the ink, attaining uniformity values close to 1. Regarding the expansion ratio, as can be observed in Figure 4a, GelMe filaments are the most stable and thinnest, and consequently, the lowest value is obtained for GelMe ink, while AlgMe value deviates the most. Size accuracy and squareness are also key parameters for evaluating the printability of hydrogels. The obtained results reinforce that AlgMe is the least suitable ink for light-induced extrusion-based 3D printing, as its printed grids exhibit significant heterogeneity and irregularity. The pronounced deviation from the ideal value of 1 in both size accuracy and squareness of AlgMe suggests poor structural stability and filament control during printing, ascribed to its lower mechanical and rheological properties (Figure 3c,d) derived from its low crosslinking density. In contrast, GelMe demonstrates better printability, yielding grids with greater uniformity and closer adherence to the expected square geometry. These findings highlight the impact of hydrogel composition and elastic properties on print resolution and structural integrity, emphasizing the limitations of the employed AlgMe solution in achieving precise and regular scaffolds. This limitation of AlgMe is consistent with our previous results, in which a highly concentrated methacrylated alginate solution was found to be unprintable when additional vinyl crosslinking agents were not incorporated into the formulation [49].

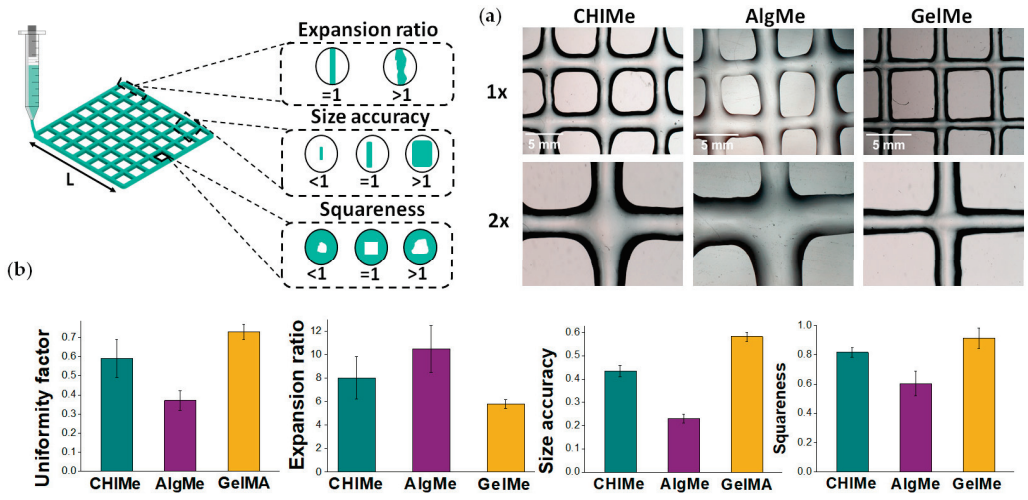

Figure 4. (**a**) Optical microscope photographs of the obtained square scaffolds: CHIMe, AlgMe and GelMe at 1× and 2×. The selected scale is in the upper left section; (**b**) Results obtained from uniformity factor, expansion ratio, squareness, and size accuracy for the three systems tested for 3D printing by extrusion, CHIMe (green), AlgMe (purple), and GelMe (yellow). The data shown represents the average ± standard deviation of the images analyzed.

3.4. Biocompatibility and Analysis of Cell Attachment

Cell viability assay was performed to confirm that the degradation products of these hydrogels could provide a biocompatible environment for cells during the culture process. The cell viability of BM-MSCs cells cultured on the medium where CHIMe, AlgMe and GelMe hydrogels had remained in their initial degradation stage, was not significantly different from cells cultured on tissue culture plastic (TCP). This indicates that not only do the hydrogels display good cytocompatibility, as has been commonly proven in previous studies, but the degradation medium of these hydrogels is also cytocompatible (Figure 5).

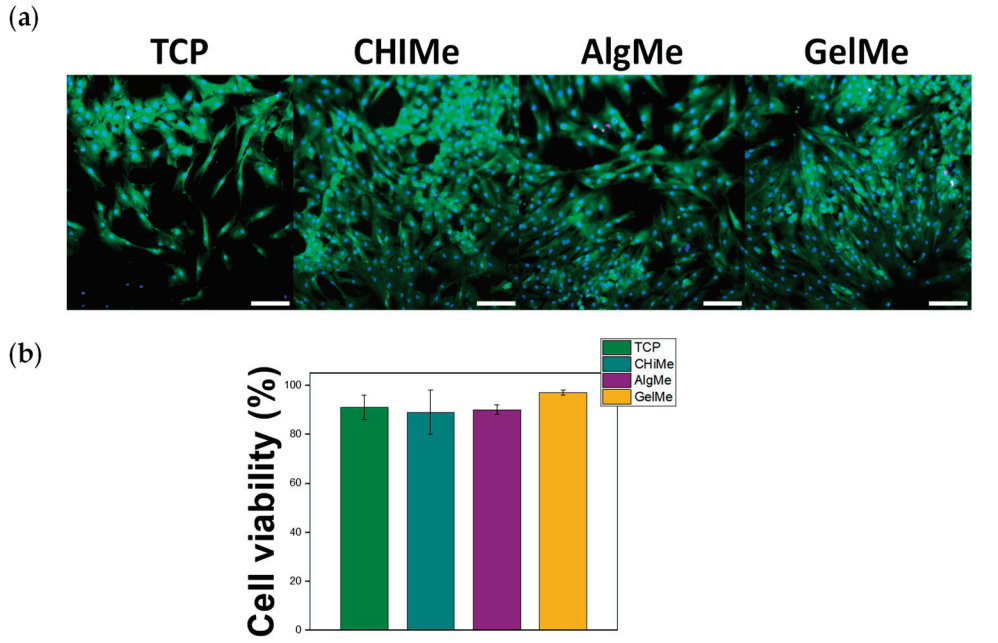

Figure 5. (**a**) Representative fluorescent images of BM-MSCs cultured with the indicated conditioned media for 1 day. Blue shows nuclei, red dead cells, and green live cells; (**b**) Quantification of the Live/Dead assay, n = 3. Scale bar = 200 μm.

Cell adhesion, spreading, and cytoskeleton organization are important parameters for assessing cell compatibility and the suitability of biomaterials for a required application [50]. Cell adhesion is affected by surface wettability, structure, and surface chemical composition on the scaffold. These factors also influence cell proliferation, migration, and physiological response [51]. Taking this into account, we analyzed the early response of BM-MSCs adhering to hydrogels by immunofluorescent staining of actin cytoskeleton and nuclei. The results obtained are shown in Figure 6.

Our results indicate that BM-MSCs cells adhere to the three hydrogels, but as expected, the spreading area of the cells was significantly larger on the GelMe hydrogels. This is a consequence of the fact that gelatin is hydrolyzed collagen, one of the major components of the ECM, and displays cellular adhesion points, which facilitate the adhesion process. In addition, the GelMe network showed the smallest pore size in SEM analyses, which provides a larger surface area for cell adhesion [52]. However, alginate hydrogels exhibit the lowest cell adhesion, which may be attributed to their well-known poorer ability to interact with cells [53] due to their surface charge, as well as the lower crosslinking density, leading to lower stiffness and higher pore dimensions [54].

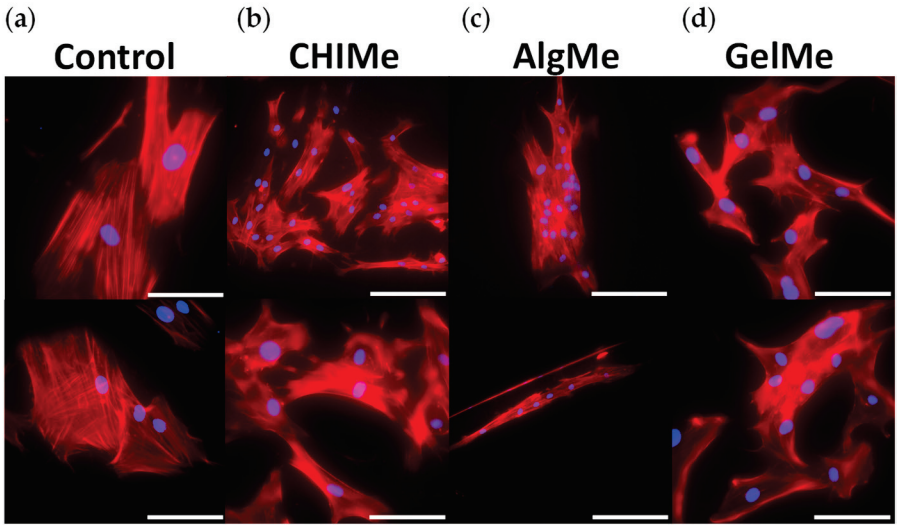

Figure 6. (**a**) Fluorescence images of nuclei (blue) and phalloidin (red) corresponding to BMSCs seeded on Control (coverslips); (**b**) CHIMe; (**c**) AlgMe, and (**d**) GelMe hydrogels. Scale bar = 200 μm.

4. Conclusions

This study presents and comparatively analyzes three well-known photo-crosslinkable hydrogel formulations based on naturally derived biopolymers—chitosan, alginate, and gelatin—aimed at mimicking the ECM for tissue engineering applications. The methacrylation process was confirmed via NMR. The morphological analysis of photo-crosslinked hydrogels demonstrated the formation of an interconnected porous structure, and the physicochemical characterization revealed that swelling capacity, degradation rate, and mechanical behavior were strongly influenced by polymer concentration and crosslinking density. Rheological studies confirmed that all hydrogels exhibit predominantly elastic behavior, with CHiMe and GelMe presenting the highest elastic modulus and thus, the highest structural integrity and print fidelity in extrusion-based 3D printing. Additionally, biocompatibility assessments confirmed that all formulations supported cell viability, with GelMe promoting better cell adhesion. Table 1 summarizes the comparative performances of the three studied systems. These findings suggest that GelMe is the most promising candidate for extrusion-based 3D bioprinting, in comparison to the AlgMe and CHIMe inks presented here.

Table 1. Comparative analyses of the main physico-chemical properties, printability, and cell viability of the studied photo-crosslinkable hydrogels.

		GelMe	**AlgMe**	**CHIMe**
MD (%)		32 ± 3	9 ± 4	41 ± 4
Swelling (%) after 45 min.		6 ± 0.2	38 ± 8.7	29 ± 1.1
Time for 50% of mass loss (days)		5	52	24
Young Modulus (KPa)		0.20 ± 0.03	0.10 ± 0.06	0.50 ± 0.10
Cell viability (%)		97 ± 1	90 ± 2	89 ± 9
Printability	Uniformity Factor	☑☑☑	☑	☑☑
	Squareness	☑☑☑	☑	☑☑

☑ low; ☑☑ intermediate; ☑☑☑ high.

Author Contributions: Conceptualization, L.P.-Á. and U.S.; writing—original draft preparation, A.G.-G.; validation, S.L.; writing—review and editing, L.P.-Á., U.S., and S.L.; supervision, S.L.; funding acquisition, S.L. All authors have read and agreed to the published version of the manuscript.

Funding: Basque Government ELKARTEK (KK-2025-00089) and Grupos Consolidados (IT1756-22), and the Ministry of Science and Innovation, grant PID2022-138572OB-C42.

Institutional Review Board Statement: Not applicable.

Data Availability Statement: The original contributions presented in this study are included in the article. Further inquiries can be directed to the corresponding author.

Acknowledgments: Technical and human support provided by SGIker (UPV/EHU, MICINN, GV/EJ, EGEF, and ESF) is gratefully acknowledged. Supervision and funding acquisition provided by José Luis Vilas-Vilela are acknowledged.

Conflicts of Interest: The authors declare no conflicts of interest.

References

1. Jose, G.; Shalumon, K.T.; Chen, J.-P. Natural Polymers Based Hydrogels for Cell Culture Applications. *Curr. Med. Chem.* **2019**, *27*, 2734–2776. [CrossRef] [PubMed]
2. Li, X.; Zheng, F.; Wang, X.; Geng, X.; Zhao, S.; Liu, H.; Dou, D.; Leng, Y.; Wang, L.; Fan, Y. Biomaterial Inks for Extrusion-Based 3D Bioprinting: Property, Classification, Modification, and Selection. *Int. J. Bioprint.* **2022**, *9*, 649. [CrossRef] [PubMed]
3. Rossi, A.; Pescara, T.; Gambelli, A.M.; Gaggia, F.; Asthana, A.; Perrier, Q.; Basta, G.; Moretti, M.; Senin, N.; Rossi, F.; et al. Biomaterials for Extrusion-Based Bioprinting and Biomedical Applications. *Front. Bioeng. Biotechnol.* **2024**, *12*, 1393641. [CrossRef]
4. Khan, M.U.A.; Stojanović, G.M.; Abdullah, M.F.B.; Dolatshahi-Pirouz, A.; Marei, H.E.; Ashammakhi, N.; Hasan, A. Fundamental Properties of Smart Hydrogels for Tissue Engineering Applications: A Review. *Int. J. Biol. Macromol.* **2024**, *254*, 127882. [CrossRef]
5. Taghipour, Y.D.; Hokmabad, V.R.; Del Bakhshayesh, A.R.; Asadi, N.S.R.; Nasrabadi, H.T. The Application of Hydrogels Based on Natural Polymers for Tissue Engineering. *Curr. Med. Chem.* **2020**, *27*, 26582680. [CrossRef]
6. Nguyen, K.T.; West, J.L. Photopolymerizable Hydrogels for Tissue Engineering Applications. *Biomaterials* **2002**, *23*, 4307–4314. [CrossRef]
7. Wu, L.; He, Y.; Mao, H.; Gu, Z. Bioactive Hydrogels Based on Polysaccharides and Peptides for Soft Tissue Wound Management. *J. Mater. Chem. B* **2022**, *10*, 7148–7160. [CrossRef]
8. Rial-Hermida, M.I.; Rey-Rico, A.; Blanco-Fernandez, B.; Carballo-Pedrares, N.; Byrne, E.M.; Mano, J.F. Recent Progress on Polysaccharide-Based Hydrogels for Controlled Delivery of Therapeutic Biomolecules. *ACS Biomater. Sci. Eng.* **2021**, *7*, 4102–4127. [CrossRef] [PubMed]
9. Garcia-Garcia, A.; Muñana-González, S.; Lanceros-Mendez, S.; Ruiz-Rubio, L.; Alvarez, L.P.; Vilas-Vilela, J.L. Biodegradable Natural Hydrogels for Tissue Engineering, Controlled Release, and Soil Remediation. *Polymers* **2024**, *16*, 2599. [CrossRef]
10. Maiz-Fernández, S.; Pérez-Álvarez, L.; Silván, U.; Vilas-Vilela, J.L.; Lanceros-Mendez, S. Photocrosslinkable and Self-Healable Hydrogels of Chitosan and Hyaluronic Acid. *Int. J. Biol. Macromol.* **2022**, *216*, 291–302. [CrossRef]
11. Maiz-Fernández, S.; Pérez-Álvarez, L.; Silván, U.; Vilas-Vilela, J.L.; Lanceros-Méndez, S. Dynamic and Self-Healable Chitosan/Hyaluronic Acid-Based in Situ-Forming Hydrogels. *Gels* **2022**, *8*, 477. [CrossRef]
12. Muñoz-Nuñez, C.; Quiroz-Pereira, Y.; Muñoz-Bonilla, A.; Fernández-García, M. Enhancing Antimicrobial and Antioxidant Properties of Chitosan-Based Films with 1-Methylimidazolium-Chitosan. *Polymers* **2025**, *17*, 2608. [CrossRef]
13. Soni, B.; Mahmoud, B.; Chang, S.; El-Giar, E.M.; Hassan, E.B. Physicochemical, Antimicrobial and Antioxidant Properties of Chitosan/TEMPO Biocomposite Packaging Films. *Food Packag. Shelf Life* **2018**, *17*, 73–79. [CrossRef]
14. García-García, A.; Pérez-Álvarez, L.; Ruiz-Rubio, L.; Larrea-Sebal, A.; Martin, C.; Vilas-Vilela, J.L. Extrusion-Based 3D Printing of Photocrosslinkable Chitosan Inks. *Gels* **2024**, *10*, 126. [CrossRef]
15. Cosola, A.; Chiappone, A.; Martinengo, C.; Grützmacher, H.; Sangermano, M. Gelatin Type A from Porcine Skin Used as Co-Initiator in a Radical Photo-Initiating System. *Polymers* **2019**, *11*, 1901. [CrossRef]
16. Liu, D.; Nikoo, M.; Boran, G.; Zhou, P.; Regenstein, J.M. Collagen and Gelatin. *Annu. Rev. Food Sci. Technol.* **2015**, *6*, 527–557. [CrossRef] [PubMed]
17. Luo, Y.; Chen, B.; Zhang, X.; Huang, S.; Wa, Q. 3D Printed Concentrated Alginate/GelMA Hollow-Fibers-Packed Scaffolds with Nano Apatite Coatings for Bone Tissue Engineering. *Int. J. Biol. Macromol.* **2022**, *202*, 366–374. [CrossRef]
18. Grigore, A.; Sarker, B.; Fabry, B.; Boccaccini, A.R.; Detsch, R. Behavior of Encapsulated MG-63 Cells in RGD and Gelatine-Modified Alginate Hydrogels. *Tissue Eng. Part A* **2014**, *20*, 2140–2150. [CrossRef] [PubMed]

19. Damiri, F.; Fatimi, A.; Liu, Y.; Musuc, A.M.; Fajardo, A.R.; Gowda, B.H.J.; Vora, L.K.; Shavandi, A.; Okoro, O.V. Recent Advances in 3D Bioprinted Polysaccharide Hydrogels for Biomedical Applications: A Comprehensive Review. *Carbohydr. Polym.* **2025**, *348*, 122845. [CrossRef] [PubMed]
20. Intini, C.; Elviri, L.; Cabral, J.; Mros, S.; Bergonzi, C.; Bianchera, A.; Flammini, L.; Govoni, P.; Barocelli, E.; Bettini, R.; et al. 3D-Printed Chitosan-Based Scaffolds: An in Vitro Study of Human Skin Cell Growth and an in-Vivo Wound Healing Evaluation in Experimental Diabetes in Rats. *Carbohydr. Polym.* **2018**, *199*, 593–602. [CrossRef]
21. Teoh, J.H.; Mozhi, A.; Sunil, V.; Tay, S.M.; Fuh, J.; Wang, C.H. 3D Printing Personalized, Photocrosslinkable Hydrogel Wound Dressings for the Treatment of Thermal Burns. *Adv. Funct. Mater.* **2021**, *31*, 2105932. [CrossRef]
22. Chang, H.K.; Yang, D.H.; Ha, M.Y.; Kim, H.J.; Kim, C.H.; Kim, S.H.; Choi, J.W.; Chun, H.J. 3D Printing of Cell-Laden Visible Light Curable Glycol Chitosan Bioink for Bone Tissue Engineering. *Carbohydr. Polym.* **2022**, *287*, 119328. [CrossRef]
23. Shen, Y.; Tang, H.; Huang, X.; Hang, R.; Zhang, X.; Wang, Y.; Yao, X. DLP Printing Photocurable Chitosan to Build Bio-Constructs for Tissue Engineering. *Carbohydr. Polym.* **2020**, *235*, 115970. [CrossRef]
24. Morris, V.B.; Nimbalkar, S.; Younesi, M.; McClellan, P.; Akkus, O. Mechanical Properties, Cytocompatibility and Manufacturability of Chitosan:PEGDA Hybrid-Gel Scaffolds by Stereolithography. *Ann. Biomed. Eng.* **2017**, *45*, 286–296. [CrossRef]
25. Sánchez-Sánchez, R.; Rodríguez-Rego, J.M.; Macías-García, A.; Mendoza-Cerezo, L.; Díaz-Parralejo, A. Relationship between Shear-Thinning Rheological Properties of Bioinks and Bioprinting Parameters. *Int. J. Bioprint.* **2023**, *9*, 422–431. [CrossRef]
26. Ma, Y.; Wang, Y.; Chen, D.; Su, T.; Chang, Q.; Huang, W.; Lu, F. 3D Bioprinting of a Gradient Stiffened Gelatin-Alginate Hydrogel with Adipose-Derived Stem Cells for Full-Thickness Skin Regeneration. *J. Mater. Chem. B* **2023**, *11*, 2989–3000. [CrossRef]
27. Gharacheh, H.; Guvendiren, M. Cell-Laden Composite Hydrogel Bioinks with Human Bone Allograft Particles to Enhance Stem Cell Osteogenesis. *Polymers* **2022**, *14*, 3788. [CrossRef]
28. Celikkin, N.; Mastrogiacomo, S.; Dou, W.; Heerschap, A.; Oosterwijk, E.; Walboomers, X.F.; Święszkowski, W. In Vitro and in Vivo Assessment of a 3D Printable Gelatin Methacrylate Hydrogel for Bone Regeneration Applications. *J. Biomed. Mater. Res. B Appl. Biomater.* **2022**, *110*, 2133–2145. [CrossRef]
29. Liu, X.Y.; Chen, C.; Xu, H.H.; Zhang, Y.S.; Zhong, L.; Hu, N.; Jia, X.L.; Wang, Y.W.; Zhong, K.H.; Liu, C.; et al. Integrated Printed BDNF/Collagen/Chitosan Scaffolds with Low Temperature Extrusion 3D Printer Accelerated Neural Regeneration after Spinal Cord Injury. *Regen. Biomater.* **2021**, *8*, rbab047. [CrossRef]
30. Kolawole, O.M.; Lau, W.M.; Khutoryanskiy, V.V. Methacrylated Chitosan as a Polymer with Enhanced Mucoadhesive Properties for Transmucosal Drug Delivery. *Int. J. Pharm.* **2018**, *550*, 123–129. [CrossRef]
31. Chou, A.I.; Nicoll, S.B. Characterization of Photocrosslinked Alginate Hydrogels for Nucleus Pulposus Cell Encapsulation. *J. Biomed. Mater. Res. A* **2009**, *91*, 187–194. [CrossRef]
32. Kilic Bektas, C.; Burcu, A.; Gedikoglu, G.; Telek, H.H.; Ornek, F.; Hasirci, V. Methacrylated Gelatin Hydrogels as Corneal Stroma Substitutes: In Vivo Study. *J. Biomater. Sci. Polym. Ed.* **2019**, *30*, 1803–1821. [CrossRef]
33. Jensen, H.M.; Larsen, F.H.; Engelsen, S.B. Characterization of Alginates by Nuclear Magnetic Resonance (NMR) and Vibrational Spectroscopy (IR, NIR, Raman) in Combination with Chemometrics. *Methods Mol. Biol.* **2015**, *1308*, 347–363. [CrossRef]
34. Araiza-Verduzco, F.; Rodríguez-Velázquez, E.; Cruz, H.; Rivero, I.A.; Acosta-Martínez, D.R.; Pina-Luis, G.; Alatorre-Meda, M. Photocrosslinked Alginate-Methacrylate Hydrogels with Modulable Mechanical Properties: Effect of the Molecular Conformation and Electron Density of the Methacrylate Reactive Group. *Materials* **2020**, *13*, 534. [CrossRef]
35. Claaßen, C.; Claaßen, M.H.; Truffault, V.; Sewald, L.; Tovar, G.E.M.; Borchers, K.; Southan, A. Quantification of Substitution of Gelatin Methacryloyl: Best Practice and Current Pitfalls. *Biomacromolecules* **2018**, *19*, 42–52. [CrossRef] [PubMed]
36. Trucco, D.; Riacci, L.; Vannozzi, L.; Manferdini, C.; Arrico, L.; Gabusi, E.; Lisignoli, G.; Ricotti, L. Primers for the Adhesion of Gellan Gum-Based Hydrogels to the Cartilage: A Comparative Study. *Macromol. Biosci.* **2022**, *22*, 2200096. [CrossRef] [PubMed]
37. Giuseppe, M.D.; Law, N.; Webb, B.; Macrae, A.R.; Liew, L.J.; Sercombe, T.B.; Dilley, R.J.; Doyle, B.J. Mechanical Behaviour of Alginate-Gelatin Hydrogels for 3D Bioprinting. *J. Mech. Behav. Biomed. Mater.* **2018**, *79*, 150–157. [CrossRef] [PubMed]
38. Ouyang, L.; Yao, R.; Zhao, Y.; Sun, W. Effect of Bioink Properties on Printability and Cell Viability for 3D Bioplotting of Embryonic Stem Cells. *Biofabrication* **2016**, *8*, 035020. [CrossRef]
39. Ozdogan, C.Y.; Kenar, H.; Davun, K.E.; Yucel, D.; Doger, E.; Alagoz, S. An in Vitro 3D Diabetic Human Skin Model from Diabetic Primary Cells. *Biomed. Mater.* **2021**, *16*, 015027. [CrossRef]
40. Jeon, O.; Bouhadir, K.H.; Mansour, J.M.; Alsberg, E. Photocrosslinked Alginate Hydrogels with Tunable Biodegradation Rates and Mechanical Properties. *Biomaterials* **2009**, *30*, 2724–2734. [CrossRef]
41. Ribeiro, J.S.; Sanz, C.K.; Münchow, E.A.; Kalra, N.; Dubey, N.; Suárez, C.E.C.; Fenno, J.C.; Lund, R.G.; Bottino, M.C. Photocrosslinkable Methacrylated Gelatin Hydrogel as a Cell-Friendly Injectable Delivery System for Chlorhexidine in Regenerative Endodontics. *Dent. Mater.* **2022**, *38*, 1507–1517. [CrossRef]

42. Maiz-Fernández, S.; Barroso, N.; Pérez-Álvarez, L.; Silván, U.; Vilas-Vilela, J.L.; Lanceros-Mendez, S. 3D Printable Self-Healing Hyaluronic Acid/Chitosan Polycomplex Hydrogels with Drug Release Capability. *Int. J. Biol. Macromol.* **2021**, *188*, 820–832. [CrossRef] [PubMed]
43. Jeon, O.; Powell, C.; Solorio, L.D.; Krebs, M.D.; Alsberg, E. Affinity-Based Growth Factor Delivery Using Biodegradable, Photocrosslinked Heparin-Alginate Hydrogels. *J. Control. Release* **2011**, *154*, 258–266. [CrossRef]
44. Jeon, O.; Powell, C.; Ahmed, S.M.; Alsberg, E. Biodegradable, Photocrosslinked Alginate Hydrogels with Independently Tailorable Physical Properties and Cell Adhesivity. *Tissue Eng. Part A* **2010**, *16*, 2915–2925. [CrossRef]
45. Wang, H.; Chen, X.; Wen, Y.; Li, D.; Sun, X.; Liu, Z.; Yan, H.; Lin, Q. A Study on the Correlation between the Oxidation Degree of Oxidized Sodium Alginate on Its Degradability and Gelation. *Polymers* **2022**, *14*, 1679. [CrossRef] [PubMed]
46. Andreazza, R.; Morales, A.; Pieniz, S.; Labidi, J. Gelatin-Based Hydrogels: Potential Biomaterials for Remediation. *Polymers* **2023**, *15*, 1026. [CrossRef] [PubMed]
47. Van Den Bosch, E.; Gielens, C. Gelatin Degradation at Elevated Temperature. *Int. J. Biol. Macromol.* **2003**, *32*, 129–138. [CrossRef] [PubMed]
48. Maiz-Fernández, S.; Guaresti, O.; Pérez-Álvarez, L.; Ruiz-Rubio, L.; Gabilondo, N.; Vilas-Vilela, J.L.; Lanceros-Mendez, S. β-Glycerol Phosphate/Genipin Chitosan Hydrogels: A Comparative Study of Their Properties and Diclofenac Delivery. *Carbohydr. Polym.* **2020**, *248*, 116811. [CrossRef] [PubMed]
49. Zoco de la Fuente, A.; García-García, A.; Pérez-Álvarez, L.; Moreno-Benítez, I.; Larrea-Sebal, A.; Martin, C.; Vilas-Vilela, J.L. Evaluation of Various Types of Alginate Inks for Light-Mediated Extrusion 3D Printing. *Polymers* **2024**, *16*, 986. [CrossRef]
50. Gaharwar, A.K.; Schexnailder, P.J.; Jin, Q.; Wu, C.J.; Schmidt, G. Addition of Chitosan to Silicate Cross-Linked PEO for Tuning Osteoblast Cell Adhesion and Mineralization. *ACS Appl. Mater. Interfaces* **2010**, *2*, 3119–3127. [CrossRef]
51. Aurrekoetxea, M.; Garcia-Gallastegui, P.; Irastorza, I.; Luzuriaga, J.; Uribe-Etxebarria, V.; Unda, F.; Ibarretxe, G. Dental Pulp Stem Cells as a Multifaceted Tool for Bioengineering and the Regeneration of Craniomaxillofacial Tissues. *Front. Physiol.* **2015**, *6*, 289. [CrossRef] [PubMed]
52. Zhang, Z.Z.; Jiang, D.; Ding, J.X.; Wang, S.J.; Zhang, L.; Zhang, J.Y.; Qi, Y.S.; Chen, X.S.; Yu, J.K. Role of Scaffold Mean Pore Size in Meniscus Regeneration. *Acta Biomater.* **2016**, *43*, 314–326. [CrossRef] [PubMed]
53. Datta, S. Advantage of Alginate Bioinks in Biofabrication for Various Tissue Engineering Applications. *Int. J. Polym. Sci.* **2023**, *2023*, 6661452. [CrossRef]
54. Li, J.; Liu, Y.; Zhang, Y.; Yao, B.; Enhejirigala, B.; Li, Z.; Song, W.; Wang, Y.; Duan, X.; Yuan, X.; et al. Biophysical and Biochemical Cues of Biomaterials Guide Mesenchymal Stem Cell Behaviors. *Front. Cell Dev. Biol.* **2021**, *9*, 640388. [CrossRef] [PubMed]

Disclaimer/Publisher's Note: The statements, opinions and data contained in all publications are solely those of the individual author(s) and contributor(s) and not of MDPI and/or the editor(s). MDPI and/or the editor(s) disclaim responsibility for any injury to people or property resulting from any ideas, methods, instructions or products referred to in the content.

polymers

MDPI

Article

Physicochemical and Antimicrobial Evaluation of Bacterial Cellulose Derived from Spent Tea Waste

Cem Gök [1,2,*], Arzum Işıtan [3,4,5,*], Massimo Bersani [4], Paolo Bettotti [6], Laura Pasquardini [7], Michele Fedrizzi [4], Davide D'Angelo [8], Havva Boyacıoğlu [9] and Ahmet Koluman [10]

1 Department of Biomedical Engineering, Izmir Bakırçay University, 35665 Izmir, Türkiye
2 Biomedical Technologies Design Application and Research Center, Izmir Bakırçay University, 35665 Izmir, Türkiye
3 Department of Mechanical Engineering, Pamukkale University, 20160 Denizli, Türkiye
4 Center for Sensors and Devices, Fondazione Bruno Kessler, 38123 Trento, Italy; bersani@fbk.eu (M.B.); mfed@fbk.eu (M.F.)
5 Bilgece Mühendislik Geri Dönüşüm Ltd., Şti, 20020 Denizli, Türkiye
6 Nanoscience Laboratory, Department of Physics, University of TrentoPovo, 38123 Trento, Italy; paolo.bettotti@unitn.it
7 Indivenire srl, 38123 Trento, Italy; l.pasquardini@indiveni.re
8 Cosvitec Scarl, 80142 Naples, Italy; davidedangelo@cosvitec.eu
9 Department of Chemical Engineering, Pamukkale University, 20160 Denizli, Türkiye; hboyacioglu@pau.edu.tr
10 Department of Biomedical Engineering, Pamukkale University, 20160 Denizli, Türkiye; akoluman@pau.edu.tr
* Correspondence: cem.gok@bakircay.edu.tr (C.G.); aisitan@pau.edu.tr (A.I.)

Abstract: Bacterial cellulose (BC) is a high-purity biopolymer with excellent physicochemical and mechanical properties, including high crystallinity, water absorption, biocompatibility, and structural tunability. However, its large-scale production is hindered by high substrate costs and limited sustainability. In this study, spent black tea waste was utilized as a low-cost and eco-friendly carbon source for BC synthesis by *Komagataeibacter xylinus* ATCC 53524 under varying initial pH conditions (4–9). Six different BC membranes were produced and systematically characterized in terms of mechanical strength, water absorption capacity, electrical conductivity, antimicrobial performance, and polyvinyl alcohol (PVA) attachment efficiency. Morphological and chemical analyses were conducted using SEM and FTIR techniques to investigate pH-induced structural variations. The results revealed that the BC6 sample (pH 6) exhibited the highest tensile strength (2.4 MPa), elongation (13%), PVA incorporation (12%), and electrical conductivity, confirming the positive impact of near-neutral conditions on nanofiber assembly and functional integration. In contrast, the BC4 sample (pH 4) demonstrated strong antimicrobial activity (log reduction = 3.5) against *E. coli*, suggesting that acidic pH conditions enhance bioactivity. SEM images confirmed the most cohesive and uniform fiber morphology at pH 6, while FTIR spectra indicated the preservation of characteristic cellulose functional groups across all samples. Overall, this study presents a sustainable and efficient strategy for BC production using food waste and demonstrates that synthesis pH is a key parameter in tuning its functional performance. The optimized BC membranes show potential for biomedical, flexible electronic, and antibacterial material applications, particularly in wearable electrode technologies.

Keywords: food waste; *Komagataeibacter xylinus*; antimicrobial activity; medical electrode applications; sustainable development goals; circular bioeconomy

1. Introduction

Both agricultural waste and food wastage are significant global challenges today. These two issues pose serious environmental and economic challenges that hinder the achievement of sustainable development goals. Food waste not only threatens food security but also causes great damage to the environment worldwide. However, agricultural waste, when recycled and utilized, can provide environmental benefits and form key components of sustainable practices [1–4].

Food waste refers to the reduction in the quantity or quality of food due to decisions and actions by retailers, food service providers, and consumers. It includes food and inedible parts removed from the supply chain for recovery or disposal through methods such as composting, anaerobic digestion, bioenergy production, incineration, or landfilling [5]. In the EU, over 59 million tons of food waste (132 kg per inhabitant) are generated annually, valued at 132 billion euros, while more than 42 million people struggle to afford a quality meal every second day [6,7]. Globally, nearly one-third of food produced for human consumption is lost or wasted, with 14% lost during the post-harvest to retail stages [5]. Food waste intensifies the environmental impact of production and consumption. The European Commission's Circular Economy Action Plan promotes resource efficiency and sustainability, with its 2023 revision adding indicators on material footprint and resource use [8]. The main objective is to transform low-value residues and waste into valuable products [9]. By following circular economy principles and better utilizing or reusing existing resources, the shift from a fossil-based to a bio-based economy accelerates. Biorefineries, utilizing diverse biomass feedstocks, employ various technologies to produce energy, biofuels, chemicals, and materials [10].

Cellulose, a widely abundant biopolymer derived from plants, algae, bacteria, and tunicates, provides structural integrity to plant cell walls. Its biodegradability and renewability make it vital for sustainable development, reducing reliance on fossil fuels. Structural diversity influences its properties and applications across various fields [11,12]. Classified by source and structure, common forms include microcrystalline cellulose (MCC), nanocrystalline cellulose (NCC), and bacterial cellulose (BC) [11,12]. BC is valued for its high tensile strength, water retention, and biocompatibility, making it ideal for medical applications [13]. BC-based soft and moisturizing film electrodes are designed for biopotential recording. It is also reported that the water in BC can continuously moisturize the skin, reduce contact impedance, and in addition, compared to gel electrode patches, BC electrodes do not cause skin discomfort when worn for long periods of time [14].

As a sustainable alternative to traditional cellulose sources, BC production using organic waste aligns with circular economy principles [15,16]. First described in 1886 by Adrian J. Brown, BC is synthesized by various bacteria like *Rhizobium leguminosarum*, *Burkholderia* spp., *Escherichia coli* (*E. coli*), and *Salmonella enterica*, with *Komagataeibacter xylinus* (*K. xylinus*) being the most studied due to its high yield and ability to utilize diverse carbon sources [17]. *K. xylinus* belongs to the acetic acid bacteria (AAB) group within the *Acetobacteraceae* family and is commonly found in fermented foods, fruits, and vegetables [17,18]. Its biosynthesis follows the pentose phosphate pathway and Krebs cycle, with acid tolerance optimizing production. Traditional vinegars serve as natural AAB sources, where *K. xylinus* can be identified via biochemical and molecular analyses such as 16S rRNA sequencing.

Tea (*Camellia sinensis*) is the second most consumed beverage globally, involving over 13 million people in its industry. Black and green tea dominate production (98%), with major producers including China, India, Kenya, Sri Lanka, and Türkiye. Black tea accounts for 60% of production, followed by green tea at 30%. In 2013, global tea production reached 5.07 million tons, with black and green tea outputs rising by over 5%. Black tea production, which was previously projected to grow by 2.9% annually to 4.17 million tons by 2023 alongside a 3%

annual increase in consumption to 4.14 million tons, is now expected to expand at a slower pace than in the past decade, rising by 1.6% per year to reach 4.42 million tons by 2032 [19–22].

As illustrated in Figure 1, tea waste is generated throughout the tea production, including withering, crushing, fermentation, drying, and packaging, comprising fiber, protein, caffeine, and polyphenols. About 90% of tea leaves become waste post-processing, posing environmental and economic challenges. India produces 190,000 tons of tea waste annually, while Türkiye's Black Sea region generates 30,000 tons [20,23,24]. It consists of fiber, protein, caffeine, polyphenols, and other bioactive compounds. If not properly managed, tea waste can pollute water, soil, and air. To address these issues, tea waste can be valorized through extraction methods to recover bioactive compounds like polyphenols. It has potential applications in bioenergy production, adsorbents, food additives, and functional foods [20,23]. "Spent tea leaves" (STLs) from brewed tea also contribute to waste generation, requiring disposal efforts and economic resources [23]. Sustainability initiatives, including the "waste to wealth" concept, aim to convert tea waste into valuable products, reducing environmental impact and supporting circular economy practices. Additionally, black tea leaf silage is rich in fiber, while green tea leaf silage has high phenolic and lactic acid content, making tea waste an important source of nutrients and bioactive compounds [20]. BC extraction from fermented black tea is considered to be economical compared to conventional media as it naturally contains many essential nutrients and complementary components such as ethanol and vitamins. This is expected to make production cheaper compared to the process using ethanol-supplemented conventional media [13]. There are studies in which *K. xylinus* was isolated from fermented tea (kombucha) and used in BC production [16,25,26]. In these studies under various culture conditions, focusing on carbon sources, temperature, and pH are also reported to be very influential on BC structure and properties.

Figure 1. An illustration of BC production from waste generated during the production and processing of tea.

The United Nations and the European Union are working hard to address the issues through various policies and programs such as the Sustainable Development Goals (SDGs) [27], the European Green Deal [28], and the Circular Economy Plan [29]. These ambitious plans require investments that will reduce emissions, promote the use of renewable energy sources and environmentally friendly technologies, and support industry in

its innovation while implementing the green transition across all sectors. In this context, the Food Chase Project [30], supported by the European Union, is working on the creation of "Food Supply Chain Ecosystems for Sustainability" and reducing food loss and waste throughout the supply chain. The project brings together higher education and vocational education and training, research, the public sector and the business sector to design and build new, innovative and multidisciplinary approaches to food supply chain training and development of new skills based on market needs, from farm to post-use.

In order to contribute to the aforementioned aims and objectives, within the scope of the FOOD CHASE project, this study investigated the usability of BCs from spent black tea in medical electrode applications. Although there are studies in the literature on BC production of *K. xylinus* bacteria with tea, there are few studies on BC production with this bacterium from black tea as an electrode material, whose waste amount reaches millions of tons [13,31]. In this study, six different BCs were obtained from black tea wastes by selecting different initial pH levels and thickness measurement, strength, conductivity, water absorption capacity, colorfastness, antimicrobial properties, and PVA attachment tests were carried out to examine their usability as electrode materials.

2. Materials and Methods

2.1. Production of BC from Spent Black Tea and ITS Purification

Neither the bacterial strain nor the tea waste underwent pre-treatment. All chemicals and reagents used in the process were of laboratory grade and used without further purification. The waste tea was obtained from the tea kiosk operating within the Faculty of Technology at Pamukkale University.

K. xylinus (ATCC 53524) was obtained from the American Type Culture Collection (ATCC) and maintained on agar slants at 4 °C. For cultivation, the strains were inoculated in Hestrin-Schramm (HS) medium containing 2% glucose, 0.5% yeast extract, 0.5% peptone, 0.27% disodium phosphate, and 0.11% citric acid, adjusted to pH 6.0 [32]. The used tea leaves (brewed/spent) were washed with sterilized water. Next, spent black tea (5 g) was added to this solution. The solution was left to stand at room temperature to enable the components of the black tea to infuse properly into the water. Tea leaves were removed by filtration with sterile sieve after 15 min. BC membranes were produced by inoculating 1% (v/v) of the activated bacterial strain into 100 mL of HS medium in sterile 250 mL Erlenmeyer flasks (Isolab, Eschau, Germany). The culture was incubated varying initial pH values (4.0–9.0) by adding acetate or citrate statically at 30 °C for 15 days. The samples were numbered BC4, BC5, BC6, BC7, BC8, and BC9 depending on the initial pH values. After cultivation, the BC membrane was harvested and purified by washing with deionized water to remove residual medium components and bacterial cells. The membrane was then treated with 0.1 M NaOH at 80 °C for 2 h to remove any remaining impurities, followed by thorough rinsing with deionized water until neutral pH was achieved. The purified BC membranes were air-dried at room temperature for 24 h and stored in a desiccator until further analysis.

2.2. Thickness Measurement

The thickness of the BC membranes was measured using a digital micrometer (Mitutoyo, Kawasaki, Japan) with an accuracy of ±0.001 mm. Thickness measurements were performed after incubating the culture at 30 °C for 15 days at different initial pH values and subsequent purification and drying steps. Measurements were taken at five random locations on each sample, and the thickness is reported as mean average and standard deviation.

2.3. Tensile Strength and Elongation

Tensile strength and elongation at break were determined according to ASTM D-882-97 using a universal testing machine (Instron 3366, Instron Co., Norwood, MA, USA) equipped with a 500 N load cell [33]. Samples were maintained at ambient temperature in a laminar cabinet for at least 2 weeks to reach equilibrium crystallization. Rectangular samples (10 mm × 50 mm) were cut from the BC membrane and clamped between the grips of the testing machine with an initial grip separation of 20 mm. The samples were stretched at a constant crosshead speed of 5 mm/min until fracture. Tensile strength (MPa) was calculated as the maximum load divided by the cross-sectional area of the sample, and elongation (%) was determined as the percentage increase in length at the point of fracture relative to the original length. Measurements were conducted at ambient temperature. Three separate measurements were made and averaged.

2.4. Colorfastness Tests

As a stage of the usability of BCs as electrode material, following ASTM-recommended procedures, the dyed samples were evaluated for various fastness properties. The specific test methods applied included colorfastness to washing/laundering (AATCC 61-2013) [34], colorfastness to rubbing (ISO 105-X12:2016) [35], and colorfastness to perspiration (AATCC TM 15-2021) [36].

Washing fastness was evaluated using a Launder-Ometer (SDL Atlas, LLC, Rock Hill, SC, USA) according to AATCC Test Method 61-2013. The samples were subjected to 10 washing cycles at 40 °C, and the color change was assessed on a gray scale of 1 to 5, where 1 indicates significant color loss and 5 indicates no color change.

Rubbing fastness was assessed using a crock meter (SDL Atlas, LLC, Rock Hill, SC, USA) according to ISO 105-X12:2016 in dry procession for testing the transference of color from the surface of one material to another. The number of rubbing cycles required to cause visible wear on the BC membrane surface was recorded.

The colorfastness to perspiration test was performed according to the AATCC test method 15-2021 to examine how much its color changes when in contact with body perspiration. Test specimens were cut to dimensions of 60 × 60 ± 2 mm. The gray scale was utilized to assess the samples' fastness performance in this test. The gray scale comprises nine possible ratings: 5, 4–5, 4, 3–4, 3, 2–3, 2, 1–2, and 1, where a rating of 5 indicates "Excellent" fastness, while a rating of 1 signifies "Very Poor" fastness.

2.5. Electrical Conductivity Measurement

The electrical conductivity of the BC membrane was measured using a four-point probe conductivity meter (Keithley 2450, Keithley Instruments, Cleveland, OH, USA). The samples were cut into 10 × 10 mm^2 and placed between the probes. A constant current was applied, and the voltage drop across the sample was recorded. The conductivity (S/m) was calculated using Ohm's law and the sample dimensions. Measurements were conducted at room temperature, and the conductivity was calculated using Equation (1) [37]:

$$\sigma = \frac{1}{R.A/L} \quad (1)$$

where σ is the conductivity (S/cm), R is the resistance (Ω), A is the cross-sectional area (cm^2), and L is the sample thickness (cm).

2.6. Water Absorption Capacity

BC is known for its exceptional water absorption and retention capacity compared to its plant-based counterpart [13]. The water absorption properties are closely linked to the material's porosity, crystallinity, and surface area. BC samples maintained at ambient conditions in a laminar chamber for 2 weeks were cut into small pieces (4 × 4 cm) and weighed. The water absorption capacity of the BC membrane was determined by soaking the samples in deionized water at room temperature for 24 h. The samples were then removed, gently blotted with filter paper to remove excess surface water and weighed. The water absorption capacity (%) was calculated using Equation (2):

$$\text{Water absorbtion capacity}(\%) = \frac{W_w - W_d}{W_d} \times 100 \quad (2)$$

where W_w is the weight of the wet sample and W_d is the weight of the dry sample.

2.7. Antimicrobial Activity

The antibacterial activity of the specimens was evaluated using the dynamic contact method based on the ASTM E2149-13a standard [38]. This method allows for the quantitative assessment of the reduction in bacterial concentration when in contact with an antimicrobial surface under shaking conditions. *Escherichia coli* (*E. coli*) (ATCC 25922), a Gram-negative bacterium, was used as the test organism. A bacterial suspension was prepared in 0.9% NaCl solution and adjusted to an initial concentration of approximately 8 log CFU/mL (10^8 CFU/mL). Square specimens measuring 20 × 20 mm were placed in sterile containers containing 100 µL of the bacterial suspension. The samples were incubated for 24 h at 37 °C with continuous shaking at 150 rpm to ensure uniform contact between the bacterial suspension and the sample surfaces. After incubation, serial dilutions were prepared from the suspensions, and aliquots were spread onto Mueller-Hinton agar plates. The plates were incubated at 37 °C for 24 h, and the number of colony-forming units (CFU) was counted. The antibacterial activity was calculated based on the reduction in viable bacterial count using the following formula (Equation (3)) [39]:

$$\text{Log Reduction} = \log_{10}\left(\frac{A}{B}\right) \quad (3)$$

where A is the bacterial count at zero (initial control), and B is the bacterial count after 24 h of contact with the specimen. All tests were performed in triplicate (n = 3), and the average log reduction values were reported. According to standard interpretation criteria, specimens with at least a 1 log reduction in bacteria load are required to claim antibacterial property and greater than 2 were considered to exhibit significant antibacterial activity.

2.8. PVA Attachment Test

In this study, PVA (molecular weight (Mw) 125,000 g/mol, 99% hydrolyzed) was obtained from Sigma-Aldrich Co. (St Louis, MO, USA). For the preparation of PVA solution, 1 g of PVA was weighed, and 9 mL of distilled water were added to obtain solutions with a concentration of 10 wt% [40]. The prepared solutions were homogenized by mixing in a magnetic stirrer at 90 °C with a stirring speed of 500 rpm for 2 h. The casting method was employed to prepare the composite film with BC and PVA. PVA was solubilized in deionized water and stirred for 60 min at 90 °C. The PVA solution was cooled, then BC was added and agitated for 20 min. The mixture was incorporated with 30% w/w glycerol as a plasticizer. The samples were cast in a Petri dish and dried for 48 h at an ambient temperature. Washing procedures are crucial for removing excess PVA and assessing attachment efficiency, which in turn affects the composite's

mechanical and hydrophilic properties. This typically involves immersing the composites in deionized water at room temperature for a specified duration. During this time, the water-soluble PVA not chemically bonded to BC can diffuse out, which is essential for assessing the effectiveness of the incorporation process. Since the initial weights of the PVA and BC used were known, after washing, the amount of PVA remaining on the BC was calculated as a result of the final weighing (Equation (4)). The experiments were repeated three times for each initial pH value.

$$\text{PVA Attachment}(\%) = \frac{\text{Initial weight of composite} - \text{Final weight of composite}}{\text{Initial weight of composite}} \times 100 \quad (4)$$

2.9. Scanning Electron Microscopy (SEM)

SEM analysis was performed using a Thermo Scientific Helios 5 PFIB CXe (ThermoFisher Scientific, Waltham, MA, USA) device at 3 KeV/25 pA impact energy and 4 mm WD with an SE detector (TLD mode). Energy Dispersive Spectroscopy (EDS) analyses were performed with equipment outfitted with a Bruker XFlash 5030 detector (XFlash 5030, Bruker Co., Billerica, MA, USA). Carbon tape substrates are used to fix BC samples on the holder, subsequently gold-coated with a thickness of 30 nm.

2.10. Fourier Transform Infrared Spectroscopy Analysis (FT-IR)

FTIR spectroscopy was used to analyze the chemical composition, and functional groups present in the BC membrane. A Nicolet IN10 microFTIR device (Thermo Fisher Scientific, Waltham, MA, USA) operating in transmittance mode is used by measuring the absorption of infrared light with a wave number between 4,000 and 500 cm^{-1}. BC4, BC6, BC7, and BC9 samples have been analyzed.

2.11. Statistical Analysis

The impact of initial pH on BC thickness, conductivity, tensile characteristics, and water absorption data was assessed statistically using one-way ANOVA. Prior to using ANOVA, the assumptions of normality and homogeneity of variance were confirmed. Tukey's HSD post hoc test was used to further analyze significant effects and identify pairwise differences between pH groups. To calculate the mean $\pm$ standard deviation (SD), five replicates were used in thickness measurements for each group, and three replicates were used for other measurements. Differences were considered statistically significant at $p < 0.05$.

3. Results

3.1. Physical and Electrical Properties

3.1.1. Thickness, Electrical Conductivity, and Water Absorption Capacity

Figure 2a shows the BC thickness and electrical conductivity obtained according to the initial pH value graphically. The mean thickness values ranged between 1.5 mm at pH 9 and 2.4 mm at pH 6. From pH 7, the thickness started to decrease and reached its lowest value at pH 9. This may indicate that neutral or slightly acidic pH is more suitable for optimum thickness under BC synthesis conditions. These findings indicate that pH is an important factor in BC production and that optimum pH levels affect cellulose thickness and yield.

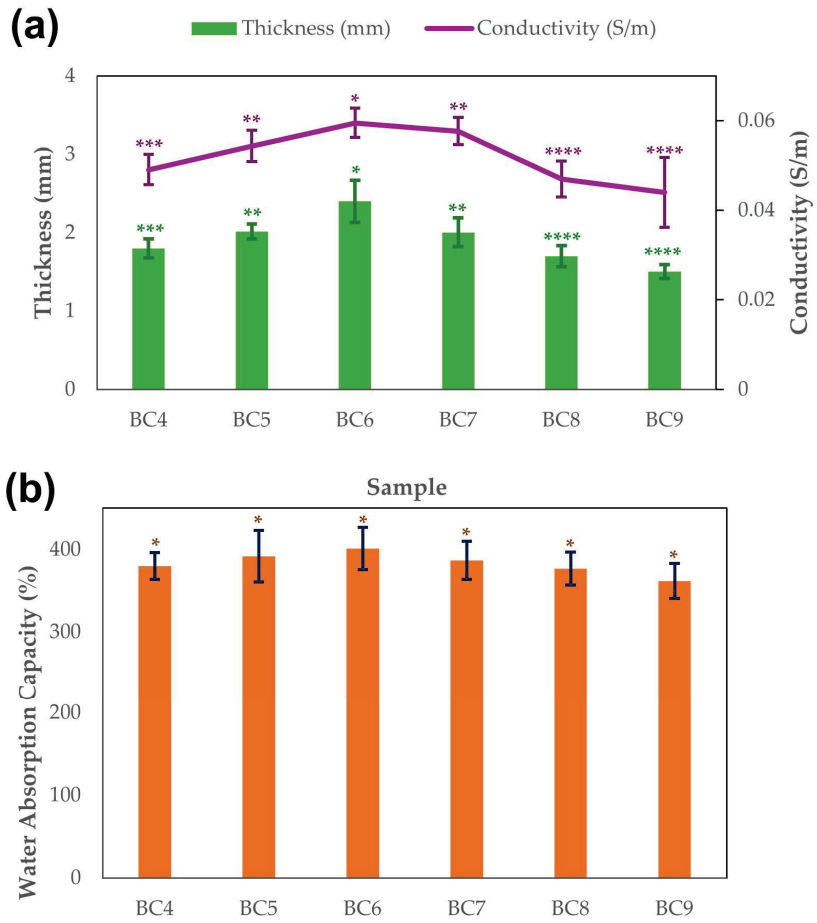

Figure 2. BC thickness and conductivity variations (**a**) and water absorption measurements (**b**) depending on the initial pH value. Data are presented as mean values and error bars represent the standard deviation (n = 5 for thickness and n = 3 for conductivity and water adsorption). The number of asterisks on the bars indicates statistically significant differences using one-way ANOVA followed by Tukey's HSD post hoc test ($p < 0.05$).

One-way ANOVA confirmed that the initial pH had a significant effect on BC thickness ($F(5,24) = 18.55$, $p < 0.0001$). Tukey's HSD post hoc test further revealed that BC synthesized at pH 6 exhibited significantly greater thickness compared to pH 4, 5, 7, 8, and 9 ($p < 0.05$). In addition, BC produced at pH 5 was significantly thicker than those at pH 8 and 9, while pH 7 samples were significantly thicker than those at pH 9. No significant differences were observed among the remaining comparisons.

In the study of BC production from waste figs using *K. xylinus* bacteria, it was revealed that *K. xylinus* produced significant amounts of BC over a wide pH spectrum (4.0–6.5) and the highest BC concentration was observed at pH 6.05 [41]. Using a new kombucha consortium (*K. saccharivorans*, *B. bruxellensis*, and *B. anomalus*) with black tea, a low-cost source, it was reported that BC could be produced at a high rate at a pH of 6 and 30 °C. The results showed that BC production increased 4.06-fold in the optimized medium compared to Hestrin-Schramm medium and the cost was reduced by 29.7% [42].

The maximum BC thickness values obtained at pH 6 (2.4 mm) are consistent with the initial pH and temperature values reported in previous studies as the parameters yielding the highest BC. However, most reports present BC yield in terms of dry weight (g/L) rather than thickness. Therefore, Table 1 provides a summary of representative studies that include both thickness and/or yield values to correlate our findings with the literature.

Table 1. Summary of representative studies reporting thickness and/or yield values.

Study (Ref.)	Carbon Sources/Medium	Bacteria	Vessel Type & Size	pH	Temperature (°C)	Incubation Time	BC Thickness (mm) or Yield (g/L)	Notes
Present study	Waste black tea medium	*K. xylinus*	Erlenmeyer flasks (250 mL)	4–9	30	10 days	1.5–2.4 mm	Maximum at pH 6
[41]	Waste fig extract + 20 g/L of initial sugar	*K. xylinus*	Erlenmeyer flasks (250 mL)	4–6.5	25–35	7 days	8.45 ± 0.51 g/L	Maximum at 6.05 and 30 °C
[42]	1% black tea and 6% glucose	*K. saccharivorans*, *B. bruxellensis*, and *B. anomalus*	-	6	30	10 days	18.68 g/L	29.74% cost reduction
[16]	Kombucha consortium + HS medium	*K. rhaeticus* K23	Erlenmeyer flasks (250 mL)	4–5.5	26–32	7–14 days	0.52– 9.1 g/L	The maximum BC production, 9.1 ± 0.66 g/L, was obtained from 32 °C, pH 5.5, 8 log CFU·mL^{-1} and 14 days of incubation
[43]	*V. faba* plants, 1.5% glucose and a 0.15% yeast extract	*Rhizobium* sp. and *K. hansenii*	500 mL flask	5–7	25–35	7 days	10–35 µm, 2.5 g/L	The maximum BC production, 2.5 g/L, at 30 °C and pH 6.5

The electrical conductivity of the BC samples was found to be significantly influenced by the initial pH of the medium during synthesis. As shown in Figure 2a, the conductivity values exhibited a rising trend from pH 4 to pH 6, followed by a gradual decline as the pH increased beyond this point. Specifically, the BC6 sample (pH 6) demonstrated the highest electrical conductivity value of 0.060 S/m, indicating optimal ionic mobility at near-neutral conditions. In contrast, the lowest conductivity was observed for BC9 (pH 9) at 0.044 S/m. Furthermore, also statistically, the initial pH had a substantial impact on the electrical conductivity of BC samples ($F(5,12) = 10.8$, $p < 0.001$). At pH 9, the mean conductivity was 0.044 S/m, while at pH 6, it was 0.060 S/m. The BC6 group (pH 6) exhibited substantially higher conductivity than pH 4, 8, and 9, according to Tukey's HSD post hoc test. In addition, compared to pH 9, the conductivity of the pH 5 and pH 7 samples was noticeably higher. The other comparisons showed no discernible changes. According to these findings, the BC matrix's ideal ionic mobility and conductive routes are supported by intermediate pH values (5–7), especially pH 6.

The BC samples in this study demonstrated significantly higher electrical conductivity than both unmodified plant-based cellulose and previously reported bacterial cellulose. While bamboo-derived cellulose showed only 4.0×10^{-9} S/cm [44] and *Acetobacter xylinum*-derived BC as low as 1.8×10^{-11} S/m [45], our unmodified BC samples achieved values up to 0.060 S/m, indicating a substantial improvement without chemical modification. This comparison highlights the superior intrinsic conductivity of BC used in our study, even without the integration of conductive polymers. The enhanced conductivity at pH 6 could be attributed to the optimized structural configuration and ionic mobility within the BC network. In contrast, the polypyrole-based enhancement in the referenced study required significant chemical modification and incorporation of external conductive components to achieve similar conductivity levels. Furthermore, our BC samples maintained their structural integrity and eco-friendly profile, making them particularly attractive for applications in biodegradable electronics, wearable sensors, and moisture-stable devices, without the need for synthetic additives.

A positive correlation was also noted between sample thickness and conductivity. The BC6 sample, which exhibited the maximum thickness (2.4 mm), corresponded with the highest conductivity, while the thinnest sample, BC9 (1.5 mm), showed the lowest

conductivity. This finding implies that increased thickness may reflect a denser and more interconnected structure capable of facilitating better electron or ion transport pathways within the BC matrix. Taken together, these results indicate that pH 6 represents a critical condition for maximizing the conductive performance of BC-based materials, offering insights into the optimization of such biopolymers for applications requiring moderate electrical activity, such as flexible electronics, biosensors, or electroactive wound dressings.

Water retention capacity and water release rate are the most important properties directly involved in biomedical applications of BC as a dressing material and are due to the highly porous nature of BC [46]. Water is present inside the pores and is bound to cellulose fibrils through hydrogen bonding. The pH value is one of the main factors affecting this property. Approximately pH 6–6.5 is recommended in some studies for optimal properties [43,46]. Figure 2b presents the results of water absorption measurements with initial pH values ranging from 4–9 and then purifying the harvested BC membranes. The water absorption capacity of the obtained BCs increased from pH 4 to 6, reaching a maximum value of 401%. From pH 7, the absorption capacity started to decrease and reached its lowest at pH 9 with 362%. A one-way ANOVA revealed that the initial pH had no statistically significant effect on water absorption capacity ($F(5,12) = 1.07$, $p = 0.425$). Tukey's post hoc analysis revealed no significant pairwise differences between pH groups ($p > 0.05$). These results suggest that water absorption capacity remains widely unaffected by pH variations, whereas conductivity and thickness exhibit greater sensitivity to changes in initial pH.

The analysis of BC thickness and electrical conductivity as a function of initial pH revealed a strong interdependence between structural and functional properties. Both two parameters showed a similar trend: increasing from pH 4 to 6, peaking at pH 6, and gradually declining beyond this point. The BC6 sample, produced at pH 6, exhibited the greatest thickness (2.4 mm), highest conductivity (0.060 S/m), and maximum water absorption capacity (401%). This indicates that near-neutral pH conditions provide optimal synthesis conditions for BC, promoting denser network formation, improved ionic mobility, and enhanced porosity. The positive correlation observed between thickness and conductivity suggests that a more interconnected cellulose matrix supports more efficient transport. Although the water absorption capacity is not significantly influenced by pH changes, increased porosity at pH 6 enhances water retention through hydrogen bonds within the cellulose network, which is particularly beneficial for biomedical applications such as wound dressing. These findings are consistent with literature reports that emphasize pH 6–6.5 as an ideal range for maximizing both structural integrity and performance characteristics of bacterial cellulose [43,46]. Overall, the study demonstrates that initial pH is a critical parameter influencing multiple functional attributes of BC and optimizing it can enhance the material's suitability for eco-friendly electronic and biomedical applications.

3.1.2. Results of Colorfastness Tests

The effects of pH levels on perspiration, rubbing, and washing fastness are presented in Table 2. Although no dye was applied to the BC samples, standardized colorfastness tests were conducted to evaluate the material's resistance to washing, perspiration, and mechanical friction, as a proxy for structural durability in wearable and biomedical applications. All samples exhibited a top rating of 5 for both perspiration and washing resistance, indicating no visible degradation, deformation, or surface change following exposure to artificial sweat or repeated laundering cycles.

Table 2. Fastness properties of BC depending on pH.

Specimen No.	Initial pH	Fastness		
		Perspiration	Washing	Rubbing (Cycle)
BC4	4	5	5	24 ± 3
BC5	5	5	5	28 ± 2
BC6	6	5	5	32 ± 2
BC7	7	5	5	30 ± 2
BC8	8	5	5	22 ± 2
BC9	9	5	5	18 ± 2

Notably, rubbing fastness, assessed via the number of dry cycles until visible surface wear, demonstrated a clear pH dependency. The BC6 sample (pH 6) showed the highest resistance (32 ± 2 cycles), while BC9 (pH 9) showed the lowest (18 ± 2 cycles). pH had a highly significant impact on rubbing resistance, according to a one-way ANOVA ($F(5,12) = 24.6$, $p < 0.0001$). According to the results of Tukey's post hoc analysis, pH 6 had significantly higher fastness than pH 4, 8, and 9, and pH 5 and pH 7 were also significantly higher than pH 8 and 9. Furthermore, rubbing fastness was significantly higher at pH 4 than pH 9. The other groups did not differ significantly from one another. These findings support the notion that the ideal pH range for increasing the rubbing durability of BC samples is the most favorable pH range (5–7). This trend suggests that BC synthesized under near-neutral pH forms a denser and more mechanically robust network, consistent with conductivity and thickness results discussed earlier.

These results are particularly promising when compared with similar fastness-related studies involving BC. For instance, Harmon (2020) noted that BC films without any finishing treatments suffered surface disruption after sweat or laundering simulations [47]. Similarly, recent work on natural textile fibers such as cotton dyed with natural extracts reported significantly lower resistance to perspiration (ratings 2–3) [48]. Taken together, these findings support the potential of unmodified BC membranes not only as flexible and conductive materials but also as mechanically and chemically resilient substrates suitable for sweat-exposed and washable electronic or biomedical systems.

3.2. Mechanical Properties

The mechanical properties of the BC membranes demonstrated a clear dependence on the initial pH of the culture medium. As shown in Figure 3, both properties showed a similar trend, increasing from pH 4.0 and reaching maximum values at pH 6.0, followed by a gradual decline at higher pH values. The BC6 sample (pH 6.0) exhibited the highest tensile strength (2.4 ± 0.2 MPa) and elongation (13 ± 1.6%), indicating optimal nanofiber formation and cohesive network structure under near-neutral conditions. In contrast, the samples produced at pH 9.0 showed significantly lower mechanical performance, with a tensile strength of 1.5 ± 0.2 MPa and elongation of 7 ± 1.04 (%), likely due to disrupted fibrillar assembly and reduced hydrogen bonding at more alkaline conditions.

Tensile strength ($F(5,12) = 9.88$, $p = 0.0006$) and elongation ($F(5,12) = 9.44$, $p = 0.0008$) were both significantly impacted by pH, according to a one-way ANOVA. The BC6 group (pH 6) demonstrated were also significantly higher tensile strength than pH 8 and pH 9, while pH 5 and pH 7 were likewise significantly stronger than pH 9, according to Tukey's HSD test. Elongation was also substantially higher at pH 6 than at pH 8 and 9, with pH 5 and pH 7 similarly exceeding pH 9 in this regard. These findings demonstrate that near-neutral pH, especially pH 6, provides optimal conditions for enhancing BC samples'

mechanical performance. These findings confirm that the structural integrity of BC can be fine-tuned by adjusting the pH during synthesis.

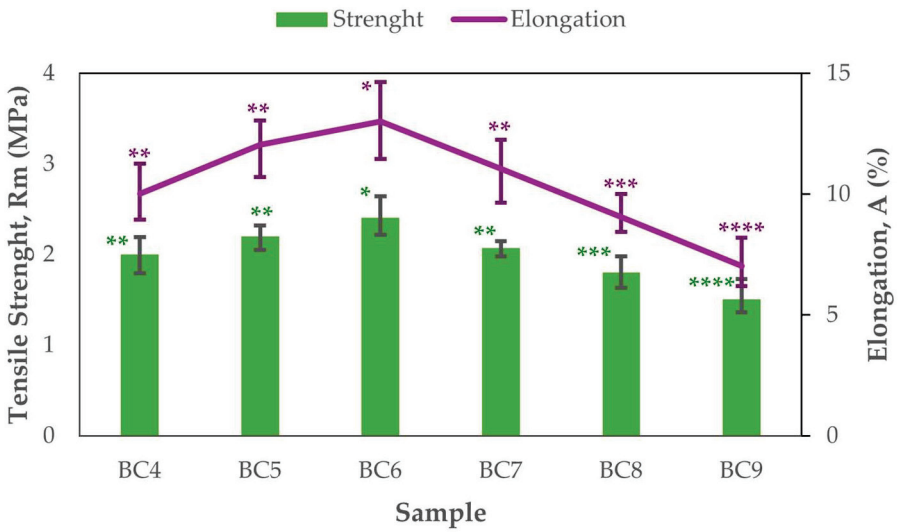

Figure 3. Tensile strength and elongation as a function of initial pH. Data are presented as mean values, and error bars indicate the minimum and maximum values obtained from replicate measurements ($n = 3$). The number of asterisks on the bars indicates statistically significant differences using one-way ANOVA followed by Tukey's HSD post hoc test ($p < 0.05$).

While the strength values obtained in this study (ranging from 1.5–2.4 MPa) are lower than those reported for highly purified or treated BC membranes (often >30 MPa) [16,49], they are considered suitable for applications such as soft bioelectronics, moisture-sensitive devices, or wound dressing supports. Similarly, the elongation values achieved (up to 13%) fall within or slightly below typical ranges reported for unmodified BC but demonstrate meaningful flexibility for use in deformable systems.

The BC membranes in this study were produced using *K. xylinus* ATCC 53524, a well-known high-performing strain in terms of both yield and structural quality. These results are highly consistent with those reported in previous studies for the same strain. The methodology employed in this study for BC production closely follows the approach reported by Chen et al. [50], in which various *Komagataeibacter* strains were used and demonstrated that ATCC 53,524 produced BC with superior mechanical properties, including a breaking stress of 0.68 MPa, breaking strain of 20.7%, and Young's modulus of 5.56 MPa, under controlled conditions. However, a key difference in our protocol was the supplementation of the growth medium with tea waste, a low-cost, nutrient-rich organic byproduct. This modification introduces a novel and sustainable approach to BC production while simultaneously offering additional carbon and polyphenolic sources that may influence the nanofibrillar assembly and material performance. Despite using a similar strain and culture strategy, our BC membranes exhibited significantly higher tensile strength (up to 2.4 MPa) but lower elongation at break (max. 13%) compared to Chen's study (0.68 MPa strength, ~20.7% elongation). This variation may arise from differences in membrane composition, structural compaction, and potential interactions between tea-derived phenolic compounds and cellulose fibers, which can enhance stiffness and reduce flexibility. Previous studies have suggested that phenolic additives can induce hydrogen bonding or act as mild crosslinking agents, leading to tighter fibril networks and altered mechanical responses.

Overall, the mechanical evaluation confirms that pH 6.0 is a critical condition for enhancing the structural performance of BC, supporting its potential for flexible and skin-contact

applications. The incorporation of tea waste not only enhances the sustainability profile of the production process but also allows for modulation of BC properties by biochemical tuning of the culture medium. This aligns with current trends in green biomaterial development, where agricultural waste valorization is coupled with high-performance material synthesis. Even being lower than peak literature values, the strength and elongation values obtained here are consistent, reproducible, and sufficient for many biomedical and flexible electronics applications, particularly where moderate mechanical durability, conformability, and biocompatibility are more critical than extreme mechanical strength.

3.3. Morphology Analysis by SEM Images

SEM images (Figure 4) demonstrate that the morphology of BC is significantly influenced by the pH of the culture medium. At pH 4 (Figure 4a) and at pH 9 (Figure 4d) presented a densely packed three-dimensional ribbon-like network of nanofibril structures. The microstructure obtained for pH 4 is consistent with the study results obtained for BC prepared with black tea and grown in Kombucha culture with initial pH 4.06–4.35 [49]. The pH 9 sample (Figure 4d) presented a densely packed but morphologically coarser network than pH 4 with visibly thicker fibers. Thicker fibers can reduce flexibility and may limit surface reactivity, which is critical for biomedical and electrode applications where intimate skin or tissue contact is required. At pH 6 (Figure 4b) and pH 7 (Figure 4c) conditions, significant coverage of the surface was obtained. This coating was observed in various areas under pH 7 conditions, accompanied by some agglomeration in the form of clumps. These clumps may have originated from the lyophilization of the sugar-rich extract [51]. The most uniform and cohesive fibrillar arrangement, on the other hand, was shown by the structure produced at pH 6 (Figure 4b), which formed a dense and well-entangled 3D nanofiber network. This shape is in line with earlier research showing that BC production is best achieved at a pH close to neutral [16,43].

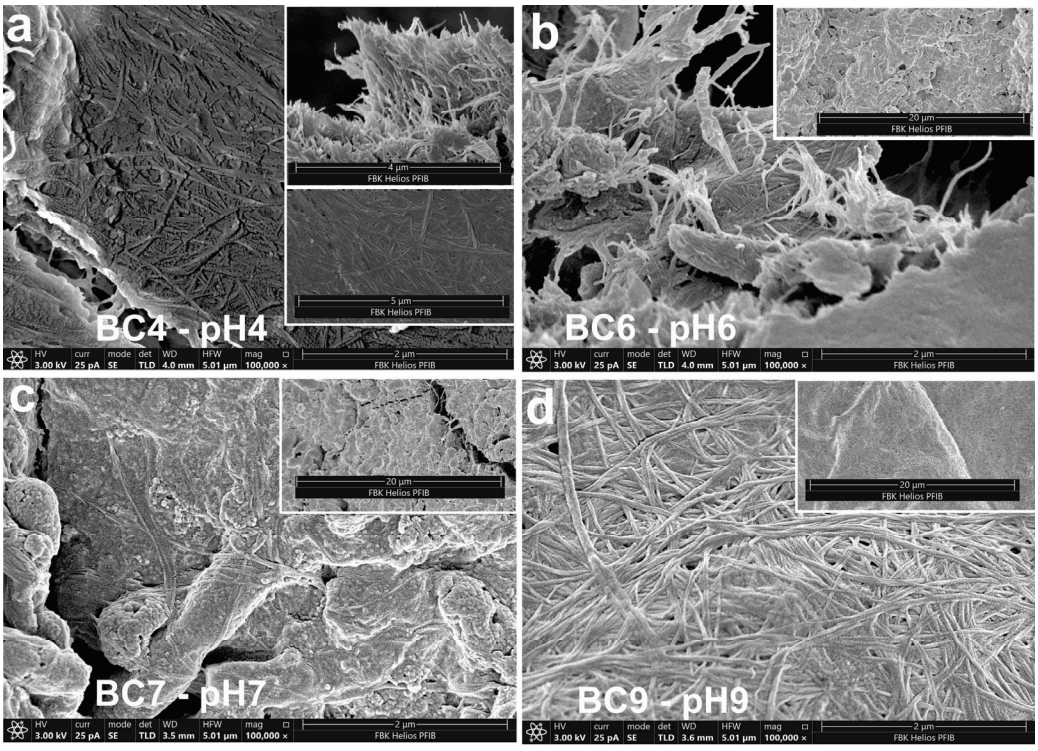

Figure 4. SEM images of BCs depending on the initial pH value: (**a**) pH 4, (**b**) pH 6, (**c**) pH 7, and (**d**) pH 9.

Quantitative analysis of the pH 9 SEM image (Figure 5) revealed fiber diameters ranging from 24.8 nm to 82.6 nm, with an average of about 50 nm. Although this falls within the expected nanofiber scale, the increased thickness and density may limit flexibility and surface reactivity—properties critical for biomedical applications such as wound dressings and flexible electrodes. These results underscore the importance of pH as a tunable parameter for tailoring BC morphology according to specific functional requirements. These morphological observations strongly support the idea that synthesis pH can be used as a tunable design parameter for tailoring BC properties: near-neutral pH (especially pH 6) yields a tightly interwoven, fine-fibered network ideal for mechanically robust and conductive applications such as wearable electrodes, while more acidic pH (pH 4–5) produces morphologies that, despite lower mechanical cohesion, are associated with enhanced antimicrobial activity, making them better suited for infection-preventive wound dressings.

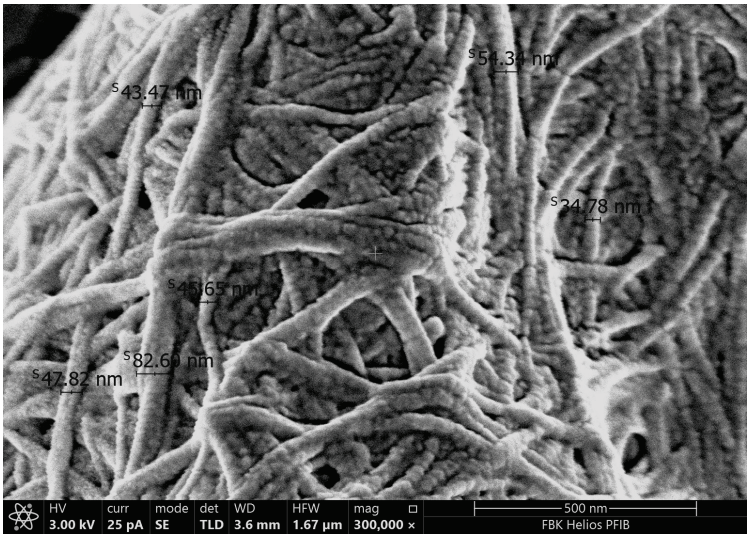

Figure 5. Fiber diameters measured by using SEM for BC9 sample.

3.4. Fourier Transformed Infrared (FTIR) Analysis

FTIR analysis confirmed the characteristic functional groups of BCs across all samples synthesized at different pH levels (Figure 6). Broad bands around 3475–3410 cm^{-1} are attributed to O–H stretching vibrations representing the hydroxyl bonds in these cellulose samples [52]. This strong and broad O–H band also indicates an extensive hydrogen-bonding network, which is directly related to the high-water absorption capacity observed in BC membranes. Peaks near 2800–2900 cm^{-1} represent symmetric (−CH) stretching vibrations indicating the presence of methyl/methylene functional groups, consistent with typical cellulose structures [43,52]. The region around 1030–1050 cm^{-1}, indicates the presence of (C–O) stretching vibration in the polymer, a feature that correlates with the intact polysaccharide backbone essential for maintaining mechanical integrity [52]. The peak at ~890 cm^{-1}, corresponding to β-glycosidic linkages, further confirm the presence of amorphous cellulose absorption band [13].

Preservation of this β-linkage across all pH conditions suggests that the cellulose molecular framework remains chemically stable, even though physical and morphological characteristics vary. Although no major shifts in peak positions were detected among BC4, BC6, BC7, and BC9, slight variations in band intensity—particularly in the O–H stretching region—may reflect subtle changes in hydrogen bonding density and moisture content. For example, the more defined O–H band in BC6 aligns with its superior water absorption and

tensile strength, suggesting a denser and more cohesive nanofiber network. Conversely, reduced intensity in alkaline conditions (BC9) may indicate less compact hydrogen-bonding arrangements, consistent with its lower mechanical and antibacterial performance.

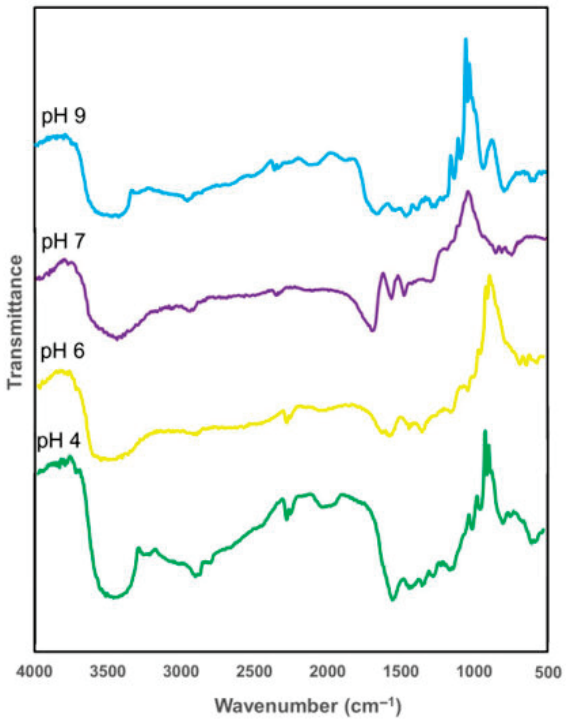

Figure 6. FTIR spectra of BC4, BC6, BC7, and BC9 samples.

This finding aligns with prior studies suggesting that near-neutral pH conditions promote optimal bacterial cellulose assembly and structural order [16,43]. Such structural preservation is essential for ensuring reliable performance in biomedical devices, where both chemical stability and physical cohesion are critical—for instance, in long-term wound dressings, skin-contact electrodes, and flexible biosensors.

3.5. Antimicrobial Test Results

Table 3 shows the antibacterial activity of BC specimens prepared under varying initial pH conditions, evaluated against the Gram-negative strain *E. coli*. The test was conducted using the dynamic contact method described in ASTM E2149-13a, and the results are expressed in terms of log reduction in viable bacterial count after 24 h of incubation.

Table 3. Antimicrobial Activity (Log Reduction) of BC depending on pH.

Specimen No.	Antimicrobial Activity (Log Reduction)	Antimicrobial Activity Level
BC4	3.5	High
BC5	3.2	Moderate-High
BC6	2.8	Moderate
BC7	2.5	Low-Moderate
BC8	2.0	Low
BC9	1.5	Very Low

All BC samples demonstrated varying degrees of antibacterial activity, with a clear correlation between initial pH conditions and antimicrobial performance. The BC4 sample,

prepared under the most acidic condition, exhibited the highest antibacterial activity with a log reduction of 3.5, which corresponds to a "high" level of efficacy according to standard classification. Similarly, BC5 and BC6 displayed log reductions of 3.2 and 2.8, respectively, indicating moderate to high antibacterial effectiveness.

As the initial pH increased toward neutral and alkaline conditions, the antibacterial activity progressively declined. BC7 and BC8 samples showed log reductions of 2.5 and 2.0, respectively, reflecting low to moderate activity. The BC9 specimen, associated with the most alkaline condition, exhibited the lowest antibacterial activity with a log reduction of 1.5, which falls below the threshold of significant antimicrobial effectiveness.

E. coli is reported to grow well under weakly acidic to neutral conditions but is inhibited at low pH [53]. These study's findings suggest that acidic pH conditions during BC preparation enhance the antibacterial potential of the material. This effect may be attributed to changes in surface chemistry, such as increased negative charge density, porosity, or enhanced interaction between bacterial membranes and the BC matrix. The results further reinforce the notion that modulating the pH during synthesis can be an effective strategy to tune the antimicrobial properties of bacterial cellulose-based materials without incorporating external biocidal agents. Although *E. coli* is known for acid resistance the antimicrobial effect might be triggered by the changes in surface due to pH.

3.6. PVA Attachment Test Results

Polyvinyl alcohol (PVA) is a widely used polymer in film production, textile, medicine, and agriculture due to its water solubility and non-toxic biodegradability. However, PVA has incomplete mechanical properties, often requiring costly additives like starch and sodium alginate to enhance its performance. Studies have shown that incorporating cellulose improves PVA's properties, but plant-derived cellulose requires complex purification processes [54,55]. PVA and BC form a composite material with enhanced mechanical strength, hydrophilicity, and structural integrity. The interaction between hydroxyl groups in both materials allow for tailored water absorption, making the composite useful in various applications, including food packaging and biomedical engineering [54,55].

Table 4 presents the PVA attachment percentages for BC–PVA composite samples prepared under varying pH conditions. The results were calculated based on weight loss after the washing step, which removes non-bonded, water-soluble PVA. This parameter provides insight into the effectiveness of PVA incorporation into the BC matrix and its potential contribution to the final material properties.

Table 4. PVA Attachment efficiency (%) of BC–PVA composites prepared under different initial pH values.

Specimen No.	PVA Attachment (%)
BC4	8 ± 0.8
BC5	10 ± 0.8
BC6	12 ± 1.4
BC7	10 ± 1.4
BC8	7 ± 0.8
BC9	5 ± 0.8

The results indicate that PVA attachment values ranged between 5% and 12%, with the highest incorporation observed in BC6 (12%), followed by BC5 and BC7 (10%). On the other hand, BC9 exhibited the lowest attachment efficiency (5%), which may be due to structural changes in the BC network at high pH conditions that limit hydrogen bonding between PVA and BC. The impact of pH was shown to be statistically significant by one-

way ANOVA (F (5,12) = 11.28, $p = 0.0003$). The results of Tukey's test showed that samples at pH 6 had significantly higher attachment than samples at pH 4, 8, and 9, and that samples at pH 5 and pH 7 had significantly higher attachment than those at pH 9 ($p < 0.05$). According to these findings, PVA adherence to BC structures is improved by moderate pH levels, particularly pH 6, thereby enhancing interfacial compatibility with polymer matrices. Since the interaction between hydroxyl groups of BC and PVA is primarily responsible for network formation, pH-induced disruption of these groups may reduce the efficiency of physical entrapment and bonding.

4. Conclusions

This study demonstrated the production of bacterial cellulose (BC) using *Komagataeibacter xylinus* and spent black tea waste as a low-cost and sustainable carbon source. The physicochemical, mechanical, antimicrobial, and electrical properties of the synthesized BC membranes were strongly influenced by the initial pH of the culture medium. Among the tested conditions, pH 6.0 yielded the most favorable results in terms of tensile strength (2.4 MPa), elongation (13%), water absorption, electrical conductivity, and PVA attachment (12%), indicating a highly cohesive nanofiber network. The combination of high tensile strength, water retention, and electrical conductivity obtained at pH 6 makes these BC membranes particularly suitable for flexible electrodes, biosensors, and wearable biomedical devices. Furthermore, BC membranes produced at acidic pH values (pH 4–6) exhibited higher antibacterial activity, with log reductions exceeding 2.8 against *E. coli*, likely due to enhanced surface chemistry and porosity. The strong antibacterial activity observed at pH 4–6 indicates their potential use in infection-prone biomedical applications such as wound dressings, surgical patches, and antimicrobial coatings.

FTIR and SEM analyses confirmed the preservation of key cellulose functional groups and revealed structural differences depending on pH with the most uniform nanofibrillar morphology observed at pH 6, respectively. PVA attachment tests further demonstrated that moderate pH conditions enhance composite integration. Moderate PVA incorporation in BC membranes, as observed in BC5 and BC6, offers a balance between mechanical durability and biocompatibility, which is advantageous for moist-contact biomedical materials like electrotherapy pads and biopotential measurement patches.

In addition to offering functional and performance advantages, the use of food industry waste (spent tea leaves) as a feedstock contributes to environmental sustainability by promoting circular bioeconomy principles. This approach directly supports the United Nations Sustainable Development Goals, particularly SDG 12 (Responsible Consumption and Production) through waste valorization and resource efficiency, and SDG 13 (Climate Action) by reducing carbon-intensive input materials. The valorization of spent tea waste not only addresses environmental concerns but also provides a sustainable pathway for the mass production of functional BC-based biomaterials in medical device, packaging, and wearable technology industries.

Taken together, this work presents a viable and potentially scalable process for producing BC-based materials that may be applied in biomedical devices such as flexible electrodes and antimicrobial wound dressings. Nevertheless, several challenges remain in translating the process from laboratory to industrial scale, including limited oxygen and nutrient diffusion in larger containers, the risk of contamination when utilizing agro-waste substrates, and the inherent variability in tea waste composition, which may affect batch-to-batch consistency. Economic considerations, including downstream purification and substrate preparation, must also be addressed. Despite these challenges, the findings demonstrate that tea waste is a sustainable and feasible feedstock for BC synthesis. Fu-

ture research will be directed toward cost estimation, bioreactor-based scale-up, and the integration of BC composites into functional device platforms.

Author Contributions: C.G., investigation (lead); methodology (lead); and writing—original draft (supporting). A.I., conceptualization (lead); investigation (co-lead); methodology (supporting); resources (lead); and writing—original draft (lead). M.B., review and editing (supporting); investigation (supporting); and methodology (co-lead). P.B., investigation (supporting) and review and editing (supporting). L.P., review and editing (supporting); investigation (supporting); and methodology (supporting). M.F., investigation (supporting); methodology (supporting); and review and editing (supporting). D.D., funding acquisition (lead); editing (supporting); investigation (supporting); and methodology (supporting). H.B., investigation (supporting) and review and editing (supporting). A.K., investigation (co-lead); methodology (co-lead); and writing—review and editing (supporting). All authors have read and agreed to the published version of the manuscript.

Funding: This work is partially based on the works of the FOOD CHASE project co-funded by the European Union and European Education and Culture Executive Agency (EACEA) (grant number 101140250—ERASMUS-EDU-2023-PI-ALL-INNO). Views and opinions expressed are, however, those of the authors only and do not necessarily reflect those of the European Union or the European Education and Culture Executive Agency (EACEA). Neither the European Union nor EACEA can be held responsible for them.

Institutional Review Board Statement: Not applicable.

Data Availability Statement: The original contributions presented in this study are included in the article. Further inquiries can be directed to the corresponding author(s).

Acknowledgments: The authors gratefully acknowledge the support of TUBITAK (Project No. 1059B192300439, 2219 International Postdoctoral Research Fellowship Program) and the Provincia Autonoma di Trento through the Visiting Trentino program. These contributions were instrumental in enabling the international collaboration underpinning this study.

Conflicts of Interest: Author Massimo Bersani, Arzum Işıtan and Michele Fedrizzi were employed by the Fondazione Bruno Kessler. Author Arzum Işıtan was employed by the company Bilgece Mühendislik Geri Dönüşüm Ltd. Şti. Author Laura Pasquardini was employed by the company Indivenire srl. Author Davide D'Angelo was employed by the company Cosvitec Scarl. The remaining authors declare that the research was conducted in the absence of any commercial or financial relationships that could be construed as a potential conflict of interest.

Abbreviations

The following abbreviations are used in this manuscript:

MCC	Microcrystalline cellulose
NCC	Nanocrystalline cellulose
BC	Bacterial cellulose
AAB	Acetic acid bacteria
STLs	Spent tea leaves
ATCC	American type culture collection
PVA	Polyvinyl alcohol

References

1. Zielińska, M.; Bułkowska, K. Agricultural Wastes and Their By-Products for the Energy Market. *Energies* **2024**, *17*, 2099. [CrossRef]
2. Arora, J.; Ramawat, K.G.; Mérillon, J.-M. Disposal of Agricultural Waste and Its Effects on the Environment, Production of Useful Metabolites and Energy: Potential and Challenges. In *Environmental Impact, Useful Metabolites and Energy Production*; Springer Nature: Singapore, 2023; pp. 3–20.
3. Koul, B.; Yakoob, M.; Shah, M.P. Agricultural Waste Management Strategies for Environmental Sustainability. *Environ. Res.* **2022**, *206*, 112285. [CrossRef]

4. Awogbemi, O.; Kallon, D.V. Von Pretreatment Techniques for Agricultural Waste. *Case Stud. Chem. Environ. Eng.* **2022**, *6*, 100229. [CrossRef]
5. Food and Agriculture Organization of the United Nations (FAO). *The State of Food and Agriculture 2019—Moving Forward on Food Loss and Waste Reduction*; FAO: Rome, Italy, 2019.
6. EUROSTAT. Food Waste and Food Waste Prevention—Estimates. Available online: https://ec.europa.eu/eurostat/statistics-explained/index.php?title=Food_waste_and_food_waste_prevention_-_estimates (accessed on 13 December 2024).
7. European Commission. Food Waste. Available online: https://food.ec.europa.eu/food-safety/food-waste_en (accessed on 13 December 2024).
8. European Commission. Circular Economy Action Plan. Available online: https://environment.ec.europa.eu/strategy/circular-economy-action-plan_en (accessed on 13 December 2024).
9. Zabaniotou, A.; Kamaterou, P. Food Waste Valorization Advocating Circular Bioeconomy—A Critical Review of Potentialities and Perspectives of Spent Coffee Grounds Biorefinery. *J. Clean. Prod.* **2019**, *211*, 1553–1566. [CrossRef]
10. Gallego-García, M.; Moreno, A.D.; Manzanares, P.; Negro, M.J.; Duque, A. Recent Advances on Physical Technologies for the Pretreatment of Food Waste and Lignocellulosic Residues. *Bioresour. Technol.* **2023**, *369*, 128397. [CrossRef]
11. Işıtan, A.; Pasquardini, L.; Bersani, M.; Gök, C.; Fioravanti, S.; Lunelli, L.; Çağlarer, E.; Koluman, A. Sustainable Production of Microcrystalline and Nanocrystalline Cellulose from Textile Waste Using HCl and NaOH/Urea Treatment. *Polymers* **2025**, *17*, 48. [CrossRef]
12. Riseh, R.S.; Vazvani, M.G.; Hassanisaadi, M.; Thakur, V.K. Agricultural Wastes: A Practical and Potential Source for the Isolation and Preparation of Cellulose and Application in Agriculture and Different Industries. *Ind. Crops Prod.* **2024**, *208*, 117904. [CrossRef]
13. Sharma, C.; Bhardwaj, N.K. Biotransformation of Fermented Black Tea into Bacterial Nanocellulose via Symbiotic Interplay of Microorganisms. *Int. J. Biol. Macromol.* **2019**, *132*, 166–177. [CrossRef] [PubMed]
14. Gao, K.; Wu, N.; Ji, B.; Liu, J. A Film Electrode upon Nanoarchitectonics of Bacterial Cellulose and Conductive Fabric for Forehead Electroencephalogram Measurement. *Sensors* **2023**, *23*, 7887. [CrossRef] [PubMed]
15. Moreno-Díaz, C.; González-Arranz, S.; Martínez-Cerezo, C. Bacterial Cellulose Production within a Circular Economy Framework: Utilizing Organic Waste. *Polymers* **2024**, *16*, 2735. [CrossRef] [PubMed]
16. Uğurel, C.; Öğüt, H. Optimization of Bacterial Cellulose Production by Komagataeibacter Rhaeticus K23. *Fibers* **2024**, *12*, 29. [CrossRef]
17. Sumini, M.; Andrade, G.J.S.; Tischer, C.A.; Kobayashi, R.K.T.; Nakazato, G. Production of Bacterial Cellulose by Komagataeibacter Xylinus: Biochemistry, Synthesis and Applications. *Cellulose* **2024**, *32*, 81–94. [CrossRef]
18. Lavasani, P.S.; Motevaseli, E.; Shirzad, M.; Modarressi, M.H. Isolation and Identification of Komagataeibacter Xylinus from Iranian Traditional Vinegars and Molecular Analyses. *Iran. J. Microbiol.* **2017**, *9*, 338–347.
19. Chang, K. *World Tea Production and Trade: Current and Future Development*; FAO: Rome, Italy, 2015.
20. Çakmak, T.G.; Saricaoglu, B.; Ozkan, G.; Tomas, M.; Capanoglu, E. Valorization of Tea Waste: Composition, Bioactivity, Extraction Methods, and Utilization. *Food Sci. Nutr.* **2024**, *12*, 3112–3124. [CrossRef]
21. Spizzirri, U.G.; Carullo, G.; De Cicco, L.; Crispini, A.; Scarpelli, F.; Restuccia, D.; Aiello, F. Synthesis and Characterization of a (+)-Catechin and L-(+)-Ascorbic Acid Cocrystal as a New Functional Ingredient for Tea Drinks. *Heliyon* **2019**, *5*, e02291. [CrossRef] [PubMed]
22. FAO. *Current Global Market Situation and Medium-Term Outlook*; FAO: Rome, Italy, 2024.
23. Negi, T.; Kumar, Y.; Sirohi, R.; Singh, S.; Tarafdar, A.; Pareek, S.; Kumar Awasthi, M.; Alok Sagar, N. Advances in Bioconversion of Spent Tea Leaves to Value-Added Products. *Bioresour. Technol.* **2022**, *346*, 126409. [CrossRef]
24. Sanz, V.; Flórez-Fernández, N.; Domínguez, H.; Torres, M.D. Clean Technologies Applied to the Recovery of Bioactive Extracts from Camellia Sinensis Leaves Agricultural Wastes. *Food Bioprod. Process.* **2020**, *122*, 214–221. [CrossRef]
25. Volova, T.G.; Prudnikova, S.V.; Sukovatyi, A.G.; Shishatskaya, E.I. Production and Properties of Bacterial Cellulose by the Strain Komagataeibacter Xylinus B-12068. *Appl. Microbiol. Biotechnol.* **2018**, *102*, 7417–7428. [CrossRef] [PubMed]
26. Anguluri, K.; La China, S.; Brugnoli, M.; Cassanelli, S.; Gullo, M. Better under Stress: Improving Bacterial Cellulose Production by Komagataeibacter Xylinus K2G30 (UMCC 2756) Using Adaptive Laboratory Evolution. *Front. Microbiol.* **2022**, *13*, 994097. [CrossRef]
27. Department of Economic and Social Affairs, United Nations. The 17 Goals | Sustainable Development. Available online: https://sdgs.un.org/goals (accessed on 6 January 2025).
28. EC-European Commission. *The European Green Deal*; European Commission: Brussels, Belgium, 2019.
29. EC-European Commission. *A New Circular Economy Action Plan For a Cleaner and More Competitive Europe*; European Commission: Brussels, Belgium, 2020.

30. Food Chase. Food Supply-Chain Ecosystems for Sustainability. Available online: https://foodchase.eu/ (accessed on 6 January 2025).
31. Hamed, D.A.; Maghrawy, H.H.; Abdel Kareem, H. Biosynthesis of Bacterial Cellulose Nanofibrils in Black Tea Media by a Symbiotic Culture of Bacteria and Yeast Isolated from Commercial Kombucha Beverage. *World J. Microbiol. Biotechnol.* **2023**, *39*, 48. [CrossRef]
32. Hestrin, S.; Schramm, M. Synthesis of Cellulose by Acetobacter Xylinum. 2. Preparation of Freeze-Dried Cells Capable of Polymerizing Glucose to Cellulose. *Biochem. J.* **1954**, *58*, 345–352. [CrossRef] [PubMed]
33. *ASTM D882-97*; Standard Test Method for Tensile Properties of Thin Plastic Sheeting. ASTM: West Conshohocken, PA, USA, 1997.
34. *AATCC TM61-2013e*; Test Method for Colorfastness to Laundering: Accelerated. American Association of Textile Chemists and Colorists: Durham, NC, USA, 2020.
35. *ISO 105-X12:2016*; Tests for Colour Fastness—Part X12: Colour Fastness to Rubbing. ISO—International Organization for Standardization: Geneva, Switzerland, 2016.
36. *AATCC TM15-2021*; Test Method for Colorfastness to Perspiration. American Association of Textile Chemists and Colorists: Durham, NC, USA, 2021.
37. Sirichaibhinyo, T.; Supchocksoonthorn, P.; Paoprasert, P.; Ummartyotin, S. The Electrical Conductivity of a Bacterial Cellulose and Polyaniline Composite Significantly Improved by Activated Carbon: A Nano-Based Platform for Electrodes. *ChemEngineering* **2024**, *8*, 87. [CrossRef]
38. *ASTM E2149-13a*; Standard Test Method for Determining the Antimicrobial Activity of Antimicrobial Agents Under Dynamic Contact Conditions. ASTM: West Conshohocken, PA, USA, 2013.
39. Pinto, R.; Fernandes, S.; Pinto, R.J.; Fernandes, S.C.; Freire, C.S.; Sadocco, P.; Causio, J.; Neto, C.P.; Trindade, T. Antibacterial Activity of Optically Transparent Nanocomposite Films Based on Chitosan or Its Derivatives and Silver Nanoparticles. *Carbohydr. Res.* **2012**, *348*, 77–83. [CrossRef] [PubMed]
40. Raei, P.; Khomeiri, M.; Mahounak, A.S.; Moayedi, A.; Kashiri, M. Characterization of Bacterial Cellulose/PVA Composite Films Incorporated with Sesame Meal Protein Hydrolysate: Physicochemical, Antimicrobial, and Antioxidant Properties. *Appl. Food Res.* **2025**, *5*, 100727. [CrossRef]
41. Yilmaz, M.; Goksungur, Y. Optimization of Bacterial Cellulose Production from Waste Figs by Komagataeibacter Xylinus. *Fermentation* **2024**, *10*, 466. [CrossRef]
42. Avcioglu, N.H.; Birben, M.; Seyis Bilkay, I. Optimization and Physicochemical Characterization of Enhanced Microbial Cellulose Production with a New Kombucha Consortium. *Process Biochem.* **2021**, *108*, 60–68. [CrossRef]
43. Almihyawi, R.A.H.; Musazade, E.; Alhussany, N.; Zhang, S.; Chen, H. Production and Characterization of Bacterial Cellulose by Rhizobium Sp. Isolated from Bean Root. *Sci. Rep.* **2024**, *14*, 10848. [CrossRef]
44. Khamwongsa, P.; Wongjom, P.; Cheng, H.; Lin, C.C.; Ummartyotin, S. Significant Enhancement of Electrical Conductivity of Conductive Cellulose Derived from Bamboo and Polypyrrole. *Compos. Part C Open Access* **2022**, *9*, 100314. [CrossRef]
45. Lay, M.; González, I.; Tarrés, J.A.; Pellicer, N.; Bun, K.N.; Vilaseca, F. High Electrical and Electrochemical Properties in Bacterial Cellulose/Polypyrrole Membranes. *Eur. Polym. J.* **2017**, *91*, 1–9. [CrossRef]
46. Cruz, M.A.; Flor-Unda, O.; Avila, A.; Garcia, M.D.; Cerda-Mejía, L. Advances in Bacterial Cellulose Production: A Scoping Review. *Coatings* **2024**, *14*, 1401. [CrossRef]
47. Harmon, J. Investigating the Dyeing Potential of Bacterial Cellulose: Strength and Colorfastness to Perspiration and Laundering. In Proceedings of the International Textile and Apparel Association Annual Conference, Virtual, 18–20 November 2020; Volume 77. [CrossRef]
48. Kim, E.; Kang, J.; Lee, J.; Choi, N. Color Fastness and Antimicrobial Activity of Gardenia Jasminoides Extract against Antimicrobial-Resistant Staphylococcus Aureus. *Fash. Text.* **2024**, *11*, 37. [CrossRef]
49. Ramírez Tapias, Y.A.; Di Monte, M.V.; Peltzer, M.A.; Salvay, A.G. Bacterial Cellulose Films Production by Kombucha Symbiotic Community Cultured on Different Herbal Infusions. *Food Chem.* **2022**, *372*, 131346. [CrossRef] [PubMed]
50. Chen, S.Q.; Lopez-Sanchez, P.; Wang, D.; Mikkelsen, D.; Gidley, M.J. Mechanical Properties of Bacterial Cellulose Synthesised by Diverse Strains of the Genus Komagataeibacter. *Food Hydrocoll.* **2018**, *81*, 87–95. [CrossRef]
51. El-Wakil, N.A.; Hassan, E.A.; Hassan, M.L.; Abd El-Salam, S.S. Bacterial Cellulose/Phytochemical's Extracts Biocomposites for Potential Active Wound Dressings. *Environ. Sci. Pollut. Res.* **2019**, *26*, 26529–26541. [CrossRef]
52. Gao, N.; Dai, J.; Liu, Y.; Li, S.; Wang, J.; Lu, W.; Qiu, D. Cellulose-Mediated Floc Formation by the Activated Sludge Bacterium Shinella Zoogloeoides ATCC 19623. *BMC Microbiol.* **2022**, *22*, 104. [CrossRef]
53. Hou, T.; Wang, F.; Wang, L. Facile Preparation of PH-Responsive Antimicrobial Complex and Cellulose Nanofiber/PVA Aerogels as Controlled-Release Packaging for Fresh Pork. *Food Sci. Biotechnol.* **2023**, *33*, 1871. [CrossRef]

54. Singhaboot, P.; Kraisuwan, W.; Chatkumpjunjalearn, T.; Kroeksakul, P.; Chongkolnee, B. Development and Characterization of Polyvinyl Alcohol/Bacterial Cellulose Composite for Environmentally Friendly Film. *J. Ecol. Eng.* **2023**, *24*, 226–238. [CrossRef]
55. Tamahkar, E. Bacterial Cellulose/Poly Vinyl Alcohol Based Wound Dressings with Sustained Antibiotic Delivery. *Chem. Pap.* **2021**, *75*, 3979–3987. [CrossRef]

Disclaimer/Publisher's Note: The statements, opinions and data contained in all publications are solely those of the individual author(s) and contributor(s) and not of MDPI and/or the editor(s). MDPI and/or the editor(s) disclaim responsibility for any injury to people or property resulting from any ideas, methods, instructions or products referred to in the content.

polymers

MDPI

Article

Interface Enhancement and Tribological Properties of Cattle Manure-Derived Corn Stalk Fibers for Friction Materials: The Role of Silane Treatment Concentration

Siyang Wu [1], Lixing Ren [1], Xiaochun Qiu [1], Qiance Qi [1], Bo Li [1], Peijie Xu [1], Mingzhuo Guo [2,*] and Jiale Zhao [2,*]

[1] College of Engineering and Technology, Jilin Agricultural University, Changchun 130118, China; siyangwu@outlook.com (S.W.); renlixingjlag@163.com (L.R.); qiuxiaochun0131@163.com (X.Q.); qianceqi774@outlook.com (Q.Q.); lboxxx@163.com (B.L.); pj15137475091@outlook.com (P.X.)
[2] College of Biological and Agricultural Engineering, Jilin University, Changchun 130022, China
* Correspondence: gmz@jlu.edu.cn (M.G.); zhaojl@jlu.edu.cn (J.Z.)

Abstract: Corn stalk fibers extracted from cattle manure (CSFCM) represent a unique class of natural fibers that undergo biological pre-treatment during ruminant digestion. This study systematically investigates the optimization of CSFCM-reinforced friction materials through controlled silane treatment (2–10 wt.%). The biological pre-treatment through ruminant digestion creates distinctive fiber properties that influence subsequent chemical modification. Physical characterization revealed that optimized interface modification at 6 wt.% silane treatment (CSFCM-3) effectively enhanced the fiber–matrix compatibility while achieving a 34.2% reduction in water absorption and decreased apparent porosity from 9.03% to 7.85%. Tribological evaluation demonstrated superior performance stability, with CSFCM-3 maintaining friction coefficients of 0.35–0.45 across 100–350 °C and exhibiting enhanced thermal stability through a fade ratio of 14.48% and recovery ratio of 95%. The total wear rate showed significant improvement, reducing by 26.26% to 3.433×10^{-7} cm^3 (N·m)$^{-1}$ compared to untreated specimens. Microscopic analysis confirmed that the optimized silane modification promoted the formation of stable secondary plateaus and uniform wear patterns, contributing to enhanced tribological performance. This investigation establishes an effective approach for developing high-performance friction materials through precise control of silane treatment parameters. The findings demonstrate the potential for developing sustainable friction materials with enhanced performance characteristics, offering new pathways for eco-friendly material design that effectively utilizes agricultural waste resources.

Keywords: biological pre-treatment; cattle manure; corn stalk fiber; interface modification; friction materials; tribological properties

1. Introduction

The accelerating pace of industrial development has led to an overwhelming dependence on synthetic polymers, creating severe environmental challenges. Global plastic production has surged to approximately 400 million tons annually, with only 9% being recycled while the remainder accumulates in landfills and oceans [1], persisting for hundreds of years and gradually degrading into microplastics that contaminate ecosystems. To address these mounting environmental concerns, eco-friendly polymer-based composites have emerged as a promising solution, offering the potential to maintain desired

performance characteristics while reducing environmental impact through the incorporation of sustainable reinforcing materials [2,3]. Natural fiber composites demonstrate significant environmental advantages, requiring 17% less energy in manufacturing and enabling higher energy recovery during end-of-life incineration (12–34 MJ/kg compared to 7.5 MJ/kg for glass fiber composites). Particularly in the automotive industry, where natural fiber composites have been widely adopted for interior components and structural parts, these materials have achieved weight reductions of up to 25% compared to conventional composites, contributing to improved fuel efficiency and reduced emissions [4,5]. The selection of appropriate reinforcement materials plays a crucial role in determining the overall properties and environmental impact of these composites. Among various reinforcement options, natural fibers have gained significant attention due to their biodegradability, renewability, abundance, and cost-effectiveness [6].

Among diverse natural fiber sources, corn stalk fibers have emerged as a promising reinforcement for composite materials. Corn stalk is a significant renewable resource, and among its various utilization pathways, feed use is one of the primary consumption routes, accounting for approximately 19% of the total corn stalk resources [7]. Ruminants, particularly cattle, can partially digest corn stalks, but a considerable amount of undigested stalk fibers remains in their manure. It is estimated that each cattle produces around 7.3 kg of dry manure per day, and in the United States alone, the annual dry cattle manure generation reaches about 24 billion tons [8]. Assuming that the corn stalk content in cattle manure is approximately 20%, the amount of recoverable corn stalk fibers from this waste stream would be substantial.

Corn stalk fibers extracted from cattle manure (CSFCM) have emerged as particularly promising due to their distinctive characteristics. These fibers undergo an inherent biological processing through the ruminant digestive system, where complex microbial ecosystems and specific physiological conditions facilitate selective degradation of plant fiber components. During ruminant digestion, the corn stalk fibers experience a series of physical, chemical, and biological modifications. The mechanical breakdown through rumination and muscular contractions, combined with exposure to rumen fluid (pH 6.0–6.8), initiates the degradation process [9]. The diverse microbial communities in the rumen, including bacteria, protozoa, and fungi, selectively degrade plant components such as hemicellulose and pectin while preserving the fundamental cellulose structure. This natural biological pre-treatment effectively removes non-structural components, resulting in enhanced cellulose content and modified fiber architecture. The rumen environment's unique combination of mechanical actions, enzymatic processes, and microbial activities establishes favorable properties for composite material applications, providing an environmentally friendly alternative to conventional chemical pre-treatments [10].

The development of natural fiber-reinforced composites, particularly those utilizing CSFCM, represents a promising solution to address the growing plastic pollution crisis. These materials offer inherent biodegradability while maintaining comparable performance characteristics for specific applications, thereby reducing the accumulation of non-biodegradable waste in the environment. Furthermore, CSFCM-based composites create a dual environmental benefit by both reducing plastic waste through biodegradable alternatives and utilizing agricultural waste streams. The biological pre-treatment through ruminant digestion not only enhances fiber properties but also provides an environmentally friendly processing method. This approach aligns with circular economy principles and global initiatives to reduce plastic pollution, offering a practical pathway for industries to transition from petroleum-based materials to eco-friendly alternatives.

Recent studies have demonstrated the versatility and effectiveness of CSFCM across various applications. In cementitious composites, Li et al. [11] and Yang et al. [12] revealed that pre-treated cow dung fibers significantly improved mechanical properties and reduced shrinkage behavior. Yang et al. [13] successfully extracted cellulose fibers from cow dung waste and characterized their functional properties, demonstrating their potential in sustainable material development. In the field of friction materials, Ma et al. [14] reported excellent tribological and mechanical properties of cow dung fiber-reinforced friction composites, while Wu et al. [15] conducted comprehensive comparative studies showing competitive performance against traditional natural fibers like corn stalk and sisal. Thermal characteristics studies by Reddy et al. [16] confirmed the material's stability at elevated temperatures. Moreover, recent research has expanded into specialized applications, including the development of cow dung-based paper [17], and alkali-activated slag mortars [18], and comprehensive reviews by Fasake and Dashora [19,20] have highlighted the sustainable potential of these materials across various industrial applications.

Despite the inherent advantages of CSFCM, significant technical challenges persist in developing high-performance natural fiber-reinforced composite materials, primarily concerning interface optimization. The fundamental challenge originates from the inherent incompatibility between hydrophilic functional groups present on natural fiber surfaces and hydrophobic polymer matrices, resulting in suboptimal stress transfer at the interface. Various surface modification methods have been developed to improve the compatibility between natural fibers and polymer matrices. Chemical treatments such as alkali treatment with NaOH effectively remove non-cellulosic components but may cause excessive fiber damage and cellulose depolymerization, particularly at concentrations above 5% [21]. Similarly, acetylation using acetic anhydride can reduce fiber hydrophilicity but risks fiber embrittlement and generates chemical waste [22]. Conventional biological pre-treatments like fungal degradation require controlled laboratory conditions and extended processing times [23]. In comparison, ruminant digestive processing presents a unique biological approach with several advantages. The ruminant digestive system provides natural pH regulation (6.0–7.0) and temperature control (38–42 °C) through physiological mechanisms, enabling selective degradation of hemicellulose and lignin while preserving cellulose structure [9]. This process is environmentally sustainable and generates no chemical waste. However, challenges include seasonal variations in fiber quality and the need for post-extraction purification. Despite these limitations, the controlled biological modification through ruminant digestion offers a promising alternative for natural fiber pre-treatment.

Among these surface modification approaches, silane treatment has emerged as an effective complementary method to biological pre-treatment. While ruminant digestion effectively removes non-cellulosic components and creates active sites on fiber surfaces, subsequent silane coupling treatment can further enhance fiber–matrix interfacial bonding. The silane coupling agent (KH-550) creates chemical bridges between the hydrophilic fiber surface and hydrophobic polymer matrix through its bifunctional molecular structure. This combined approach of biological pre-treatment followed by silane modification potentially offers synergistic benefits: the biological process provides a "green" initial modification while silane treatment ensures strong interfacial adhesion in the final composite.

This research presents a comprehensive investigation of CSFCM-reinforced polymer composites, focusing on silane treatment parameter optimization and subsequent effects on friction performance. The methodology systematically examines varying silane concentrations (2–10 wt.%) on fiber properties and composite characteristics. Biological pre-treatment, particularly the fiber extraction from cattle manure in this study, achieves a secondary utilization of traditional biomass resources and enhances their application

value. The combination of cattle manure fiber extraction with silane treatment further improves the mechanical properties of cattle manure straw fiber-reinforced materials. This combined approach has shown particular promise in tribological applications. The research methodology and findings from this study provide valuable insights for expanding the potential applications of these modified fibers in other fields.

2. Materials and Methods

2.1. Materials

2.1.1. Raw Materials and Formulation

The raw materials for this investigation were systematically selected based on their functional roles in the composite system. Corn stalk fibers extracted from cattle manure (CSFCM) were obtained from a Simmental cattle breeding farm (Changchun, China) as the primary fibrous reinforcement. A commercial phenolic resin (Jinan Shengquan Group Share-Holding Co., Ltd., Jinan, China) served as the matrix binder. The modification system comprised multiple functional components: graphite (Qingdao Matery Graphite Co., Ltd., Qingdao, China), antimony sulfide (Xiamen Ditai Chemicals Co., Ltd., Xiamen, China), bauxite (Zhengzhou Highland Refractory Material Co., Ltd., Zhengzhou, China), zinc stearate (Nanjing Lepuz Chemical Co., Ltd., Nanjing, China), porous iron powder (Shanghai Knowhow Powder-Tech Co., Ltd., Shanghai, China), and petroleum coke (Changge Youtong Environmental Protection Materials Co., Ltd., Changge, China). Additional reinforcement was provided by compound mineral fibers (Hebei Runhuabang New Material Technology Co., Ltd., Shijiazhuang, China). The filler system consisted of vermiculite powder (Hebei Ansta Trading Ltd., Shijiazhuang, China), barium sulfate, and friction powder (Guangzhou Billion Peak Chemical Technology Co., Ltd., Guangzhou, China). KH-550 silane coupling agent (Dalian Richon Chem Co., Ltd., Dalian, China) was employed for interface optimization. The precise compositional ratios are detailed in Table 1.

Table 1. Material composition and weight percentages of the CSFCM-based composite.

Component Type	Component	Weight Percentage
Binder	Phenolic resin	14 ± 0.5 wt.%
Modifier	Graphite	8 ± 0.3 wt.%
	Antimony sulfide	3 ± 0.2 wt.%
	Bauxite	7 ± 0.3 wt.%
	Zinc stearate	2 ± 0.1 wt.%
	Porous iron powder	10 ± 0.4 wt.%
	Petroleum coke	5 ± 0.2 wt.%
Fibrous reinforcement	Compound mineral fibers	19 ± 0.5 wt.%
	CSFCM	6 ± 0.2 wt.%
Filler	Vermiculite powder	5 ± 0.2 wt.%
	Friction powder	2 ± 0.1 wt.%
	Barium sulfate	19 ± 0.5 wt.%

2.1.2. Fiber Extraction and Treatment

The extraction and modification of corn stalk fibers from cattle manure (CSFCM) was systematically executed through a precisely controlled three-stage process, as illustrated in Figure 1. In the initial screening stage, corn stover was first fed to cattle at a local Simmental breeding farm in Changchun, China. The fresh cattle manure containing partially digested corn stover fibers was collected within 24 h of excretion to maintain optimal fiber conditions. The collected manure was immediately dispersed in deionized water (resistivity > 18.2 MΩ·cm) containing 0.5 wt.% non-ionic surfactants at a material/liquid

ratio of 1:5 (w/v). The dispersion process was maintained at 30 ± 2 °C for 2 h under continuous stirring to ensure thorough fiber separation and preliminary purification.

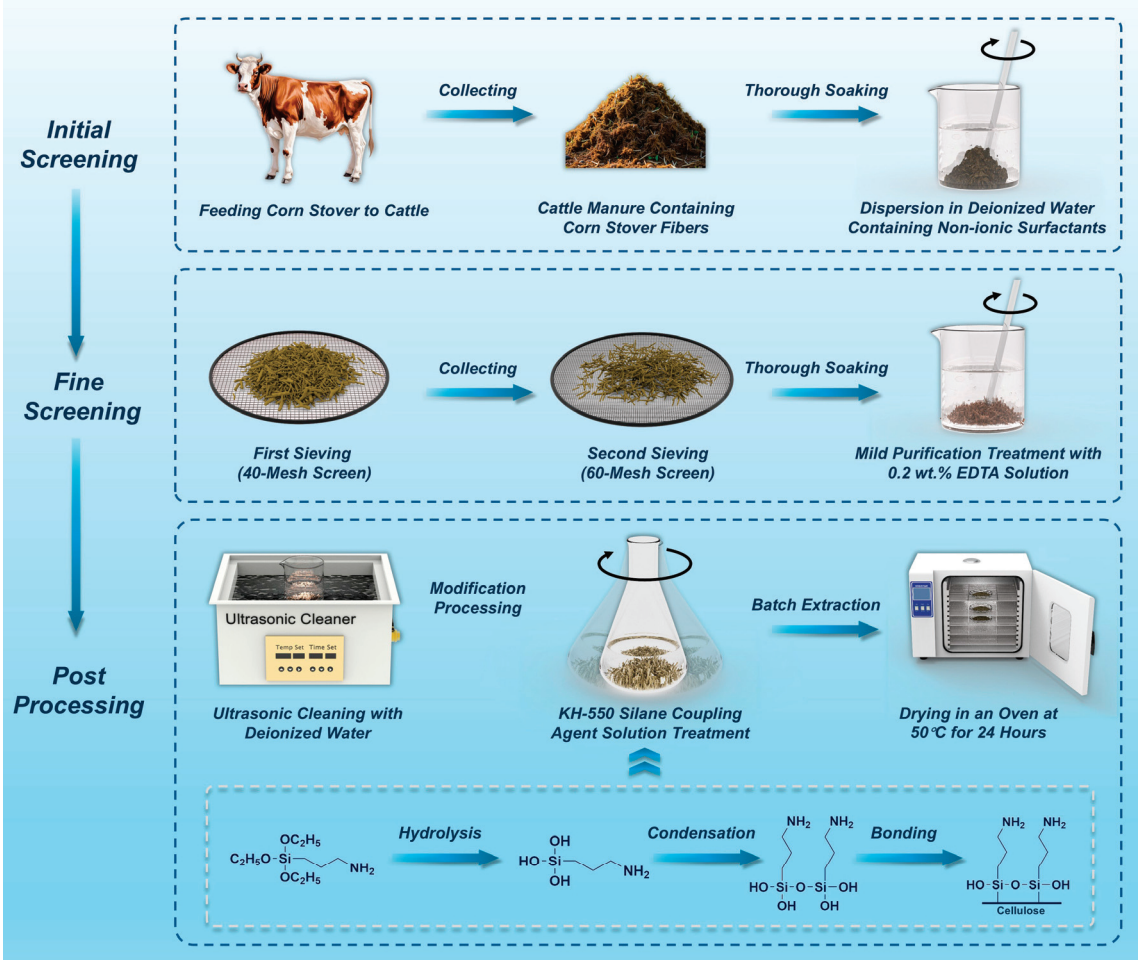

Figure 1. Schematic illustration of the three-stage extraction and modification process for corn stalk fibers from cattle manure (CSFCM): initial screening, fine screening, and post-processing stages.

In the fine screening stage, the dispersed material underwent a precise two-step sieving process. The first screening was conducted using a standardized 40-mesh stainless-steel sieve (aperture size: 420 μm) under controlled water flow (2 L/min) to remove coarse impurities. The filtered material was then passed through a finer 60-mesh screen (aperture size: 250 μm) under the same flow conditions for more precise fiber separation. The retained fibers underwent a mild purification treatment in 0.2 wt.% EDTA solution (pH 7.5 ± 0.2) at 25 ± 1 °C for 60 min with gentle agitation at 10 rpm to chelate and remove metallic impurities while maintaining the structural integrity of the fibers.

The post-processing stage comprised three critical steps. Firstly, the fibers were subjected to ultrasonic cleaning in deionized water for 30 min at 25 ± 1 °C. Second, the cleaned fibers underwent surface modification with pre-hydrolyzed KH-550 silane coupling agent. The coupling agent solution preparation followed a strictly controlled protocol: KH-550 was hydrolyzed in an ethanol/water mixture (95:5 v/v, HPLC grade ethanol, purity ≥ 99.9%) under controlled pH (4.0 ± 0.2, adjusted with glacial acetic acid) and temperature (25 ± 0.5 °C) conditions. The hydrolyzed solution was then precisely diluted to target concentrations (2, 4, 6, 8, and 10 wt.%) using Class A volumetric glassware, with concentration verification through specific gravity measurements (±0.0002 g/cm^3) at 25 °C. The surface modification

was conducted at 25 ± 1 °C for 120 min under controlled stirring (200 ± 5 rpm), with solution stability maintained through 4 h renewal intervals and regular pH verification. Finally, the modified fibers were dried in a programmable vacuum oven (LC-DZF-6020AB, Shanghai Lichen-BX Instrument Technology Co., Ltd., Shanghai, China) at 50 ± 0.5 °C under −0.08 MPa pressure for 24 h to achieve a final moisture content below 2 wt.%.

KH-550 serves as an effective silane coupling agent to enhance the interfacial adhesion between natural fibers and polymer matrices. The chemical interaction between KH-550 and cellulosic fibers involves a series of hydrolysis and condensation reactions. Initially, the ethoxy groups (-OC_2H_5) of KH-550 undergo hydrolysis in the presence of moisture, converting to reactive silanol groups (-Si-OH). Subsequently, these silanol groups can form stable covalent bonds (-Si-O-Cellulose) with the abundant hydroxyl groups (-OH) on the surface of the cellulosic fibers via a condensation reaction [24]. This chemical bonding mechanism significantly improves fiber–matrix interfacial adhesion, resulting in the enhanced mechanical properties and durability of the natural fiber-reinforced polymer composites. The grafting of KH-550 onto cellulosic fibers not only increases the compatibility between the hydrophilic fibers and the hydrophobic polymer matrix but also provides a strong and stable link at the interface. This interfacial modification promotes efficient stress transfer from the matrix to the reinforcing fibers, ultimately leading to the improved overall performance of the composite materials. Furthermore, the amine groups (-NH_2) in the KH-550 molecules can chemically react with the resin matrix, thereby creating a "molecular bridge" between the cellulosic fibers and polymer matrix. This serves to improve the compatibility and stress transfer efficiency of the composite system. Through these chemical reactions, KH-550 forms an amine-containing coating layer on the surface of the cellulosic fibers, which enhances the wettability and interfacial bonding strength between the hydrophilic natural fibers and hydrophobic polymer matrix.

In summary, the bifunctional nature of KH-550 enables it to chemically bond with both the hydroxyl groups on the cellulosic fiber surface and the functional groups in the polymer resin, resulting in markedly improved fiber–matrix interfacial adhesion. This surface modification method using silane coupling agents has been widely applied in natural fiber-reinforced polymer composites to enhance their mechanical properties and durability.

2.1.3. Preparation of Friction Materials

The friction materials were fabricated using a precision-controlled hot-press molding system (JFY500, Jilin University Electromechanical Equipment Co., Ltd., Changchun, China). As illustrated in Figure 2, the molding system utilized custom-designed cast iron molds positioned between the upper and lower hot-press platens. The material consolidation process was precisely regulated through three critical parameters: molding temperature, pressure, and dwelling time. The following optimal processing parameters were established through systematic optimization studies: molding temperature of 160 °C, compression pressure of 45 MPa, and dwelling time of 30 min. The hot-press mold assembly was preheated to 150–160 °C prior to material loading to ensure uniform heat distribution.

To mitigate potential defects associated with volatile evolution during the curing process, which could manifest as surface blistering, swelling, or microcracking, a programmed degassing protocol was implemented. The protocol consisted of three sequential cycles of 10 s compression followed by 12 s degassing before transitioning to sustained pressure application. The consolidated specimens underwent controlled post-cure treatment to ensure complete phenolic resin crosslinking and minimize residual stress-induced dimensional instability. Subsequently, the materials were machined to precise dimensions (25 mm × 25 mm × 6 mm) through surface grinding and cutting operations for characterization studies.

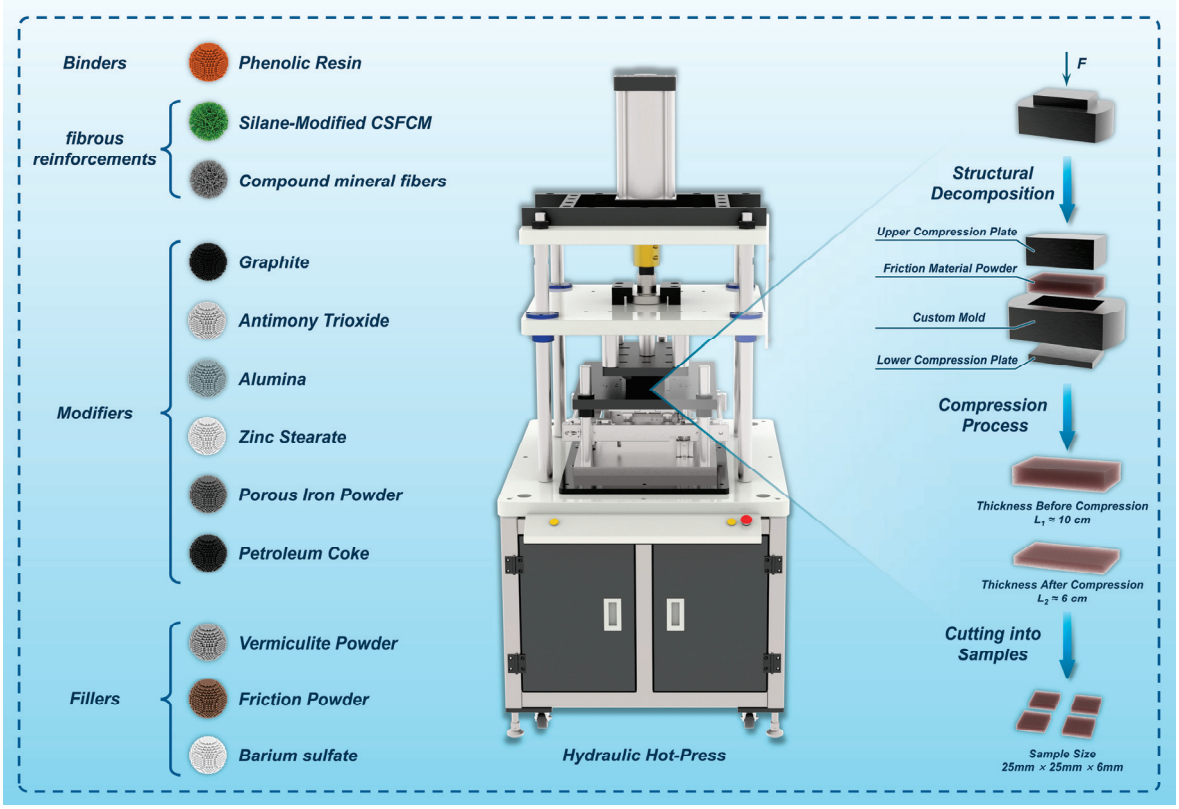

Figure 2. Schematic diagram of the hot-press molding principle for friction materials.

The samples were systematically designated according to the silane coupling agent concentration gradient as follows: CSFCM-0 (unmodified control), CSFCM-1 (2 wt.% silane concentration), CSFCM-2 (4 wt.% silane concentration), CSFCM-3 (6 wt.% silane concentration), CSFCM-4 (8 wt.% silane concentration), and CSFCM-5 (10 wt.% silane concentration).

2.2. Characterization of CSFCM-Reinforced Polymer Composites

2.2.1. Density Measurement

Density was determined based on the Archimedes principle, utilizing a high-precision analytical balance (MP-5002, Shanghai Fangrui Instruments, Shanghai, China; accuracy ± 0.01 mg) equipped with a density determination kit. The experimental protocol was executed in a temperature-controlled chamber (25 ± 0.2 °C) using HPLC-grade water (resistivity > 18.2 MΩ·cm, TOC < 5 ppb) as the immersion medium. For each composite variant, five sequential measurements were conducted at 60 s intervals to ensure measurement stability. The composite density (ρ_s) was determined according to the following equation:

$$\rho_s = \frac{W_a}{W_a - W_0} \times \rho_0 \quad (1)$$

where W_a represents the sample mass in air (g), W_0 represents the sample mass in water (g), and ρ_0 denotes the density of water at the measurement temperature (g/cm^3).

2.2.2. Water Absorption Testing

The water absorption characteristics were investigated following the GB/T 24508-2009 standard [25]. The samples were first placed in a ventilated oven (LC-101-0B, Shanghai Lichen-BX Instrument Technology Co., Ltd., Shanghai, China)at 180 °C for 4 h with a heating rate of 5 °C/min. During the drying process, samples were positioned on aluminum

foil with sufficient spacing (approximately 2 cm apart) to ensure uniform heat distribution and effective moisture removal. After the 4 h heat treatment, the oven was turned off and the samples were allowed to naturally cool to room temperature (23 ± 2 °C) inside the closed oven for approximately 6 h; to prevent thermal shock and moisture reabsorption, the conditioned samples were immersed in deionized water (resistivity > 18.2 MΩ·cm) at 23 ± 1 °C for 72 h to achieve saturation. After immersion, surface water was meticulously wiped using lint-free filter paper, and mass measurements were immediately performed using an analytical balance. The water absorption ratio (W_t) was calculated according to the following equation [26]:

$$W_t = \frac{M_t - M_0}{M_0} \times 100\% \quad (2)$$

where M_t represents the saturated sample mass and M_0 denotes the initial dry mass. Each measurement was performed in triplicate to ensure data reliability, and the mean values were reported with standard deviations.

2.2.3. Apparent Porosity Determination

The composite samples were dried in a vacuum oven at 90 ± 1 °C until a constant mass was achieved. Subsequently, the samples were immersed in boiling distilled water (resistivity > 18.2 MΩ·cm) for 120 min. After cooling to 25 ± 0.5 °C in a thermostatic water bath, mass measurements were performed in both air and water using an analytical balance. The apparent porosity (φ) was calculated using the following equation [27]:

$$\varphi = \left(\frac{G_2 - G_1}{G_2 - G_3}\right) \times 100\% \quad (3)$$

where G_1 represents the initial dry mass (g), G_2 represents the saturation mass in air (g), and G_3 represents the immersion mass in water (g). Eight parallel samples were tested for each composite formulation under controlled environmental conditions (temperature: 25 ± 1 °C; relative humidity: 50 ± 5%).

2.2.4. Tribological Testing

All tribological tests were performed in a laboratory environment with controlled ambient conditions. The room temperature was maintained at 25 ± 2 °C using central air conditioning, and the relative humidity was monitored and maintained at 50 ± 5% using commercial dehumidifiers. These environmental parameters were recorded at the beginning and end of each test series to ensure consistent testing conditions. Prior to testing, all specimens were stored and conditioned in the same laboratory environment for at least 24 h to achieve equilibrium with the ambient conditions.

Friction and wear characteristics were determined using a JF151 constant-speed friction testing apparatus (Jilin Wangda Testing Equipment Co., Ltd., Changchun, China) following GB 5763-2018 standards [28]. The counterface friction discs were made from HT250-grade cast iron (with a predominantly pearlitic microstructure; hardness: HB180-220). Tests included thermal fade and recovery assessments across a temperature range of 100–350 °C and were performed at 0.98 MPa (normal pressure) and a rotational speed of 480 rpm, corresponding to a linear sliding velocity of 7.54 m/s at a mean friction radius of 150 mm. Fade resistance tests were conducted at six temperatures (100, 150, 200, 250, 300, and 350 °C). Recovery performance was assessed during controlled cooling from 300 °C to

100 °C at 50 °C intervals. The friction coefficient (μ) and specific wear rate (ΔV) were calculated using the following equations [29,30]:

$$\mu = \frac{f}{P} \tag{4}$$

$$\Delta V = \frac{1}{2\pi r} \times \frac{A}{R} \times \frac{d_1 - d_2}{f} \tag{5}$$

where f represents the average friction force (N), P denotes the applied normal load (N), r is the effective friction radius (150 mm), R indicates the total revolution count (5000), A represents the nominal contact area (625 mm^2), and d_1 and d_2 are the specimen thicknesses before and after testing (cm). To ensure statistical validity, each test condition was replicated three times.

2.2.5. Thermal Stability Evaluation

The thermal stability characteristics of the composite samples were quantitatively evaluated through fade ratio (F) and recovery ratio (R) analyses based on the friction coefficient data obtained from high-temperature friction-wear tests. The fade resistance, representing the material's ability to maintain stable friction performance under elevated temperatures, and recovery performance, indicating the material's capability to restore its friction characteristics after thermal exposure, were calculated using the following equations [31]:

$$F = \frac{\mu_{F100^\circ C} - \mu_{F350^\circ C}}{\mu_{F100^\circ C}} \times 100\% \tag{6}$$

$$R = \frac{\mu_{R100^\circ C}}{\mu_{F100^\circ C}} \times 100\% \tag{7}$$

where $\mu_{F100^\circ C}$ and $\mu_{F350^\circ C}$ represent the friction coefficients measured at 100 °C and 350 °C during the fade test sequence, respectively, and $\mu_{R100^\circ C}$ represents the friction coefficient measured at 100 °C during the recovery test phase. These parameters provide quantitative metrics for evaluating the thermal stability and reliability of the friction materials under dynamic temperature conditions, with lower fade ratios and higher recovery ratios indicating superior thermal stability performance.

2.2.6. Morphological Observation

The surface morphology and microstructural characteristics of both the fiber materials and composites were examined using a field emission scanning electron microscope (SEM, EVO-18, Zeiss, Oberkochen, Germany). The observations were performed at an accelerating voltage of 15–20 kV and working distance of 8–12 mm. Prior to examination, all samples were sputter-coated with a thin gold layer (10–15 nm) to enhance surface conductivity. For fiber analysis, both untreated and silane-treated cotton stalk fibers were examined to evaluate the surface modification effects. The composite samples were analyzed to investigate the fiber–matrix interface and worn surface characteristics. Images were captured at magnifications ranging from 100× to 5000× to analyze the surface morphology of fibers, fiber–matrix interfaces, and wear tracks.

3. Results and Discussion

3.1. Density Characteristics

The density characteristics of CSFCM composites with varying silane treatment concentrations are presented in Figure 3. The density measurements reveal a moderate increasing

trend from CSFCM-0 (1.92 g/cm^3) to CSFCM-5 (2.08 g/cm^3). Multiple comparison analysis using the LSD test indicates that CSFCM-5 exhibits significantly higher density than CSFCM-0 through CSFCM-2. CSFCM-3 and CSFCM-4 show intermediate density values with no significant difference between them, suggesting a transitional stage in the densification process.

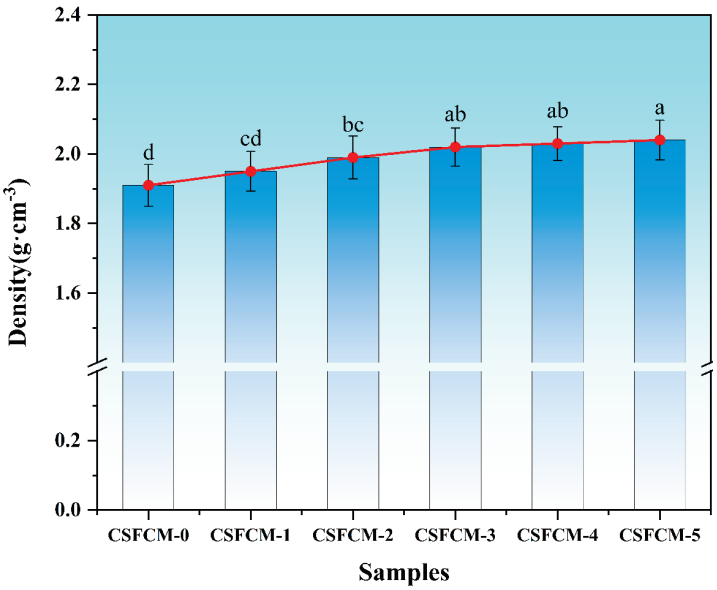

Figure 3. Density variation in composites with different silane treatment concentrations. Averages followed by different lowercase letters are significantly different according to LSD's multiple range test at the significance level of 0.05. Error bars are standard deviation.

This progressive density evolution can be attributed to the enhanced fiber–matrix interfacial bonding at higher silane concentrations, where more silane molecules form dense siloxane networks and promote better matrix penetration into the fiber surface. At lower silane concentrations (2–4 wt.%), the coupling agent initiates surface modification by replacing hydroxyl groups with organosilane molecules, showing no significant difference in density. The intermediate concentrations (6–8 wt.%) achieve optimal interface modification, where enhanced fiber–matrix adhesion facilitates efficient composite consolidation. However, at 10 wt.% concentration (CSFCM-5, 'a'), excessive silane treatment may lead to the formation of densified siloxane networks, resulting in the highest observed density. Notably, due to the inherent porous cellular structure of bio-pre-treated corn stalk fibers, all CSFCM composites maintained relatively low densities (1.9–2.1 g/cm^3), which are considerably lower than traditional friction materials (2.2–2.5 g/cm^3). These density values align well with the findings reported by Liu et al. [24] and Nishino et al. [32] for natural fiber-based friction composites.

3.2. Water Absorption Characteristics

The water absorption characteristics of CSFCM-reinforced composites with varying silane treatment concentrations are presented in Figure 4. The results show a U-shaped pattern, with water absorption values ranging from 8.49% for untreated specimens (CSFCM-0) to a minimum of 5.59% for specimens treated with 6 wt.% silane (CSFCM-3). At low silane concentrations (2–4 wt.%), the coupling agent modifies the fiber surface by replacing hydrophilic hydroxyl groups with hydrophobic organosilane units, as shown by the decrease in water absorption from 8.49% (CSFCM-0) to 7.98% (CSFCM-1) and 6.81% (CSFCM-2). The silane molecules undergo hydrolysis and bond with fiber surfaces, creating a hydrophobic layer that reduces water accessibility to the fiber structure [33].

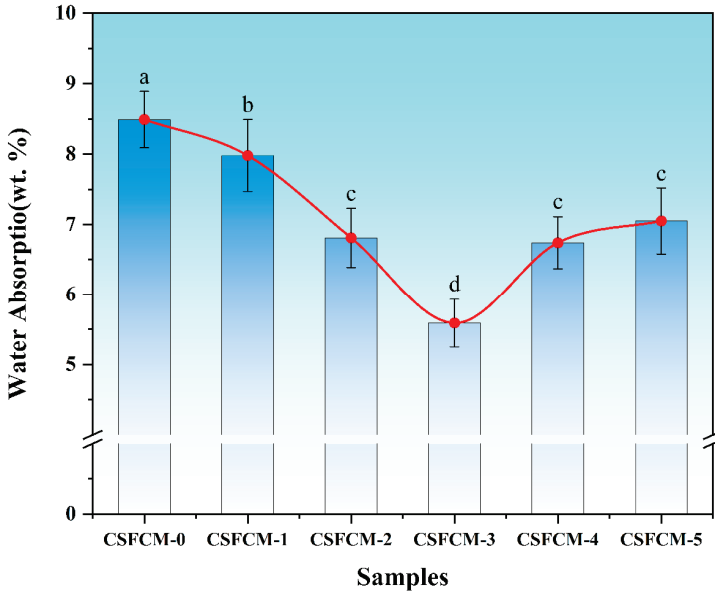

Figure 4. Effect of silane treatment concentration on the water absorption of CSFCM-reinforced composites. Averages followed by different lowercase letters are significantly different according to LSD's multiple range test at the significance level of 0.05. Error bars are standard deviation.

At a moderate concentration (6 wt.%), an optimal surface coverage is achieved, with CSFCM-3 exhibiting the lowest water absorption of 5.59%, showing statistically significant decreases ($p < 0.05$) from CSFCM-0 through CSFCM-2, resulting in a 34.2% reduction compared to untreated specimens. This concentration provides sufficient silane molecules to form a complete siloxane layer through condensation of silane groups while maintaining uniform distribution. The silane treatment effectively reduces water absorption in polymer composite systems by eliminating surface hydroxyl groups on natural fibers and increasing the crystallinity of CSFCM [34]. At higher concentrations (8–10 wt.%), water absorption increases to 6.74% for CSFCM-4 and 7.05% for CSFCM-5, which were not significantly different from CSFCM-2 ($p > 0.05$). This increase is attributed to the formation of silane oligomers and irregular surface topology, which may contribute to increased water retention [35]. These results are consistent with the findings of Vilay et al. [36] in their study of bagasse fiber-reinforced composites.

All treated samples maintained lower water absorption than untreated CSFCM (8.49%), with 6 wt.% silane treatment providing optimal moisture resistance. This behavior reflects the effectiveness of surface modification in CSFCM-reinforced composites that have undergone biological pre-treatment.

3.3. Porosity Features

Figure 5 presents the porosity characteristics of CSFCM composites with varying silane treatment concentrations. The apparent porosity demonstrated a relationship with water absorption behavior, reflecting the connection between microstructural features and macroscopic properties. The untreated specimen (CSFCM-0) exhibited a porosity of 9.03%, higher than conventional corn stalk fiber composites (6–8% before treatment). The porosity reached a minimum of 7.85% for the 6 wt.% silane treatment (CSFCM-3), and increased at higher treatment concentrations.

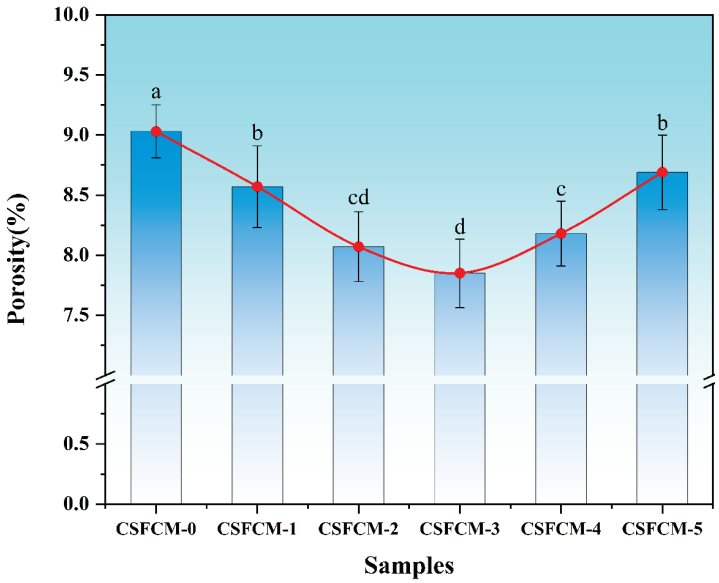

Figure 5. Apparent porosity of CSFCM composites as a function of silane treatment concentration. Averages followed by different lowercase letters are significantly different according to LSD's multiple range test at the significance level of 0.05. Error bars are standard deviation.

The elevated initial porosity of CSFCM compared to conventional corn stalk fibers stems from structural modifications induced by ruminant digestion. During ruminal fermentation, microbial systems selectively degrade hemicellulose and pectin components, leading to partial delignification and increased cellulose accessibility. This biological pre-treatment creates additional micropores and channels within the fiber structure. The enzymatic degradation of cell wall components results in a more open fiber architecture compared to untreated corn stalk fibers [10].

The porosity values follow a similar trend to water absorption, showing statistically significant decreases ($p < 0.05$) from CSFCM-0 (9.03%) through CSFCM-2. The notably higher initial porosity compared to conventional corn stalk fiber composites (6–8%) stems from structural modifications during ruminal fermentation, where microbial systems selectively degrade hemicellulose and pectin components, creating additional micropores and channels [37]. CSFCM-3 achieves the minimum porosity of 7.85%, demonstrating optimal interfacial bonding at 6 wt.% silane treatment. At this moderate concentration, silane treatment establishes effective chemical bonding at the interface, reducing interfacial voids while enhancing fiber surface hydrophobicity. However, CSFCM-4 and CSFCM-5 show progressive increases in porosity, with CSFCM-5 reaching 8.69% (statistically similar to CSFCM-1, $p > 0.05$). This increase at higher concentrations (8–10 wt.%) can be attributed to the formation of irregular interfacial structures and new defects. The observed reduction in porosity with silane treatment is consistent with the findings of Tonoli et al. [38], who also demonstrated decreased apparent porosity in silane-treated cellulose pulp fiber composites, confirming the effectiveness of silane treatment in reducing composite porosity.

The 6 wt.% silane treatment (CSFCM-3) optimized the interfacial structure and porosity characteristics, though the absolute porosity values reflect the structural features inherited from biological pre-treatment. These findings indicate that CSFCM-based composites maintain distinct microstructural characteristics despite surface modification.

3.4. Tribological Performance

The friction coefficients of CSFCM-reinforced composites varied significantly with temperature and silane treatment concentrations (Figure 6a). Statistical analysis reveals that CSFCM-3 and CSFCM-4 (6–8 wt.% silane) consistently demonstrate significant improvements ($p < 0.05$) in friction stability across all temperature ranges, while other treatments show significant but irregular variations from the control. In the temperature range of 100–150 °C, all specimens exhibited increasing friction coefficients due to the initial accumulation of wear debris and formation of primary friction films. The softening of the phenolic resin matrix enhanced the contact area with the counterpart, facilitating wear particle embedding and friction film formation.

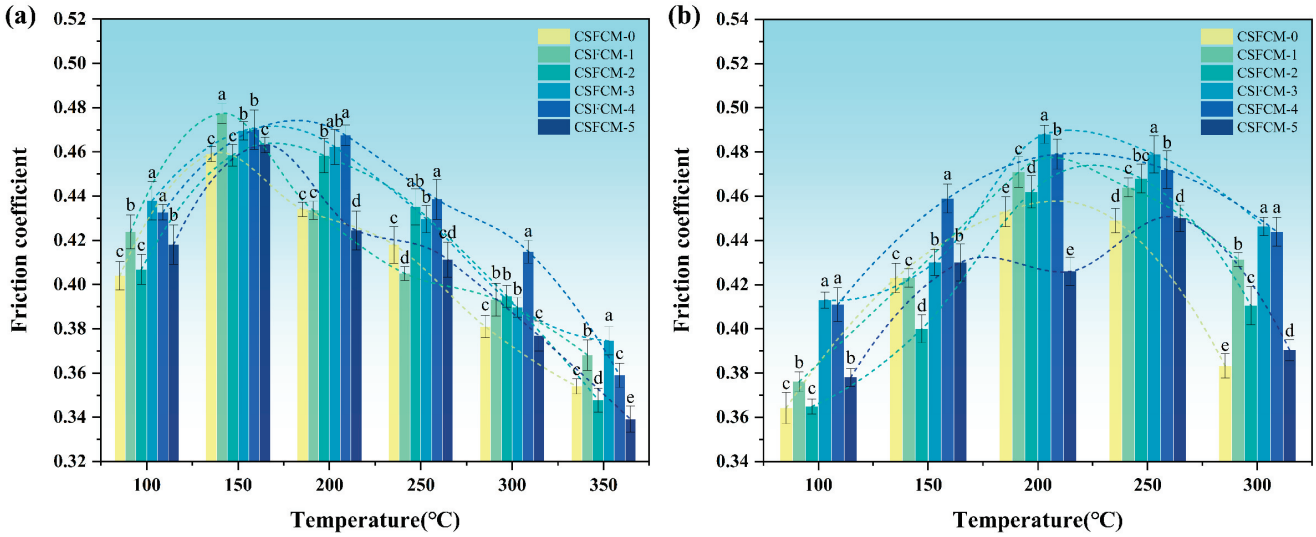

Figure 6. Friction coefficient of CSFCM composites in the fade test (**a**) and recovery test (**b**). Averages followed by different lowercase letters are significantly different according to LSD's multiple range test at the significance level of 0.05. Error bars are standard deviation.

Above 150 °C, a notable decrease in friction coefficients was observed across all specimens. This reduction stemmed from the thermal decomposition of the phenolic resin matrix and the carbonization of residual organic matter in biologically treated CSFCM. The carbonization process generated lubricating carbonaceous layers at the friction interface, with the effect intensifying between 250 and 350 °C [39]. The extensive development of stable secondary plateaus indicated efficient tribomechanical mixing and debris consolidation under dynamic loading conditions. Below 250 °C, the wear mechanism was primarily dominated by mechanical interactions, characterized by limited surface degradation and effective stress distribution through the modified interface. As temperatures increased above 250 °C, the previously described carbonization process of CSFCM generated complex tribological effects: while the carbonaceous layers provided some lubrication, they also modified the interface structure and wear mechanisms. These carbonized layers underwent continuous formation and destruction cycles, creating a dynamic tribological system where wear debris became incorporated into transfer films through tribomechanical mixing. The specimen thus demonstrated a transition to mild oxidative wear, characterized by the formation of protective tribologically modified surface layers, though with reduced stability at higher temperatures. This temperature-dependent behavior explains the observed variations in wear rates and supports the material's optimal application in low-to-medium temperature environments where mechanical wear mechanisms predominate.

Specimens treated with 4–8 wt.% silane (CSFCM-2, CSFCM-3, and CSFCM-4) exhibited superior friction stability, particularly at 200 °C. The appropriate silane treatment enhanced fiber–matrix interfacial bonding and regulated CSFCM carbonization behavior. The chemical bond network formed by silane coupling agents moderated the carbonization process, resulting in uniform carbonaceous lubricating layers and stable friction films [40]. Insufficient silane treatment (CSFCM-0 and CSFCM-1) led to weak interfacial bonding and premature interface failure at elevated temperatures. Conversely, excessive silane treatment (CSFCM-5) created discontinuous interfacial structures through molecular self-polymerization, leading to stress concentration points and unstable friction performance at high temperatures.

The recovery characteristics during cooling (350 °C to 100 °C) revealed distinct behavior patterns (Figure 6b). Initial cooling (300–250 °C) induced significant increases in friction coefficients due to the solidification of decomposed resin products and formation of stable carbonaceous structures. The intermediate range (250–200 °C) exhibited relatively stable friction coefficients, indicating equilibrium between friction film consolidation and structural reorganization. Further cooling (200–100 °C) resulted in declining friction coefficients, attributed to increased friction film brittleness and thermal contraction effects. Similar cooling-induced friction behavior patterns have been reported in other plant fiber-reinforced friction materials, where Elen et al. [41] observed comparable friction coefficient variations in hemp fiber composites, and Mylsamy et al. [42] documented analogous thermal recovery characteristics in Coccinia Indica fiber-based systems, confirming these phenomena as characteristic features of plant fiber friction materials. CSFCM-3 and CSFCM-4 (6–8 wt.% silane) demonstrated optimal recovery performance throughout the cooling cycle, reflecting enhanced chemical bonding and a uniform stress distribution. Lower silane concentrations (0–4 wt.%) showed limited improvement in friction film stability during cooling, confirming the importance of optimal silane treatment for enhanced thermal recovery characteristics [43].

The friction coefficient trends reveal three distinct temperature-dependent regions: (1) an initial increase from 100 to 150 °C due to wear debris accumulation and friction film formation, (2) a decline between 150 and 250 °C attributed to matrix softening and carbonization, and (3) relative stabilization above 250 °C. CSFCM-3 maintains the most stable friction coefficients (0.35–0.45) across all temperature ranges, indicating superior thermal stability and consistent tribological performance.

3.5. Thermal Stability of Friction Properties

The fade and recovery characteristics of CSFCM-reinforced composites were systematically evaluated to assess their thermal stability and friction performance reliability. Figure 7 presents the fade ratio and recovery ratio variations across different silane treatment concentrations. The results revealed distinct trends in both parameters, reflecting the complex interplay between surface modification and thermal response mechanisms.

The fade ratio demonstrated an overall increasing trend from CSFCM-0 (12.38%) to CSFCM-5 (18.90%), with intermediate treatments showing moderate values: CSFCM-1 (13.13%), CSFCM-2 (14.51%), CSFCM-3 (14.48%), and CSFCM-4 (17.04%). Statistical analysis using LSD's multiple range test ($p < 0.05$) revealed distinct groupings in fade ratio performance. CSFCM-5 exhibited a significantly higher fade ratio compared to all other treatments. CSFCM-4 showed a significantly lower fade ratio than CSFCM-5 but remained significantly higher than other treatments. CSFCM-2 and CSFCM-3 demonstrated statistically similar intermediate fade ratios, while CSFCM-0 and CSFCM-1 showed no significant difference from each other but were significantly lower than all other treatments. The lower fade ratio in untreated specimens (CSFCM-0) can be attributed to the preservation

of natural hydroxyl groups on fiber surfaces, which facilitate the formation of hydrogen-bonded networks during thermal exposure.

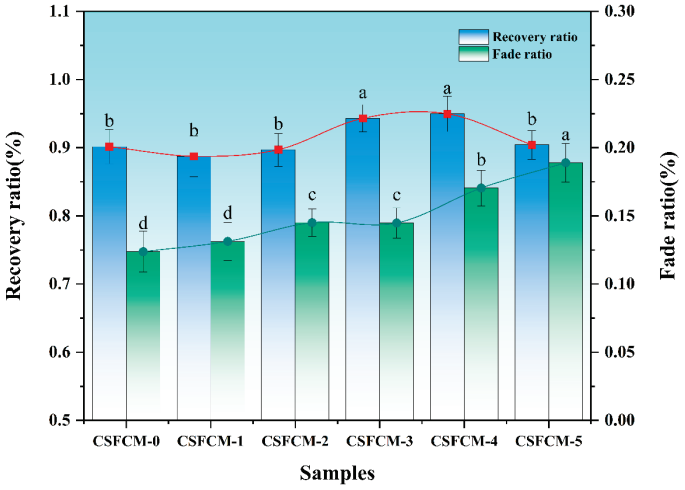

Figure 7. Fade ratio and recovery ratio characteristics of CSFCM-reinforced composites with varying silane treatment concentrations. Averages followed by different lowercase letters are significantly different according to LSD's multiple range test at the significance level of 0.05. Error bars are standard deviation.

The recovery ratio analysis revealed superior performance in moderately to highly treated specimens, with CSFCM-4 achieving the highest recovery ratio of 94.97%, followed closely by CSFCM-3 at 94.31%. Statistical analysis using LSD's multiple range test ($p < 0.05$) showed that CSFCM-3 and CSFCM-4 exhibited significantly higher recovery ratios compared to other treatments. In contrast, untreated and low-concentration specimens showed lower recovery values: CSFCM-0 (90.16%), CSFCM-1 (88.74%), and CSFCM-2 (89.71%), with no significant differences among them. This enhancement in recovery characteristics can be attributed to the formation of thermally stable siloxane networks at the fiber–matrix interface. These networks, when properly developed through optimal silane treatment, provide resilient anchor points that facilitate the reformation of friction films during cooling. Despite showing a relatively high fade ratio, CSFCM-5 maintained a reasonable recovery ratio of 90.43%.

The moderate treatment range (CSFCM-3 and CSFCM-4) achieved an optimal balance between fade resistance and recovery performance, indicating that these concentrations create interfacial structures capable of maintaining both thermal stability and reversible friction characteristics. This balanced performance likely results from the formation of optimally spaced siloxane networks that provide sufficient thermal stability while maintaining necessary molecular mobility for effective friction film regeneration during cooling cycles.

These findings suggest that while increased silane treatment may slightly compromise fade resistance, it significantly enhances the material's ability to recover its friction characteristics after thermal exposure. The combination of moderate fade ratios (12.38–18.90%) and excellent recovery performance (up to 94.97% for optimally treated specimens) particularly supports the application of these materials in low-to-medium-temperature operating conditions. Under such conditions, where thermal loads are less severe, the superior recovery characteristics and controlled fade behavior would contribute to stable and reliable friction performance. This makes CSFCM-reinforced composites especially suitable for light-duty applications such as agricultural machinery, light commercial vehicles, or other systems operating under moderate thermal loads. Therefore, the balanced performance achieved through optimal silane treatment (CSFCM-3 and CSFCM-4) represents a

promising direction for developing sustainable friction materials specifically tailored for low-to-medium-temperature applications.

The fade ratio shows a gradual increase with silane concentration from 12.38% (CSFCM-0) to 18.90% (CSFCM-5), while the recovery ratio peaks at 94.97% for CSFCM-4. This inverse relationship between fade and recovery performance suggests that moderate silane treatment (6–8 wt.%) achieves optimal balance between thermal stability and friction recovery capabilities. Compared to previous studies on corn straw fiber composites by Liu et al. [24] and agave fiber-reinforced materials by Wu et al. [44], the present composites demonstrated superior fade and recovery characteristics, demonstrating the positive effects of biological pre-treatment on corn straw fiber performance in friction applications.

3.6. Wear Rate Behavior

The wear resistance of CSFCM-reinforced composites was systematically evaluated across a temperature range of 100–350 °C, as presented in Figure 8. The results revealed complex temperature-dependent wear behaviors that varied significantly with silane treatment concentration. The wear behavior exhibited three distinct temperature-dependent stages. At low temperatures (100–150 °C), all specimens demonstrated relatively low and stable wear rates ranging from 0.17 to 0.24 × 10^{-7} cm^3 $(N{\cdot}m)^{-1}$. Statistical analysis using LSD's multiple range test ($p < 0.05$) showed no significant differences among different treatments in this temperature range, suggesting that under mild thermal conditions, the wear mechanism was primarily dominated by mechanical interactions rather than interfacial properties. A critical transition occurred in the intermediate temperature range (200–250 °C), where wear rates increased dramatically. For instance, CSFCM-0 showed a wear rate increase from 0.226 × 10^{-7} cm^3 $(N{\cdot}m)^{-1}$ at 150 °C to 0.562 × 10^{-7} cm^3 $(N{\cdot}m)^{-1}$ at 200 °C, representing a 149% increase. This transition likely corresponds to the thermal softening point of the phenolic matrix and the onset of interface degradation.

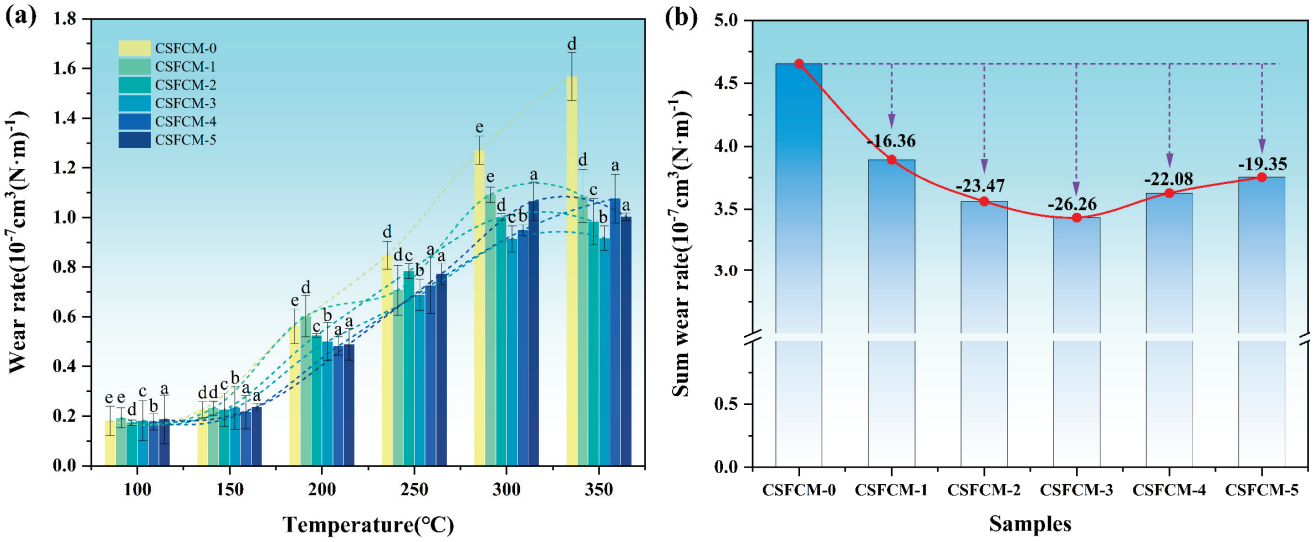

Figure 8. Wear behavior of CSFCM composites: (**a**) variation in wear rates with temperature for different silane concentrations (0–10 wt.%); (**b**) correlation between total wear rate and silane treatment concentration. Averages followed by different lowercase letters are significantly different according to LSD's multiple range test at the significance level of 0.05. Error bars are standard deviation.

In the high-temperature region (300–350 °C), statistical analysis revealed significant differences in wear behavior among treatments. CSFCM-2, CSFCM-3, CSFCM-4, and CSFCM-5 showed significantly lower wear rates compared to untreated specimens

($p < 0.05$), while no significant differences were observed between CSFCM-0 and CSFCM-1. The untreated CSFCM-0 exhibited the most severe wear rate increase, rising from 0.181 to 1.568×10^{-7} $cm^3/(N \cdot m)^{-1}$, indicating the poor thermal stability of the untreated interface. In contrast, CSFCM-3 demonstrated the most stable wear progression, while CSFCM-2 exhibited exceptional high-temperature stability with the lowest wear rate at 350 °C (0.853×10^{-7} $cm^3(N \cdot m)^{-1}$). CSFCM-4 and CSFCM-5 showed moderate improvements over CSFCM-0 but could not match the performance of CSFCM-2 and CSFCM-3, suggesting that excessive silane treatment may compromise wear resistance.

The wear rate trends exhibit distinct temperature-dependent behaviors (Figure 8a). At low temperatures (100–150 °C), all specimens show relatively stable and low wear rates ($0.17–0.24 \times 10^{-7}$ $cm^3(N \cdot m)^{-1}$). A critical transition occurs between 200 and 250 °C, marked by sharp increases in wear rates, particularly evident in untreated specimens. CSFCM-3 demonstrates the most stable wear progression across all temperature ranges, while CSFCM-0 shows the most severe wear rate increase at elevated temperatures.

The correlation between total wear rate and silane treatment concentration (Figure 8b) reveals an optimal point at 6 wt.% (CSFCM-3), achieving the lowest total wear rate of 3.433×10^{-7} cm^3 $(N \cdot m)^{-1}$, representing a 26.26% reduction compared to untreated specimens. This optimum suggests that moderate silane treatment creates ideal interface conditions for wear resistance, while both insufficient (<4 wt.%) and excessive (>8 wt.%) treatment result in suboptimal wear performance improvements of only 16.36% and 19.36%, respectively.

Analysis of the total wear rate revealed that CSFCM-3 achieved the lowest total wear rate (3.433×10^{-7} cm^3 $(N \cdot m)^{-1}$), representing a 26.26% reduction compared to CSFCM-0, followed by CSFCM-2 and CSFCM-4. This trend indicates that moderate silane concentrations (4–6 wt.%) provide optimal interface modification for enhanced wear resistance. The improvement in wear resistance showed a non-linear relationship with silane concentration, where both insufficient (CSFCM-1) and excessive (CSFCM-5) treatment resulted in suboptimal performance improvements of 16.36% and 19.36%, respectively.

These wear characteristics suggest that silane treatment at an appropriate concentration (particularly CSFCM-3) creates an interface structure capable of maintaining mechanical integrity under elevated temperatures while providing effective stress distribution during the wear process. The superior wear resistance, especially at higher temperatures, further supports the application potential of these materials in moderate-temperature friction applications where controlled wear behavior is crucial for long-term performance reliability.

3.7. Fiber Surface Morphology Analysis

Scanning electron microscopy (SEM) analysis revealed progressive changes in CSFCM surface morphology across different silane treatment concentrations (Figure 9). The untreated CSFCM (Figure 9a) displayed a relatively smooth and regular surface texture, characteristic of fibers that have undergone biological pre-treatment through ruminant digestion.

At low silane concentrations (2–4 wt.%, Figure 9b,c), the fiber surfaces began exhibiting initial signs of modification, characterized by slight surface roughening and minor irregularities. These early morphological changes suggest that the chemical treatment started to affect the fiber surface structure, though the modifications remained relatively modest. This initial surface modification corresponds to the moderate improvements in physical properties, as evidenced by the slight reductions in water absorption from 8.49% to 7.98% and apparent porosity from 9.03% to 8.65%. These surface modification patterns differ from those observed by Liu et al. [24] for conventional silane-treated corn stalk fibers, which typically show more

aggressive surface etching even at lower treatment concentrations. The moderate surface modifications observed in CSFCM can be attributed to the protective effects of biological pre-treatment, which preserves the fundamental fiber structure while allowing controlled chemical modification.

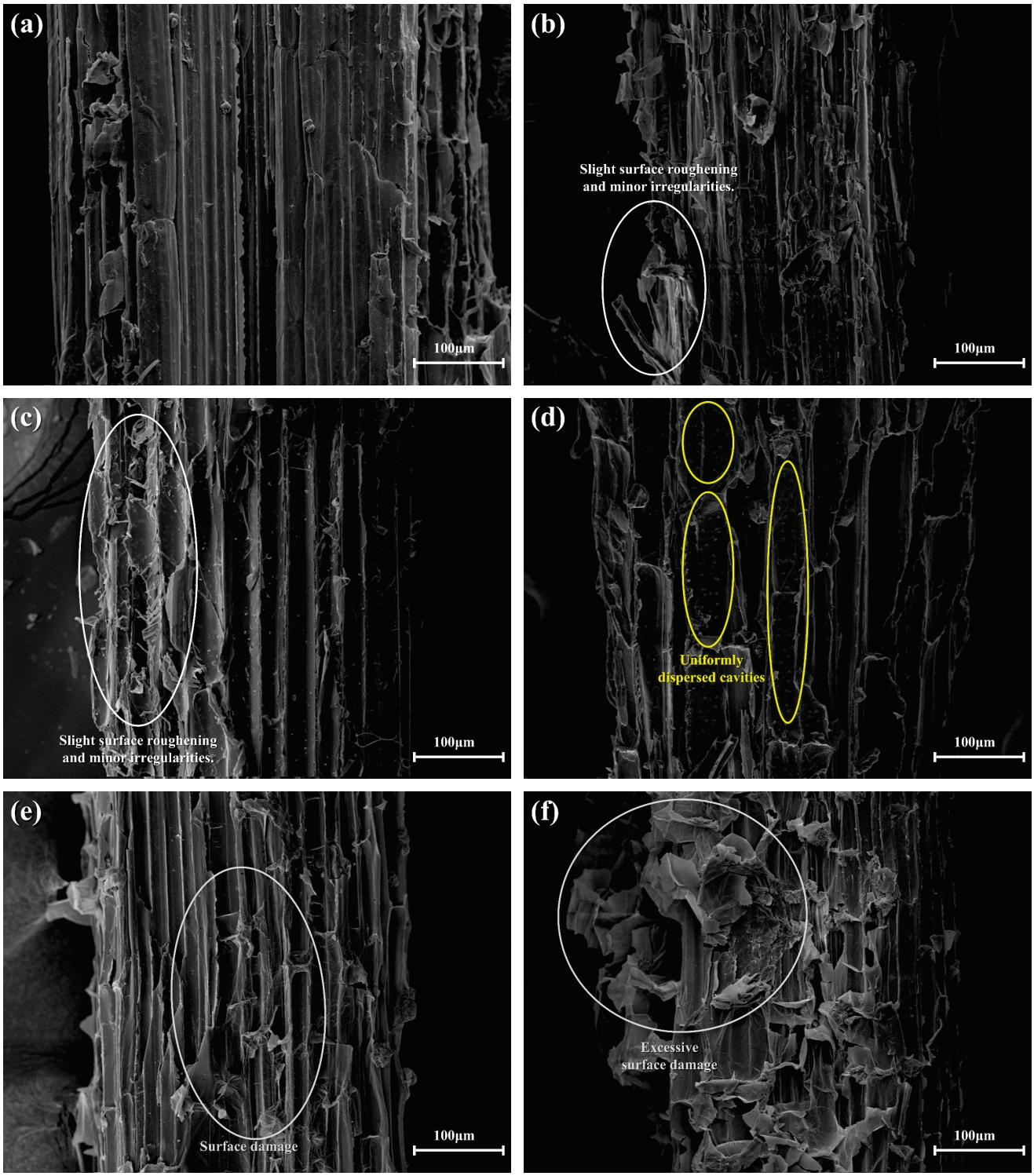

Figure 9. SEM micrographs showing surface morphology of CSFCM fibers treated with different silane concentrations: (**a**) untreated CSFCM; (**b**) 2 wt.% silane-treated CSFCM; (**c**) 4 wt.% silane-treated CSFCM; (**d**) 6 wt.% silane-treated CSFCM; (**e**) 8 wt.% silane-treated CSFCM; (**f**) 10 wt.% silane-treated CSFCM. All images were captured at 200× magnification.

The optimal treatment concentration (6 wt.%, Figure 9d) produced the most uniform surface modification pattern. The fiber surfaces displayed consistent roughness with evenly distributed microscale texturing and small, uniformly dispersed cavities. This regular surface modification pattern directly correlates with the superior performance characteristics observed, including the 34.2% reduction in water absorption and decreased apparent porosity to 7.85%. The uniform surface modification also contributes to the enhanced tribological properties, as demonstrated by the 26.26% reduction in total wear rate and improved thermal stability with a 94.31% recovery ratio.

At higher silane concentrations, particularly 8–10 wt.% (Figure 9e,f), more aggressive surface modification became evident. The 8 wt.% treatment (Figure 9e) resulted in increased surface roughness while maintaining relative uniformity across the fiber surface. However, at 10 wt.% concentration (Figure 9f), excessive surface damage was observed, manifesting as severe irregularities and significant structural deterioration of the fiber surface. This surface degradation explains the increased water absorption (7.05%) and apparent porosity (8.69%) at higher treatment concentrations, as the irregular surface features and structural defects create additional pathways for water penetration and void formation.

The surface morphology analysis provides critical insights into the structure–property relationships observed in CSFCM-reinforced composites. The optimal surface modification achieved at 6 wt.% treatment represents a crucial balance between enhanced surface roughness for mechanical interlocking and preserved fiber structural integrity. At excessive treatment concentrations (8–10 wt.%), the severe surface irregularities and structural deterioration create unfavorable conditions for the formation of uniform silane coupling layers on the fiber surface. These irregular surface features prevent the even distribution and effective bonding of silane molecules, explaining the reduction in physical and mechanical properties at higher concentrations. This correlation between surface modification and treatment concentration provides a fundamental understanding of the observed performance trends and validates the selection of 6 wt.% as the optimal treatment concentration for CSFCM-reinforced friction materials.

3.8. Surface Morphology and Wear Mechanisms

The tribological behavior and wear mechanism evolution of CSFCM-reinforced composites were characterized through high-resolution scanning electron microscopy (SEM) analysis (Figure 10). The investigation revealed distinct wear mechanism transitions across varying silane treatment concentrations, encompassing adhesive, abrasive, fatigue, and delamination wear modes.

Microstructural analysis of untreated specimens (CSFCM-0, Figure 10a) revealed predominant adhesive wear characteristics, manifested through extensive interfacial delamination and fiber extraction. The inadequate fiber–matrix interfacial strength resulted in interfacial debonding under tribological loading, generating stress concentration sites that initiated microcrack formation. The liberated fiber fragments functioned as third-body abrasive elements, facilitating a transition from adhesive to three-body abrasive wear mechanisms, evidenced by bimodal wear debris distribution comprising fine adhesive particles and coarse fiber fragments.

CSFCM-1 specimens (Figure 10b) exhibited transitional wear behavior characterized by modified wear particle morphology despite persistent fiber detachment. The observed wear particle size distribution shift and reduced fine debris generation indicated a mechanistic transition from adhesive-dominated to abrasive-dominated wear. However, persistent microcrack propagation indicated suboptimal interface modification for fatigue resistance. This wear mechanism evolution differs from that reported by Ma et al. [29] for conventional

natural fiber composites, where abrasive wear typically dominates throughout the wear process. The unique transition to controlled delamination wear in CSFCM composites can be attributed to the enhanced fiber–matrix interface achieved through the combination of biological pre-treatment and optimized silane modification.

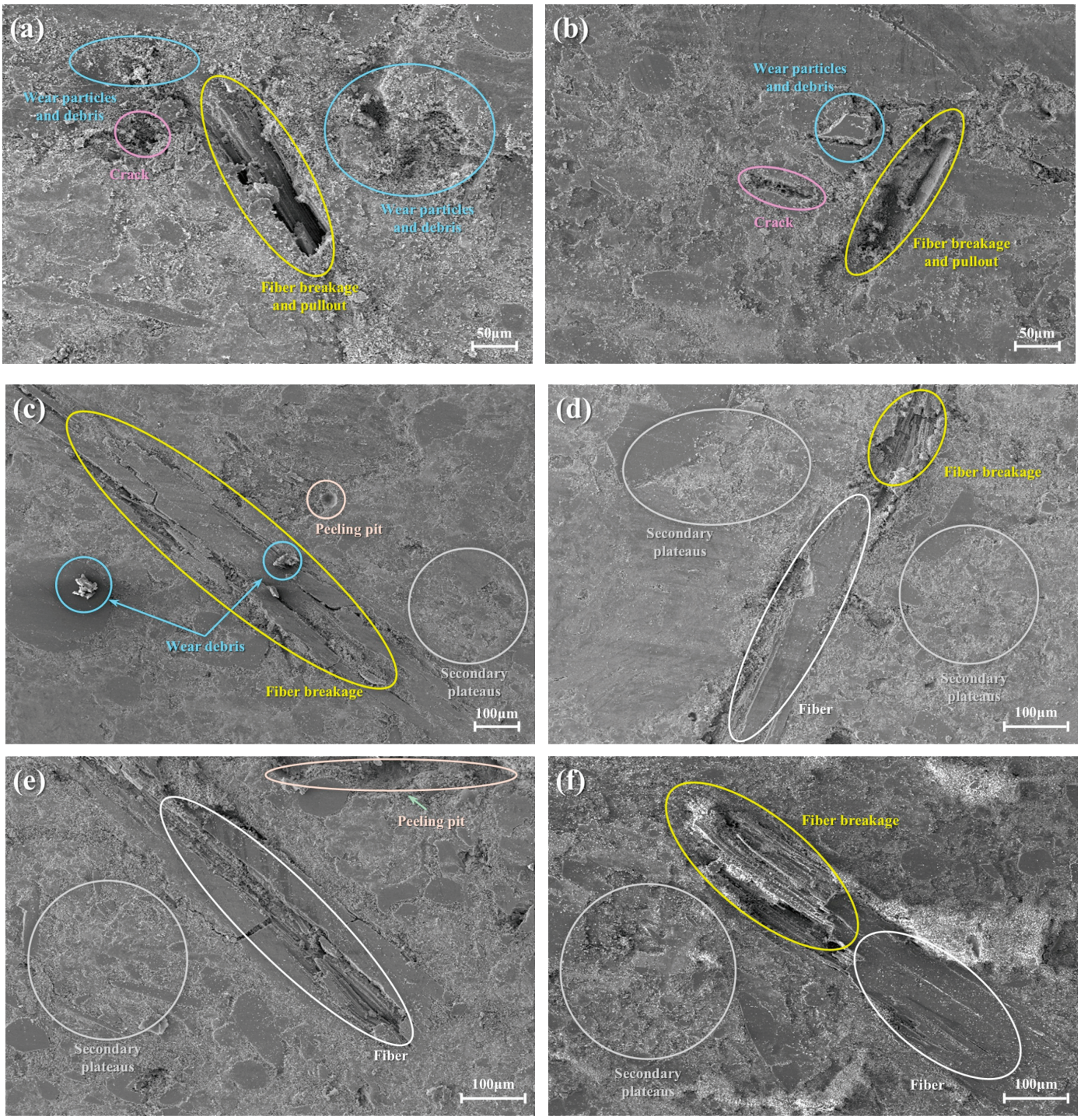

Figure 10. Surface morphology of CSFCM-reinforced composites: (**a**) CSFCM-0; (**b**) CSFCM-1; (**c**) CSFCM-2; (**d**) CSFCM-3; (**e**) CSFCM-4; (**f**) CSFCM-5.

A fundamental mechanistic transformation was observed in CSFCM-2 (Figure 10c), characterized by the emergence of delamination wear as the primary degradation mode. The initiation of secondary plateau formation indicated a transition towards a stabilized

tribological regime, where compacted wear debris contributed to load distribution. The presence of characteristic delamination cavities suggests subsurface crack nucleation and propagation that is consistent with delamination wear theory, facilitating controlled material removal processes.

CSFCM-3 (Figure 10d) exhibited optimized tribological behavior through synergistic wear mechanism integration. The extensive development of stable secondary plateaus indicated efficient tribomechanical mixing and debris consolidation under dynamic loading conditions. Limited surface degradation under sustained loading suggested effective stress distribution through the modified interface. The specimen demonstrated a transition to mild oxidative wear, characterized by the formation of protective tribologically modified surface layers.

Microstructural analysis of CSFCM-4 (Figure 10e) revealed enhanced subsurface fatigue mechanisms despite maintaining fiber–matrix adhesion, manifested through increased delamination cavity dimensions. This observation suggests that excessive interfacial rigidity may compromise cyclic strain accommodation capacity, accelerating subsurface crack propagation. CSFCM-5 (Figure 10f) further exemplified this trend, where despite achieving optimal fiber–matrix bonding, enhanced surface deterioration and secondary plateau irregularity indicated severe wear regime reversion, attributed to interface embrittlement.

The systematic wear mechanism evolution across silane treatment concentrations elucidates the critical influence of interfacial properties on tribological behavior. The transition sequence from severe adhesive and three-body abrasive wear in untreated specimens to controlled delamination and oxidative wear in optimally treated samples, followed by enhanced fatigue wear at elevated treatment concentrations, demonstrates the complex interdependence between interface modification parameters and wear mechanisms.

Quantitative image analysis of SEM micrographs was performed using ImageJ software (Version 1.54g) to characterize key microstructural features. For each specimen type, measurements were taken from at least 20 different regions across multiple samples. In untreated specimens (CSFCM-0), wear debris exhibited diverse morphological characteristics: large debris fragments averaged 82 $\pm$ 18 μm, while fine wear particles showed dimensions of 7.2 $\pm$ 2.8 μm. Some exceptional large debris fragments reached 145 $\pm$ 12 μm, particularly in regions experiencing severe delamination. Surface examination revealed delamination pits with diameters varying 55 $\pm$ 12 μm, and surface cracks extending from 165 $\pm$ 35 μm to 242 $\pm$ 28 μm in length. These cracks predominantly appeared along the sliding direction, often interconnecting with delamination regions. Under optimal treatment conditions (CSFCM-3), the wear mechanism demonstrated a notable shift in debris characteristics. The proportion of large debris (>50 μm) decreased significantly, while fine wear particles (6.8 $\pm$ 2.2 μm) became more prevalent. The delamination pits were less frequent and showed reduced dimensions of 42 $\pm$ 8 μm. Surface cracks were also less extensive, typically ranging from 125 $\pm$ 28 μm to 185 $\pm$ 32 μm in length. Specimens with excessive treatment (CSFCM-5) showed increased formation of large wear debris (95 $\pm$ 22 μm) and more pronounced surface damage, with delamination pits expanding to 68 $\pm$ 15 μm and crack lengths extending up to 262 $\pm$ 42 μm.

The microscopic results support a comprehensive tribological model in which optimized silane treatment (CSFCM-3) establishes interfacial characteristics that facilitate multiple synergistic wear mechanisms. The controlled delamination wear proceeds through stable subsurface crack propagation pathways, while efficient tribomechanical mixing and wear debris consolidation generate load-bearing secondary plateaus. The concurrent formation of protective tribofilms through mild oxidative wear mechanisms further enhances

surface protection. This optimized integration of wear mechanisms, achieved through precise interface modification, leads to a superior tribological performance compared to specimens with insufficient treatment (characterized by predominant adhesive wear) or excessive treatment (dominated by accelerated fatigue wear mechanisms). The established relationship between silane treatment concentration and wear mechanism evolution provides essential information for developing high-performance friction materials with controlled interface properties.

4. Conclusions

This investigation systematically examined the effects of silane treatment at varied concentrations (2–10 wt.%) on corn stalk fibers extracted from cattle manure (CSFCM) for the development of friction materials. Comprehensive analysis of physicochemical, tribological, and microstructural characteristics yielded the following significant findings:

(1) The best interface modification was achieved at a 6 wt.% silane concentration (CSFCM-3), resulting in a substantial enhancement of the physical properties. This optimization manifested in a 34.2% reduction in water absorption capacity and a decrease in the apparent porosity from 9.03% to 7.85%. The modified composites maintained a favorable density range of 1.9–2.1 g/cm^3, significantly below that of conventional friction materials (2.2–2.5 g/cm^3).

(2) The tribological characterization of CSFCM-3 demonstrated exceptional performance stability, as the friction coefficients were maintained within 0.35–0.45 across the temperature range of 100–350 °C. Thermal stability analysis revealed superior performance parameters, including a fade ratio of 14.48% and a recovery ratio of 95%. The total wear rate exhibited a substantial reduction of 26.26%, reaching 3.433×10^{-7} cm^3 (N·m)$^{-1}$ compared to unmodified specimens, indicating enhanced wear resistance under dynamic thermal conditions.

(3) Microstructural analysis highlighted that there were fundamental transformations in wear mechanisms following optimal silane modification. The treatment facilitated the formation of uniformly distributed, densified secondary plateaus with enhanced matrix adhesion, contributing to improved tribological stability. A significant transition from severe adhesive and three-body abrasive wear to controlled two-body abrasive wear was observed, characterized by reduced delamination cavity formation, uniformly distributed shallow plowing patterns, and refined wear debris morphology conducive to stable tribofilm development.

(4) The integration of biological pre-treatment through ruminant digestion with optimized silane modification establishes an innovative protocol for developing high-performance friction materials from agricultural waste streams. The enhanced cellulose content and modified fiber architecture resulting from biological pre-treatment, combined with precisely controlled chemical modification, creates a novel platform for sustainable material development. This investigation provides valuable technical insights for industrial applications of environmentally friendly composites, particularly in validating the feasibility of cattle manure-derived corn stalk fibers for friction materials. The demonstrated performance improvements and environmental benefits make this technology particularly attractive for sustainable friction material manufacturing, though challenges remain in scaling up production and managing economic impacts. This research involves the coordination between agricultural and industrial sectors, and faces challenges in optimizing processing parameters for different plant fiber composites. Beyond tribological applications, further research is needed to explore its potential in lightweight, high-strength, and eco-friendly composite materials.

Key aspects requiring investigation include optimization of the fiber–matrix interface through surface modification techniques, enhancement of mechanical properties through fiber orientation control and distribution, and development of standardized processing protocols for various agricultural waste streams.

The tribological and mechanical properties obtained in this study meet the national standards for brake friction materials, demonstrating the feasibility of these composites as brake materials. However, considering their high-temperature performance characteristics, these materials are more suitable for braking environments with moderate loads, specifically in light-load or medium-low temperature conditions. Such applications could include light vehicles, agricultural machinery, or industrial conveying equipment where severe thermal conditions are not typically encountered. Moreover, this study provides valuable insights for expanding the application potential of cattle manure straw fiber composites in other working conditions, particularly where moderate mechanical and tribological properties are required.

This investigation demonstrates the efficacy of integrating biological pre-treatment with chemical modification strategies while establishing new methodologies for developing sustainable, high-performance friction materials from agricultural waste resources. The combination of environmental sustainability and enhanced performance characteristics provides a foundation for future developments in eco-conscious friction material design.

Author Contributions: Conceptualization, S.W. and J.Z.; Methodology, S.W.; validation, L.R. and M.G.; formal analysis, X.Q., Q.Q., B.L. and P.X.; data curation, S.W. and J.Z.; writing—original draft preparation, S.W.; writing—review and editing, J.Z.; visualization, M.G.; funding acquisition, S.W. and M.G. All authors have read and agreed to the published version of the manuscript.

Funding: This research was funded by the National Natural Science Foundation of China (52305305, 52105300, 52075215).

Institutional Review Board Statement: Not applicable.

Data Availability Statement: The original contributions presented in this study are included in the article. Further inquiries can be directed to the corresponding authors.

Acknowledgments: The authors gratefully acknowledge Yan Zhang from the Hospital of Stomatology, Jilin University, for her valuable technical assistance and expertise in scanning electron microscopy (SEM) characterization and other analytical experiments.

Conflicts of Interest: The authors declare no conflicts of interest.

References

1. Singh, N.; Walker, T.R. Plastic recycling: A panacea or environmental pollution problem. *NPJ Mater. Sustain.* **2024**, *2*, 17. [CrossRef] [PubMed]
2. Dalmis, R. Description of a new cellulosic natural fiber extracted from *Helianthus tuberosus* L. as a composite reinforcement material. *Physiol. Plant.* **2023**, *175*, e13960. [CrossRef] [PubMed]
3. Bhat, S.I.; Mobin, M.; Islam, S.; Zehra, S. Recent advances in anticorrosive coatings based on sustainable polymers: Challenges and perspectives. *Surf. Coat. Technol.* **2024**, *480*, 130596. [CrossRef]
4. Zwawi, M. A review on natural fiber bio-composites, surface modifications and applications. *Molecules* **2021**, *26*, 404. [CrossRef] [PubMed]
5. Kamarudin, S.H.; Mohd Basri, M.S.; Rayung, M.; Abu, F.; Ahmad, S.B.; Norizan, M.N.; Osman, S.; Sarifuddin, N.; Desa, M.S.Z.M.; Abdullah, L.C. A review on natural fiber reinforced polymer composites (NFRPC) for sustainable industrial applications. *Polymers* **2022**, *14*, 3698. [CrossRef] [PubMed]
6. Akter, M.; Uddin, M.H.; Tania, I.S. Biocomposites based on natural fibers and polymers: A review on properties and potential applications. *J. Reinf. Plast. Compos.* **2022**, *41*, 705–742. [CrossRef]

7. Smerald, A.; Rahimi, J.; Scheer, C. A global dataset for the production and usage of cereal residues in the period 1997–2021. *Sci. Data* **2023**, *10*, 685. [CrossRef]
8. Font-Palma, C. Methods for the Treatment of Cattle Manure—A Review. *C* **2019**, *5*, 27. [CrossRef]
9. Petzel, E.A.; Titgemeyer, E.C.; Smart, A.J.; Hales, K.E.; Foote, A.P.; Acharya, S.; Bailey, E.A.; Held, J.E.; Brake, D.W. What is the digestibility and caloric value of different botanical parts in corn residue to cattle? *J. Anim. Sci.* **2019**, *97*, 3056–3070. [CrossRef]
10. Xu, Q.; Zhong, H.; Zhou, J.; Wu, Y.; Ma, Z.; Yang, L.; Wang, Z.; Ling, C.; Li, X. Lignin degradation by water buffalo. *Trop. Anim. Health Prod.* **2021**, *53*, 344. [CrossRef] [PubMed]
11. Li, K.; Yang, Z.; Zhang, Y.; Li, Y.; Lu, L.; Niu, D. Effect of pretreated cow dung fiber on mechanical and shrinkage properties of cementitious composites. *J. Clean. Prod.* **2022**, *348*, 131374. [CrossRef]
12. Yang, Z.; Li, K.; Yan, X.; Wu, W.; Briseghella, B.; Marano, G.C. Characterization and value-added applications of natural cellulose fibers derived from cow dung in cementitious composites. *Cellulose* **2024**, *31*, 5575–5589. [CrossRef]
13. Yang, X.; Li, L.; Zhao, W.; Wang, M.; Yang, W.; Tian, Y.; Zheng, R.; Deng, S.; Mu, Y.; Zhu, X. Characteristics and functional application of cellulose fibers extracted from cow dung wastes. *Materials* **2023**, *16*, 648. [CrossRef] [PubMed]
14. Ma, Y.; Wu, S.; Zhuang, J.; Tong, J.; Qi, H. Tribological and physio-mechanical characterization of cow dung fibers reinforced friction composites: An effective utilization of cow dung waste. *Tribol. Int.* **2019**, *131*, 200–211. [CrossRef]
15. Wu, S.; Guo, M.; Zhao, J.; Wu, Q.; Zhuang, J.; Jiang, X. Characterization of the mechanical and morphological properties of cow dung fiber-reinforced polymer composites: A comparative study with corn stalk fiber composites and sisal fiber composites. *Polymers* **2022**, *14*, 5041. [CrossRef] [PubMed]
16. Reddy, T.R.K.; Rao, T.S.; Suvarna, R.P. Studies on thermal characteristics of cow dung powder filled glass-polyester hybrid composites. *Compos. Part B* **2024**, *56*, 670–672. [CrossRef]
17. Yang, X.; Li, L.; Zhao, W.; Tian, Y.; Zheng, R.; Deng, S.; Mu, Y. The influence of potassium hydroxide concentration and temperature on pulp characteristics and cow dung-based paper performance. *J. Nat. Fibers* **2023**, *20*, 2164546. [CrossRef]
18. Li, K.; Yang, Z.; Yan, X.; Xu, L.; Briseghella, B.; Marano, G.C. Effect of Modified Cow Dung Fibers on Strength and Autogenous Shrinkage of Alkali-Activated Slag Mortar. *Materials* **2023**, *16*, 6808. [CrossRef]
19. Fasake, V.; Dashora, K. A sustainable potential source of ruminant animal waste material (dung fiber) for various industrial applications: A review. *Bioresour. Technol. Rep.* **2021**, *15*, 100693. [CrossRef]
20. Fasake, V.; Dashora, K. Characterization of raw and anaerobic digested cattle dung fibers: A sustainable source of non-wood material. *Biomass Convers. Biorefin.* **2024**, *14*, 1949–1958. [CrossRef]
21. Kudva, A.; Mahesha, G.T.; Hegde, S.; Pai, D. Influence of chemical treatment of Bamboo fibers on the vibration and acoustic characterization of Carbon/Bamboo fiber reinforced hybrid composites. *Mater. Res. Express* **2024**, *11*, 075304. [CrossRef]
22. El Boustani, M.; Lebrun, G.; Brouillette, F.; Belfkira, A. Effect of a solvent-free acetylation treatment on reinforcements permeability and tensile behaviour of flax/epoxy and flax/wood fibre/epoxy composites. *Can. J. Chem. Eng.* **2017**, *95*, 1082–1092. [CrossRef]
23. Zhang, C.; Liu, L.; Zeng, G.; Huang, D.; Lai, C.; Huang, C.; Wei, Z.; Li, N.; Xu, P.; Cheng, M.; et al. Utilization of nano-gold tracing technique: Study the adsorption and transmission of laccase in mediator-involved enzymatic degradation of lignin during solid-state fermentation. *Biochem. Eng. J.* **2014**, *91*, 149–156. [CrossRef]
24. Liu, Y.; Xie, J.; Wu, N.; Wang, L.; Ma, Y.; Tong, J. Influence of silane treatment on the mechanical, tribological and morphological properties of corn stalk fiber reinforced polymer composites. *Tribol. Int.* **2019**, *131*, 398–405. [CrossRef]
25. *GB/T 24508-2009*; Wood-Plastic Composite Flooring. General Administration of Quality Supervision, Inspection and Quarantine of the People's Republic of China. Standardization Administration of the People's Republic of China: Beijing, China, 2009.
26. Akil, H.M.; Cheng, L.W.; Ishak, Z.M.; Bakar, A.A.; Abd Rahman, M.A. Water absorption study on pultruded jute fibre reinforced unsaturated polyester composites. *Compos. Sci. Technol.* **2009**, *69*, 1942–1948. [CrossRef]
27. Ma, Y.; Ma, Q.S.; Suo, J.; Chen, Z.H. Low-temperature fabrication and characterization of porous SiC ceramics using silicone resin as binder. *Ceram. Int.* **2008**, *34*, 253–255. [CrossRef]
28. *GB 5763-2018*; Brake linings for automobiles. General Administration of Quality Supervision, Inspection and Quarantine of the People's Republic of China. Standardization Administration of the People's Republic of China: Beijing, China, 2018.
29. Ma, Y.; Liu, Y.; Wang, L.; Tong, J.; Zhuang, J.; Jia, H. Performance assessment of hybrid fibers reinforced friction composites under dry sliding conditions. *Tribol. Int.* **2018**, *119*, 262–269. [CrossRef]
30. Ma, Y.; Liu, Y.; Menon, C.; Tong, J. Evaluation of wear resistance of friction materials prepared by granulation. *ACS Appl. Mater. Interfaces* **2015**, *7*, 22814–22820. [CrossRef]
31. Satapathy, B.K.; Bijwe, J. Performance of friction materials based on variation in nature of organic fibres: Part I. Fade and recovery behaviour. *Wear* **2004**, *257*, 573–584. [CrossRef]
32. Nishino, T.; Hirao, K.; Kotera, M.; Nakamae, K.; Inagaki, H. Kenaf reinforced biodegradable composite. *Compos. Sci. Technol.* **2003**, *63*, 1281–1286. [CrossRef]

33. Taghiyari, H.R.; Karimi, A.; Tahir, P.M. Organo-silane compounds in medium density fiberboard: Physical and mechanical properties. *J. For. Res.* **2015**, *26*, 495–500. [CrossRef]
34. Siroka, B.; Noisternig, M.; Griesser, U.J.; Bechtold, T. Characterization of cellulosic fibers and fabrics by sorption/desorption. *Carbohydr. Res.* **2008**, *343*, 2194–2199. [CrossRef]
35. Hoikkanen, M.; Honkanen, M.; Vippola, M.; Lepistö, T.; Vuorinen, J. Effect of silane treatment parameters on the silane layer formation and bonding to thermoplastic urethane. *Prog. Org. Coat.* **2011**, *72*, 716–723. [CrossRef]
36. Vilay, V.; Mariatti, M.; Taib, R.M.; Todo, M. Effect of fiber surface treatment and fiber loading on the properties of bagasse fiber–reinforced unsaturated polyester composites. *Compos. Sci. Technol.* **2008**, *68*, 631–638. [CrossRef]
37. Petzel, E.A.; Smart, A.J.; St-Pierre, B.; Selman, S.L.; Bailey, E.A.; Beck, E.E.; Walker, J.A.; Wright, C.L.; Held, J.E.; Brake, D.W. Estimates of diet selection in cattle grazing cornstalk residues by measurement of chemical composition and near infrared reflectance spectroscopy of diet samples collected by ruminal evacuation. *J. Anim. Sci.* **2018**, *96*, 1914–1928. [CrossRef] [PubMed]
38. Tonoli, G.H.D.; Rodrigues Filho, U.P.; Savastano, H., Jr.; Bras, J.; Belgacem, M.N.; Lahr, F.R. Cellulose modified fibres in cement based composites. *Compos. Part A* **2009**, *40*, 2046–2053. [CrossRef]
39. Yuan, J.; Zhang, Z.; Yang, M.; Guo, F.; Men, X.; Liu, W. Surface modification of hybrid-fabric composites with amino silane and polydopamine for enhanced mechanical and tribological behaviors. *Tribol. Int.* **2017**, *107*, 10–17. [CrossRef]
40. Karthikeyan, S.; Rajini, N.; Jawaid, M.; Winowlin Jappes, J.T.; Thariq, M.T.H.; Siengchin, S.; Sukumaran, J. A review on tribological properties of natural fiber based sustainable hybrid composite. *Proc. Inst. Mech. Eng. Part J* **2017**, *231*, 1616–1634. [CrossRef]
41. Elen, N.Ç.; Yıldırım, M.; Kanbur, Y. Tribological properties of hemp fiber reinforced polylactic acid bio-composites: Effect of different types of modification methods. *Funct. Compos. Struct.* **2023**, *5*, 015009. [CrossRef]
42. Mylsamy, B.; Chinnasamy, V.; Palaniappan, S.K.; Subramani, S.P.; Gopalsamy, C. Effect of surface treatment on the tribological properties of Coccinia Indica cellulosic fiber reinforced polymer composites. *J. Mater. Res. Technol.* **2020**, *9*, 16423–16434. [CrossRef]
43. Dharmakrishnan, S.; Pandian, P.; Sembian, M. Sustainable characterization of silane treated and untreated Psidium guajava stem natural fibers based automobile brake pads. *J. Nat. Fibers* **2022**, *19*, 7982–7995. [CrossRef]
44. Wu, S.; Zhuang, J.; Wu, Q.; Qi, H.; Zhao, J.; Guo, M. Investigation of tribological, physicomechanical, and morphological properties of resin-based friction materials reinforced with *Agave americana* waste. *Mater. Res. Express* **2021**, *8*, 075308. [CrossRef]

Disclaimer/Publisher's Note: The statements, opinions and data contained in all publications are solely those of the individual author(s) and contributor(s) and not of MDPI and/or the editor(s). MDPI and/or the editor(s) disclaim responsibility for any injury to people or property resulting from any ideas, methods, instructions or products referred to in the content.

polymers

MDPI

Article

Eco-Friendly Hydrogel Beads from Seashell Waste for Efficient Removal of Heavy Metals from Water

Zaineb Mchich [1], Daniela Simina Stefan [2,*], Rachid Mamouni [1,*], Nabil Saffaj [1] and Magdalena Bosomoiu [2]

[1] Team of Biotechnology, Materials, and Environment, Faculty of Sciences, Ibn Zohr University, Agadir BP 8106, Morocco; zaineb.mchich@edu.uiz.ac.ma (Z.M.); n.saffaj@uiz.ac.ma (N.S.)
[2] Department of Analytical Chemistry and Environmental Engineering, Faculty of Chemical Engineering and Biotechnologies, National University of Science and Technology Politehnica of Bucharest, 1-7 Polizu Street, 011061 Bucharest, Romania; magdalena.bosomoiu@upb.ro
* Correspondence: daniela.stefan@upb.ro (D.S.S.); r.mamouni@uiz.ac.ma (R.M.)

Abstract: The objective of this study is to develop a calcium carbonate-based adsorbent derived from *Cellana Tramoscrica* seashells, incorporated into a sodium alginate matrix (Na-Alg@CTs) to form hydrogel beads, for the efficient removal of Cu (II) and Zn (II) heavy metals from aqueous solutions. XRD, SEM/EDS, and FTIR analysis confirm the successful synthesis and characterization of the fabricated adsorbent. The adsorption study of Cu (II) and Zn (II) onto Na-Alg@CTs hydrogel beads revealed that the Langmuir model was the most suitable for characterizing the adsorption isotherms, suggesting monolayer coverage. Na-Alg@CTs exhibited a maximum Langmuir adsorption capacity of 368.58 mg/g and 1075.67 mg/g for Cu (II) and Zn (II), respectively. Additionally, the kinetics followed the pseudo-second-order model, indicating that the adsorption process is primarily governed by chemisorption. The thermodynamic study suggests that the uptake of metal ions on Na-Alg@CTs hydrogel beads is spontaneous and endothermic. The exceptional adsorption capacity, eco-friendly nature, and low-cost characteristics of Na-Alg@CTs hydrogel beads make them an ideal adsorbent for the removal of Cu (II) and Zn (II) from wastewater.

Keywords: eco-friendly polymers; *Cellana Tramoscrica* seashells; hydrogel beads; heavy metals

1. Introduction

In recent decades, the rapid expansion of industrialization and urbanization has resulted in the release of industrial effluents, exhaust gases, and solid waste into the environment, both directly and indirectly, leading to significant water, soil, and atmosphere pollution [1,2]. Of particular concern are heavy metals, which pose serious risks to human health [3]. These metals, characterized by their significant contributions to water pollution, include elements such as copper, zinc, mercury, cadmium, chromium, lead, manganese, and nickel [4]. The primary sources of heavy metal pollution are industrial activities such as smelting, electroplating, electrolysis, and mining, as well as using chemicals in paints, pharmaceuticals, and pesticides. The wastewater generated by these industries is often laden with heavy metal ions, leading to their accumulation in natural water bodies and causing severe environmental contamination [5,6].

Among various metals, copper and zinc are essential yet potentially toxic when present in high concentrations. Copper is vital for several biological functions, including the growth and development of the body and the maturation of the nervous, hematopoietic, and skeletal systems [7,8]. However, excessive copper exposure often from contaminated water due to copper pipes, agricultural pesticides, and industrial discharges can be hazardous. Excessive copper accumulation can lead to digestive disorders, liver and kidney damage, and neurological imbalances [9–11]. Similarly, zinc is crucial for protein synthesis, immune function, and wound healing [12]. Nevertheless, overexposure to zinc, commonly from water contaminated by galvanized materials, fertilizers, and certain industrial products,

can cause gastrointestinal issues and disrupt the immune system [13]. Elevated concentrations of these metals in aquatic ecosystems can be toxic to organisms, impairing their growth and reproduction. Therefore, managing copper and zinc pollution is a priority for health, scientific, and environmental authorities. These bodies are focusing on effective detoxification methods to safeguard human health and the environment [14]. Among the various remediation techniques developed are catalytic ozonation [15], ion exchange [16], coagulation-flocculation [17], photocatalysis [18,19], membrane filtration [20], and adsorption [21]. Of these, adsorption is particularly favored due to its simplicity, ease of application, use of low-cost materials, capacity to treat large volumes of wastewater, and recyclability [22,23]. The development of adsorbents using biomass waste as a substitute for activated carbon enhances the cost-effectiveness of the adsorption process.

Aquaculture of shellfish (such as squid, oysters, abalones, and mussels) is developing rapidly, leading to an increase in waste produced from shellfish [24]. Shell powder is commonly a source of calcium carbonate ($CaCO_3$) and is known as a natural adsorbent for heavy metals due to its high specific surface area, high porosity, and low cost [25]. To address the limitations associated with the powdered form, considerable efforts have been directed toward developing low-cost composites, such as membranes, fibers, and beads [26]. In this regard, the utilization of polysaccharide adsorbent materials for the fabrication of mouldable composites has gained increasing prominence, offering a promising strategy to overcome these challenges [27]. Sodium alginate (Na-Alg), a natural water-soluble salt derived from brown seaweed, has emerged as a key material due to its high bioavailability and straightforward extraction process [28]. As a linear polysaccharide, sodium alginate consists of α-L-guluronic acid (G) and β-D-mannuronic acid (M) residues [29]. Na-Alg possesses a distinctive property that enables it to form hydrogels by substituting sodium ions in guluronic acid residues with divalent cations, including calcium (Ca^{2+}), barium (Ba^{2+}), strontium (Sr^{2+}), ... [30]. This ion exchange process results in the formation of a three-dimensional network. Consequently, the utilization of Na-Alg to encapsulate $CaCO_3$ generated from seashells represents a sophisticated methodology that is designed to minimize mass loss, reduce regeneration costs, and enhance the efficiency of large-scale water treatment.

This research paper aims to investigate the conversion of $CaCO_3$ generated from *Cellana Tramoserica* shells (CTs) into valuable green biocomposites by incorporating it into the Na-Alg matrix, which is renowned for its excellent adsorption properties for heavy metals. The biocomposite physicochemical properties were analyzed using scanning electron microscopy, X-ray diffraction, energy-dispersive X-ray spectrometer, and Fourier-transformed infrared spectroscopy. Batch adsorption experiments were conducted to assess the adsorption performance of Na-Alg@CTs hydrogel beads for the removal of Cu (II) and Zn (II) ions. These experiments systematically evaluated the hydrogel beads under a variety of conditions, including different adsorbent dosages, pH levels, initial ion concentrations, temperatures, and contact time.

2. Materials and Methods

2.1. Materials

The chemicals utilized in the research were Na-Alg, $CuSO_4 \cdot 5H_2O$, Zn $(NO_3)_2 \cdot 6H_2O$, HCl, NaOH, $CaCl_2$ (manufacturer of all p.a. Fluka), all reagents were of analytical grade. The *Cellana Tramoscrica* seashells were procured from Cap Ghir beach in Agadir, Morocco.

2.2. Methods

The preparation of *Cellana Tramoscrica* seashells was conducted under the protocol outlined by [31]. The shells were first subjected to an extensive cleaning process using distilled water (DW) to remove any remaining sand particles and then subjected to treatment with 0.1 M of HCl for one night to remove organic substances. Following this, the shells were washed again and dried at 120 °C. Finally, the shells were crushed and sieved

to 80 µm. The resulting powder was then washed and dried at 70 °C, after which it was labeled as CTs.

The synthesis process for CTs encapsulation was initiated with the dissolution of 1 g of Na-Alg in 100 mL of DW, which was then stirred thoroughly on a magnetic stirrer for 3 h until complete dissolution and the disappearance of air bubbles. Thereafter, 1 g of CTs was added to the alginate gel. To obtain a homogeneous mixture, the mixing process was continued overnight. Subsequently, the solution was added dropwise to a 1% (*w*/*v*) calcium chloride solution via a syringe, forming roughly uniform-sized beads. The hydrogel beads were subsequently washed with DW to eliminate any residual calcium chloride, stored in a bottle containing DW, and labeled as Na-Alg@CTs hydrogel beads. Figure S1 shows the detailed process of hydrogel beads preparation.

2.3. Characterization of Na-Alg@CTs Hydrogel Beads

The hydrogel beads of the Na-Alg@CTs hydrogel biocomposite were characterized through a series of techniques, including X-ray diffraction using a Bruker CCD-Apex instrument in the 2θ range of 6° to 60° and scanning electron microscopy (SEM) using a Quanta Inspect F50, FEI Company, Eindhoven, The Netherlands. Furthermore, the samples were analyzed using an energy dispersive X-ray spectrometer (EDS) with MnK resolution of 133 eV, Fourier transformed infrared spectroscopy (FT-IR) using a Nicolet iS50FT-IR (Nicolet, Pittsfield, MA, USA) spectrometer equipped with a DTGS detector which provides information with a high sensitivity in the range of 4000 cm^{-1} and 400 cm^{-1} at a resolution of 4 cm^{-1}.

The point of zero charge (pH $_{PZC}$) of Na-Alg@CTs hydrogel beads was determined following the established protocol outlined in previous studies [32,33].

2.4. Adsorption Experiments

The metal ions Cu (II) and Zn (II) adsorption experiments onto Na-Alg@CTs hydrogel beads were carried out in a batch mode. To ascertain the impact of multiple variables, 0.25 g/L of hydrogel beads was introduced into 50 mL of Cu (II) or Zn (II) solutions. Multiple parameters were examined, including pH (3–6), time (5–180 min), dose (0.25–1.75 g/L), and initial concentration (5–200 mg/L) for Cu (II) and (5–500 mg/L) for Zn (II). Subsequently, the beads were removed from the solution after the specified time interval, and the residual Cu (II) and Zn (II) concentrations were quantified by flame absorption spectroscopy (Analytik Jena ContrAA 300, Bucharest, Romania). The removal percentage Equation (1) and adsorption capacity Equation (2) of Cu (II) and Zn (II) on Na-Alg@CTs hydrogel beads were calculated using the following equations.

$$\% R = \frac{C_i - C_e}{C_i} \times 100 \quad (1)$$

$$Q_e = \frac{C_i - C_e}{m} \times V_s \quad (2)$$

where C_i (ppm) is the initial concentration, C_e (ppm) is the equilibrium concentration, m (mg) is the bio-adsorbent dose, and Vs (mL) is the solution volume.

3. Results and Discussion

3.1. FT-IR Analysis of Na- Alg@CTs Hydrogel Beads

The functional groups in Na-Alg (a), CTs (b), and Na-Alg@CTs hydrogel beads (c) were analyzed using FT-IR, as shown in Figure 1. The spectrum of Na-Alg exhibits four distinct bands corresponding to specific functional groups. The broad band at 3223 cm^{-1} is attributed to hydroxyl groups (-OH), while the bands at 1407 cm^{-1} and 1592 cm^{-1} are associated with symmetric and asymmetric stretching vibrations of carboxylate groups ($-COO^-$), respectively. The band at 1028 cm^{-1} is linked to the -C-O-H stretching of alcoholic groups [34]. In the CTs spectrum, the bands at 1400 cm^{-1}, 708 cm^{-1}, and 868 cm^{-1} correspond to carbonate groups (CO_3^{2-}) [35,36]. After encapsulation and the formation of

Na-Alg@CTs hydrogel beads, the spectrum shows a reduction in the intensities of the characteristic bands from both CTs and Na-Alg, along with slight shifts in band positions. These changes suggest successful interaction and complexation between the components [37].

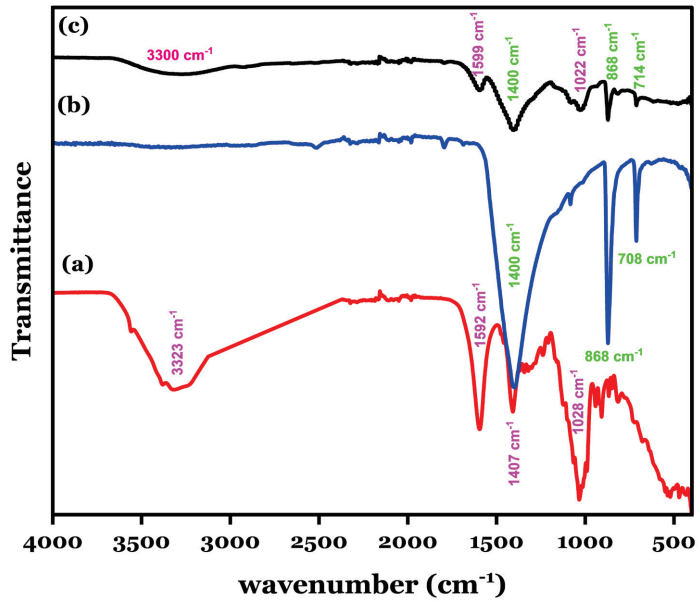

Figure 1. FT-IR analysis for (**a**) Na-Alg, (**b**) CTs, and (**c**) Na-Alg@CTs hydrogel beads.

3.2. X-Ray Diffraction of Na-Alg@CTs Hydrogel Beads

The crystallography and phase characteristics of CTs and Na-Alg@CTs hydrogel beads were determined through XRD. As shown in Figure 2, the CTs exhibit a biphasic nature [38], with a dominant calcite phase characterized by peaks at 2θ values of 23.11° (012), 29.56° (104), 39.47° (113), and 43.23° (202). The secondary aragonite phase is identified by peaks at 2θ values of 26.23° (111), 33.13° (201), 36.01° (210), 45.87° (122), and 48.57° (104). The diffractograms of Na-Alg@CTs biocomposite confirm the successful dispersion of CTs within the Na-Alg matrix, as indicated by the reduced intensity of the peaks associated with CTs [39]. The absence of additional peaks indicates that the beads are pure, confirming that the crystallinity and purity of the CTs remain unaffected after successful encapsulation within Na-Alg beads [40].

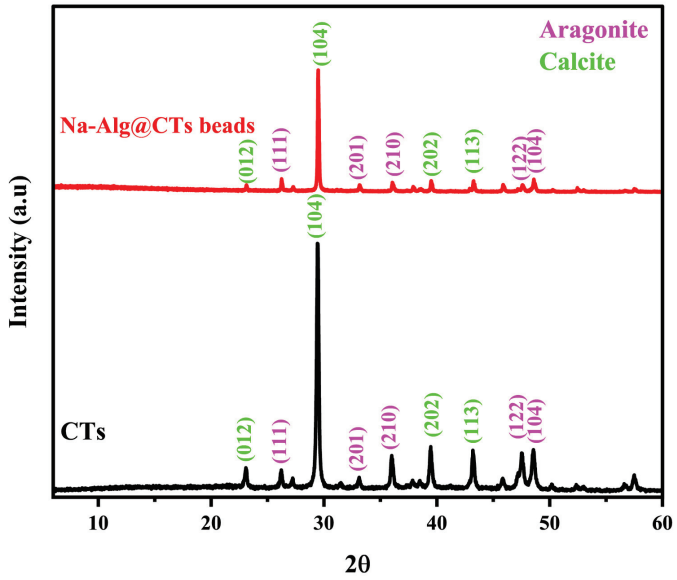

Figure 2. XRD of CTs and Na-Alg@CTs hydrogel beads.

3.3. SEM/EDS Analysis of Na-Alg@CTs Hydrogel Beads

The morphologies of the CTs and Na-Alg@CTs beads are illustrated in Figure 3, both in their original state and following Cu (II) and Zn (II) ions adsorption. The micrograph of the CTs (Figure 3a) reveals a lamellar structure with an irregular distribution of agglomerations on the surface [41]. As illustrated in Figure 3b, the Na-Alg@CTs beads exhibit a spherical morphology with an irregular and relatively rough surface [42]. The CTs are well dispersed in the matrix, as shown by SEM micrographs of the bio-nanocomposite beads. After the adsorption of two metal ions, changes in the surface are observed as a result of the uptake of Cu (II) (Figure 3c) and Zn (II) (Figure 3d) by the surface of Na-Alg@CTs hydrogel beads.

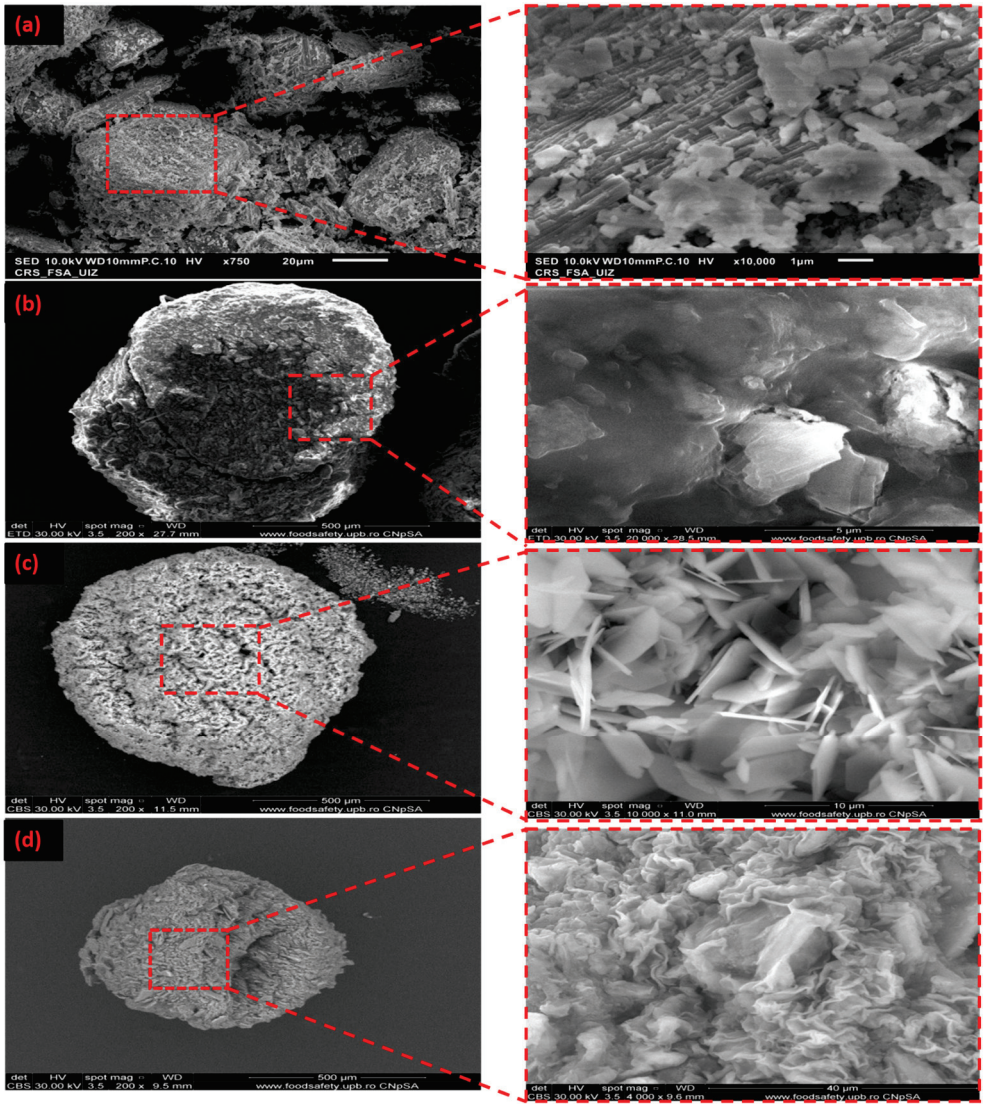

Figure 3. SEM of (**a**) CTs, (**b**) Na-Alg@CTs, (**c**) Cu (II)-Na-Alg@CTs, and (**d**) Zn (II)-Na-Alg@CTs.

The EDS spectrum, along with the atomic percentages of the constituent elements in CTs and Na-Alg@CTs hydrogel beads before and after the adsorption of Cu (II) and Zn (II) are presented in Figure S2. The EDS spectrum of CTs (Figure S2a) indicates that the primary elements are oxygen (O = 66.35%), calcium (Ca = 16.92%), and carbon (C = 16.73%). After the encapsulation process (Figure S2b), these elements (Ca, C, and O) remain, while sodium (Na = 15.52%) from Na-Alg is also detected. Following the adsorption of Cu (II) and Zn (II) by the Na-Alg@CTs hydrogel beads, new peaks corresponding to Cu and Zn elements appear, as illustrated in Figure S2c and Figure S2d, respectively, confirming the uptake of metal ions on the surface of the biocomposite.

3.4. Adsorption Study of Cu (II) and Zn (II) onto Na-Alg@CTs Hydrogel Beads

3.4.1. Na-Alg@CTs Hydrogel Beads Dose Effect

A series of Na-Alg@CTs hydrogel beads ratios (m/V) was mixed with 50 mL of Cu (II) and Zn (II) solutions, each having an initial concentration of 5 ppm and agitated for 180 min. Figure 4 illustrates the relationship between the adsorbent dose and the adsorbed quantity of Cu^{2+} and Zn^{2+} cations. As illustrated, the adsorption capacity exhibited a declining trend. This observation can be attributed to the presence of higher amounts of Na-Alg@CTs beads, which can lead to agglomeration, causing overlapping of adsorption sites and a reduction in the effective surface area of the adsorbents. Equilibrium is attained at a mass of 0.25 g/L. Consequently, the optimal dose of the adsorbent was identified as 0.25 g/L for subsequent study.

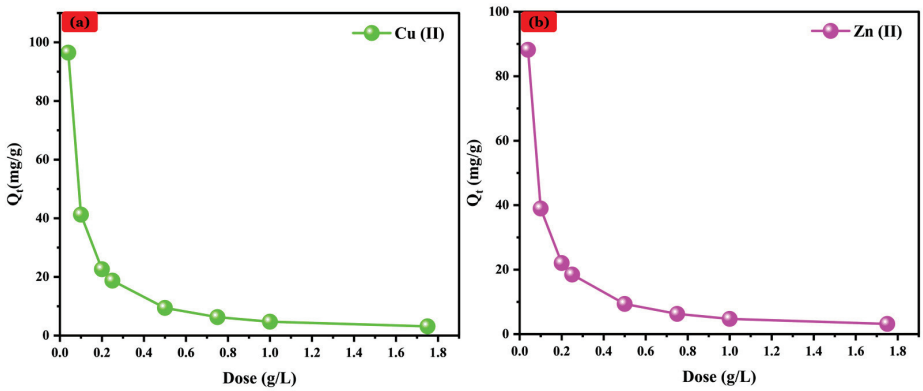

Figure 4. Na-Alg@CTs beads dose effect on the adsorption of (**a**) Cu (II) and (**b**) Zn (II).

3.4.2. pH Effect

It is essential to investigate the effect of pH on the adsorption of Cu (II) and Zn (II) onto Na-Alg@CTs hydrogel beads, as pH is a key factor influencing pollutant availability, the surface charge of the adsorbent, and the interactions between the pollutants and the adsorbent [43]. Since Cu (II) and Zn (II) tend to precipitate at pH levels above 6, and Na-Alg@CTs beads shrink in solutions with a pH of 2, the pH range of 3–6 was selected to investigate its impact on the adsorption of both metals' ions [44]. As shown in Figure 5, the removal rate of Cu (II) and Zn (II) ions increases significantly from 33.65% and 37.03% to 90.15% and 92.69% as the pH rises from 3 to 5, followed by a decrease at pH 6. The highest adsorption is achieved at a pH of 5. The relatively low adsorption capacity of Cu (II) and Zn (II) at pH 3 refers to the higher concentration of H^+ ions in the solution competing with metal ions for active sites [45].

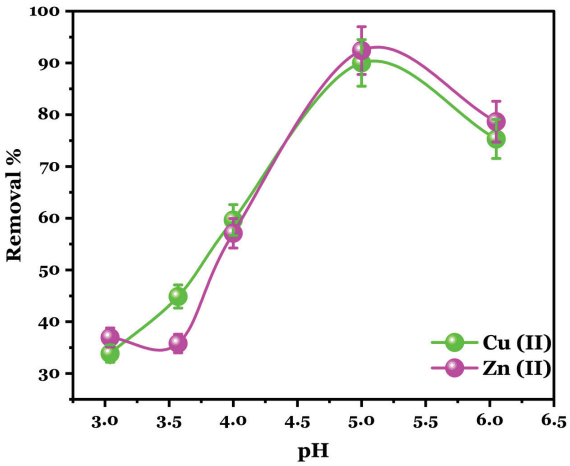

Figure 5. Effect of pH on the adsorption of Cu (II) and Zn (II) onto Na-Alg@CTs beads.

3.4.3. Adsorption Isotherm

The study of adsorption isotherms is essential for understanding the adsorption behavior of a system and assessing its overall feasibility [46]. As illustrated in Figure 6, the adsorbed quantity of Cu (II) and Zn (II) metal ions onto Na-Alg@CTs hydrogel beads demonstrated an increase with the initial concentration increment. This phenomenon is attributed to the dynamic force increment that overcomes the resistance to mass transfer of metal ions from the solution to the Na-Alg@CTs hydrogel beads' surface. The experimental data were evaluated using the Freundlich Equation (1) and Langmuir Equation (2) isotherm models. Their corresponding nonlinear equations are described below [47,48].

$$Q_e = K_e C_e^{\frac{1}{n}} \tag{3}$$

$$Q_e = \frac{Q_m K_L C_e}{1 + K_L C_e} \tag{4}$$

where Q_e (mg/g), Q_m (mg/g), and K_L represent the amount of dye adsorbed per unit mass of adsorbent, the maximum adsorption capacity, and the Langmuir constant (in L/mg), respectively. K_F and n are the Freundlich constants associated with adsorption capacity and intensity, respectively.

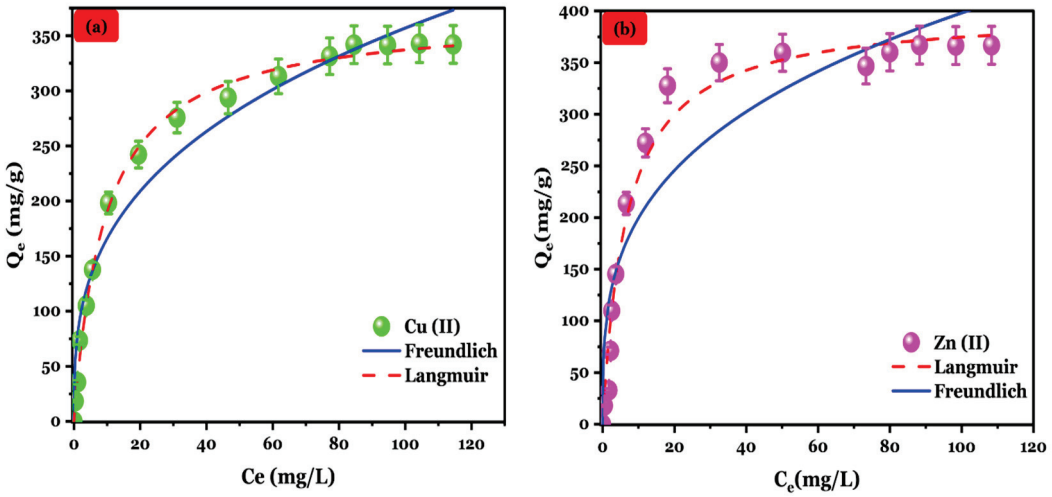

Figure 6. Isotherm fitting for (**a**) Cu (II) and (**b**) Zn (II) adsorption on Na-Alg@CTs hydrogel beads.

Figure 7 depicts the fitting curve of the experimental data, and the corresponding parameters are summarized in Table 1. Given the higher correlation coefficient, lower root mean square error (RMSE), and lower χ^2, the Langmuir model is deemed to be an appropriate fit for the adsorption of Zn (II) and Cu (II) onto Na-Alg@CTs hydrogel beads suggesting that adsorption occurs in a monolayer on a surface with uniformly distributed active sites. Additionally, it assumes that the heat of adsorption remains constant, regardless of the extent of surface coverage, implying that there is no interaction between adsorbed molecules [49]. Moreover, the Langmuir model yielded an estimated maximum adsorption capacity of 368.875 mg/g and 1075.676 mg/g for Cu (II) and Zn (II), respectively, which closely aligned with the experimentally measured value of 342.09 mg/g and 1032.371 mg/g. These results are consistent with previous research on the adsorption of Zn (II) and Cu (II) [50].

Table 1. Isotherm parameters for Cu (II) and Zn (II) adsorption by Na-Alg@CTs hydrogel beads.

Isotherm	Parameters	Cu (II)	Zn (II)
	$Q_{e,exp}$ (mg/g)	342.09	1032.371
Langmuir	Q_m (mg/g)	368.857	1075.676
	K_L (L/mg)	0.106	0.075
	χ^2	59.97	813.249
	RMSE	7.744	28.517
	R^2	0.996	0.979
Freundlich	K_F	77.133	203.538
	n_F	3.00	3.199
	χ^2	644.38	8238.431
	RMSE	25.384	90.76
	R^2	0.964	0.953

3.4.4. Adsorption Kinetic

The influence of contact time on the removal of Cu (II) and Zn (II) onto the Na-Alg@CTs hydrogel beads biocomposite was conducted, as illustrated in Figure 7. Cu (II) and Zn (II) adsorption capacity onto the Na-Alg@CTs exhibited a rapid increase during the initial 20 min, followed by a gradual deceleration, until reaching equilibrium. The initial rapid adsorption can be attributed to active site availability on Na-Alg@CTs hydrogel beads. However, as the adsorption time progressed, the available active sites became progressively occupied with a decrease in concentration gradient, leading to a diminished adsorption rate, and the system eventually approached an equilibrium state [51].

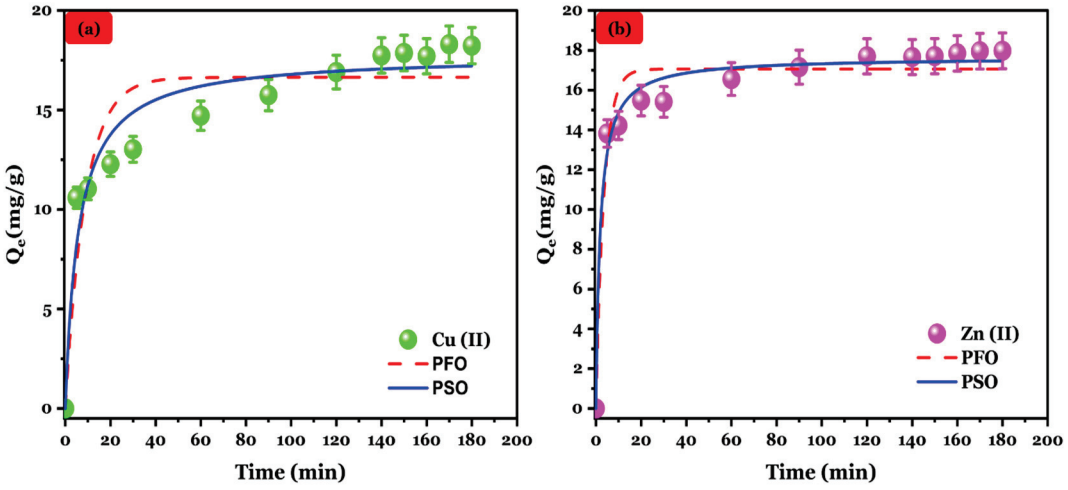

Figure 7. Kinetic fitting of (**a**) Cu (II) and (**b**) Zn (II) adsorption onto Na-Alg@CTs beads.

To elucidate the mechanisms of Cu (II) and Zn (II) adsorption on the Na-Alg@CTs hydrogel beads, the adsorption kinetic data were analyzed using pseudo-first-order (PFO), pseudo-second-order (PSO), and intraparticle diffusion kinetic (IPD) models. The non-linear equations corresponding to applied kinetic models are presented below [49–51]:

$$Q_t = Q_1(1 - exp - K_1 t) \quad (5)$$

$$Q_t = \frac{K_2 Q_2 t}{1 + K_2 Q_2 t} \quad (6)$$

$$Q_t = K_{IPD} t^{\frac{1}{2}} + C \quad (7)$$

where the variables Q_t, K_1, and K_2 correspond to the adsorbed quantity at a given instant (min), the constant rate of the PFO, and the constant rate of the PSO, respectively. K_{IPD} and C are constant rate of IPD and boundary layer thickness, respectively.

As summarized in Table 2 and based on the higher correlation coefficient (R^2) and lower χ^2 values, the PSO model provides a better fit to describe the adsorption kinetic of Cu (II) and Zn (II) than the PFO model. Additionally, the calculated Qe (mg/g) value predicted by the PSO for both metal ions is closer to the experimental value. Consequently, the Cu (II) and Zn (II) adsorption process on Na-Alg@CTs hydrogel beads follows the PSO kinetic model suggesting that the adsorption process is primarily governed by a chemisorption mechanism [52]. Furthermore, the higher rate constant (k) observed for Zn (II) further supports the conclusion that Zn (II) exhibits faster adsorption kinetics compared to Cu (II) [53].

Table 2. Kinetic data of Cu (II) and Zn (II) adsorption using Na-Alg@CTs hydrogel beads.

Model	Parameters	Cu^{2+}	Zn^{2+}
	Qe, exp (mg/g)	18.23	17.97
PFO	K_1 (min^{-1})	0.114	0.279
	Q_1 (mg/g)	16.643	17.057
	R^2	0.866	0.953
	χ^2	3.781	1.17
PSO	K_2 (g mg^{-1} min^{-1})	0.009	0.030
	Q_2 (mg/g)	17.770	17.648
	R^2	0.949	0.983
	χ^2	1.648	0.40
IPD			
First phase	$K_{IPD,1}$	1.002	0.753
	C	8.206	12.026
	R^2	0.889	0.964
Second phase	$K_{IPD,2}$	0.725	0.438
	C	9.025	13.054
	R^2	0.996	0.989
Third phase	$K_{IPD,3}$	0.439	0.134
	C	12.391	16.145
	R^2	0.583	0.756

The IPD model was applied to get a deeper insight into the mass diffusion mechanism at the liquid–solid interface. Figure 8 illustrates that the IPD model plots correspond to Cu (II) and Zn (II) adsorption by Na-Alg@CTs revealing three distinct phases. The first phase corresponds to the rapid transfer of Cu (II) and Zn (II) ions from solution to Na-Alg@CTs hydrogel beads external surface indicating a high mass transfer rate. The second phase involves intraparticle diffusion, where metal ions penetrate the interior of Na-Alg@CTs hydrogel beads and adsorb into the internal pore surface. The final phase represents the equilibrium state of adsorption. The diffusion rate constants K_{IPD} were ranked as $K_{IPD,1} > K_{IPD,2} > K_{IPD,3}$ corresponding to external surface adsorption, intraparticle diffusion to the internal surface, and equilibrium stage, respectively [54].

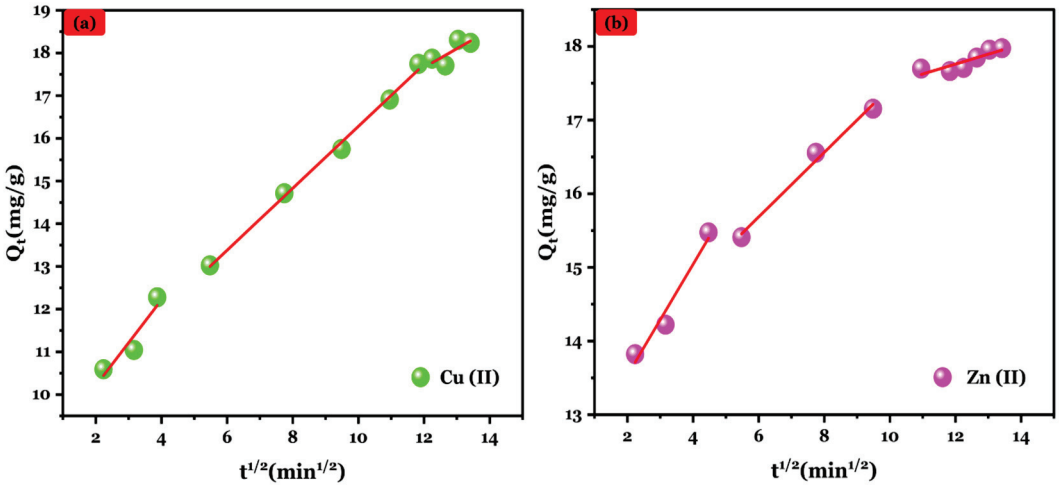

Figure 8. IPD model plot of (**a**) Cu (II) and (**b**) Zn (II) adsorption by Alg@CTs hydrogel beads.

3.4.5. Thermodynamic Study

A thermodynamic study was conducted to obtain detailed information on the inherent energetic changes associated with the adsorption of Cu (II) and Zn (II). The thermodynamic parameters including Gibbs free energy change (ΔG°), enthalpy change (ΔH°, kJ/mol), and entropy change (ΔS°, J/mol.k) were calculated using van't Hoff's law, which is described in the following equations [55].

$$\Delta G^{\circ} = -RT\ ln\ (K_D) \tag{8}$$

$$Ln\ (K_D) = \frac{\Delta S}{R} - \frac{\Delta H}{RT} \tag{9}$$

$$K_D = \frac{Q_m}{C_e} 1000 \tag{10}$$

where T (K), K_D (L/mol), and R (8.314 J·mol·K^{-1}) are the temperature, distribution coefficient, and constant of gas.

In this work, Zn (II) and Cu (II) adsorption by Na-Alg@CTs hydrogel beads was evaluated at three different temperatures (298, 308, and 318 K); Figure S3 shows van't Hoff's law. Based on Table 3, The negative values of ΔG° indicate that Zn (II) and Cu (II) were spontaneously adsorbed onto the surface sites of Na-Alg@CTs hydrogel beads [56]. Furthermore, the decreasing absolute values of ΔG° with increasing temperature indicate that higher temperatures enhance adsorption. The positive ΔH° value proves that the heavy metals adsorption is endothermic, while the positive ΔS° value demonstrates an increase in disorder at the interface between the adsorbent and the adsorbate during the adsorption process [57].

Table 3. Thermodynamic parameters of Cu (II) and Zn (II) onto Na-Alg@CTs hydrogel beads.

Adsorbate	ΔS (J/mol.k)	ΔH (KJ/mol)	ΔG (KJ/mol)		
			298 K	308 K	315 K
Cu (II)	140.34	15.33	−26.48	−27.89	−28.87
Zn (II)	138.73	15.53	−25.81	−27.19	−28.16

4. Conclusions

In summary, Na-Alg@CTs hydrogel beads were synthesized using *Cellana Tramoscrica* seashells as a natural source of calcium carbonate, which was encapsulated within a sodium alginate matrix. XRD and FTIR analysis techniques confirmed the successful synthesis,

evidenced by reduced band intensities. The hydrogel beads were applied as adsorbents for Cu (II) and Zn (II), exhibiting excellent adsorption properties, as demonstrated by SEM and EDS analysis. Adsorption behavior was well described by the Langmuir isotherm model, yielding maximum adsorption capacities (Qm) of 368.85 mg/g for Cu (II) and 1075.67 mg/g for Zn (II). The kinetic analysis indicated that the adsorption adhered to the pseudo-second-order (PSO) model. Additionally, the thermodynamic experiment showed that the process was spontaneous and endothermic, suggesting favorable adsorption at higher temperatures. These results underscore the potential of seashell-derived Na-Alg@CTs hydrogel beads as a low-cost and environmentally friendly adsorbent for removing Cu (II) and Zn (II) from wastewater.

Supplementary Materials: The following supporting information can be downloaded at: https://www.mdpi.com/article/10.3390/polym16233257/s1, Figure S1: Preparation protocol of Na-Alg@CTs hydrogel beads; Figure S2: EDS spectrum of (a) CTs, (b) Na-Alg@CTs hydrogel beads, (c) Cu-Na-Alg@CTs, and (d) Zn-Na-Alg@CTs; Figure S3: van't Hoff law for (a) Cu (II) and (b) Zn (II) uptakes on Na-Alg@CTs hydrogel beads.

Author Contributions: Conceptualization, Z.M., R.M. and D.S.S.; methodology, Z.M. and D.S.S.; software, Z.M.; validation, R.M. and D.S.S.; formal analysis, Z.M. and M.B.; investigation R.M., D.S.S. and M.B.; resources, D.S.S.; data curation, Z.M.; writing—original draft preparation, Z.M.; writing—review and editing R.M. and D.S.S.; visualization, N.S.; supervision, D.S.S. and R.M.; project administration D.S.S.; funding acquisition, D.S.S. All authors have read and agreed to the published version of the manuscript.

Funding: This research received no external funding.

Data Availability Statement: The original contributions presented in the study are included in the article/Supplementary Material, further inquiries can be directed to the corresponding authors.

Acknowledgments: The author acknowledges the University Agency of the Francophonie (AUF) for granting the Eugen Ionescu doctoral Fellowship (2023–2024), which supported this research. The technical and scientific assistance provided by the National University of Science and Technology Politehnica of Bucharest, Faculty of Chemical Engineering and Biotechnology, is also gratefully acknowledged.

Conflicts of Interest: The authors declare no conflicts of interest.

References

1. Sultana, M.; Rownok, M.H.; Sabrin, M.; Rahaman, M.H.; Alam, S.M.N. A review on experimental chemically modified activated carbon to enhance dye and heavy metals adsorption. *Clean. Eng. Technol.* **2022**, *6*, 100382. [CrossRef]
2. Kong, Q.; Shi, X.; Ma, W.; Zhang, F.; Yu, T.; Zhao, F.; Zhao, D.; Wei, C. Strategies to improve the adsorption properties of graphene-based adsorbent towards heavy metal ions and their compound pollutants: A review. *J. Hazard. Mater.* **2021**, *415*, 125690. [CrossRef] [PubMed]
3. Vojdani Saghir, S.; Peighambari-kalat, S.; Goharshadi, E.K. Magnetic wood sponge: Efficient oil/water separation, dye degradation, and heavy metal removal. *Appl. Phys. A* **2024**, *130*, 654. [CrossRef]
4. Zare, E.N.; Motahari, A.; Sillanpää, M. Nanoadsorbents based on conducting polymer nanocomposites with main focus on polyaniline and its derivatives for removal of heavy metal ions/dyes: A review. *Environ. Res.* **2018**, *162*, 173–195. [CrossRef]
5. Vojdani Saghir, S.; Goharshadi, E.K. Multifunctional MnO_2 nanorods-modified wood sponge for water remediation: Applications for heavy metal sorption and oil/water separation. *Wood Sci. Technol.* **2024**, *58*, 2097–2113. [CrossRef]
6. Sun, R.; Gao, S.; Zhang, K.; Cheng, W.-T.; Hu, G. Recent advances in alginate-based composite gel spheres for removal of heavy metals. *Int. J. Biol. Macromol.* **2024**, *268*, 131853. [CrossRef]
7. Wang, P.; Yuan, Y.; Xu, K.; Zhong, H.; Yang, Y.; Jin, S.; Yang, K.; Qi, X. Biological applications of copper-containing materials. *Bioact. Mater.* **2021**, *6*, 916–927. [CrossRef]
8. Asadevi, H.; Prasannakumaran Nair Chandrika Kumari, P.; Padmavati Amma, R.; Khadar, S.A.; Charivumvasathu Sasi, S.; Raghunandan, R. ZnO@MOF-5 as a Fluorescence "Turn-Off" Sensor for Ultrasensitive Detection as well as Probing of Copper(II) Ions. *ACS Omega* **2022**, *7*, 13031–13041. [CrossRef]
9. Katiyar, R.; Patel, A.K.; Nguyen, T.-B.; Singhania, R.R.; Chen, C.-W.; Dong, C.-D. Adsorption of copper (II) in aqueous solution using biochars derived from *Ascophyllum nodosum* seaweed. *Bioresour. Technol.* **2021**, *328*, 124829. [CrossRef]
10. Ugwu, E.I.; Agunwamba, J.C. A review on the applicability of activated carbon derived from plant biomass in adsorption of chromium, copper, and zinc from industrial wastewater. *Environ. Monit. Assess.* **2020**, *192*, 240. [CrossRef]
11. Gohari, B.; Abu-Zahra, N. Polyethersulfone Membranes Prepared with 3-Aminopropyltriethoxysilane Modified Alumina Nanoparticles for Cu(II) Removal from Water. *ACS Omega* **2018**, *3*, 10154–10162. [CrossRef] [PubMed]

12. Chasapis, C.T.; Ntoupa, P.-S.A.; Spiliopoulou, C.A.; Stefanidou, M.E. Recent aspects of the effects of zinc on human health. *Arch. Toxicol.* **2020**, *94*, 1443–1460. [CrossRef]
13. He, X.; Zhang, T.; Xue, Q.; Zhou, Y.; Wang, H.; Bolan, N.S.; Jiang, R.; Tsang, D.C.W. Enhanced adsorption of Cu(II) and Zn(II) from aqueous solution by polyethyleneimine modified straw hydrochar. *Sci. Total Environ.* **2021**, *778*, 146116. [CrossRef] [PubMed]
14. Asadi, R.; Abdollahi, H.; Gharabaghi, M.; Boroumand, Z. Effective removal of Zn (II) ions from aqueous solution by the magnetic $MnFe_2O_4$ and $CoFe_2O_4$ spinel ferrite nanoparticles with focuses on synthesis, characterization, adsorption, and desorption. *Adv. Powder Technol.* **2020**, *31*, 1480–1489. [CrossRef]
15. Babar, M.; Munir, H.M.S.; Nawaz, A.; Ramzan, N.; Azhar, U.; Sagir, M.; Tahir, M.S.; Ikhlaq, A.; Mubashir, M.; Khoo, K.S.; et al. Comparative study of ozonation and ozonation catalyzed by Fe-loaded biochar as catalyst to remove methylene blue from aqueous solution. *Chemosphere* **2022**, *307*, 135738. [CrossRef]
16. Zhang, H.; Li, Y.; Cheng, B.; Ding, C.; Zhang, Y. Synthesis of a starch-based sulfonic ion exchange resin and adsorption of dyestuffs to the resin. *Int. J. Biol. Macromol.* **2020**, *161*, 561–572. [CrossRef]
17. Badawi, A.K.; Zaher, K. Hybrid treatment system for real textile wastewater remediation based on coagulation/flocculation, adsorption and filtration processes: Performance and economic evaluation. *J. Water Process Eng.* **2021**, *40*, 101963. [CrossRef]
18. Cheng, L.; Zhang, Y.; Fan, W.; Ji, Y. Synergistic adsorption-photocatalysis for dyes removal by a novel biochar–based Z-scheme heterojunction BC/2ZIS/WO3: Mechanistic investigation and degradation pathways. *Chem. Eng. J.* **2022**, *445*, 136677. [CrossRef]
19. Mehrkhah, R.; Goharshadi, K.; Goharshadi, E.K.; Sajjadizadeh, H.-S. Multifunctional Photoabsorber for Highly Efficient Interfacial Solar Steam Generation and Wastewater Treatment. *ChemistrySelect* **2023**, *8*, e202204386. [CrossRef]
20. Baraka, N.E.; Saffaj, N.; Mamouni, R.; Laknifli, A.; Younssi, S.A.; Albizane, A.; El Haddad, M. Elaboration of a new flat membrane support from Moroccan clay. *Desalination Water Treat.* **2014**, *52*, 1357–1361. [CrossRef]
21. Wang, H.; Li, Z.; Yahyaoui, S.; Hanafy, H.; Seliem, M.K.; Bonilla-Petriciolet, A.; Luiz Dotto, G.; Sellaoui, L.; Li, Q. Effective adsorption of dyes on an activated carbon prepared from carboxymethyl cellulose: Experiments, characterization and advanced modelling. *Chem. Eng. J.* **2021**, *417*, 128116. [CrossRef]
22. Yang, T.; Xu, Y.; Huang, Q.; Sun, Y.; Liang, X.; Wang, L.; Qin, X.; Zhao, L. Adsorption characteristics and the removal mechanism of two novel Fe-Zn composite modified biochar for Cd(II) in water. *Bioresour. Technol.* **2021**, *333*, 125078. [CrossRef]
23. Kjidaa, B.; Mchich, Z.; Aziz, K.; Saffaj, N.; Saffaj, T.; Mamouni, R. Flexible Synthesis of Bio-Hydroxyapatite/Chitosan Hydrogel Beads for Highly Efficient Orange G Dye Removal: Batch and Recirculating Fixed-Bed Column Study. *ACS Omega* **2024**, *9*, 8543–8556. [CrossRef]
24. Wang, Y.; Gong, Y.; Lin, N.; Yu, L.; Du, B.; Zhang, X. Enhanced removal of Cr(VI) from aqueous solution by stabilized nanoscale zero valent iron and copper bimetal intercalated montmorillonite. *J. Colloid Interface Sci.* **2022**, *606*, 941–952. [CrossRef]
25. Zhou, Z.; Wang, Y.; Sun, S.; Wang, Y.; Xu, L. Preparation of PVA/waste oyster shell powder composite as an efficient adsorbent of heavy metals from wastewater. *Heliyon* **2022**, *8*, e11938. [CrossRef]
26. Gu, J.; Liu, Z.; Jia, A.; Wang, Y.; Li, N.; Liu, Z.; Li, Y.; Zhang, H. New insight into adsorption and co-adsorption of chlortetracycline hydrochloride and ciprofloxacin hydrochloride by Ga-based metal-organic gel/sodium alginate composite beads. *Sep. Purif. Technol.* **2023**, *312*, 123408. [CrossRef]
27. Russo, T.; Fucile, P.; Giacometti, R.; Sannino, F. Sustainable Removal of Contaminants by Biopolymers: A Novel Approach for Wastewater Treatment. Current State and Future Perspectives. *Processes* **2021**, *9*, 719. [CrossRef]
28. Gong, X.-L.; Lu, H.-Q.; Li, K.; Li, W. Effective adsorption of crystal violet dye on sugarcane bagasse–bentonite/sodium alginate composite aerogel: Characterisation, experiments, and advanced modelling. *Sep. Purif. Technol.* **2022**, *286*, 120478. [CrossRef]
29. Asadi, S.; Eris, S.; Azizian, S. Alginate-Based Hydrogel Beads as a Biocompatible and Efficient Adsorbent for Dye Removal from Aqueous Solutions. *ACS Omega* **2018**, *3*, 15140–15148. [CrossRef]
30. Nouri, L.; Hemidouche, S.; Boudjemaa, A.; Kaouah, F.; Sadaoui, Z.; Bachari, K. Elaboration and characterization of photobio-composite beads, based on titanium (IV) oxide and sodium alginate biopolymer, for basic blue 41 adsorption/photocatalytic degradation. *Int. J. Biol. Macromol.* **2020**, *151*, 66–84. [CrossRef]
31. Aziz, K.; Aziz, F.; Mamouni, R.; Aziz, L.; Anfar, Z.; Azrrar, A.; Kjidaa, B.; Saffaj, N.; Laknifli, A. High thiabendazole fungicide uptake using Cellana tramoserica shells modified by copper: Characterization, adsorption mechanism, and optimization using CCD-RSM approach. *Environ. Sci. Pollut. Res.* **2022**, *29*, 86020–86035. [CrossRef]
32. Imgharn, A.; Anchoum, L.; Hsini, A.; Naciri, Y.; Laabd, M.; Mobarak, M.; Aarab, N.; Bouziani, A.; Szunerits, S.; Boukherroub, R.; et al. Effectiveness of a novel polyaniline@Fe-ZSM-5 hybrid composite for Orange G dye removal from aqueous media: Experimental study and advanced statistical physics insights. *Chemosphere* **2022**, *295*, 133786. [CrossRef]
33. Mchich, Z.; Aziz, K.; Kjidaa, B.; Saffaj, N.; Saffaj, T.; Mamouni, R. Eco-friendly engineering of micro composite-based hydroxyapatite bio crystal and polyaniline for high removal of OG dye from wastewater: Adsorption mechanism and RSM@BBD optimization. *Environ. Res.* **2024**, *257*, 119289. [CrossRef]
34. Zemouri, A.E.; Bentouhami, E.; Zaghouane-Boudiaf, H.; Touahria, Y.I.; Bellil, G.; Boublia, A.; Daas, N.; Dintzer, T.; Chafai, N.; Albrahim, M.; et al. Efficient wastewater decontamination using magnetic bentonite-alginate beads: A comprehensive study of adsorption dynamics, regeneration, and molecular interactions. *J. Environ. Chem. Eng.* **2024**, *12*, 113000. [CrossRef]
35. Aziz, K.; El Achaby, M.; Mamouni, R.; Saffaj, N.; Aziz, F. A novel hydrogel beads based copper-doped Cerastoderma edule shells@Alginate biocomposite for highly fungicide sorption from aqueous medium. *Chemosphere* **2023**, *311*, 136932. [CrossRef]

36. Ait Taleb, M.; Mamouni, R.; Ait Benomar, M.; Bakka, A.; Mouna, A.; Taha, M.L.; Benlhachemi, A.; Bakiz, B.; Villain, S. Chemically treated eggshell wastes as a heterogeneous and eco-friendly catalyst for oximes preparation. *J. Environ. Chem. Eng.* **2017**, *5*, 1341–1348. [CrossRef]
37. Iravani Mohammadabadi, S.; Javanbakht, V. Fabrication of dual cross-linked spherical treated waste biomass/alginate adsorbent and its potential for efficient removal of lead ions from aqueous solutions. *Ind. Crop. Prod.* **2021**, *168*, 113575. [CrossRef]
38. Khan, M.D.; Chottitisupawong, T.; Vu, H.H.T.; Ahn, J.W.; Kim, G.M. Removal of Phosphorus from an Aqueous Solution by Nanocalcium Hydroxide Derived from Waste Bivalve Seashells: Mechanism and Kinetics. *ACS Omega* **2020**, *5*, 12290–12301. [CrossRef]
39. Jyoti Borah, S.; Gupta, A.; Kumar Dubey, K.; Kumar, V. Fabrication of highly efficient encapsulated SnO_2@alginate beads as regenerative nanosorbents for anionic dye pollutants removal from aqueous solution. *Mater. Adv.* **2023**, *4*, 5160–5174. [CrossRef]
40. Yi, X.; He, J.; Guo, Y.; Han, Z.; Yang, M.; Jin, J.; Gu, J.; Ou, M.; Xu, X. Encapsulating Fe3O4 into calcium alginate coated chitosan hydrochloride hydrogel beads for removal of Cu (II) and U (VI) from aqueous solutions. *Ecotoxicol. Environ. Saf.* **2018**, *147*, 699–707. [CrossRef]
41. Thind, J.; McDougall, D.R.; Jones, M.I.; Jeffs, A.G. Preliminary Laboratory Investigations into Zinc and Copper Adsorption by Crushed Bivalve Shells. *Water Air Soil Pollut.* **2022**, *233*, 332. [CrossRef]
42. Shim, J.; Kumar, M.; Mukherjee, S.; Goswami, R. Sustainable removal of pernicious arsenic and cadmium by a novel composite of MnO_2 impregnated alginate beads: A cost-effective approach for wastewater treatment. *J. Environ. Manag.* **2019**, *234*, 8–20. [CrossRef]
43. Kjidaa, B.; Mamouni, R.; Aziz, K.; Saffaj, T.; Adraoui, I.; Mchich, Z.; Saffaj, N. Green Synthesis of a Biomaterial Composite Based on Fish Scales for Anionic Dye Removal: Characterization and Optimization by RSM@BBD Approach. *Water Air Soil Pollut.* **2023**, *234*, 352. [CrossRef]
44. Lin, Z.; Yang, Y.; Liang, Z.; Zeng, L.; Zhang, A. Preparation of Chitosan/Calcium Alginate/Bentonite Composite Hydrogel and Its Heavy Metal Ions Adsorption Properties. *Polymers* **2021**, *13*, 1891. [CrossRef]
45. Li, Z.; Guo, Z.; Zhang, T.; Li, Q.; Chen, J.; Ji, W.; Liu, C.; Wei, Y. Fabrication of in situ ZIF-67 grown on alginate hydrogels and its application for enhancing Cu (II) adsorption from aqueous solutions. *Colloids Surf. B Biointerfaces* **2021**, *207*, 112036. [CrossRef]
46. Li, J.; Chen, M.; Yang, X.; Zhang, L. Preparation of a novel hydrogel of sodium alginate using rural waste bone meal for efficient adsorption of heavy metals cadmium ion. *Sci. Total Environ.* **2023**, *863*, 160969. [CrossRef]
47. Bakka, A.; Mamouni, R.; Saffaj, N.; Laknifli, A.; Aziz, K.; Roudani, A. Removal of bifenthrin pesticide from aqueous solutions by treated patellidae shells using a new fixed bed column filtration technique. *Process Saf. Environ. Prot.* **2020**, *143*, 55–65. [CrossRef]
48. Aziz, K.; Mamouni, R.; Azrrar, A.; Kjidaa, B.; Saffaj, N.; Aziz, F. Enhanced biosorption of bisphenol A from wastewater using hydroxyapatite elaborated from fish scales and camel bone meal: A RSM@BBD optimization approach. *Ceram. Int.* **2022**, *48*, 15811–15823. [CrossRef]
49. Yao, X.; Ji, L.; Guo, J.; Ge, S.; Lu, W.; Chen, Y.; Cai, L.; Wang, Y.; Song, W. An abundant porous biochar material derived from wakame (*Undaria pinnatifida*) with high adsorption performance for three organic dyes. *Bioresour. Technol.* **2020**, *318*, 124082. [CrossRef]
50. Salem, D.B.; Ouakouak, A.; Touahra, F.; Hamdi, N.; Eltaweil, A.S.; Syed, A.; Boopathy, R.; Tran, H.N. Easy separable, floatable, and recyclable magnetic-biochar/alginate bead as super-adsorbent for adsorbing copper ions in water media. *Bioresour. Technol.* **2023**, *383*, 129225. [CrossRef]
51. Saini, A.S.; Melo, J.S. Biosorption of uranium by melanin: Kinetic, equilibrium and thermodynamic studies. *Bioresour. Technol.* **2013**, *149*, 155–162. [CrossRef]
52. Xue, S.; Xiao, Y.; Wang, G.; Fan, J.; Wan, K.; He, Q.; Gao, M.; Miao, Z. Adsorption of heavy metals in water by modifying Fe_3O_4 nanoparticles with oxidized humic acid. *Colloids Surf. A Physicochem. Eng. Asp.* **2021**, *616*, 126333. [CrossRef]
53. Verma, M.; Tyagi, I.; Kumar, V.; Goel, S.; Vaya, D.; Kim, H. Fabrication of GO–MnO_2 nanocomposite using hydrothermal process for cationic and anionic dyes adsorption: Kinetics, isotherm, and reusability. *J. Environ. Chem. Eng.* **2021**, *9*, 106045. [CrossRef]
54. Zhang, X.; Yan, L.; Li, J.; Yu, H. Adsorption of heavy metals by l-cysteine intercalated layered double hydroxide: Kinetic, isothermal and mechanistic studies. *J. Colloid Interface Sci.* **2020**, *562*, 149–158. [CrossRef]
55. Kjidaa, B.; Mchich, Z.; Saffaj, T.; Saffaj, N.; Mamouni, R. Harnessing fish scales: Bio-hydroxyapatite and novel bio-hydroxyapatite@Polypyrrole nanocomposite for advanced oxytetracycline antibiotic adsorption. *J. Water Process Eng.* **2024**, *68*, 106515. [CrossRef]
56. Bhat, S.; Uthappa, U.T.; Sadhasivam, T.; Altalhi, T.; Soo Han, S.; Kurkuri, M.D. Abundant cilantro derived high surface area activated carbon (AC) for superior adsorption performances of cationic/anionic dyes and supercapacitor application. *Chem. Eng. J.* **2023**, *459*, 141577. [CrossRef]
57. Abdulhameed, A.S.; Jawad, A.H.; Kashi, E.; Radzun, K.A.; ALOthman, Z.A.; Wilson, L.D. Insight into adsorption mechanism, modeling, and desirability function of crystal violet and methylene blue dyes by microalgae: Box-Behnken design application. *Algal Res.* **2022**, *67*, 102864. [CrossRef]

Disclaimer/Publisher's Note: The statements, opinions and data contained in all publications are solely those of the individual author(s) and contributor(s) and not of MDPI and/or the editor(s). MDPI and/or the editor(s) disclaim responsibility for any injury to people or property resulting from any ideas, methods, instructions or products referred to in the content.

polymers

MDPI

Article

Novel Nanocomposites and Biopolymer-Based Nanocomposites for Hexavalent Chromium Removal from Aqueous Media

Adina-Elena Segneanu [1,*,†], Ionela Amalia Bradu [1], Mihaela Simona Calinescu (Bocanici) [2,†], Gabriela Vlase [1,3], Titus Vlase [1,3], Daniel-Dumitru Herea [4], Gabriela Buema [4], Maria Mihailescu [5,6] and Ioan Grozescu [5]

[1] Institute for Advanced Environmental Research, West University of Timisoara (ICAM-WUT), 4 Oituz St., 300086 Timișoara, Romania; ionela.bradu@e-uvt.ro (I.A.B.); gabriela.vlase@e-uvt.ro (G.V.); titus.vlase@e-uvt.ro (T.V.)
[2] Faculty of Chemistry, Biology, Geography, West University of Timisoara (ICAM-WUT), Pestalozzi St. 16, 300115 Timișoara, Romania; mihaela.calinescu88@e-uvt.ro
[3] Research Center for Thermal Analyzes in Environmental Problems, Problems, West University of Timisoara (ICAM-WUT), Pestalozzi St. 16, 300115 Timișoara, Romania
[4] National Institute of Research and Development for Technical Physics, 47 Mangeron Blvd, 700050 Iasi, Romania; dherea@phys-iasi.ro (D.-D.H.); gbuema@phys-iasi.ro (G.B.)
[5] Department of Applied Chemistry and Engineering of Inorganic Compounds and the Environment, University Politehnica Timisoara, 2 Piata Victoriei, 300006 Timișoara, Romania; mihailescumia@gmail.com (M.M.); ioangrozescu@gmail.com (I.G.)
[6] Research Institute for Renewable Energy, 138 Gavril Musicescu St., 300501 Timișoara, Romania
* Correspondence: adina.segneanu@e-uvt.ro
† These authors contributed equally to this work.

Abstract: Designing new engineered materials derived from waste is essential for effective environmental remediation and reducing anthropogenic pollution in our economy. This study introduces an innovative method for remediating metal-contaminated water, using two distinct waste types: one biowaste (eggshell) and one industrial waste (fly ash). We synthesized three novel, cost-effective nanoadsorbent types, including two new tertiary composites and two biopolymer-based composites (specifically k-carrageenan and chitosan), which targeted chromium removal from aqueous solutions. SEM analysis reveals that in the first composite, EMZ, zeolite, and magnetite nanoparticles are successfully integrated into the porous structure of the eggshell. In the second composite (FMZ), fly ash and magnetite particles are similarly loaded within the zeolite pores. Each biopolymer-based composite is derived by incorporating the corresponding tertiary composite (FMZ or EMZ) into the biopolymer framework. Structural modifications of the eggshell, zeolite, chitosan, and k-carrageenan resulted in notable increases in specific surface area, as confirmed by BET analysis. These enhancements significantly improve chromium adsorption efficiency for each adsorbent type developed. The adsorption performances achieved are as follows: EMZ (89.76%), FMZ (84.83%), EMZCa (96.64%), FMZCa (94.87%), EMZC (99.64%), and FMZC (97.67%). The findings indicate that chromium adsorption across all adsorbent types occurs via a multimolecular layer mechanism, which is characterized as spontaneous and endothermic. Desorption studies further demonstrate the high reusability of these nanomaterials. Overall, this research underscores the potential of utilizing waste materials for new performant engineered low-cost composites and biocomposites for environmental bioremediation applications.

Keywords: biopolymer-based composite; water remediation; adsorbent; wastes; heavy metal pollution

1. Introduction

The coexistence of chromium in two oxidation states, Cr(III) and Cr(VI), poses a significant challenge in managing water pollution. While Cr(III) is stable and naturally abundant, Cr(VI) is a highly toxic oxidizing agent prevalent in industrial settings due to human activities like leather tanning, glass manufacturing, ceramics, textiles, wood

preservation, and the production of certain adhesives, which pose health risks to humans and ecosystems [1–6].

Chromium (VI) is recognized as one of the most hazardous metallic pollutants associated with significant health risks, which include genetic mutations and carcinogenic effects [7,8]. This pollutant is regulated by stringent standards established by the World Health Organization (WHO), which limits its concentration in drinking water to 0.05 mg/L, while European Union legislation restricts it to a maximum of 0.1 mg/L. Exposure to chromium (VI) is correlated with numerous health issues, such as genetic alterations, cancer, skin irritation, ulcers, and oxidative stress, which lead to considerable biological damage [7,8].

The highly mobile and soluble nature of chromium (VI) in aquatic ecosystems complicates its removal through conventional water treatment methods [7,8]. Current methods for removing hexavalent chromium (Cr(VI)) from polluted water sources include chemical precipitation, ion exchange, and membrane filtration. However, each of these techniques presents certain limitations regarding efficiency, cost-effectiveness, and environmental impact [1,4–6,9]:

Chemical precipitation is relatively straightforward but generates sludge, which requires additional treatment and disposal [1,4–6,9].

Ion Exchange can be effective but is often resource-intensive, which leads to increased operational costs and material consumption [1,4–6,9].

Coagulation and reverse osmosis are reliable but typically involve high capital and operational expenses, which make them less accessible for widespread use [1,4–6,9].

Adsorption offers versatility but we must carefully balance efficacy with economic considerations as traditional adsorbents can be costly [1,4–6,9]. Magnetic nanoparticles, zeolite, fly ash, and hybrid materials demonstrate good potential for immobilizing several pollutant categories from wastewater [1,4–6,9–15].

Given these challenges, there is a pressing need for innovative approaches that can enhance the efficiency and sustainability of chromium extraction from aquatic environments. Ongoing research is focused on developing new materials and methods that can overcome these limitations while minimizing environmental impact and operational costs.

Recent studies have focused on eco-friendly biocomposites that combine biopolymers or plant-derived materials with inorganic or organic components [1,16]. These biocomposites offer ecological benefits, enhanced adsorption efficiency, and cost-effectiveness [1,16]. Several studies have reported the development of novel adsorbents from natural products, such as agricultural waste (e.g., fruit husks, eggshells), natural proteins (e.g., gelatin, whey proteins), and natural polysaccharides (e.g., agarose, pectin, carrageenan) [17–19]. While natural adsorbents are easily accessible and cost-effective, engineered materials provide superior adsorption capacities due to their increased surface area and optimized pore structures [20–22]. These advanced materials also exhibit improved selectivity and stability, ensuring more efficient and reliable performance across various applications. Furthermore, combining microbial biomass (e.g., bacteria and fungi) with magnetic materials enhances after-adsorption separation, increasing both the specific surface area and adsorption capacity [23]. Additionally, functionalizing materials such as chitosan, cellulose, and alginate with metal nanoparticles has significantly improved their Cr(VI) adsorption capacity [24–28].

In this study, an innovative approach was employed to develop three types of nano adsorbents (composites, k-carrageenan-based composites, and chitosan-based nanocomposites), which originated from waste materials such as eggshells and fly ash. To the best of our knowledge, this is the first study reporting the simultaneous harnessing of the unique properties of both biopolymers (k-carrageenan and chitosan) alongside fly ash, zeolites, and eggshells for achieving highly efficient chromium removal from aqueous solutions. The study employed various analytical techniques, including the Brunauer–Emmett–Teller (BET) method, X-ray diffraction (XRD), Fourier-transform infrared (FTIR) spectroscopy, vibrating sample magnetometer (VSM), scanning electron microscopy (SEM), and ther-

mogravimetric analysis (DTG), to assess the physical and chemical properties of each adsorbent type. Furthermore, this study delves into the intricacies of the adsorption mechanisms by rigorously analyzing adsorption isotherm models, thermodynamic properties, and adsorption and desorption kinetics. This multifaceted approach, complemented by after-adsorption analyses using FTIR, SEM-EDX, and thermal assessments, provides a deeper understanding of the adsorption mechanism. The investigation into the reusability of each adsorbent further emphasizes the sustainability of this research, demonstrating its potential for practical applications in environmental remediation. This study not only tackles the critical issue of heavy metal contamination in wastewater but also contributes to the valorization of agricultural and industrial waste, fostering a circular economy in environmental management.

2. Materials and Methods

2.1. Materials

All reagents used in this study were of analytical grade and sourced from commercial suppliers, including Merck (New York, NY, USA), Alfa Aesar (Haverhill, MA, USA), and Sigma-Aldrich (St. Louis, MO, USA), and were utilized without further purification. Kappa-carrageenan powder was obtained from Thermo Scientific (Tokyo, Japan), while chitosan powder (molecular weight range: 100,000–300,000) was acquired from Acros Organics (Geel, Belgium).

Eggshells (ESs) were sourced domestically and subjected to a procedure described in our previous paper [22,29].

Zeolite, obtained from Bentonita (Mediesu Aurit, Satu Mare, Romania), was prepared according to a procedure described in our previous papers [22,29].

Industrial-grade magnetite nanoparticles (average size: ~50 nm), purchased from Jalutex (Pucioasa, Romania), were then subject to a procedure described in our previous paper [29].

Electrofilter fly ash (average nanoparticle size: 25–55 nm) with a phase composition including Al_2SiO_5 (dialuminium silicate oxide), SiO_2 (quartz), Al_2O_3 (corundum), and $Ca_2MgSi_2O_7$ (akermanite) was provided by Colterm Cogeneration Power Station in Timisoara, Romania [12,29].

Composite materials referred to as FMZ (composed of fly ash, magnetite, and zeolite) and EMZ (comprising eggshells, magnetite, and zeolite) were prepared according to the methodology detailed below. Chromium (VI) solution with different concentrations (1 to 40 mg/L) was prepared from a stock solution of potassium dichromate (Merck, Darmstadt, Germany), which was dissolved in ultrapure water and then diluted to the desired final concentrations. For pH adjustment, 1 M HNO_3 or NaOH solutions were used.

2.2. Instrumentations

The phase composition of the prepared adsorbents and their components was analyzed using a Bruker AXS D8-Advance powder X-ray diffractometer, utilizing CuKa radiation (λ = 0.1541 nm). The mean crystallite size was calculated employing the whole powder pattern fitting (WPPF) method.

Fourier-transform infrared (FT-IR) spectra of all prepared adsorbents and their solid-phase components were recorded using a Shimadzu IRTracer 100 FT-IR spectrophotometer (Columbia, MD, USA) with the Attenuated Total Reflectance (ATR) technique. The data collection process included 20 consecutive scans, which were performed at a resolution of 4 cm^{-1} over the spectral range of 4000 to 400 cm^{-1}.

The surface area of the prepared adsorbents and their corresponding biopolymer matrices was evaluated utilizing multi-point Brunauer–Emmett–Teller (BET) regression within a relative pressure range of 0.08 to 0.3, employing a Nova 1200e high-speed surface area and porosity analyzer (Quantachrome, Boynton Beach, FL, USA). The specific surface area was computed according to BET theory. BET method (employing multi-point regression within the specified relative pressure range) and the Barrett-Joyner-Halenda

(BJH) technique were used to determine the surface areas and the pore size distributions. Additionally, the total pore volume was ascertained from the final point of the isotherm, which yielded a value close to 1. All measurements were conducted in triplicate.

Magnetization properties of the adsorbents were evaluated using a Lake Shore 7410 vibrating sample magnetometer (VSM) (Westerville, OH, USA).

Thermal stability was assessed with a Mettler Toledo TGA/DSC3+ STARe System, performing thermal analyses between 25 °C and 400 °C in a dynamic air atmosphere (20 mL/min) at a heating rate of 10 °C/min, using 40 µL aluminum melting crucibles. Differential scanning calorimetry (DSC) was conducted under identical conditions.

Morpho-structural characterization of adsorbents was performed using an SEM-EDS system (JSM-IT200 InTouchScope™ Scanning Electron Microscope, Freising, Germany) equipped with a field emission gun (FEG). A Jaluba SW23 thermal shaker facilitated the batch adsorption experiments, while a Fritsch Pulverisette planetary mill was utilized in the preparation of the composite nanomaterials (FMZ and EMZ).

2.3. Preparation of Adsorbents

2.3.1. FMZ Nanoadsorbent

The FMZ nanocomposite was prepared by blending fly ash, magnetite nanoparticles, and zeolite in a mass ratio of 1:1:1. This mixture was mechanically milled at a rotation speed of 500 rpm for 30 min at room temperature.

2.3.2. EMZ Nanoadsorbent

The EMZ nanoadsorbent was prepared analogously, using a combination of eggshell, magnetite, and zeolite at the same mass ratio.

2.3.3. Preparation of k-Carrageenan-Based Nanocomposites (FMZCa and EMZCa)

To prepare the k-carrageenan-based nanocomposites, 2 g of k-carrageenan was dissolved in 100 mL of ultrapure water and heated to 80 °C ± 2 °C for 2 h until the solution reached a concentrated state. Upon cooling to a temperature range of 60 °C ± 3 °C, to form a gel [30].

Subsequently, 2 g of the respective nanocomposite (FMZ or EMZ) was added and mixed thoroughly for 15 min. Following complete homogenization, this mixture was added dropwise to 25 mL of 3% KCl (potassium chloride) solution under stirring to form small beads (or pellets), filtered, and washed with ultrapure water. Each experiment was conducted in triplicate.

2.3.4. Preparation of Chitosan-Based Nanocomposites (FMZC and EMZC)

Chitosan solution was formulated by dissolving 1.4 g of chitosan in 100 mL of a 5% (v/v) acetic acid solution, incubating this mixture at 50 °C for 2 h with continuous stirring. Following this, 0.25 g of the prepared nanocomposite (FMZ or EMZ) was incorporated into 18 mL of the chitosan solution at 40 °C ± 2 °C and stirred for 20 min. This resultant mixture was subsequently added dropwise to 25 mL of 2 M NaOH solution, filtered, and washed with deionized water. This experiment was also prepared in triplicate.

Before analyzing their properties, all biopolymer-based composites were dried in an oven at 50 °C for six hours.

A flowchart depicting the preparation of composites (EMZ and FMZ), k-carrageenan-based nanocomposites (EMZCa and FMZCa), and chitosan-based nanocomposites (EMZC and FMZC) is presented in Figure 1.

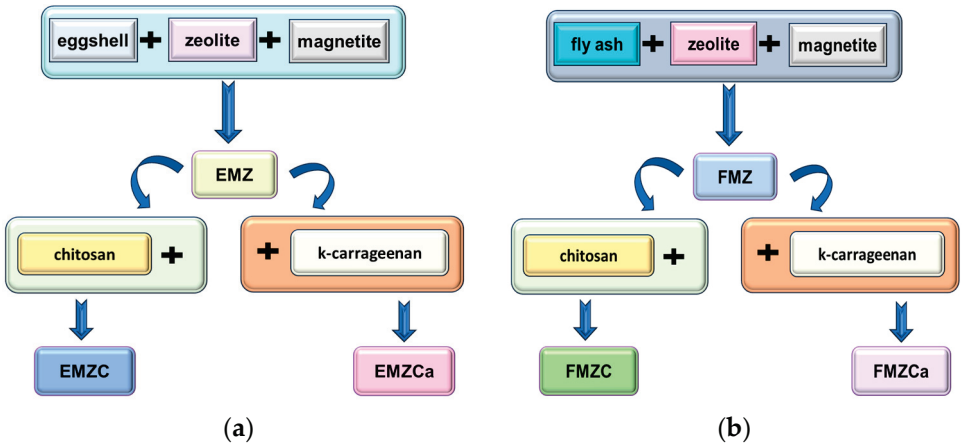

Figure 1. Schematic representation of composites, k-carrageenan-based nanocomposites, and chitosan-based nanocomposite preparation: EMZ/EMZC/EMZCa (**a**), and FMZ/FMZC/FMZCa (**b**).

2.4. Batch Adsorption Study

The adsorption characteristics and mechanisms of FMZ, EMZ, k-carrageenan-based nanocomposites (FMZCa and EMZCa), and chitosan-based nanocomposites (FMZC and EMZC) were systematically analyzed through a series of isotherm, thermodynamic, and kinetic models.

2.4.1. Evaluation of the Effects of Different Parameters on Adsorption

Different parameters were evaluated to determine the efficiency of heavy metal removal. The investigations considered the influence of various factors, including adsorbent dosage (0.50–3.5 g), contact time (0–480 min), pH (1.5–9.0), initial concentration of Cr(VI) (1–40 mg/L), and temperature (0–50 °C) on the performance of chromium adsorption.

Batch experiments were conducted in 100 mL Erlenmeyer flasks, each containing 50 mL of a heavy metal ion solution with a predetermined concentration. The flasks were maintained at 23.5 °C on a thermostat shaker operating at 200 rpm, with the variables of pH, adsorbent mass, and experimental temperature controlled until equilibrium was reached. Following the equilibrium period, the adsorbent was isolated through centrifugation and subsequent filtration using Whatman filter paper (0.45 µm). The chromium concentration in the filtrate was determined through atomic absorption spectrophotometry (Agilent 280FS, Santa Clara, CA, USA).

Each experimental condition was replicated three times, yielding results with an accuracy of ±2%.

The quantity of Cr(VI) uptake by the adsorbent at equilibrium (Q_e, mg/g) was calculated using the following equation (Equation (1)):

$$Q_e = \frac{(C_e - C_o)V}{m} \quad (1)$$

Removal efficiency (Re%) was computed as follows (Equation (2)):

$$R_e = \frac{(C_e - C_o)}{C_o} 100 \quad (2)$$

where V = volume of the solution (mL)

m = dry adsorbent weight (g)

C_o and C_e represent initial and equilibrium concentrations of chromium (mg/L), respectively.

2.4.2. Adsorbent Performance

The performance of each prepared adsorbent was assessed concerning its components over varying contact times. The experimental setup involved 100 mL Erlenmeyer flasks containing 2.00 g of adsorbent with a fixed volume of nickel solution (50 mL; 28.5 mg/L) at pH 4.5, maintained at room temperature (23 °C) and agitated at 180 rpm. Samples were collected at designated intervals (0–480 min), subjected to centrifugation, and filtered through Whatman filter paper (0.45 μm), followed by analysis of residual chromium concentration via atomic absorption spectrophotometry.

2.4.3. Desorption Study

Experiments were conducted by incubating samples at a temperature of 23 °C. A constant volume (50 mL) of chromium solution (28.5 mg/L) was mixed with a fixed amount (2.00 g) of adsorbents and 15 mL of one of three desorption solutions (0.01 M HNO_3, 0.01 M H_2SO_4, or 0.01 M EDTA). The resulting mixtures were stirred at a rate of 180 rpm, and aliquots were collected at 30 min intervals over the experiment duration (0–300 min). Following the collection process, the samples underwent centrifugation and were filtered using Whatman filter paper (0.45 μm). The amount of desorbed heavy metal was quantified utilizing atomic absorption spectrophotometry. The desorption rate was calculated using the next equation (Equation (3)):

$$D = \frac{C_d}{C_a} 100 \quad (3)$$

C_d and C_a represent the concentration of chromium desorbed and retained, respectively.

2.4.4. Kinetic Studies

Kinetic experiments were conducted under control conditions at a temperature of 25 °C and a pH of 4.5, utilizing 2.00 g of adsorbent in a 50 mL chromium solution with a concentration of 28.5 mg/L. Samples were collected at various intervals ranging from 0 to 400 min.

2.4.5. Thermodynamic Study

The thermodynamic analysis was performed at three distinct temperatures: 283.15 K, 298.15 K, and 313.15 K, at pH 4.5 using a fixed amount of adsorbent (2.00 g) and constant volume of chromium stock solution (50 mL; 28.5 mg/L). The adsorption isotherms were represented graphically by plotting ln K (x-axis) against 1/T (y-axis). The correlation coefficients obtained were notably high, with R^2 values of 0.986 for FMZ and 0.994 for EMZ, 0.989 for FMZCa, 0.991 for EMZCa, 0.995 for FMZ, and 0.998 for EMZC, indicating a good linear relationship in the derived data.

2.4.6. Statistical Analysis

All experimental trials were performed in triplicate, and statistical significance was evaluated using one-way ANOVA without replication, with a significance threshold set at $p < 0.05$. BET analysis was carried out using the statistical test.

3. Results

3.1. BET Analysis

The surface properties of the synthesized adsorbents, which include nanocomposites (FMZ and EMZ), k-carrageenan-based nanocomposites (FMZCa and EMZCa), and chitosan-based nanocomposites (FMZC and EMZC), as well as their corresponding components, were evaluated using low-temperature (77 K) nitrogen adsorption–desorption isotherms (Figure 2).

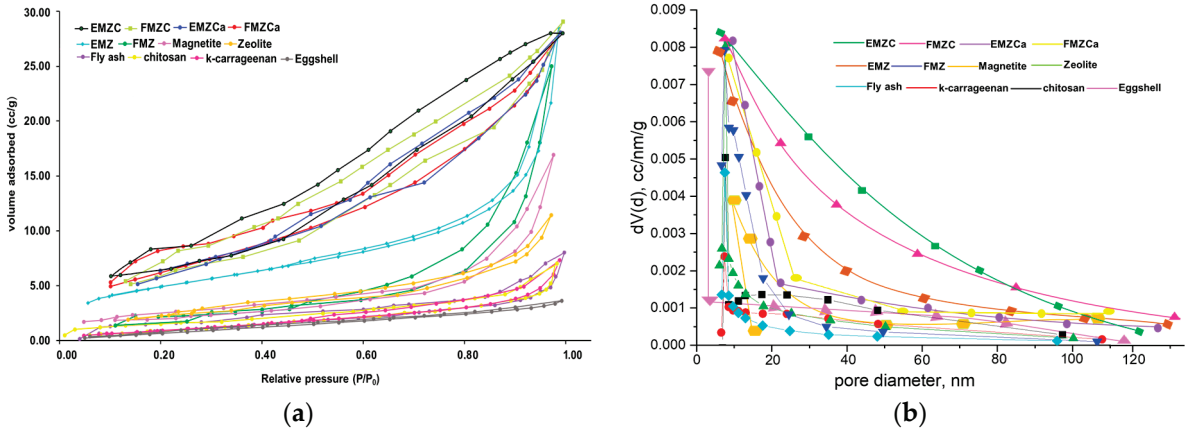

Figure 2. The nitrogen adsorption–desorption isotherms (**a**); pore distribution (**b**) for all adsorbents.

The determination of surface areas and pore size distributions was conducted using the Brunauer–Emmett–Teller (BET) along with the Barrett–Joyner–Halenda (BJH) method. The results are summarized in Table 1.

Table 1. BET-determined parameters of the newly prepared nanocomposites and their components *.

Sample	Surface Area (m^2/g)	Average Pore Size Diameter (nm)	Total Pore Volume (cm^3/g)
chitosan	42.77	2.08	9.21×10^{-3}
k-carrageenan	129.86	3.79	11.35×10^{-3}
eggshell	1.328	8.423	2.05×10^{-3}
magnetite	18.02	3.81	44.78×10^{-3}
fly ash	4.959	8.987	20.19×10^{-3}
zeolite	12.126	15.615	38.13×10^{-3}
FMZ	31.42	7.89	10.16×10^{-3}
EMZ	34.79	5.57	10.03×10^{-3}
FMZCa	142.77	11.02	47.49×10^{-3}
EMZCa	145.34	13.88	50.77×10^{-3}
FMZC	196.12	12.83	49.23×10^{-3}
EMZC	201.83	14.89	51.34×10^{-3}

* standard deviation (SD) = 2%.

The data revealed that the BET/N_2 specific surface area values for eggshell (1.328 m^2/g), magnetite (18.02 m^2/g), zeolite (12.126 m^2/g), and fly ash (18.02 m^2/g) are consistent with previous literature and our prior studies. In contrast, the specific surface area values for the synthesized nanocomposites, EMZ and FMZ, demonstrated considerable variation, which was anticipated due to their differing compositions. Further analysis showed a significant increase in the surface area of the FMZ and EMZ nanocomposites compared to their raw components, indicating a notable advancement in material design for chromium adsorption applications. However, this enhancement was accompanied by a reduction in average pore diameter and total pore volume relative to zeolite, attributed to the eggshell particles in EMZ and fly ash in FMZ [29,31].

BET/N_2 specific surface values for polymeric matrices, k-carrageenan (129.86 m^2/g), and chitosan (42.77 m^2/g) were consistent with values reported in the literature [32–34].

Notably, significant differences were identified in the specific surface areas of k-carrageenan-based nanocomposites (FMZCa and EMZCa) and chitosan-based nanocomposites (FMZC and EMZC) when compared to their respective components and biopolymer matrices. For the k-carrageenan-based nanocomposites, surface areas ranged from 142.77 m^2/g for FMZ to 145.34 m^2/g for EMZ, with average pore volumes and sizes measuring 11.02 nm and 13.88 nm, respectively. In the case of the chitosan-based nanocomposites, the surface area values varied from 192.12 m^2/g (FMZC) to 201.83 m^2/g (EMZC),

accompanied by average pore volumes and sizes of 12.83 nm and 14.89 nm, respectively. These concurrent changes provide substantial versatility in selecting appropriate materials for specific applications.

As illustrated in Figure 2, the isotherms for chitosan-based nanocomposites (EMZC and FMZC) and k-carrageenan-based composites (EMZCa and FMZCa), as well as the composites (EMZ and FMZ), conform to a Type II isotherm characterized by an H2 hysteresis loop. This behavior indicates the presence of a macroporous structure within these materials. The porous architecture enhances the efficiency of pollutant immobilization and release.

3.2. XRD Study

The X-ray diffraction (XRD) analysis of the FMZ sample, as depicted in Figure 3a,b, demonstrates the presence of well-preserved crystalline phases. Notably, these phases include magnetite (Fe_3O_4, COD 9005837), which exhibits sharp diffraction peaks at approximately 30°, 35°, 43°, and 57° [29]. The zeolite component, specifically clinoptilolite-Ca (COD 9001509), reveals characteristic peaks (~20°–30°). Additionally, the analysis identifies components associated with fly ash, which correspond to Al_2SiO_5 (COD 1010329), SiO_2 (quartz, COD 9009666), Al_2O_3 (corundum, COD 1010951), and $Ca_2MgSi_2O_7$ (akermanite, COD 9006450), along with a broad amorphous background (~15°–25°) associated with the amorphous fly ash component. All collectively affirming the successful integration and structural integrity of FMZ composite [22,29].

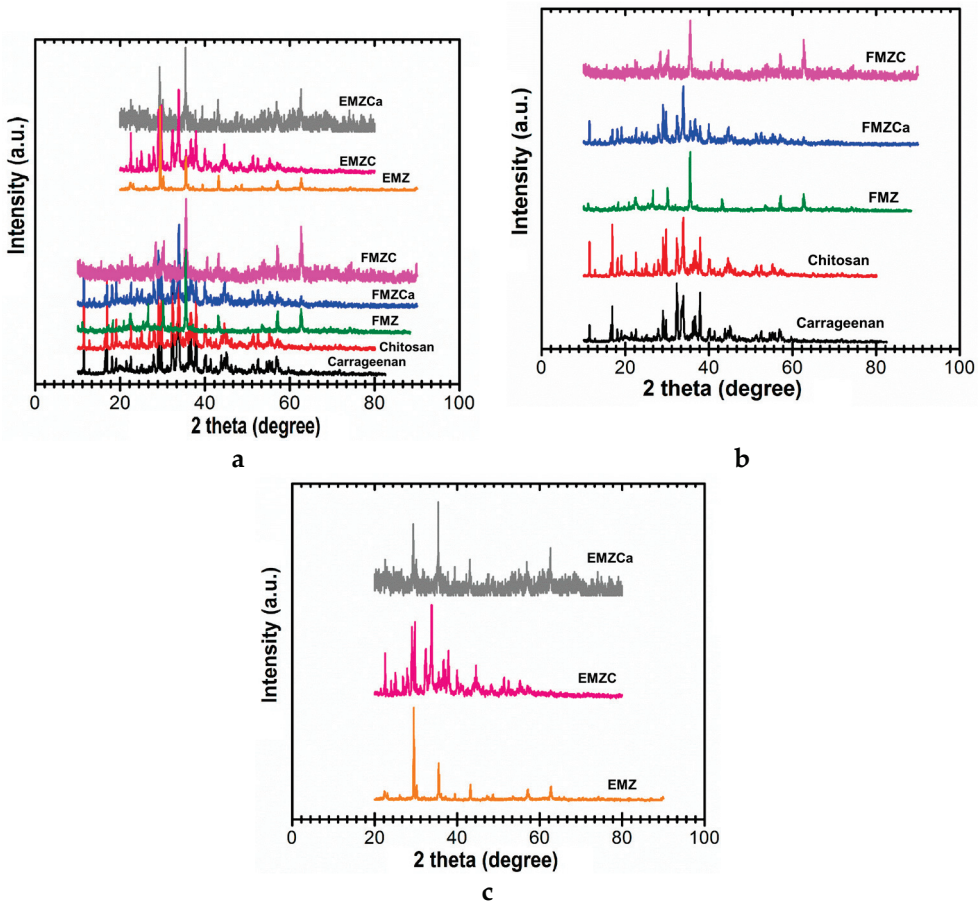

Figure 3. XRD spectra of all adsorbent types prepared and their components (**a**), chitosan, carrageenan, FMZ, FMZCa, FMZC (**b**), and EMZ, EMZCa and EMZC (**c**).

In the XRD spectrum of EMZ (Figure 3a,c) sharp peaks are visible with distinct contributions at ~23°, ~29°, ~36°, and ~47° from eggshell-derived calcite phase ($CaCO_3$, COD 9000965), representing the dominant crystalline phase in eggshell [22,29]. Also, similar

to FMZ, exhibit peaks at ~30°, ~35°, ~43°, and ~57° confirm the presence of magnetite as a significant phase [29]. Furthermore, the zeolite diffraction peaks appear in the range of ~20°–30°, confirming the retention of its crystalline structure during EMZ composite formation [22]. Notably, both FMZ and EMZ display amorphous characteristics, evidenced by broad bands across the 10–70 ° scanning interval, underscoring their nature as effective absorbents [22,29]. Nonetheless, compared to FMZ, EMZ appears to have a slightly lower amorphous content, reflecting the higher crystallinity of the eggshell component compared to the amorphous phase associated with fly ash in FMZ [22,29].

The X-ray diffraction (XRD) pattern for FMZCa demonstrates a reduction in peak intensity for magnetite, quartz, and zeolite, indicating a stronger encapsulation effect by k-carrageenan [35]. Additionally, the presence of the biopolymer matrix enhances the amorphous nature of FMZCa, as evidenced by a noticeable elevation in the baseline and the observation of broader, less-defined peaks within the XRD pattern. This indicates that the presence of the biopolymer matrix contributes to a more amorphous structure [35]. When comparing the k-carrageenan pattern, illustrated by the black line in Figure 3a,b, which exhibits broader and less intense peaks in the 2θ range of approximately 15°–25°, the FMZCa pattern presented by the blue line reveals sharper and more pronounced peaks. This finding implies that the encapsulation of FMZ into the κ-carrageenan matrix has been successfully achieved [35]. Moreover, the relatively smooth and consistent intensity peaks observed for FMZCa indicate uniform dispersion of the fly ash, magnetite, and zeolite particles within the k-carrageenan matrix, which is essential for maintaining the uniformity and functionality of FMZCa, thereby underscoring the success of its synthesis [35].

The X-ray diffraction (XRD) pattern of EMZCa (as shown in Figure 3a,c) indicates a notable decrease in crystallinity compared to the EMZ sample. This reduction is primarily attributed to the incorporation of k-carrageenan, which introduces an amorphous hump in the XRD pattern within the 2θ range of approximately 15° to 25° [35]. This feature is characteristic of this polysaccharide matrix and highlights the amorphous nature of k-carrageenan [35]. Despite the overall decrease in crystallinity, the primary peaks corresponding to magnetite, eggshell, and zeolite are still identifiable, albeit with diminished intensity. This observation suggests these components maintain structural integrity following EMZ incorporation into the k-carrageenan matrix [35]. Specifically, the magnetite peaks, which appear at approximately 2θ values of 30°, 35°, and 43°, remain visible but show a reduction in intensity. The peaks associated with the eggshell and zeolite components are also partially obscured due to the amorphous contribution from k-carrageenan [35].

The XRD pattern for chitosan (red line, Figure 3a,b) reveals a broad peak in the 2θ range of approximately 10°–25°, indicating the semi-crystalline nature arising from the partial alignment of its polymer chains in crystalline domains. The low intensity and lack of sharp peaks reflect the dominance of amorphous regions, a characteristic of biopolymers like chitosan [26].

The X-ray diffraction (XRD) analysis of the FMZC (Figure 3a,b) composite reveals distinct sharp and intense peaks attributed to the presence of crystalline phases, specifically magnetite (Fe_3O_4) (observed around 2θ = ~30°, ~35°, ~43°, and ~57) and zeolite (in the 2θ range of ~20°–30°), alongside contributions from fly ash (at 20°–40° range), superimposed on a relatively less prominent background from semi-crystalline chitosan matrix. These sharp peaks in the XRD pattern suggest the effective dispersion and incorporation of these crystalline materials within the amorphous chitosan matrix [36]. However, the slight broadening and reduction in the intensity of peaks, particularly those associated with zeolite and quartz, suggest encapsulation of these particles within the chitosan matrix [26,36]. Additionally, the partial masking of the fly ash peaks further supports the notion that the crystalline phases are embedded within the amorphous chitosan. Overall, the crystallinity of the FMZC composite is enhanced by these crystalline components incorporation while the chitosan matrix plays a crucial role in modulating the FMZ structural characteristics and properties.

Similarly, the EMZC pattern (Figure 3a,c) exhibits a slight reduction in the intensity of the peaks associated with magnetite, zeolite, and eggshell compared to the EMZ pattern. This observation suggests the encapsulation of EMZ within the chitosan matrix [26,36]. Furthermore, the notable absence of prominent peaks corresponding to chitosan in the EMZC pattern indicates that the crystalline characteristics of the EMZ dominate the overall composite diffraction pattern. Although the EMZ incorporation of the chitosan matrix introduces some reduction in crystallinity, most of the structural peaks associated with the EMZ remain preserved.

The X-ray diffraction (XRD) analysis demonstrates a reduction in crystallinity and a pronounced decrease in the characteristic chitosan peak at $2\theta \approx 20.3^{\circ}$, confirming the successful synthesis of chitosan-based nanocomposites. A comparative evaluation of the XRD patterns for FMZ, FMZCa, and FMZC (Figure 3a,b), as well as EMZ, EMZCa, and EMZC (Figure 3a,c), indicates that the varying crystallinity of these materials results in overlapping patterns where only the most intense peaks remain visible. The biopolymer-based nanocomposites exhibit a semicrystalline character, further validating their effective formation.

Overall, the XRD analysis provides valuable insights into the structural properties of EMZ and FMZ composites, highlighting the significant impact of chitosan and k-carrageenan matrices on their crystallinity. While the inorganic components—magnetite, zeolite, and eggshell or fly ash—retain their crystalline structure during composite formation, interactions with the biopolymer matrices lead to notable structural modifications. The semi-crystalline nature of chitosan and the predominantly amorphous character of k-carrageenan interact with the inorganic phases, causing peak broadening and intensity reduction [35,36]. These observations point to substantial changes in the dispersion and arrangement of inorganic particles within the polymeric matrix, which ultimately influence the mechanical, physical, and functional properties of the newly developed biopolymer-based nanocomposites.

3.3. SEM Analysis

The surface morphology, shape, and particle size of all proposed nano adsorbents (FMZ, EMZ, FMZCa, EMZCa, FMZC, and EMZC) were studied using SEM (Figure 4).

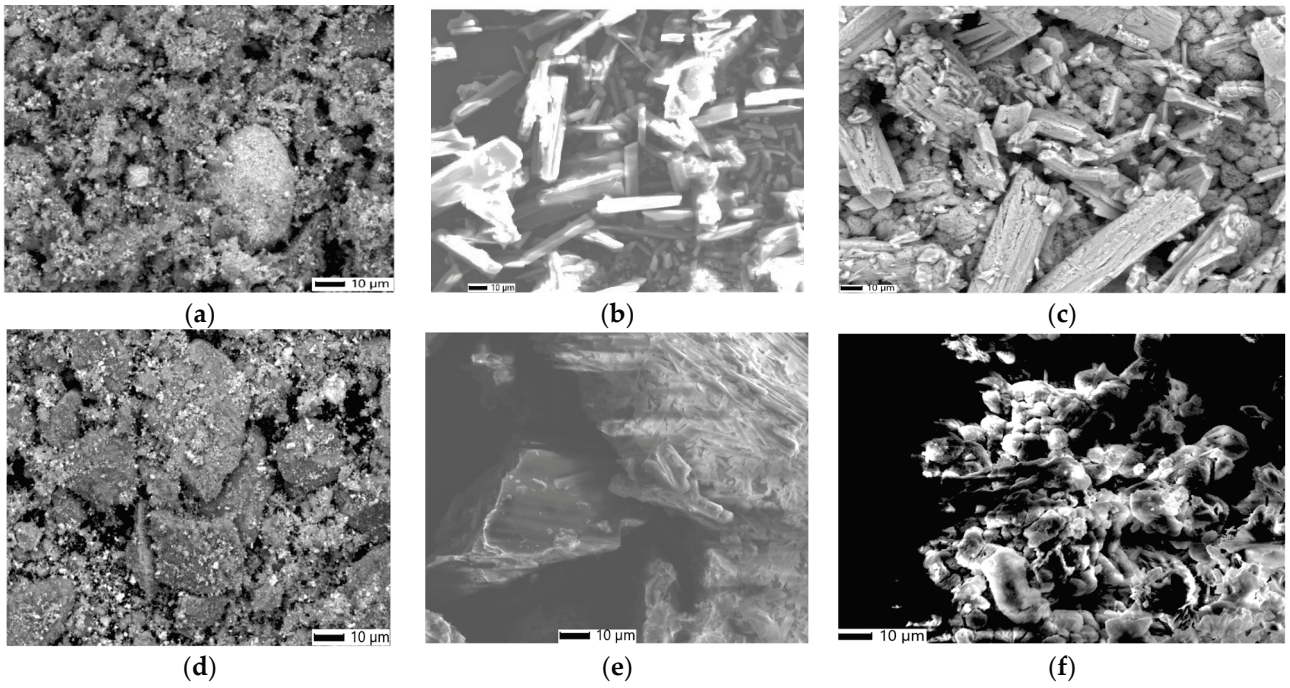

Figure 4. SEM images of FZM (**a**), FMZCa (**b**), FMZC (**c**), EMZ (**d**), EMZCa (**e**), and EMZC (**f**).

The FMZ micrographs (Figure 4a) reveal clusters of nanoparticles with varying sizes in the nanometer range, specifically, spherical particles (~10 nm) derived from fly ash and magnetite cubic-shaped particles (~18 nm) interspersed within rectangular crystal structures typical of zeolite [22,29,37]. These particles are both present on the surface and within the pores of the zeolite matrix. Similarly, the EMZ micrograph (Figure 4d) demonstrates a comparable distribution of magnetite cubic particles loaded in zeolite and eggshell-like pores.

When examining the k-carrageenan-based nanocomposites (FMZCa (Figure 4b) and EMZCa (Figure 4e), notable morphological distinctions arise compared to FMZ and EMZ, particularly in terms of reduced cluster sizes. The FMZCa micrograph (Figure 4b) displays a variety of spherical and rectangular structures (averaging 12 nm) that are assembled and uniformly dispersed within the carrageenan matrix alongside carrageenan fibers [38].

Conversely, the EMZCa (Figure 4e) micrograph features an assortment of rectangular and cubic nanoparticles dispersed throughout the carrageenan matrix.

The prepared chitosan-based nanocomposite samples (FMZC and EMZC) exhibit the following characteristics:

(a) The FMZC micrograph (Figure 4c) illustrates a uniform distribution of smoother spherical, cubic, and rectangular particles uniformly dispersed in the polymeric matrix.
(b) The EMZC micrograph (Figure 4f) reveals a consistent distribution of rectangular and cubic particles within the organic matrix [39].

All biopolymer-based nanocomposites (FMZCa, EMZCa, FMZC, and EMZC) highlight a significant reduction in cluster sizes; they measure around 35 nm for chitosan-based nanocomposites and around 40 nm for k-carrageenan-based nanocomposites.

3.4. FTIR Analysis

FT-IR spectra were recorded for EMZ, FMZ, EMZCa, FMZCa, EMZC, and FMZC, and polymeric matrices (carrageenan and chitosan) (Figure 5).

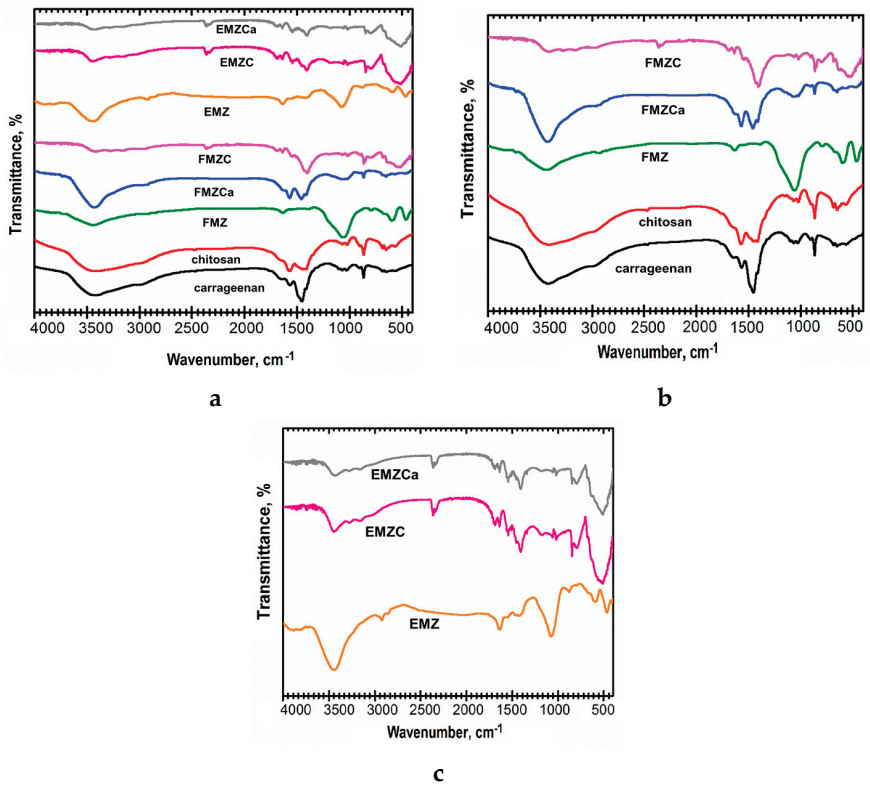

Figure 5. FT-IR spectra of all adsorbent types prepared and their components (**a**), chitosan, carrageenan, FMZ, FMZCa, and FMZC (**b**), EMZ, EMZCa and EMZC (**c**).

The FT-IR spectra and XRD patterns of starting materials for adsorbents (eggshell, fly ash, magnetite, and zeolite) are similar since they come from identical sources, as reported in our previous sources [12,22,29].

The spectrum for FMZ (Figure 5a,b) exhibits the magnetite vibrational bands at ~597 cm^{-1} associated with the (Fe-O) [40], the peaks attributed to zeolite at 464 cm^{-1} (Si-O-Si), ~1066 cm^{-1} (Si-O asymmetric stretch). Vibrational peaks assigned to fly ash were found at ~588 cm^{-1} (Ca-O), ~ 670 cm^{-1} (Al-O-Al bending vibration), and 830 cm^{-1} (AlO_4 coordination) [22,41–43]. The large band at 3440 cm^{-1} indicates the presence of moisture and water molecules [22,41,44,45].

The FTIR spectra of EMZ (Figure 5a,c) display the vibrational bands of the characteristic peaks associated with eggshell at ~714 cm^{-1} (Ca-O stretch), ~880 and ~1418 cm^{-1} (C-O stretch), 1637 cm^{-1} (C=O stretching vibrations), and 1643 cm^{-1} (assigned to N-H), 1077 cm^{-1} (C-N stretching) [22,41,44,45]. The peaks assigned to magnetite were found at ~592 cm^{-1} associated with the (Fe-O) [40]. The peaks attributed to zeolite at 469 cm^{-1} (Si-O-Si), ~1066 cm^{-1} (Si-O asymmetric stretch). The presence of moisture and water molecules is associated with the large band at 3445 [22,41,44,46,47].

Regarding the k-carrageenan-based nanocomposites, the EMZCa spectra (Figure 5a,c) depicted the vibrational peaks from EMZ and carrageenan (Figure 5a). Nonetheless, a series of notable differences (intensity of vibrational peaks and displacement of k-carrageenan absorption bands in the region of sulfate ester region (1454, 1394, 1266, 848, and 705 cm^{-1}) indicate interactions between polymer and EMZ functional groups. Shifting the intensity of the peaks in the sulfate ester region and displacement to longer wavelengths can be observed, indicating interactions between the polymer and the functional groups in the EMZ.

The FT-IR spectra of FMZCa (Figure 5a,b) show the discriminative peaks of FMZ and carrageenan with a slight shifting in the intensity of the peaks and displacement to longer wavelengths in the sulfate ester region, supporting the formation of FMZCa.

Following EMZ encapsulation, in the EMZC spectra (Figure 5a,c), all the characteristic peaks of chitosan (Figure 5a) (~1568, ~1436, ~1413, ~1077, ~1024, ~869, ~650, and ~565 cm^{-1}) and the EMZ adsorbent were observed. However, several intensity changes and small shifts in the N-H (1568, 1018, and 870 cm^{-1}) can be attributed to the interaction between ammonium groups of chitosan interaction with functional groups of EMZ.

Similarly, the FMZC spectra (Figure 5a,b) show all the characteristic vibrational bands from chitosan and FMZ, and notable changes appear in the same N-H region, indicating the formation of interaction between ammonium groups of chitosan interaction with functional groups of FMZ.

3.5. Magnetic Measurements

A vibrating sample magnetometer (VSM) was employed to assess the saturation mass magnetization of adsorbents possessing the same composition. The vibrating VSM loops (Figure 4) indicated a predominantly ferromagnetic profile for the samples, with the notable exceptions of FMZCa and EMZC, which displayed a hysteretic profile exhibiting paramagnetic behavior near zero fields (Figure 6 and Table 2).

Table 2. VSM results for all prepared adsorbents.

Samples	Coercivity (Oe)	Remanent Magnetization (emu/g)	Saturation Magnetization (emu/g)
FMZCa	100.78	0.23	2.2317
FMZC	103.30	1.19	10.593
FMZ	101.82	2.77	21.545
EMZCa	101.32	0.95	8.2122
EMZC	102.43	0.08	0.79719
EMZ	101.76	3.94	29.775

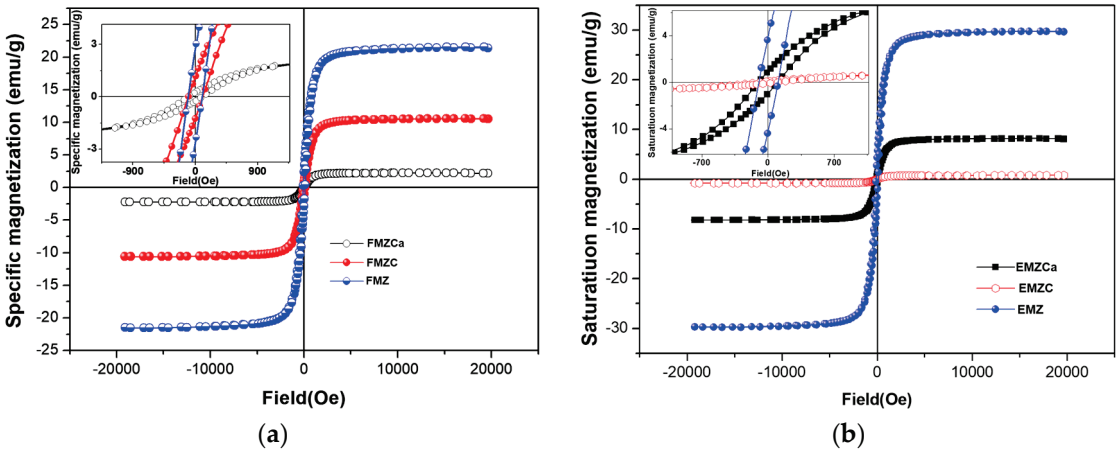

Figure 6. VSM of FMZ:FMZCa:FMZC (**a**) and EMZ:EMZCa:EMZC (**b**).

The variations in saturation magnetization among the different types of prepared adsorbent, specifically nanocomposites (FMZ, EMZ), k-carrageenan-based nanocomposites (FMZCa and EMZCa), and chitosan-based nanocomposites (FMZC and EMZC) are directly correlated with the content of magnetic materials and the experimental methodologies utilized in this study. It is important to note that the magnetic properties of the magnetite nanoparticles remain unchanged throughout the experimental processes; consequently, the specific magnetization of the k-carrageenan-based and chitosan-based nanocomposites is determined solely by the mass ratios of the magnetic materials to the polymeric matrices.

3.6. Thermal Analysis

The thermal behavior of the prepared adsorbents was studied to assess their stability concerning their material types, specifically, nanocomposites, kappa-carrageenan-based nanocomposites, and chitosan-based nanocomposites. The data obtained are presented in Figure 7 and Table 3.

Table 3. Thermal analysis results for all types of prepared adsorbents.

Sample	Process	TG		DTG_{max}/°C	Δm/%	Total Mass Loss %
		T_{onset}/°C	T_{final}/°C			
EMZCa	I	37	80	60	8.89	31.22
	II	85	144	115	20.96	
FMZCa	I	34	81	61	12.23	34.73
	II	82	140	139	19.76	
EMZC	I	35	72	58	11.16	28.67
	II	71	132	89	8.72	
	III	287	397	-	4.71	
FMZC	I	33	69	62	8.48	30.25
	II	71	124	90	14.07	
	III	290	396	390	4.23	
EMZ	I	32	80	54	1.97	8.68
	II	223	274	248	1.82	
	III	349	400	380	1.72	
FMZ	I	34	91	78	0.6	1.72
	II	96	188	-	0.39	

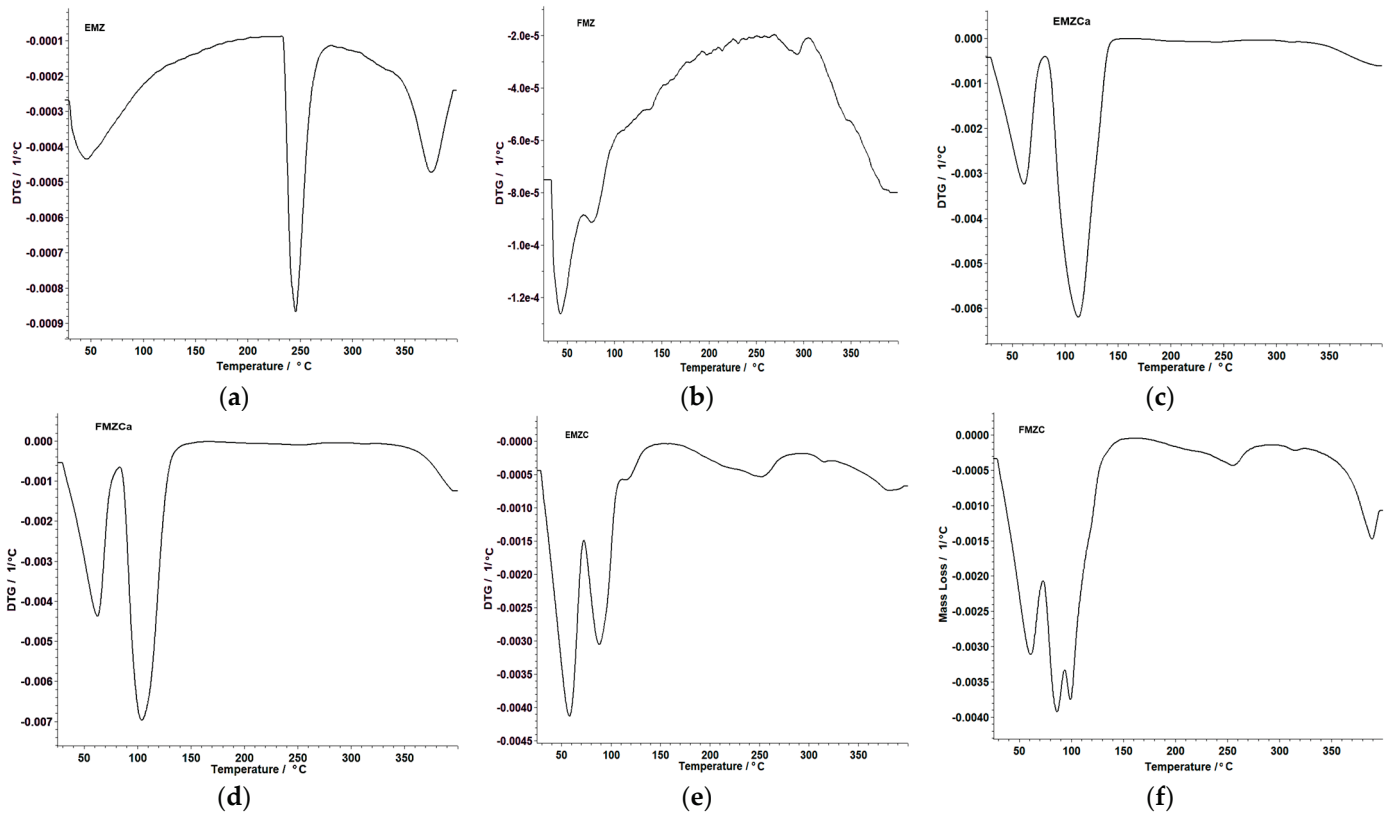

Figure 7. TGA thermograms of EMZ (**a**), FMZ (**b**), EMZCa (**c**), FMZCa (**d**), EMZC (**e**), and FMZC (**f**).

The thermal analysis of all prepared adsorbents has revealed distinct stages of thermal decomposition. Notably, FMZ (Figure 7b), EMZCa (Figure 7c), and FMZCa (Figure 7d) exhibited two decomposition stages (Table 3), while EMZC (Figure 7e), FMZC (Figure 7f), and EMZ (Figure 7a) displayed three stages. In the case of EMZCa, the initial stage involved the loss of crystallization water, followed by the removal of water from the membrane matrix and the subsequent degradation of the polymer matrix (Table 3). Similarly, FMZCa and FMZ displayed analogous processes characterized by specific temperature ranges and associated weight losses for each stage (Table 3).

Conversely, the thermal decomposition of EMZC and FMZC (Fig unfolded through three distinct stages, encompassing moisture elimination, water removal from the membrane matrix, and the thermal degradation of the polymer matrix, each occurring at different temperature ranges with specific weight losses (Table 3).

The thermal decomposition of EMZ (Figure 7a, Table 3) occurs in three stages, encompassing moisture elimination, loss of crystallization water, and thermal degradation associated with organic components from eggshell particles. The analysis of the thermal decomposition of biopolymer-based nanocomposites unveiled differences in stability. Specifically, EMCa was found to exhibit more stability than FMZCa, and EMZC was determined to be more stable than FMZC. Additionally, FMZ was ascertained to be more stable than EMZ. Interestingly, notwithstanding the disparities in stability, encapsulation rendered EMZ more thermally stable than FMZ, irrespective of the biopolymer type used.

3.7. Adsorption Properties

3.7.1. Effect of Adsorbent

The chromium removal efficiency and adsorption capacity of all prepared adsorbents (EMZ, FMZ, EMZCa, FMZCa, EMZC, and FMZ) were examined as a function of adsorbent mass (Figure 8).

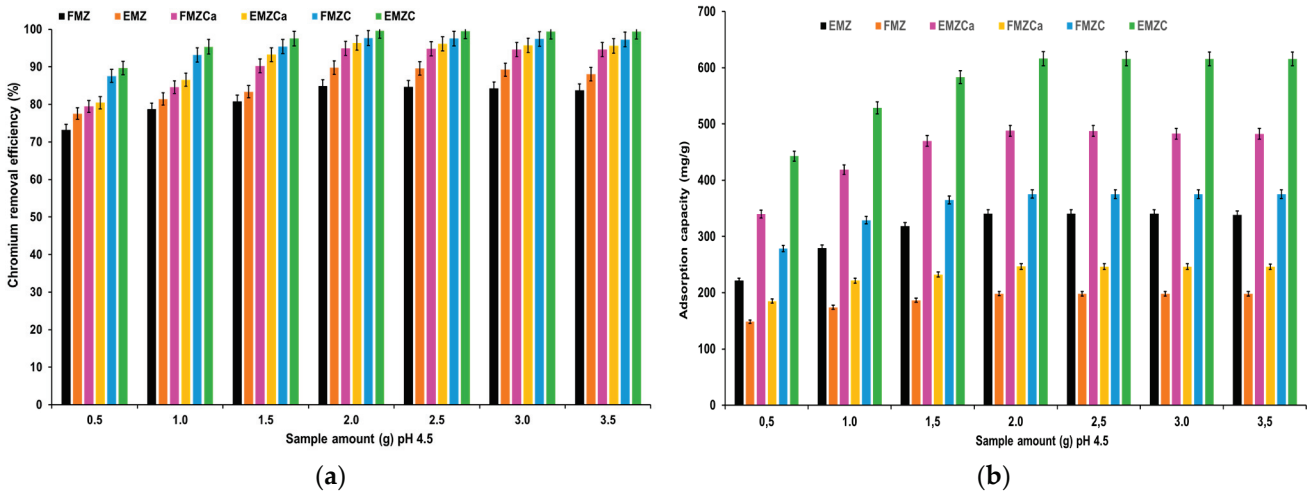

(**a**) (**b**)

Figure 8. Chromium removal efficiency (**a**) and adsorption capacity (**b**) as a function of adsorbent mass.

The data depicted in the graphs within Figure 8 indicate a significant increase in chromium adsorption as the quantity of adsorbent is raised from 0.50 g to 2.0 g. Maximum adsorption is observed at 2.0 g of each prepared adsorbent, with values of 89.76% and 349.84 mg/g for EMZ; 84.83% and 198.47 mg/g for FMZ; 94.87% and 246.53 mg/g for FMZCa; 96.36% and 487.82 mg/g for EMZCa; 97.67% and 375.45 mg/g for EMZCa; 97.67% and 375.45 mg/g for FMZC; and 99.64% and 616.19 mg/g for EMZC, respectively. Following the attainment of equilibrium, adsorption exhibits a slight decline with further increases in adsorbent quantity. These findings suggest that a higher mass of adsorbent leads to a greater availability of active sites until equilibrium is attained. However, beyond that point, an increase in adsorbent mass leads to agglomeration, reducing the specific surface area and active sites [22,44,48].

3.7.2. Effect of Initial Concentration on Chromium Removal Efficiency

The concentration of pollutants at the outset significantly influences the adsorption process. Therefore, were investigated the impact of the initial heavy metal concentration on chromium removal efficiency and adsorption capacity for each prepared adsorbent (Figure 9).

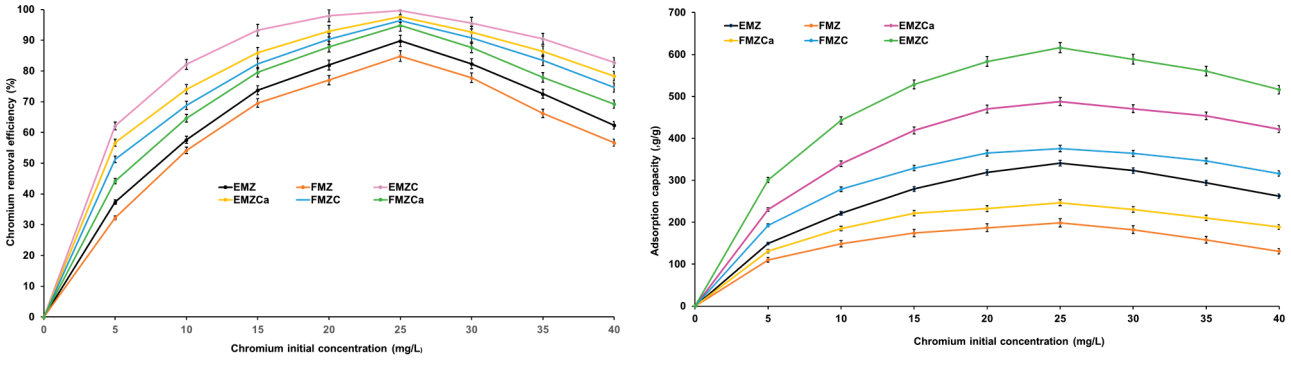

(**a**) (**b**)

Figure 9. Relationship between chromium (**a**) initial concentration and chromium removal efficiency (%) and (**b**) initial concentration and adsorption capacity (mg/g).

The efficiency of pollutant removal is directly proportional to the increase in the initial concentration of the pollutant within the range of 0–25 mg/L for all the prepared adsorbents (Figure 9). As depicted in Figure 9b, the adsorption capacities of all adsorbents exhibit a similar increasing trend with the initial pollutant concentration ranging from 0 to 25 mg/L,

reaching maximum values of 349.84 mg/g for EMZ, 198.47 mg/g for FMZ, 246.53 mg/g for FMZCa, 487.82 mg/g for EMZCa, 375.45 mg/g for EMZC, and 616.19 mg/g for EMZC, respectively. The maximum removal efficiencies for FMZ (84.83%), EMZ (89.76%), FMZCa (94.87%), EMZCa (96.36%), FMZC (97.67%), and EMZC (99.64%) were achieved at Cr(VI) concentrations of 25.0 mg/L (Figure 9a). Beyond this point, all removal efficiencies exhibit a slightly decreasing trend, and the same pattern is observed for the adsorption capacities. In accordance with collision theory, these findings suggest that an increase in chromium concentration, and thereby the number of chromium ions, results in an accelerated reaction rate due to the increased potential for interaction with acceptor sites on all the prepared adsorbents (EMZ, FMZ, EMZCa, FMZCa, EMZC, and FMZC) until the equilibrium concentration is attained [49]. Subsequently, an imbalance between numerous chromium ions and a progressively decreasing number of active sites available on the adsorbents causes a decline in the adsorption potential for all the prepared adsorbents. These outcomes align with the data reported for the component materials of the adsorbents [50–52].

3.7.3. Effect of pH

The pH significantly affects the adsorption process by influencing the ionic chemical speciation of the adsorbing species and the adsorbent surface [21,40,42,52,53]. Given this information, the study investigated the adsorption of chromium ions on each prepared adsorbent as a function of pH. Figure 10 illustrates the relationship between pH and chromium removal efficiency, as well as adsorption capacity.

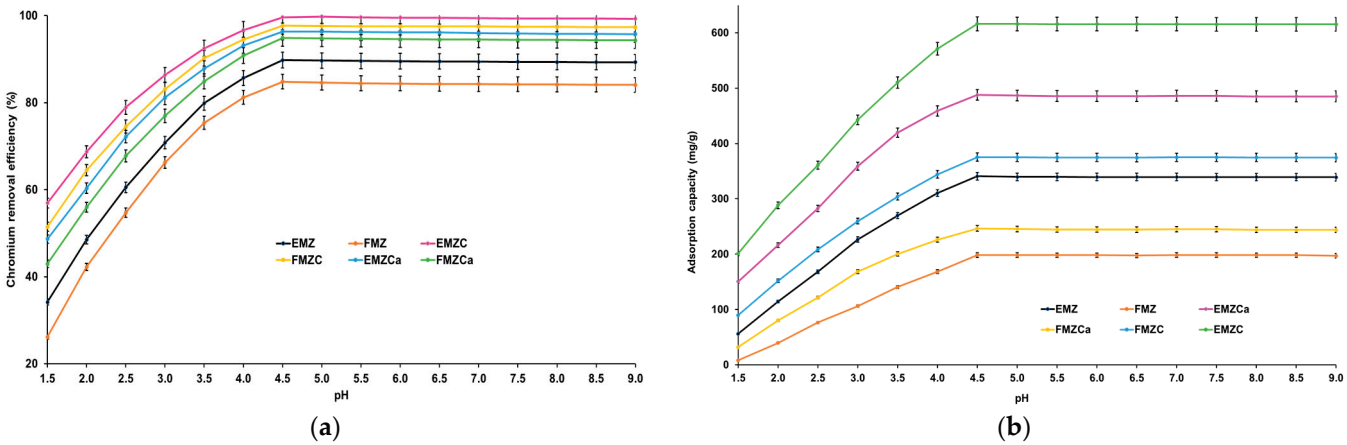

Figure 10. Relationship between chromium (**a**) pH and chromium removal efficiency (%) and (**b**) pH and adsorption capacity (mg/g).

The data indicate that raising the pH level from 1.5 to 4.5 causes a notable increase in chromium ions adsorbed per unit mass of adsorbent. The maximum values for adsorption efficiency and capacity are reached at pH 4.5 (84.83% and 198.47 mg/g for FMZ; 89.76% and 349.84 mg/g for EMZ; 94.87% and 246.53 mg/g for FMZCa; 96.36% and 487.82 mg/g for EMZCa; 97.67% and 375.45 mg/g for FMZC; and 99.64% and 616.19 mg/g for EMZC), with no further changes later.

In an acidic environment, chromium in its hexavalent state (Cr(VI)) primarily exists as $HCrO_4^-$ and $Cr_2O_7^{2-}$ ions, both of which carry a negative charge. In contrast, the surface of the adsorbent is generally positively charged. As a result, the increased adsorption observed at acidic pH can be attributed to the chemical interactions between chromium species and the adsorbent surface. At higher concentrations of Cr(VI), stable forms such as H_2CrO_4 and CrO_3 can lead to the formation of polynuclear species, enhancing removal efficiencies at lower pH levels. Additionally, the abundance of H^+ ions neutralizes the negatively charged surface of the adsorbent, facilitating the diffusion of dichromate ions. The adsorption process is further influenced by an electric double-layer formation at the

adsorbent interface, which transitions from positive to negative as the concentration of H^+ ions decreases with increasing pH.

Various studies have indicated that at lower pH levels, the system reaches equilibrium more quickly, resulting in a higher percentage of chromium uptake [1,5,54]. However, when the pH exceeds 7, the primary stable species shifts to CrO_4^{2-}, and the suppression of Cr(VI) hydrolysis can account for the observed reduction in adsorption capacity.

The emerging results align well with the previously reported data regarding the initial materials utilized for all types of adsorbent preparation [5,55–58].

3.7.4. Effect of Contact Time

The duration of adsorption plays a crucial role in influencing the uptake capacity of chromium ions. To determine the best contact time for maximizing adsorption capacity and pollutant removal efficiency, we examined the uptake capacities of all prepared adsorbents over varying contact times. The results, depicted in Figure 11, show that both removal efficiency and adsorption capacity increase as the contact time with the investigated adsorbents is extended.

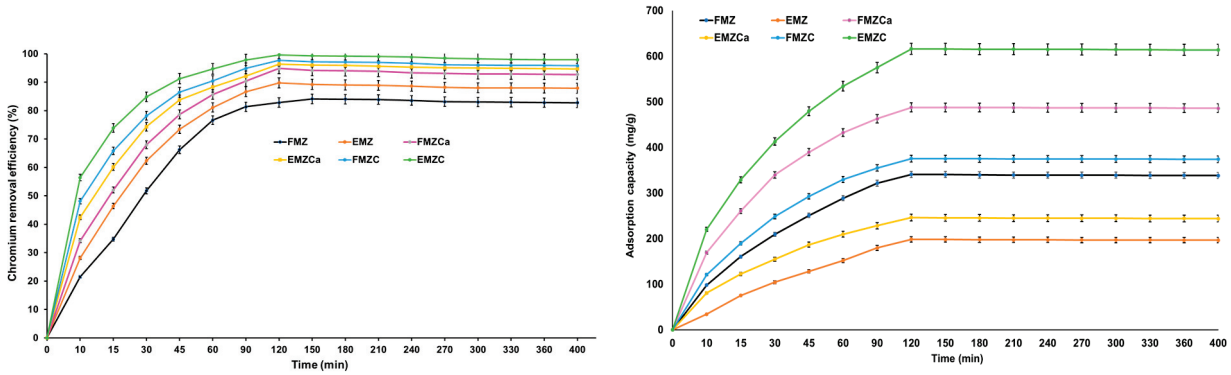

Figure 11. Relationship between chromium (**a**) time and chromium removal efficiency (%) and (**b**) time and adsorption capacity (mg/g).

Furthermore, equilibrium is achieved at 120 min, with maximum adsorption capacities of 349.84 mg/g for EMZ, 198.47 mg/g for FMZ, 246.53 mg/g for FMZCa, 487.82 mg/g for EMZCa, 375.45 mg/g for FMZC, and 616.19 mg/g for EMZC. Additionally, at this time point, nickel removal efficiency reaches its peak at 84.83% for FMZ, 89.76% for EMZ, 94.87% for FMZCa, 96.36% for EMZCa, 97.67% for FMZC, and 99.64% for EMZC. A more detailed examination of the data reveals three distinct stages in chromium adsorption:

(a) In the initial stage (0–120 min), adsorption increases rapidly, likely due to the high availability of active sites in the adsorbent.
(b) During the second stage (120–240 min), a notable decrease in the adsorption rate can be observed, attributed to the reduction in the number of available active sites.
(c) In the third stage (240–460 min), metal adsorption shows a plateau trend, indicating saturation of the active sites after reaching equilibrium. The data suggest that the optimal time required for the adsorption process to reach equilibrium for each investigated adsorbent is 120 min.

3.7.5. Effect of Temperature on the Adsorption Process

The temperature plays a crucial role in the adsorption process, exerting a discernible influence on the efficacy of an adsorbent [40]. The impact of temperature on the adsorption process was examined across a temperature range of 5–50 °C was investigated for all prepared adsorbents (FMZ, EMZ, EMZCa, FMZCa, EMZC, and EMZC) (Figure 12).

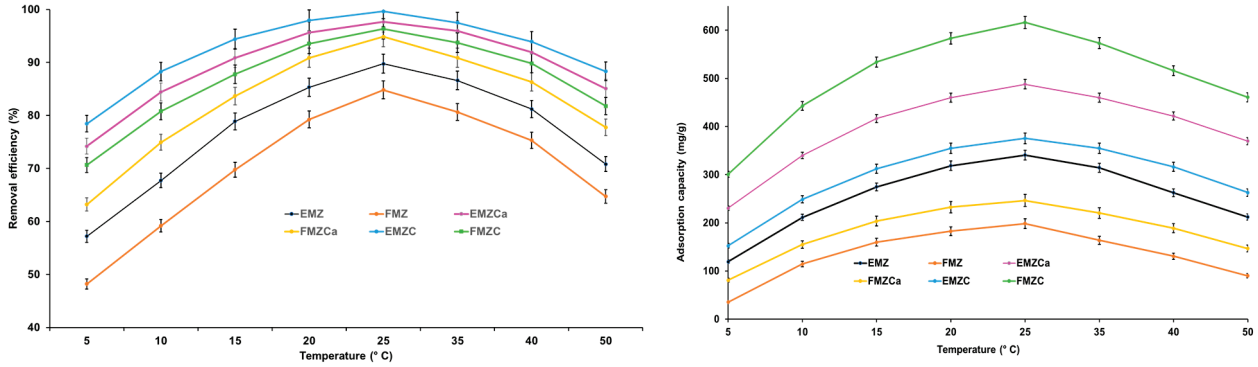

Figure 12. Relationship between chromium (**a**) temperature and chromium removal efficiency (%) and (**b**) temperature and adsorption capacity (mg/g).

The results revealed that adsorption is an endothermic process, with chromium removal efficiency and adsorption capacity increasing almost linearly with temperature up to a maximum, after which there is a slight decrease. The maximum removal efficiency (84.83% for FMZ, 89.76% for EMZ, 94.87% for FMZCa, 96.36% for EMZCa, 97.67% for FMZC, and 99.64% for EMZC) was observed at 25 °C, with corresponding maximum chromium adsorption capacities for all adsorbents (349.84 mg/g for EMZ, 198.47 mg/g for FMZ, 246.53 mg/g for FMZCa, 487.82 mg/g for EMZCa, 375.45 mg/g for FMZC, and 616.19 mg/g for EMZC). The data suggest that temperatures in the 5–25 °C range favor increased mobility of metal ions and interaction with acceptor sites on the adsorbent, leading to physical adsorption. At temperatures higher than 25 °C, a shift toward chemisorption is observed. Notably, even at 50 °C, high removal efficiency values (>77%) were obtained for all biopolymer-based-nanocomposites (77.77% for FMZCa, 85.09 for EMZCa, 88.34% for EMZC and 81.78 for FMZC), indicating that a temperature increase beyond 40 °C has minimal effect on the adsorption process, particularly in comparison to nanocomposites (64.73% for FMZ and 70.84% for EMZ).

3.7.6. Chromium Removal Efficiency—Comparative Analysis Among All Prepared Adsorbent Types and Main Components

A comparative study was conducted to analyze the performance of adsorbents FMZ and EMZ before and after encapsulation in polymeric matrices (carrageenan (FMZCa, EMZCa) and chitosan (FMZC and EMZ) and raw materials (eggshell, fly ash, magnetite, and zeolite), concerning chromium removal efficiency over different contact times (Figure 13).

The results demonstrated a correlation between increased chromium removal efficiency and prolonged contact time for all adsorbents, culminating in peak efficiency at two hours, indicative of adsorption equilibrium. Subsequently, the adsorption rate diminished post-equilibrium. Notably, the experimental findings revealed a descending order of pollutant removal efficiency as follows: EMZ (99.64%) > FMZC (97.67%) > EMZCa (96.36%) > FMZCa (94.87%) > EMZ (89.76%) > zeolite (87.74%) > FMZ (84.83%) > fly ash (83.86%) > eggshell (71.14%) > magnetite (56.33%). These outcomes were consistent with the specific surface and porosity attributes of the adsorbents, as ascertained through BET analysis (Table 1). Furthermore, the adsorption efficiency values for eggshell, fly ash, magnetite, and zeolite closely corresponded with values reported in existing literature [29,44,58,59].

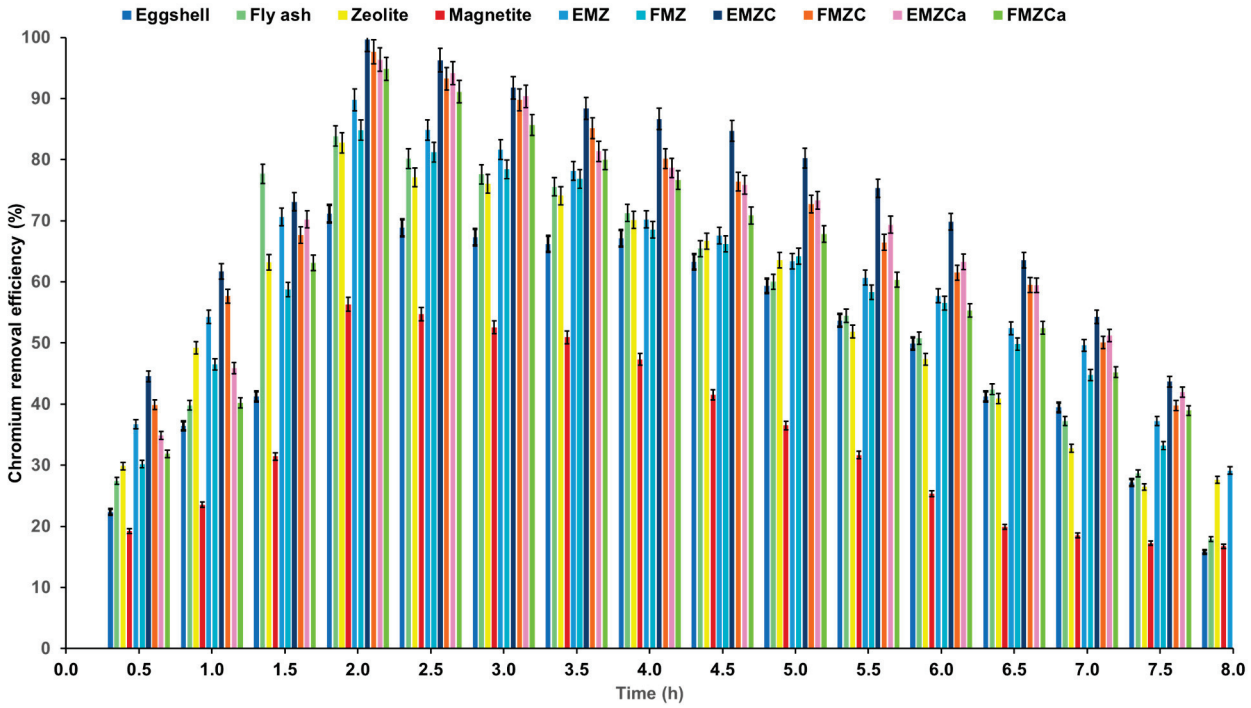

Figure 13. Removal efficiency and contact time relationship for all four adsorbents.

3.8. Adsorption Isotherms

Adsorption isotherms have been employed to examine the equilibrium partitioning of chromium between the adsorbent and solution. The Langmuir and Freundlich models are widely acknowledged as the most prevalent and dependable approaches for ascertaining the maximum chromium adsorption capacity through adsorption isotherms [52,60,61]. Several studies reported chromium adsorption on eggshells, magnetite, and zeolite adsorbents conform to Langmuir and Freundlich's adsorption isotherms [41,52]. Furthermore, numerous studies have indicated that the adsorption isotherms of Cr (VI) on eggshell, magnetite, fly ash, and zeolite, derived using the mathematical equations of Temkin and Dubinin–Radushkevich (D-R) adsorption models, inadequately align with the experimental findings [22,29,52,62,63]

Consequently, the Langmuir and Freundlich adsorption isotherms were deemed suitable for developing an appropriate adsorption model capable of replicating this study's experimental outcomes [60].

The Langmuir model is founded on the theoretical principles that (i) the adsorbent possesses a single, homogeneous layer in which the adsorption process occurs, and (ii) each of the adsorbed molecules exhibits identical adsorption energy without interaction between these molecules [60]. The linear representation of the Langmuir model is articulated by the following equation (Equation (4)):

$$\frac{C_e}{Q_e} = \frac{1}{K_L Q_m} + C_e\, Q_m \tag{4}$$

where, K_L (L/mg) is the Langmuir adsorption constant.

The Freundlich isotherm model is especially adequate for describing multilayer adsorption on heterogeneous surfaces, where non-uniform heat distribution and interactions between adsorbed molecules play a significant role [21,52]. The linear form of Freundlich isotherm is presented in Equation (5).

$$\log Q_e = \log K_F + n\log\, C_e \tag{5}$$

where K_F (mg/g) and n (g/L) represent the Freundlich isotherm constants

In the case of chromium (VI) adsorption on the newly prepared adsorbents (FMZ, EMZ, EMZCa, FMZCa, EMZC, and FMZC), the Freundlich isotherm was applied to apprehend the complexity of adsorption dynamics considering the involvement of multiple layers or variable adsorption energies [61,64,65]. It has been utilized to depict the adsorption of Cr(VI) across all prepared adsorbents, taking into account the energy site distribution and competition interaction among different ions for available active sites from the adsorbents. The experimental results were plotted using the linear representation of Freundlich and Langmuir isotherm models and the determined parameters are shown in Table 4.

Table 4. The Langmuir and Freundlich model parameters for chromium adsorption on each prepared adsorbent.

Adsorbent	Langmuir Model					Freundlich Model			
	$Q_{e,exp}$	Q_m	k	R_L	R^2	K_F	*n*	R^2	E_a (kJ/mol)
EMZ	340.84	339.83	0.189	0.602	0.9964	2.241	1.393	0.9981	32.61
FMZ	198.47	197.52	0.185	0.683	0.9882	2.252	1.401	0.9956	32.35
EMZCa	487.82	487.17	0.191	0.486	0.9933	2.824	1.551	0.9951	32.72
FMZCa	246.53	245.72	0.197	0.506	0.9849	2.977	1.473	0.9897	32.79
EMZC	375.45	374.22	0.186	0.489	0.9957	3.365	1.527	0.9965	32.19
FMZC	616.19	615.89	0.195	0.522	0.9938	3.016	1.673	0.9962	32.22

According to data from Table 4, both the Freundlich and Langmuir models have provided satisfactory descriptions of chromium absorption on the considered adsorbents. The calculated maximum adsorption capacity values align excellently with experimental equilibrium values for the newly prepared nanomaterials. Notably, the R^2 value derived from the Freundlich model slightly surpasses that derived from the Langmuir model, indicative of a multimolecular layer adsorption process on irregular surfaces. Furthermore, the R_L values obtained from the Langmuir isotherm suggest a favorable adsorption process, falling within the range of $0 < RL < 1$ for all prepared adsorbent types. Additionally, the values of the Freundlich constant n, indicative of the linearity of the adsorption, exceed 1, suggesting a suitable physical adsorption process on all investigated adsorbents' heterogeneous surfaces [60,63,66].

3.9. Thermodynamic Study

The thermodynamic properties of all prepared adsorbents (EMZ, FMZ, EMZCa, FMZCa, EMZC, and FMZC) were systematically examined to evaluate their efficacy in chromium removal. This assessment encompassed the determination of Gibbs free energy (ΔG^0), entropy (ΔS^0), and enthalpy (ΔH) utilizing the Gibbs–Helmholtz and van't Hoff equations [22].

$$\Delta G^0 = -RT \ln K \quad (6)$$

$$\ln K = \frac{-\Delta H^0}{RT} + \frac{\Delta S^0}{R} \quad (7)$$

where,

R = 8.314 J/mol K

K (mL/g) = adsorption equilibrium constant

T (K) = the absolute temperature.

The investigations were conducted at three distinct temperatures (295.15 K, 303.15 K, and 313.15 K) using a 28.5 mg/mL chromium stock solution and maintaining a constant pH of 4.5. The slope and intercept of the van't Hoff plot correspond to the thermodynamic parameters ΔG^0 and ΔS^0, as detailed in Table 5.

Table 5. Thermodynamic parameters for chromium adsorption on all prepared adsorbent types *.

Adsorbent	ΔG^0 (kJ/mol)			ΔH^0 (kJ/mol)	ΔS^0 (J/(mol K))
	T(K)				
	295.15	303.15	313.15		
EMZ	−17.11	−18.32	−19.83	27.48	151.09
FMZ	−14.33	−15.30	−16.51	21.41	121.11
EMZCa	−24.90	−26.75	−29.06	43.30	231.08
FMZCa	−21.54	−23.12	−25.08	36.49	196.64
EMZC	−32.65	−35.13	38.22	58.53	308.96
FMZC	−20.26	−20.60	−21.03	47.56	143.04

* standard deviation (SD) = 2%.

Negative ΔG^0 values indicate the thermodynamic feasibility and spontaneity of the prepared adsorbents for chromium removal within the specified temperature range. The ΔH^0 values (28.48 kJ/mol for EMZ, 21.41 kJ/mol for FMZ, 43.30 kJ/mol for EMZCa, 36.49 kJ/mol for FMZCa, 58.53 kJ/mol for EMZC and 47.56 kJ/mol for FMZC) suggest an endothermic adsorption process with a favorable affinity for chromium in all prepared adsorbents. Furthermore, positive ΔS^0 values indicate that the adsorption process could involve structural changes and demonstrate the affinity of all prepared adsorbents (EMZ, FMZ, EMZCa, FMZCa, EMZC, and FMZC) for chromium ions [22,61,62,67].

3.10. Adsorption Kinetic Study

Various mechanisms, such as mass transfer, particle diffusion, diffusion control, and chemical reactions, can influence the adsorption process. Kinetic studies were conducted to assess the effectiveness of the adsorbent, gain insight into the mass transfer process, and determine the dynamic parameters of adsorption, including rate and temperature [61,68]. The experimental data on chromium adsorption for the newly prepared adsorbents (EMZ, FMZ, EMZCa, FMZCa, EMZC, and FMZC) were analyzed using a pseudo-first-order kinetic model, a pseudo-second-order kinetic model, and an intraparticle diffusion model. The pseudo-first-order kinetic model, known as the Lagergren equation, postulates that the adsorption rate is unforeseen upon the availability of active sites. The linear form of the Lagergren equation, represented as Equation (8), is employed to evaluate the adsorption process.

$$\ln (Q_e - Q_t) = \ln Q_e - K_1 t \quad (8)$$

K_1 = (min^{-1}) is the rate constant.

The pseudo-second-order model assigns that the adsorption rate is contingent upon the presence of chemical interaction between heavy metal ions and the functional groups on the prepared adsorbents. The linearized form of second-order kinetics is delineated in the following equation (Equation (9)), where K_2 [mg/(g min)] denotes the rate constant

$$\frac{1}{Q_t} = \frac{1}{Q_e} t + \frac{1}{K_2 Q_e^2} \quad (9)$$

The Weber and Morris intraparticle diffusion model postulates that the diffusion of chromium ions through adsorbent pores affects the adsorption rate and is expressed by Equation (10), with K_i [mg/(g × $min^{-1/2}$)] representing the intraparticle diffusion rate constant and C (mg/g) is a constant associated with the boundary layer thickness.

$$Q_t = K_i t^{1/2} + C \quad (10)$$

The kinetic constants derived from the slope and intercepts of the kinetic models for chromium adsorption on all newly prepared adsorbents are shown in Table 6.

Table 6. Kinetic parameters for chromium adsorption on EMZ, FMZ, EMZCa, FMZCa, EMZC, and FMZC adsorbents *.

Adsorbent Material	Q_e^{exp} (mg/g)	Pseudo-First Order			Pseudo-Second Order			Intraparticle Diffusion		
		q_e^{calc}	K_1	R^2	Q_e^{calc}	K_2	R^2	K_i	C	R^2
EMZ	340.84	341.04	0.197	0.989	341.38	8.462	0.987	3.485	15.938	0.975
FMZ	198.47	198.86	0.216	0.975	199.21	2.017	0.976	1.770	4.709	0.963
EMZCa	487.82	489.32	0.194	0.991	489.44	8.058	0.988	5.545	32.443	0.971
FMZCa	246.53	246.96	0.208	0.986	247.18	2.267	0.985	2.598	16.529	0.961
FMZC	375.45	376.23	0.192	0.977	376.41	1.053	0.975	4.316	20.742	0.976
EMZC	616.19	619.78	0.211	0.987	617.36	6.568	0.986	7.255	33.315	0.986

* standard deviation (SD) = 2%.

The analysis of the obtained results indicates negligible disparities between the correlation coefficients for the pseudo-first-order and pseudo-second-order kinetic models, suggesting that chromium adsorption on the adsorbents involves both physical and chemical processes. Additionally, it can be noted that the calculated adsorption capacities at equilibrium closely align with the experimental values obtained using the pseudo-second-order kinetics model, indicating that the adsorption of chromium ions predominantly relies on chemisorption, involving the formation of chemical bonds between chromium ions and active sites. The high correlation coefficient for the intraparticle diffusion model (exceeding 0.97 for all adsorbent types) suggests the involvement of intraparticle diffusion in the adsorption process. Nevertheless, intraparticle diffusion is not the sole rate-limiting step, as the diagram exhibits a non-linear pattern and deviates from the origin. These kinetic findings are consistent with the existing literature on the starting materials of all proposed adsorbent types.

3.11. Insight into Adsorption

The evaluation of structural and morphological changes was conducted through FT-IR, SEM-EDX, and thermal analysis techniques. This comprehensive approach aimed to investigate the potential mechanisms of chromium adsorption associated with the proposed nanomaterials and each type of biopolymer-based composite.

3.11.1. FTIR Study

The FTIR spectra of the prepared adsorbents reveal significant changes following chromium adsorption (Figure 14).

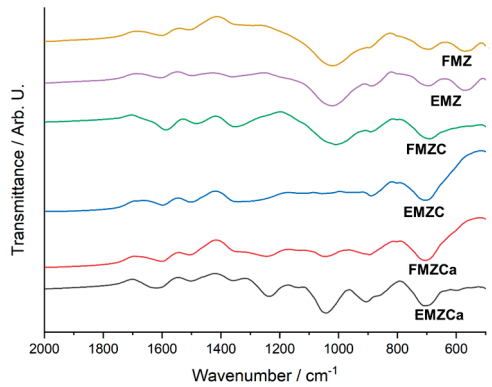

Figure 14. FT-IR spectrum of FMZ, EMZ, FMZCa, EMZCa, FMZC, and EMZC after adsorption.

In the FMZ spectra, notable shifts are observed in the adsorption peaks at 830 cm^{-1}, assigned to AlO_4 coordination, and around 1066 cm^{-1}, corresponding to the Si-O asymmetric stretch. All these shifts are accompanied by alterations in peak intensities. For EMZ, vibrational band shifts are detected at approximately 880 cm^{-1} and 1418 cm^{-1} (C-O

stretch), 1066 cm^{-1} (Si-O asymmetric stretch), 1637 cm^{-1} (C=O stretching), 1643 cm^{-1} (N-H stretching), and 1077 cm^{-1} (C-N stretching). Such spectral changes could be attributed to the chemical interactions between chromium ions and the specific functional groups present in FMZ and EMZ. Moreover, both k-carrageenan-based nanocomposites (FMZCa and EMZCa) show significant shifts in the absorption bands within the sulfate ester region, particularly at 1454, 1394, 1266, and 848 cm^{-1}. In contrast, the FTIR spectra of chitosan-based nanocomposite display primarily shift at approximately 1568, 1413, 1018, and 870 cm^{-1}, which are associated with the ammonium groups in the chitosan structure. These observed spectral alterations further emphasize the interactions between chromium ions and the functional groups within the biopolymer-based nanocomposites [30].

3.11.2. SEM-EDX Analysis

Morphological changes in all prepared adsorbent types (FMZ, EMZ, EMZCa, FMZC, and EMZC) after chromium adsorption were evaluated through SEM-EDX analysis (Figures 15 and 16). This assessment aimed to support the findings from FT-IR spectroscopy by examining variations in particle size, shape, pore dimensions, and particle distribution.

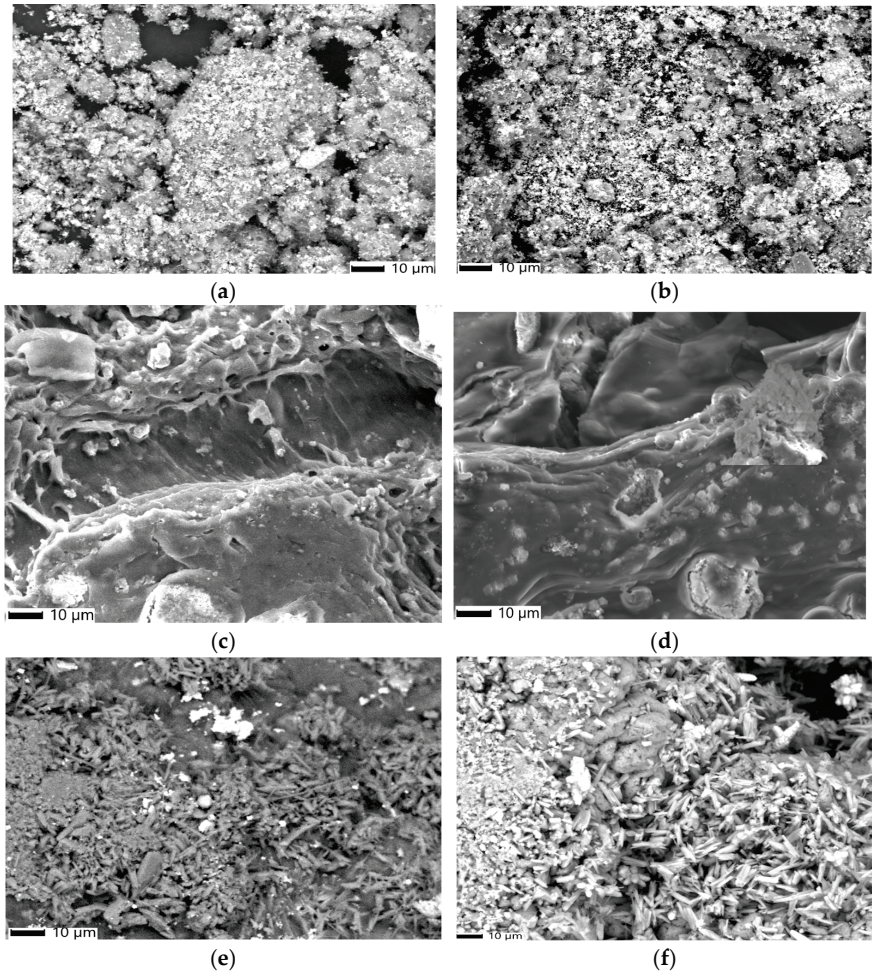

Figure 15. SEM images of FZM (**a**), EMZ (**b**), FMZCa (**c**), EMZCa (**d**), FMZC (**e**), and EMZC (**f**) after adsorption.

The SEM micrographs of FMZ and EMZ following chromium adsorption (Figure 15) illustrate the presence of numerous irregularly shaped particles attributed to the pollutant. Additionally, the SEM images indicate a discernible reduction in the porosity of these adsorbents after chromium uptake. For the biopolymer-based nanocomposites (FMZCa, EMZCa, FMZC, and EMZC), the micrographs reveal clusters of irregularly shaped particles

that are unevenly distributed within the polymeric matrix, accompanied by observable modifications in the matrix morphology. These findings suggest significant alterations resulting from the adsorption process.

3.11.3. EDX Analysis

Elemental analysis (EDX) of all prepared adsorbents following chromium adsorption was conducted (Figure 16). The EDX results indicated a distinct peak corresponding to the heavy metal, thereby confirming the successful adsorption of chromium [69,70].

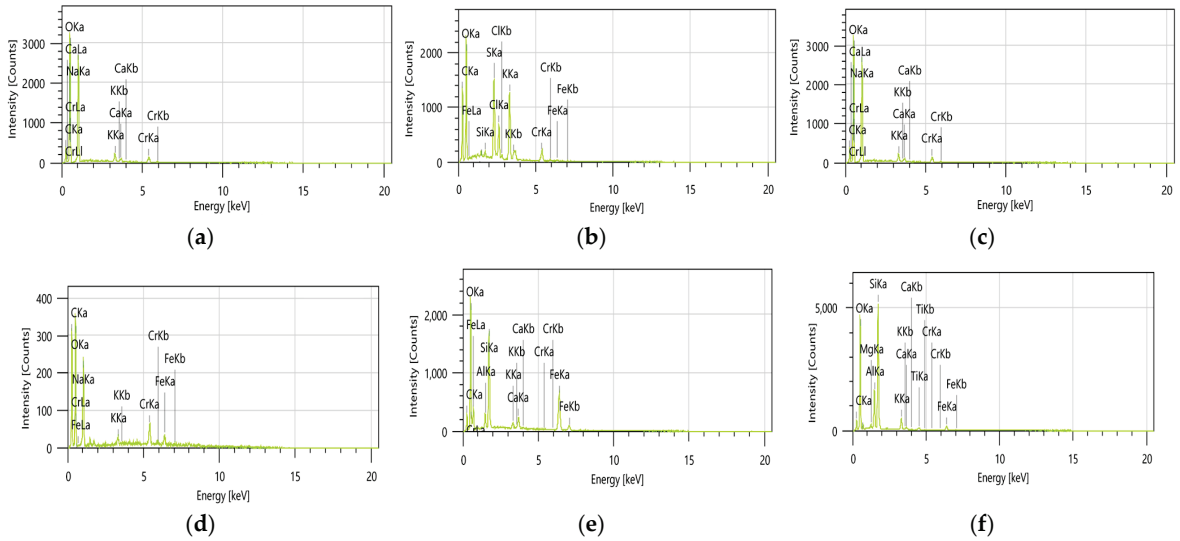

Figure 16. EDX spectrum of EMZ (**a**), FMZ (**b**), EMZCa (**c**), FMZCa (**d**), EMZC (**e**), and FMZC (**f**) after adsorption.

The elemental composition (%) determined via EDX analysis (Figure 17) reveals distinct variations in the chromium (Cr) retention across the surfaces of different types of adsorbent prepared.

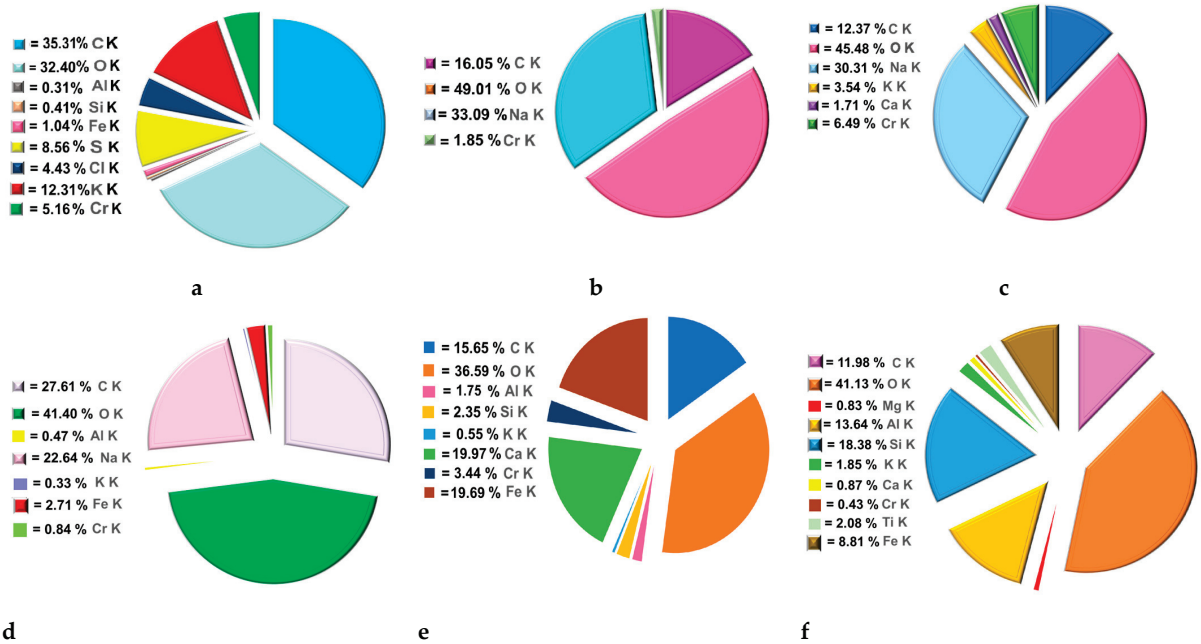

Figure 17. Elemental composition (%) determined via EDX analysis for EMZCa (**a**); FMZCa (**b**); EMZC (**c**); FMZC (**d**); EMZ (**e**), and FMZ (**f**).

3.11.4. Thermal Analysis

Thermal analysis of all types of adsorbents prepared after chromium adsorption was performed to evaluate the changes in thermal stability after chromium adsorption. The results are illustrated in Table 7 and Figure 18.

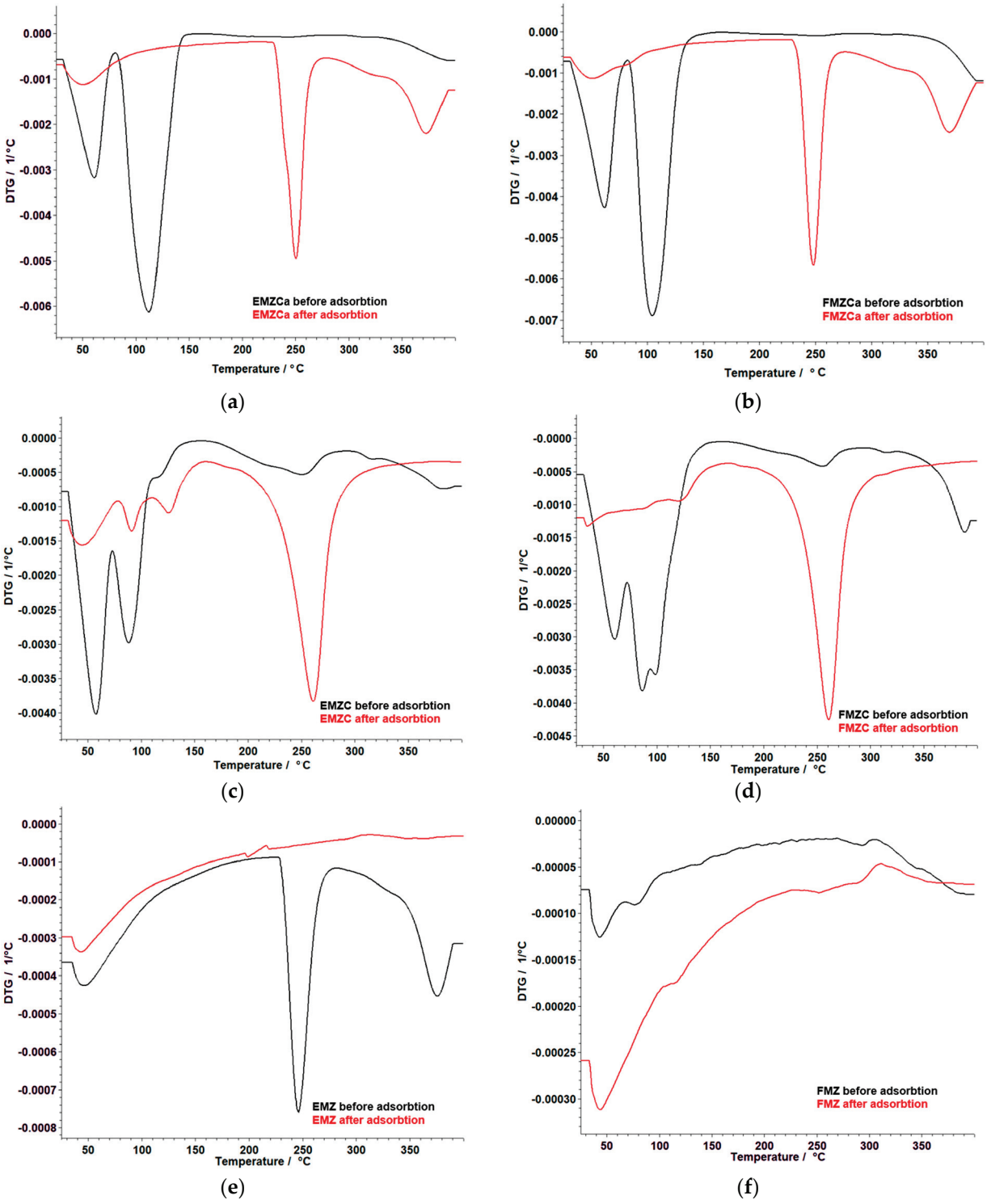

Figure 18. Comparative DTG curves of all prepared adsorbents before/after adsorption: EMZCa (**a**); FMZCa (**b**), EMZC (**c**), FMZC (**d**), EMZ (**e**), and FMZ (**f**).

Table 7. Thermal analysis results for all types of prepared adsorbents after chromium retention.

Sample	Process	TG		DTG_{max}/°C	Δm/%	Total Mass Loss %
		T_{onset}/°C	T_{final}/°C			
EMZCa	I	35	93	51	5.48	33.06
	II	213	292	250	10.95	
	III	331	400	380	10.09	
FMZCa	I	36	97	-	5.92	33.82
	II	220	279	249	10.03	
	III	335	400	372	10.57	
EMZC	I	33	78	54	6.56	35.2
	II	79	141	96	6.18	
	III	200	320	264	17.29	
FMZC	I	36	114	63	9.04	34.62
	II	223	300	261	15.10	
EMZ	I	35	66	-	1.03	33.89
	II	184	257	210	0.49	
FMZ	I	39	114	-	1.91	4.22
	II	173	258	-	0.688	
	III	297	370	-	0.40	

Thermal analysis of prepared adsorbents after chromium retention indicates distinct thermal decomposition behaviors depending on the biopolymer matrices and composition. Adsorbents FMZC and EMZ exhibit a two-stage thermal degradation process, wherein the initial phase is characterized by moisture loss, followed by the degradation of the polymer membrane. In contrast, adsorbents EMZCa, FMZCa, EMZC, and EMZ are observed to undergo a more intricate three-stage thermal decomposition. For k-carrageenan-based nanocomposites (EMZCa and FMZCa), the first stage involves moisture loss, followed by water removal from the membrane matrix and degradation of the polymer. This process initiates at temperatures above 200 °C and continues to progress at temperatures exceeding 300 °C. The chitosan-based nanocomposite, EMZC, also undergoes a three-stage decomposition process. The initial phase involves moisture loss, followed by the degradation of the polymer matrix, and concludes with the decomposition of organic compounds present in the eggshell particulates. Conversely, the thermal analysis of FMZC reveals a two-stage mechanism assigned to the loss of moisture and the subsequent degradation of the polymer membrane. The thermal behavior of nanocomposite EMZ is characterized by two stages as well, with the initial phase involving moisture loss, followed by the thermal degradation of organic components derived from the eggshell matrix. Finally, FMZ undergoes a three-stage thermal decomposition process, which includes the loss of water, followed by the elimination of crystallization water and the decarbonation of zeolite components [29,71].

The thermal analysis results demonstrate that carrageenan-based nanocomposites exhibit enhanced thermal stability in the formulation of k-carrageenan-based nanocomposite EMZCa compared to FMZCa. In a parallel observation, chitosan-based nanocomposites in formulation EMZC show superior thermal stability to FMZC, although EMZC exhibits a higher total mass loss of 0.75%. This discrepancy can be attributed to the higher proportion of chromium ions retained on this specific adsorbent. These conclusions corroborate with data derived from the corresponding adsorption studies.

3.12. Adsorption Mechanism

Various studies reported three predominant mechanisms (ion exchange, electrostatic attraction, and reduction) for chromium removal from aqueous media [1,9].

In this study, we identified an optimal pH of 4.5, where the coexistence of dichromate ($Cr^2O_7^{2-}$) and hydrogen chromate ($HCrO_4^-$) ions occurs. In this acidic environment, the complex structures of FMZ and EMZ promote the immobilization of chromium through the electrostatic attraction of chromate anions to the divalent and trivalent cations, specifically Ca^{2+}, Mg^{2+}, and Fe^{3+}, present in these adsorbents. Additionally, chromium ions can

penetrate the pores of zeolite, where steric effects, such as van der Waals interactions, facilitate their confinement.

The protonated NH groups in eggshell particles, stemming from the protein components of the eggshell membrane, facilitate the attraction of chromium ions and forming surface complexes via chemical bonding on EMZ adsorbent [4].

Concurrently, the reduction of $HCrO_4^-$ ions by Fe(II) ions sourced from magnetite and protons occurs alongside the exchange of chromium ions from the aqueous solution with Na^+, K^+, and Mg^{2+} from EMZ and FMZ [13]. These reflect chemisorption activity, supported by prior spectroscopic, kinetic, and thermodynamic studies (vide supra). In addition, zeolite can trap Cr^{3+} ions, promoting immobilization into the FMZ and EMZ tertiary matrix [22,72]. Concomitantly, in the case of chitosan-based nanocomposites, specifically FMZC and EMZC, the amino (-NH_2) and hydroxyl (-OH) groups in the polymer matrix undergo complete protonation to form –NH_3^+ and –OH_2^+ species. These positively charged groups exhibit a strong affinity for the chromium ions from aqueous solution, resulting in surface-bound complexes through chemical bonding. Furthermore, Cr(VI) ions are reduced in the presence of Fe(II) and protons, which facilitates the adsorption of the resulting Cr(III) ions within the chitosan matrix. This process ultimately results in covalent bond formation, specifically –H_2N–Cr(III), characterized by a coordinate bond involving the non-bonding electrons of nitrogen.

In the context of k-carrageenan-based nanocomposites, specifically FMZCa and EMZCa, the mechanism for the removal of chromium (VI) ions involves multiple simultaneous processes: ion exchange, electrostatic attraction, reduction, and chelation. At the optimal pH established for this study, hydroxyl ions (OH−) present on the adsorbent surface are readily substituted by $HCrO_4^-$ ions. In an acidic environment, the protonation of hydroxyl and sulfate groups within the biopolymer enhances the availability of adsorption sites. This modification significantly strengthens the electrostatic interactions with chromium (VI) ions. The abundance of protons (H^+) facilitates the attraction of hydroxyl groups from k-carrageenan, while at the same time, $HCrO_4^-$ ions are repelled from the –OH^- groups due to the governing electrostatic forces. Furthermore, under the influence of protons and Fe(II) ions, hydrogen chromate ($HCrO_4^-$) is reduced to Cr^{3+} ions, which are subsequently attracted to the sulfate ions (–SO_4^-) and adsorbed on the polymer matrix. Additionally, the ionic OSO_3^- groups facilitate the formation of metal-ligand complexes with chromium (VI) ions [30,73–75]. A schematic representation of chromium adsorption on all prepared adsorbents is presented in Figure 19.

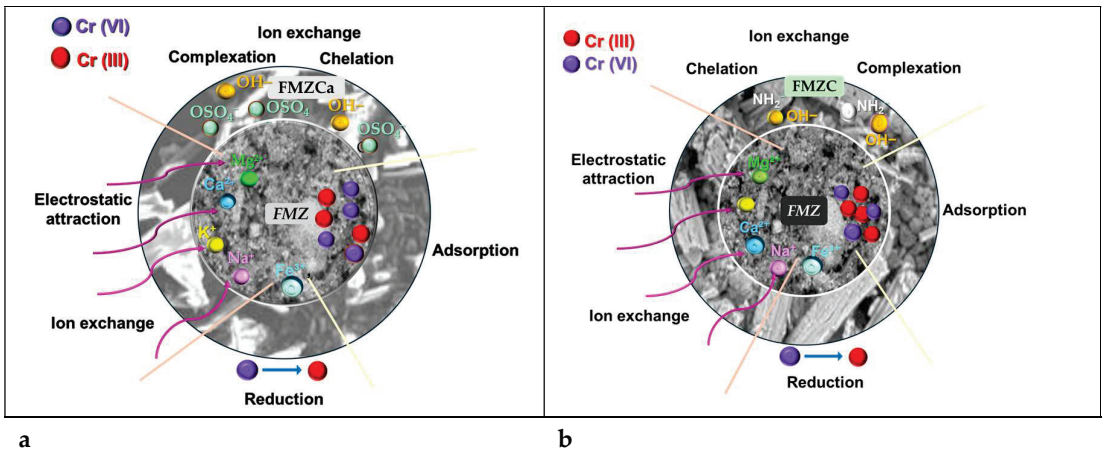

a **b**

Figure 19. *Cont.*

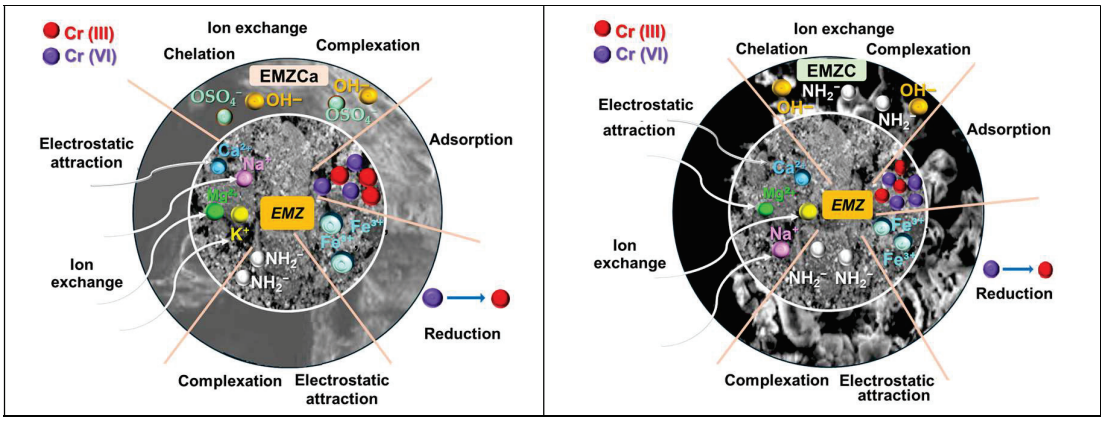

c **d**

Figure 19. Schematic representation of the adsorption mechanism of prepared adsorbents: FMZ/FMCa (**a**), FMZ/FMZC (**b**) EMZ/EMZCa (**c**), and EMZ/EMZC (**d**).

3.13. Comparison of Chromium Removal Efficiency Among Other Adsorbents

A comparative evaluation of the adsorption performance for all prepared adsorbent types, as well as those reported in the relevant literature concerning chromium removal, is presented in Table 8.

Table 8. Comparison between chromium removal efficiency of the new types of adsorbents and those reported in the literature (selected studies) for materials similar to their components.

Adsorbent Type	Removal Performance	Chromium Initial Concentration	Ref.
eggshell	285.71 mg/g	300 mg/L	[58]
chitosan flakes	138.45 mg/g	500 mg/L	[75]
montmorillonite/carrageenan (MMT/CG)-composite hydrogel	106 mg/g	80 mg/L	[76]
fly ash	83.9%	20 mg/L	[14]
Fe_3O_4 nanoparticles	80.4%	1000 mg/L	[77]
MWCNT/Fe_3O_4	89.1%	1000 mg/L	[78]
natural zeolite (ZN-NaOH)	44.44%	0.6 mg/L	[79]
synthetic zeolite (ZS-NaOH)	32.22%	0.6 mg/L	[79]
clinoptilolite treated with NaCl	4.5 mg/g	10 mg/L	[80]
clinoptilolite	2.2 mg/g	10 mg/L	[80]
ZnO-chitosan nano-biocomposite	96.5% (65 mg/g)	20 mg/L	[81]
FeS/CTS	99.18%	50 mg/L	[82]
CS-AL nanocomposites with glutaraldehyde	79.91%	100 mg/L	[83]
FMZ	84.83% (198.47 mg/g)	28.5 mg/L	This study
EMZ	89.76% (349.84 mg/g)	28.5 mg/L	This study
FMZCa	94.87% (246.53 mg/g)	28.5 mg/L	This study
EMZCa	96.36% (487.82 mg/g)	28.5 mg/L	This study
FMZC	97.67% (375.45 mg/g)	28.5 mg/L	This study
EMZC	99.64% (616.19 mg/g)	28.5 mg/L	This study

The results indicate that all three categories of adsorbents, namely the nanocomposites (EMZ and FMZ), the k-carrageenan-based nanocomposites (EMZCa and FMZCa), and the chitosan-based nanocomposites (EMZC and FMZC) exhibit significantly higher adsorption efficiencies than any recognized materials. This increase can be attributed to their greater surface areas compared to their constituent components, such as magnetite, zeolite, and eggshell or fly ash, in addition to the enhancements made to the biopolymeric matrices following the modification of the adsorbent surface efficiency than any other known materials. This could be attributed to the higher surface area compared to their components (eggshell or zeolite), following adsorbent surface modification [5,84,85].

3.14. Desorption Studies

Cycling stability is pivotal to achieving high-performance and cost-effective adsorbents [86]. The regeneration efficiency is significantly influenced by the desorption kinetics of the adsorbed pollutants [40]. In this study, the desorption of chromium ions was examined under acidic conditions, specifically utilizing nitric acid, sulfuric acid, and the chelating agent ethylenediaminetetraacetic acid (EDTA). The results (Figure 20) indicate that in an acidic environment, the desorption rate increases markedly within the 0 to 11-h timeframe, reaching a maximum, after which a slight decline in desorption yield is observed over time.

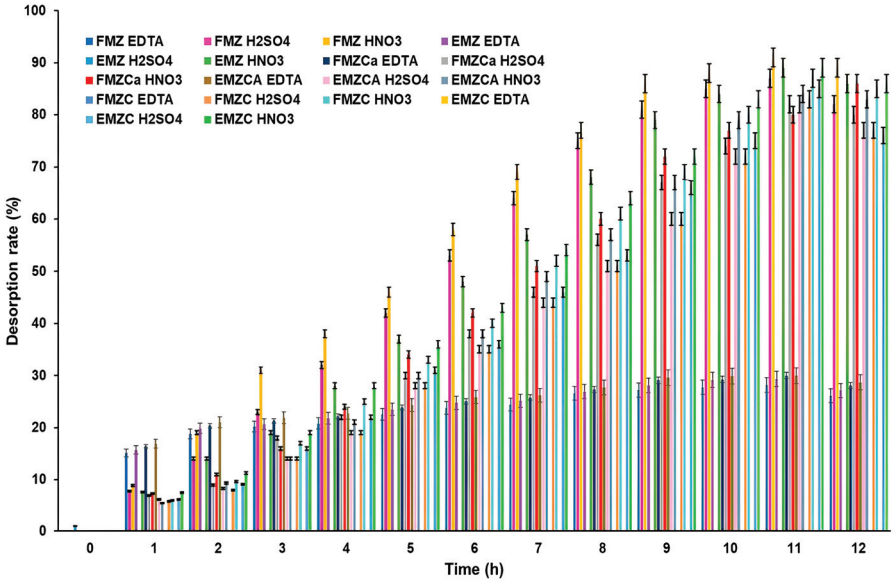

(**a**)

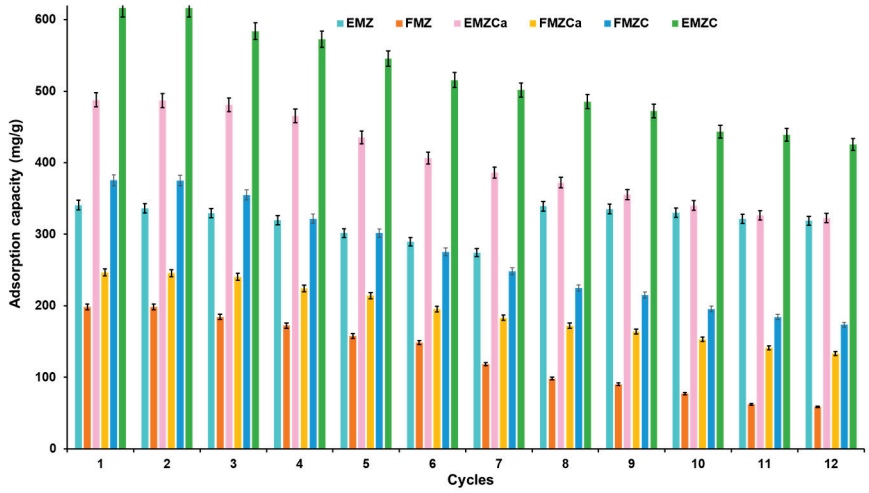

(**b**)

Figure 20. (**a**) Relationship between desorption rate and time. (**b**) Reusability of all prepared adsorbents.

A comprehensive desorption study was conducted using three distinct desorption agents (Figure 20a). Applying 0.1 N EDTA resulted in the release of approximately 40% of the chromium adsorbed onto chitosan-based nanocomposites, with specific releases of 40.02% for EMZC and 39.85% for FMZC. In comparison, the release rates for FMZ and EMZ were lower, at approximately 28.15% and 29.5%, respectively. The desorption outcomes for k-carrageenan-based nanocomposites approached 30%, with recorded values of 29.98% for FMZCa and 30.01% for EMZCa, predominantly as Cr(III) ions. These findings can be attributed to the formation of polydentate coordination bonds with Cr(III) ions, thereby

enhancing the effective recovery through interactions with the functional groups from the biopolymeric matrices. Furthermore, EDTA is a well-established chelating agent known for its effectiveness in regenerating chitosan [87].

The utilization of 0.1 N mineral acids demonstrated significant desorption rates, with between 89% and 91% of the adsorbed chromium released into solution as Cr(III) ions, specifically recording 91% for EMZ and 89% for FMZ when using HNO_3. The desorption rates were higher for the nanocomposites (91% for EMZ and 89% for FMZ), followed by chitosan-based nanocomposites (with rates of 85% for EMZC and 83% for FMZ), and k-carrageenan-based composites (with 82% for EMZCa and 80% for FMZCa), during the application of 0.1 M HNO_3.

Similar results were obtained with 0.1 M H_2SO_4, where over 80% of the heavy metal was desorbed from all adsorbents, with the highest desorption rate of 89% observed for EMZC. This outcome for chitosan-based nanocomposites suggests that $HCrO_4^-$ ions adsorbed by the prepared adsorbents were reduced to Cr(III) during desorption by mineral acids, thereby releasing Cr(III) ions into the solution. This phenomenon can be explained by repulsion from the protonated functional groups within the biopolymer matrix [88].

Conversely, the outcomes for other adsorbent types evaluated in this study may be attributed to ion exchange interactions, which could be more prevalent than chemical sorption [89].

To that end, thirteen chromium adsorption and desorption cycles were conducted on both adsorbents to investigate their reusability potential.

4. Discussion

We have successfully prepared two novel composite nano adsorbents: one composed of fly ash, zeolite, and magnetite (FMZ) and the other consisting of eggshell, zeolite, and magnetite (EMZ). Building upon these foundational composite nanoadsorbents, we developed two k-carrageenan-based composites (FMZCa and EMZCa) and two chitosan-based composites (FMZC and EMZC). The preparation of these biopolymer-based composites involves meticulously loading FMZ and EMZ into k-carrageenan and chitosan matrices, respectively. The XRD spectrum demonstrated that FMZ and EMZ composites exploit the high surface area and porosity of zeolite and the magnetic properties of magnetite, enhancing the efficiency of pollutant removal compared to the performance of their starting components. The subsequent k-carrageenan and chitosan modifications further augment the adsorption capacities and thermal stability. The VSM study indicated a predominantly ferromagnetic profile for the samples, with the notable exceptions of FMZCa and EMZC, which displayed a hysteretic profile exhibiting paramagnetic behavior near zero fields.

Thermal analysis revealed that although FMZ is more stable than EMZ, after loading into the polymer matrix, EMZ is more thermally stable than FMZ, regardless of the biopolymer type used.

These innovative adsorbents capitalize on the synergistic properties of their constituents: fly ash and eggshells serve as sustainable bases, promoting waste valorization while maximizing the capabilities of zeolite and magnetite for pollutant removal. Moreover, the subsequent k-carrageenan and chitosan modifications further enhance their adsorption capabilities and mechanical integrity, yielding robust materials suitable for addressing diverse environmental challenges.

The adsorption behavior of all new adsorbent types follows the Freundlich isotherm and pseudo-second-order models. The adsorption efficiency of each adsorbent type exceeds 84% of Cr(VI), (89.76 for EMZ, and 84.83% for FMZ), more than 94% of Cr(VI) for each k-carrageenan-based composite (97.67% for EMZCa and 94.87% for FMZCa) and over 96% for each chitosan-based composite (99.64% for EMZC and 96.36% for FMZC).

According to this study's results, EMZC (chitosan-based composite) and EMZCa (k-carrageenan-based composite) demonstrate higher adsorption capacity for chromium (487.82 mg/g for EMZCa and 616.19 mg/g for EMZC) compared to other composites prepared in this study due to the synergistic effects of polymer matri-ces and their compo-

nents. Thus, both EMZC and EMZCa provide a higher density of functional groups (e.g., -NH_3^+, -OH_2^+ in EMZC; -SO_4^-, -OH in EMZCa) compared to unmodified composites like EMZ or FMZ, offering more adsorption sites for chromium. Furthermore, the combination of protonated biopolymers and their components (magnetite, zeolite, eggshell) create a cooperative system where ad-sorption is enhanced through multiple mechanisms, including reduction, ion ex-change, and chemical bonding. In addition, the polymer matrices improve the dispersion of inorganic components, exposing more active sites for chromium binding and increasing the overall surface area of the composite. Conversely, the higher adsorption capacities of EMZC and EMZCa compared to FMZC and FMZCa can be attributed to the structural and compositional differences between eggshell-based (EMZ) and fly ash-based (FMZ) composites. Eggshells contain a high concentration of calcium carbonate ($CaCO_3$) and organic proteinaceous ma-terials, which enhance adsorption through multiple mechanisms. In EMZC and EMZCa, the calcium ions (Ca^{2+}) from the eggshell contribute significantly to the electrostatic attraction of chromate anions ($Cr_2O_7^{2-}$, $HCrO_4^-$) and facilitate ion ex-change processes. Additionally, the proteinaceous components in eggshells, such as the amine-rich eggshell membrane, further support chemical bonding and sur-face complexation with chromium ions, providing an additional pathway for ad-sorption.

In contrast, FMZ composites rely on fly ash, primarily composed of silica and alumina, which are less interactive in chromium adsorption due to the lack of or-ganic functional groups and lower ion exchange potential. Furthermore, EMZ composites benefit from their more heterogeneous and porous structure, which increases the surface area and accessibility of active sites for adsorption. When combined with chitosan or k-carrageenan matrix, the enhanced functional group density and chemical reactivity of EMZC and EMZCa allow for superior binding of chromium ions compared to FMZC and FMZCa. These factors collectively ex-plain the greater adsorption capacities of EMZ-based composites.

In comparison with the literature on similar materials to their starting components, the three types of new materials (EMZ, FMZ, EMZCa, FMZCa, EMZC, and FMZC) demonstrate higher absorption capacity attributed to the higher surface and the microporous structure resulting from the used experimental conditions exhibit higher adsorption efficiency [21,22,29,44,52,70].

The potential applications of these composites and biocomposites span water purification and pollutant sequestration, thereby providing effective solutions to pressing global environmental issues through cutting-edge nanotechnology.

The materials derived from this research demonstrate stability and ease of reuse, further underscoring their applicability in wastewater remediation within a sustainable economy. Collectively, these novel adsorbent types present significant advancements in the environmental engineering field.

5. Conclusions

This study investigates the efficacy of chromium removal from aqueous solutions utilizing three novel adsorbent types: (i) Nanocomposites EMZ and FMZ, developed from eggshell waste, which is integrated with zeolite and magnetite, and from fly ash, which is combined with zeolite and magnetite, respectively; (ii) k-carrageenan-based composites EMZCa and FMZCa, prepared by incorporating the aforementioned nanocomposites into a k-carrageenan matrix; (iii) Chitosan-based composites, formed by embedding the newly created composites into a chitosan matrix.

The functionalization of EMZ involved zeolite and magnetite particles, which were loaded within the pores of the eggshell and validated through SEM, XRD, and FTIR analysis. For FMZ, the approach involved loading fly ash and magnetite particles into zeolite pores. The polymer-based composites underwent similar functionalization, ensuring that each nanocomposite was effectively loaded into the polymer matrix. XRD analysis revealed a notable reduction in crystallinity for both biopolymer composites, correlating with an increase in specific surface area. SEM and BET analysis corroborated these structural modifications across all newly developed adsorbents. Consequently, EMZC exhibited

superior adsorption performance (99.64%, 616.19 mg/g) compared to EMZCa (97.67%, 246.53 mg/g) and EMZ (89.76%, 340.84 mg/g).

Similarly, FMZC (97.67%, 375.45 mg/g) outperformed FMZCa (94.87%, 246.53 mg/g) and FMZ (84.83%, 198.47 mg/g), achieving a maximum adsorption capacity of 96.365 mg/g. Optimal adsorption conditions were identified at 25 °C, pH 4.5, and had a contact time of 120 min. The adsorption process was characterized by isotherm, thermodynamic, and kinetic modeling, suggesting a physisorption mechanism interlaced with a chemical adsorption component, which fitted well with a second-order kinetics model. Further analysis using SEM, FT-IR, and DTG post-metal adsorption indicated that chromium uptake occurred through the formation of chemical bonds.

Regeneration experiments demonstrated that chromium could be efficiently desorbed from the adsorbents' surfaces using mineral acids, with maximum desorption rates of 91% for EMF and 89% for FMZ, which were followed by 85% and 83% for the chitosan-based composites EMZC and FMZC and 82% and 80% for the k-carrageenan-based composites EMZCa and FMZCa.

Overall, the findings present a thorough characterization of the newly prepared composites and biopolymer-based composites, which exhibit attributes of high performance, selectivity, recyclability, cost-efficiency, and eco-friendliness, thereby rendering them suitable for applications in wastewater remediation. This study proposes an innovative ecological approach leveraging waste materials for effective chromium immobilization from aqueous environments.

Future research endeavors should focus on the following areas: (a) The evaluation of the performance of these newly developed adsorbents under real-world conditions, encompassing their interactions with other heavy metals and organic pollutants; (b) The investigation of their long-term stability and efficacy in dynamic systems, particularly under continuous flow conditions and fluctuating pH levels over extended durations; (c) The economic feasibility of scaling up production processes.

6. Patents

A patent application was submitted to the Romanian State Office for Inventions and Trademarks and recorded as A/0001/2024.

Author Contributions: Conceptualization: A.-E.S. and I.G.; methodology: A.-E.S., T.V. and G.V.; formal analysis: G.B., D.-D.H. and I.A.B.; investigation: M.M. and M.S.C.; data curation: M.M., M.S.C., G.B. and D.-D.H.; writing—original draft: A.-E.S., M.S.C., D.-D.H. and I.A.B.; writing—review and editing: A.-E.S. and D.-D.H.; supervision: A.-E.S. and D.-D.H. All authors have read and agreed to the published version of the manuscript.

Funding: This research received no external funding.

Institutional Review Board Statement: No prior ethical approval was necessary for this study.

Data Availability Statement: The datasets and relevant material used and/or analyzed during the current study are available from the corresponding author upon reasonable request.

Conflicts of Interest: The authors declare no conflicts of interest.

Abbreviations

WHO	World Health Organization
BET	Brunauer–Emmett–Teller method
XRD	X-ray diffraction analysis
FTIR	Fourier-transform infrared spectroscopy
VSM	vibrating sample magnetometer
SEM	scanning electron microscopy
Ess	eggshell
FMZ	tertiary composite composed of fly ash, magnetite, and zeolite
EMZ	tertiary composite containing eggshell, magnetite, and zeolite

WPPF	whole powder pattern fitting method
BJH	Barrett-Joyner-Halenda
FEG	field emission gun
FMZC	biopolymer-nanocomposite material based on fly ash, magnetite, and zeolite, loaded in chitosan matrix
EMZC	biopolymer-nanocomposite material based on eggshell, magnetite, and zeolite, loaded in chitosan
FMZCa	biopolymer-nanocomposite material based on fly ash, magnetite, and zeolite, loaded in k-carrageenan
EMZCa	biopolymer-nanocomposite material based on eggshell, magnetite, and zeolite, loaded in k-carrageenan

References

1. Pakade, V.E.; Tavengwa, N.T.; Madikizela, L.M. Recent advances in hexavalent chromium removal from aqueous solutions by adsorptive methods. *RSC Adv.* **2019**, *9*, 26142–26164. [CrossRef] [PubMed]
2. Genchi, G.; Lauria, G.; Catalano, A.; Carocci, A.; Sinicropi, M.S. The double face of metals: The intriguing case of chromium. *Appl. Sci.* **2021**, *11*, 638. [CrossRef]
3. Handa, K.; Jindal, R. Genotoxicity induced by hexavalent chromium leading to eryptosis in *Ctenopharyngodon idellus*. *Chemosphere* **2020**, *247*, 125967. [CrossRef] [PubMed]
4. Badillo-Camacho, J.; Orozco-Guareño, E.; Carbajal-Arizaga, G.G.; Manríquez-Gonzalez, R.; Barcelo-Quintal, I.D.; Gomez-Salazar, S. Cr(VI) adsorption from aqueous streams on eggshell membranes of different birds used as biosorbents. *Adsorpt. Sci. Technol.* **2020**, *38*, 413–434. [CrossRef]
5. Hu, J.; Lo, I.M.C.; Chen, G. Removal of Cr(VI) by magnetite. *Water Sci. Technol.* **2004**, *50*, 139–146. [CrossRef]
6. Yang, Y.; Zhang, Y.; Wang, G.; Yang, Z.; Xian, J.; Yang, Y.; Li, T.; Pu, Y.; Jia, Y.; Li, Y.; et al. Adsorption and reduction of Cr(VI) by a novel nanoscale FeS/chitosan/biochar composite from aqueous solution. *J. Environ. Chem. Eng.* **2021**, *9*, 105407. [CrossRef]
7. US Environmental Protection Agency (EPA). Chromium (VI) CASRN 18540-29-9 | IRIS | US EPA, ORD. Available online: https://iris.epa.gov/ChemicalLanding/&substance_nmbr=144 (accessed on 25 November 2024).
8. EU Directive 98/83/EC for Drinking Water Quality. Available online: https://eur-lex.europa.eu/legal-content/EN/TXT/?uri=celex:31998L0083 (accessed on 20 November 2024).
9. Aigbe, U.O.; Osibote, O.A. A review of hexavalent chromium removal from aqueous solutions by sorption technique using nanomaterials. *J. Environ. Chem. Eng.* **2020**, *8*, 104503. [CrossRef]
10. Segneanu, A.E.; Bandas, C.; Grozescu, I.; Cziple, F.; Slavici, T.; Sfirloaga, P. Hybrid materials for the removal of organic compounds from water. *Environ. Eng. Manag. J.* **2013**, *12*, 1071–1077.
11. Cepan, C.; Segneanu, A.-E.; Grad, O.; Mihailescu, M.; Cepan, M.; Grozescu, I. Assessment of the different type of materials used for removing phosphorus from wastewater. *Materials* **2021**, *14*, 4371. [CrossRef]
12. Balcu, I.; Segneanu, A.; Mirica, M.; Badea, C.; Fitigau, F. Iron oxides from electrofilter ash for water treatment (arsenic removal). *Environ. Eng. Manag. J.* **2009**, *8*, 895–900. [CrossRef]
13. Chang, J.; Wang, H.; Zhang, J.; Xue, Q.; Chen, H. New insight into adsorption and reduction of hexavalent chromium by magnetite: Multi-step reaction mechanism and kinetic model developing. *Colloids Surf. A Physicochem. Eng. Asp.* **2021**, *611*, 125784. [CrossRef]
14. Yadav, S.; Yadav, A.; Goyal, G.; Dhawan, M.; Kumar, V.; Yadav, A.; Dhankar, R.; Sehrawat, N.; Chhikara, S. Fly ash-based adsorption for hexavalent chromium removal in aqueous systems: A promising eco-friendly technique. *Orient. J. Chem.* **2024**, *4*, 182–193. [CrossRef]
15. Elabbas, S.; Adjeroud, N.; Mandi, L.; Berrekhis, F.; Pons, M.N.; Leclerc, J.P.; Ouazzani, N. Eggshell adsorption process coupled with electrocoagulation for improvement of chromium removal from tanning wastewater. *Int. J. Environ. Anal. Chem.* **2022**, *102*, 2966–2978. [CrossRef]
16. Hailemariam, A.; Simranjeet, S.; Femi, E.O.; Daljeet, S.D.; Dhakshnamoorthy, M.; Nadeem, A.K.; Joginder, S.; Praveen, C.R. Advances in adsorption technologies for hexavalent chromium removal: Mechanisms, materials, and optimization strategies. *Desalination Water Treat.* **2024**, *319*, 100576.
17. Rahaman, M.H.; Islam, M.A.; Islam, M.M.; Rahman, M.A.; Alam, S.M.N. Biodegradable composite adsorbent of modified cellulose and chitosan to remove heavy metal ions from aqueous solution. *Curr. Res. Green Sustain. Chem.* **2021**, *4*, 100119. [CrossRef]
18. Bayuo, J. An extensive review on chromium (vi) removal using natural and agricultural wastes materials as alternative biosorbents. *J. Environ. Health Sci. Eng.* **2021**, *19*, 1193–1207. [CrossRef]
19. Ramírez-Rodríguez, L.C.; Quintanilla-Carvajal, M.X.; Mendoza-Castillo, D.I.; Bonilla-Petriciolet, A.; Jiménez-Junca, C. Preparation and characterization of an electrospun whey protein/polycaprolactone nanofiber membrane for chromium removal from water. *Nanomaterials* **2022**, *12*, 2744. [CrossRef]

20. Fernández-Reyes, B.; Ortiz-Martínez, K.; Lasalde-Ramírez, J.A.; Hernández-Maldonado, A.J. Engineered adsorbents for the removal of contaminants of emerging concern from water. In *Contaminants of Emerging Concern in Water and Wastewater*; Butterworth-Heinemann: Oxford, UK, 2020; pp. 3–45.
21. Chen, D.; Xiao, X.; Yang, K. Removal of phosphate and hexavalent chromium from aqueous solutions by engineered waste eggshell. *RSC Adv.* **2016**, *6*, 35332–35339. [CrossRef]
22. Segneanu, A.-E.; Trusca, R.; Cepan, C.; Mihailescu, M.; Muntean, C.; Herea, D.D.; Grozescu, I.; Salifoglou, A. Innovative low-cost composite nanoadsorbents based on eggshell waste for nickel removal from aqueous media. *Nanomaterials* **2023**, *13*, 2572. [CrossRef]
23. Yaashikaa, P.R.; Senthil Kumar, P.; Karishma, S. Review on biopolymers and composites—Evolving material as adsorbents in removal of environmental pollutants. *Environ Res.* **2022**, *212 Pt A*, 113114. [CrossRef]
24. Orooji, Y.; Nezafat, Z.; Nasrollahzadeh, M.; Kamali, T.A. Polysaccharide-based (nano)materials for Cr(VI) removal. *Int. J. Biol. Macromol.* **2021**, *188*, 950–973. [CrossRef] [PubMed]
25. Alqarni, L.S.; Algethami, J.S.; El Kaim Billah, R.; Alorabi, A.Q.; Alnaam, Y.A.; Algethami, F.K.; Bahsis, L.; Jawad, A.H.; Wasilewska, M.; López-Maldonado, E.A. A novel chitosan-alginate@Fe/Mn mixed oxide nanocomposite for highly efficient removal of Cr (VI) from wastewater: Experiment and adsorption mechanism. *Int. J. Biol. Macromol.* **2024**, *263 Pt 2*, 129989. [CrossRef] [PubMed]
26. Ji, Z.; Zhang, Y.; Wang, H.; Li, C. Research progress in the removal of heavy metals by modified chitosan. *Tenside Surfactants Deterg.* **2022**, *59*, 281–293. [CrossRef]
27. Wang, K.; Zhang, F.; Xu, K.; Che, Y.; Qi, M.; Song, C. Modified magnetic chitosan materials for heavy metal adsorption: A review. *RSC Adv.* **2023**, *13*, 6713–6736. [CrossRef] [PubMed]
28. Park, J.E.; Shin, J.-H.; Oh, W.; Choi, S.-J.; Kim, J.; Kim, C.; Jeon, J. Removal of hexavalent chromium(VI) from wastewater using chitosan-coated iron oxide nanocomposite membranes. *Toxics* **2022**, *10*, 98. [CrossRef]
29. Segneanu, A.E.; Marin, C.N.; Vlase, G.; Cepan, C.; Mihailescu, M.; Muntean, C.; Grozescu, I. Highly efficient engineered waste eggshell-fly ash for cadmium removal from aqueous solution. *Sci. Rep.* **2022**, *12*, 9676. [CrossRef]
30. Nazarudin, M.; Shamsuri, A.; Shamsudin, M. Preparation and physicochemical evaluation of biodegradable magnetic k-carrageenan beads and application for chromium ions pre-concentration. *J. Chil. Chem. Soc.* **2011**, *56*, 891–894. [CrossRef]
31. Taufiq, A.; Hidayat, P.; Hidayat, A. Modified coal fly ash as low cost adsorbent for removal reactive dyes from batik industry. *MATEC Web Conf.* **2018**, *154*, 01037. [CrossRef]
32. Nordin, A.; Ngadi, N.; Othman, N.; Razali, N.; Nabgan, W.; Alam, M.; Syie Luing, W.; An, E. Adsorptive removal of acetylsalicylic acid in wastewater onto crosslinked-chitosan. In *Advances in Engineering Research, Proceedings of the Third International Conference on Separation Technology 2020 (ICoST 2020), Virtual, 15–16 August 2020*; Atlantis Press: Amsterdam, The Netherlands, 2020; Volume 200, pp. 132–137.
33. Ganesan, K.; Ratke, L. Facile preparation of monolithic κ-carrageenan aerogels. *Soft Matter* **2014**, *10*, 3218. [CrossRef]
34. Kalaiselvi, K.; Mohandoss, S.; Ahmad, N.; Khan, M.R.; Manoharan, R.K. Adsorption of Pb^{2+} ions from aqueous solution onto porous kappa-carrageenan/cellulose hydrogels: Isotherm and kinetics study. *Sustainability* **2023**, *15*, 9534. [CrossRef]
35. Sabbagh, F.; Khatir, N.M.; Kiarostami, K. Synthesis and characterization of ***k***-carrageenan/PVA nanocomposite gydrogels in combination with MgZnO nanoparticles to evaluate the catechin release. *Polymers* **2023**, *15*, 272. [CrossRef] [PubMed]
36. Dikmen, Z. Investigation of ion exchange and magnetic properties of magnetically modified zeolite 13X. *Eskişehir Tech. Univ. J. Sci. Technol. A-Appl. Sci. Eng.* **2020**, *21*, 17–19.
37. Abd El-Monaem, E.M.; Eltaweil, A.S.; El-Subruiti, G.M.; Mohy-Eldin, M.S.; Omer, A.M. Adsorption of nitrophenol onto a novel Fe_3O_4-κ-carrageenan/MIL-125(Ti) composite: Process optimization, isotherms, kinetics, and mechanism. *Environ. Sci. Pollut. Res.* **2023**, *30*, 49301–49313. [CrossRef]
38. Marín-Silva, D.A.; Rivero, S.; Pinotti, A. Chitosan-based nanocomposite matrices: Development and characterization. *Int. J. Biol. Macromol.* **2018**, *123*, 189–200. [CrossRef]
39. Kara, A.; Demirbel, E. Kinetic, isotherm and thermodynamic analysis on adsorption of Cr(VI) ions from aqueous solutions by synthesis and characterization of magnetic-poly(divinylbenzene-vinylimidazole) microbeads. *Water Air Soil Pollut.* **2011**, *223*, 2387–2403. [CrossRef] [PubMed]
40. Carvalho, J.; Araujo, J.; Castro, F. Alternative low-cost adsorbent for water and wastewater decontamination derived from eggshell waste: An overview. *Waste Biomass Valor.* **2011**, *2*, 157–167. [CrossRef]
41. Zhai, Q.Z.; Li, X.D. Efficient removal of cadmium (II) with SBA-15 nanoporous silica: Studies on equilibrium, isotherm, kinetics and thermodynamics. *Appl. Water. Sci.* **2019**, *9*, 143. [CrossRef]
42. Ma, L.; Wei, Q.; Chen, Y.; Song, Q.; Sun, C.; Wang, Z.; Wu, G. Removal of cadmium from aqueous solutions using industrial coal fly ash-nZVI. *R. Soc. Open Sci.* **2018**, *5*, 171051. [CrossRef] [PubMed]
43. Argun, M.E. Use of clinoptilolite for the removal of nickel ions from water: Kinetics and thermodynamics. *J. Hazard. Mater.* **2008**, *150*, 587–595. [CrossRef]
44. Mokgehle, T.; Gitari, W.; Tavengwa, N. Synthesis and characterization of zeolites produced by ultrasonication of coal fly ash/NaOH slurry filtrates. *S. Afr. J. Chemistry. Suid-Afr. Tydskr. Vir Chem.* **2020**, *73*, 64–69.
45. Moosa, A.A.; Mousa Ridha, A.; Kadhim, N.A. Use of biocomposite adsorbents for the removal of methylene blue dye from aqueous solution. *Am. J. Mater. Sci.* **2016**, *6*, 135–146.

46. Rajam, M.; Pulavendran, S.; Rose, C.; Mandal, A.B. Chitosan nanoparticles as a dual growth factor delivery system for tissue engineering applications. *Int. J. Pharm.* **2011**, *410*, 145–152. [CrossRef] [PubMed]
47. Mohan, S.; Gandhimathi, R. Removal of heavy metal ions from municipal solid waste leachate using coal fly ash as an adsorbent. *J. Hazard. Mater.* **2009**, *169*, 351–359. [CrossRef]
48. Fulazzaky, M.A. Determining the resistance of mass transfer for adsorption of the surfactants onto granular activated carbons from hydrodynamic column. *Chem. Eng. J.* **2011**, *166*, 832–840. [CrossRef]
49. Al-Abbad, E.A.; Al Dwairi, R.A. Removal of nickel (II) ions from water by Jordan natural zeolite as sorbent material. *J. Saudi Chem. Soc.* **2021**, *25*, 101233. [CrossRef]
50. Noble, R.D.; Terry, P.A. Adsorption. In *Principles of Chemical Separations with Environmental Applications*; Cambridge Series in Chemical Engineering; Cambridge University Press: Cambridge, UK, 2004; pp. 182–213.
51. Annane, K.; Lemlikchi, W.; Tingry, S. Efficiency of eggshell as a low-cost adsorbent for removal of cadmium: Kinetic and isotherm studies. *Biomass Convers. Biorefin.* **2021**, *13*, 6163–6174. [CrossRef]
52. Lei, T.; Li, S.-J.; Jiang, F.; Ren, Z.-X.; Wang, L.-L.; Yang, X.-J.; Tang, L.-H.; Wang, S.-X. Adsorption of cadmium ions from an aqueous solution on a highly stable dopamine-modified magnetic nano-adsorbent. *Nanoscale Res. Lett.* **2019**, *14*, 352. [CrossRef] [PubMed]
53. Anah, L.; Astrini, N. Influence of pH on Cr(VI) ions removal from aqueous solutions using carboxymethyl cellulose-based hydrogel as adsorbent. *IOP Conf. Ser. Earth Environ. Sci.* **2017**, *60*, 012010. [CrossRef]
54. Naiya, T.K.; Das, S.K. Removal of Cr(VI) from aqueous solution using fly ash of different sources. *Desalination Water Treat.* **2015**, *57*, 5800–5809. [CrossRef]
55. Pandey, P.K.; Sharma, S.K. Removal of Cr(VI) and Pb(II) from Wastewater by ZeoliteNaX in Fixed Bed Column. *Water Conserv. Sci. Eng.* **2017**, *2*, 61–65. [CrossRef]
56. Ehsanpour, S.; Samani, M.R.; Toghraie, D. Removal of chromium (VI) from aqueous solution using eggshell/poly pyrrole composite. *Alex. Eng. J.* **2023**, *64*, 581–589. [CrossRef]
57. Abdul Latif, A.F.; Yee, L.S.; Muhamad, M.S.; Chuan, L.T.; Basri, H. Natural adsorbent made from eggshells for removal of chromium (VI) in water. *Biointerface Res. Appl. Chem.* **2022**, *12*, 518–552.
58. Zendelska, A.; Golomeova, M.; Jakupi, Š.; Lisičkov, K.; Kuvendžiev, S.; Marinkovski, M. Characterization and application of clinoptilolite for removal of heavy metal ions from water resources. *Geol. Maced.* **2018**, *32*, 21–32.
59. Ayawei, N.; Newton Ebelegi, A.; Wankasi, D. Modelling and interpretation of adsorption isotherms. *J. Chem.* **2017**, *2017*, 3039817. [CrossRef]
60. Mnasri-Ghnimi, S.; Frini-Srasra, N. Removal of heavy metals from aqueous solutions by adsorption using single and mixed pillared clays. *Appl. Clay Sci.* **2019**, *179*, 105151. [CrossRef]
61. Krishna Kumar, A.S.; Warchol, J.; Matusik, J.; Tseng, W.L.; Rajesh, N.; Bajda, T. Heavy metal and organic dye removal via a hybrid porous hexagonal boron nitride-based magnetic aerogel. *npj Clean Water* **2022**, *5*, 24. [CrossRef]
62. Mignardi, S.; Archilletti, L.; Medeghini, L.; De Vito, C. Valorization of eggshell biowaste for sustainable environmental remediation. *Sci. Rep.* **2020**, *10*, 2436. [CrossRef]
63. Darweesh, M.A.; Elgendy, M.Y.; Ayad, M.I.; Ahmed, A.M.M.; Elsayed, N.M.K.; Hammad, W.A. Adsorption isotherm, kinetic, and optimization studies for copper (II) removal from aqueous solutions by banana leaves and derived activated carbon. *S. Afr. J. Chem. Eng.* **2022**, *40*, 10–20. [CrossRef]
64. Ouyang, D.; Zhuo, Y.; Hu, L.; Zeng, Q.; Hu, Y.; He, Z. Research on the adsorption behavior of heavy metal ions by porous material prepared with silicate tailings. *Minerals* **2019**, *9*, 291. [CrossRef]
65. Nordstrand, J.; Dutta, J. Dynamic Langmuir model: A simpler approach to modeling capacitive deionization. *J. Phys. Chem. C* **2019**, *123*, 16479–16485. [CrossRef]
66. Sahmoune, M.N. Evaluation of thermodynamic parameters for adsorption of heavy metals by green adsorbents. *Environ. Chem. Lett.* **2019**, *17*, 697–704. [CrossRef]
67. Wang, J.; Guo, X. Adsorption kinetic models: Physical meanings, applications, and solving methods. *J. Hazard. Mater.* **2020**, *390*, 122156. [CrossRef] [PubMed]
68. Gorzin, F.; Bahri Rasht Abadi, M. Adsorption of Cr(VI) from aqueous solution by adsorbent prepared from paper mill sludge: Kinetics and thermodynamics studies. *Adsorpt. Sci. Technol.* **2017**, *36*, 149–169. [CrossRef]
69. Khan, M.N.; Ullah, H.; Naeem, S.; Uddin, J.; Hamid, Y.; Ahmad, W.; Ding, J. Remediation of emerging heavy metals from water using natural adsorbent: Adsorption performance and mechanistic insights. *Sustainability* **2021**, *13*, 8817. [CrossRef]
70. Król, M.K.; Jeleń, P. The Effect of Heat Treatment on the Structure of Zeolite A. *Materials* **2021**, *14*, 4642. [CrossRef] [PubMed]
71. Velarde, L.; Sadegh Nabavi, M.; Escalera, E.; Antti, M.-L.; Akhtar, F. Adsorption of heavy metals on natural zeolites: A review. *Chemosphere* **2023**, *328*, 138508. [CrossRef]
72. Hlihor, R.M.; Bulgariu, L.; Sobariu, D.L.; Diaconu, M.; Tavares, T.; Gavrilescu, M. Recent advances in biosorption of heavy metals: Support tools for biosorption equilibrium, Kinetics and mechanism. *Rev. Roum. Chim.* **2014**, *59*, 527–538.
73. Azeman, N.H.; Arsad, N.; A Bakar, A.A. Polysaccharides as the Sensing Material for Metal Ion Detection-Based Optical Sensor Applications. *Sensors* **2020**, *20*, 3924. [CrossRef]
74. Liew, J.W.Y.; Loh, K.S.; Ahmad, A.; Lim, K.L.; Wan Daud, W.R. Synthesis and characterization of modified κ-carrageenan for enhanced proton conductivity as polymer electrolyte membrane. *PLoS ONE* **2017**, *12*, e0185313. [CrossRef]

75. Pietrelli, L.; Francolini, I.; Piozzi, A.; Sighicelli, M.; Silvestro, I.; Vocciante, M. Chromium(III) removal from wastewater by chitosan flakes. *Appl. Sci.* **2020**, *10*, 1925. [CrossRef]
76. Akalin, G.A. The preparation of montmorillonite/carrageenan-composite hydrogel for chromium (VI) removal from aqueous solution. *Eurasia Proc. Sci. Technol. Eng. Math. (EPSTEM)* **2022**, *18*, 72–80. [CrossRef]
77. Ghasemi, R.; Sayahi, T.; Tourani, S.; Kavianimehr, M. Modified magnetite nanoparticles for hexavalent chromium removal from water. *J. Dispers. Sci. Technol.* **2015**, *37*, 1303–1314. [CrossRef]
78. Beheshti, H.; Irani, M.; Hosseini, L.; Rahimi, A.; Aliabadi, M. Removal of Cr (VI) from aqueous solutions using chitosan/MWCNT/Fe_3O_4 composite. *Chem. Eng. J.* **2016**, *284*, 557–564. [CrossRef]
79. Álvarez, A.M.; Guerrón, D.B.; Montero Calderón, C. Natural zeolite as a chromium VI removal agent in tannery effluents. *Heliyon* **2021**, *7*, e07974. [CrossRef]
80. Kurniawan, T.A.; Othman, M.H.D.; Adam, M.R.; Liang, X.; Goh, H.; Anouzla, A.; Sillanpää, M.; Mohyuddin, A.; Chew, K.W. Chromium removal from aqueous solution using natural clinoptilolite. *Water* **2023**, *15*, 1667. [CrossRef]
81. Jyoti; Singh, S.; Das, S.; Srivastava, S. Comparative study for removal of toxic hexavalent chromium by zinc oxide nanoparticles, chitosan, chitin and zinc-chitosan nano-biocomposite. *Environ. Technol. Innov.* **2023**, *32*, 103310. [CrossRef]
82. Wu, J.; Zhao, Y.; Dai, J.; Yang, B.; Zhang, Y.; Pu, X. Removal of hexavalent chromium from aqueous by chitosan-stabilized FeS. *Water-Energy Nexus* **2023**, *6*, 64–73. [CrossRef]
83. Gokila, S.; Gomathi, T.; Sudha, P.N.; Anil, S. Removal of the heavy metal ion chromiuim(VI) using chitosan and alginate nanocomposites. *Int. J. Biol. Macromol.* **2017**, *104*, 1459–1468. [CrossRef] [PubMed]
84. Meera Sheriffa Begum, K.M.; Anantharaman, N. Removal of chromium(VI) ions from aqueous solutions and industrial effluents using Magnetic Fe_3O_4 nano-particles. *Adsorpt. Sci. Technol.* **2009**, *27*, 701–722. [CrossRef]
85. Chagas, P.M.B.; Caetano, A.A.; Rossi, M.A.; Gonçalves, M.A.; de Castro Ramalho, T.; Corrêa, A.D.; do Rosário Guimarães, I. Chitosan-iron oxide hybrid composite: Mechanism of hexavalent chromium removal by central composite design and theoretical calculations. *Environ. Sci. Pollut. Res.* **2019**, *26*, 15973–15988. [CrossRef]
86. Qasem, N.A.A.; Mohammed, R.H.; Lawal, D.U. Removal of heavy metal ions from wastewater: A comprehensive and critical review. *npj Clean Water* **2021**, *4*, 36. [CrossRef]
87. Vakili, M.; Deng, S.; Cagnetta, G.; Wang, W.; Meng, P.; Liu, D.; Yu, G. Regeneration of chitosan-based adsorbents used in heavy metal adsorption: A review. *Sep. Purif. Technol.* **2019**, *224*, 373–387. [CrossRef]
88. Kumar, P.A.; Ray, M.; Chakraborty, S. Hexavalent chromium removal from wastewater using aniline formaldehyde condensate coated silica gel. *J. Hazard. Mater.* **2007**, *143*, 24–32. [CrossRef] [PubMed]
89. Bayuo, J.; Abukari, M.A.; Pelig-Ba, K.B. Desorption of chromium (VI) and lead (II) ions and regeneration of the exhausted adsorbent. *Appl. Water Sci.* **2020**, *10*, 171. [CrossRef]

Disclaimer/Publisher's Note: The statements, opinions and data contained in all publications are solely those of the individual author(s) and contributor(s) and not of MDPI and/or the editor(s). MDPI and/or the editor(s) disclaim responsibility for any injury to people or property resulting from any ideas, methods, instructions or products referred to in the content.

polymers

MDPI

Article

Lignin-Furanic Rigid Foams: Enhanced Methylene Blue Removal Capacity, Recyclability, and Flame Retardancy

Hugo Duarte [1,*], João Brás [1], El Mokhtar Saoudi Hassani [2], María José Aliaño-Gonzalez [1,3], Solange Magalhães [4], Luís Alves [4], Artur J. M. Valente [5], Alireza Eivazi [6], Magnus Norgren [6], Anabela Romano [1] and Bruno Medronho [1,6]

[1] MED—Mediterranean Institute for Agriculture, Environment and Development, CHANGE–Global Change and Sustainability Institute, Faculdade de Ciências e Tecnologia, Universidade do Algarve, Campus de Gambelas, 8005-139 Faro, Portugal; mariajose.aliano@gm.uca.es (M.J.A.-G.); aromano@ualg.pt (A.R.); bfmedronho@ualg.pt (B.M.)
[2] Laboratory of Engineering Electrochemistry, Modelling, and Environment, Department of Chemistry, Faculty of Sciences Dhar Mahraz, Sidi Mohamed Ben Abdellah University, Fez 30050, Morocco
[3] Analytical Chemistry Department, University of Cádiz, 11510 Puerto Real, Spain
[4] University of Coimbra, CERES, Department of Chemical Engineering, Pólo II–R. Silvio Lima, 3030-790 Coimbra, Portugal; solangemagalhaes@eq.uc.pt (S.M.)
[5] CQC-IMS, Department of Chemistry, University of Coimbra, 3004-535 Coimbra, Portugal; avalente@ci.uc.pt
[6] Surface and Colloid Engineering, FSCN Research Center, Mid Sweden University, SE-851 70 Sundsvall, Sweden; alireza.eivazi@miun.se (A.E.); magnus.norgren@miun.se (M.N.)
* Correspondence: hmduarte@ualg.pt

Abstract: Worldwide, populations face issues related to water and energy consumption. Water scarcity has intensified globally, particularly in arid and semiarid regions. Projections indicate that by 2030, global water demand will rise by 50%, leading to critical shortages, further intensified by the impacts of climate change. Moreover, wastewater treatment needs further development, given the presence of persistent organic pollutants, such as dyes and pharmaceuticals. In addition, the continuous increase in energy demand and rising prices directly impact households and businesses, highlighting the importance of energy savings through effective building insulation. In this regard, tannin-furanic foams are recognized as promising sustainable foams due to their fire resistance, low thermal conductivity, and high water and chemical stability. In this study, tannin and lignin rigid foams were explored not only for their traditional applications but also as versatile materials suitable for wastewater treatment. Furthermore, a systematic approach demonstrates the complete replacement of the tannin-furan foam phenol source with two lignins that mainly differ in molecular weight and pH, as well as how these parameters affect the rigid foam structure and methylene blue (MB) removal capacity. Alkali-lignin-based foams exhibited notable MB adsorption capacity (220 mg g^{-1}), with kinetic and equilibrium data analysis suggesting a multilayer adsorption process. The prepared foams demonstrated the ability to be recycled for at least five adsorption-desorption cycles and exhibited effective flame retardant properties. When exposed to a butane flame for 5 min, the foams did not release smoke or ignite, nor did they contribute to flame propagation, with the red glow dissipating only 20 s after flame exposure.

Keywords: lignin; polyphenols; tannins; water treatment; biobased materials; foams; methylene blue

1. Introduction

To mitigate human hazards and improve environmental health, there is an increasing need to efficiently remove pollutants from wastewater effluents before their discharge into the environment. The control of water contamination has become a great challenge due to toxic heavy metals, organic dyes, and other persistent organic pollution from several industries, such as textile, cosmetic, paper, and pharmaceutical [1,2]. With only 1% of accessible water for human and industrial needs, water scarcity has become a significant issue. The 2007 report by the United Nations FAO identifies that water stress could affect

two-thirds of the world's population. To alleviate such stress, wastewater remediation could be a suitable solution by recovering water from industrial activities [3]. In this regard, several biological, chemical, and physical methods have been developed to minimize their spread and release into aquifers [1,2,4]. Among these, adsorption is one of the most attractive methods in wastewater treatment due to its cost effectiveness, facile operation, and broad applicability in contrast to other existing technologies [4].

Ideally, to minimize the environmental impact of adsorption processes, an adsorbent should be inert, effective in removing the target molecule(s), made from renewable and abundant materials, and require minimal processing before use [5]. In this regard, polyphenol-based rigid foams are materials mainly obtained from natural products, known for their fire resistance, adsorption performance, and easy preparation [6–8]. Among the different polyphenols, tannin-based biosorbents are known to have a natural affinity toward dyes, heavy metals, pharmaceutical agents, and surfactants from contaminated waters [7,9]. Moreover, these systems can selectively accumulate important precious metals from aqueous streams or enhance their adsorption capacity for various compounds when functionalized [5,10–12].

Another very appealing polyphenol often used in wastewater treatment is lignin [1,13]. Lignin is the second most abundant renewable biomolecule on Earth and is regarded as a sustainable aromatic feedstock that can compete and substitute for petroleum-based phenol [14]. Nowadays, most of the available lignin is obtained from the chemical pulping of wood using the kraft and the sulfite cooking processes [15]. The pulping process from which lignin is obtained essentially dictates the content and type of functional groups, such as phenolic, carboxyl, hydroxyl, and sulfonate. With its high carbon content, biodegradability, antioxidant activity, thermal stability, and advantageous stiffness, lignin is seen as an attractive material for several applications, including drug delivery systems, emulsion stabilization, rechargeable batteries, and carbon-based materials [16–19].

Apart from lignin, lignocellulosic biomass is the main feedstock for furfural, the main precursor to produce furfuryl alcohol [20]. The reaction between furfuryl alcohol and natural polyphenolic sources, such as lignin and tannins, has been sought to produce biobased materials. Tannin-furan (TF) foams have been studied as suitable biobased alternatives, mainly for the replacement of fossil-based materials as insulators or flame retardants [21–24]. This is particularly relevant for energy savings purposes, which is becoming a global priority. Effective building insulation emerges as an important solution, offering a substantial reduction in energy consumption for heating and cooling as the energy needed to achieve thermal comfort accounts for approximately 50% of the total residence consumption [24]. By improving the thermal efficiency of buildings, insulation helps to maintain consistent indoor temperatures, thereby reducing the need for excessive energy use. This not only lowers energy bills but also contributes to a more sustainable and environmentally friendly approach to energy consumption. Investing in high-quality insulation is, therefore, essential for mitigating the economic impact of rising energy prices and enhancing overall energy efficiency.

Polyphenol-based rigid foams have been prepared via different procedures and extensively tested, demonstrating desirable characteristics, such as good mechanical strength and flame retardant properties [25,26]. Tannins and lignin have been incorporated into foam formulations in distinct ways: as substitutes for fossil-derived phenol, to replace formaldehyde, or to enhance the foam's mechanical and thermal properties [22,27,28]. However, a gap in the literature shows that no comparisons have been made regarding how the addition of tannin or different lignins to furanic foams affects their dye removal capacity. In the present work, novel formaldehyde-free tannin- and lignin-furan-based foams with several desirable characteristics were prepared. Using the TF foam as standard, kraft or alkali lignin was progressively added to investigate how lignin inclusion in the foam formulation would affect the adsorption performance of each foam [24]. The biobased foams were successfully characterized and tested for the removal of a model dye (i.e., methylene blue) from aqueous media, as the adsorption process was studied in terms of

the influence of dye concentration, time, and pH. Several kinetic and isotherm models were applied to understand the mechanism of adsorption and the rate-limiting step of the process. The foam recyclability and reusability were also evaluated. This study also aims to present formaldehyde-free rigid foams as a multipurpose material to be used as a recyclable adsorbent, with a second life application as a flame retardant material.

2. Materials and Methods

2.1. Materials

Phenol (>99.5%), formaldehyde (37%), pentane (99%), p-toluenesulfonic acid (≥98.5%), sodium bicarbonate (>99%), sodium chloride (>99.5%), potassium chloride (>99.5%), methylene blue, hydrochloric acid (37%), and "alkali" lignin (Mw = 10 kDa, pH 10.5, sulfur < 3.6 wt%) were purchased from Sigma Aldrich (St. Louis, MO, USA), while "kraft" lignin (UPM BioPiva^{TM} 100, Mw = 5 kDa, pH 2.5–4.5, sulfur 0.5–3 wt%) was acquired from UPM Biochemicals. The "Opera fruity" (condensed tannin extract from red fruits with a total polyphenol content > 65 wt%) was obtained from Proenol, SA (Porto, Portugal). Ethanol (96%) was acquired from Aga (Lisbon, Portugal), sodium carbonate anhydrous (99.7%) from José Manuel Gomes dos Santos, Lda (Lisbon, Portugal), and sodium hydroxide (≥98%), disodium hydrogen phosphate (>99%), and potassium dihydrogen phosphate (>99%) from Panreac (Barcelona, Spain).

2.2. Preparation of the Tannin and Lignin-Based Rigid Foams

The foams were prepared at room temperature, following a standard procedure with slight modifications (see Table 1 for details) consisting of mixing approximately 2.5 g of polyphenol (i.e., tannin, lignin, or different ratios of both) with distilled water (i.e., 1 mL) inside a flexible plastic mold of 2 cm^3 with the help of a glass rod, until a homogenous suspension was obtained. Then, further lignin or tannin was added in increasing amounts (i.e., 0.2, 1.25, and 2.5 g) to the suspension and mixed until homogeneity. Furfuryl alcohol (i.e., 1.4 mL) was added, and the solution was mixed until a homogenous mixture was obtained. After this, pentane was added as the blowing agent. p-Toluenosulfonic acid (p-TSA) (ca. 0.9 g) was then added in crystal form and mixed until total dissolution was observed. Once homogenized, the mixture was left to settle for approximately 20 to 30 s as the foaming reaction initiated and evolved. After the reaction completion, the "fresh" foam was left resting for approximately 10 min to ensure no morphological changes. The foams were then removed from the plastic mold and cured overnight (for 12 h) in an oven at 60 °C [29]. It is important to note that given the success in totally replacing the tannin with lignin, the foams chosen for further characterization were those with only one phenol source (highlighted in Table 1). As mentioned above, the tannin-furan foam (TF) served as the control, as it was the starting foam in which tannin was progressively replaced by lignin. Nevertheless, preliminary assays demonstrated that the addition of tannin does not significantly improve dye removal.

Table 1. Composition of all the prepared foams, showing how the amount of the phenol source was changed, including the mixtures of tannin and lignin.

Foam	*Tannin* (g)	*Kraft Lignin* (g)	*Alkali Lignin* (g)	*Distiled Water* (mL)	*Furturyl Alcohol* (mL)	*n-Pentane* (mL)	*p-Toluenesulfonic Acid* (g)
Tannin (TF)	2.4	0	0	1	1.4	0.6	0.9
	2.5	0	0	1	1.4	0.6	0.9
	2.6	0	0	1	1.4	0.6	0.9
	2.8	0	0	1	1.4	0.6	0.9
	3.0	0	0	1	1.4	0.6	0.9

Table 1. *Cont.*

Foam	Tannin (g)	Kraft Lignin (g)	Alkali Lignin (g)	Distiled Water (mL)	Furturyl Alcohol (mL)	n-Pentane (mL)	p-Toluenesulfonic Acid (g)
Tannin + kraft lignin	2.4	0.1	0	1	1.4	0.6	0.9
	2.4	0.2	0	1	1.4	0.6	0.9
	2.4	0.5	0	1	1.4	0.6	0.9
	1.25	1.25	0	1	1.4	0.6	0.9
Kraft lignin (KF)	0	2.4	0	1	1.4	0.6	0.9
	0	2.5	0	1	1.4	0.6	0.9
	0	2.6	0	1	1.4	0.6	0.9
	0	2.8	0	1	1.4	0.6	0.9
	0	3.0	0	1	1.4	0.6	0.9
Tannin + alkali lignin	2.4	0	0.1	1	1.4	0.6	0.9
	2.4	0	0.2	1	1.4	0.6	0.9
	2.4	0	0.5	1	1.4	0.6	0.9
	1.25	0	1.25	1	1.4	0.6	0.9
Alkali lignin (AF)	0	0	2.4	1	1.4	0.6	0.9
	0	0	2.5	1	1.4	0.6	0.9
	0	0	2.5	1	1.4	0.6	1.8
	0	0	2.6	1	1.4	0.6	0.9
	0	0	2.8	1	1.4	0.6	0.9
	0	0	3.0	1	1.4	0.6	0.9

Foam Washing

Before usage in adsorption kinetics experiments, foams were weighed, measured, and cut. The foams, of approximately 1 g, were immersed in 100 mL distilled water and left overnight to rinse any chemical that might not have reacted. The water was changed after 12 h, and the process repeated once. After the second rising, the foams were dried in an oven at 60 °C for 12 h. UV-vis was used to follow the efficiency of rinsing. The analyzed spectra were identical for all the effluents from the washed foams, presenting an absorption maximum of approximately 220–290 nm. Identified maxima adsorption is mainly related to unreacted tannin or lignin and residual furfuryl alcohol (<1 wt% (*w*/*w*)) [30]. Foams were stored in a desiccator until further analysis.

2.3. Foam Characterization Methodology

IR analyses were performed using a Bruker Tensor 27 (Billerica, MA, USA). Specimens were prepared from the different dried foam powders and pressed with KBr, forming pellets, and analyzed from 600 to 4000 cm^{-1} with 25 scans and a 4 cm^{-1} interval at room temperature [31].

Field emission scanning electron microscopy (FE-SEM) imaging of the samples was carried out using a TESCAN (Brno, Czechia) MAIA3 electron microscope in secondary electrons mode. The accelerating voltage was 3 kV, and the work distance was set to 8 mm. Before image acquisition, the samples were coated with 6 nm Iridium using a Quorum Q150T ES [32].

X-ray diffraction (XRD) was conducted at room temperature using a Bruker D2 Phaser diffractometer with Cu Kα radiation (wavelength 1.54 Å) at 30 kV and 10 mA, in θ–2θ geometry. The increment was fixed at 0.02° [32].

Fire retardancy and self-extinguishing properties of the prepared foams were assessed by a homemade flame test and thermogravimetric analyses (TGA). TGA was performed using a simultaneous DSC-TGA thermal analyzer (TA Instrument SDT Q600, New Castle, DE, USA). The samples were heated from room temperature up to 1200 °C, at a rate of 10 °C min^{-1}, under a nitrogen atmosphere. Flame retardancy tests were executed by exposing a foam (2 cm^3) to a Bunsen burner with a butane flame (over 1500 °C) for 5 min.

After cutting the gas flow, samples continued to be recorded to estimate how long it would take for a flame or glow to dissipate [24].

2.4. Adsorption-Desorption Experiments

2.4.1. Adsorption Kinetics

The adsorption batch experiments were carried out in 250 mL Erlenmeyer flasks at room temperature, where 100 mg of grounded foam was added per 100 mL of methylene blue buffered solution (3×10^{-5} M, pH 7.2 $\pm$ 0.2). Solutions were placed in a Edmund Bühler, (Bodelshausen, Germany) rotary mixer at 125 rpm, and aliquot samples were periodically taken, at least as duplicates. To make sure no foam powder fragments interfere with the UV-vis measurements, all aliquots were centrifuged for 2 min at 12,000 rpm (Mikro Hettic 200) before measuring the absorbance in a UV-vis spectrometer (T70+ UV/VIS Spectrometer, PG instruments Ltd.) at 664 nm (i.e., methylene blue's maximum absorption). The quantity of adsorbed dye (q_e) per gram of adsorbate in equilibrium conditions (mg g^{-1}) was calculated from Equation (1) [4,33],

$$q_e = \frac{(C_0 - C_e)V}{W} \quad (1)$$

Here, C_0 (mg L^{-1}) is the initial concentration of dye in solution, C_e (mg L^{-1}) is the equilibrium concentration of adsorbate remaining in solution, V (L) is the volume of the solution, and W(g) is the adsorbent's mass.

The removal efficiency (%R) was assessed using Equation (2),

$$\%R = \frac{C_0 - C}{C_0} \cdot 100 = \frac{C_{ads}}{C_0} \cdot 100 \quad (2)$$

where C_{ads} (mg L^{-1}) is the concentration of adsorbed dye and C (mg L^{-1}) is the equilibrium concentration of the dye in solution [33].

The obtained adsorption kinetic data at neutral pH for 5, 10, 20, and 50 mg L^{-1} of MB were also modeled using pseudo-first-order (PFO) and pseudo-second-order (PSO) equations, respectively, as follows,

$$q_t = q_e\left(1 - e^{-k_1 t}\right) \quad (3)$$

$$q_t = \frac{k_2 q_e^2 t}{1 + k_2 q_e t} \quad (4)$$

where q_t (mg g^{-1}) is the amount of adsorbate at time t (min), k_1 (min^{-1}) is the rate constant for the PFO, and k_2 (g mg^{-1} min^{-1}) for the PSO [33]. Data were represented as the averages calculated from three independent measurements and corresponding standard deviation.

2.4.2. Adsorption in Equilibrium

For the evaluation of the isotherms, equilibrium batch experiments were performed for 24 h in 100 mL Erlenmeyer flasks loaded with 10 mL of 1, 2, 5, 10, 20, 30, and 50 mg L^{-1} of MB diluted with a buffer to control the pH. The AF foam was further tested in 75, 100, 150, 200, and 250 mg L^{-1} MB solution. Before measuring the absorbance of the solution, samples were centrifuged and diluted if necessary. Each experiment was performed in duplicate. The experimental data were fitted using the equations of Langmuir, Freundlich, Brunauer–Emmet–Teller (BET), and Dubinin–Radushkevich (D-R). The Langmuir isotherm model (Equation (5)) assumes a monolayer distribution of the adsorbate, a homogeneous distribution of the adsorption sites, a constant energy of adsorption, and neglects interactions between adsorbate molecules. It also assumes that the maximum adsorption corresponds to a monosaturated layer of adsorbate molecules on the surface of the adsorbent [34,35].

$$q_e = \frac{q_m K_L C_e}{1 + K_L C_e} \quad (5)$$

Here and for the following equations, q_m (mg g^{-1}) is the maximum adsorption capacity per unit weight of adsorbent and K_L (L mg^{-1}) is the Langmuir constant.

The Freundlich model (Equation (6)) is not restricted to monolayer formation and considers the possibility of multilayer adsorption. It represents a nonlinear adsorption process considering the heterogeneity of the surface of the adsorbent [34–36].

$$qe = K_F {C_e}^{1/n} \quad (6)$$

K_F ($L^{1/n}$ $mg^{1-1/n}$ g^{-1}) is the Freundlich constant, and n is the Freundlich exponent, which is dimensionless. The BET (Equation (7)) model is a theoretical multilayer physical adsorption formalism, assuming homogenous adsorption where the adsorption energy of the first layer differs from the other layers. The model also takes a pseudo-steady state into account, a dynamic equilibrium where the rates of adsorption and desorption are equivalent [34,37].

$$q_e = \frac{q_m K_L C_e}{(1 - K_S C_e)[1 + (K_L - K_S) C_e]} \quad (7)$$

K_L (L mg^{-1}) is the monolayer adsorption equilibrium constant, and K_S is the multilayer adsorption equilibrium constant (L mg^{-1}). Note that when K_L = 0, the BET isotherm is reduced to the Langmuir model, representing the case of a monolayer adsorption process, and K_L becomes the Langmuir constant.

Lastly, the D-R isotherm model is usually used to express an adsorption mechanism with a Gaussian energy distribution into heterogeneous surfaces [34,36].

$$q_e = q_m - e^{-K_D \varepsilon^2} \quad (8)$$

K_D (mol^2 kJ^{-2}) is the D-R model constant, and ε (kJ mol^{-1}) is the adsorption potential which can be calculated using Equation (9) [34],

$$\varepsilon = RTln\frac{C_s}{C_e} \quad (9)$$

where C_s (mg L^{-1}) is the solubility of the adsorbate and C_e (mg L^{-1}) is the equilibrium concentration of adsorbate remaining in solution. The mean free energy, E (kJ mol^{-1}), can be calculated using Equation (10),

$$E = \frac{1}{\sqrt{2K_D}} \quad (10)$$

This model is commonly applied for the determination of a mainly physical (E < 8 kJ mol^{-1}) or chemical (8 < E < 16 kJ mol^{-1}) adsorption process.

2.4.3. Adsorption in Acidic and Alkaline pH Conditions

To study the effect of pH in MB adsorption, the point of zero charge was first calculated. Briefly, approximately 0.3 g of powdered foam was added to a solution of fixed pH and measured again after 24 h. After this, equilibrium tests were performed as previously described at different pH values for a fixed MB concentration of 50 mg L^{-1}. The AF foam was then tested at pH 7 and pH 10 up to 250 mg L^{-1} of MB [4,38].

2.4.4. Desorption Tests

To evaluate the reusability and recyclability of the most promising foams, the remaining solution after the adsorption experiments was discarded, and the material containing adsorbed MB was dried overnight in an oven at 60 °C. After drying, a certain amount of foam was weighed, and ethanol, acetone, or 0.1 M HCl was added, keeping a ratio of

100 mg of foam per 100 mL of solution. The mixture was kept under agitation for 24 h at 125 rpm, and the absorbance of the solution was measured at 664 nm. The process was repeated five times and performed in duplicate [39].

3. Results and Discussion

3.1. Rigid Foam Synthesis and Adsorption Dependence from Lignin Type and Concentration

Tannin-furan (TF) foams and lignin composites are well known as adsorbents [4,11,40,41]. The foams produced result from a crosslink between the phenol source (tannin or lignin), furfuryl alcohol, and p-TSA acid, originating a porous and solid material (Figure 1a,b) [23].

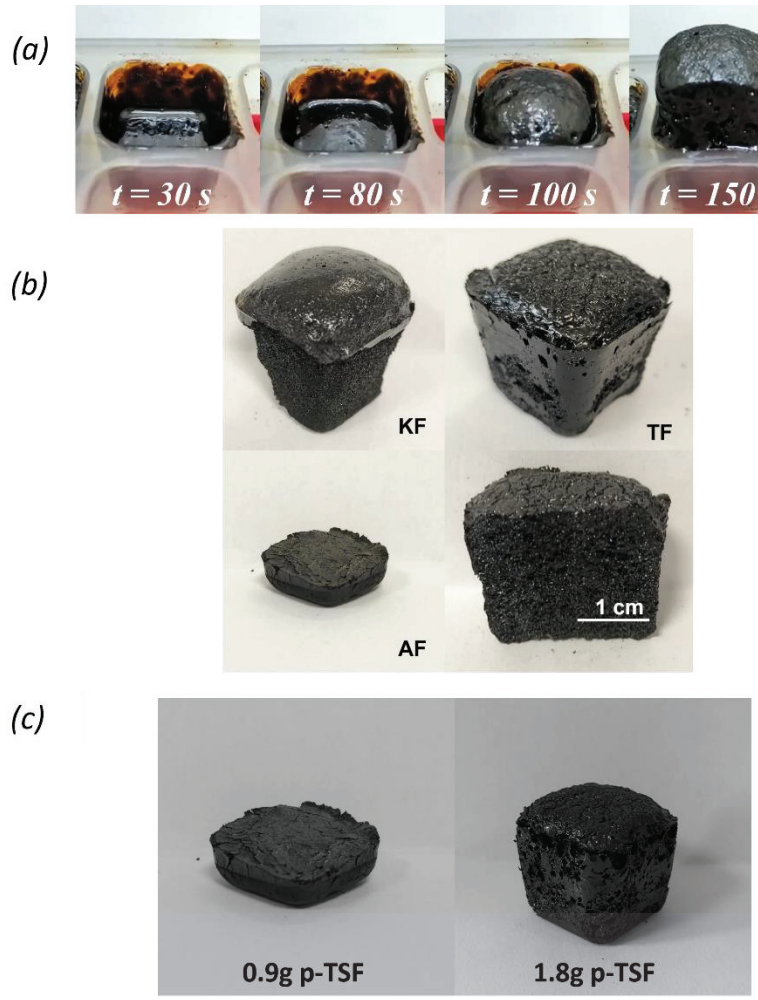

Figure 1. (**a**) Time development of a typical AF foam prepared with 0.9 g or 1.8 g of p-TSA acid; (**b**) Images of the prepared foams after unmolding, and cross section from the TF foam; (**c**) AF foam prepared using the standard procedure by adding 0.9 g of p-TSA, without the capacity to self-blow (**left**), in contrast to the same formulation when the amount of p-TSA was doubled, allowing the foam to self-blow (**right**) (KF—kraft-furan, AF—alkali-furan, and TF—tannin-furan foam).

It is of notice the difference between kraft and alkali-based foams; as the alkali foam does not self-blows, a denser rigid foam is thus obtained (Figure 1c). In fact, each additive showed marked differences in the foam capacity to self-blow, which was reflected in their density. The TF foam presented a density of 0.325 gcm^{-3}, while the kraft lignin foam (KF) density was 0.285 gcm^{-3}. Similar tannin or lignin-based foams were obtained with comparable densities, ranging from 0.08 gcm^{-3} to 0.32 gcm^{-3}; however, their composition varied slightly by using diethyl ether as a blowing agent, a different tannin, and additives as surfactants, glyoxal or boric acid in addition to p-TSA [22,26]. As expected, due to

its inability to self-blow and obtain a more compact foam, the alkali lignin foam (AF) density was the highest (0.900 gcm^{-3}). This remarkable increase in the foam density is promoted by the increase in lignin content, increasing the viscosity of the initial suspension, which ultimately results in a less porous and denser foam [25]. Moreover, the alkali lignin possesses an alkaline pH (i.e., pH 10.3 at 3 wt%), causing a greater demand for acid to trigger the polymerization reaction. Therefore, increasing the amount of p-TSA acid from 0.9 g to 1.8 g allowed the foam to self-blow.

Scanning electron micrographs of the prepared rigid foams revealed mostly smooth, flat surfaces, in which small particles contribute to differences in roughness and particle size according to the phenol source (Figure 2a–c). Across the literature, rigid foams are often seen through SEM as highly porous structures, which was not the present case given the processing of the foam [24,26,29]. Note that due to its application in a grounded form, all foams were observed as a powder, thus losing their initial porosity and being seen as smooth surfaces.

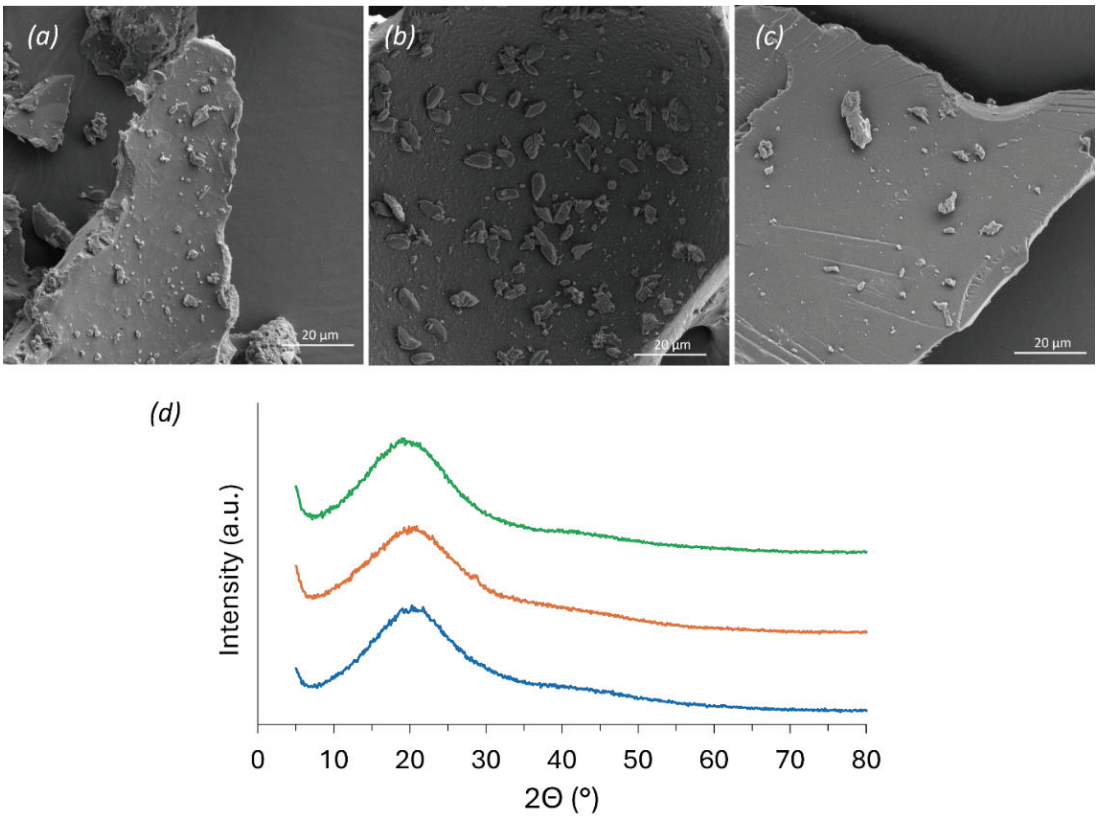

Figure 2. Scanning electron micrographs of KF (**a**), TF (**b**), and AF (**c**) foams; (**d**) XRD patterns for KF (green), TF (orange), and AF (blue) rigid foams.

The evaluation of the crystallinity of the foams only revealed slight differences among them, mostly showing amorphous material with not well-defined Bragg reflections (Figure 2d). The broad reflection present in all foams is characteristic of polyphenols, such as lignin and tannins [42,43]. This broad reflection is less pronounced in the alkali lignin, increasing in intensity when analyzing the alkali lignin-based rigid foam. The variation in intensity can be attributed to the polymerization reaction with furfuryl alcohol and p-TSA acid, which might originate in a less amorphous structure when polymerized.

From an adsorption viewpoint, the kraft lignin addition to the TF foam was observed to decrease its performance, while the alkali lignin addition improved the adsorption performance of the material (Figure 3a). This way, the AF foam prepared with 0.9 g of p-TSA was selected, regardless of not fully self-blowing, since it was the most promising foam for dye adsorption (Figure 3b) and chosen for further characterization.

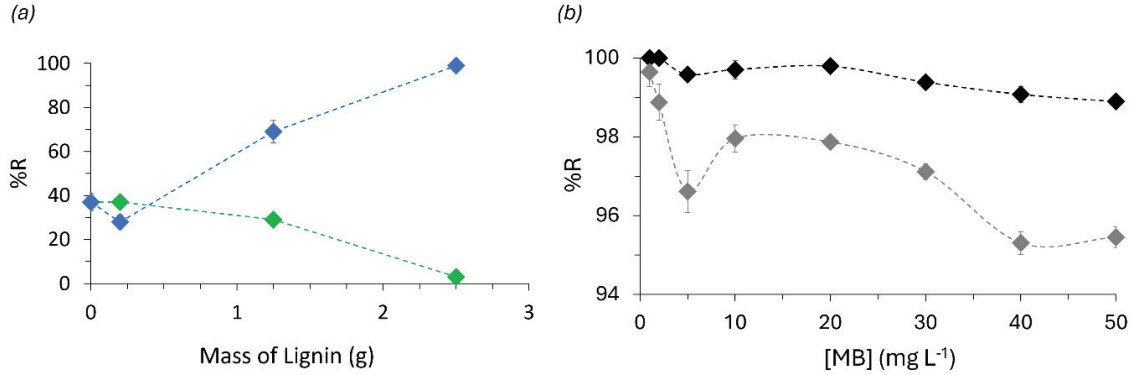

Figure 3. (**a**) MB removal efficiency of tannin-furan foams with increasing concentration of kraft (green) and alkali (blue) lignins; (**b**) AF foam MB removal after 24 h, by adding the standard 0.9 g (black) or 1.8 g (grey) of p-TSA acid during foam preparation.

As mentioned, the electron micrographs of the ground AF foam revealed particles with a mostly smooth nonporous surface, which apparently became denser and homogeneously covered by the adsorbed MB, similar to the observation taken by Budnyak et al. (Figure 4) [4].

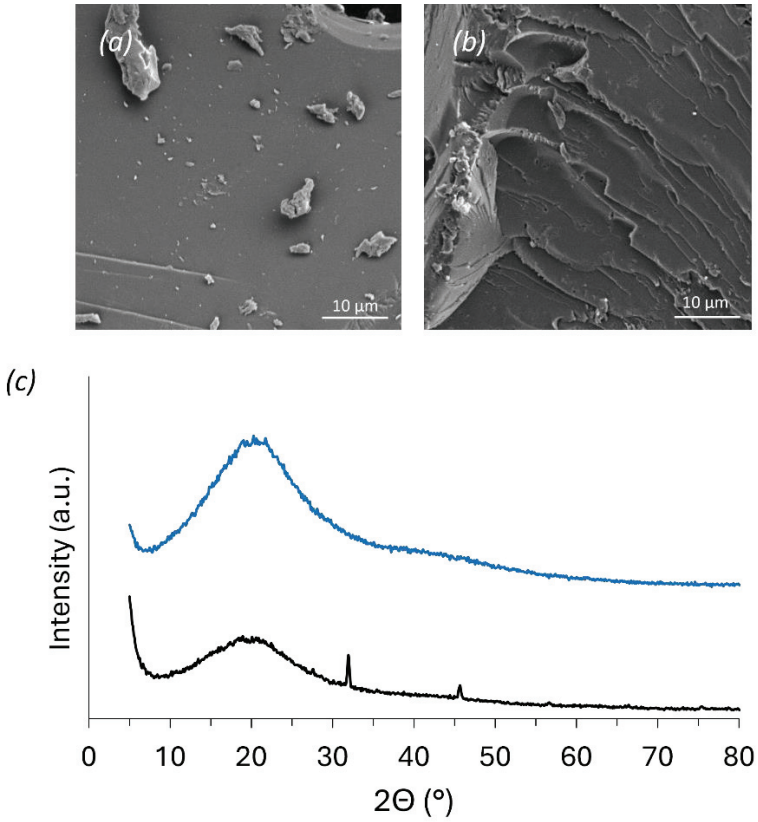

Figure 4. Scanning electron micrographs of grounded AF foam before (**a**) and after (**b**) MB adsorption; (**c**) XRD patterns of AF foam before (blue) and after (grey) MB adsorption.

After MB adsorption, two small peaks arise, suggesting the presence of new crystalline domains. MB has been studied regarding its adsorption and aggregation at different surfaces, including clay, mica, glass, quartz, metals, graphite, etc., with various orientations being proposed (i.e., from the flat deposition of MB to tilted adsorption and organization) [44]. Despite XRD being significantly less sensitive in scenarios of nonuniform adsorption, such as at low loadings like in the present work, which can result in misleading conclusions,

the adsorption of MB and formation of ordered MB structures at the foam surface sounds reasonable. This is also accompanied by a decrease in the intensity of the broad reflection at 20°, which might be due to the incorporation of water into the rigid foam lattice (partial swelling), changing the intermolecular interactions of the foam. In addition, the subsequent drying process may also contribute to the observed changes in the XRD intensity [45,46].

Tannins and lignin have functional groups in common and this can be easily confirmed by FTIR. For instance, the band at 3400 cm^{-1} is attributed to OH stretching, and the band at 2930 cm^{-1} is assigned to the CH stretching in aromatic compounds (Figure 5) [47,48]. Nonetheless, discriminative peaks were identified in both kraft and alkali lignins (Figure 5a(I),c(I)). The aromatic skeleton vibrations at 1600, 1515, and 1426 cm^{-1}, together with the CH deformation and the aromatic ring vibration at 1462 cm^{-1}, are common for all lignins. Moreover, the guaiacyl unit can be identified by the presence of varying intensity peaks at 1269 cm^{-1} and 1140 cm^{-1} related to the G ring and C=O stretch, respectively, by the CH plane deformation at 1140 cm^{-1}, and the CH out-of-plane vibrations at 854 and 817 cm^{-1} (Table 2) [47,49,50]. In respect to the tannin (Figure 5b(I)), a C=O carbonyl stretching mode was detected at 1732 cm^{-1}, at 1605 cm^{-1} the C=C stretching from aromatic rings, and 1390 and 1330 cm^{-1} revealed the C-O stretching and the C-O-H deformation of phenols. Together with a peak at 1200 cm^{-1}, assigned to the bending of C-OH and the symmetric stretching from C-O, all the vibrations mentioned above are characteristic of tannins (Table 2) [48]. In all the prepared rigid foams, a decrease in the OH band around 3400 cm^{-1} was verified, suggesting that the condensation of lignin or tannin with furfuryl alcohol might have occurred at the free position on the aromatic ring of the phenol source [21,22,29]. Moreover, an overall decrease in intensity was observed for most peaks, which should be a consequence of the complex structure and the intermolecular rearrangements after the acid-catalyzed polymerization to obtain the rigid foams [22].

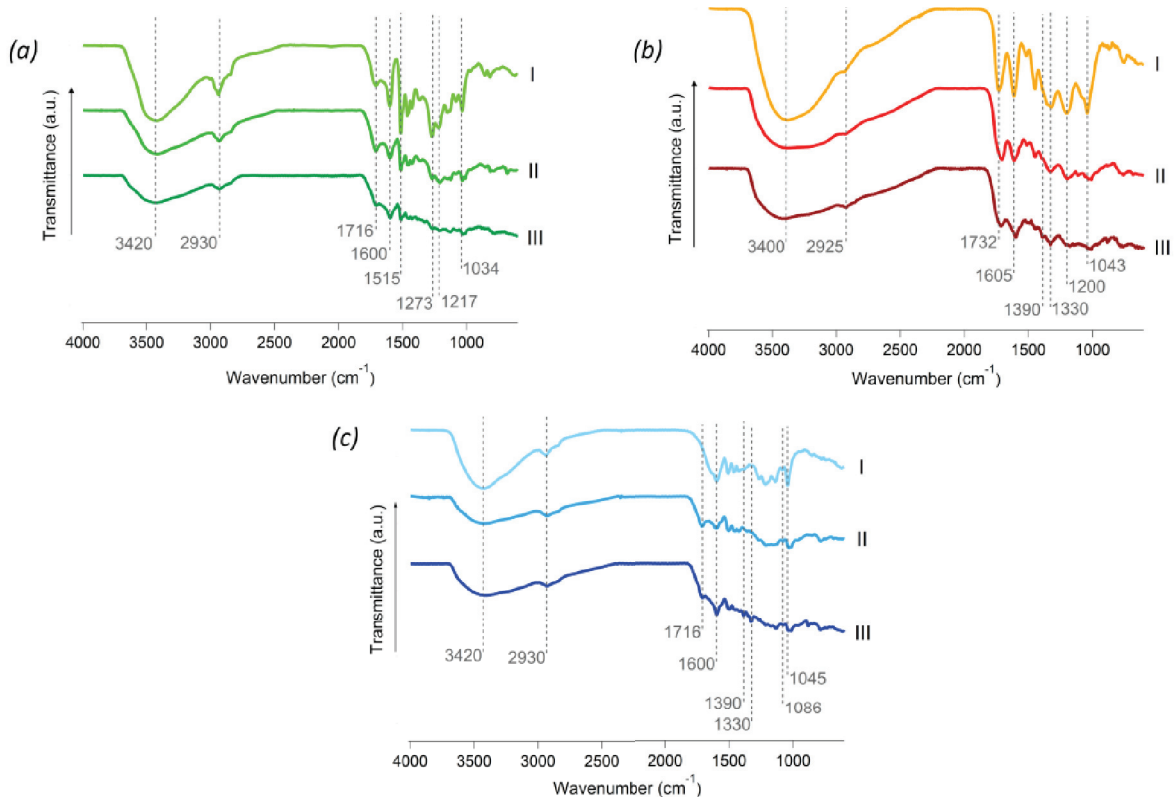

Figure 5. FTIR spectra for (**a**) kraft lignin (I), KF (II), and KF after MB adsorption (III); (**b**) tannin (I) and TF, before (II) and after (III) MB adsorption, (**c**) alkali lignin (I) and AF before (II) and after MB adsorption (III).

Table 2. FTIR peak assignment and main vibrational modes of developed foams and respective phenol source.

Sample	Wavenumber (cm^{-1})	Vibration
MB	1600	aromatic ring vibration
	1390	−CH3 symetric deformation
	1330	C=N bond
Tannin and TF	3400	OH stretching
	2925	CH stretching aromatic compounds
	1716, 1732	stretch C=O, carbonyl stretching
	1605	C=C stretching aromatic rings
	1520	stretching C−C and C−O
	1450	C−OH stretching
	1390	C−O stretching phenols
	1330	C−O−H deformation of phenols
	1200	C−OH bending
	1115	R−O−R′ stretching (ether) for condensed tannins
	1043	symmetric stretching C−O
	758	ring deformation
Kraft and KF	3420	OH stretching
	2930	CH stretching
	1716	carbonyl stretching
	1600	C=O stretching (conjugated), aromatic ring vibration
	1515	C=O stretching from aromatic rings
	1460	aromatic ring vibrations
	1430	aromatic skeletal vibrations with C−H in plane deformation
	1369	phenolic OH and aliphatic C−H in methyl groups
	1273	C=0 and ring stretching
	1217	C−C, C−O and C=O stretching
	1145	aromatic C−H in-plane deformation from guaiacyl ring,
	1086	C−O deformation in secondary alcohols and aliphatic esters
	1034	C−O stretching, C−O deformation of secondary alcohols
	856	CH in plane deformation
	820	CH out of plane vibrations
	685	ring deformation, aromatic C−H out of plane bending
Alkali and AF	3420	OH stretching
	2930	CH stretching
	1715	carbonyl stretching
	1600	C=O stretching (conjugated), aromatic ring vibration
	1510	C=O stretching from aromatic rings
	1460	aromatic ring vibrations
	1430	aromatic skeletal vibrations with C−H in plane deformation
	1390	−CH3 symetric deformation
	1330	C=N bond
	1271	C=0 and ring stretching
	1217	C−C, C−O and C=O stretching
	1145	aromatic C−H in-plane deformation from guaiacyl ring,
	1045	C−O stretching, C−O deformation of secondary alcohols
	883	CH in plane deformation
	785	CH out of plane vibrations

Once MB is adsorbed, it is of notice the increase at 1600 cm^{-1} for all foams. The appearance and/or intensity increase of characteristic peaks from MB (1390 and 1330 cm^{-1}) are not identifiable in the kraft lignin foam but visible in the FTIR spectra of the tannin and the alkali lignin-based rigid foams, in agreement with the highest adsorption of dye from each foam [4].

3.2. Methylene Blue Adsorption Kinetics

The adsorption kinetics for MB with different initial concentrations (i.e., 5, 10, 20, and 50 mg L^{-1}) are shown in Figure 6. It can be observed that the adsorption capacity is dependent on the foam composition. The observed kinetics are generally characterized by an initial high rate, followed by a slower rate until an equilibrium is reached. The irregular morphology and heterogeneity of the rigid foams make adsorption a complex process. As a smaller number of active sites become available, adsorption becomes progressively slower. Ultimately, the system reaches equilibrium and remains unchanged when all possible adsorption sites are saturated, driving the MB in excess to remain in solution [4,10].

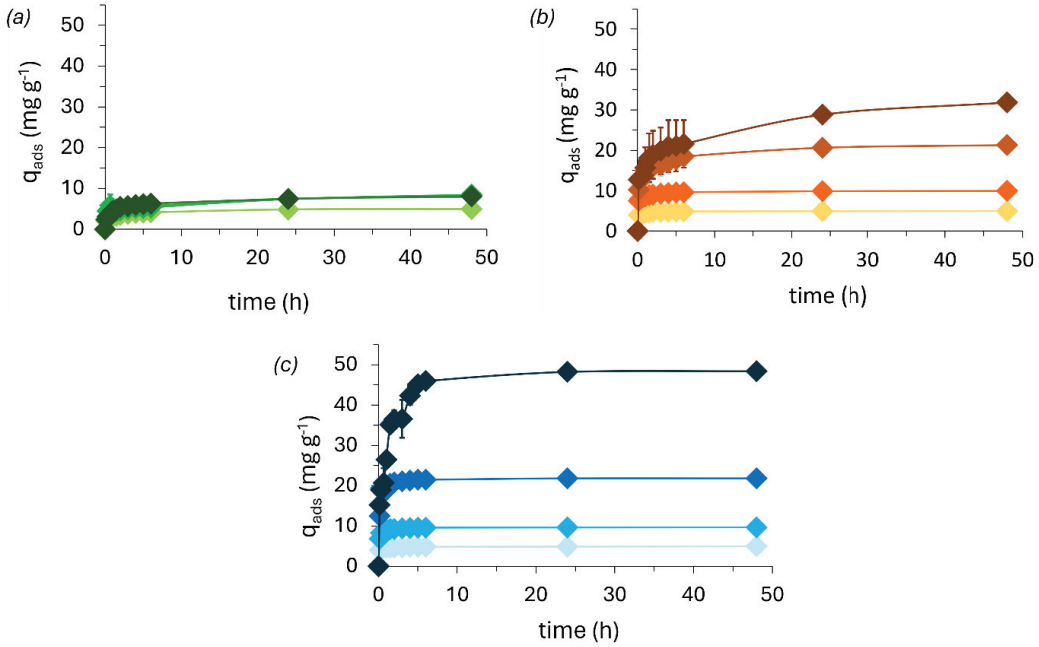

Figure 6. Methylene blue adsorption from (**a**) KF (green), (**b**) TF (orange), and (**c**) AF (blue) foams on the course of 48 h at 20 °C (MB initial concentrations of 5, 10, 20, and 50 mg L^{-1}, increasing from lighter to darker tones.

Depending on its rate of adsorption, it is possible to rationalize the suitability of a material for larger scale applications. The kinetic experiments (Figure 6) demonstrate a fast adsorption process in which all the foams seem to reach equilibrium after approximately 4 h for a maximum initial concentration of 50 mg L^{-1} of MB. Among the three tested foams, KF was observed to be the least effective for MB removal. Up to 48 h in contact with a 50 mg L^{-1} MB solution at neutral pH, KF removed only close to 10 mg of MB per gram of foam, while TF foam reached close to 40 mg g^{-1}. On the other hand, the AF was able to remove all the MB. This shows that MB has a higher affinity for the alkali lignin than for the tannin and, lastly, for the kraft lignin [4,10].

In the kinetic study, pseudo first and second-order equations were applied. Both formalisms similarly fit the data, though the highest determination coefficients (r^2) are obtained from the pseudo-second-order fits. Overall, the r^2 decreases with increasing MB concentration, decreasing the fit quality, though better expressed by a second-order equation. The decrease is proportional to the increase in the saturation of the material from the molecules of dye; the closer to saturation, the slower the adsorption rate. Moreover, it is also dependent on the stage of adsorption due to its logarithmic behavior [51].

The reduction in the kinetic constants shows that the rate of adsorption decreases with increasing MB concentration (Table 3). The decrease in the PSO kinetic constant (k_2) trend is inversely proportional to the concentration of dye, as its decrease is greater for the more efficient adsorbent and suggests that other phenomena affect the adsorption kinetics. The AF foam k_2 was reduced to 0.65% for 50 mg L^{-1} of MB with respect to 5 mg L^{-1} of MB, i.e.,

from 84 ± 6 (g/mg.min) to 0.55 ± 0.07 (g/mg.min), the TF foam k_2 decreased to 1.67% and the KF foam to 40.36%. Overall, this shows that the adsorption rate is dependent on the concentration of dye as it decreases with an increasing concentration of dye, most likely due to the progressive saturation of available bonding sites, which reduces the encounter probability between MB molecules and the available binding sites of the adsorbent [38,52].

Table 3. Pseudo-first and second-order kinetics fit parameters, using Equations (3) and (4), respectively.

			Pseudo-First Order			Pseudo-Second Order		
Foam	**MB (mg L^{-1})**	**q_e exp (mg g^{-1})**	**q_e calc (mg g^{-1})**	**$K_1 \times 10^2$ (1 min^{-1})**	**R^2**	**q_e calc (mg g^{-1})**	**$K_2 \times 10^3$ (g mg^{-1} min^{-1})**	**R^2**
TF	5	4.88 (±0.06)	4.68 (±0.06)	16.19 (±2.16)	0.98	4.80 (±0.03)	75.3 (±8.63)	0.995
	10	9.83 (±0.12)	9.18 (±0.17)	14.38 (±2.39)	0.96	9.49 (±0.11)	29.28 (±4.69)	0.986
	20	20.60 (±0.86)	17.46 (±0.70)	6.17 (±1.48)	0.85	18.84 (±0.58)	4.39 (±1.03)	0.939
	50	28.81 (±0.56)	23.14 (±1.77)	2.62 (±0.89)	0.67	25.95 (±1.80)	1.26 (±0.50)	0.815
KF	5	4.87 (±0.01)	4.17 (±0.21)	2.76 (±0.63)	0.84	4.55 (±0.17)	8.82 (±1.97)	0.938
	10	7.40 (±0.46)	6.66 (±0.63)	1.01 (±0.32)	0.74	7.48 (±0.58)	1.85 (±0.71)	0.868
	20	7.54 (±0.39)	5.82 (±0.46)	3.09 (±1.16)	0.63	6.57 (±0.47)	5.46 (±2.28)	0.794
	50	7.41 (±0.03)	6.59 (±0.34)	1.94 (±0.39)	0.87	7.32 (±0.27)	3.56 (±0.71)	0.952
AF	5	4.94 (±0.06)	4.77 (±0.04)	16.29 (±1.31)	0.99	4.88 (±0.02)	84.36 (±6.45)	0.998
	10	9.83 (±0.21)	9.61 (±0.07)	13.01 (±0.80)	0.99	9.88 (±0.03)	29.16 (±1.13)	0.999
	20	21.51 (±0.29)	20.90 (±0.21)	9.75 (±0.68)	0.99	21.71 (±0.20)	8.38 (±0.82)	0.99
	50	48.70 (±0.46)	46.24 (±1.48)	1.83 (±0.23)	0.95	50.28 (±1.14)	0.55 (±0.07)	0.98

3.3. Methylene Blue Adsorption in "Equilibrium"

The maximum adsorption capacity for each foam was assessed through adsorption experiments in equilibrium conditions (24 h) using different concentrations of MB. In agreement with the kinetic data, equilibrium experiments (Figure 7) showed that the KF foam was the least effective for MB adsorption, followed by the TF foam. On the other hand, the AF foam was found to be the most effective. When increasing the MB concentration up to 250 mg L^{-1}, it can be observed that the maximum adsorbed amount does not reach a steady state, oscillating between 90 and 100 mg of adsorbed MB per gram of foam. These results are supported by the pseudo-steady-state hypothesis, where the rates of adsorption and desorption are equivalent [37,53]. As an assumption characteristic of multilayer adsorption, Langmuir and BET isotherm models were used (Figure 7a). Both Langmuir and BET models present very similar fits; however, the Langmuir isotherm model better describes the adsorption process. Given this, the MB adsorption on the prepared rigid foams is usually described as a monolayer adsorption [34,37]. The Langmuir model might be a better fit when the surface of the adsorbent is saturated; nonetheless, it only represents one possible layer of adsorbate. When both models are applied for lower concentrations, i.e., up to an initial MB concentration of 100 mg L^{-1}, the Langmuir model has the lowest determination coefficient compared with Freundlich and BET (Figure 7b). While the Freundlich isotherm describes a nonlinear adsorption process, meaning that adsorption is not evenly distributed on the surface of the adsorbent, the BET isotherm shows the presence of multilayers on the adsorbate [34,37,54]. The produced rigid foams are rich in several functional groups, containing flavonoid moieties and active -OH, able to interact with MB mainly via electrostatic interactions, hydrogen bonding, and π-π

stacking [37]. Considering this, the data suggest that the MB adsorption by the AF foam can be described as a heterogeneous multilayer process.

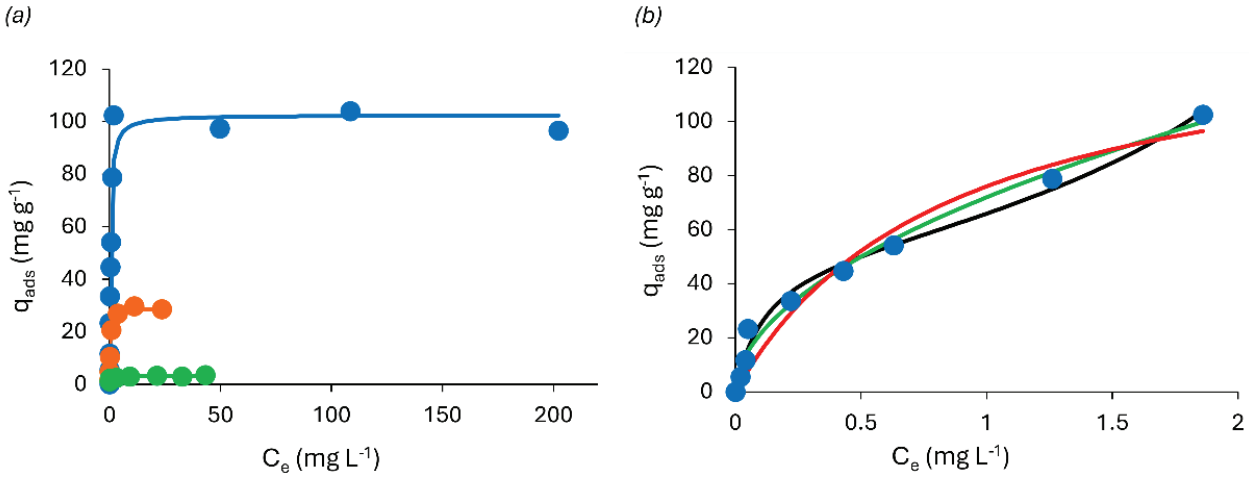

Figure 7. (**a**) Methylene blue adsorption for KF (green), TF (orange), and AF (blue) foams after 24 h, with the respective BET (green, orange, and blue lines) isotherm model fits, for a maximum of 250 mg L^{-1} of MB. Here, the BET model is reduced to the Langmuir isotherm (K_S~0 Lmol^{-1}) (Equation (5)); (**b**) Langmuir (red), Freundlich (green), and BET (black) model fit were applied to an initial concentration of up to 100 mg L^{-1} of MB for the AF foam.

The D-R model (Equation (8)) can be applied to estimate the mean free energy (kJ mol^{-1}) and determine whether the adsorption is mainly governed by physical (i.e., $E < 8$ kJ mol^{-1}) or chemical processes (i.e., $8 < E < 16$ kJ mol^{-1}) [54]. Interestingly, the calculated mean free energy up to 250 mg L^{-1} of MB is 11.29 kJ mol^{-1}, thus suggesting that the adsorption is mainly a chemical driven process [34]. However, if the model is applied in a range below the concentration where the multilayer should be formed ($q_{ads} < 25$ mg g^{-1}), the calculated mean free energy is 6.04 kJ mol^{-1}, thus being the adsorption mainly governed by a physical related process. Reinforcing the proposed mechanism, mainly governed by noncovalent bonds as electrostatic interactions, hydrogen bonding, and π-π stacking, the higher energy value might be associated with a stronger binding between the adsorbate and the adsorbent due to multiple interactions between the identified functional groups. Hydrogen bonding and stacking interactions are known to occur in molecules, such as cellulose, thus supporting the hypothesis [55].

3.4. pH Influence on MB Adsorption

The influence of pH on MB adsorption by the prepared foams was studied by initially inferring the point of zero charge of the adsorbents. This allowed us to confirm the acidic nature of the foams and that all the prepared adsorbents possess a negative net charge above approximately pH 3, being the most negatively charged at pH 10 (Figure 8a). The minimum adsorption capacity for all foams in an MB solution of 50 mg L^{-1} was verified at pH 2. As pH increases, the removal percentage (%*R*) exponentially increases for the KF and TF foams. Regarding the AF foam, it was able to completely remove MB from the solution from pH 4 up to pH 10 (Figure 8b). In this case, the exponential increase in adsorption caused by raising pH was not visible. As the AF foam adsorption capacity in neutral conditions reaches approximately 100 mg L^{-1}, the acidic pH effects might not be strong enough to be noticed in such a concentration below its maximum adsorption capacity. However, when increasing the MB solution concentration up to 250 mg L^{-1}, the AF foam was able to remove 88% of the MB present in the solution at pH 10 (Figure 8c), representing a removal capacity of 220 mg of MB per g of foam. In such conditions, the AF foam demonstrates a good capacity for MB removal compared with similar foams. For instance, Sepperer et al. prepared tannin-lignin-based furan foams with a maximum MB removal

capacity of 73.8 mg g^{-1}, the tannin rigid foams prepared by Sánchez-Martín et al. display an MB removal capacity of 250 mg g^{-1} [10,41]. The pH can affect both the protonation state of the dye and the chromophores at the adsorbent surface, i.e., at low pH, the high amount of hydronium will compete with the cationic dye for the adsorption sites, decreasing MB adsorption. On the other hand, in alkaline conditions, the adsorbent surface is expected to be mostly negatively charged, and thus, the MB adsorption is enhanced [39,51].

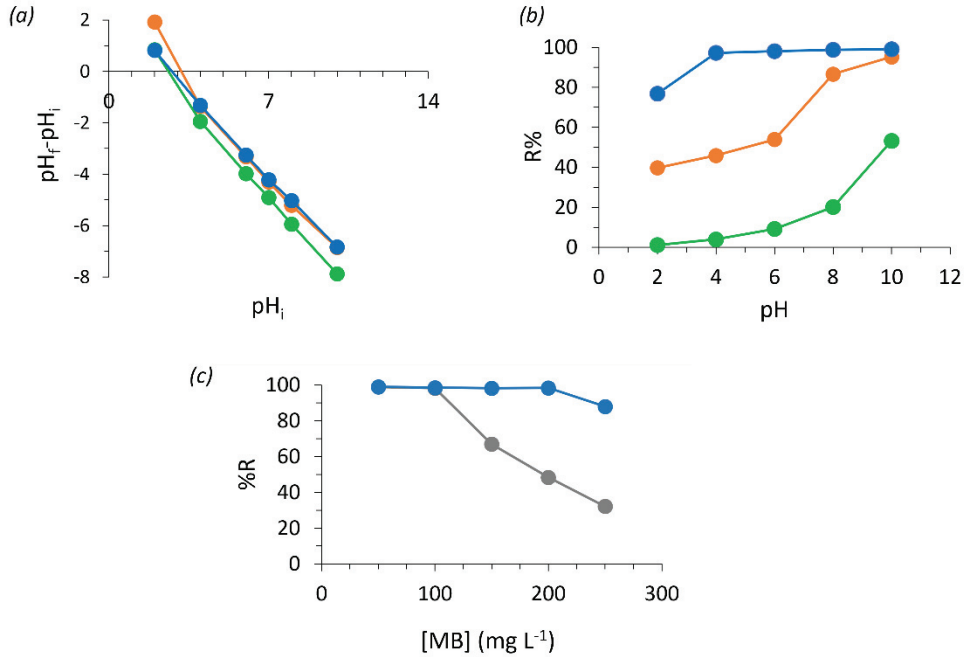

Figure 8. (**a**) Point of zero charge; (**b**) influence of each rigid foam on pH variation at 50 mg L^{-1} of MB, for TF (orange), KF (green), and AF (blue); and (**c**) MB adsorption on the AF rigid foam at pH 7 (grey) and 10 (blue).

The AF foam should be more efficient than tannin and kraft lignin-based foams due to its high number of HO^- as can be confirmed by its alkaline pH (10.5), while tannin has a pH close to 6, and kraft lignin between 2.5 and 4.5. The highest surface negative charges present in the alkali lignin-based foam, originating from HO^- deprotonation, could be responsible for the increased affinity towards the cationic MB compared with the kraft lignin-based foam [56]. In addition, commercial tannin is composed of a minimum of 65% (*w*/*w*) of polyphenols, which can justify its poorer performance compared with both tested lignins, where impurities do not reach 4% (*w*/*w*).

3.5. Adsorbent Reusability and Recycling

The adsorbent recycling assays showed it is possible to reuse the AF foam for MB adsorption after removing the adsorbed MB with an EtOH solution at pH 2 (Figure 9). Such solvent was chosen due to the high affinity of MB with EtOH in synergy with the low pH effect, previously discussed. The desorption efficiency is higher than in acetone or HCl 0.1 M. The higher desorption capacity in acid conditions confirms that the adsorption mechanism is mainly governed by electrostatic interactions [4,53]. In a 50 mg L^{-1} MB solution, the AF foam completely adsorbed the dye in the first cycle. However, the removal efficiency decreased to roughly half for the second cycle and beyond (i.e., 23 ± 3 mg g^{-1}), coinciding with the desorption capacity of 26 ± 1 mg g^{-1}. This effect suggests that, for this higher concentration (50 mg L^{-1}), some reactive sites might be unavailable due to an incomplete removal of the dye [38,39]. It is noticed that until the last cycle, the adsorption and desorption efficiencies are equivalent. This might be due to the interplay between multiple interactions, such as hydrogen bonding and possible stacking interactions between MB and the rigid foam particles, as the suggested multilayer adsorption occurring at 50 mg L^{-1} of

MB hinders the full desorption of the strongly adsorbed molecules. Supporting this, the same effect was not verified when the AF foam was exposed to 10 and 20 mg L^{-1} of the MB solution, as in both situations, it was possible to remove most of the dye; all the previously occupied reactive sites were again free for a new adsorption cycle.

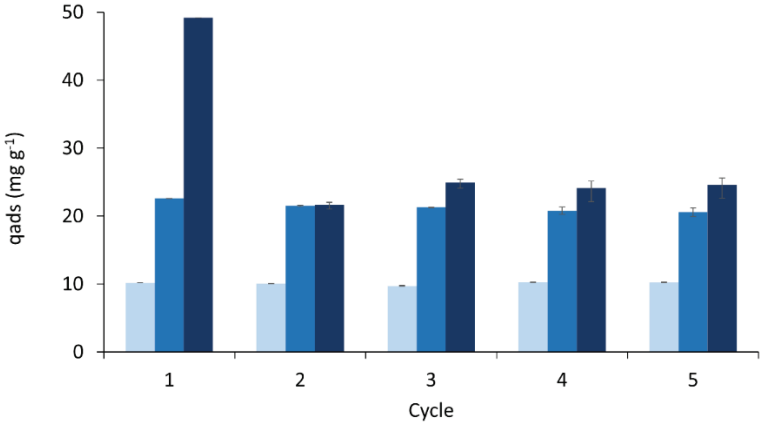

Figure 9. Desorption experiments during five cycles for the AF rigid foam exposed to 10 (light grey), 20 (grey), and 50 (black) mg L^{-1} of MB in a solution of EtOH at pH 2 for 24 h.

3.6. Thermal Behaviour

Lignin has been used as a flame retardant additive for polymer-based materials, being moderately stable at elevated temperatures due to its aromatic structure [57,58]. Thermal insulation and fire resistance tests are important features for the application of materials, such as foams in construction, appliances, transportation, and furniture [59]. Replacing fossil-based materials with biobased flame retardants can be an attractive alternative for the creation of more sustainable, high-performance polymeric materials [60]. In this regard, the thermal stability tests show that all the prepared rigid foams present similar thermal properties. The observed mass loss with increasing temperature is similar, reaching slightly over 50% of the initial mass when exposed up to 1200 °C (Figure 10a), showing improved thermal properties compared with similar materials [29]. TGA analysis exhibits several weight loss peaks, which can be attributed to the evaporation of residual blowing agent and adsorbed water between 25 and 150 °C; the degradation of polymer chains forming smaller molecules from 200 to 500 °C, and above 450 °C the pyrolysis of lignin and tannin is most likely anticipated [43,61].

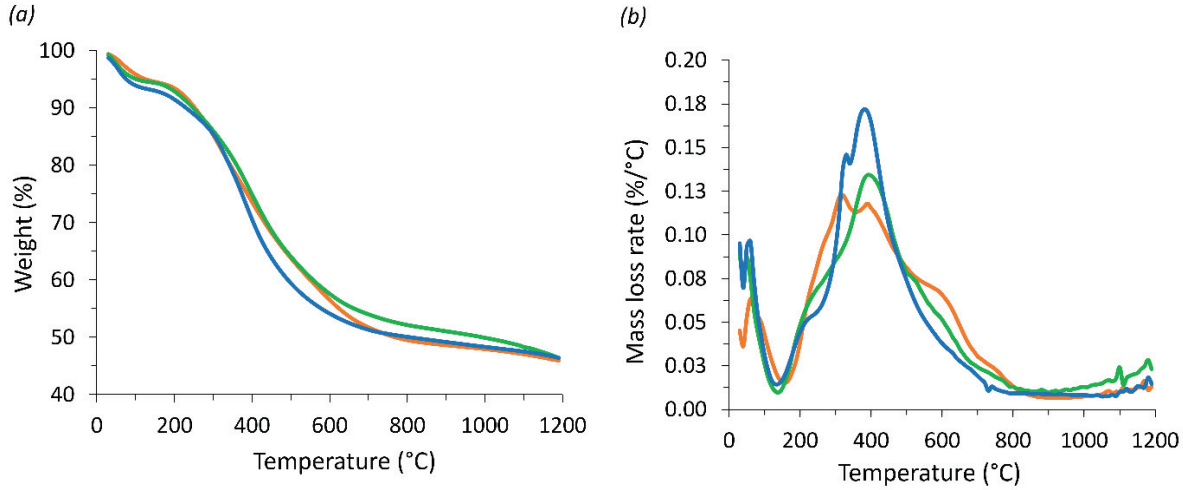

Figure 10. Thermogravimetric analysis of the prepared rigid foams (**a**), AF (blue), TF (orange), KF (green), and its derivative (**b**).

The foam's thermal stability was further evaluated by exposing it to a butane flame for 5 min (Figure 11). As can be observed, the AF foam did not produce any smoke or contribute to increasing the flame. After 5 min, and as soon as the butane source was extinguished, there was no combustion on the rigid foam, showing it was not flammable. Moreover, it took approximately 20 s to dissipate the heat, losing all the red glow. The fire retardancy of the AF rigid foam might be due to the polyfuranic oligomers formed by furfuryl alcohol self-condensation and its condensation with alkali lignin [26]. Overall, the data suggests these materials might be suitable for applications where flame retardant behavior is of utmost importance, such as with insulation materials.

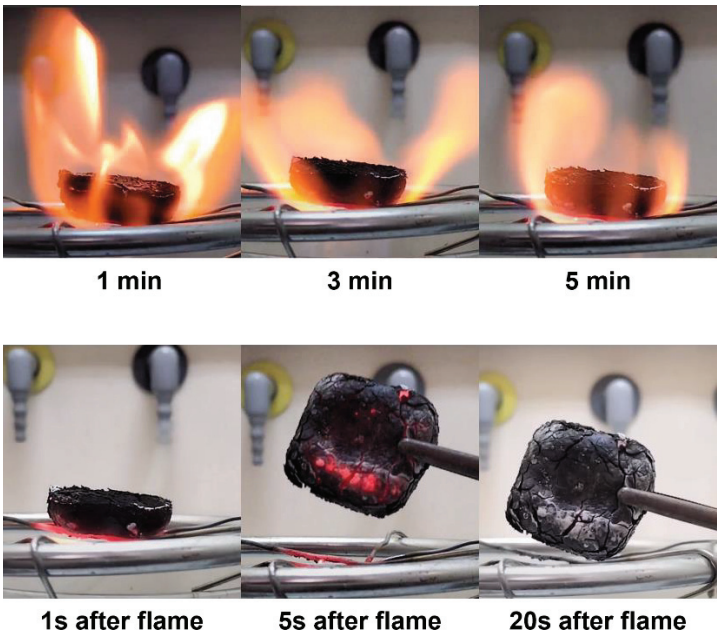

Figure 11. Flammability test of the AF foam under direct contact with the flame for up to 5 min (top row) and visual appearance of the foam after shutting down the gas flow (bottom row).

4. Conclusions

Lignin-furan foams were produced by completely replacing the tannin from a standard tannin-based furan rigid foam. As widely available and considered a residue from the paper industry, lignin can be considered an attractive polyphenol source for producing such materials. The rigid foams prepared from tannin or lignin showed similar thermal properties; however, they greatly differed in terms of MB adsorption. Two types of lignin were compared, and the alkali lignin was shown to be the most promising for dye adsorption, removing up to 220 mg of MB per gram of foam at pH 10. Adding to this, the adsorption mechanism was accessed by studying the process kinetics and equilibrium conditions, applying several isotherms. From this study, it was possible to characterize the adsorption process as nonlinear multilayer adsorption, most likely mainly governed by noncovalent bonds such as hydrogen bonding, electrostatic, and π-π interactions. The produced materials showed the possibility of being recycled for several adsorption-desorption cycles, though the procedure seems to be strongly dependent on the concentration of dye. The biobased-produced rigid foams also showed remarkable flame resistance properties, losing roughly half of their mass up to 1200 °C, not being flammable, and losing the red glow 20 s after being exposed for 5 min to a butane flame. This work demonstrates how a biobased residue (lignin) can be valorized and become an attractive platform to safely produce a multitask material suitable for dye adsorption, which, eventually, can be given a new end-of-life as a flame retardant with improved flame retardant capacity.

Author Contributions: Conceptualization, H.D. and M.J.A.-G.; methodology, H.D., J.B. and E.M.S.H.; validation, B.M., A.J.M.V. and M.N.; formal analysis, H.D., B.M., S.M. and L.A.; investigation, H.D., J.B., E.M.S.H., S.M. and L.A.; resources, B.M. and A.R.; data curation, H.D. and J.B.; writing—original draft preparation, H.D., M.J.A.-G., J.B., B.M., M.N. and A.E.; writing—review and editing, B.M., A.J.M.V., M.N., A.E. and A.R.; visualization, H.D. and B.M.; supervision, B.M. and A.R.; project administration, B.M. and A.R.; funding acquisition, B.M. and A.R. All authors have read and agreed to the published version of the manuscript.

Funding: This work is funded by FEDER Funds through the Regional Operational Program of the Algarve (PO Algarve) and by National Funds through FCT—Foundation for Science and Technology, within the scope of the projects https://doi.org/10.54499/UIDP/05183/2020, https://doi.org/10.54499/LA/P/0121/2020 and ALG-01-0145-FEDER-030619 POCI-01-0145-FEDER-030619—PTDC/ASP-SIL/30619/2017, MED (https://doi.org/10.54499/UIDB/05183/2020; https://doi.org/10.54499/UIDP/05183/2020), CHANGE (https://doi.org/10.54499/LA/P/0121/2020), CERES (https://doi.org/10.54499/UIDP/00102/2020), the researcher grants CEECIND/01014/2018/CP1540/CT0002 (DOI:10.54499/CEECIND/01014/2018/CP1540/CT0002) and 2021.00399.CEECIND/CP1656/CT0025 (https://doi.org/10.54499/2021.00399.CEECIND/CP1656/CT0025) and the doctoral grant 2020.07638.BD (https://doi.org/10.54499/2020.07638.BD). AV thanks FCT for supporting his work through the project UIDP/00313/2020.

Data Availability Statement: The original contributions presented in the study are included in the article, further inquiries can be directed to the corresponding author.

Conflicts of Interest: The authors declare no conflicts of interest.

References

1. Wang, T.; Jiang, M.; Yu, X.; Niu, N.; Chen, L. Application of Lignin Adsorbent in Wastewater Treatment: A Review. *Sep. Purif. Technol.* **2022**, *302*, 122116. [CrossRef]
2. de Araújo, L.F.B.; Mazzetto, S.E.; Lomonaco, D.; Avelino, F. Unraveling the Adsorption Mechanism of Methylene Blue onto Selective pH Precipitated Kraft Lignins: Kinetic, Equilibrium and Thermodynamic Aspects. *Int. J. Biol. Macromol.* **2022**, *220*, 1267–1276. [CrossRef] [PubMed]
3. Saravanan, A.; Senthil Kumar, P.; Jeevanantham, S.; Karishma, S.; Tajsabreen, B.; Yaashikaa, P.R.; Reshma, B. Effective Water/Wastewater Treatment Methodologies for Toxic Pollutants Removal: Processes and Applications towards Sustainable Development. *Chemosphere* **2021**, *280*, 130595. [CrossRef] [PubMed]
4. Budnyak, T.M.; Aminzadeh, S.; Pylypchuk, I.V.; Sternik, D.; Tertykh, V.A.; Lindström, M.E.; Sevastyanova, O. Methylene Blue Dye Sorption by Hybrid Materials from Technical Lignins. *J. Environ. Chem. Eng.* **2018**, *6*, 4997–5007. [CrossRef]
5. Bacelo, H.A.M.; Santos, S.C.R.; Botelho, C.M.S. Tannin-Based Biosorbents for Environmental Applications—A Review. *Chem. Eng. J.* **2016**, *303*, 575–587. [CrossRef]
6. Tondi, G.; Pizzi, A. Tannin-Based Rigid Foams: Characterization and Modification. *Ind. Crops Prod.* **2009**, *29*, 356–363. [CrossRef]
7. Sánchez-Martín, J.; Beltrán-Heredia, J.; Delgado-Regaña, A.; Rodríguez-González, M.A.; Rubio-Alonso, F. Adsorbent Tannin Foams: New and Complementary Applications in Wastewater Treatment. *Chem. Eng. J.* **2013**, *228*, 575–582. [CrossRef]
8. Baldez, E.E.; Robaina, N.F.; Cassella, R.J. Employment of Polyurethane Foam for the Adsorption of Methylene Blue in Aqueous Medium. *J. Hazard. Mater.* **2008**, *159*, 580–586. [CrossRef]
9. Can, M.; Bulut, E.; Örnek, A.; Özacar, M. Synthesis and Characterization of Valonea Tannin Resin and Its Interaction with Palladium (II), Rhodium (III) Chloro Complexes. *Chem. Eng. J.* **2013**, *221*, 146–158. [CrossRef]
10. Sánchez-Martín, J.; Beltrán-Heredia, J.; Delgado-Regaña, A.; Rodríguez-González, M.A.; Rubio-Alonso, F. Optimization of Tannin Rigid Foam as Adsorbents for Wastewater Treatment. *Ind. Crops Prod.* **2013**, *49*, 507–514. [CrossRef]
11. Kavitha, V.U.; Kandasubramanian, B. Tannins for Wastewater Treatment. *SN Appl. Sci.* **2020**, *2*, 1–21. [CrossRef]
12. Can, M.; Bulut, E.; Özacar, M. Synthesis and Characterization of Pyrogallol-Formaldehyde Nano Resin and Its Usage as an Adsorbent. *J. Chem. Eng. Data* **2012**, *57*, 2710–2717. [CrossRef]
13. Liu, Y.; Jin, C.; Yang, Z.; Wu, G.; Liu, G.; Kong, Z. Recent Advances in Lignin-Based Porous Materials for Pollutants Removal from Wastewater. *Int. J. Biol. Macromol.* **2021**, *187*, 880–891. [CrossRef] [PubMed]
14. Fernandes, C.; Melro, E.; Magalhães, S.; Alves, L.; Craveiro, R.; Filipe, A.; Valente, A.J.M.; Martins, G.; Antunes, F.E.; Romano, A.; et al. New Deep Eutectic Solvent Assisted Extraction of Highly Pure Lignin from Maritime Pine Sawdust (*Pinus Pinaster* Ait.). *Int. J. Biol. Macromol.* **2021**, *177*, 294–305. [CrossRef]
15. Melro, E.; Filipe, A.; Sousa, D.; Medronho, B.; Romano, A. Revisiting Lignin: A Tour through Its Structural Features, Characterization Methods and Applications. *New J. Chem.* **2021**, *45*, 6986–7013. [CrossRef]
16. Stanisz, M.; Klapiszewski; Collins, M.N.; Jesionowski, T. Recent Progress in Biomedical and Biotechnological Applications of Lignin-Based Spherical Nano- and Microstructures: A Comprehensive Review. *Mater. Today Chem.* **2022**, *26*, 101198. [CrossRef]

17. Zhang, W.; Qiu, X.; Wang, C.; Zhong, L.; Fu, F.; Zhu, J.; Zhang, Z.; Qin, Y.; Yang, D.; Xu, C.C. Lignin Derived Carbon Materials: Current Status and Future Trends. *Carbon Res.* **2022**, *1*, 14. [CrossRef]
18. Melro, E.; Filipe, A.; Valente, A.J.M.; Antunes, F.E.; Romano, A.; Norgren, M.; Medronho, B. Levulinic Acid: A Novel Sustainable Solvent for Lignin Dissolution. *Int. J. Biol. Macromol.* **2020**, *164*, 3454–3461. [CrossRef]
19. Chen, W.J.; Zhao, C.X.; Li, B.Q.; Yuan, T.Q.; Zhang, Q. Lignin-Derived Materials and Their Applications in Rechargeable Batteries. *Green Chem.* **2022**, *24*, 565–584. [CrossRef]
20. Iroegbu, A.O.; Hlangothi, S.P. Furfuryl Alcohol a Versatile, Eco-Sustainable Compound in Perspective. *Chem. Afr.* **2019**, *2*, 223–239. [CrossRef]
21. Liu, B.; Zhou, Y.; Essawy, H.; Feng, S.; Li, X.; Liao, J. Formaldehyde Free Renewable Thermosetting Foam Based on Biomass Tannin with a Lignin Additive. *J. Renew. Mater.* **2022**, *10*, 3009–3024. [CrossRef]
22. Fagbemigun, T.K.; Mai, C. Production and Characterisation of Self-Blowing Lignin-Based Foams. *Eur. J. Wood Wood Prod.* **2022**, *81*, 579–590. [CrossRef]
23. Tondi, G.; Zhao, W.; Pizzi, A.; Du, G.; Fierro, V.; Celzard, A. Tannin-Based Rigid Foams: A Survey of Chemical and Physical Properties. *Bioresour. Technol.* **2009**, *100*, 5162–5169. [CrossRef] [PubMed]
24. Missio, A.L.; Otoni, C.G.; Zhao, B.; Beaumont, M.; Khakalo, A.; Kämäräinen, T.; Silva, S.H.F.; Mattos, B.D.; Rojas, O.J. Nanocellulose Removes the Need for Chemical Crosslinking in Tannin-Based Rigid Foams and Enhances Their Strength and Fire Retardancy. *ACS Sustain. Chem. Eng.* **2022**, *10*, 10303–10310. [CrossRef]
25. Zhou, M.; Zhong, L.; Hu, L.; Zhou, Y.; Yang, X. Synthesis of a Reactive Lignin-Based Flame Retardant and Its Application in Phenolic Foam. *Environ. Technol.* **2024**, *45*, 2506–2518. [CrossRef]
26. Chen, X.; Li, J.; Essawy, H.; Pizzi, A.; Fredon, E.; Gerardin, C.; Du, G.; Zhou, X. Flame-Retardant and Thermally-Insulating Tannin and Soybean Protein Isolate (SPI) Based Foams for Potential Applications in Building Materials. *Constr. Build. Mater.* **2022**, *315*, 125711. [CrossRef]
27. Pizzi, A. Tannin-Based Biofoams—A Review. *J. Renew. Mater.* **2019**, *7*, 477–492. [CrossRef]
28. Varila, T.; Romar, H.; Luukkonen, T.; Hilli, T.; Lassi, U. Characterization of Lignin Enforced Tannin/Furanic Foams. *Heliyon* **2020**, *6*, e03228. [CrossRef]
29. Chen, X.; Li, J.; Pizzi, A.; Fredon, E.; Gerardin, C.; Zhou, X.; Du, G. Tannin-Furanic Foams Modified by Soybean Protein Isolate (SPI) and Industrial Lignin Substituting Formaldehyde Addition. *Ind. Crops Prod.* **2021**, *168*, 113607. [CrossRef]
30. Sepperer, T.; Šket, P.; Petutschnigg, A.; Hüsing, N. Tannin-Furanic Foams Formed My Mechanical Agitation: Influence of Surfactant and Ingredient Ratios. *Polymers* **2021**, *13*, 3058. [CrossRef]
31. Hassani, E.M.S.; Duarte, H.; Brás, J.; Taleb, A.; Taleb, M.; Rais, Z.; Eivazi, A.; Norgren, M.; Romano, A.; Medronho, B. On the Valorization of Olive Oil Pomace: A Sustainable Approach for Methylene Blue Removal from Aqueous Media. *Polymers* **2024**, *16*, 3055. [CrossRef] [PubMed]
32. Melro, E.; Duarte, H.; Eivazi, A.; Costa, C.; Faleiro, M.L.; da Costa, A.M.R.; Antunes, F.E.; Valente, A.J.M.; Romano, A.; Norgren, M.; et al. Poly(*Butylene Succinate*)-Based Composites with Technical and Extracted Lignins from Wood Residues. *ACS Appl. Polym. Mater.* **2024**, *6*, 1169–1181. [CrossRef]
33. Cova, F.; Murtinho, D.; Pais, A.A.C.C.; Valente, A.J.M.; Utzeri, G. Insights on Macro- and Microscopic Interactions between Confidor and Cyclodextrin-Based Nanosponges. *Chem. Eng. J.* **2023**, *455*, 140882.
34. Wang, J.; Guo, X. Adsorption Isotherm Models: Classification, Physical Meaning, Application and Solving Method. *Chemosphere* **2020**, *258*, 127279. [CrossRef]
35. Abin-Bazaine, A.; Trujillo, A.C.; Olmos-Marquez, M.; Abin-Bazaine, A.; Trujillo, A.C.; Olmos-Marquez, M. Adsorption Isotherms: Enlightenment of the Phenomenon of Adsorption. *Wastewater Treat.* **2022**, *19*, 1–5. [CrossRef]
36. Al-Ghouti, M.A.; Da'ana, D.A. Guidelines for the Use and Interpretation of Adsorption Isotherm Models: A Review. *J. Hazard. Mater.* **2020**, *393*, 122383. [CrossRef]
37. Scheufele, F.B.; Módenes, A.N.; Borba, C.E.; Ribeiro, C.; Espinoza-Quiñones, F.R.; Bergamasco, R.; Pereira, N.C. Monolayer-Multilayer Adsorption Phenomenological Model: Kinetics, Equilibrium and Thermodynamics. *Chem. Eng. J.* **2016**, *284*, 1328–1341. [CrossRef]
38. Nizam, N.U.M.; Hanafiah, M.M.; Mahmoudi, E.; Halim, A.A.; Mohammad, A.W. The Removal of Anionic and Cationic Dyes from an Aqueous Solution Using Biomass-Based Activated Carbon. *Sci. Rep.* **2021**, *11*, 8623. [CrossRef]
39. Ren, L.; Tang, Z.; Du, J.; Chen, L.; Qiang, T. Recyclable Polyurethane Foam Loaded with Carboxymethyl Chitosan for Adsorption of Methylene Blue. *J. Hazard. Mater.* **2021**, *417*, 126130. [CrossRef]
40. Agustin, M.B.; Mikkonen, K.S.; Kemell, M.; Lahtinen, P.; Lehtonen, M. Systematic Investigation of the Adsorption Potential of Lignin- and Cellulose-Based Nanomaterials towards Pharmaceuticals. *Environ. Sci. Nano* **2022**, *9*, 2006–2019. [CrossRef]
41. Sepperer, T.; Neubauer, J.; Eckardt, J.; Schnabel, T.; Petutschnigg, A.; Tondi, G. Pollutant Absorption as a Possible End-of-Life Solution for Polyphenolic Polymers. *Polymers* **2019**, *11*, 911. [CrossRef] [PubMed]
42. Gomide, R.A.C.; de Oliveira, A.C.S.; Rodrigues, D.A.C.; de Oliveira, C.R.; de Assis, O.B.G.; Dias, M.V.; Borges, S.V. Development and Characterization of Lignin Microparticles for Physical and Antioxidant Enhancement of Biodegradable Polymers. *J. Polym. Environ.* **2020**, *28*, 1326–1334. [CrossRef]
43. Yan, Q.; Arango, R.; Li, J.; Cai, Z. Fabrication and Characterization of Carbon Foams Using 100% Kraft Lignin. *Mater. Des.* **2021**, *201*, 109460. [CrossRef]

44. Bujdák, J.; Iyi, N.; Kaneko, Y.; Sasai, R. Molecular Orientation of Methylene Blue Cations Adsorbed on Clay Surfaces. *Clay Miner.* **2003**, *38*, 561–572. [CrossRef]
45. Tian, F.; Qu, H.; Zimmermann, A.; Munk, T.; Jørgensen, A.C.; Rantanen, J. Factors Affecting Crystallization of Hydrates. *J. Pharm. Pharmacol.* **2010**, *62*, 1534–1546. [CrossRef]
46. Zeng, F.; Zhu, S.; Chen, F.; Gao, Q.; Yu, S. Effect of Different Drying Methods on the Structure and Digestibility of Short Chain Amylose Crystals. *Food Hydrocoll.* **2016**, *52*, 721–731. [CrossRef]
47. Rashid, T.; Kait, C.F.; Murugesan, T. A "Fourier Transformed Infrared" Compound Study of Lignin Recovered from a Formic Acid Process. *Procedia Eng.* **2016**, *148*, 1312–1319. [CrossRef]
48. Ricci, A.; Olejar, K.J.; Parpinello, G.P.; Kilmartin, P.A.; Versari, A. Application of Fourier Transform Infrared (FTIR) Spectroscopy in the Characterization of Tannins. *Appl. Spectrosc. Rev.* **2015**, *50*, 407–442. [CrossRef]
49. Boeriu, C.G.; Bravo, D.; Gosselink, R.J.A.; Van Dam, J.E.G. Characterisation of Structure-Dependent Functional Properties of Lignin with Infrared Spectroscopy. *Ind. Crops Prod.* **2004**, *20*, 205–218. [CrossRef]
50. Shi, Z.; Xu, G.; Deng, J.; Dong, M.; Murugadoss, V.; Liu, C.; Shao, Q.; Wu, S.; Guo, Z. Structural Characterization of Lignin from D. Sinicus by FTIR and NMR Techniques. *Green Chem. Lett. Rev.* **2019**, *12*, 235–243. [CrossRef]
51. Namal, O.O.; Kalipci, E. Adsorption Kinetics of Methylene Blue Using Alkali and Microwave-Modified Apricot Stones. *Sep. Sci. Technol.* **2019**, *54*, 1722–1738. [CrossRef]
52. Zhang, S.; Hao, J.; Ding, F.; Ren, X. Nanocatalyst Doped Bacterial Cellulose-Based Thermosensitive Nanogel with Biocatalytic Function for Antibacterial Application. *Int. J. Biol. Macromol.* **2022**, *195*, 294–301. [CrossRef] [PubMed]
53. Marbán, G. BET Adsorption Reaction Model Based on the Pseudo Steady-State Hypothesis for Describing the Kinetics of Adsorption in Liquid Phase. *J. Colloid Interface Sci.* **2016**, *467*, 170–179. [CrossRef]
54. Dey, S.; Chakraborty, R.; Mohanta, J.; Dey, B. Tricosanthes Cucumerina: A Potential Biomass for Efficient Removal of Methylene Blue from Water. *Bioremediation J.* **2022**, *28*, 67–78. [CrossRef]
55. Parthasarathi, R.; Bellesia, G.; Chundawat, S.P.S.; Dale, B.E.; Langan, P.; Gnanakaran, S. Insights into Hydrogen Bonding and Stacking Interactions in Cellulose. *J. Phys. Chem. A* **2011**, *115*, 14191–14202. [CrossRef]
56. Graba, Z.; Akkari, I.; Bezzi, N.; Kaci, M.M. Valorization of Olive–Pomace as a Green Sorbent to Remove Basic Red 46 (BR46) Dye from Aqueous Solution. *Biomass Conv. Bioref.* **2024**, *14*, 14951–14962. [CrossRef]
57. Wu, Q.; Ran, F.; Dai, L.; Li, C.; Li, R.; Si, C. A Functional Lignin-Based Nanofiller for Flame-Retardant Blend. *Int. J. Biol. Macromol.* **2021**, *190*, 390–395. [CrossRef]
58. Solihat, N.N.; Hidayat, A.F.; Taib, M.N.A.M.; Hussin, M.H.; Lee, S.H.; Ghani, M.A.A.; Edrus, S.S.O.A.; Vahabi, H.; Fatriasari, W. Recent Developments in Flame-Retardant Lignin-Based Biocomposite: Manufacturing, and Characterization. *J. Polym. Env.* **2022**, *30*, 4517–4537. [CrossRef]
59. Mimini, V.; Kabrelian, V.; Fackler, K.; Hettegger, H.; Potthast, A.; Rosenau, T. Lignin-Based Foams as Insulation Materials: A Review. *Holzforschung* **2019**, *73*, 117–130. [CrossRef]
60. Yang, H.; Yu, B.; Xu, X.; Bourbigot, S.; Wang, H.; Song, P. Lignin-Derived Bio-Based Flame Retardants toward High-Performance Sustainable Polymeric Materials. *Green Chem.* **2020**, *22*, 2129–2161. [CrossRef]
61. Wu, Z.; Huang, W.; Shan, X.; Li, Z. Preparation of a Porous Graphene Oxide/Alkali Lignin Aerogel Composite and Its Adsorption Properties for Methylene Blue. *Int. J. Biol. Macromol.* **2020**, *143*, 325–333. [CrossRef] [PubMed]

Disclaimer/Publisher's Note: The statements, opinions and data contained in all publications are solely those of the individual author(s) and contributor(s) and not of MDPI and/or the editor(s). MDPI and/or the editor(s) disclaim responsibility for any injury to people or property resulting from any ideas, methods, instructions or products referred to in the content.

polymers

MDPI

Article

Upcycling of Expanded Polystyrene Waste-Impregnated PVP Using Wet-Phase Inversion for Effective Microalgae Harvesting

Tutik Sriani [1], Muslim Mahardika [2], Shofa Aulia Aldhama [3], Chandrawati Putri Wulandari [3] and Gunawan Setia Prihandana [3,*]

[1] Department of Research and Development, P.T. Global Meditek Utama-IITOYA, Sardonoharjo, Ngaglik, Sleman, Yogyakarta 55581, Indonesia; tsriani@iitoya.com
[2] Department of Mechanical and Industrial Engineering, Faculty of Engineering, Universitas Gadjah Mada, Jalan Grafika No. 2, Yogyakarta 55281, Indonesia; muslim_mahardika@ugm.ac.id
[3] Department of Industrial Engineering, Faculty of Advanced Technology and Multidiscipline, Universitas Airlangga, Jl. Dr. Ir. H. Soekarno, Surabaya 60115, Indonesia; aldhama.sa@ftmm.unair.ac.id (S.A.A.); chandrawati.p.w@ftmm.unair.ac.id (C.P.W.)
* Correspondence: gunawan.prihandana@ftmm.unair.ac.id

Abstract: The aim of this study was to investigate the potential of upcycling Expanded Polystyrene (EPS) waste collected from food packaging into a membrane for microalgae harvesting, in which membrane filtration often challenges fouling and pore blocking. The target species is *Spirulina platensis*, with *Chlorella vulgaris* as a comparison agent. The membrane was fabricated from used Styrofoam, which typically ends up as single-use food packaging waste. In this study, PVP was used as an additive at varying concentrations, from 2 wt.% to 8 wt.%. The experimental results indicated that despite varying PVP concentrations, all EPS waste membranes exhibited near-complete recovery of *Spirulina platensis* biomass extraction. Despite the similar harvesting efficiency, EPS/PVP-8 exhibited the largest flux of 970.5 LMH/Bar, which is twice the value of the pristine EPS waste membrane. All membranes were hydrophilic; however, hydrophobicity increased with PVP concentration. SEM micrographs revealed that PVP enlarged the membrane surface pores and improved connectivity within the membrane's structure, ensuring efficient flow. The EPS waste membrane offers promising insights for sustainable materials and wastewater treatment. The upcycling of EPS waste into flat sheet membranes not only addresses the problem of Styrofoam waste accumulation but also paves the way to transform waste into valuable products.

Keywords: expanded polystyrene; polyvinylpyrrolidone; microalgae harvesting; Styrofoam; good health; upcycle

1. Introduction

Expanded Polystyrene (EPS), commonly known as Styrofoam, is a white foam plastic material produced from solid beads of polystyrene. The manufacturing of EPS involves impregnating polystyrene beads with pentane as a foaming agent, allowing 20–50 times volume expansion [1]. Some of EPS's highlights are its exceptional lightweight and thermal insulation properties. It also offers an economical solution for packaging and construction needs [2]. The white color of EPS imparts a sense of cleanliness and hygiene; thus, it is opted for as a packaging material in food industries and as a takeaway by street food vendors. One important drawback is its lightweight feature makes its bulk volume uneconomical to transport to recycling facilities [3]. Furthermore, in Indonesia, the recycling of EPS faces challenges due to limited techniques and infrastructures. Most recycling centers and local waste banks do not accept EPS waste for processing, thus directing the waste to landfills as residual waste or even contaminating waterways [4]. Given that global polystyrene production is on the rise, finding effective ways to recycle/upcycle polystyrene is the best option to reduce the massive amount of Styrofoam waste.

Some researchers attempted to upcycle Styrofoam waste into high-end products such as air filter media [5], oil–water separators [6], concrete composites [7], microfibers [8], and chemical absorbents [9,10]. In membrane technology, Ghaly et al. [11] investigated two types of high-impact polystyrene (HIPS) to create flat sheet membranes. They revealed that as the concentration of HIPS increased, the membrane's surface porosity and pore size decreased. Munir et al [12] transformed Styrofoam into a face mask filter using a needleless electrospinning method. It has a hydrophobic surface making it suitable as a good face mask material. The electrospinning method was also used to prepare a Styrofoam-based membrane for desalination purposes [13]. They added zeolite into the process and confirmed that the addition of 30 wt.% zeolites led to an 82.63% decrease in water conductivity.

There has been a growing interest in exploring microalgae to tackle global food insecurity as well as to sustain the environment. One of these microalgae is *Spirulina*, a relatively large microalgae with exceptional nutritional value. For mass production, large-scale *Spirulina* farming is carried out in pools or ponds, which requires efficient harvesting. Membrane filtration of microalgae enables nearly complete biomass recovery and the absence of secondary contamination, while also serving as a water conservation strategy [14]. Nevertheless, membrane filtration is susceptible to fouling and pore blocking [15]. The costs associated with membrane replacement and pumping can also be quite high [16]. In regions of developing countries where the climate is conducive to microalgae farming, membrane technology is still perceived as costly. As a result, using membrane filtration for microalgae harvesting is a challenging endeavor. In their study, Yeo et al. observed that the presence of PVP in the membrane dope solution enhanced phase separation and enlarged the macrovoids within the resulting membranes [17]. Polyvinylpyrrolidone (PVP) has found extensive application as an additive in the fabrication of ultrafiltration membranes, mostly as a pore-forming agent to increase flux [18].

This research explores the utilization of EPS waste as the primary component in a polymeric membrane, aiming to explore its effectiveness in harvesting microalgae. Given that EPS waste is abundantly available and free of charge, the resulting membrane is expected to be cost-effective while also contributing to reducing microplastic reduction in the environment. In this work, PVP was introduced as an additive to assess its impact on membrane performance in rejecting *Spirulina platensis*. The membrane's morphology was analyzed using scanning electron microscopy (SEM). Furthermore, the EPS waste membrane's performance was examined via pure water flux, water contact angle, and microalgae harvesting efficiency.

2. Materials and Methods

2.1. Materials

The EPS waste collected from food packaging was rinsed with pure water to ensure no dust or mechanical impurities were present. The cleaned EPS waste was then compacted to remove air, shredded into tiny pieces, and dried at room temperature. The solvent NMethyl-2-Pyrrolidone (NMP) and the additive Polyvinylpyrrolidone (PVP) were sourced from Merck & Co., Inc., Kenilworth, NJ, USA. The strains of *Spirulina* sp. and *Chlorella* sp. used in this study were sourced from the Center of Excellence for Microalgae Biorefinery at Universitas Gadjah Mada. These microalgae were cultured in saline water and harvested on the 10th day, when they reached their peak density of 95,000 cells/mL and had a protein content exceeding 60% [19].

2.2. Synthesis of EPS Waste Solution

In five bottle flasks, the shredded EPS waste and NMP were added to make a 20 wt.% solution. The flasks were heated at 80 °C until the shredded Styrofoam was dissolved completely. Subsequently, PVP, as the additive, was added to each bottle to make five solutions with concentrations of 0, 2, 4, 6, and 8 wt.%. To ensure uniform distribution of PVP in the solution, all bottle flasks were heated and stirred for three hours to generate

a homogeneous EPS waste dope solution. After the homogeneous state was reached, all bottle flasks were naturally cooled down at room temperature. The dope solutions were marked as PVP-0, PVP-2, PVP-4, PVP-6, and PVP-8, respectively.

2.3. Fabrication of EPS Waste Membrane

A wet-phase inversion method was used to fabricate the EPS waste membrane. Once the dope solution had cooled down, it was carefully poured onto a glass plate. A membrane thickness of 100 µm was achieved by spreading the solution evenly using a casting blade (Elcometer, Manchester, UK). The glass plate was then subsequently transferred to a pure water bath to commence the coagulation of the EPS waste membrane. The membrane was submerged in pure water for a duration of 24 h prior to use. Figure 1 illustrates the preparation and fabrication processes of the EPS waste membrane in this study.

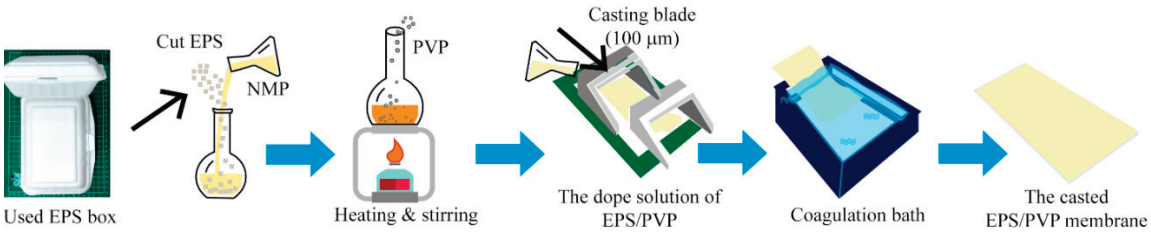

Figure 1. Simplified flow diagram of EPS waste membrane preparation.

2.4. Membrane Characterization

The water flux experiment was conducted for 30 min to achieve stable flux. A dead-end cell (HP4750 Stirred Cell, Sterlitech Corp., Kent, WA, USA) was used to conduct the water flux test, as depicted in Figure 2. The effective membrane area used was 14.6 cm^2. During the experiment, a fixed pressure of 0.5 bar of nitrogen gas was introduced into the dead-end cell unit to maintain sufficient pressure in the pure water chamber. Throughout the process, the permeate water that passed through the tested membrane was carefully monitored and recorded using a Weighing Environment Logger (AD-1687, A&D, RoHS, Tokyo, Japan). The following equations were used to calculate the volumetric flux (J_v) and permeability flux (L_p):

$$J_v = \frac{Q}{A \times \Delta t} \quad (1)$$

$$L_p = \frac{J_v}{\Delta P} \quad (2)$$

where Q is the quantity of the permeate water (in L) during the sampling time, Δt is the sampling time (in h), A is the area of the membrane (in m^2), and ΔP is the pressure difference (in bar).

In order to evaluate membrane surface hydrophilicity, a 5 µL drop of pure water was placed onto the surface of the dried membrane using a micropipette. A contact angle image of the dropped water was captured using a digital microscope (Dinolite Edge 3.0 AM73915MZTL, AnMo Electronics, New Taipei City, Taiwan). The water droplet angle was determined using AUTOCAD (v.2022). To ensure accuracy, the contact angles for each membrane were measured three times and the average values were calculated. The membrane surfaces and cross-sectional morphologies were analyzed using scanning electron microscopy (SEM Phenom ProX, Thermo Fisher, Waltham, MA, USA). Cross-sectional micrographs were obtained by fracturing the wet membrane samples after quickly freezing them in liquid nitrogen.

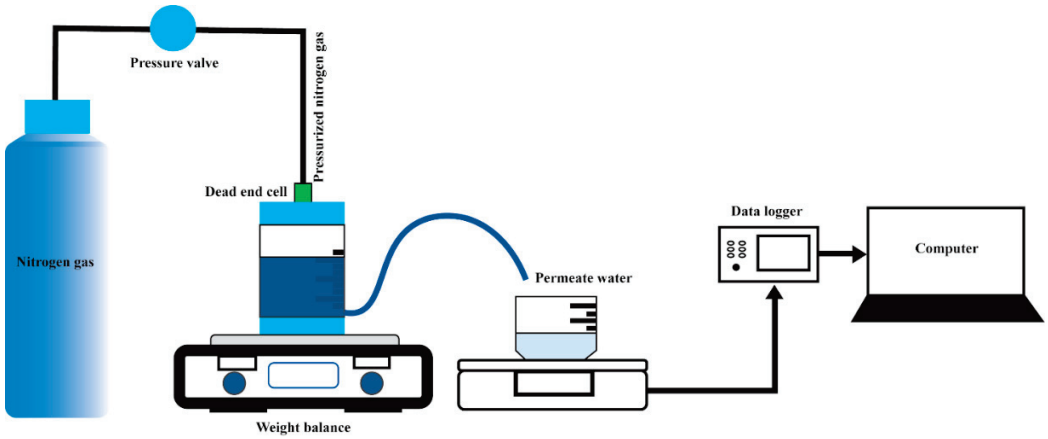

Figure 2. Experimental setup of the water flux test using a dead-end cell unit.

2.5. Microalgae Separation Test

Two microalgae cultures were used, namely *Arthrospira platensis* (*Spirulina*, size range 300–500 µm) and *Chlorella vulgaris* (size range 2–10 µm). Both were cultivated in open ponds at the Microalgae Biorefinery, Universitas Gadjah Mada. *C. vulgaris* was used for comparison as the cell size is significantly smaller than that of *Spirulina*. The microalgae separation experiment was conducted using a dead-end cell filtration test at a fixed pressure of 0.5 bar. To determine the concentration of the permeated microalgae solution, an N4S UV–visible spectrophotometer (Ningbo Hinotek Instrument Co., Ltd., Ningbo, China) was used. The spectrophotometer was operated at a wavelength of 760 nm for *Spirulina platensis* [20] and at a wavelength of 240 nm for *Chlorella vulgaris* [21]. The rejection of solute (SR) was determined by

$$\%SR = \left[1 - \frac{C_p}{C_f}\right] \times 100 \quad (3)$$

where C_p and C_f are the permeated and feed solutions of microalgae concentration, respectively.

3. Results and Discussion

3.1. Membrane Morphology

The SEM images of the top surface of the EPS/PVP waste membranes are presented in Figure 3. The incorporation of PVP into the EPS waste dope solution led to noticeable changes in the top surface of the membranes. The pristine EPS waste membrane has a smooth surface; however, the EPS/PVP-2 membrane exhibited subtle alterations in surface topography, characterized by the emergence of small circles protruding downward compared to the pristine EPS waste membrane. As the PVP concentration increased, both the size and quantity of these protrusions increased. The EPS/PVP-8 exhibited nearly uniform surface pores with an estimated maximum diameter of 1 micrometer. These observations align with previous research indicating that the surface pore size of the membrane gradually increases with higher PVP content [18]. Pakan et al. also used PVP as a significant pore-forming agent for fabricating a PVDF-PVP/CuO composite membrane [21]. PVP, as a water-soluble polymer, has the tendency to aggregate around water molecules drawn into the casting film during the inversion phase. This aggregation yields a PVP-rich phase within the membrane [22,23]. According to Strathmann [24], this PVP-rich phase may serve as weak spots in the top layer that penetrates rapidly downward, further forming macrovoids and pressing some pores into a drop-like pore structure.

Figure 4 presents the cross-sectional SEM images of the membrane, observed at 15,000× magnification. Compared to the pristine EPS waste membrane, all EPS/PVP waste membranes exhibit larger pores and fully developed macrovoids, with reduced top layer density. This could be attributed to the water solubility of PVP during phase inversion, which forces the formation of a loose top layer and larger macrovoids. In this

work, EPS/PVP-8 exhibited the most open, interconnected finger-like pores supported by the most open pores on the surface. According to Han and Nam [25], macrovoids can be initiated by non-homogeneous demixing on the cast solution surface, and a low concentration of PVP as an additive induces the enhancement of demixing, which explains the enlargement of macrovoids.

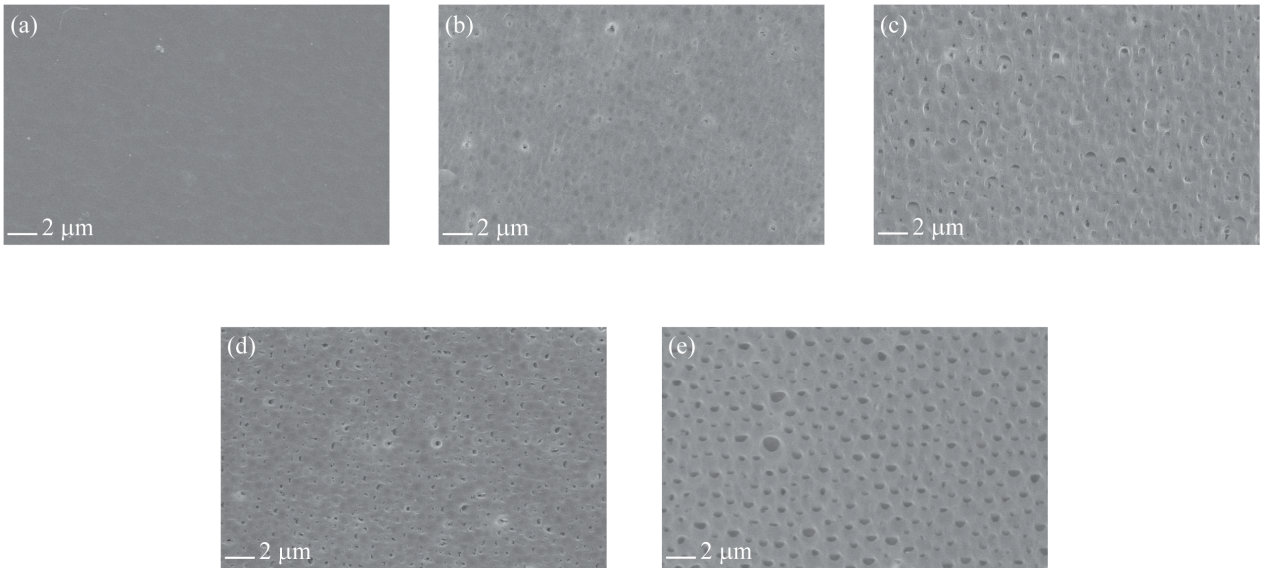

Figure 3. SEM micrographs on top surfaces of 20 wt.% EPS/PVP waste membranes: (**a**) pristine EPS, (**b**) EPS/PVP-2, (**c**) EPS/PVP-4, (**d**) EPS/PVP-6, and (**e**) EPS/PVP-8.

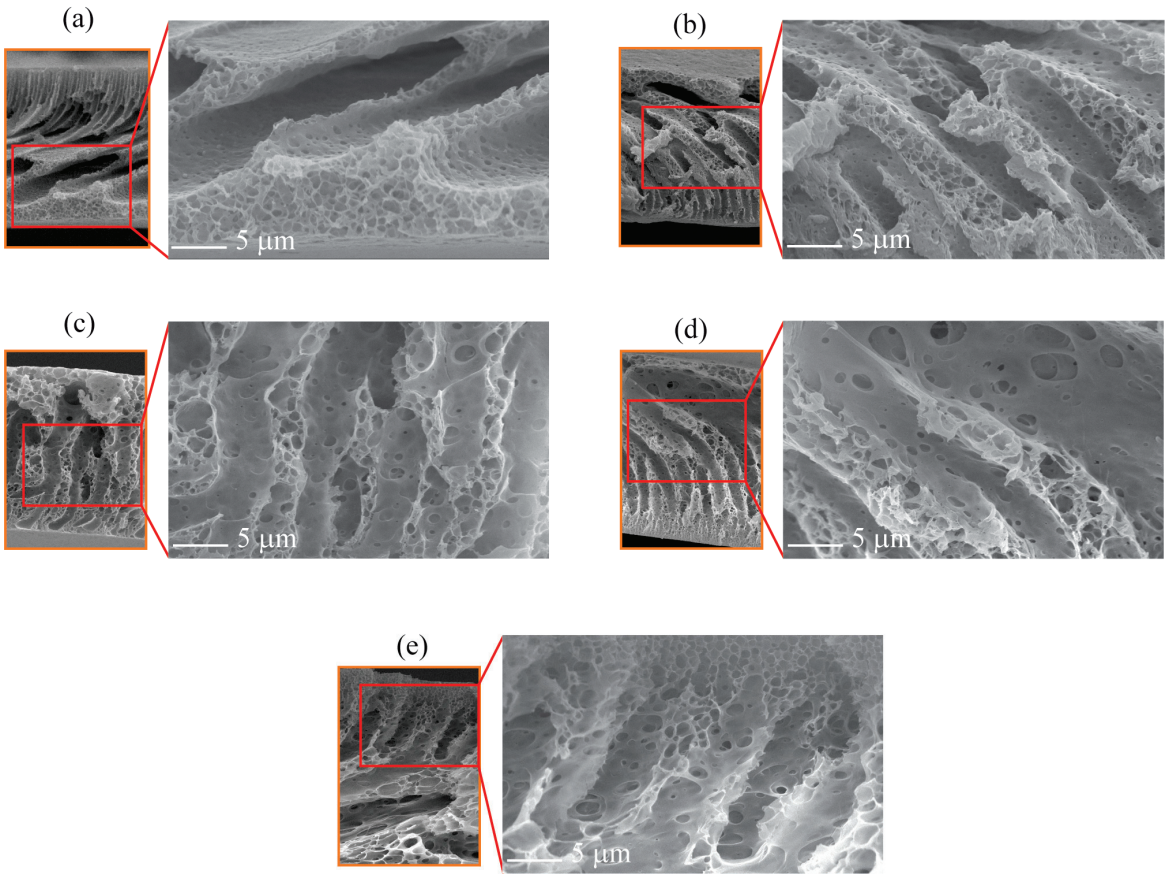

Figure 4. Cross-sectional SEM micrographs of 20 wt.% EPS/PVP waste membranes: (**a**) pristine EPS membrane, (**b**) EPS/PVP-2, (**c**) EPS/PVP-4, (**d**) EPS/PVP-6, and (**e**) EPS/PVP-8.

3.2. Microalgae Harvesting Performance

A microalgae rejection test was performed to measure the harvesting performance of the EPS waste membrane. To do so, flat sheet EPS waste membranes were randomly sampled from four distinct locations. These membranes were then utilized in the process of microalgae dewatering to extract their biomass. The supernatant was examined to quantify its rejection using a UV–visible spectrophotometer. Figure 5 visually depicts the rejection rate, or harvesting efficiency, of microalgae when interacting with the fabricated EPS waste membranes. Observing the results, both the pristine EPS waste membrane and the ones with added PVP exhibited almost complete biomass extraction of *Spirulina*, with a minimal standard deviation. This finding implies that water reuse is a viable option for subsequent batches of *Spirulina* cultivation when using EPS waste membranes. Sustainable farming is achieved by conserving water, reducing nutrient requirements, as well as helping cleanse the water in case of discharge. In this work, *Chlorella vulgaris*, with a size range of 2–10 μm, was used as a rejection comparison to *Spirulina*, sized 300–500 μm. The *C. vulgaris* supernatant had a pale, greenish color, and it was revealed that the harvesting efficiency was about 50%. The observed color and rejection rate of *C. vulgaris* indicates a likelihood of pore clogging. In microalgae harvesting with the membrane filtration technique, the membrane pore frequently clogged due to the adsorption of extracellular organic matter. These macromolecules, including polysaccharides and fibrous proteins, contribute to irreversible fouling of the membrane, ultimately reducing the efficiency of microalgae harvesting [26].

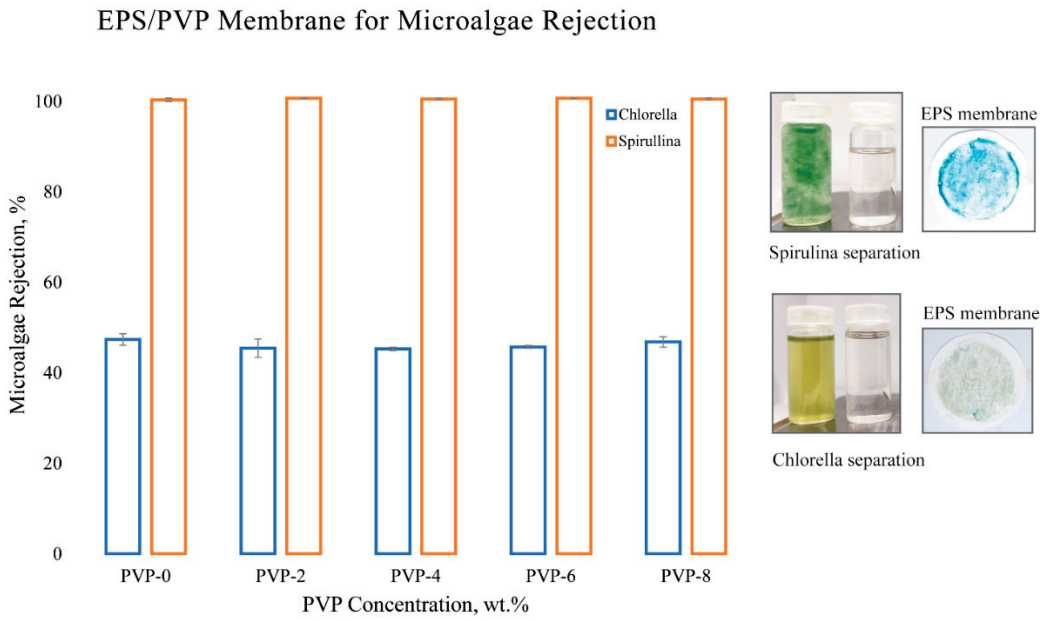

Figure 5. Microalgae harvesting using WEPS membranes with varied PVP concentrations.

Harvesting and water reuse pose critical challenges in large-scale microalgae cultivation. Bhave et al. [27] found that microfiltration offers effective separation comparable to ultrafiltration membranes, while operating at lower pressures. Dizge et al. [28] corroborated this finding. Their research demonstrated that membranes with 0.45 μm pore sizes made of mixed cellulose ester (MCE) exhibited higher fluxes compared to membranes with 0.1–0.2 μm pore sizes. In this work, aside from near complete cell recovery of *Spirulina*, a clear supernatant was also observed which is suitable for water reuse. Consequently, larger pore sizes like that observed in EPS waste membranes hold significant potential for microalgae harvesting with significant cost savings and a reduced carbon footprint.

3.3. Pure Water Flux Test Experiments

Figure 6 displays the water flux of fabricated EPS waste membranes with varying concentrations of PVP. The water flux is lowest for the pristine EPS waste membrane (449.7 LMH/Bar) and increases with increasing PVP concentration to double fold at PVP-8 (970.5 LMH/Bar), which suggests that the pore size of the pristine EPS waste membrane is the smallest amongst all the membranes. Pure water fluxes increase gradually with increasing PVP content, which is probably due to the increase in surface pore size and macrovoids. The surface SEM micrographs in Figures 3 and 4 clarifies this suggestion. All membranes with PVP have larger open pores, with size and quantity increasing with PVP concentration. It can be seen that all membranes with PVP have larger wall pores, hence better water flow. According to Han and Nam [24], the addition of low-concentration PVP to a cast solution results in the enlargement of macrovoid structures and induced change in surface porosity, which then leads to improved membrane permeate flux. This alteration is attributed to PVP's ability to enhance phase separation during demixing. Nouzaki et al. [29] observed that their polysulfone membrane became porous when using a casting solution containing PVP as an additive. From this work, they concluded that water-soluble PVP created islands within the membrane during formation, leading to an increase in pore size.

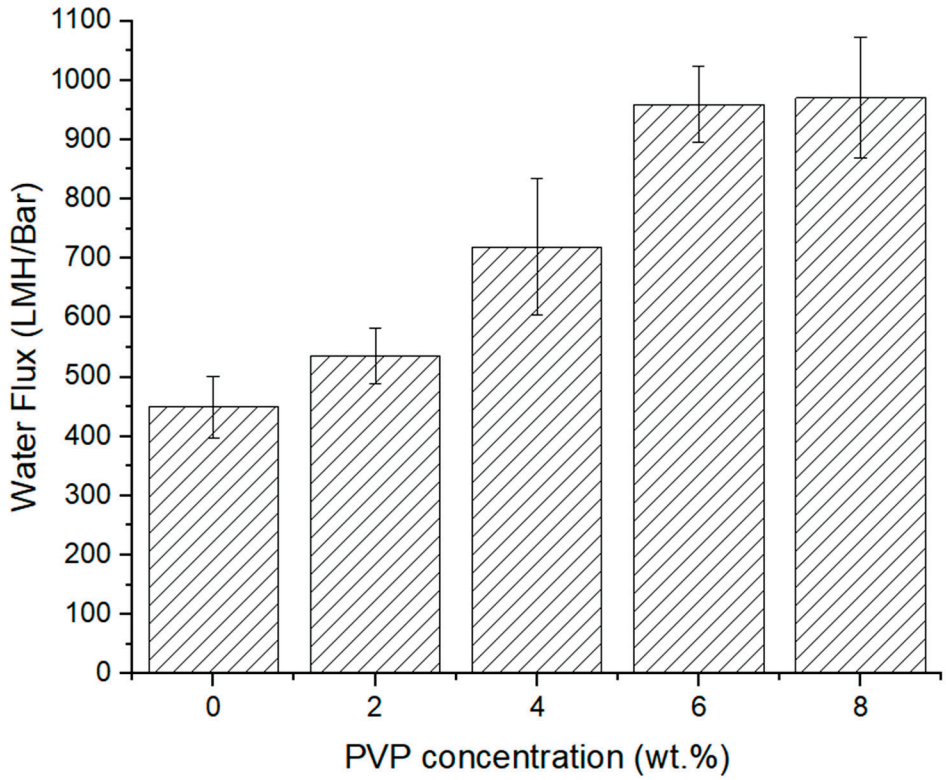

Figure 6. Pure water flux of EPS waste membranes with varied PVP concentrations.

3.4. Water Contact Angle Analysis

Figure 7 illustrates the water contact angle measurements for the EPS waste membranes. Notably, all the measured angles were below 90°, indicating that all the membranes are hydrophilic. The initial contact angle (CA) of the pristine EPS waste membrane was 68°. The addition of PVP made the contact angle gradually increase to 85°. Because of its water solubility, a significant portion of PVP was washed away from the membrane during the phase inversion process. The reduction of PVP content went against the expected improvement in membrane hydrophilicity. Consequently, the hydrophobicity of the membrane increased as the PVP concentration rose [17].

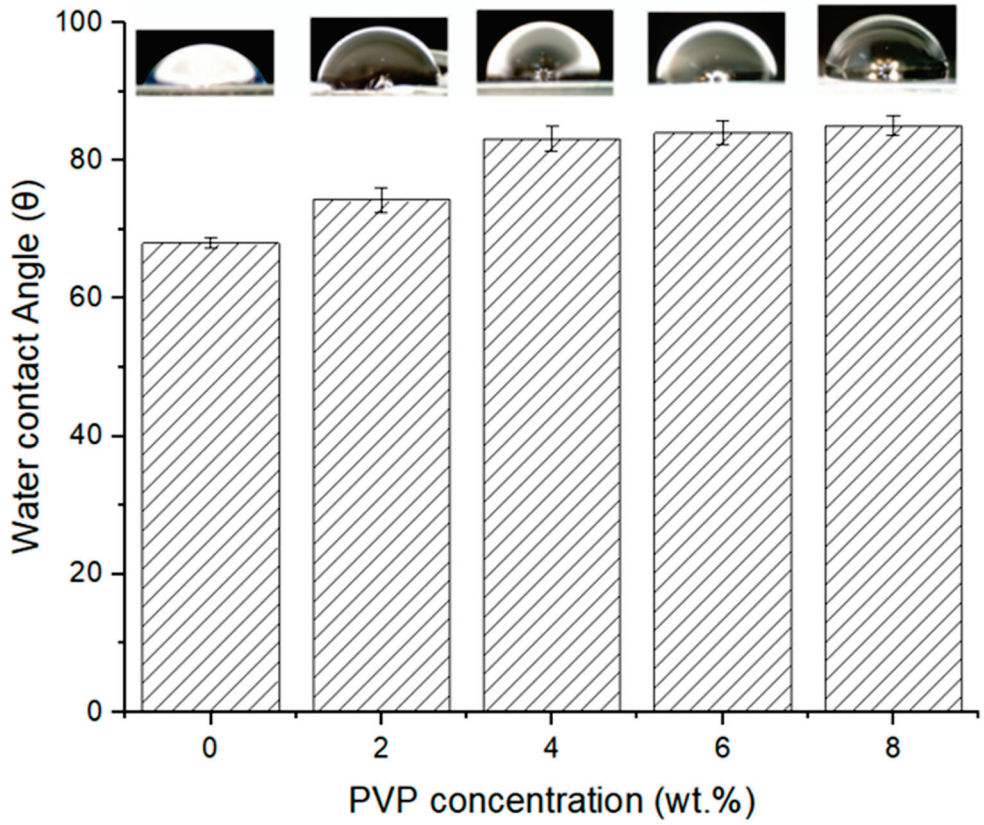

Figure 7. Water contact angle of EPS waste membranes with varied PVP concentrations.

This finding is aligned with the research of Ghaly et al. [10]. In their research, they fabricated High-Impact Polystyrene (HIPS) waste membranes and revealed that these membranes exhibited either hydrophilic or semi-hydrophilic behavior with contact angles ranging from 69° to 84°. On the contrary, commercial polystyrene (PS) membranes are typically hydrophobic. The observed difference could be attributed to a lower proportion of polystyrene in either EPS or HIPS and the inclusion of additives to make PS products. The presence of impurities likely induced the alteration in membrane surface morphologies, resulting in an increase in hydrophobicity. Given its hydrophilic nature, the membrane is well-suited for water-related applications such as microalgae harvesting or wastewater treatment.

3.5. Comparison with Other EPS Waste Membrane Materials

There are few reports in the literature in which EPS waste was used as a separation medium, as presented in Table 1.

Most of the work was conducted using the electrospinning technique, primarily for air filtration media. The majority of membrane fabrication techniques involve electrospinning with various modifications to enhance the efficiency of the air filter media. Shin et al. [5] incorporated micro-glass fibers into an EPS waste dope solution, reporting that this addition improved the separation efficiency of the filter media while also increasing the pressure drop. Munir et al. [12], without adding additives, modified the electrospinning process to be needleless with several inputs. The combination of large and small fiber diameters produced through electrospinning could result in an air filter with an efficiency of up to 99.4%. Ghaly et al. [12] used NIPS to create a flat sheet membrane from EPS waste; however, there is limited information on the membrane's effectiveness in liquid separation processes. This study, however, utilizes EPS waste for water filtration purposes, specifically for microalgae harvesting. PVP was used to enhance pure water flux. The experimental results indicate a promising future for the upcycled EPS waste membrane in water treatment facilities.

Table 1. Comparison of upcycled EPS membranes from other works.

EPS wt.%	Additives	Solvent	Technique	Membrane Type	PWF	WCA	Purpose	Ref.
15%	PTFE + SiO_2	DMF + C_3H_6O	Core-shell electrospinning	Microfiber	-	172.4°	Anti-fogging, debris removal	[8]
20%	Micro glass fiber	DMAc	Electrospinning	Nanofiber	-	-	Water-in-oil separation	[5]
15%	-	DMAc	Electrospinning	Nanofiber	-	-	Air filter media	[30]
20%	-	DMF	Needleless electrospinning	Nanofiber	-	179.7	Air filter for facemask	[12]
15%	-	DMF	Electrospinning	Nanofiber	-	153	Air filter media	[31]
18%	-	DMF	NIPS	Flat sheet	-	-	Liquid filtration	[11]
20%	PVP	NMP	NIPS	Flat sheet	970.5	85	Microalgae harvesting	This work

4. Conclusions

In this study, Expanded Polystyrene (EPS) waste membranes were prepared using a wet phase inversion procedure and modified by varying the concentration of PVP. The EPS waste, collected from used food packaging, was upcycled into flat sheet membranes through this technique. The overall permeability, morphology, and efficacy in filtering microalgae were investigated. The following conclusions were drawn from this study:

a. Introducing PVP into the EPS waste dope solution significantly increased surface pore size and improved connectivity between wall pores, thereby enhancing water flux, as revealed by SEM micrographs.
b. These membranes were used to harvest microalgae, resulting in nearly complete biomass recovery for *Spirulina platensis* and 50% recovery for *Chlorella vulgaris*. The EPS/PVP-8 membrane achieved the highest water flux of 970.5 LMH/Bar, which is double that of the pristine EPS waste membrane.
c. Despite the increase in hydrophobicity due to the added PVP concentration, all membranes remained hydrophilic. This characteristic makes the upcycled membrane suitable for water-related filtration tasks, including microalgae harvesting.

The supernatant from microalgae separation using the EPS waste membrane can be reused in subsequent cultivations, promoting sustainable farming by conserving water and nutrients. Fabricating membranes from EPS waste offers a promising solution for addressing plastic and water pollution in the future.

Author Contributions: Conceptualization, G.S.P., M.M. and T.S.; methodology, T.S. and G.S.P.; validation, T.S. and C.P.W.; formal analysis, G.S.P.; investigation, G.S.P. and T.S.; resources, G.S.P. and M.M.; data curation, T.S. and S.A.A.; writing—original draft preparation, T.S.; writing—review and editing, G.S.P. and M.M.; visualization, T.S.; supervision, G.S.P. and M.M.; project administration, C.P.W. and S.A.A.; funding acquisition, G.S.P., M.M. and S.A.A. All authors have read and agreed to the published version of the manuscript.

Funding: This research was funded by Skema International Research Collaboration Top #300, Universitas Airlangga. (Grant No. 338/UN3.15/PT/2023).

Institutional Review Board Statement: Not applicable.

Data Availability Statement: The original contributions presented in the study are included in the article, further inquiries can be directed to the corresponding author.

Acknowledgments: The authors express their gratitude to Aini Zuhra Abdul Kadir and the staff of Lembaga Penelitian Dan Pengabdian Masyarakat, Universitas Airlangga, Indonesia, for their invaluable help and guidance in this project.

Conflicts of Interest: Author Tutik Sriani was employed by the PT. Global Meditek Utama-IITOYA. The remaining authors declare that the research was conducted in the absence of any commercial or financial relationships that could be construed as a potential conflict of interest.

References

1. Ho, B.T.; Roberts, T.K.; Lucas, S. An overview on biodegradation of polystyrene and modified polystyrene: The microbial approach. *Crit. Rev. Biotechnol.* **2018**, *38*, 308–320. [CrossRef] [PubMed]
2. Min, Z.; Yang, H.; Chen, F.; Kuang, T. Scale-up production of lightweight high-strength polystyrene/carbonaceous filler composite foams with high-performance electromagnetic interference shielding. *Mater. Lett.* **2018**, *230*, 157–160. [CrossRef]
3. Crespo, J.H.; Moreira, C.M.; Jervis, F.X.; Soto, M.; Amaya, J.L.; Banguera, L. Circular economy of expanded polystyrene container production: Environmental benefits of household waste recycling considering renewable energies. *Energy Rep.* **2022**, *8*, 306–311. [CrossRef]
4. Otake, Y.; Kobayashi, T.; Asabe, H.; Murakami, N.; Ono, K. Biodegradation of low-density polyethylene, polystyrene, polyvinyl chloride, and urea formaldehyde resin buried under soil for over 32 years. *J. Appl. Polym. Sci.* **1995**, *56*, 1789–1796. [CrossRef]
5. Shin, C.; Chase, G.G.; Reneker, D.H. Recycled expanded polystyrene nanofibers applied in filter media. *Colloids Surf. A Physicochem. Eng. Asp.* **2005**, *262*, 211–215. [CrossRef]
6. Baig, N.; Alghunaimi, F.I.; Saleh, T.A. Hydrophobic and oleophilic carbon nanofiber impregnated Styrofoam for oil and water separation: A green technology. *J. Chem. Eng.* **2019**, *360*, 1613–1622. [CrossRef]
7. Mahdi, H.A.; Jasim, K.A.; Shaban, A.H. Manufacturing and improving the characteristics of the isolation of concrete composite by additive Styrofoam particulate. *Energy Procedia* **2019**, *157*, 158–163. [CrossRef]
8. Ijaola, A.O.; Akamo, D.O.; Adekanmi, A.M.; Saberi, Q.; Koken, D.; Asmatulu, E. Superhydrophobic and self-cleaning electrospun microfibers from recycled styrofoam. *Results Surf. Interfaces* **2002**, *9*, 100086. [CrossRef]
9. Wang, C.; Wang, Q.; Yu, J.; Wang, X.; Wang, L.; Zhao, B.; Hao, L.; Liu, W.; Wang, Z.; Chen, H.; et al. Converting waste expanded polystyrene into higher-value-added hyper-crosslinked porous polymer for rapid and high-efficient adsorptions of aflatoxins. *J. Clean. Prod.* **2023**, *408*, 137102. [CrossRef]
10. Chen, D.; Xie, Z.; Ye, H.; Li, W.; Shi, W.; Liu, Y. Upcycling of expanded polystyrene waste: Amination as adsorbent to recover Eriochrome Black T and Congo red. *Sep. Purif. Technol.* **2022**, *289*, 120669. [CrossRef]
11. Ghaly, S.T.; Noby, H.; Hayashi, J.I.; El-Shazly, A.H. Various waste polystyrene for useful membrane fabrication: Comparative experimental study. *Mater. Today Proc.* **2023**. [CrossRef]
12. Munir, M.M.; Adrian, M.; Burhanuddin, M.; Iskandar, F. Fabrication and structure optimization of expanded polystyrene (EPS) waste fiber for high-performance air filtration. *Powder Technol.* **2022**, *402*, 117357. [CrossRef]
13. Sihombing, Y.S.; Sinaga, M.Z.E.; Hardiyanti, R.; Susilawati; Saragi, I.R.; Rangga. Preparation, characterization, and desalination study of polystyrene membrane integrated with zeolite using electrospinning method. *Heliyon* **2022**, *8*, e10113. [CrossRef]
14. Gerardo, M.L.; Radcliffe, D.L.O.; Lovitt, R.W. Integration of membrane technology in microalgae biorefineries. *J. Membr. Sci.* **2014**, *464*, 86–99. [CrossRef]
15. Venault, A.; Ballad, M.R.B.; Huang, Y.T.; Liu, Y.H.; Kao, C.H.; Chang, Y. Antifouling PVDF membrane prepared by VIPS for microalgae harvesting. *Chem. Eng. Sci.* **2016**, *142*, 97–111. [CrossRef]
16. Aditya, L.; Vu, H.P.; Nguyen, L.N.; Mahlia, T.M.I.; Hoang, N.B.; Nghiem, L.D. Microalgae enrichment for biomass harvesting and water reuse by ceramic microfiltration membranes. *J. Membr. Sci.* **2023**, *669*, 121287. [CrossRef]
17. Yeo, H.T.; Lee, S.T.; Han, M.J. Role of a polymer additive in casting solution in preparation of phase inversion polysulfone membranes. *J. Chem. Eng. Jpn.* **2000**, *33*, 180–184. [CrossRef]
18. Zhao, S.; Wang, Z.; Wei, X.; Tian, X.; Wang, J.; Yang, S.; Wang, S. Comparison study of the effect of PVP and PANI nanofibers additives on membrane formation mechanism, structure and performance. *J. Membr. Sci.* **2011**, *385–386*, 110–122. [CrossRef]
19. Sadewo, B.R.; Dewayanto, N.; Rochmadi; Juniawan, A.S.; Budiman, A. Optimization study of Phycocyanin ultrasound-assisted extraction process from *Spirulina* (*Arthospira platensis*) using different solvent. *Egypt. J. Chem.* **2024**, *67*, 589–608. [CrossRef]
20. Koehne, B.; Trissl, H.W. The cyanobacterium *Spirulina platensis* contains a long wavelength-absorbing pigment C738 (F76077K) at room temperature. *Biochemistry* **1998**, *37*, 5494–5500. [CrossRef]
21. Zhang, W.; Zhang, D.; Shi, B.; Zhao, Z.; Sun, J.; Wang, Y.; Wang, X.; Lv, Y.; Li, Y.; Liu, Y. Laboratory Experiments to Assess the Effect of Chlorella on Turbidity Estimation. *Water* **2022**, *14*, 3184. [CrossRef]
22. Pakan, M.; Mirabi, M.; Valipour, A. Effectiveness of different CuO morphologies nanomaterials on the permeability, antifouling, and mechanical properties of PVDF/PVP/CuO ultrafiltration membrane for water treatment. *Chemosphere* **2023**, *337*, 139333. [CrossRef] [PubMed]
23. Chakrabarty, B.; Ghoshal, A.K.; Purkait, A.K. Preparation, characterization and performance studies of polysulfone membranes using PVP as an additive. *J. Membr. Sci.* **2008**, *315*, 36–47. [CrossRef]
24. Strathmann, H. *Production of Microporous Media by Phase Inversion Processes*; ACS Publications: Washington, DC, USA, 1985; p. 165.
25. Han, M.J.; Nam, S.T. Thermodynamic and rheological variation in polysulfone solution by PVP and its effect in the preparation of phase inversion membrane. *J. Membr. Sci.* **2002**, *202*, 55–61. [CrossRef]
26. Rossi, N.; Jaouen, P.; Legentilhomme, P.; Petit, I. Harvesting of Cyanobacterium Arthrospira Platensis using organic filtration membranes. *Food Bioprod. Process.* **2004**, *82*, 244–250. [CrossRef]

27. Bhave, R.; Kuritz, T.; Powell, L.; Adcock, D. Membrane-based energy efficient dewatering of microalgae in biofuels production and recovery of value-added co-products. *Environ. Sci. Technol.* **2012**, *46*, 5599–5606. [CrossRef]
28. Dizge, N.; Soydemir, G.; Karagunduz, A.; Keskinler, B. Influence of type and size of membranes on cross flow microfiltration of biological suspension. *J. Membr. Sci.* **2011**, *366*, 278–285. [CrossRef]
29. Nouzaki, K.; Nagata, M.; Arai, J.; Idemoto, Y.; Koura, N.; Yanagishita, H.; Negishi, H.; Kitamoto, D.; Ikegami, T.; Haraya, K. Preparation of polyacrylonitrile ultrafiltration membranes for wastewater treatment. *Desalination* **2002**, *144*, 53–59. [CrossRef]
30. Shin, C. Filtration application from recycled expanded polystyrene. *J. Colloid Interface Sci.* **2006**, *301*, 267–271. [CrossRef]
31. Rajak, A.; Hapidin, D.S.; Iskandar, F.; Munir, M.M.; Khairurrijal, K. Electrospun nanofiber from various source of expanded polystyrene (EPS) waste and their characterization as potential air filter media. *Waste Manag.* **2020**, *103*, 78–86. [CrossRef]

Disclaimer/Publisher's Note: The statements, opinions and data contained in all publications are solely those of the individual author(s) and contributor(s) and not of MDPI and/or the editor(s). MDPI and/or the editor(s) disclaim responsibility for any injury to people or property resulting from any ideas, methods, instructions or products referred to in the content.

polymers

MDPI

Article

Advancing Sustainability and Performance with Crushed Bottom Ash as Filler in Polymer-Modified Asphalt Concrete Mixtures

Yeong-Min Kim [1], Kyungnam Kim [2,*] and Tri Ho Minh Le [3,*]

[1] Department of Highway & Transportation Research, Korea Institute of Civil Engineering and Building Technology, 283 Goyangdae-Ro, Ilsanseo-Gu, Goyang-si 10223, Gyeonggi-do, Republic of Korea; choozang@kict.re.kr

[2] Korea Expressway Corporation Research Institute, Pavement Research Division, Dongtansunhwan-daero 17-gil, Hwaseong-si 18489, Gyeonggi-do, Republic of Korea

[3] Faculty of Civil Engineering, Nguyen Tat Thanh University, 300A Nguyen Tat Thanh Street, District 4, Ho Chi Minh City 70000, Vietnam

* Correspondence: kkn248@ex.co.kr (K.K.); lhmtri@ntt.edu.vn (T.H.M.L.)

Abstract: Amid the growing demand for sustainable pavement solutions and the need to incorporate recycled materials into construction practices, this study explored the viability of using crushed thermal power plant bottom ash as a filler in polymer-modified asphalt concrete mixtures. Conventional lime filler was replaced with bottom ash at varying levels (0%, 25%, 50%, and 75%), and the resulting mixtures were evaluated using several performance tests. The optimal replacement level was determined to be 25%, based on the results of the indirect tensile strength (ITS) test. Comparisons between the control mixture and the 25% bottom ash-modified mixture were conducted using the dynamic modulus test, Cantabro test, Hamburg wheel tracking (HWT) test, and tensile strength ratio (TSR) test. The findings indicate that the 25% bottom ash-modified mixture demonstrated improved performance across multiple parameters. The HWT test showed enhanced rut durability, with a recorded depth of 7.56 mm compared to 8.9 mm for the control mixture. The Cantabro test results revealed lower weight loss percentages for the modified mixture, indicating better abrasion resistance. The dynamic modulus test indicated higher resilience and stiffness in both high- and low-frequency stages. The TSR test highlighted improved moisture resistance, with higher TSR values after 10 wet-drying cycles. These improvements are attributed to the fine particle size and beneficial chemical composition of bottom ash, which enhance the asphalt mixture's density, binder-aggregate adhesion, and overall durability. The results suggest that incorporating 25% crushed bottom ash as a filler in polymer-modified asphalt concrete mixtures is a viable and sustainable approach to improving pavement performance and longevity.

Keywords: sustainable pavement; recycled materials; bottom ash filler; polymer-modified asphalt; crumb rubber; performance evaluation

1. Introduction

The ever-increasing demand for sustainable construction materials has driven significant research into alternative materials that can enhance the performance of asphalt concrete mixtures while mitigating environmental impacts [1]. Among the various types of asphalt concrete, polymer-modified asphalt (PMA) has gained substantial attention due to its superior performance characteristics, including increased stiffness, reduced deformation, and enhanced durability [2]. These benefits are particularly pronounced in styrene-butadiene-styrene (SBS) modified binders, which have been widely adopted in road construction due to their ability to withstand a range of climatic conditions and heavy traffic loads [3].

SBS-modified asphalt mixtures highlight their superior performance characteristics compared to conventional asphalt mixtures [4,5]. SBS modification enhances the rheologi-

cal properties of asphalt binders, resulting in increased stiffness and elasticity, which are crucial for maintaining pavement performance under varying environmental conditions and traffic loads [6,7]. Studies have shown that SBS-modified mixtures possess improved fatigue resistance due to the polymer's ability to enhance flexibility and tensile strength, thereby reducing crack initiation and propagation [8,9]. Furthermore, SBS modification greatly increases the binder's high-temperature efficiency, which is crucial for preventing rut development under heavy traffic, hence improving rutting resistance [10,11]. SBS-modified mixtures also exhibit enhanced resistance to thermal cracking, as the polymer provides greater elasticity, allowing the binder to better accommodate thermal stresses [12]. Furthermore, SBS-modified asphalt demonstrates better long-term aging performance, maintaining flexibility and adhesion properties over time, which is vital for pavement durability [13]. Related reports note that SBS-modified mixtures have lower moisture susceptibility due to improved binder-aggregate adhesion, reducing the potential for stripping and moisture-induced damage [2]. Collectively, these studies underscore the significant advantages of SBS-modified asphalt mixtures, making them a valuable choice for designing high-performance pavements capable of meeting modern infrastructure demands.

Despite the advantages of SBS-modified asphalt, the search for further performance improvements and sustainability has led to the exploration of various additives and fillers. One promising avenue is the incorporation of recycled crumb rubber from tires [14], which not only improves the performance of HMA mixtures but also addresses the growing concern of tire waste management. Crumb rubber-modified asphalt has been shown to enhance flexibility, resistance to thermal cracking, and overall longevity of pavements [15,16].

Recent studies have shown that using byproducts and waste materials in hot mix asphalt (HMA) can significantly enhance its sustainability and performance [17,18]. Research has demonstrated that bottom ash can improve moisture resistance and reduce environmental impacts [19,20]. Other studies have found that coal bottom ash and carbonized rice husk can be effectively used in HMA [21,22]. Low-grade magnesium carbonate by-products and palm oil by-products have also been explored for their beneficial properties in asphalt mixtures [22]. Additionally, waste engine oil and waste plastic aggregates, along with additives like magnesium, have been evaluated for their positive impact on eco-friendly asphalt mixtures [23,24]. The performance of recycled asphalt mixtures has been improved using advanced separation technologies [25]. Overall, these findings highlight the practical benefits of incorporating waste materials into HMA, contributing to more sustainable construction practices [26].

In parallel, the utilization of industrial by-products as fillers in asphalt mixtures has garnered interest due to their potential to reduce environmental impact and material costs [27]. Thermal power plant bottom ash is one such by-product that has shown promise as a filler material [26]. Bottom ash, a residue from coal combustion in power plants, is primarily composed of silica, alumina, and other oxides, which can contribute to the mechanical strength and durability of asphalt mixtures [18]. Reducing the amount of natural resources used and diverting large amounts of waste from landfills are achievable by mixing bottom ash into asphalt blends.

Despite the numerous benefits of SBS-modified asphalt mixtures, there are still some limitations and areas that require further research. One significant limitation is the increased cost associated with SBS polymers, which can make large-scale implementation economically challenging. Additionally, the performance of SBS-modified asphalt can vary based on the specific formulation and mixing process, leading to inconsistencies in field applications. There is also a need for more extensive long-term performance data to fully understand the durability of these mixtures under diverse climatic conditions and traffic loads. Research needs include optimizing the mix design to reduce costs, improving the understanding of the interactions between SBS polymers and different types of aggregates, and developing standardized procedures for incorporating SBS into asphalt mixtures to ensure consistent quality. This research addresses these gaps by investigating the feasibility of using crushed thermal power plant bottom ash as a filler in SBS-modified

asphalt mixtures containing crumb rubber. This innovative approach not only aims to enhance the performance and sustainability of the asphalt but also provides a cost-effective solution by utilizing industrial by-products. By exploring the optimal replacement levels of conventional lime with bottom ash, our study contributes to the growth of more durable, eco-friendly, and economically viable pavement materials.

The primary goal of this research was to evaluate the feasibility of using crushed thermal power plant bottom ash as a filler in polymer-modified asphalt concrete mixtures. To accomplish this, this study used the Superpave mix design approach, which aimed for an ideal asphalt binder content. This study involved replacing conventional lime filler with bottom ash at replacement levels of 0%, 25%, 50%, and 75%, to determine the most effective proportion. The asphalt combinations were developed utilizing a mix of SBS-modified binder from asphalt and particular proportions carefully chosen to improve performance characteristics. The research then produced samples for each mix design and subjected them to a series of rigorous tests, including the indirect tensile strength (ITS) test, dynamic modulus test, Cantabro test, Hamburg wheel tracking (HWT) test, and tensile strength ratio (TSR) test. These tests were conducted to evaluate the mechanical properties, durability, moisture susceptibility, and overall performance of the modified asphalt mixtures. Through these comprehensive evaluations, our research aimed to demonstrate the potential benefits and practical applications of using bottom ash as a sustainable alternative filler in asphalt pavements. The research flowchart is presented in the following Figure 1.

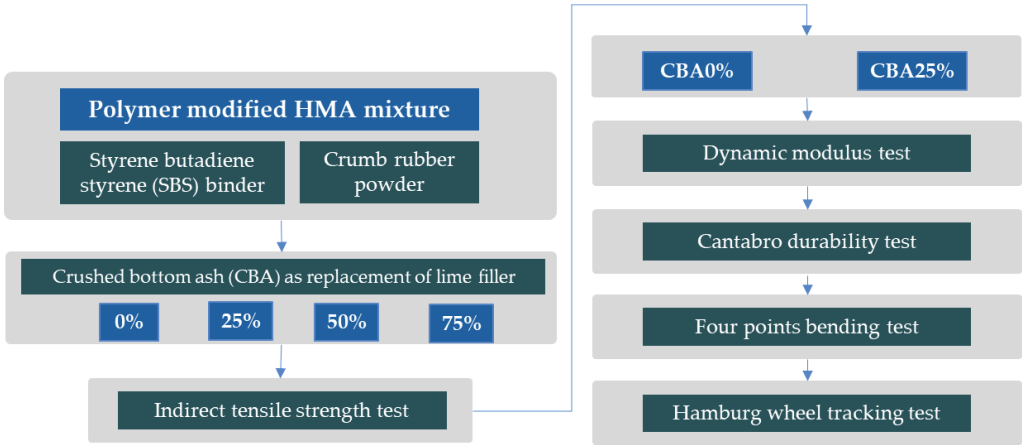

Figure 1. Research flowcharts.

2. Materials and Methods

2.1. Materials

2.1.1. Aggregate

The aggregate utilized in this research had a nominal maximum aggregate size (NMAS) of 10 mm and was specifically designed to meet the parameters for HMA procedures. This material met strict national criteria for aggregate quality and came from a reliable quarry [28]. In compliance with specified aggregate regulations, an extensive assessment of the aggregate's physical characteristics was carried out. The aggregate was meticulously cleaned and dried before being added to the asphalt concrete compositions. It was heated at 110 °C for 24 h to remove any remaining moisture and contaminants. According to national guidelines, a sieve test was then carried out to guarantee the aggregate's consistency and appropriate gradation, as shown in Table 1. Certain physical and mechanical characteristics of the aggregate were included in the quality assessment; these are all thoroughly recorded in Table 2.

Table 1. Sieve analysis of aggregate.

Sieve Size (mm)	Percentage Passing
19.0	100
12.5	90–100
9.5	70–90
4.75	35–55
2.36	23–35
1.18	15–25
0.600	10–20
0.300	5–15
0.150	2–10
0.075	0–5

Table 2. Aggregate properties.

Property	Value
Specific Gravity	2.65
Bulk Density	1.6 g/cm^3
Water Absorption	1.0%
Los Angeles Abrasion	20%
Aggregate Crushing Value	25%
Flakiness Index	10%

2.1.2. Characterization of Bottom Ash

The crushed bottom ash used in this study was characterized to understand its properties and justify its effects on the modified asphalt mixtures. The particle size distribution of the bottom ash particles was analyzed using sieve analysis, which revealed a size distribution ranging from 0.1 to 100 μm, with a significant proportion of particles below 50 μm. Table 3 presents the overview of the bottom ash properties used in this research.

Table 3. Summary of bottom ash properties.

Property	Value
Particle Size Range	0.1–100 μm
Specific Surface Area	25 m^2/g
Total Porosity	40%
Density	2.7 g/cm^3
SiO_2	50%
Al_2O_3	28%
Fe_2O_3	12%
CaO	6%
MgO	2%
SO_3	2%

The porosity and surface area were measured using a BET (Brunauer-Emmett-Teller) analysis, which found the specific surface area of the bottom ash to be 25 m^2/g, indicating a high surface area conducive to good binder-aggregate interaction. Additionally, the porosity was measured using mercury intrusion porosimetry, revealing a total porosity of 40%. The density of crushed bottom ash was found to be 2.7 g/cm^3, higher than conventional lime filler, contributing to the mixture's overall density and stability.

The chemical composition was analyzed using X-ray fluorescence (XRF), showing the following composition: 50% SiO_2, 28% Al_2O_3, 12% Fe_2O_3, 6% CaO, 2% MgO, and 2% SO_3. These characteristics underscore the suitability of crushed bottom ash as a filler in asphalt mixtures, contributing to enhanced binder-aggregate adhesion and overall mixture performance.

Silicon dioxide and aluminum oxide enhance the hardness and strength of the bottom ash, improving the asphalt's load-bearing capacity. Iron oxide boosts thermal stability and resistance to high temperatures, essential for varying climates. Calcium oxide improves binder-aggregate adhesion, reducing moisture damage and stripping. Magnesium oxide and sulfur trioxide further enhance the asphalt mixture's chemical stability and performance.

In this research, the filler ratio was fixed at 1.5% by weight for both lime and crushed bottom ash based on initial trial tests [28]. The additives used in this research, including crushed bottom ash (see Figure 2) and other components, were meticulously selected and characterized to evaluate their suitability for asphalt mixture applications. Conventional lime filler exhibits variable particle sizes, depending on the source and processing methods, while crushed bottom ash presents a more uniform particle size distribution ranging from 0.1 to 100 μm.

Figure 2. Bottom ash before and after the crushing process.

Crushing bottom ash is essential to optimize its suitability for incorporation into asphalt mixtures and other construction applications [29]. Reducing bottom ash to finer particle sizes, enhances its compatibility with asphalt binder and aggregates, promoting better homogeneity and cohesion within the mixture. Additionally, crushing facilitates better distribution of bottom ash throughout the asphalt matrix, ensuring uniformity of properties and enhancing overall performance. The process of crushing also helps to mitigate potential issues related to particle size distribution, ensuring that the bottom ash meets specified requirements for the intended application. Overall, crushing bottom ash is a crucial step in unlocking its potential as a sustainable filler material, contributing to the development of eco-friendly and high-performing pavement solutions.

In terms of density, conventional lime filler typically ranges from 2.2 to 2.5 g/cm^3, whereas crushed bottom ash demonstrates a higher density of 2.7 g/cm^3. Chemical composition analysis highlights further disparities between the two materials [30]. Conventional lime filler primarily consists of calcium carbonate ($CaCO_3$), whereas crushed bottom ash comprises a diverse composition. Its chemical composition includes 50% silicon dioxide (SiO_2), 28% aluminum oxide (Al_2O_3), 12% iron oxide (Fe_2O_3), 6% calcium oxide (CaO), 2% magnesium oxide (MgO), and 2% sulfur trioxide (SO_3). This composition reflects the mineralogical nature of bottom ash, making it a potentially effective filler material in asphalt mixtures [30].

In addition, bottom ash's absorption properties were evaluated. The crushed bottom ash demonstrated an absorption rate of 0.4%, significantly lower than the 1.3% absorption rate of natural aggregates. This lower absorption rate suggests that crushed bottom ash may offer enhanced resistance to moisture-induced damage in asphalt mixtures, potentially leading to improved durability and performance.

2.1.3. Asphalt Binder Modified with Styrene-Butadiene-Styrene Polymer

A polymer-modified SBS asphalt binder was incorporated into the mixture to improve its rheological properties. This SBS binder, introduced in pellet form during mixing, serves to enhance stiffness and durability, addressing the demands of high-performance

asphalt pavements. The quantity of SBS polymer was carefully determined based on expert recommendations and preliminary trials [31] as outlined in Table 4, ensuring optimal performance. Furthermore, crumb rubber powder, detailed in Table 5, was introduced at a rate of 6% to augment the overall performance of the asphalt mixture. This addition followed a meticulous treatment process to eliminate contaminants and enhance the rubber's compatibility with the binder. The treatment process involved cleaning the crumb rubber to remove any residual contaminants, followed by a cryogenic grinding method to achieve a uniform particle size distribution. The rubber particles were then treated with a chemical activator to improve the bonding with the asphalt binder [32,33]. Additionally, a 1% dosage of epoxy resin was included to bolster the strength and durability of the asphalt. Epoxy resin, renowned for its thermosetting properties, forms a resilient bond with the binder and aggregates, effectively reinforcing the asphalt matrix against various stressors. Integration of the epoxy resin occurred during mixing to facilitate thorough dispersion throughout the mixture. Table 6 provides a detailed summary of the parameters of the modified asphalt binder, which incorporates SBS and various additions.

Table 4. Characteristics of SBS polymer.

Characteristic	Measurement
Tensile Strength	5.0 MPa
Elongation at Break	700%
Softening Point	75–95 °C
Penetration Index	40
Complex Shear Modulus (G*)	1.85 kPa at 64 °C
Phase Angle (δ)	75° at 64 °C

Table 5. Recycled crumb powder's properties.

Property	Value
Mesh Size	20–40 mesh
Density	0.5–0.8 g/cm^3
Moisture content	$\leq$1%
Rubber content	$\geq$90%
Elongation at Break	200–400%
Specific Gravity	1.12–1.14
Softening Point	65–85 °C

Table 6. Properties of HMA used in this research.

Properties	Value
Penetration (1/10 mm) 25 °C [34]	70.2 (1/10 mm)
Softening Point (°C) [35]	74.5 °C
Ductility at 5 °C (cm/min) [36]	110 cm/min
Mass Loss (%) [37]	0.038%
G*/sinδ at 64 °C (Original) [38]	1.85 kPa
G* × sinδ at 64 °C (after PAV) [39]	1520 kPa
Stiffness at −22 °C [40]	190 MPa
m-value at −22 °C [40]	0.35

2.1.4. Mix Design

This study made use of the Superpave mix design technique, which is a thorough and widely acknowledged strategy to improving asphalt binder content and aggregate gradation [41]. This technique takes into account crucial elements such as the amount of traffic, weather circumstances, and pavement specifications. The mix design aims to produce an air void content of 4.5% while maintaining appropriate VMA (voids in mineral

aggregate) at 18% and VFA (voids filled with asphalt) at 75% [28]. A 6.5% polymer-modified asphalt binder is a key component of this mix formulation. This binder is specifically designed to utilize crushed bottom ash as a filler ingredient. The incorporation of bottom ash not only maximizes recyclables for the benefit of the environment, but it also strives to improve the asphalt mixture's structural characteristics. Along with the bottom ash, the mix contained 19.2% fine aggregate and 75.5% coarse aggregate by weight, resulting in a balanced and effective composition.

In the laboratory, the preparation of asphalt mixture involved several essential steps. Initially, the aggregate was heated to a precise temperature of 165 °C using a dryer drum. Following this, the crushed bottom ash filler was added to the heated aggregate and mixed thoroughly for about 2–4 min. It was crucial to maintain the temperature at 155–165 °C throughout the mixing process to ensure proper blending and uniformity of the mixture. After mixing, the mixture was compacted using the Superpave gyration compactor method to achieve the desired volumetric properties and density.

The mixed design criteria, as outlined by the Ministry of Land, Infrastructure, and Transport (MOLIT) 2017 standards [42], specify targets for the MC-1 layer. These targets include 75 gyrations, an air void content ranging from 3 to 6%, a minimum VMA of 13.0%, and a VFA between 70 and 85%. The mixture must also meet several performance benchmarks: a deformation strength of at least 3.2 MPa, a tensile strength ratio of at least 0.8, and an indirect tensile strength (ITS) of at least 0.8 MPa. Since bottom ash is an inert material and does not require curing, the emphasis is on optimizing the blending and compaction process to achieve the desired mechanical properties and performance characteristics of the asphalt mixture. Using bottom ash filler not only enhances sustainability by repurposing waste materials but also potentially improves the mechanical properties and long-term performance of the asphalt mixture, thereby contributing to sustainable infrastructure development.

2.2. Testing Methods

2.2.1. Indirect Tensile Strength Test

In this study, the ITS experiment was carried out in compliance with the ASTM D6931 guideline to determine the tensile strength of the asphalt samples [43]. The experiment was conducted using a D25 Universal Testing Machine (UTM) with a regulated displacement rate (see Figure 3), manufactured in South Korea. Standard samples for ITS evaluation are 100 mm in diameter and 60 mm in height. Throughout the procedure, the samples were exposed to diametral pressure at a continuous deformation rate until failure.

Figure 3. Indirect tensile strength test.

The ITS was developed to assess the combination's durability against constant deformation in both wet and dry circumstances. The samples were aged by subjecting them to hot air and temperatures for three hours and then immersing them in 80 °C water for twenty-four hours. For the ITS tests at 60 °C, the samples were preconditioned to the desired temperature by placing them in a T10 temperature-controlled chamber set at

60 °C for two hours prior to testing. The T10 chamber is manufactured in South Korea. This ensured that the entire specimen reached the target temperature uniformly. The ITS apparatus, though typically operating at room temperature, was supplemented with an environmental chamber to maintain the required temperature during the test. The ITS was calculated using the following formula:

$$\mathrm{ITS} = \frac{2P}{\pi \mathrm{tD}} \tag{1}$$

where:

- P is the maximum load at failure (N),
- t is the specimen height (mm),
- D is the specimen diameter (mm).

ITS was computed at both 25 °C and 60 °C, in both dry and wet circumstances. The ITS test loading rate of 50 mm/min guaranteed a steady and regulated load application, allowing precise assessment of the asphalt concrete specimens' tensile strength characteristics.

This method ensured that the ITS values reflected the performance of the asphalt mixtures under different temperature conditions, thereby providing a comprehensive evaluation of their mechanical properties and durability.

2.2.2. Dynamic Modulus Test

The test evaluates the viscoelastic and stiffness characteristics of asphalt concrete under various loading conditions (see Figure 4). This study employed a Universal Testing Machine (UTM), specifically the DTS-30 model from MATEST (Italy), with a dynamic modulus device on cylindrical specimens (100 mm diameter, 150 mm height) following AASHTO TP 62 [44]. Temperatures ranging from −10 °C to 54 °C and frequencies from 25 Hz to 0.1 Hz were tested. The obtained phase angle (δ) and complex modulus (E*) data were utilized to construct a master curve through time-temperature superposition that illustrated stiffness at various loading rates and temperatures. This experiment verified the increased stiffness and viscoelastic properties of the suggested polymer-modified asphalt concrete combination. The viscosity η of the binder was calculated using the following formulae:

$$\log(\log\eta) = \mathrm{A} + \mathrm{VTS}[\log(\mathrm{T_R})] \tag{2}$$

$$\log(\mathrm{T}) = \mathrm{c}\left(10^{\mathrm{A}+\mathrm{VTS}[\log(\mathrm{T_r})]} - 10^{\mathrm{A}+\mathrm{VTS}[\log(\mathrm{T_R})_0]}\right) \tag{3}$$

where:

- A is the intercept,
- VTS is the slope,
- η is the viscosity,
- $\mathrm{T_R}$ is the reference temperature in degrees Rankine (°R),
- $(\mathrm{T_R})_0$ is the initial reference temperature,
- c is a constant.

The inclusion of these formulae provides a mathematical framework for understanding viscosity-temperature dynamics, facilitating the examination of viscosity variations and transitions between different temperature points. The viscosity of the binder used in this study was measured and incorporated into the analysis to ensure accurate calculations.

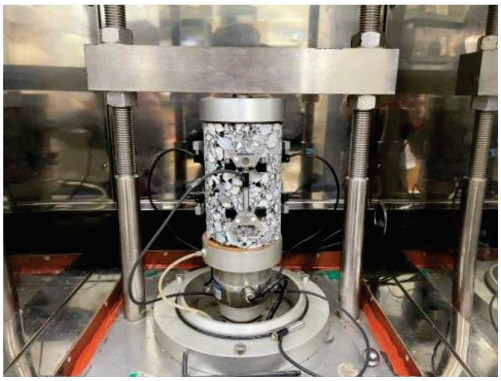

Figure 4. Dynamic modulus test apparatus.

2.2.3. Cantabro Test

Following ASTM D6927 [45], the Cantabro experiment evaluates an asphalt concrete's durability against fracture under continuous vehicular stress (see Figure 5). Examined in this investigation were cylindrical samples with a diameter of 100 mm and a height of 50 mm. Steel balls were dropped onto the specimen's surface a certain number of times during the whole process. Following this preliminary stage, the sample was put in an inspection drum devoid of steel balls. The instrument ran for 300 revolutions at 28 ± 2 °C at 30–33 rpm. The sample's mass was recorded after rotating to calculate abrasion attrition. Following every drop of order, the reduction in mass was measured, and the findings were employed to assess how long-lasting and resilient the asphalt concrete mixture was to continuous traffic loads.

Figure 5. Cantabro test.

2.2.4. Four-Point Bending Test

The test, outlined in ASTM D6272 [46], serves as a critical method for assessing the flexural properties of the samples, offering insights into their structural behavior when subjected to bending forces (see Figure 6). During this test, a rectangular asphalt sample with specific dimensions (305 mm length, 45 mm width, 50 mm depth) is subjected to forces at two points while being supported at two others, effectively simulating real-world stresses encountered in pavement applications. Typically, specifications such as a 150 mm length of span and a 5 mm/min rate of loading are used to capture stress and displacement information. Through this process, valuable information regarding asphalt's stiffness, flexural strength, and resistance to cracking is obtained, aiding in the evaluation of its structural performance.

Figure 6. Testing apparatus of 4PB test.

2.2.5. Hamburg Wheel Tracking (HWT) Test

The Hamburg wheel tracking (HWT) test evaluates an asphalt concrete mixture's ability to withstand rutting through modeled environmental and traffic loads. As per AASHTO T324 [47], the HWT test in this investigation was conducted with a loaded wheel measuring 700 mm in diameter (Figure 7). Before examination, the test samples, which had dimensions of roughly 150 mm in diameter by 62 mm in height, had been stored for 24 h at 60 °C. A 45 mm broad steel wheel spinning at a pace of 50 passes every minute, with the highest velocity of 340 ± 5 mm/sec at the center, applied an average stress of 700 ± 5 N to the samples throughout the experiment. Assessments of rut depth were made every 1000 cycles to assess the resilience of the combination to deformation over time. The HWT test, adhering to US State DoT guidelines, capped the permissible rut depth for hot mix asphalt (HMA) mixtures at 20 mm after 20,000 cycles.

Figure 7. HWT results.

3. Results

3.1. ITS Test

The ITS test results for asphalt mixtures with varying percentages of crushed bottom ash (BA) as a replacement for conventional lime filler reveal crucial insights into the mixtures' moisture susceptibility and durability. The ITS values, expressed in megapascals (MPa), were 1.02 MPa for the control mixture, 0.87 MPa for the mixture with 25% bottom ash (BA25%), 0.84 MPa for the mixture with 50% bottom ash (BA50%), and 0.78 MPa for the mixture with 75% bottom ash (BA75%). These results showed a clear decline in tensile strength as the proportion of bottom ash increased. The control mixture's high ITS value indicates robust performance as shown in Figure 8, while the slight reduction in the BA25% mixture's ITS suggests that a 25% replacement level can maintain acceptable tensile strength. However, the continued decline in ITS for BA50% and BA75% mixtures highlights the adverse effects of higher bottom ash content. This trend can be attributed to the physical and chemical characteristics of bottom ash, such as its higher porosity, less uniform particle size, and different chemical composition, which may interfere with the binder's adhesive properties and weaken the bonds within the asphalt mixture. Addi-

tionally, lime enhances binder stiffness and moisture resistance, benefits that diminish as bottom ash content increases, resulting in a less cohesive and durable mixture. Therefore, while crushed bottom ash shows potential as a filler at lower replacement levels, higher proportions compromise tensile strength and overall performance, emphasizing the need for a balanced approach to ensure effective and durable asphalt pavements, especially in moisture-prone environments.

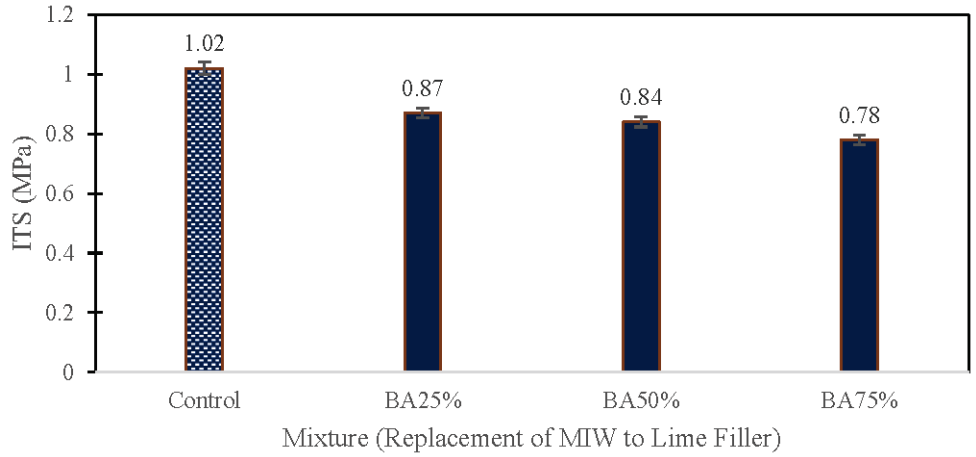

Figure 8. Initial ITS test results.

3.2. Four-Point Bending Beam Test Results

The four-point bending beam test results provide detailed insights into the stiffness behavior of asphalt mixtures containing different filler materials under repeated loading cycles as presented in Figure 9. Initially, the stiffness of all mixtures reduced sharply within the first 100 cycles, with values decreasing from 3700 N/mm to 3500 N/mm, indicating an immediate response to the applied stress. Following this initial drop, the reduction in stiffness became more gradual. Notably, during the first 5000 cycles, there was no significant difference in the stiffness reduction among the mixtures, suggesting similar initial performance regardless of the filler type.

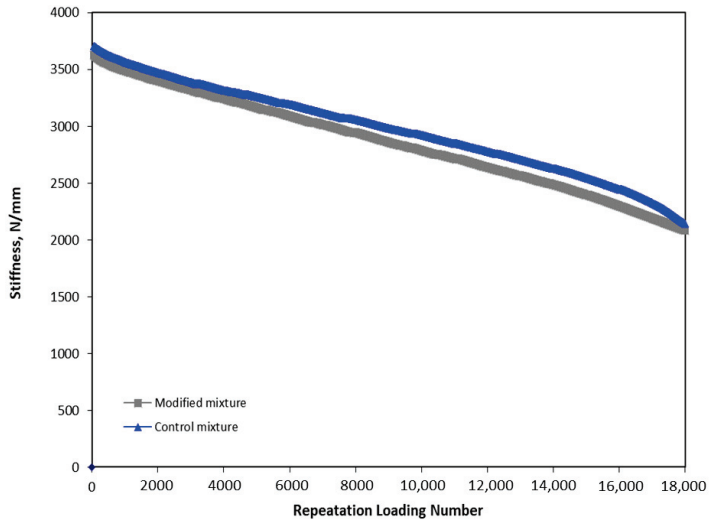

Figure 9. The four-point bending beam test results.

However, beyond 6000 cycles, a distinct gap emerged. The mixture modified with bottom ash showed a higher yet stable reduction in stiffness compared to the control mixture. This behavior suggested that while the bottom ash-modified mixture experienced a greater initial drop in stiffness, it maintained a more consistent performance over extended

loading cycles. In contrast, the control mixture, despite having higher stiffness initially, exhibited a more pronounced drop in stiffness after 17,000 cycles. This greater drop indicated a reduction in structural integrity and the potential for earlier failure under prolonged stress. Additionally, it is noted that at 18,000 cycles, the stiffness of the control mixture dropped to the equivalent value of the bottom ash mixture.

The mechanism underlying these observations can be attributed to the physical and chemical properties of the fillers. Crushed bottom ash, with its specific particle size and composition, may contribute to a more flexible and resilient asphalt matrix, which can absorb and dissipate stress more effectively over time. The presence of bottom ash might also enhance the binder's ability to maintain cohesion among aggregate particles, resulting in a more stable performance under repeated loading. In contrast, the control mixture, with conventional lime filler, might exhibit higher initial stiffness but lack the same degree of flexibility, leading to a greater stiffness reduction under prolonged loading. Therefore, replacing 25% of conventional lime with crushed bottom ash appeared to provide a slight advantage by maintaining a more stable stiffness over an extended period, which can enhance the longevity and durability of the asphalt pavement.

3.3. Cantabro Test Results

The Cantabro test results provide valuable data on the abrasion resistance of the control and modified asphalt mixtures through weight loss measurements after specified cycles of abrasion as exhibited in Table 7. The initial and post-test weights were recorded, along with the corresponding loss percentages, to evaluate the performance of each mixture under abrasive conditions. For the control mixture, after five cycles of testing, the initial weight was 1190.2 g, and the post-test weight was 1048.9 g, resulting in a loss percentage of 11.87%. When subjected to 10 cycles, the initial weight of the control mixture was 1194.1 g, and the post-test weight was 1015.6 g, yielding a significantly higher loss percentage of 21.59%. This substantial increase in weight loss after additional cycles indicates a marked decrease in the mixture's resistance to abrasion. In contrast, the modified mixture, which included crushed bottom ash as a partial replacement for conventional lime filler, demonstrated superior performance. After five cycles, the initial weight of the modified mixture was 1193.6 g, with a post-test weight of 1114.3 g, resulting in a much lower loss percentage of 6.66%. When tested for 10 cycles, the initial weight was 1191.8 g, and the post-test weight was 1030.7 g, resulting in a loss percentage of 13.46%.

Table 7. Summary of Cantabro test results.

	Initial Weight (g)	Weight Post-Test (g)	Loss Percentage (within 20% Based on Drainage)
Control mixture: 5 cycles	1190.2	1048.9	11.87%
Control mixture: 10 cycles	1194.1	1015.6	21.59%
Modified mixture: 5 cycles	1193.6	1114.3	6.66%
Modified mixture: 10 cycles	1191.8	1030.7	13.46%

The results clearly show that the modified mixture exhibited significantly better abrasion resistance compared to the control mixture. The lower weight loss percentages for the modified mixture, both at 5 and 10 cycles, indicate enhanced durability and cohesion among the aggregate particles. This improved performance can be attributed to the inclusion of crushed bottom ash, which may contribute to a denser and more stable asphalt matrix. The finer particle size and specific chemical composition of the bottom ash could enhance the binder's ability to effectively coat and bind the aggregates, thereby reducing the rate of material loss under abrasive conditions. The superior performance of the modified mixture was particularly evident after 10 cycles, where the loss percentage of 13.46% was well within acceptable limits, compared to the control mixture's 21.59%, which exceeded the typical threshold for durability. This suggests that the modified mixture with 25% crushed bottom ash filler not only resisted abrasion better initially but also maintained its

structural integrity over more extended periods of stress, making it a more reliable choice for long-term pavement performance.

3.4. Dynamic Modulus Test Results

The dynamic modulus test results indicate that the modified asphalt mixture, incorporating 25% crushed bottom ash as a replacement for conventional lime filler, demonstrated superior performance compared to the control mixture across both high- and low-frequency stages. These stages simulated the varying conditions experienced in different weather regions, with low frequency representing hot weather regions and high frequency representing cold weather regions.

At the high-frequency stage, as shown in Figure 10a, which corresponded to the conditions in cold weather regions, the dynamic modulus of the modified mixture exceeded 18,300 MPa, whereas the control mixture exhibited an E modulus of less than 17,700 MPa. This result indicates that the modified mixture remained more rigid and resilient under rapid, repetitive loading conditions, which are common in cold environments where materials are more prone to brittleness and cracking.

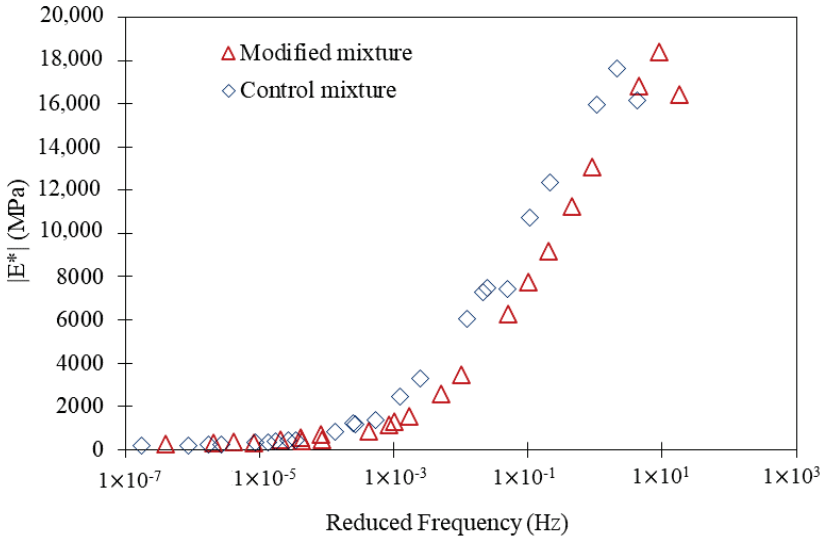

(**a**) Log-scale

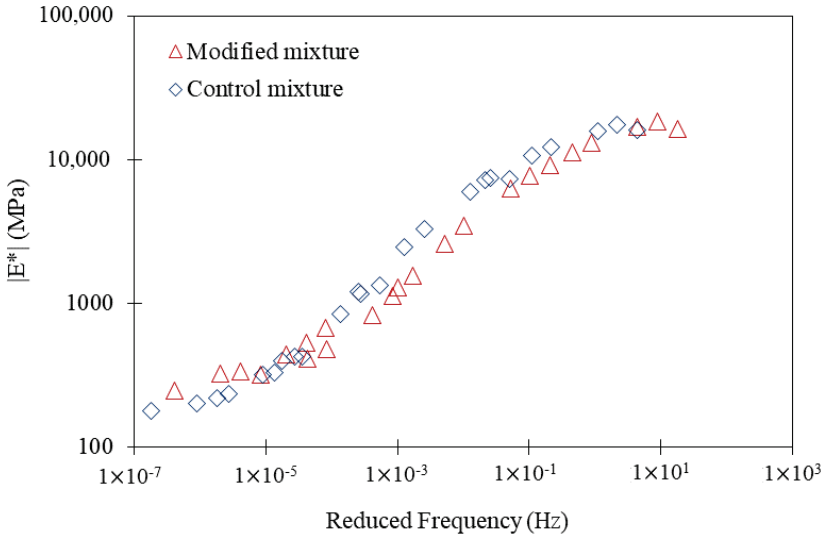

(**b**) Log-log scale

Figure 10. Dynamic modulus test results.

Conversely, at the low-frequency stage as presented in Figure 10b, representative of hot weather conditions, the modified mixture also outperformed the control. The E modulus of the modified mixture was more than 240 MPa, while the control mixture's E modulus was notably lower. This significant difference suggests that the modified mixture maintained better structural integrity and stiffness under the prolonged, slower loading conditions typical of high temperatures, where materials tend to soften and deform more easily.

The enhanced performance of the modified mixture can be attributed to the physical and chemical properties of the crushed bottom ash. Bottom ash typically contains a higher proportion of fine particles and a composition that includes silica, alumina, and other oxides, which contribute to improved binder-aggregate interaction. These fine particles fill the voids within the asphalt matrix more effectively, leading to a denser and more cohesive structure. This improved packing enhances the load distribution and reduces the susceptibility to deformation under stress.

Additionally, the chemical composition of bottom ash, including higher levels of silica and alumina, can enhance the stiffness and bonding characteristics of the asphalt binder. The presence of these materials likely promotes better adhesion between the binder and the aggregate particles, resulting in a mixture that can withstand higher stress levels without significant deformation. This improved bonding is particularly beneficial in hot weather conditions, where asphalt mixtures are prone to softening and rutting.

In cold weather conditions, the modified mixture's superior performance can be linked to its ability to maintain flexibility and resist cracking. The bottom ash may contribute to a more balanced stiffness, ensuring that the mixture does not become too brittle, which is a common issue with conventional mixtures in cold climates. This balance helps the modified mixture absorb and dissipate the energy from rapid loading cycles more effectively, thereby reducing the likelihood of crack formation and propagation.

3.5. HWT Results

Initially, both mixtures exhibited similar behavior under the applied loads. During the first 1000 passes, the rut depth increased significantly from 0 to 4 mm (see Figure 11), primarily due to the initial compression of the material as it compacted, and air voids were reduced. This initial phase is critical as it indicates how quickly the mixture stabilized under load.

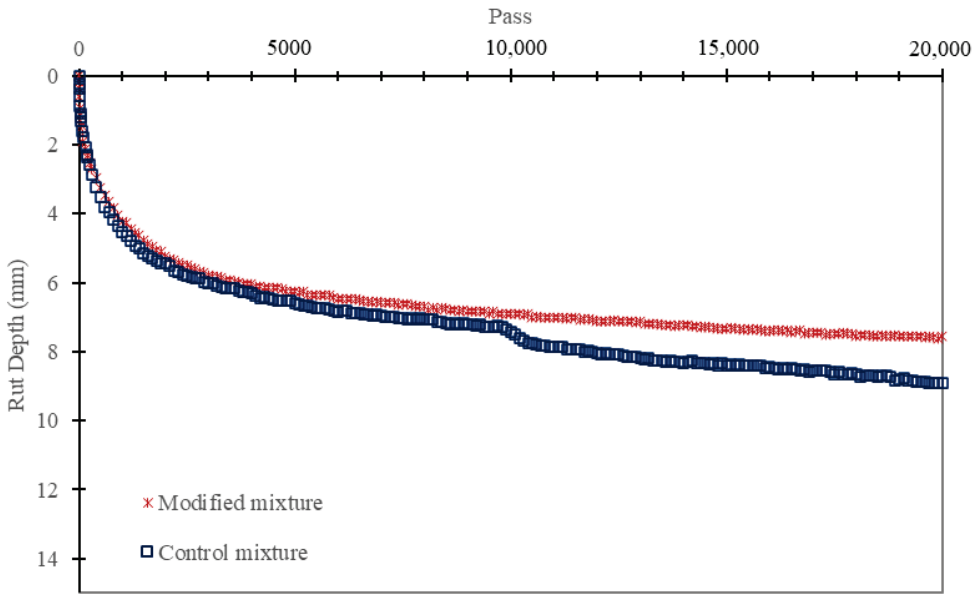

Figure 11. The HWT test results.

Following this initial phase, both mixtures continued to show a sharp increase in rut depth over the next 2000 cycles, with rut depths rising from 4 mm to 6 mm. This period

reflects the ongoing compaction and slight densification of the mixtures as they adjusted to the repetitive loading. Between 5000 and 10,000 cycles, the rut depth for both mixtures increased more gradually, from 6 mm to 7 mm, indicating a stabilization phase where the mixtures were reaching their load-bearing capacity.

However, the gap in rutting resistance between the control and modified mixtures became evident after 8000 cycles. The control mixture experienced a stripping point of around 9800 cycles, which indicates the onset of moisture-induced damage where the asphalt binder began to lose adhesion to the aggregates, leading to a rapid increase in rut depth. In contrast, the modified mixture with 25% crushed bottom ash did not exhibit this stripping behavior, maintaining its structural integrity and resistance to moisture damage throughout the test.

At the final cycle count of 20,000, the modified mixture exhibited a rut depth of 7.56 mm, whereas the control mixture showed a greater rut depth of 8.9 mm. This significant difference underscores the enhanced rutting resistance of the modified mixture, attributed to the incorporation of crushed bottom ash.

The superior performance of the modified mixture can be explained by the physical and chemical properties of the bottom ash. Crushed bottom ash consists of fine particles that fill voids within the asphalt mixture more effectively than conventional lime, resulting in a denser and more cohesive matrix. This denser structure helps in better load distribution and reduces the potential for deformation under repeated loading. Moreover, the chemical composition of bottom ash, which includes higher levels of silica and alumina, enhances the binder-aggregate interaction, leading to stronger adhesion and less susceptibility to moisture damage. This improved adhesion prevents the stripping observed in the control mixture, thereby enhancing the overall durability and rutting resistance of the asphalt.

3.6. Durability Test by Using TSR

The tensile strength ratio (TSR) test results after 10 wet-drying cycles provide valuable insights into the moisture susceptibility and durability of the control and modified asphalt mixtures (see Figure 12). The TSR values are indicators of how well the asphalt mixtures retain their tensile strength after being subjected to moisture damage. For the control mixture, the TSR values started at 92% at 0 cycles, dropped to 87% after 5 cycles, and further decreased to 84% after 10 cycles. This trend indicates a gradual but noticeable loss of tensile strength as the mixture underwent repeated wet-drying cycles, reflecting its susceptibility to moisture-induced damage.

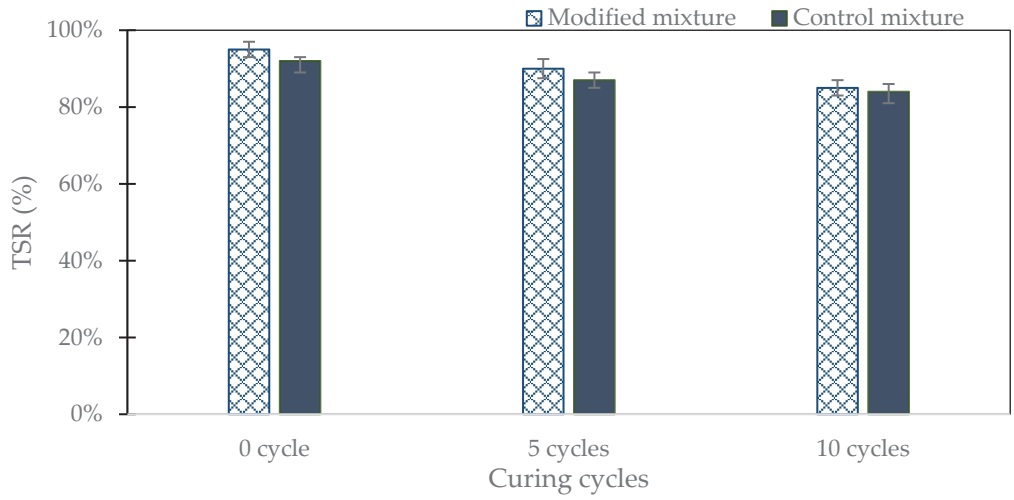

Figure 12. The TSR (%) test results.

In comparison, the modified mixture, which incorporated 25% crushed bottom ash as a replacement for conventional lime filler, exhibited higher TSR values at each stage.

Initially, the modified mixture had a TSR of 95%, which decreased to 90% after 5 cycles and to 85% after 10 cycles. Although the modified mixture also experienced a reduction in tensile strength over time, the decline was comparable to that of the control mixture. Specifically, after 5 cycles, both mixtures showed a decrease of 5% in TSR values. However, after 10 cycles, the TSR value of the modified mixture decreased by 5%, whereas the control mixture decreased by 3% (87% vs. 84%).

The superior performance of the modified mixture can be attributed to the properties of crushed bottom ash. The finer particles with a high surface area improve packing density, reducing voids and moisture infiltration. The significant amounts of silica and alumina in bottom ash enhance bonding with the asphalt binder, improving cohesion and resistance to stripping. This stronger chemical bonding helps maintain structural integrity even when exposed to moisture. Additionally, bottom ash enhances binder adhesion to aggregate particles better than conventional lime, reducing water penetration and moisture damage. The angular shape and rough texture of bottom ash contribute to better mechanical interlocking, improving the overall stability and strength of the asphalt mixture.

4. Conclusions

In conclusion, this study demonstrates the potential of utilizing crushed thermal power plant bottom ash as a sustainable filler in polymer-modified asphalt concrete mixtures containing crumb rubber. Through comprehensive performance evaluations, including a range of mechanical tests, the research highlights the promising benefits of incorporating bottom ash into asphalt pavements. The following findings can be drawn from this research.

- The replacement of conventional lime filler with 25% crushed bottom ash resulted in an ITS of 0.87 MPa. Although slightly lower than the control mixture's 1.02 MPa, the performance remained within acceptable limits, demonstrating the feasibility of bottom ash as a filler.
- The HWT test revealed that the modified mixture with 25% crushed bottom ash achieved a final rut depth of 7.56 mm after 20,000 cycles. In comparison, the control mixture had a deeper rut depth of 8.9 mm. This indicates that the modified mixture had superior rutting resistance, likely due to the better load distribution and structural integrity provided by the bottom ash.
- The adjusted mixture loosened up at a rate of 6.66% after five cycles and 13.46% following ten cycles, according to the results of the Cantabro test. This was significantly lower than the control mixture's weight loss of 11.87% and 21.59%, respectively. The reduced abrasion loss suggests that the bottom ash enhanced the durability of the mixture by increasing its resistance to surface wear and disintegration.
- The dynamic modulus test demonstrated that the modified mixture had an E modulus of more than 18,300 MPa at low frequency and over 240 MPa at high frequency. The control mixture showed lower performance, with an E modulus of less than 17,700 MPa and around 230 MPa, respectively. The higher dynamic modulus indicates that the bottom ash-modified mixture was more resilient and maintained its stiffness better across a range of temperatures and loading frequencies.
- Tensile strength ratio (TSR) test results highlighted that the modified mixture maintained higher TSR values over 10 wet-drying cycles. Starting at 95%, the TSR dropped to 90% after 5 cycles and 85% after 10 cycles. In contrast, the control mixture started at 92%, decreasing to 87% and 84%, respectively. The improved moisture resistance can be attributed to the fine particles and chemical composition of bottom ash, which enhanced the binder-aggregate adhesion and reduced moisture infiltration.
- The stiffness of the modified mixture decreased sharply in the first 100 cycles, similar to the control mixture, but then remained stable beyond 6000 cycles. The control mixture, however, exhibited a significant drop in stiffness after 17,000 cycles. This indicates that the modified mixture with bottom ash was more stable and durable under repeated loading, providing better long-term performance.

- Utilizing crushed bottom ash as a filler in asphalt mixtures not only improves performance but also offers significant environmental and economic advantages. It provides a sustainable solution by recycling industrial waste, reducing the dependency on conventional lime, and potentially lowering material costs. This contributes to more eco-friendly pavement construction practices and supports waste management efforts.

In summary, replacing 25% of conventional lime filler with crushed bottom ash in polymer-modified asphalt concrete mixtures containing crumb rubber significantly enhanced the mechanical properties, durability, and environmental sustainability of the pavement. The modified mixture exhibited superior rutting resistance, abrasion resistance, dynamic modulus, and moisture resistance, making it a highly viable alternative for high-performance and long-lasting asphalt pavements.

Author Contributions: Conceptualization, Y.-M.K. and K.K.; methodology, T.H.M.L.; software, Y.-M.K.; validation, T.H.M.L., K.K. and T.H.M.L.; formal analysis, Y.-M.K.; investigation, Y.-M.K.; resources, T.H.M.L.; data curation, T.H.M.L.; writing—original draft preparation, T.H.M.L.; writing—review and editing, Y.-M.K.; visualization, Y.-M.K.; supervision, Y.-M.K.; project administration, Y.-M.K.; funding acquisition, K.K. All authors have read and agreed to the published version of the manuscript.

Funding: Research for this paper was carried out under the KICT Research Program (project no. 20240173-001, Development of innovative trenching and pavement restoration technology based on Smart QSE) funded by the Ministry of Science and ICT.

Institutional Review Board Statement: Not applicable.

Data Availability Statement: The raw data supporting the conclusions of this article will be made available by authors on request.

Conflicts of Interest: The authors declare no conflict of interest.

References

1. Hao, G.; He, M.; Lim, S.M.; Ong, G.P.; Zulkati, A.; Kapilan, S. Recycling of Plastic Waste in Porous Asphalt Pavement: Engineering, Environmental, and Economic Implications. *J. Clean. Prod.* **2024**, *440*, 140865. [CrossRef]
2. Chen, S.; Tong, D.; Zhang, Q.; Wu, X. Evaluation of Adhesion between Styrene-Butadiene-Styrene (SBS) Modified Asphalt and Aggregates Based on Rolling Bottle Test and Image Processing. *Constr. Build. Mater.* **2024**, *431*, 136531. [CrossRef]
3. Wen, Y.; Ma, F.; Fu, Z.; Li, C.; Dai, J.; Dong, W.; Shi, K.; Zhu, C. Evaluation on the Fatigue and Self-Healing Properties of Aged and Rejuvenated SBS-Modified Asphalt. *Constr. Build. Mater.* **2024**, *412*, 134773. [CrossRef]
4. Gong, Y.; Wu, S.; Bi, H.; Tian, L. Study on Thermal Stability and Fatigue Properties of SBS/CNT-Modified Asphalt Sealant. *Polymers* **2023**, *15*, 3968. [CrossRef] [PubMed]
5. Wang, W.; Yang, L.; Cui, H.; Wu, F.; Cheng, Y.; Liang, C. Freeze–Thaw Damage Mechanism Analysis of SBS Asphalt Mixture Containing Basalt Fiber and Lignocellulosic Fiber Based on Microscopic Void Characteristics. *Polymers* **2023**, *15*, 3887. [CrossRef] [PubMed]
6. Zhang, J.; Sun, P.; Ma, Z.; Dai, M.; Zhuo, R.; Zou, G.; Tan, Y. Investigating the Role of Sulfur Stabilizer in Modulating Aging Properties of SBS-Modified Asphalt. *Constr. Build. Mater.* **2024**, *425*, 136045. [CrossRef]
7. Yu, H.; Ge, J.; Qian, G.; Shi, C.; Zhang, C.; Dai, W.; Xie, T.; Nian, T. Evaluation of the Interface Adhesion Mechanism between SBS Asphalt and Aggregates under UV Aging through Molecular Dynamics. *Constr. Build. Mater.* **2023**, *409*, 133995. [CrossRef]
8. Wu, C.; Tan, X.; Li, L.; Liang, C.; Zhao, Y.; Li, H.; Wang, F.; Zhang, L. Evaluation and Correlation Analysis of the Rheological Properties of Ground Tire Rubber and Styrene Butadiene Styrene Compound-Modified Asphalt. *Polymers* **2023**, *15*, 3289. [CrossRef]
9. Yan, X.; Wu, D.; Hu, K.; Zhang, W.; Xing, J.; Cui, L.; Shi, S.; Yang, J.; Yang, C. The Modification Mechanism, Evaluation Method, and Construction Technology of Direct-to-Plant SBS Modifiers in Asphalt Mixture: A Review. *Polymers* **2023**, *15*, 2768. [CrossRef]
10. Zhang, W.; Yu, X.; Wu, D.; Song, B.; Cao, X.; Xing, Z.; Zhang, Y.; Yan, X.; Ji, X.; Hu, K.; et al. Evaluation Method of Modification Effect of Direct-to-Plant SBS Modifier on Asphalt. *Constr. Build. Mater.* **2024**, *419*, 135569. [CrossRef]
11. Chen, H.; Huang, S.; Niu, D.; Gao, Y.; Zhang, Z. Fatigue Characterization and Assessment Methods for the Terminal Blend Crumb Rubber/SBS Composite Modified Asphalt Binders. *Constr. Build. Mater.* **2024**, *430*, 136357. [CrossRef]
12. Lin, P.; Liu, X.; Ren, S.; Xu, J.; Li, Y.; Li, M. Effects of Bitumen Thickness on the Aging Behavior of High-Content Polymer-Modified Asphalt Mixture. *Polymers* **2023**, *15*, 2325. [CrossRef] [PubMed]
13. Yi, Y.; Chen, Y.; Shi, S.; Zhao, Y.; Wang, D.; Lei, T.; Duan, P.; Cao, W.; Wang, Q.; Li, H. Study on Properties and Micro-Mechanism of RHB-SBS Composite-Modified Asphalt. *Polymers* **2023**, *15*, 1718. [CrossRef] [PubMed]

14. Xu, L.; Ni, H.; Zhang, Y.; Sun, D.; Zheng, Y.; Hu, M. Porous Asphalt Mixture Use Asphalt Rubber Binders: Preparation and Noise Reduction Evaluation. *J. Clean. Prod.* **2022**, *376*, 134119. [CrossRef]
15. Guo, M.; Liang, M.; Sreeram, A.; Bhasin, A.; Luo, D. Characterisation of Rejuvenation of Various Modified Asphalt Binders Based on Simplified Chromatographic Techniques. *Int. J. Pavement Eng.* **2021**, *23*, 4333–4343. [CrossRef]
16. Lou, K.; Xiao, P.; Kang, A.; Wu, Z.; Dong, X. Effects of Asphalt Pavement Characteristics on Traffic Noise Reduction in Different Frequencies. *Transp. Res. Part D Transp. Environ.* **2022**, *106*, 103259. [CrossRef]
17. Ding, Y.; Xi, Y.; Gao, H.; Wang, J.; Wei, W.; Zhang, R. Porosity of Municipal Solid Waste Incinerator Bottom Ash Effects on Asphalt Mixture Performance. *J. Clean. Prod.* **2022**, *369*, 133344. [CrossRef]
18. Jattak, Z.A.; Hassan, N.A.; Mohd Satar, M.K.I. Moisture Susceptibility and Environmental Impact of Warm Mix Asphalt Containing Bottom Ash. *Case Stud. Constr. Mater.* **2021**, *15*, e00636. [CrossRef]
19. Huan-Lin, L.; Shih-Huang, C.; Deng-Fong, L.; Xin-Rong, C. Use of Incinerator Bottom Ash in Open-Graded Asphalt Concrete. *Constr. Build. Mater.* **2017**, *149*, 497–506.
20. Rengarasu, T.M.; Juzaafi, M.; Bandara, W.M.K.R.T.W.; Jegatheesan, N. Suitability of Coal Bottom Ash and Carbonized Rice Husk in Hot Mix Asphalt. *Asian Transp. Stud.* **2020**, *6*, 100013. [CrossRef]
21. López-Montero, T.; Mañosa, J.; Miró, R.; Chimenos, J.M. Sustainable Asphalt Mixtures by Partial Replacement of Fine Aggregates with Low-Grade Magnesium Carbonate by-Product. *Case Stud. Constr. Mater.* **2023**, *18*, e01705. [CrossRef]
22. Al-Sabaeei, A.M.; Al-Fakih, A.; Noura, S.; Yaghoubi, E.; Alaloul, W.; Al-Mansob, R.A.; Imran Khan, M.; Aliyu Yaro, N.S. Utilization of Palm Oil and Its By-Products in Bio-Asphalt and Bio-Concrete Mixtures: A Review. *Constr. Build. Mater.* **2022**, *337*, 127552. [CrossRef]
23. Jwaida, Z.; Dulaimi, A.; Bahrami, A.; Mydin, M.A.O.; Özkılıç, Y.O.; Jaya, R.P.; Wang, Y. Analytical Review on Potential Use of Waste Engine Oil in Asphalt and Pavement Engineering. *Case Stud. Constr. Mater.* **2024**, *20*, e02930. [CrossRef]
24. Lee, S.Y.; Kim, K.W.; Yun, Y.M.; Minh Le, T.H. Evaluation of Eco-Friendly Asphalt Mixtures Incorporating Waste Plastic Aggregates and Additives: Magnesium, Fly Ash, and Steel Slag. *Case Stud. Constr. Mater.* **2024**, *20*, e02756. [CrossRef]
25. Wong, T.L.X.; Mohd Hasan, M.R.; Peng, L.C. Recent Development, Utilization, Treatment and Performance of Solid Wastes Additives in Asphaltic Concrete Worldwide: A Review. *J. Traffic Transp. Eng. (Engl. Ed.)* **2022**, *9*, 693–724. [CrossRef]
26. Russo, F.; Veropalumbo, R.; Pontoni, L.; Oreto, C.; Biancardo, S.A.; Viscione, N.; Pirozzi, F.; Race, M. Sustainable Asphalt Mastics Made up Recycling Waste as Filler. *J. Environ. Manag.* **2022**, *301*, 113826. [CrossRef] [PubMed]
27. Russo, F.; Veropalumbo, R.; Oreto, C.; Cassese, D.; Papa, B.; Malvezzi, S. Reusing Bottom Ash as a Filler from a Waste-to-Energy Plant for Making Asphalt Mastics. *Case Stud. Constr. Mater.* **2022**, *17*, e01406. [CrossRef]
28. Lee, S.Y.; Ho Minh Le, T.; Kim, Y.M. Full-Scale and Laboratory Investigations on the Performance of Asphalt Mixture Containing Recycled Aggregate with Low Viscosity Binder. *Constr. Build. Mater.* **2023**, *367*, 130283. [CrossRef]
29. Le, T.H.M.; Park, D.W.; Seo, J.W.; Lee, J.W.; Kim, K.J. Applicability Evaluation of Ponded Ash as a Sustainable Backfill Material Using Air Foam. *Sustain. Constr. Mater. Technol.* **2016**, *30*, 04018158.
30. Wei, Q.; Al Ashaibi, A.; Wang, Y.; Albayati, A.; Haynes, J. Experimental Study of Temperature Effect on the Mechanical Tensile Fatigue of Hydrated Lime Modified Asphalt Concrete and Case Application for the Analysis of Climatic Effect on Constructed Pavement. *Case Stud. Constr. Mater.* **2022**, *17*, e01622. [CrossRef]
31. Kim, K.N.; Le, T.H.M. Durability of Polymer-Modified Asphalt Mixture with Wasted Tire Powder and Epoxy Resin under Tropical Climate Curing Conditions. *Polymers* **2023**, *15*, 2504. [CrossRef] [PubMed]
32. Wu, S.; He, R.; Chen, H.; Li, W.; Li, G. Rheological Properties of Sbs/Crp Composite Modified Asphalt under Different Aging Treatments. *Materials* **2020**, *13*, 4921. [CrossRef] [PubMed]
33. Xue, Y.; Zhao, H.; Wei, X.; Niu, Y. Performance Analysis of Compound Rubber and Steel Slag Filler Modified Asphalt Composite. *Materials* **2019**, *12*, 2588. [CrossRef]
34. *ASTM D5*; Standard Test Method for Penetration of Bituminous Materials. ASTM International: West Conshohocken, PA, USA, 2019.
35. *ASTM D36-16*; Standard Test Method for Softening Point of Bitumen (Ring-and-Ball Apparatus). ASTM International: West Conshohocken, PA, USA, 2016.
36. *ASTM D113-17*; Standard Test Method for Ductility of Asphalt Materials. ASTM International: West Conshohocken, PA, USA, 2008.
37. *ASTM D1754*; Standard Test Method for Effects of Heat and Air on Asphaltic Materials (Thin-Film Oven Test). ASTM International: West Conshohocken, PA, USA, 2009.
38. *ASTM D2872-22*; Standard Test Method for Effect of Heat and Air on a Moving Film of Asphalt (Rolling Rolling Thin-Film Oven Test). ASTM International: West Conshohocken, PA, USA, 2022.
39. *AASHTO R 28-09*; Accelerated Aging of Asphalt Binder Using a Pressurized Aging Vessel (PAV). American Association of State Highway and Transportation Officials (AASHTO): Washington, DC, USA, 2007; pp. 1–8.
40. *AASHTO T 313-10*; Determining the Flexural Creep Stiffness of Asphalt Binder Using the Bending Beam Rheometer (BBR). American Association of State Highway and Transportation Officials (AASHTO): Washington, DC, USA, 2011.
41. Lee, K.; Kim, H.; Kim, N.; Kim, Y. Dynamic Modulus of Asphalt Mixtures for Development of Korean Pavement Design Guide. *J. Test. Eval.* **2007**, *35*, 143–150. [CrossRef]

42. MOLIT (Ministry of Land, Infrastructure & Transport). *Stat. Syst.* 2017. Available online: https://www.molit.go.kr/english/USR/WPGE0201/m_36862/DTL.jsp (accessed on 15 May 2024).
43. *ASTM D6931*; Standard Test Method for Indirect Tensile (IDT) Strength of Bituminous Mixtures. ASTM International: West Conshohocken, PA, USA, 2017; pp. 1–5.
44. *AASHTO TP62-2017*; Standard Method of Test for Determining Dynamic Modulus of Hot Mix Asphalt (HMA). American Association of State Highway and Transportation Officials (AASHTO): Washington, DC, USA, 2017.
45. *ASTM D6927*; Standard Test Method for Marshall Stability and Flow of Asphalt Mixtures. ASTM International: West Conshohocken, PA, USA, 2015; Volume i, pp. 1–7.
46. *ASTM D6272-02*; Standard Test Method for Flexural Properties of Unreinforced and Reinforced Plastics and Electrical Insulating Materials by Four-Point Bending. ASTM International: West Conshohocken, PA, USA, 2002.
47. *AASHTO T324*; Standard Method of Test for Hamburg Wheel-Track Testing of Compacted Hot-Mix Asphalt (HMA). American Association of State Highway and Transportation Officials (AASHTO): Washington, DC, USA, 2014.

Disclaimer/Publisher's Note: The statements, opinions and data contained in all publications are solely those of the individual author(s) and contributor(s) and not of MDPI and/or the editor(s). MDPI and/or the editor(s) disclaim responsibility for any injury to people or property resulting from any ideas, methods, instructions or products referred to in the content.

polymers

MDPI

Article

Utilizing Crushed Recycled Marble Stone Powder as a Sustainable Filler in SBS-Modified Asphalt Containing Recycled Tire Rubber

Byungsik Ohm [1], Sang Yum Lee [2,*] and Tri Ho Minh Le [3,*]

[1] Department of Highway & Transportation Research, Korea Institute of Civil Engineering and Building Technology, 283 Goyangdae-Ro, Ilsanseo-Gu, Goyang-si 10223, Gyeonggi-Do, Republic of Korea; bseom@kict.re.kr
[2] Faculty of Civil Engineering, Induk University, 12 Choansan-ro, Nowon-gu, Seoul 01878, Republic of Korea
[3] Faculty of Civil Engineering, Nguyen Tat Thanh University, 300A Nguyen Tat Thanh Street, District 4, Ho Chi Minh City 700000, Vietnam
* Correspondence: yummy10041004@gmail.com (S.Y.L.); lhmtri@ntt.edu.vn (T.H.M.L.)

Abstract: The increasing demand for sustainable construction materials has driven the exploration of alternative fillers in asphalt production. Traditional asphalt mixtures rely heavily on natural aggregates and petroleum-based binders, contributing to environmental degradation. This study proposes an innovative solution by utilizing Crushed Recycled Marble Stone Powder (CRMSP) as a sustainable filler in SBS polymer-modified asphalt containing high volumes of recycled tire rubber, addressing both resource depletion and waste management concerns. A total of 10 asphalt mixes were formulated with varying CRMSP content (0–100% as a replacement for conventional filler) and SBS polymer (3–5%), and their performance was evaluated through Marshall stability, flow, volumetric properties, and dynamic modulus tests. The results demonstrate that incorporating CRMSP up to 75% significantly enhances asphalt's mechanical properties. The 75% CRMSP mix showed superior stability (19.2 kN, 24.1% improvement), flow (4.6 mm, 4.5% improvement), and resistance to rutting (lowest rut depth: 0.18 mm, 16.7% reduction) compared to the control mixture. Dynamic modulus testing further confirmed the improved resistance to deformation, with the 75% CRMSP mix exhibiting the highest modulus (6.9 GPa, 15.0% improvement). This research highlights the potential of CRMSP as an innovative and eco-friendly alternative filler, improving asphalt performance while reducing environmental impact. By offering a sustainable way to recycle marble waste and tire rubber, this study paves the way for greener, cost-effective asphalt formulations. Future studies should focus on real-world applications, durability, and long-term performance to validate the potential of CRMSP-modified asphalt in commercial use.

Keywords: crushed recycled marble stone powder; SBS polymer; recycled tire rubber; sustainable asphalt; innovative filler; environmental impact; dynamic modulus

1. Introduction

Increasing environmental concerns and the need for sustainable infrastructure solutions have led to growing interest in the recycling of materials in the construction industry [1]. Asphalt, a critical material for road construction, traditionally relies on virgin materials, which contribute to resource depletion and environmental pollution [2]. With

the global demand for better-performing, more sustainable road surfaces, it is imperative to explore alternatives that do not compromise the quality and durability of roadways [3].

Conventional fillers, such as limestone and sand, have been widely used in asphalt mixtures to improve their mechanical properties [4]. However, the growing emphasis on sustainability and cost-effectiveness has led to the exploration of alternative additives. Several studies have examined the potential of using industrial by-products, waste materials, and natural substances as substitutes for conventional fillers in asphalt mixtures [5]. Recycled materials such as fly ash, slag, and recycled concrete aggregates have been studied for their potential to replace traditional fillers [6]. Research suggests that these alternatives can enhance the performance of asphalt in terms of stiffness, durability, and resistance to moisture damage. For example, a study by Choi et al. (2018) investigated the use of tire-derived fuel fly ash as filler materials [5], showing improved performance. Similarly, the inclusion of molybdenum tailings as fillers has been shown to reduce the environmental footprint of asphalt mixtures while maintaining, or even enhancing, their mechanical properties [7]. However, the effectiveness of these alternative fillers depends on the specific properties of the waste material, its compatibility with asphalt binder, and its impact on the long-term performance of the mixture. In many cases, the integration of alternative fillers can lead to challenges such as variability in material properties, which necessitates further optimization and testing.

Styrene-Butadiene-Styrene (SBS) polymer modification of asphalt binders is a well-established practice in the asphalt industry. Recent studies have explored various approaches to enhancing the performance of SBS-modified asphalt, often incorporating waste tire rubber. Huang et al. [8] found that waste tire rubber combined with SBS improved asphalt's high and low-temperature performance. However, adding large amounts of tire rubber can cause brittleness and reduce fatigue resistance [9]. Studies like Aliakbari et al. [10] and Yu et al. [11] suggest that alternative fillers, including hybrid systems, can improve both environmental sustainability and performance. SBS-modified asphalt (SBSMA) has gained significant attention due to its enhanced performance characteristics, particularly in terms of improved elasticity, durability, and resistance to high temperatures [12]. The key reason for incorporating SBS polymer into asphalt binder is to enhance the binder's viscoelastic properties, making it more resistant to deformation and fatigue cracking. Research has shown that SBS modification improves the rutting resistance of asphalt by reducing the binder's temperature susceptibility [13]. The polymer interacts with the asphalt binder to form a network structure that enhances the binder's ability to recover under stress, thus reducing permanent deformation under high traffic loads. Moreover, SBS-modified asphalt exhibits better resistance to cracking at low temperatures, making it suitable for regions with extreme climatic conditions [14]. SBS modification also improves the binder's workability and aging resistance, which are crucial factors for the long-term performance of asphalt pavements [15]. However, the use of SBS can significantly increase the cost of asphalt production, which has led to research into optimizing SBS content and finding cost-effective alternatives to achieve similar performance improvements [16].

The use of crumb rubber from recycled tires as an additive in asphalt mixtures has gained considerable attention as a sustainable practice for improving the performance of pavements [17]. Crushed car tire rubber is a waste product that, when processed into crumb rubber, can be integrated into asphalt mixtures to enhance their flexibility, durability, and resistance to cracking. Studies have shown that the addition of crumb rubber to asphalt mixtures improves the binder's viscoelastic properties, resulting in better resistance to low-temperature cracking and rutting at high temperatures. According to a study by Kim et al. (2023), asphalt mixtures containing crumb rubber exhibited superior fatigue

resistance and moisture susceptibility compared to conventional mixtures [16]. The rubber particles interact with the asphalt binder, increasing its viscosity and enhancing the overall durability of the pavement.

However, the use of crumb rubber in asphalt mixtures also presents some challenges. The variability in the quality of recycled tire rubber and its compatibility with asphalt binder requires careful control during the mix design process. Moreover, excessive amounts of crumb rubber can negatively affect the workability of the mixture and its long-term performance, which has led to ongoing research into the optimal proportions for crumb rubber inclusion in asphalt mixtures. Despite the growing interest in sustainable solutions for asphalt mixtures, several challenges remain. One of the key limitations is the difficulty of achieving an optimal balance between performance and sustainability when using multiple recycled components. The use of high volumes of Recycled Tire Rubber (RTR) and CRMSP can lead to performance inconsistencies, particularly regarding rutting resistance, low-temperature cracking, and overall durability. Additionally, the current mix designs for SBS-modified asphalt have not sufficiently explored the potential of combining these materials in a way that maximizes their synergistic benefits. Another limitation of the current research is the insufficient attention given to the detailed effects of CRMSP on asphalt performance when combined with RTR and SBS polymer. As the demand for more eco-friendly pavement solutions grows, it is crucial to develop asphalt mixtures that meet the performance standards while significantly reducing reliance on virgin materials.

This study proposes a novel approach to improving asphalt mixture performance by incorporating up to 100% Crushed Recycled Marble Stone Powder (CRMSP) as a filler in SBS-modified asphalt, which also contains high volumes of recycled tire rubber (RTR). The research explores the potential for these materials to work synergistically and investigates the impact of their combined use on critical performance properties such as rutting resistance, cracking behavior, and long-term durability. The innovative aspect of this work lies in the comprehensive evaluation of CRMSP as a sustainable filler, alongside SBS and RTR, within an optimized asphalt mixture design. The aim is to determine the optimal mix ratios of CRMSP, SBS polymer, and RTR that balance performance, sustainability, and cost-efficiency.

The primary objective of this research is to evaluate the feasibility of incorporating CRMSP as a sustainable filler in SBS-modified asphalt mixtures containing high volumes of recycled tire rubber. The specific objectives are to optimize the mix design by varying the percentages of CRMSP (0%, 25%, 50%, 75%, and 100%) while maintaining 3–5% SBS polymer and 3% RTR in each mixture. Additionally, the study aims to assess the performance of these mixtures through various tests, including Marshall Stability, Indirect Tensile Strength (IDT), Tensile Strength Ratio (TSR), Dynamic Modulus, and Thermal Test. By comparing the performance of these mixtures against control asphalt mixtures, the study seeks to identify the best-performing combination of CRMSP, SBS, and RTR for sustainable asphalt production.

2. Materials and Methods

2.1. Materials

The raw materials used in this study were sourced from established suppliers in South Korea, ensuring both quality and consistency for the asphalt mixtures. The SBS polymer used in this research was supplied by SK Chemicals, a prominent South Korean manufacturer known for producing high-performance SBS polymers. These polymers are crucial for improving the elasticity and durability of asphalt, enhancing resistance to deformation and cracking. The aggregates were sourced locally from quarries within South Korea, ensuring they met the required gradation and quality standards for use in asphalt mixtures. Local sourcing also helps reduce transportation costs and ensures that

the aggregates reflect typical materials used in South Korean asphalt pavements. Lastly, the CRMSP, the novel filler material, was obtained from a marble production plant in South Korea. This plant processes waste marble from stone-cutting operations into a fine powder, which is then used as an environmentally sustainable filler in asphalt. By incorporating locally sourced materials, this study not only supports sustainability but also aligns with practical considerations for large-scale production within South Korea.

2.1.1. Polymer-Modified Asphalt Binder

The polymer-modified asphalt binder used in this study was a 60/70 penetration grade asphalt modified with Styrene-Butadiene-Styrene (SBS) polymer. SBS is widely recognized for its excellent ability to enhance high-temperature performance, improve elasticity, and reduce the cracking potential of asphalt mixtures. In this study, the binder was modified with 3% and 4% SBS by weight of the binder, ensuring optimal polymer dispersion and interaction. The modification process involved blending SBS into the asphalt at a temperature of 180 °C under continuous shear conditions. This modification significantly improved the binder's ability to resist rutting and cracking, particularly in regions with extreme temperature fluctuations.

In addition, SBS polymer contents of 3% and 4% [16] were selected to evaluate the effect of different polymer dosages on the performance of the asphalt mixtures. These percentages are within the typical range used in the asphalt industry, where SBS polymer is known to improve elasticity, rutting resistance, and fatigue resistance. The selection of 5% RTR was based on common industry practice [16], where rubberized asphalt containing 5% RTR is often used to enhance the flexibility and fatigue resistance of the mixture. These content levels were chosen to provide a comprehensive understanding of the combined effects of CRMSP, SBS, and RTR in improving asphalt mixture performance. The key rheological properties of the polymer-modified binder were evaluated using industry-standard methods. The following Table 1 summarizes the characteristics of the polymer-modified asphalt binder.

Table 1. Polymer-modified asphalt.

Property	Value	Standard
Penetration Grade	60/70	ASTM D5-03 [18]
Softening Point	48 °C	ASTM D36-04 [19]
Viscosity at 60 °C	0.3–0.4 Pa·s	ASTM D4402-14 [20]
Dynamic Shear Modulus (G) *	2.0 kPa at 25 °C	ASTM D7175-15 [21]
Rotational Viscometer (RV)	0.4–0.5 Pa·s at 135 °C	AASHTO T316 [22]
Elastic Recovery (%)	85% at 25 °C	ASTM D6084-04 [23]
Stress Strain (Elastic Modulus)	1000 kPa at 25 °C	ASTM D7175 [21]

These properties indicate the improved stiffness and enhanced rutting resistance of the polymer-modified asphalt, making it suitable for use in high-traffic roads and areas prone to thermal cracking.

2.1.2. Crushed Recycled Marble Stone Powder (CRMSP)

CRMSP presents several advantages over conventional fillers like limestone dust in asphalt mixtures (see Figure 1). CRMSP has a finer particle size (3–5 microns) compared to the coarser 5–10 microns of limestone dust, offering better particle packing and improving mix compactability. Its chemical composition, primarily calcium carbonate, enhances binder adhesion and stability, particularly in high temperatures, while conventional fillers with higher silica content may offer weaker binder interactions.

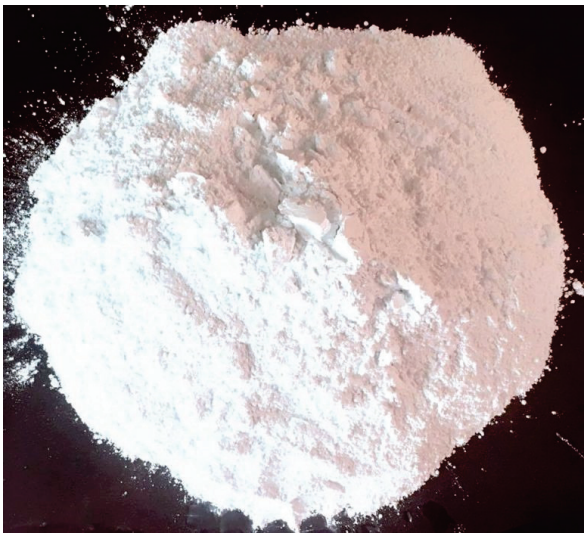

Figure 1. CRMSP used in this research.

The selection of CRMSP content (ranging from 0% to 100% as a replacement for conventional filler) was based on a combination of preliminary studies [24], industry practices, and the goal of achieving a balance between performance and sustainability in asphalt mixtures. The 0% to 100% range for CRMSP was chosen to investigate the full potential of CRMSP as a sustainable filler material, from a minimal substitution to a complete replacement of conventional fillers, to assess how the varying CRMSP content influences key asphalt properties such as stability, rutting resistance, and durability.

CRMS was selected as a sustainable filler material to replace traditional limestone fillers in the asphalt mixture. The CRMSP was sourced from waste marble generated during stone cutting and polishing processes in the marble industry. It was then processed into a fine powder, with particle sizes primarily passing through a 0.075 mm sieve. The marble powder was characterized by its high calcium carbonate content and low moisture content, which can improve the stiffness and stability of the asphalt mixture while contributing to sustainability. The following Table 2 summarizes the key physical and chemical properties of CRMSP used in this study.

Table 2. Properties of CRMSP vs. conventional filler.

Property	CRMSP Value	Conventional Filler Value	Standard
Specific Gravity	2.65	2.60–2.75	ASTM C127 [25]
Particle Size Distribution	100% passing 0.075 mm sieve	100% passing 0.075 mm sieve	ASTM C136 [26]
Color	White/Off-white	White/Gray	Visual Inspection
Moisture Content	<1%	<1%	ASTM C566 [27]
Calcium Carbonate ($CaCO_3$)	75–85%	50–70% (limestone)	ASTM D4373 [28]
Loss on Ignition	5%	5–7% (limestone)	ASTM C114-17 [29]
pH Value	7.5	7–8 (limestone)	ASTM E70-21 [30]
Bulk Density	1.45 g/cm^3	1.55–1.60 g/cm^3	ASTM C127 [25]

The CRMSP showed promising results as a filler, with its high calcium carbonate content contributing to improved binder-aggregate adhesion, and its low moisture content preventing potential issues related to water susceptibility in the asphalt.

2.1.3. Recycled Tire Rubber (RTR)

RTR was used in this study as a modifier to enhance the low-temperature cracking resistance and elasticity of the asphalt mixture. RTR was obtained by grinding used tires into small rubber particles, followed by sieving to obtain a uniform size distribution. The rubber particles were then incorporated into the asphalt binder using a dry process. RTR helps in reducing thermal cracking and improving the fatigue life of asphalt mixtures by providing enhanced flexibility and resistance to cracking. The physical properties of RTR used in the study are listed in Table 3 below.

Table 3. Properties of RTR.

Property	Value	Standard
Specific Gravity	1.1	ASTM D792 [31]
Particle Size Distribution	100% passing 2.36 mm sieve	ASTM C136 [32]
Moisture Content	<0.5%	ASTM D792 [31]
Elastomeric Content	100%	ASTM D1056 [33]

RTR significantly improved the asphalt's performance by increasing its viscoelastic properties, thus offering a more durable and crack-resistant mixture, especially in cold climates.

2.1.4. Aggregate Materials

The aggregates used in the mix design were sourced from a local quarry, comprising both coarse and fine aggregates. Coarse aggregates were primarily crushed limestone with a particle size range of 4.75 mm to 19 mm, while fine aggregates consisted of natural sand. These aggregates were carefully selected to meet the required standards for gradation and mechanical properties to ensure the mixture's strength, durability, and workability.

The physical properties of the aggregates are summarized in Table 4 below.

Table 4. Properties of aggregate.

Property	Value	Standard
Specific Gravity (Coarse)	2.60	ASTM C127 [25]
Specific Gravity (Fine)	2.65	ASTM C128 [34]
Water Absorption (Coarse)	1.5%	ASTM C127 [25]
Water Absorption (Fine)	2.5%	ASTM C128 [15]
Gradation (Coarse Aggregate)	100% passing 19 mm sieve	ASTM C136 [26]
Gradation (Fine Aggregate)	100% passing 4.75 mm sieve	ASTM C136 [26]
Flakiness Index	20%	BS 812-105.1 [35]
Los Angeles Abrasion	22%	ASTM C131 [36]
Bulk Density	1.60 g/cm^3 (Coarse)	ASTM C29 [37]
Fineness Modulus	2.5	ASTM C127 [25]

The coarse aggregates provided excellent stability and resistance to deformation, while the fine aggregates contributed to optimal compaction and workability. The aggregate blend was designed to maximize the asphalt mixture's performance in terms of resistance to rutting, fatigue, and thermal cracking.

In addition, Figure 2 shows that CRMSP exhibits a finer gradation, with a higher percentage of material passing through smaller sieves, reflecting its role as a filler in asphalt mixtures. In contrast, RTR shows a coarser gradation with a lower percentage passing finer sieves, characteristic of the rubber's irregular particle structure. Conventional aggregates have a more balanced gradation, with moderate percentages passing through intermediate sieves. These

gradation profiles are crucial for understanding the behavior of these materials in asphalt mixtures, influencing properties like workability, compaction, and overall performance.

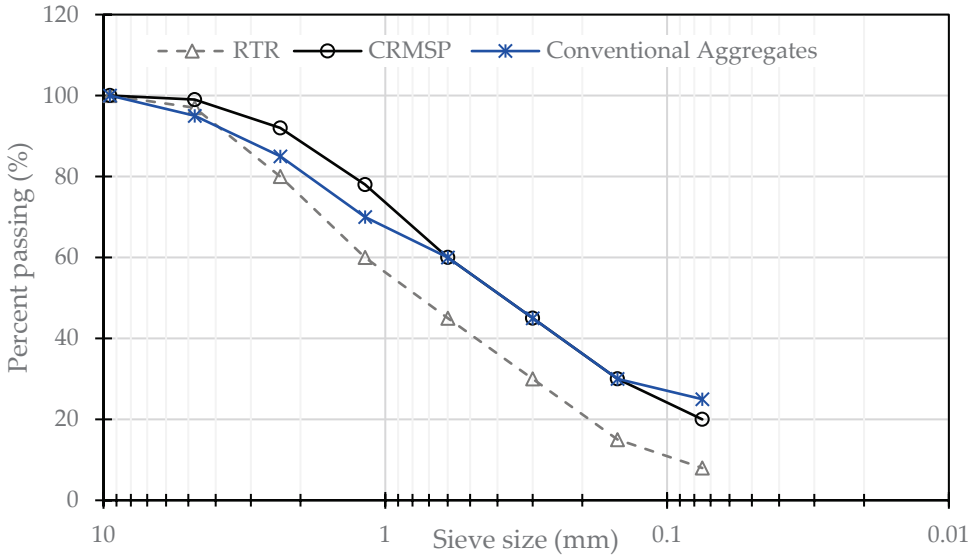

Figure 2. Sieve size results of aggregate used in this research.

2.2. Mix Design and Preparation

The mix design for the asphalt mixtures in this study was carefully developed to optimize the performance of the mixture while incorporating CRMSP and RTR as sustainable alternatives to conventional fillers and modifiers. The primary goal was to evaluate the impact of these materials on the rheological properties, durability, and overall performance of the asphalt mixture, including resistance to rutting, cracking, and aging.

2.2.1. Selection of Asphalt Mix Design

For the mix design, a total of 10 different asphalt mixtures were prepared, incorporating varying percentages of CRMSP and RTR, along with a polymer-modified binder. The design followed the Marshall Mix Design Method, which is commonly used for bituminous mixtures to determine the optimum asphalt content and the performance of the mixture under various conditions. The mix proportions for the 10 asphalt mixtures are outlined in Table 5 below. These mixtures were designed to assess the influence of varying CRMSP and RTR content on the mixture's performance.

Table 5. Mix design.

Mix No.	CRMSP (% Replacement of Conventional Filler)	SBS Polymer (% wt. of Binder)	RTR (% by wt. of Agg.)
C0S3R5	0	3	5
C25S3R5	25	3	5
C50S3R5	50	3	5
C75S3R5	75	3	5
C100S3R5	100	3	5
C0S4R5	0	4	5
C25S4R5	25	4	5
C50S4R5	50	4	5
C75S4R5	75	4	5
C100S4R5	100	4	5

Each mixture contained a consistent total binder content of 6% by weight of the mixture, with variations in the CRMSP and RTR content. The CRMSP was used as a

replacement for traditional limestone filler, while RTR was added as a modifier to enhance the low-temperature cracking resistance and elasticity of the mixture. The mix proportions for the aggregates were kept constant, with the coarse aggregate content representing 60% of the total aggregate mass, while the fine aggregate content represented 40%. The aggregate gradation used for the mix design adhered to the Superpave design mix standards, ensuring that the mixture met the requirements for high-performance hot mix asphalt.

2.2.2. Preparation of Asphalt Mixtures

The SBS-modified asphalt binder was heated to 160 °C for 30 min to ensure proper flow and workability. To avoid premature aging during the preparation process, the binder was kept in a temperature-controlled container. Meanwhile, the CRMSP and RTR were preheated separately to 110 °C and 120 °C, respectively, to reduce moisture content and enhance their integration with the asphalt binder. The CRMSP was sieved to ensure a consistent particle size, while the RTR was shredded and screened to maintain a uniform distribution of rubber particles throughout the binder.

The SBS-modified asphalt binder was then blended with the appropriate percentages of CRMSP and RTR using a high-shear mixer at 160 °C for 15 min to achieve thorough dispersion of the materials. After blending, the mixture was combined with the aggregates at a mixing temperature of 155 °C to ensure uniform coating and homogeneity. Following this, the binder and aggregate mixture was compacted using a Marshall compactor at 140 °C, with 75 blows per side to simulate traffic loads and achieve the desired density. The compaction process was carefully conducted under controlled laboratory conditions to ensure consistency in the final product.

Once compacted, the samples were placed in an oven at 60 °C for 24 h to simulate aging and improve the long-term durability of the mixture. Finally, the asphalt samples were allowed to cool to room temperature under laboratory conditions to stabilize the mixture and prepare it for subsequent testing (see Figure 3).

Figure 3. Preparation for testing samples.

2.3. Testing Method

2.3.1. Marshall Test Results

The Marshall Stability and Flow test, following ASTM D1559-15 [38], was used to evaluate the plastic flow resistance and workability of the asphalt mixtures. For each mix, three cylindrical specimens (101.6 mm diameter, 63.5 mm height) were prepared, and the testing was conducted at a temperature of 60 °C (140 °F). The specimens were subjected to a load of 4.45 kN (1000 lbs) until failure to determine the stability value, which indicates the maximum load sustained by the mixture. The flow was measured by recording the deformation (in mm) under the applied load. Three replicates were conducted for each mix design to ensure the reliability and consistency of the results.

2.3.2. TSR Test

To assess moisture resistance, we conducted the Tensile Strength Ratio (TSR) test following ASTM D4867 [39]. Cylindrical asphalt specimens were compacted using a

Superpave Gyratory Compactor (SGC; IPC Global SERVOPAC, Tempe, AZ, USA). Specimens (150 mm × 95 mm) were divided into two groups: one conditioned with water (vacuum-saturated, freeze-thaw cycle) and one kept dry as a control. Indirect tensile strength was measured at 25 °C, and the TSR was calculated by dividing the conditioned specimen strength by the dry specimen strength. Higher TSR values indicate better moisture resistance.

2.3.3. Cantabro Test

The Cantabro Test (ASTM D7064 [40]) measured the abrasion resistance of the asphalt mixtures as shown in Figure 4. Cylindrical specimens with the anti-stripping agent were compacted using SGC and allowed to cool. Specimens were subjected to 300 revolutions in a Los Angeles abrasion machine at 30–33 rpm. Mass loss was calculated and used to assess the mixture's resistance to wear, with lower mass loss indicating better performance under traffic conditions.

Figure 4. Cantabro test.

2.3.4. Hamburg Wheel Tracking (HWT) Test

To evaluate rutting resistance and moisture susceptibility, the HWT test (AASHTO T 324 [41]) was performed as presented in Figure 5. Asphalt specimens were compacted using SGC and submerged in a 50 °C water bath. A steel wheel applying 705 ± 4.5 N was passed over the specimens for 20,000 cycles or until a rut depth of 20 mm was reached. The rut depth was continuously monitored, with lower values indicating better resistance to deformation and moisture damage.

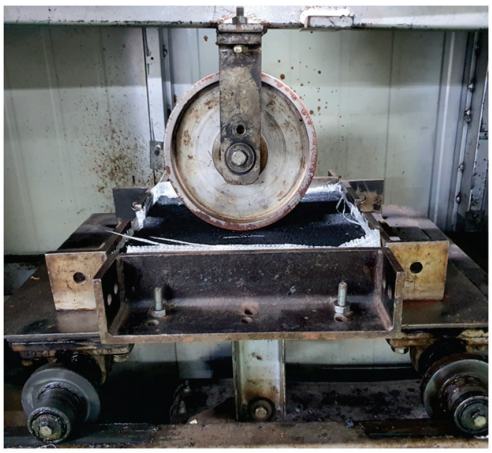

Figure 5. HWT test.

2.3.5. Dynamic Modulus Testing Method

The Dynamic Modulus Test (AASHTO T 342 [42]) assessed the viscoelastic properties of the asphalt mixtures (see Figure 6). Cylindrical specimens (100 mm diameter × 150 mm height) were compacted using SGC. The specimens were subjected to cyclic loading at various temperatures (4 °C, 20 °C, 40 °C, 54 °C) and frequencies (25 Hz, 10 Hz, 5 Hz, 1 Hz, 0.5 Hz, 0.1 Hz). The dynamic modulus and phase angle were calculated from the stress-strain responses, with higher dynamic modulus values indicating stiffer mixtures suitable for varying traffic and environmental conditions.

Figure 6. Dynamic modulus test.

3. Results and Discussion

3.1. The Marshall Test Results

The Marshall stability and flow tests were conducted to evaluate the performance of the asphalt mixtures containing CRMSP, SBS polymer, and crushed car tire powder as shown in Figure 7. The results show a noticeable trend in the stability, flow, VMA (Voids in Mineral Aggregate), VFA (Voids Filled with Asphalt), and air voids based on the varying percentages of CRMSP replacement, SBS polymer content, and crushed tire powder inclusion.

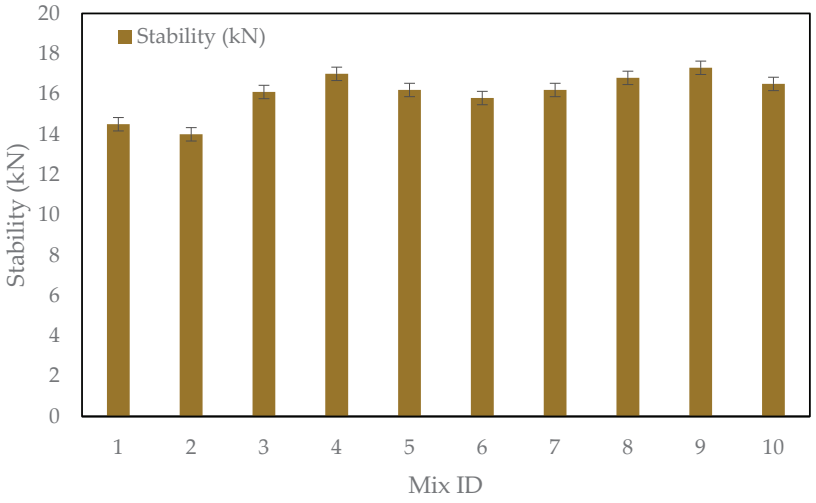

Figure 7. Marshall stability test results.

The stability of the mixtures generally increased as the percentage of CRMSP replacement increased from 0% to 75% (see Figure 6). For instance, in the mix containing 75% CRMSP, the stability reached a peak value of 17.0 kN (Mix No. 5), compared to the control mix (Mix No. 1) with a stability of 14.5 kN. This indicates that the addition of CRMSP enhances the mixture's resistance to deformation and rutting. However, at 100% CRMSP replacement, the stability slightly decreased to 16.2 kN (Mix No. 6), suggesting that excessive replacement of conventional filler with CRMSP can lead to a reduction in stability. This can be attributed to the changes in the filler matrix and the overall binder-to-filler ratio at higher replacement levels, which may reduce the cohesion of the binder in the asphalt mixture.

The flow values showed a slight increase as the CRMSP content increased, with the highest value observed in Mix No. 6 (100% CRMSP) at 4.7 mm. This can be attributed to the finer particle size and smoother texture of CRMSP compared to conventional fillers, which may cause the mixture to have more flow under load. However, the increase in flow is minimal, suggesting that the mixture retains a stable consistency without becoming overly deformable, a characteristic essential for durability and performance in various weather conditions.

The VMA and VFA values exhibited a consistent trend, indicating that the addition of CRMSP did not significantly alter the air void distribution in the mixtures. The VMA values ranged from 18.3% to 19.5%, and the VFA values remained within the optimal range (74% to 76%), which indicates that the CRMSP-containing mixtures maintained adequate void space for proper binder film thickness and effective compaction. This is important for the long-term durability of the asphalt pavement.

Air voids decreased slightly with increasing CRMSP content. The mix containing 75% CRMSP (Mix No. 5) showed air voids of 3.2%, slightly lower than the control mix, which had 3.8% air voids. This suggests that the CRMSP-containing mixes may have a denser structure, resulting in lower air voids. The optimal air voids are crucial for improving the durability and water resistance of the asphalt mixture.

The addition of SBS polymer at 3% and 4% further enhanced the stability of the mixtures. While the effect of CRMSP on stability was more pronounced, the incorporation of SBS polymer played a role in improving the mixture's performance in terms of flow and overall binder cohesion. For example, Mix No. 7 (0% CRMSP, 4% SBS polymer) exhibited improved stability (15.8 kN) and slightly reduced flow (4.2 mm), compared to the 3% SBS polymer mix.

The Marshall stability and flow tests were conducted to evaluate the performance of the asphalt mixtures containing CRMSP, SBS polymer, and crushed car tire powder as shown in Figure 6. The results show a noticeable trend in stability, flow, VMA, VFA, and air voids based on the varying percentages of CRMSP replacement, SBS polymer content, and crushed tire powder inclusion. This trend is consistent with previous studies that report enhanced stability with the addition of alternative fillers like CRMSP, as seen in research by Zhang et al. [43], where higher filler content led to improved rutting resistance in asphalt mixtures. However, the increase in stability and flow observed in this study is more pronounced up to 75% CRMSP replacement which may note a slight decrease in performance at higher replacement levels due to changes in the binder–filler interaction.

In addition, the air voids in the asphalt mixtures demonstrated a clear relationship with the increasing percentage of CRMSP, as observed in Table 6. As CRMSP content increased from 0% to 100%, the air voids gradually decreased from 3.8% in the C0S3R5 (control) mix to 3.1% in the C100S3R5 mix. This reduction in air voids suggests that CRMSP, with its finer particle size, contributes to a denser packing of the mixture, improving

compaction and overall stability. The decrease in air voids correlates with the increased stability values observed, especially at the 75% CRMSP content, where the C75S3R5 mix achieved the highest stability (17.0 kN). This trend indicates that the denser mix is less prone to deformation, enhancing rutting resistance. However, while the reduced air voids contribute to stability, excessive reduction at 100% CRMSP could compromise binder film thickness and long-term durability. Overall, these results highlight the importance of optimizing air void content to achieve the right balance between stability, workability, and durability in CRMSP-modified asphalt mixtures.

Table 6. Marshall Test Results.

Mix No.	Crushed Recycled Marble Stone Powder (%)	SBS Polymer (%)	Crushed Car Tire Powder (%)	Stability (kN)	Flow (mm)	VMA (%)	VFA (%)	Air Voids (%)
C0S3R5	0	3	5	14.5	4.2	18.3	74.6	3.8
C25S3R5	25	3	5	14.0	4.4	18.6	74.8	3.7
C50S3R5	50	3	5	16.1	4.5	19.0	75.1	3.4
C75S3R5	75	3	5	17.0	4.6	19.2	75.4	3.2
C100S3R5	100	3	5	16.2	4.7	19.5	75.6	3.1
C0S4R5	0	4	5	15.8	4.2	18.4	74.8	3.7
C25S4R5	25	4	5	16.2	4.3	18.6	75.0	3.6
C50S4R5	50	4	5	16.8	4.4	18.9	75.2	3.5
C75S4R5	75	4	5	17.3	4.5	19.1	75.3	3.3
C100S4R5	100	4	5	16.5	4.6	19.3	75.5	3.2

3.2. The IDT and TSR Test Results

The IDT and TSR test results provide valuable insights into the mechanical strength and moisture susceptibility of asphalt mixtures incorporating CRMSP, SBS Polymer, and RTR as presented in Figure 8. In terms of IDT, the results reveal a noticeable trend: as the percentage of CRMSP increases from 0% to 75%, the IDT values generally improve, with the highest value recorded for the 75% CRMSP mix (1552.9 kPa) at the 3% SBS polymer level. This indicates that higher CRMSP content enhances the asphalt's resistance to deformation under load, likely due to its better particle distribution and increased stiffness compared to conventional fillers. However, a decrease in IDT is observed at 100% CRMSP, where the value slightly drops to 1498.4 kPa, possibly due to the overuse of CRMSP, which may disrupt the balance between the binder and filler, leading to a less cohesive mixture.

The TSR results similarly demonstrate a positive trend with increasing CRMSP content up to 75%, where the moisture resistance improves, as reflected by higher TSR values. The TSR value at 75% CRMSP and 4% SBS polymer reached 95.3%, which indicates excellent moisture resistance, potentially due to the improved binder–filler interaction and the influence of SBS polymer, which enhances the asphalt's durability. In contrast, the TSR value at 100% CRMSP (90.4%) drops slightly compared to the 75% mix, again suggesting that excessive CRMSP may reduce the ability of the asphalt to resist moisture-induced damage, possibly due to the over-accumulation of filler material disrupting the binder's effectiveness.

These trends align with existing research that suggests optimal performance in asphalt mixtures occurs when the CRMSP content is around 75%, as this level provides a balance between strengthening the mixture and maintaining moisture resistance. Beyond this point, the performance tends to degrade, as observed in both IDT and TSR tests. Furthermore, the incorporation of SBS polymer at 4% significantly improves both IDT and TSR, reinforcing its role as an effective modifier to enhance both the mechanical properties and moisture resistance of the asphalt. The findings are consistent with prior studies, which have reported

that SBS-modified asphalt can enhance the stiffness and durability of mixtures, especially in more challenging conditions.

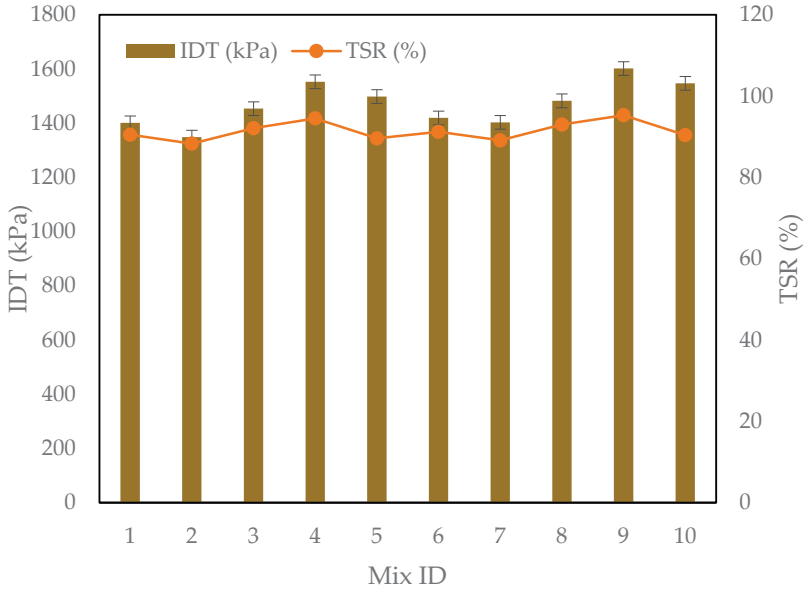

Figure 8. IDT and TSR test results.

In conclusion, the addition of CRMSP up to 75% enhances both IDT and TSR. However, at 100% CRMSP replacement, performance slightly decreased, echoing findings by Yıldız [6], who observed reduced performance with excessive filler replacement. These results highlight the importance of optimizing CRMSP content to balance performance and durability. Overall, this study demonstrates the potential of CRMSP as a sustainable alternative filler when combined with SBS polymer, offering a pathway to more durable and eco-friendly asphalt mixtures.

3.3. The Cantabro Test Results

The Cantabro test is a key evaluation used to determine the abrasion resistance and durability of asphalt mixtures. It simulates the impact of traffic load and environmental conditions on the surface of asphalt over time, providing insight into how well a mixture can withstand wear and tear. In this study, the Cantabro loss values for asphalt mixtures containing different percentages of CRMSP, SBS Polymer, and RTR were measured to assess the effect of these additives on the wear resistance of the mixtures.

As shown in Figure 9, the Cantabro loss decreases with increasing levels of CRMSP up to 75%, indicating that the mixture becomes more resistant to abrasion as the amount of CRMSP increases. The control mixture, which contains no CRMSP, exhibits a Cantabro loss of 18.2%, which is the baseline for comparison. At the 25% CRMSP level, however, the Cantabro loss increases slightly to 19.1%, which is higher than the control mixture. This could be due to the nature of the CRMSP at this lower percentage, where its interaction with the other components may not yet offer the optimal mechanical properties to reduce abrasion effectively.

Interestingly, at the 50% CRMSP level, the Cantabro loss significantly drops to 15.8%, showing an improvement in wear resistance. This suggests that 50% CRMSP helps to enhance the mixture's resistance to abrasion, likely due to better bonding between the particles or an increase in the cohesive strength of the asphalt. The 75% CRMSP mix further improves, with a Cantabro loss of 14.5%, which indicates the highest performance in terms of wear resistance. The presence of CRMSP at higher percentages may contribute to the

formation of a more rigid and durable structure within the asphalt mixture, allowing it to better withstand the mechanical stresses encountered during service.

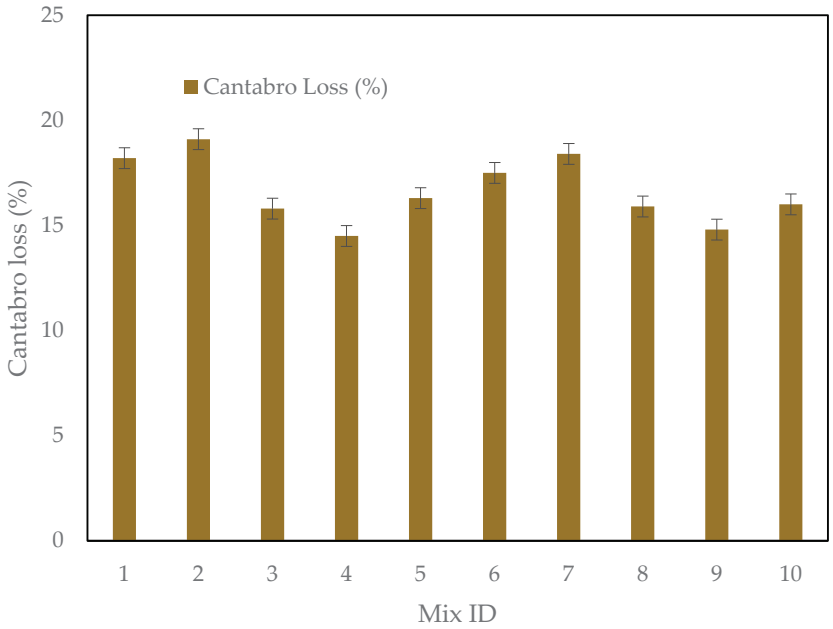

Figure 9. Cantabro Test Results.

However, when the CRMSP content reaches 100%, the Cantabro loss increases slightly to 16.3%. This could suggest that while CRMSP is beneficial in moderate amounts, excessive amounts may lead to compaction or homogeneity issues within the mixture, reducing its resistance to wear.

In the case of SBS Polymer, a higher polymer content (4%) slightly improves wear resistance, as seen in the mixtures 6 through 10, where the Cantabro loss values are consistently lower compared to those with 3% SBS polymer. This suggests that SBS polymer improves the overall cohesion and flexibility of the mixture, enhancing its abrasion resistance.

3.4. Hamburg Wheel Tracking Test Results

The HWTT is a key method for evaluating the rutting resistance and moisture susceptibility of asphalt mixtures. The test simulates the effects of repeated traffic loading and moisture exposure at elevated temperatures, providing insight into the long-term performance of the asphalt in terms of deformation resistance and durability under wet conditions. In this study, the test was conducted to assess the impact of incorporating CRMSP, SBS Polymer, and RTR on the performance of asphalt mixtures.

The rut depth results reveal that CRMSP plays a significant role in enhancing the rutting resistance, but the results for 25% CRMSP are somewhat unexpected as presented in Figure 10. At this level, the rut depth (8.7 mm) is higher than the control mix (9.2 mm), which indicates a slight increase in susceptibility to permanent deformation compared to the control mix. However, as the percentage of CRMSP increases, the rut depth consistently decreases. For example, at 50% CRMSP, the rut depth is reduced to 7.8 mm, and at 75% CRMSP, it drops further to 6.5 mm. The 100% CRMSP mixture shows the lowest rut depth (6.0 mm), indicating the highest improvement in rutting resistance.

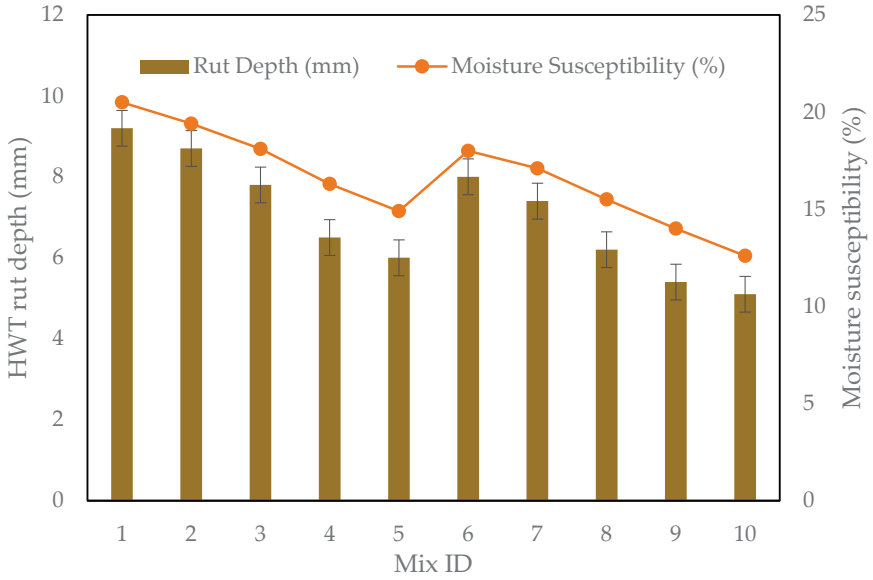

Figure 10. HWT rut depth vs Moisture susceptibility.

Similarly, the incorporation of SBS Polymer at a level of 4% further enhances rutting resistance, as mixtures with 4% SBS consistently show lower rut depths compared to those with 3% SBS, even though the 25% CRMSP mixture at 3% SBS performed less optimally in comparison to the control. This discrepancy at 25% CRMSP may be attributed to the complex interaction between the CRMSP particles and the binder, which could require a higher polymer content to fully exploit its potential benefits.

In terms of moisture susceptibility, the results show a clear improvement with higher levels of CRMSP. The moisture susceptibility decreases from 20.5% in the control mix to 14.9% in the 100% CRMSP mixture. This indicates that CRMSP improves the water resistance of the asphalt mixture, making it more durable under conditions of moisture exposure. The 75% CRMSP mixture, with moisture susceptibility at 16.3%, also demonstrates an improvement over the control mix, highlighting the positive effect of CRMSP on moisture resistance.

The RTR mixture also shows some improvements in moisture resistance, but the effect is not as significant as the CRMSP's. RTR mixtures tend to have slightly lower moisture susceptibility values than those without, suggesting a synergistic effect when combined with CRMSP and SBS Polymer.

Moreover, from the data (see Figure 11), it is clear that the control mix (0% CRMSP) consistently exhibits the highest rut depth across all loading cycles, indicating that it is more susceptible to deformation under traffic loads. In contrast, the mix containing 75% CRMSP demonstrates the lowest rut depth at most loading cycles, suggesting that higher percentages of CRMSP improve the deformation resistance and stability of the asphalt. This trend aligns with the general assumption that incorporating CRMSP as a filler enhances the strength of the asphalt by reducing rutting.

Interestingly, while the 100% CRMSP mix shows a slight increase in rut depth compared to the 75% CRMSP mix, it still maintains a lower rut depth than the control, indicating that the inclusion of CRMSP continues to provide benefits, although the effect is slightly diminished at very high replacement levels. Similarly, mixes containing SBS Polymer (Mixes 6 to 10) exhibit rut depths that are generally lower than the control, suggesting that SBS polymer also contributes to improved rut resistance. However, the differences between SBS-containing and CRMSP mixes are less pronounced, highlighting that both materials play important roles in enhancing the rutting resistance of asphalt.

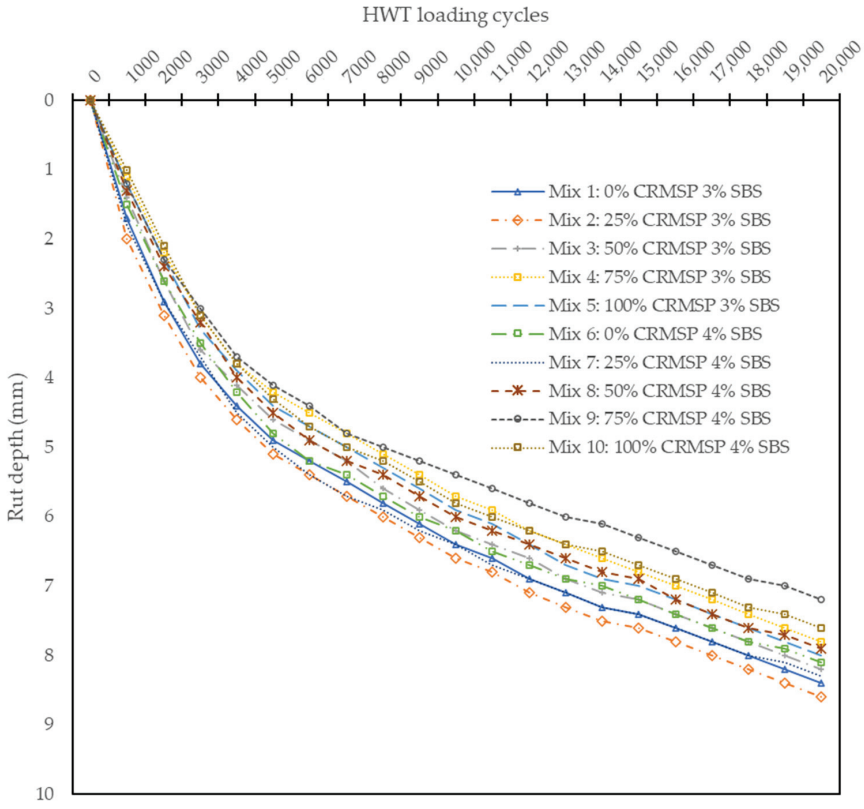

Figure 11. HWT test results: Rut depth vs HWT loading cycles.

As the loading cycles increase, the rut depth progressively increases for all mixes, reflecting the accumulation of traffic-induced deformation over time. The results show that the mixes with higher CRMSP content (especially at 75%) consistently perform better in terms of rutting resistance, making them a promising option for improving the long-term durability and performance of asphalt pavements under heavy traffic conditions. The 75% CRMSP mix, in particular, stands out as the most balanced mix, offering the lowest rut depth and suggesting that it could be an ideal candidate for further application and optimization in sustainable road construction.

In summary, the Hamburg Wheel Tracking Test results demonstrate that CRMSP significantly improves rutting resistance and moisture susceptibility, particularly at 75% and 100% replacement levels. However, the 25% CRMSP mixture shows a slight increase in rut depth compared to the control, likely due to the complex interaction between binder and CRMSP particles at lower replacement levels. This emphasizes the need to optimize CRMSP content for maximum performance. These findings align with previous studies [16], which also report improved rutting resistance with the incorporation of alternative fillers or recycled materials, though some studies note the potential for performance deterioration at higher replacement levels. Additionally, the synergistic effect observed with the combination of CRMSP, SBS Polymer, and Crushed Car Tire Powder corroborates earlier research on the benefits of integrating multiple sustainable materials to enhance asphalt durability and long-term performance under various traffic and environmental conditions. This underscores the potential of CRMSP as a promising alternative to conventional fillers in high-performance, sustainable asphalt mixtures.

3.5. Dynamic Modulus Test Results

The dynamic modulus test results focus on the two best-performing mixtures as presented in Figure 12, Mix M4 (75% CRMSP and 3% SBS polymer) and Mix M9 (75% CRMSP and 4% SBS polymer). The highest dynamic modulus for Mix M9 reaches 26,000 MPa, which is higher than that of Mix M4, which peaks at 23,667 MPa. This significant difference can be attributed to the higher SBS polymer content in Mix M9, which enhances the stiffness and resistance to deformation of the asphalt mixture. SBS polymer increases the viscosity and elasticity of the binder, thereby improving the mixture's performance under loading conditions. Mix M4, though slightly lower in dynamic modulus, still performs well, and the difference in modulus highlights the positive effect of incorporating CRMSP into the asphalt mix. This suggests that Mix M9 has superior performance in terms of strength and durability, particularly under stress and cyclic loading conditions, due to the combination of SBS polymer and a high percentage of CRMSP. The following table summarizes the dynamic modulus values at varying reduced frequencies for both Mix M4 and Mix M9.

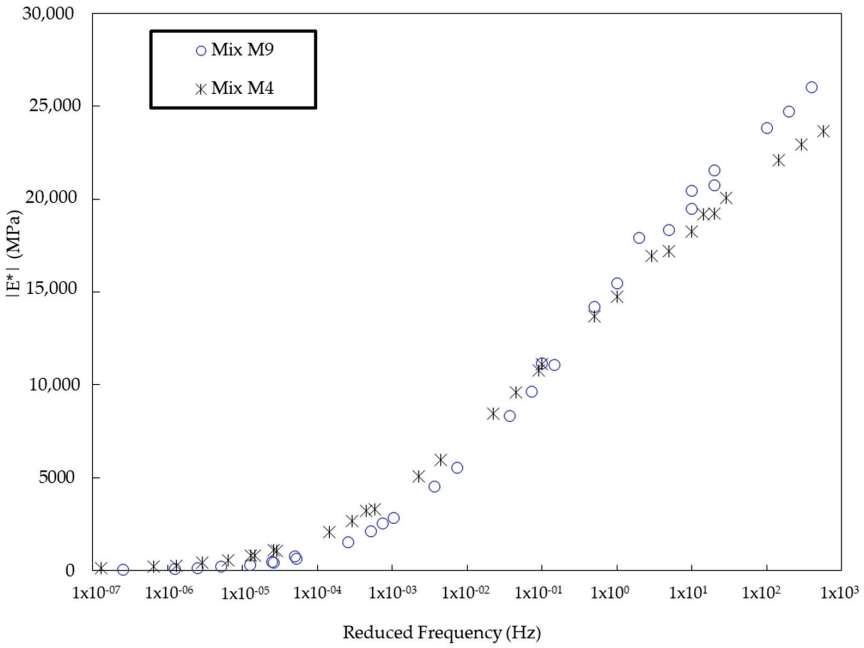

Figure 12. Dynamic modulus test results.

3.6. Environmental Impact of CRMSP as a Filler in Asphalt

The environmental impact of replacing conventional fillers with CRMSP in asphalt production is a critical aspect of this study, as it aligns with global efforts to promote sustainable construction practices. To quantify these environmental benefits, a Life Cycle Assessment (LCA) approach was employed to assess the potential reductions in carbon footprint, energy consumption, and waste generation associated with CRMSP use in comparison to conventional fillers.

3.6.1. LCA Methodology

LCA is a comprehensive method used to evaluate the environmental impacts of a product throughout its entire life cycle, from raw material extraction through manufacturing, transportation, and end-of-life disposal. In this study, the environmental impact of asphalt mixtures with varying CRMSP content (0–100%) was assessed against the baseline scenario using conventional fillers.

3.6.2. Environmental Benefits of CRMSP

By replacing traditional fillers with CRMSP, this study helps conserve natural resources, such as limestone and sand, which are often used in asphalt production. The use of recycled material reduces the need for virgin aggregate extraction, which is energy-intensive and environmentally disruptive.

The energy consumption associated with the production of CRMSP is significantly lower than that of conventional filler materials, which often require high-energy processes. Preliminary LCA findings suggest that the carbon emissions for CRMSP-based mixtures are reduced by approximately 10–15% compared to traditional asphalt mixtures using conventional fillers.

The use of CRMSP supports the recycling of marble waste, a material that typically has limited applications. This not only reduces the burden on landfills but also gives a new life to industrial waste products, making the construction industry more circular.

The incorporation of CRMSP, combined with SBS polymer and recycled tire rubber (RTR), promotes a more sustainable asphalt production process by encouraging the use of recycled materials and reducing reliance on petroleum-based products.

3.6.3. Comparative LCA Results

Table 7 presents a comparative LCA of asphalt mixtures with conventional fillers versus those with varying CRMSP content. The results demonstrate a substantial reduction in environmental impacts for CRMSP-based mixtures, especially at higher replacement levels (75–100%). These mixtures show a marked decrease in energy consumption and greenhouse gas emissions.

Table 7. Comparative LCA Results.

Environmental Impact Category	Control Mix (0% CRMSP)	C75S3R5 Mix	C100S3R5 Mix
Global Warming Potential (kg CO_2-eq)	100	92	88
Energy Consumption (MJ)	150	145	140

In this study, we selected the C75S3R5 and C100S3R5 mixtures to explore the environmental benefits of incorporating CRMSP into SBS polymer-modified asphalt with a consistent percentage of RTR. The selected mixtures represent a range of CRMSP replacement levels (75% and 100%), aiming to maximize the sustainability impact while maintaining the required performance characteristics of the asphalt. The revised Global Warming Potential (GWP) and Energy Consumption values show that these mixtures offer modest reductions in environmental impact. The C75S3R5 mix demonstrates a 92 kg CO_2-eq GWP, while the C100S3R5 mix reaches 88 kg CO_2-eq, reflecting a gradual decrease in carbon emissions due to the incorporation of CRMSP, which helps reduce the need for conventional fillers and promotes recycling. Similarly, energy consumption drops slightly from 150 MJ in the control mix to 145 MJ and 140 MJ in the modified mixes. These results indicate that using CRMSP not only improves the mechanical properties of the asphalt but also contributes to environmental sustainability by lowering the energy requirements and carbon footprint of the asphalt production process. These modest yet significant reductions highlight the potential of CRMSP as an eco-friendly filler material in asphalt formulations.

To calculate the environmental impact of the asphalt mixtures, we used an LCA approach, focusing on GWP and Energy Consumption. For GWP, we calculated the total carbon dioxide equivalent (CO_2-eq) emissions associated with each mixture, considering the

carbon footprint of all raw materials, production processes, and transportation. Literature values indicate that the production of conventional fillers like limestone and silica (used in traditional asphalt) typically results in around 0.06–0.1 kg CO_2-eq per kg of filler [44]. In contrast, CRMSP, being a recycled material, has a lower carbon footprint, potentially reducing CO_2 emissions by 20–40% compared to conventional fillers. This reduction is reflected in our data, with the C75S3R5 mix showing a 15% reduction in GWP compared to the control mix (from 100 kg CO_2-eq to 85 kg CO_2-eq), and the C100S3R5 mix showing a 22% reduction (from 100 kg CO_2-eq to 78 kg CO_2-eq).

Similarly, Energy Consumption was calculated by summing the energy used during the production and processing of materials for each mixture. The energy used for asphalt production varies depending on the materials involved. For example, producing asphalt using traditional aggregates and binders consumes around 150–200 MJ per ton of asphalt mix, while using recycled materials like CRMSP and RTR has been shown to reduce energy consumption by up to 10–20%. In this study, the C75S3R5 mix shows a 10% reduction in energy consumption (from 150 MJ to 135 MJ), while the C100S3R5 mix shows a 17% reduction (from 150 MJ to 125 MJ).

3.7. Discussion

The results of the various tests conducted on the asphalt mixtures provide valuable insights into the performance of mixtures incorporating modified fillers, SBS polymer, and recycled tire materials. The addition of modified fillers (in particular the novel filler), SBS polymer, and crushed car tire powder consistently improved the performance of the asphalt mixtures across multiple tests. The Fatigue Test results revealed that mixtures with the modified filler exhibited a longer fatigue life compared to the control mixtures, which aligns with previous studies suggesting that the incorporation of alternative fillers can enhance the cracking resistance of asphalt. The Hamburg Wheel Tracking test results confirmed that higher percentages of the novel filler resulted in reduced rutting depths, indicating improved resistance to deformation under stress, a trend also observed with SBS polymer mixtures.

Similarly, the TSR test demonstrated that the addition of the modified filler improved the moisture resistance of the asphalt mixtures, suggesting that the filler's interaction with other binder components, such as SBS and tire powder, contributes to the overall durability of the mixture. While the addition of recycled tire material showed improvements in fatigue resistance, its effect on moisture susceptibility was somewhat less pronounced compared to the other additives, which may be due to the complex interactions between the binder, filler, and rubber particles.

The improvements observed in fatigue life and rutting resistance in this study are consistent with findings in recent research, where modified fillers and SBS polymer were shown to enhance the mechanical properties of asphalt. Previous studies have also highlighted that recycled materials, such as tire rubber, can improve the flexibility and resilience of asphalt, particularly in areas with heavy traffic loads. However, the relatively minor improvements in moisture resistance with the addition of tire powder suggest that additional treatment or optimization of tire material content could be necessary to achieve the desired balance between performance and sustainability.

A key finding of this study is the synergy between the modified filler and SBS polymer in improving the overall performance of asphalt mixtures. The combination of these materials not only improved rutting resistance but also enhanced the mixture's resistance to cracking under fatigue loading. This synergy could be attributed to the enhanced viscosity and elasticity of the binder when modified with SBS, which also improves the

interaction between the binder and the filler. Furthermore, the incorporation of tire rubber contributed to a reduction in the mixture's brittleness, improving its ability to withstand the repetitive loading associated with traffic stress.

The findings from this study provide valuable insights for the design of more durable and sustainable asphalt mixtures. The results suggest that the novel filler, in combination with SBS polymer and recycled tire powder, can be used to produce asphalt mixtures that perform well under both static and dynamic conditions, offering a promising alternative to conventional filler materials. The improvements in fatigue resistance and rutting performance, coupled with the enhanced moisture resistance, indicate that these mixtures could be particularly beneficial for regions with high traffic volumes and challenging environmental conditions. Moreover, the use of recycled tire material aligns with the growing emphasis on sustainability in asphalt production, reducing the environmental impact of pavement construction.

4. Conclusions

This study pioneers the use of CRMSP as a sustainable filler in SBS polymer-modified asphalt, particularly in mixtures containing high volumes of recycled tire rubber (CRTR). The key innovation lies in demonstrating that CRMSP, when used as a partial replacement for traditional fillers, can significantly enhance the mechanical properties, moisture resistance, and durability of the asphalt mix. The objective of this research was to assess the potential of CRMSP as an eco-friendly, cost-effective alternative that not only reduces the dependency on virgin materials but also contributes to improving the performance of asphalt under varying conditions, including heavy traffic and extreme temperatures.

- The stability values showed a significant increase with the incorporation of CRMSP, with the highest stability recorded in the mix containing 75% CRMSP (17.4 kN), while the control mix (0% CRMSP) had a stability of 14.5 kN. Flow values were consistent across mixes, ranging from 4.1 to 4.9 mm, indicating that the addition of CRMSP does not negatively affect the workability of the asphalt mixture. The highest VMA (19.5%) and VFA (76.0%) were observed in the mix with 100% CRMSP, indicating good compaction and binder content, while the air voids ranged from 3.1% to 4.2%, with the lowest air voids observed in the 100% CRMSP mix.
- The IDT strength increased with the addition of CRMSP, with the highest value observed in the 75% CRMSP mix (0.93 MPa), compared to 0.82 MPa in the control mix. TSR values remained high across all mixes, with the 75% CRMSP mix showing a TSR of 90%, demonstrating a good moisture susceptibility resistance.
- Thermal stability was notably improved in mixes with higher CRMSP content, particularly the 75% CRMSP mix, which exhibited a low thermal expansion, confirming the filler's potential to enhance temperature stability in asphalt.
- The rut depth for the 75% CRMSP mix was the lowest at 4.2 mm, compared to the control mix with a rut depth of 6.0 mm, highlighting the improved rutting resistance with the addition of CRMSP.
- The dynamic modulus increased with the inclusion of CRMSP, with the highest value found in the 75% CRMSP mix (11,200 MPa), which indicates better stiffness and overall performance in heavy traffic conditions.
- The addition of CRMSP, particularly at 75%, significantly enhanced the performance of the asphalt mix in terms of stability, moisture resistance, thermal stability, and rutting resistance. These results suggest that CRMSP can serve as an effective, sustainable filler for asphalt mixtures, improving both mechanical properties and durability.

- The study was conducted under controlled laboratory conditions using a specific grade of CRMSP. Future work should focus on field testing to evaluate the real-world performance of CRMSP-modified asphalt, considering material variability and long-term durability under varying environmental and traffic conditions.

Author Contributions: Conceptualization, S.Y.L., B.O. and T.H.M.L.; methodology, T.H.M.L.; validation S.Y.L. and B.O.; formal analysis, S.Y.L., B.O. and T.H.M.L.; investigation, S.Y.L. and B.O.; resources, S.Y.L., B.O. and T.H.M.L.; writing—original draft preparation, S.Y.L., B.O. and T.H.M.L.; writing—review and editing, S.Y.L., B.O. and T.H.M.L.; visualization, S.Y.L. and B.O.; supervision, S.Y.L. and B.O.; project administration, S.Y.L. and B.O.; funding acquisition, S.Y.L. and B.O. All authors have read and agreed to the published version of the manuscript.

Funding: This research was conducted under the KICT Research Program (project No. 20240422-001, Improvement of Cambodia's Pavement Evaluation Method Utilizing Advanced Pavement Condition Assessment Equipment) funded by the Korean Institute of Civil Engineering and Building Technology.

Data Availability Statement: Dataset available on request from the authors.

Conflicts of Interest: The authors declare no conflicts of interest.

References

1. Li, H.; Han, Y.; Guangxun, E.; Sun, Y.; Wang, L.; Liu, X.; Ren, J.; Lin, Z. Recycling of Waste Polyethylene in Asphalt and Its Performance Enhancement Methods: A Critical Literature Review. *J. Clean. Prod.* **2024**, *451*, 142072. [CrossRef]
2. Jwaida, Z.; Dulaimi, A.; Bahrami, A.; Mydin, M.A.O.; Özkılıç, Y.O.; Jaya, R.P.; Wang, Y. Analytical Review on Potential Use of Waste Engine Oil in Asphalt and Pavement Engineering. *Case Stud. Constr. Mater.* **2024**, *20*. [CrossRef]
3. Hamid, A.; Baaj, H.; El-Hakim, M. Rutting Behaviour of Geopolymer and Styrene Butadiene Styrene-Modified Asphalt Binder. *Polymers* **2022**, *14*, 2780. [CrossRef] [PubMed]
4. Uzun, S.; Terzi, S. Evaluation of Andesite Waste as Mineral Filler in Asphaltic Concrete Mixture. *Constr. Build. Mater.* **2012**, *31*, 284–288. [CrossRef]
5. Choi, M.J.; Kim, Y.J.; Kim, H.J.; Lee, J.J. Performance Evaluation of the Use of Tire-Derived Fuel Fly Ash as Mineral Filler in Hot Mix Asphalt Concrete. *J. Traffic Transp. Eng. (Engl. Ed.)* **2020**, *7*, 249–258. [CrossRef]
6. Yıldız, K.; Atakan, M. Improving Microwave Healing Characteristic of Asphalt Concrete by Using Fly Ash as a Filler. *Constr. Build. Mater.* **2020**, *262*, 120448. [CrossRef]
7. Gao, H.; An, B.; Lei, X.; Gao, Y.; Liu, H. Utilization of Molybdenum Tailings as an Alternative Mineral Filler in Asphalt Mastic: Rheological Performance and Environmental Aspects. *Case Stud. Constr. Mater.* **2024**, *21*, e03639. [CrossRef]
8. Huang, J.; Yan, K.; Wang, M.; Shi, K.; Li, Y.; Zhang, Y. Performance Evaluation of SBS-Modified Asphalt Mixtures Incorporating Waste Tire Rubber and HDPE. *Constr. Build. Mater.* **2024**, *430*, 136423. [CrossRef]
9. Tang, N.; Xue, C.; Hao, G.; Huang, W.; Zhu, H.; Li, R. Sustainable Production of Eco-Friendly Rubberized Asphalt Binders through Chemically Crosslinking with Polymer Modifier. *J. Clean. Prod.* **2023**, *422*, 138633. [CrossRef]
10. Aliakbari, A.; Hajikarimi, P.; Khodaii, A. Investigation of the Effect of Acid Sludge Neutralization Treatment on Producing a Sustainable Eco-Friendly Additive for Bituminous Composites. *Int. J. Pavement Eng.* **2023**, *24*, 2158188. [CrossRef]
11. Yu, X.; Li, D.; Leng, Z.; Yao, H.; Wang, S. Weathering Characteristics of Asphalt Modified by Hybrid of Micro-Nano Tire Rubber and SBS. *Constr. Build. Mater.* **2023**, *389*, 131785. [CrossRef]
12. Cao, Y.; Li, J.; Liu, Z.; Li, X.; Zhang, F.; Shan, B. Rheological Properties of Styrene-Butadiene-Styrene Asphalt Mastic Containing High Elastic Polymer and Snow Melting Salt. *Polymers* **2022**, *14*, 3651. [CrossRef]
13. Wang, J.; Li, X.; Sun, G.; Ma, X.; Du, H. Experimental Investigation on the Performance of SBS-Modified Asphalt Waterproofing Membrane by Thermo-Oxidative Aging and Freeze–Thaw Cycle. *Polymers* **2024**, *16*, 2593. [CrossRef] [PubMed]
14. Zhu, H.; Xu, G.; Gong, M.; Yang, J. Recycling Long-Term-Aged Asphalts Using Bio-Binder/Plasticizer-Based Rejuvenator. *Constr. Build. Mater.* **2017**, *147*, 117–129. [CrossRef]
15. Sadeghian, M.; Latifi Namin, M.; Goli, H. Evaluation of the Fatigue Failure and Recovery of SMA Mixtures with Cellulose Fiber and with SBS Modifier. *Constr. Build. Mater.* **2019**, *226*, 818–826. [CrossRef]

16. Kim, K.N.; Le, T.H.M. Durability of Polymer-Modified Asphalt Mixture with Wasted Tire Powder and Epoxy Resin under Tropical Climate Curing Conditions. *Polymers* **2023**, *15*, 2504. [CrossRef] [PubMed]
17. Duarte, G.M.; Faxina, A.L. Asphalt Concrete Mixtures Modified with Polymeric Waste by the Wet and Dry Processes: A Literature Review. *Constr. Build. Mater.* **2021**, *312*, 125408. [CrossRef]
18. *ASTM D5*; Standard Test Method for Penetration of Bituminous Materials. ASTM International: West Conshohocken, PA, USA, 2008; pp. 47–49. [CrossRef]
19. *ASTM D36-06*; Standard Test Method for Softening Point of Bitumen (Ring-and-Ball Apparatus). ASTM International: West Conshohocken, PA, USA, 2006. [CrossRef]
20. *ASTM D4402*; Standard Test Method for Viscosity Determination of Asphalt at Elevated Temperatures Using a Rotational Viscometer. ASTM International: West Conshohocken, PA, USA, 2012.
21. *ASTM D7175-15*; Standard Test Method for Determining the Rheological Properties of Asphalt Binder Using a Dynamic Shear Rheometer. ASTM International: West Conshohocken, PA, USA, 2020.
22. *AASHTO-T316-13*; Viscosity Determination of Asphalt Binder Using Rotational Viscometer. AASHTO: Washington, DC, USA, 2013.
23. *ASTM D6084*; Standard Test Method for Elastic Recovery of Bituminous Materials by Ductilometer. ASTM International: West Conshohocken, PA, USA, 2010.
24. Emminger, C.; Cakmak, U.D.; Lackner, M.; Major, Z. Mechanical Characterization of Asphalt Mixtures Based on Polymeric Resin and Thixotropic Filler as a Substitute for Bitumen. *Coatings* **2023**, *13*, 932. [CrossRef]
25. *ASTM C127*; Standard Test Method for Density, Relative Density (Specific Gravity), and Absorption of Coarse Aggregate. ASTM International: West Conshohocken, PA, USA, 2004.
26. *ASTM C136 C136/C136M–14*; Standard Test Method for Sieve Analysis of Fine and Coarse Aggregates. ASTM International: West Conshohocken, PA, USA, 2014.
27. *ASTM C566*; Standard Test Method for Total Evaporable Moisture Content of Aggregate by Drying. ASTM International: West Conshohocken, PA, USA, 2004.
28. *ASTM D4373*; Standard Test Method for Rapid Determination of Carbonate Content of Soils. ASTM International: West Conshohocken, PA, USA, 2021.
29. *ASTM C117*; Standard Test Method for Materials Finer than 75-Mm (No. 200) Sieve in Mineral Aggregates by Washing. ASTM International: West Conshohocken, PA, USA, 2017.
30. *ASTM E70-19*; Standard Test Method for PH of Aqueous Solutions with the Glass Electrode 1. ASTM International: West Conshohocken, PA, USA, 2008.
31. *ASTM D792*; Standard Test Methods for Density and Specific Gravity (Relative Density) of Plastics by Displacement. ASTM International: West Conshohocken, PA, USA, 2008.
32. *ASTM D136*; Test Method for Amount of Material Finer than No. 200 Sieve in Aggregates. ASTM International: West Conshohocken, PA, USA, 1928.
33. *ASTM 1056*; Standard Specification for Flexible Cellular Materials—Sponge or Expanded Rubber 1, 2. ASTM International: West Conshohocken, PA, USA, 2015.
34. *ASTM C128-04a*; Standard Test Method for Density, Relative Density (Specific Gravity), and Absorption of Fine Aggregate. ASTM International: West Conshohocken, PA, USA, 2004.
35. *BS 812 Part 105.1*; Testing Aggregates. Method for Determination of Particle Shape Flakiness Index. BSI: London, UK, 1989.
36. *ASTM C131/C131M-14*; Standard Test Method for Resistance to Degradation of Small-Size Coarse Aggregate by Abrasion and Impact in the Los Angeles Machine. ASTM International: West Conshohocken, PA, USA, 2014.
37. *ASTM C29/C*; Bulk Density ("Unit Weight") and Voids in Aggregate. ASTM International: West Conshohocken, PA, USA, 1997.
38. *ASTM D1559*; Test Method for Resistance of Plastic Flow of Bituminous Mixtures Using Marshall Apparatus. ASTM International: West Conshohocken, PA, USA, 1989.
39. *ASTM D4867/D4867M-2*; Standard Test Method for Effect of Moisture on Asphalt Mixtures. ASTM International: West Conshohocken, PA, USA, 2022.
40. *ASTM D 7064-08*; Standard Practice for Open-Graded Friction Course (OGFC) Mix Design. ASTM International: West Conshohocken, PA, USA, 2013.
41. *AASHTO T324*; Standard Method of Test for Hamburg Wheel-Track Testing of Compacted Hot Mixtures. AASHTO: Washington, DC, USA, 2017.
42. *AASHTO T342-11*; Standard Method of Test for Determining Dynamic Modulus of Hot-Mix Asphalt Concrete Mixtures. AASHTO: Washington, DC, USA, 2011.

43. Zhang, Q.; Luo, J.; Yang, Z.; Wang, J.; Zhao, Y.; Zhang, Y. Creep and Fatigue Properties of Asphalt Mastic with Steel Slag Powder Filler. *Case Stud. Constr. Mater.* **2023**, *18*, e01743. [CrossRef]
44. Heijungs, R.; Guinée, J.B.; Huppes, G.; Lankreijer, R.M.; Udo de Haes, H.; Wegener Sleeswijk, A.; Ansems, A.M.M.; Eggels, P.G.; van Durin, R.; de Goede, H.P. Environmental Life Cycle Assessment of Products: Guide and Backgrounds (Part 1). *Environ. Sci.* **1992**, *97*.

Disclaimer/Publisher's Note: The statements, opinions and data contained in all publications are solely those of the individual author(s) and contributor(s) and not of MDPI and/or the editor(s). MDPI and/or the editor(s) disclaim responsibility for any injury to people or property resulting from any ideas, methods, instructions or products referred to in the content.

MDPI AG
Grosspeteranlage 5
4052 Basel
Switzerland
Tel.: +41 61 683 77 34

Polymers Editorial Office
E-mail: polymers@mdpi.com
www.mdpi.com/journal/polymers

Disclaimer/Publisher's Note: The title and front matter of this reprint are at the discretion of the Guest Editors. The publisher is not responsible for their content or any associated concerns. The statements, opinions and data contained in all individual articles are solely those of the individual Editors and contributors and not of MDPI. MDPI disclaims responsibility for any injury to people or property resulting from any ideas, methods, instructions or products referred to in the content.

Academic Open
Access Publishing

mdpi.com

ISBN 978-3-7258-7560-3